Springer Tracts in Modern Physics 246

Hartmut Zabel
Michael Farle *Editors*

Magnetic Nanostructures

Spin Dynamics and Spin Transport

Springer

Springer Tracts in Modern Physics

Volume 246

For further volumes:
http://www.springer.com/series/426

Springer Tracts in Modern Physics

Springer Tracts in Modern Physics provides comprehensive and critical reviews of topics of current interest in physics. The following fields are emphasized: elementary particle physics, solid-state physics, complex systems, and fundamental astrophysics.

Suitable reviews of other fields can also be accepted. The editors encourage prospective authors to correspond with them in advance of submitting an article. For reviews of topics belonging to the above mentioned fields, they should address the responsible editor, otherwise the managing editor.

See also springer.com

Hartmut Zabel · Michael Farle
Editors

Magnetic Nanostructures

Spin Dynamics and Spin Transport

Springer

Editors
Hartmut Zabel
Fakultät für Physik und Astronomie
Ruhr-Universität Bochum
Bochum
Germany

Michael Farle
Fakultät für Physik
Universität Duisburg-Essen
Duisburg
Germany

ISSN 0081-3869 ISSN 1615-0430 (electronic)
ISBN 978-3-642-32041-5 ISBN 978-3-642-32042-2 (eBook)
DOI 10.1007/978-3-642-32042-2
Springer Heidelberg New York Dordrecht London

Library of Congress Control Number: 2012947388

Printed on acid-free paper

Springer is part of Springer Science+Business Media (www.springer.com)

Preface

This book on Magnetic Nanostructures in the Springer Series on Modern Physics contains seven chapters, highlighting several aspects of this fascinating modern field of condensed matter physics ranging from spin currents and spin torques in magnetic nanostructures to the manipulation of single spins in quantum dots. It complements the Springer book on Magnetic Heterostructures: Advances and Perspectives in Spinstructures and Spintransport published in 2008 [1]. These two books cover much of the scientific progress made possible through the collaborative effort of teams of experimental and theoretical physicists working together in a collaborative research center (SFB 491) for more than 10 years to provide a better understanding of static and dynamic magnetism in novel nanostructures.

The term "nanostructure" is not well defined. Thin films of only a few nanometers thickness are nanostructured in one direction normal to the film. However, by the term nanostructure we usually understand an object which has a size on the nanoscale in at least two directions. Artificial islands, wires, dots, rings, pillars, etc., are nanostructures when their extension is confined to the nanoscale in more than one direction. Nanostructures can be fabricated artificially or may be arranged from nanoparticles via self-assembly. The fabrication of nanostructures from different materials, metals, oxides, and semiconductors is essential for the exploration, and further development of their fascinating properties.

In the late 1990s, the interest in magnetic properties of nanostructured materials has increased dramatically. This interest was fueled for two reasons: technical and scientific. From a technical point-of-view the down-scaling of physical sizes of magnetic data bits and magnetic sensors required investigations of magnetic properties on the submicron scale. From a scientific point-of-view nanostructures—by the choice of their shape or material—offer the possibility to stabilize single magnetic domains or to tailor specific domain structures with well-defined domain walls. An early realization of magnetic nanostructures dates back to Meiklejohn and Bean, who have created magnetic nanoparticles by a bottom-up approach of naturally occurring Co/CoO [2]. The more recent interest was ignited by a publication of Cowburn, showing with magneto-optical hysteresis measurements the vortex state of domains in circular islands [3]. Shortly after, Shinjo and coworkers imaged the

vortex core in circular islands with MFM and demonstrated its stability in external fields at different angles of inclination [4]. Rüdiger and coworkers studied the development of magnetic domains in nanostructures of different shape and aspect ratio [5], and Ono demonstrated how domain walls propagate in narrow wires with a well-defined speed [6]. Katine et al. and Grollier et al. showed that spin currents can produce a torque that switches the magnetization direction in GMR devices, allowing a control via an electric field instead of a magnetic field [7, 8]. All these early experiments inspired many more experiments during the past 10–15 years. The latest twist being the arrangement of magnetic islands with single domain dipole character into two-dimensional arrays with intrinsic geometric frustration for the study of artificial spin ice [9]. In this book, only a few but important aspects of magnetic nanostructures are covered by reviews of developments which took place over the last 15 years or so.

In Chap. 1 by J. Lindner et al. and also partially in Chap. 2 spin torque experiments are discussed. The concept of spin torque was introduced independently by Slonczewski [10] and Berger [11] in the mid-1990s. They pointed out that the spin-polarized current carries an angular momentum that can switch the magnetization of a layer when the torque is absorbed by its magnetization. This leads to a new type of switching mechanism. Instead of switching via an external magnetic field in conventional GMR and TMR devices, in spin torque devices the switching is provided by a change of the direction of the spin current, i.e., by the direction of an electric field. This principle has been demonstrated for the first time by Katine et al. [7] and has inspired many new experiments and device concepts.

In Chap. 2 by M. Farle et al. the spin dynamics in magnetic nanostructures is considered. Experimental detection schemes to analyze the relaxation of the magnetization after microwave excitation are discussed. Modern techniques operating in the time domain, which are able to "visualize" the precession of the magnetization vector are discussed in connection with classical resonance techniques, detecting resonance frequencies of the precessing magnetization as well as more modern magneto-resistive schemes that are based on spin-polarized current driven ferromagnetic resonance. New schemes on how to distinguish different relaxation channels (intrinsic versus extrinsic) are discussed. Examples of how to control such phenomena are presented. For example, by gently structuring the magnetization extrinsic two-magnon scattering can be controlled, offering a bridge to the new field of lithographically patterned magnonic crystals [12] and magnonic electronics [13], possibly called "soft magnonics".

The Chap. 3 by K. B. Efetov et al. is devoted to proximity effects between superconductors and ferromagnets in nanostructures. These two ground states of the electronic system in solids are antagonistic, since ferromagnetism requires a parallel alignment of the spins, whereas conventional singlet superconductivity requires an antiparallel alignment. The proximity effect in superconductor/ferromagnet nanostructures has raised considerable interest during the last 15 years and has been reviewed at several places [14, 15]. The present review is devoted to recent experimental and theoretical progress in the physics of the proximity effect with special emphasis on the occurrence of odd triplet superconductivity, which

may occur at superconducting/ferromagnetic interfaces in case where the magnetization of the ferromagnetic layer is inhomogeneous. Recent experiments with Josephson tunneling junctions including a ferromagnetic barrier provided evidence for the existence of a long range odd triplet component of the supercurrent [16, 17]. Further topics include experimental progress concerning the realization of superconducting spin valves and experimental evidence for the existence of an inverse proximity effect [18].

Chapter 4 by H. Herper et al. on Heusler alloys includes discussions on their electronic properties and magnetic moment formation, and recognizes the importance of this class of materials for magnetic nanostructures and spintronic devices [19]. The extensive interest in Heusler alloys is due to their unique magnetic properties, such as a predicted 100 % spin polarization at the Fermi level and very high Curie temperatures, which make them suitable for various applications. The present review focusses on nanostructured Heusler alloys as needed for magneto-electronic applications, with special emphasis on the effect of composition, disorder, and structural deformation on the magnetic properties. As the quality of spintronic devices crucially depends on the interfacial properties of Heusler alloys and specific substrates, these aspects are considered in detail.

Chapter 5 on magneto-electric materials by W. Kleemann and Ch. Binek reviews a new development in magnetic nanostructures and spintronics, i.e., the control of the ferromagnetic hysteresis via the polarization of a ferroelectric material in spin valve devices. The classic magneto-electric effect was discovered by a combination of an antiferromagnet Cr_2O_3 with a switchable ferromagnetic surface magnetization in contact with a ferromagnetic layer in a spin valve device [20]. Similarly, in multiferroic materials like $BiFeO_3$ and $BiMnO_3$ similar exchange bias was controlled by the application of electric fields [21]. This review provides an overview of these new and exciting developments and shows perspectives for novel multiferroic ordering types including potential applications.

Chapter 6 by O. Hellwig et al. describes in contrast to Chaps. 1 and 2 the magneto-static properties of different nanomagnetic systems, which are commonly used in spin valve arrays, such as in bit patterns of magnetic storage media or in random access memory devices. In either case, proximity effects via magneto-static interaction are an issue. Vice versa, the magnetostatic interaction can be beneficial in magnetic dipole arrays, which form artificial spin ice structures with various degrees of frustration [9, 22]. This chapter also contains a section which treats self-organized magnetic nanocluster, which are considered as a potential route to new applications in memory devices, immunology, and cancer treatment. At the same time, magnetic nanoclusters provide new aspects for the investigation of magnetic ordering and phase transitions.

Chapter 7 which is the final chapter by A. Ludwig et al. is devoted to the discussion of spins in quantum dots. Several approaches are discussed for spin injection into quantum dots and how the spins can be detected via the circular polarization of the emitted light of quantum dot LED devices. Furthermore, spin injection concepts into single quantum dots are discussed as well as schemes for pulsed spin injection on a sub-nanosecond time scale. Finally, a theoretical

description of the minimal model for spin accumulation and relaxation in metal–semiconductor hybrids is described and extended to the case of coupled spins in distinct quantum dots.

We hope that these reviews are useful for students entering the field of magnetic nanostructures as well as experts working already in this and/or neighboring fields. Clearly, the present volume cannot treat all aspects of magnetic nanostructures because of size restrictions. But it gives an updated perspective on a good fraction of this exciting and fast developing field. For all missing parts, we would like to refer to other reviews, books, and topical monographs published on magnetic nanostructures.

Finally, we would like to thank all authors of the chapters in this book for their time, effort, and dedication to realize this book project in time in spite of all other pressing daily duties. Furthermore, we would like to thank our colleagues, who have critically read and commented selected chapters, thereby providing essential suggestions for the improvement of the content: Prof. M. Albrecht (Universität Chemnitz), Prof. H. J. Elmers (Universität Mainz), Prof. M. Fiebig (ETH Zürich), Prof. B. Hillebrands (Universität Kaiserslautern), Prof. U. Kunze (Ruhr-Universität Bochum), Prof. Strunk (Universität Regensburg). Last but not least, we would like to thank the Deutsche Forschungsgemeinschaft for supporting the collaborative research center on "Magnetic Heterostructures" (SFB 491) for the last 12 years. Without this support, this focussed research and the present book project would not have been possible.

Bochum and Duisburg — Hartmut Zabel
May 2012 — Michael Farle

References

1. H. Zabel, S.D. Bader, STMP **227**, 1 (2008)
2. W.J. Meiklejohn, C.P. Bean, Phys. Rev. **102**, 1413 (1956)
3. R.P. Cowburn, D.K. Koltsov, A.O. Adeyeye, M.E. Welland, D.M. Tricker, Phys. Rev. Lett. **83**, 1042 (1999)
4. T. Shinjo, T. Okuno, R. Hassdorf, K. Shigeto, T. Ono, Science **289**, 930 (2000)
5. U. Ruediger, J. Yu, S. Zhang, A.D. Kent, S.S.P. Parkin, Phys. Rev. Lett. **80**, 5639 (1998)
6. T. Ono, H. Miyajima, K. Shigeto, K. Mibu, N. Hosoito, T. Shinjo, Science **284**, 468 (1999)
7. J.A. Katine, F.J. Albert, R.A. Buhrman, E.B. Myers, D.C. Ralph, Phys. Rev. Lett. **84**, 3149 (2000)
8. J. Grollier, V. Cros, A. Hamzi, J.M. Georges, G. Faini, J. Ben Youssef, H. Le Gall, A. Fert, Phys. Rev. B **67**, 174402 (2003)

9. R.F. Wang, C. Nisoli, R.S. Freitas, J. Li, W. McConville, B.J. Cooley, M.S. Lund, N. Samarth, C. Leighton, V.H. Crespi, P. Schiffer, Nature **439**, 303 (2006)
10. J.C. Slonczewski, J. Magn. Magn. Mater. **159**, L1 (1996)
11. L. Berger, Phys. Rev. B **54**, 9353 (1996)
12. V.V. Kruglyak, S.O. Demokritov, D. Grundler, J. Phys. D: Appl. Phys. **43**, 264001 (2010)
13. H. Al-Wahsh, A. Akjouj, B. Djafari-Rouhani, L. Dobrzynski, Surf. Sci. Rep. **66**, 29 (2011)
14. A. Buzdin, Rev. Mod. Phys. **77**, 935 (2005)
15. F.S. Bergeret, A.F. Volkov, K.B. Efetov, Rev. Mod. Phys. **77**, 1321 (2005)
16. T.S. Khaire, M.A. Khasawneh, W.P. Pratt Jr, N.O. Birge, Phys. Rev. Lett. **104**, 137002 (2010)
17. D. Sprungmann, K. Westerholt, H. Zabel, M. Weides, H. Kohlstedt, Phys. Rev. B **82**, 060505 (2010)
18. R.I. Salikhov, I.A. Garifullin, N.N. Garif'yanov, L.R. Tagirov, K. Theis-Bröhl, K. Westerholt, H. Zabel, Phys. Rev. Lett. **102**, 087003 (2009)
19. S. Tsunegi, Y. Sakuraba, M. Oogane, K. Takanashi, Y. Ando, Appl. Phys. Lett. **93**, 112506 (2008)
20. X. Chen, A. Hochstrat, P. Borisov, W. Kleemann, Appl. Phys. Lett. **89**, 202508 (2006)
21. M. Fiebig, J. Phys. D **38**, R123 (2005)
22. E. Mengotti, L.J. Heyderman, A.F. Rodríguez, F. Nolting, R.V. Hügli, H.B. Braun, Nat. Phys. **7**, 68 (2011)

Contents

Contributors

Gerd Bacher Werkstoffe der Elektrotechnik and CeNIDE, Universität Duisburg-Essen, Bismarckstr. 81, 47057 Duisburg, Germany, e-mail: gerd.bacher@uni-due.de

Christian Binek Department of Physics and Astronomy, University of Nebraska, Lincoln, USA, e-mail: cbinek@unl.edu

Daniel E. Bürgler Electronic Properties (PGI-6) and Jülich Aachen Research Alliance, Fundamentals of Future Information Technology (JARA-FIT), Peter Grünberg Institute, Forschungszentrum Jülich GmbH, 52425 Jülich, Germany, e-mail: d.buergler@fz-juelich.de

Konstantin B. Efetov Institut für Theoretische Physik III, Ruhr-Universität Bochum, 44780 Bochum, Germany, e-mail: efetov@tp3.rub.de

Peter Entel Faculty of Physics, University of Duisburg-Essen, Lotharstraße 1, 47048 Duisburg, Germany, e-mail: entel@thp.uni-duisburg.de

Michael Farle Fakultät für Physik and Center for NanoIntegration Duisburg-Essen (CeNIDE), Universität Duisburg-Essen, Lotharstr. 1, 47057 Duisburg, Germany, e-mail: farle@uni-due.de

Ilgiz A. Garifullin Zavoisky Physical-Technical Institute RAS, Kazan 420029, Russia, e-mail: ilgiz_garifullin@yahoo.com

Nils C. Gerhardt Lehrstuhl für Photonik und Terahertztechnologie, Ruhr-Universität Bochum, 44801 Bochum, Germany, e-mail: nils.gerhardt@rub.de

Olav Hellwig San Jose Research Center, HGST, a Western Digital Company, 3403 Yerba Buena Road, San Jose, CA 95135, USA, e-mail: Olav.Hellwig@HGST.com

Heike C. Herper Faculty of Physics, University of Duisburg-Essen, Lotharstraße 1, 47048 Duisburg, Germany, e-mail: Heike.Herper@uni-due.de

Laura J. Heyderman Paul Scherrer Institut, 5232 Villigen PSI, Switzerland, e-mail: laura.heyderman@psi.ch

Henning Höpfner Lehrstuhl für Photonik und Terahertztechnologie, Ruhr-Universität Bochum, 44801 Bochum, Germany, e-mail: henning.hoepfner@rub.de

Martin R. Hofmann Lehrstuhl für Photonik und Terahertztechnologie, Ruhr-Universität Bochum, 44801 Bochum, Germany, e-mail: Martin.Hofmann@ruhr-uni-bochum.de

Wolfgang Kleemann Angewandte Physik, Universität Duisburg-Essen, 47048 Duisburg, Germany, e-mail: wolfgang.kleemann@uni-due.de

Jürgen König Theoretische Physik, Universität Duisburg-Essen and CeNIDE, 47048 Duisburg, Germany, e-mail: koenig@thp.uni-due.de

Peter Kratzer Faculty of Physics, University of Duisburg-Essen, Lotharstraße 1, 47048 Duisburg, Germany, e-mail: Peter.Kratzer@uni-due.de

Bernhard Krumme Faculty of Physics, University of Duisburg-Essen, Lotharstraße 1, 47048 Duisburg, Germany, e-mail: bernhard.krumme@gmx.de

Tilmar Kümmell Werkstoffe der Elektrotechnik and CeNIDE, Universität Duisburg-Essen, Bismarckstr. 81, 47057 Duisburg, Germany, e-mail: tilmar.kuemmell@uni-due.de

Jürgen Lindner Faculty of Physics, Center for Nanointegration (CeNIDE), University of Duisburg-Essen, Lotharstr. 1, 47057 Duisburg, Germany, e-mail: juergen.lindner@uni-due.de

Arne Ludwig Lehrstuhl für Angewandte Festkörperphysik, Ruhr-Universität Bochum, 44801 Bochum, Germany, e-mail: arne.ludwig@rub.de

Stéphane Mangin Institut Jean Lamour Boulevard des Aiguillettes, Nancy-Université, CNRS, B.P. 239, Vandoeuvre lés Nancy 54506, France, e-mail: stephane.mangin@ijl.nancyuniversite.fr

Jörg Nannen Werkstoffe der Elektrotechnik and CeNIDE, Universität Duisburg-Essen, Bismarckstr. 81, 47057 Duisburg, Germany, e-mail: joerg.nannen@uni-due.de

Oleg Petracic Jülich Centre for Neutron Science JCNS and Peter Grünberg Institute PGI, Forschungszentrum Jülich GmbH, 52425 Jülich, Germany, e-mail: o.petracic@fzjuelich.de

Tom Silva National Institute of Standards and Technology, Boulder, CO, USA, e-mail: silva@boulder.nist.gov

Björn Sothmann Département de Physique Théorique, Université de Genève, 1211 Genève 4, Switzerland, e-mail: bjorn.sothmann@unige.ch

Anatoly F. Volkov Institut für Theoretische Physik III, Ruhr-Universität Bochum, 44780 Bochum, Germany, e-mail: volkov@tp3.rub.de

Heiko Wende Faculty of Physics, University of Duisburg-Essen, Lotharstraße 1, 47048 Duisburg, Germany, e-mail: Heiko.Wende@uni-due.de

Kurt Westerholt Institut für Experimentalphysik/Festkörperphysik, Ruhr-Universität Bochum, 44780 Bochum, Germany, e-mail: kurt.westerholt@rub.de

Andreas D. Wieck Lehrstuhl für Angewandte Festkörperphysik, Ruhr-Universität Bochum, 44801 Bochum, Germany, e-mail: andreas.wieck@ruhr-uni-bochum.de

Georg Woltersdorf Department of Physics, Universität Regensburg, Universitätsstraße 31, 93040 Regensburg, Germany, e-mail: georg.woltersdorf@ur.de

Hartmut Zabel Institut für Experimentalphysik/Festkörperphysik, Ruhr-Universität Bochum, 44780 Bochum, Germany, e-mail: hartmut.zabel@ruhr-uni-bochum.de

The Influence of Magnetic Anisotropy on Current-Induced Spindynamics

Jürgen Lindner, Daniel E. Bürgler and Stéphane Mangin

Abstract The chapter provides a short and intuitive introduction to the basic concept of spin-transfer torque and the field of spin-torque driven magnetization dynamics in nanopillar systems. The influence of spin-polarized currents on magnetic nano-objects may lead to current-induced magnetization reversal as well as current-driven magnetization dynamics. The quantities that determine the critical currents for magnetization switching and the influence of the relative orientation of magnetization and current polarization are discussed. We focus on the nanopillar geometry and address the influence of magnetic anisotropy on the spin-torque driven spindynamics. Selected experimental examples are given to illustrate the interplay between magnetic anisotropy and spin-transfer torque.

1 Introduction

The first prediction and experimental verification of spin-transfer torque driven magnetization dynamics dates back to the work of Berger in the 1970s and 1980s. He predicted current-driven domain wall movement [1] and later provided the

J. Lindner (✉)
Faculty of Physics and Center for Nanointegration (CeNIDE),
University of Duisburg-Essen, Lotharstr. 1, 47057 Duisburg, Germany
e-mail: juergen.lindner@uni-due.de

D. E. Bürgler
Peter Grünberg Institute, Electronic Properties (PGI-6) and Jülich Aachen Research Alliance,
Fundamentals of Future Information Technology (JARA-FIT),
Forschungszentrum Jülich GmbH, D-52425 Jülich, Germany
e-mail: d.buergler@fz-juelich.de

S. Mangin
Institut Jean Lamour Boulevard des Aiguillettes, Nancy-Université, CNRS, B.P.239, F-54506
Vandoeuvre lés Nancy, France
e-mail: stephane.mangin@ijl.nancy-universite.fr

H. Zabel and M. Farle (eds.), *Magnetic Nanostructures,*
Springer Tracts in Modern Physics 246, DOI: 10.1007/978-3-642-32042-2_1,

experimental proof [2]. However, the current pulses used to drive the domain walls in thin films had magnitudes of 45 A, being impractical for direct application. Thus, the effect did not attract much attention. The starting signal to again study the effects of electric currents on the magnetization dynamics was given by theoretical work of Slonczewski [3] and, independently, Berger [4] in 1996, this time considering *nanostructured* ferromagnets. They predicted a spin-transfer torque resulting from the interaction between a spin-polarized current and the magnetization of the ferromagnet. A spin-polarized current carries angular momentum that may be partly transferred to the magnetization due to the angular momentum conservation principle. After the first experimental verification of current-induced magnetization reversal by Katine et al. [5] many investigations followed. It is noteworthy that the original argument of Slonczewski and Berger is quite general: As angular momentum is conserved in a system comprising itinerant electrons and local magnetic moments, any divergence of the spin-polarized current carried by itinerant electrons will be accompanied by an opposite and equal change of the angular momentum of the local moments (spin-transfer torque). Spin-transfer torque phenomena may also be seen as the inverse effect of giant magnetoresistance (GMR). Indeed, for GMR the current is affected by magnetization orientation, i.e. the resistance changes as the relative orientation of the magnetizations evolves. On the other hand, for spin-transfer torque the magnetization orientation is affected by the polarized current. Experimental verification of the spin-transfer torque has been carried out in magnetic nanowires (lateral geometry) as well as in vertical spin valve pillar structures with either metallic interlayers exploiting the GMR or insulating barriers that make use of the tunneling magnetoresistance (TMR).

This chapter does not aim at giving a complete overview about theory and experimental results on spin-torque driven dynamics. There exist excellent overview papers discussing the topic on a detailed basis (see e.g. Stiles and Miltat [6] and the series of review articles in Ref. [7–15]). Moreover, the field of current-driven domain wall motion in lateral structures will not be presented (see e.g. [16] for a detailed overview). The focus of the present paper is merely on introducing the mechanisms of current-driven magnetization dynamics in a simple yet intuitive manner (Sect. 2) and discussing the role and benefits of magnetic anisotropy in spin-torque systems (Sect. 3).

2 Spin-Torque Driven Magnetization Dynamics—Basics

Spin-transfer effects provide a local means of manipulating magnetization rather than relying on the long-range effects mediated by a remote current via its Oersted field. Potential applications include spin-transfer written magnetic random access memory (MRAM) cells [17] and high frequency non-linear spin-torque nano-oscillators [18] providing an approach for solid state memories, magnetic logic units, and chip-based, nanoscale, and tuneable microwave sources. However, several advances are needed to realize practical devices [17, 19]. For current-induced magnetization switching one key point is the reduction of the critical currents required

to reverse magnetization while maintaining the thermal stability of the free layer. There have been a range of approaches to lower the switching currents by optimizing the material properties, modifying the layer sequence or sample architecture [17, 20–24]. For spin-torque nano-oscillators, the main challenges are to increase the power and reduce the linewidth of the output signal to meet the requirements of applications and to achieve operation without applying an external field.

2.1 Origin of the Spin-Transfer Torque: A Simple Explanation

Figure 1 schematically shows the situation of an electric current flowing perpendicularly through a nanopillar structure that consists (from bottom to top) of a bottom electrode, a polarizing layer, a spacer layer, the switching layer (sometimes also called analyzing or free layer), and the top electrode. While for the electrodes non-magnetic materials with high conductivity are usually preferred (Au, Ag, or Cu), the polarizer and switching layer consist of ferromagnetic materials. The magnetization of the polarizing layer ($\mathbf{M}_\mathrm{p}$) should remain fixed, while the switching layer's magnetization is easy to rotate (note that the switching layer's magnetization denoted $\mathbf{M}_\mathrm{free}$ in Fig. 1 is simply termed $\mathbf{M}$ from now on).

In the following the basic idea of spin-torque driven magnetization reversal is explained in a simplified, yet demonstrative way. First we consider the switching of the free layer from antiparallel to parallel alignment with respect to the polarizer, which—for typical conditions, e.g. Co/Cu/Co trilayers—is achieved for electrons flowing from the polarizer to the switching layer. Opposite behavior can occur for specific material combinations [25, 26] and is called inverse current-induced magnetization switching.

Figure 1a and b shows a side and a top view of the pillar structure for an electron flow from the polarizer to the switching layer. The top view shows the direction of the magnetization at the height position indicated by the black arrow in the side view. The two spin channels are shown separately. At the polarizing layer (a) the majority spins are transmitted, while the minority spins are reflected or transformed to majority spins via spin-flip scattering processes within the polarizer. This leads to a spin polarization of the current leaving the polarizer given by $P = \left|I_\uparrow - I_\downarrow\right| / (I_\uparrow + I_\downarrow) = \left|\rho_\uparrow - \rho_\downarrow\right| / (\rho_\uparrow + \rho_\downarrow)$ [3], where $I_{\uparrow(\downarrow)}$ is the current carried by the majority(minority) spins and $\rho_{\uparrow(\downarrow)}$ the respective resistivity. The latter is usually written as $\rho_{\uparrow(\downarrow)} = 2\rho^*(1 \mp \delta)$, δ being the bulk spin asymmetry factor [27]. For a non-magnetic material $\delta = 0$ and the two spin channels have the same resistivities, while they differ in ferromagnetic materials. Assuming spin asymmetry in the bulk only, $P = \delta$ follows. However, at the interface δ may be quite different (interface spin asymmetry coefficient, often called γ), so that a more complex description is required [27]. The quantity P can be determined from tunnelling experiments into a superconductor at low temperatures. Values of P for the ferromagnetic materials Fe, Co, Ni, and Gd are 0.40, 0.35, 0.23, and 0.14 [28] and the value for Py is 0.73 [29].

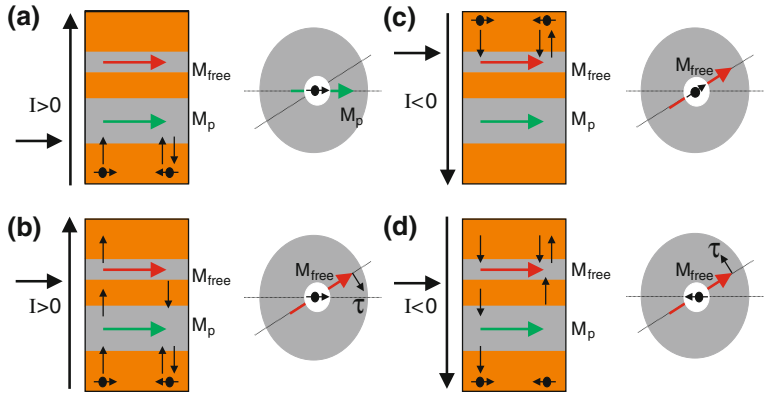

Fig. 1 Schematic *side* and *top* view on a pillar structure used for current-induced switching studies. While **a** and **b** show the situation for a current flowing from the polarizing ferromagnet to the switching layer ($I > 0$), **c** and **d** show the case of the opposite current direction. The *arrow* on the *left* side indicates for which position within the pillar the *top* view is plotted. The two channels for the different spin directions are shown separately. The direction of the spin-torque is indicated by the *arrow* labeled τ in the *top* views. Taken from [23]

Next, the spin-polarized current is injected into the spacer material. This layer is needed to magnetically de-couple polarizer and switching layer. It has, however, to be thin enough to maintain the spin polarization of the electric current. The electron's mean free path is the length scale for momentum relaxation and determines the resistivity of a material. In many materials this length is typically $\lesssim$10 nm [27]. The distance over which the spin orientation is maintained (called the spin diffusion length) is much larger because a spin-flip process can only be mediated by either exchange interaction or spin-orbit coupling at defects or impurities. For Cu the spin diffusion length can be as large as 500 nm [30]. For heavier elements, however, it is reduced due to the stronger spin-orbit coupling (for Au the spin diffusion length is about 60 nm [30]). This explains why Cu has been widely used as spacer material. In ferromagnets, due to the presence of exchange fields, the spin diffusion length is strongly reduced. In Co it is about 60 nm [31] and in Py 5 nm [29].

After passing through the spacer layer the spin-polarized current reaches the switching (or free) layer (see Fig. 1b), which we assume to have a magnetization direction slightly tilted with respect to the polarization axis of the current, i.e. the magnetization direction of the polarizing layer. In this case the spin-polarized current exhibits a transverse spin component with respect to the magnetization of the switching layer. Due to the large energy contribution of the transverse spin component due to exchange interaction, it is strongly absorbed within the interface region. It is this absorption of the transverse spin current that results in a spin-torque acting on the switching layer trying to align the magnetizations of the free layer parallel to that of the polarizer.

When the direction of the electric current is reversed as shown in Figs. 1c and d, the direction of the spin-torque also becomes reversed, i.e. the torque now destabilizes the parallel alignment of polarizer and switching layer. For this reversed current polarity, the current is first spin-polarized by flowing through the switching layer and then reaches the polarizer. At the interface, however, the direction of the magnetization of the polarizer differs with respect to the spin polarization, again due to an assumed small misalignment of the magnetizations of polarizing and free layer. This defines a new quantization axis with respect to which the incoming spin-polarized electrons are described by a superposition of spin-up and spin-down components. The component with parallel alignment is transmitted into the polarizing layer, while the antiparallel component is predominantly reflected to the switching layer, where it gives rise to a spin-torque as discussed above. Therefore, depending on current polarity, electrons transmitted through or reflected from the polarizer are responsible for the spin-torque. This implies that the situation is not symmetric with respect to the current direction and, consequently, also the spin-torques differ in magnitude.

2.2 Quantitative Model of Spin-Transfer Torque

In the following a more rigorous quantum-mechanical approach to the spin-torque effect is given similar to that of Stiles and Zangwill [32].

2.2.1 Framework of the Model

Space is defined by a direct orthogonal basis $(\mathbf{e}_x, \mathbf{e}_y, \mathbf{e}_z)$ corresponding to the three directions of space (x, y, z) with z the quantization axis. We will consider a single electron flowing in the z direction with a wave vector k, whose spin is polarized in the xz plane at an angle η with respect to the z direction (see Fig. 2). In the basis $(|\uparrow\rangle, |\downarrow\rangle)$ formed by the spin-up and the spin-down states this electron is represented by a plane wave function of the form

$$|\varphi\rangle = \frac{\exp(\mathrm{i}kz)}{\sqrt{\Omega}} \left(a|\uparrow\rangle + b|\downarrow\rangle\right), \tag{1}$$

where Ω is a normalization volume. It is incident onto a ferromagnet, whose magnetization points in the z direction. This ferromagnet is described in the Stoner model. Inside the ferromagnet, the electrons experience an exchange splitting Δ, which shifts the states of the spin-down electrons to higher energy than the spin-up electrons. Consequently, the electrons scatter at the interface with the ferromagnet from a rectangular potential energy step that depends on the spin state. For simplicity, we will consider that the height of the potential energy step is zero for the spin-up state and Δ for the spin-down state (see Fig. 2). Assuming the dispersion of free electrons and for the energy E of the electrons $E > \Delta$, the electrons have a

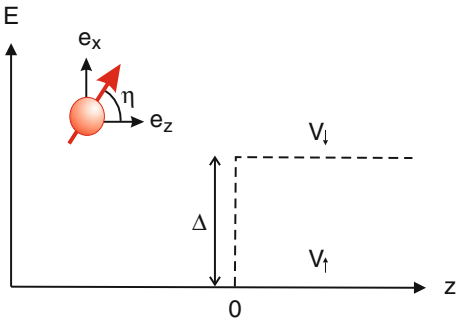

Fig. 2 Scheme of the potential energy step in the Stiles model [32]

wave vector $k = \sqrt{2mE}/\hbar$ outside the ferromagnet and wave vectors $k_\uparrow = k$ and $k_\downarrow = \sqrt{2m(E-\Delta)}/\hbar$ inside the ferromagnet for the spin-up and spin-down states, respectively.

2.2.2 Quantum Definition of Spin Current Density

In the following we discuss the calculation of spin current densities. A spin current density represents a number of spins flowing through a surface per surface and time units. It is related to the orientation of the spins in space and to the direction of their flow. Thus, it is a second order tensor quantity. Classically, it is given for a single electron by the outer product of the average electron velocity with the spin $\boldsymbol{j}_\mathbf{s} = \boldsymbol{v} \otimes \boldsymbol{s}$.

In quantum mechanics, the spin is associated to the operator $\frac{\hbar}{2}\boldsymbol{\sigma}$, where $\boldsymbol{\sigma}$ is one of the Pauli matrices. In the framework of the model described here, they are three 2×2 matrices stated in the basis $(|\uparrow\rangle, |\downarrow\rangle)$, one for each space direction,

$$\boldsymbol{\sigma}_\mathbf{x} = \begin{pmatrix} 0 & 1 \\ 1 & 0 \end{pmatrix}, \quad \boldsymbol{\sigma}_\mathbf{y} = \begin{pmatrix} 0 & -i \\ i & 0 \end{pmatrix}, \quad \boldsymbol{\sigma}_\mathbf{z} = \begin{pmatrix} 1 & 0 \\ 0 & -1 \end{pmatrix}. \tag{2}$$

The operator associated to the velocity is $\frac{\hbar}{im}\nabla$ and the average velocity of a single electron wave function $|\varphi\rangle$ is therefore $\frac{\hbar}{im}\langle\varphi|\nabla|\varphi\rangle$ related to the probability current density $\frac{\hbar}{m}\Im(\varphi^*\nabla\varphi)$. By analogy with the classical formulation, the quantum expression of the spin current density is given by

$$\boldsymbol{j}_\mathbf{s} = \frac{\hbar^2}{2m}\Im\left(\boldsymbol{\varphi}^*\boldsymbol{\sigma} \otimes \nabla\boldsymbol{\varphi}\right). \tag{3}$$

2.2.3 Calculation of the Wave Functions

To calculate the variation of spin current density, we first need to calculate the wave function of an electron flowing in the energy landscape described in Fig. 2. This is a scattering problem, so we have to calculate the expressions of the incident, reflected, and transmitted part of the wave function. The general forms are given by Eq. (1).

The incident part of the electron wave function propagates in the non-magnetic material and its projections on the spin-up and spin-down states are determined by the orientation of the spin with respect to the quantization axis. After solving a system of two equations, one obtains the expression of the incident wave function,

$$|\varphi_{\mathbf{in}}\rangle = \frac{\exp(\mathrm{i}kz)}{\sqrt{\Omega}}\left(\cos\frac{\eta}{2}|\uparrow\rangle + \sin\frac{\eta}{2}|\downarrow\rangle\right). \tag{4}$$

As soon as the incident wave function reaches the interface with the ferromagnet, one part of it is reflected and the other is transmitted through the magnet. The reflected wave function propagates in the non-magnetic material and the transmitted wave function propagates inside the ferromagnet, where the spin-up and spin-down states do not have the same wave vectors. The coordinates of the wave function in the basis $(|\uparrow\rangle, |\downarrow\rangle)$ are determined by the continuity of the wave function and its derivative with respect to the space coordinate at the interface with the ferromagnet. Solving these equations leads to the expressions for the reflected and the transmitted parts of the wave function,

$$|\varphi_{\mathbf{re}}\rangle = \frac{\exp(-\mathrm{i}kz)}{\sqrt{\Omega}}\frac{k-k_{\downarrow}}{k+k_{\downarrow}}\sin\frac{\eta}{2}|\downarrow\rangle, \tag{5}$$

$$|\varphi_{\mathbf{tr}}\rangle = \frac{\exp\left(\mathrm{i}k_{\uparrow}z\right)}{\sqrt{\Omega}}\cos\frac{\eta}{2}|\uparrow\rangle + \frac{\exp\left(\mathrm{i}k_{\downarrow}z\right)}{\sqrt{\Omega}}\frac{2k}{k+k_{\downarrow}}\sin\frac{\eta}{2}|\downarrow\rangle. \tag{6}$$

Equations (4), (5), and (6) contain all necessary ingredients to calculate the spin current density throughout the entire system.

2.2.4 Calculation of the Spin Current Densities

Each wave function contributes to the total spin current density, and we calculate the respective spin current densities taking into account that the second order tensor of the spin current density is reduced to a vector, since the wave functions propagate in z-direction only.

Applying Eq. (3) to the incident, reflected, and transmitted wave functions (4), (5), and (6) yields the spin current densities

$$\boldsymbol{j}_{\mathbf{s}}^{\mathbf{in}} = \frac{\hbar^2 k}{2m\Omega}\left(\sin\eta\mathbf{e_x} + \cos\eta\mathbf{e_z}\right), \tag{7}$$

$$\boldsymbol{j}_{\mathbf{s}}^{\mathbf{re}} = \frac{\hbar^2 k}{2m\Omega}\left(\frac{k-k_\downarrow}{k+k_\downarrow}\sin\frac{\eta}{2}\right)^2 \mathbf{e_z}, \tag{8}$$

$$\boldsymbol{j}_{\mathbf{s}}^{\mathbf{tr}} = \frac{\hbar^2 k}{2m\Omega}\Big[\sin\eta\cos\left[\left(k_\uparrow - k_\downarrow\right)z\right]\mathbf{e_x} - \sin\eta\sin\left[\left(k_\uparrow - k_\downarrow\right)z\right]\mathbf{e_y} + \left(\cos^2\frac{\eta}{2} - \frac{4kk_\downarrow}{(k+k_\downarrow)^2}\sin^2\frac{\eta}{2}\right)\mathbf{e_z}\Big]. \tag{9}$$

2.2.5 Calculation of the Spin-Transfer Torque

The expressions for the spin current densities show that the spin current density flowing on the left side of the magnet $\boldsymbol{j}_{\mathbf{s}}^{\mathbf{in}} + \boldsymbol{j}_{\mathbf{s}}^{\mathbf{re}}$ is not equal to the spin current density flowing through the magnet $\boldsymbol{j}_{\mathbf{s}}^{\mathbf{tr}}$. Therefore, the spin angular momentum of the spin-polarized current is not conserved. This net variation of spin angular momentum of the spin polarized current can be transferred to the magnetization of the ferromagnet such that the total angular momentum of the system is conserved. Assuming that the totality of this variation is transferred to the magnetization, the net variation of spin angular momentum per unit of time absorbed by the magnetization, i.e. the torque exerted on the magnetization, is given by $\boldsymbol{\tau}_{\mathbf{str}} = A(\boldsymbol{j}_{\mathbf{s}}^{\mathbf{in}} + \boldsymbol{j}_{\mathbf{s}}^{\mathbf{re}} - \boldsymbol{j}_{\mathbf{s}}^{\mathbf{tr}})$ with A the surface of the interface. Plugging Eqs. (7), (8), and (9) in this formula, the the spin-transfer torque becomes

$$\boldsymbol{\tau}_{\mathbf{str}} = A\frac{\hbar^2 k}{2m\Omega}\sin\eta\left[\left(1-\cos\left[\left(k_\uparrow - k_\downarrow\right)z\right]\right)\mathbf{e_x} + \sin\left[\left(k_\uparrow - k_\downarrow\right)z\right]\mathbf{e_y}\right]. \tag{10}$$

2.2.6 Analysis of the Spin-Transfer Torque

The model presented here shows that a spin-polarized current propagating from a non-magnetic metal to a ferromagnet loses spin angular momentum, which is transferred to the magnetization. This transfer of spin angular momentum generates a torque acting on the magnetization, the so-called spin-transfer torque, given by Eq. (10).

This novel torque is perpendicular to the magnetization and equal to zero if the magnetization and the spin polarization are perfectly collinear ($\eta = 0$ or $\eta = \pi$). The angular evolution of the spin-transfer torque with η is discussed in detail in Sect. 2.5. The spin-transfer torque also vanishes if $k_\uparrow = k_\downarrow$, indicating that it originates from the spin filtering effect of the ferromagnet.

This model also describes how the transfer of spin angular momentum could take place. The spin-transfer torque is composed of a constant term called the Slonczewski term $\tau_{\mathbf{str}}^{\mathbf{sl}} = A\frac{\hbar^2 k}{2m\Omega}\sin\eta\mathbf{e_x}$, which is absorbed at the interface due to the potential energy step. It is equal to the component of the incident spin current density perpendicular to the magnetization. The remaining terms of the spin-transfer torque

in Eq. (10) form a term $\tau_{\mathbf{str}}^{\mathbf{fl}} = A\frac{\hbar^2 k}{2m\Omega}\left(\cos\left[\left(k_\uparrow - k_\downarrow\right)z\right]\mathbf{e_x} + \sin\left[\left(k_\uparrow - k_\downarrow\right)z\right]\mathbf{e_y}\right)$. This term is called field-like because its action on the magnetization is the same as that of an external field applied in z-direction: The magnetization precesses around the z axis. The field-like term is due to oscillations of the transmitted spins around the effective magnetic field as they propagate through the ferromagnet. The wavelength of these precessions $\frac{2\pi}{k_\uparrow - k_\downarrow}$ is very short for typical transition metals, i.e. of the order of few atomic layers. In a more rigorous calculation, one has to take into account the fact that the electronic states contributing to the current lie on different parts of the Fermi surface (in other word they propagate in different space directions). Therefore, their precessions are neither in phase nor of the same wavelength. Integrating over all contributing states at the interface, their precessions quickly dephase and the mean value of the field-like term becomes very small. In the end, the spin-transfer torque mainly originates from the absorption of the component of the incident spin current density perpendicular to the magnetization, at least in a spin-valve with a metallic spacer material:

$$\boldsymbol{\tau}_{\mathbf{str}} \simeq A(\boldsymbol{j}_{\mathbf{s}}^{\mathbf{in}} \cdot \mathbf{e_x})\mathbf{e_x} = A\frac{\hbar^2 k}{2m\Omega}\sin\eta\mathbf{e_x}. \tag{11}$$

Indeed, in magnetic tunnel junctions, where the spacer is an insulator, the transport of the spin current from the polarizer to the free layer is due to tunneling. The tunneling probability depends exponentially on the component of the electron momentum perpendicular to the tunneling barrier leading to a strong k-space selection even for amorphous barrier materials such as AlO_x. In addition, matching of the band structures in epitaxial junctions can select a few specific states to dominate the tunneling current. This is most prominent in epitaxial Fe/MgO/Fe junctions [33, 34]. Under these conditions, the dephasing/averaging process mentioned above for metallic junctions is less efficient. Therefore, the field-like term remains sizable and has to be taken into account when dealing with insulating spacers. This also holds when the ferromagnet is a magnetic semiconductor.

Finally, we want to mention that this model gives the false impression that the existence of a spin current is always associated with a charge current in the same space region. Spin currents can actually flow in parts of a device, where there is no charge current. As a consequence, the spin-transfer effect can occur in a ferromagnet that does not carry a charge current. This is a phenomenon pointed out by Slonczewski [35] when calculating the interlayer exchange coupling in magnetic tunnel junctions. Pure spin currents have recently been studied intensely in non-local geometries of multiterminal devices, where a charge current is injected between two selected terminals and a spin current can diffuse in other parts of the device, where it is probed via further terminals. A first experimental demonstration of pure spin-current-induced reversible magnetization switching was given by Yang et al. [36].

2.3 Macrospin Description: Landau–Lifshitz–Gilbert Equation

Within the macrospin approximation, i.e. assuming that the magnetization of the switching layer can be treated as a macroscopic vector, one can easily derive a term attributed to the spin-torque that is added to the Landau–Lifshitz–Gilbert (LLG) equation of motion and can be used to describe the current-induced spin dynamics. A polarized current with the polarization direction given by the magnetization direction of the polarizing layer is assumed to enter into the switching layer. Based on the result of the previous sections we consider the transverse component of the electron's magnetic moment that is given by $\Delta\mu_e^{\perp} = P\mu_e \sin\eta$, with the spin polarization P and the angle η between the spin polarization direction and the magnetization of the switching layer. Using the relation $\gamma = g\mu_B/\hbar$ for the gyromagnetic ratio, one derives $\Delta\mu_e^{\perp} = P\,|\gamma|\sin\eta\cdot\hbar/2$. The relation between the angular momentum L_e of the electron and its magnetic moment $\mu_e = -\,|\gamma|\,L_e$ yields for the (transverse) angular momentum transfer $\Delta L_e = -\frac{P\hbar}{2}\sin\eta$. For $\mathrm{d}N = I\,\mathrm{d}t/\,|e|$ electrons (I being the electric current, e the electron's charge) one obtains $\Delta L_e^{\mathrm{all}} = -\frac{P\hbar}{2}\frac{I\,\mathrm{d}t}{e}\sin\eta$, which can be directly converted into the term $\frac{\mathrm{d}\mu_e^{\mathrm{all}}}{\mathrm{d}t} = |\gamma|\,P\frac{\hbar}{2|e|}I\sin\eta$. This provides an expression for the total change in magnetic moment, if the complete injected transverse spin angular momentum is absorbed. Using finally $M = \mu/V$ (V: volume of switching layer) as a definition of the switching layer's magnetization and identifying $\mathrm{d}\mu_e^{\mathrm{all}}/\mathrm{d}t$ as the total magnetic moment change due to the spin-polarized current, the time derivative of the magnetization of the switching layer, when written in vectorial form, is

$$\frac{\mathrm{d}\mathbf{M}}{\mathrm{d}t} = -\frac{\hbar}{2\,|e|}\frac{|\gamma|\,PI}{M^2V}\mathbf{M}\times(\mathbf{M}\times\mathbf{i}_S) = -\frac{\hbar}{2\,|e|}\frac{|\gamma|\,PJ}{M^2d}\mathbf{M}\times\left(\mathbf{M}\times\mathbf{m}_p\right). \tag{12}$$

Here, $\mathbf{i}_S$ is the unit vector of the spin current, $\mathbf{m}_p$ the unit vector of the magnetization in the polarizer, $J = I/A$ the current density, and d the thickness of the switching layer ($V = A\cdot d$ with the cross section A of the switching layer). Note that the sign of the spin-transfer torque vector describes the fact that for a positive prefactor (i.e. for a positive current flowing from the polarizer to the free layer) the torque prefers a parallel alignment of the two magnetizations (see also Fig. 1). The complete LLG equation of motion including spin-torque effects is given by

$$\frac{\mathrm{d}\mathbf{M}}{\mathrm{d}t} = -\,|\gamma|\,\mathbf{M}\times\mathbf{B}_{\mathrm{eff}} + \frac{\alpha}{M}\mathbf{M}\times\frac{\mathrm{d}M}{\mathrm{d}t} - |\gamma|\,\frac{a_J}{M}\mathbf{M}\times\left(\mathbf{M}\times\mathbf{m}_p\right) - |\gamma|\,a_J\xi\mathbf{M}\times\mathbf{m}_p \tag{13}$$

with the factor a_J given by $a_J(P,\eta) = \hbar/(2\,|e|\,Md)\cdot g(P,\eta)J$. Here, we have replaced P by a more general function $g(P,\eta)$ for reasons that will be discussed below. a_J has the dimension of a magnetic field and characterizes the amplitude of the spin-transfer torque. For completeness we have introduced a term proportional to $\mathbf{M}\times\mathbf{m}_p$ in addition to the so-called Slonczewski term derived in Eq. (12). The additional term was introduced in [37], where it was shown that the spin current

also gives rise to an effective field parallel to the polarizer's magnetization, which in general also contributes to magnetization reversal. Note that a field-like term already appeared in the discussion of the simple model used in Sect. 2.2.5 [see Eq. (10)]. ξ is a measure of the relative strength of the two terms and has been shown to be a function of the thickness of the free layer divided by the length λ_J, $\xi = f(d/\lambda_J)$ [37]. λ_J describes the typical length scale on which the exchange interaction between the local magnetic moments of the ferromagnet and the spins of the conduction electrons of the spin-polarized current operates, finally resulting in the spin polarization of the current being aligned parallel to the local magnetization. Since it is the transverse spin component of the spin-polarized electrons that is absorbed on the length scale of λ_J it sometimes is called transverse spin diffusion length. Using $\lambda_J = 2.5\,\text{nm}$ and a typical experimental thickness of about $d = 2.5\,\text{nm}$, yields $\xi \approx 0.3$. For $d > \lambda_J$, however, ξ rapidly decreases to zero. The Slonczewski term has a dependence on d/λ_J, too, given by a different function $h(d/\lambda_J)$. While $h \approx 0.8$ for $d = 2.5\,\text{nm}$ and $\lambda_J = 2.5\,\text{nm}$, $h = 1$ in the limit of large d values. Thus, the prefactor of the Slonczewski term approaches the $1/d$ behavior as in Eq. (12).

Note, that the simple calculation presented above did not take into account that the spin polarization P itself is a function of the relative orientation of the magnetization of polarizer and switching layer given by the angle η. Formally this dependence can be accounted for by replacing the constant P by the spin efficiency function $g(P, \eta)$, as in Eq. (13). The explicit form of $g(P, \eta)$ is discussed in Sect. 2.5

The effective magnetic field $\mathbf{B}_{\text{eff}}$ is composed of all magnetic fields acting on the magnetization of the switching layer. In general, $B_{\text{eff}} = B_0 + B_{\text{dip}} + B_{\text{ip}} + B_{\text{oop}}/2$, where B_0 is the externally applied magnetic field, B_{dip} the dipolar field originating from the stray field of the polarizer acting on the switching layer, B_{ip} is the in-plane anisotropy field, and B_{oop} the effective perpendicular anisotropy field of the free layer, given by the sum of the shape anisotropy field and the intrinsic out-of-plane anisotropy field, i.e. $B_{\text{oop}} = B_{\text{shape}} - B_\perp = \mu_0 M - B_\perp$. Obviously, choosing appropriate geometries and materials with specific anisotropy contributions allows for tailoring the properties of spin-torque systems.

We note that the effective field—*excluding* the effective field due to spin-torque, see Eq. (12)—can be derived from an expression of the free energy F of the system. To show this for a simple example we consider a system in which the free energy is supposed to depend only on the angle θ of the magnetization with respect to an anisotropy axis. If θ_B is the angle of the external field relative to this axis, the free energy can be written as $F = F_a - M \cdot B_0 \cos(\theta - \theta_B)$, where the first term is the anisotropy energy and the second the Zeeman contribution of the external field. The equilibrium angle of M can be found from $\frac{\partial F}{\partial \theta} = 0 = \frac{\partial F_a}{\partial \theta} + M \cdot B_0 \sin(\theta - \theta_B) = \frac{\partial F_a}{\partial \theta} + |\mathbf{M} \times \mathbf{B}_0|$. This equation means that in equilibrium the torque $\mathbf{M} \times \mathbf{B}_0$ due to the external field is balanced by the torque due to the magnetic anisotropy field given by $-\frac{\partial F_a}{\partial \theta}$ (the opposite sign indicates that the torques are antiparallel). When B_0 causes a turn of M of $\delta\theta$, the torque due to the anisotropy field is proportional to $\delta\theta$ and given by $-\frac{\partial F_a}{\partial \theta} = c \cdot \delta\theta$. Thus, for $\delta\theta \to 0$ $c = -\frac{\partial^2 F_a}{\partial \theta^2}\Big|_{\delta\theta=0}$ and the equilibrium

condition becomes $c \cdot \delta\theta + M \cdot B_0 \sin\delta\theta \approx -\left.\frac{\partial^2 F_a}{\partial\theta^2}\right|_{\delta\theta=0} \cdot \delta\theta + M \cdot B_0 \delta\theta = 0$. From this equation the anisotropy field is found to be

$$B_a = -\frac{1}{M} \cdot \left.\frac{\partial^2 F_a}{\partial\theta^2}\right|_{\delta\theta=0} \tag{14}$$

Note that the derivative has to be taken at the equilibrium angle, for which $\delta\theta = 0$. In contrast to the effective field due to anisotropies the 'spin-torque' effective field given by Eq. (12) cannot be derived from a 'spin-torque' free energy. This has been discussed in detail by Stiles [38].

From a stability analysis of the LLG equation including the spin-transfer torque term it is possible to derive the critical current threshold for which the free layer's orientation becomes unstable. This is an important information since for the application of current-induced switching, integration with existing electronic technology requires switching current densities below 10^5–10^6 A/cm^2 [17]. The critical current in general is given by

$$I_c = \frac{2e}{\hbar}\frac{\alpha M V}{g(P,\eta)} B_{\text{eff}}. \tag{15}$$

Therefore, the critical current density depends apart from the material properties entering $g(P,\eta)$ on all details that define B_{eff}. We will discuss the two cases of in-plane and perpendicularly magnetized switching layers in Sects. 3.1 and 3.2, respectively.

2.4 Current-Induced Magnetization Oscillations

As discussed in [39, 40] the LLG equation of motion as given by Eq. (13) can be rewritten in the form (for details, see Appendix).

$$\begin{aligned}\frac{1}{|\gamma|}\frac{\mathrm{d}\mathbf{M}}{\mathrm{d}t} &= -A \cdot \mathbf{M} \times \left(\mathbf{B}_{\text{eff}} - \alpha a_J \mathbf{m}_p\right) \\ &\quad -A \cdot \frac{\mathbf{M}}{M} \times \left[\mathbf{M} \times \left(\alpha \mathbf{B}_{\text{eff}} + a_J \mathbf{m}_p\right)\right].\end{aligned} \tag{16}$$

Here, $A = 1/(1+\alpha^2)$. Note that we have neglected the field-like term given in Eq. (13) and solely considered the Slonczewski term. The form of Eq. (16) clearly shows that the Slonczewski spin-torque term introduces two contributions: One has precessional character, the other within the second term on the right hand side of Eq. (16) generates additional damping or antidamping. The sign of a_J and the direction of $\mathbf{m}_p$ with respect to $\mathbf{B}_{\text{eff}}$ decide if the spin-torque increases or decreases the Gilbert damping. An interesting situation arises if the spin-torque contribution compensates or even overcompensates the Gilbert damping. In this case the

spin-transfer torque can *drive* magnetization dynamics. Indeed, current-driven magnetization oscillations have been observed experimentally in many different systems (see e.g. [41–45]).

In the macrospin approximation the current-driven magnetization dynamics results in precession-like motion of the magnetization vector, but with much larger excitation (cone) angles (as large as 180°) and strong deviations from circular precession due to anisotropy. The shape anisotropy of the thin-film geometry, for instance, tends to flatten the precession trajectory to an ellipse with large excursions of the dynamic magnetization in the sample plane and smaller ones in the perpendicular direction (for examples see Fig. 7). These oscillatory dynamic modes are not attainable with magnetic fields alone. When relaxing the macrospin approximation, spin wave excitations have to be considered in addition to the uniform precession-like modes.

Any oscillatory motion of the free layer magnetization with respect to the fixed layer results, due to the GMR or TMR effect in the ferromagnet/spacer/ferromagnet layered structure, in a variation of the resistance. Therefore, the DC current that gives rise to the spin-torque excitations generates a periodic voltage drop across the pillar. The frequencies are typically similar to those of ferromagnetic resonance (FMR) experiments, i.e. in the GHz range. This phenomenon can be employed for fabricating nanoscale microwave generators, whose frequency can be tuned by varying the DC current and/or the external field [43, 46]. Such devices are called spin-torque nano-oscillators (STNO). A detailed theoretical discussion of STNO properties in the framework of non-linear auto-oscillator theory has been given by Slavin and Tiberkevich [47].

2.5 Comparison of Spin-Transfer Models—Efficiency Functions

The difference between the various models that have been applied to quantitatively describe the spin-transfer torque is mainly resulting from different expressions for the magnitude and angular dependence of the spin-torque efficiency function $g(P, \eta)$ introduced in Eq. (13).

The calculation of the spin-torque efficiency function $g(P, \eta)$ was addressed by different authors using different approaches. In the simplest approximation as the one used in Sect. 2.2 the angular dependence of the spin-torque magnitude is symmetric and proportional to $\sin(\eta)$ (see Fig. 3a). The factor $\sin(\eta)$ results from the double-cross product in Eq. (12) that represents the transversal component of the incident spin current and is common to all models. Therefore, in the simple model of Sect. 2.2 the spin-torque efficiency function is a constant, $g(P, \eta) = P$. In general, however, the magnitude of the spin-torque is connected to the spin-dependent transport properties of the structure and, thus, transport calculations have to be performed. In the first publication on spin-torque Slonczewski assumed purely ballistic transport and included spin-dependent scattering at the *interfaces* only, i.e. no scattering is allowed when the electrons propagate from one interface to another [3]. In this limit $g(P, \eta)$ takes the form

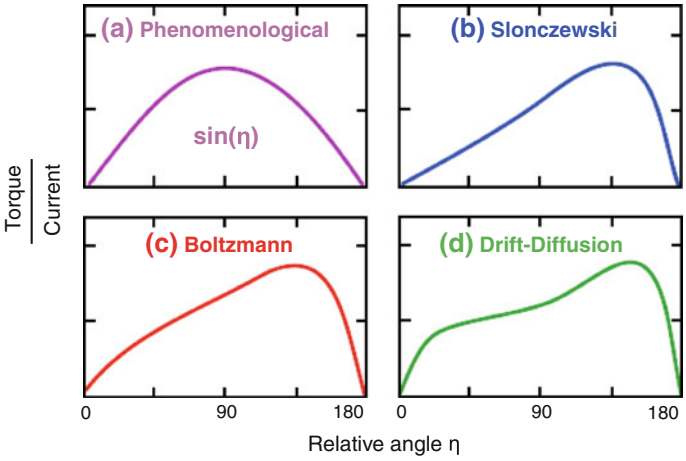

Fig. 3 Angular variation of the spin-torque (the quantity $a_J \sin(\eta)$ is plotted) in various approaches: **a** for $a_J = 1$, **b** according to a model by Slonczewski that assumes purely ballistic transport and interface scattering only [3], **c** for the most general approach given by a solution of the Boltzmann equation [48], and **d** for the drift-diffusion approximation assuming fully diffusive transport [50, 51]

$$g_{\text{ballistic}}(P, \eta) = \left[-4 + (3 + \cos\eta) \frac{(1+P)^3}{4P^{3/2}} \right]^{-1} . \tag{17}$$

Figure 3b shows the spin-torque for $J > 0$ (electrons flowing from the polarizer to the switching layer) as a function of η (i.e. the quantity $a_J \cdot \sin(\eta)$, see Sect. 2.3) for the Slonczewski approach. For exact parallel and antiparallel alignment of the two magnetizations the torque vanishes and in between the curve is asymmetric with larger values for near antiparallel alignment. The torque is positive for the whole range of η values indicating that the parallel alignment is favored. The torque increases more rapidly with η when starting from the antiparallel orientation. For a negative current (i.e. electron flow from switching layer to polarizer) the shape of the torque curve would be the same but with negative torque values preferring an antiparallel alignment. As the current needed to induce magnetization switching is correlated to the slope of the torque curve, the shape of the curve implies that one needs a higher current density for switching from the parallel to the antiparallel orientation (torque increases less rapidly with the angle η when starting from parallel alignment) than for switching from antiparallel to parallel alignment. This is indeed observed in most experiments (see e.g. the first experiment by Katine et al. [5] and discussion in Sect. 3.2.1).

A more rigorous way to treat the transport of electrons is to use the Boltzmann equation, which assumes that the electronic system can be described by the local occupation probability as given by the distribution function $f(\mathbf{r}, \mathbf{k}, t)$ of well-defined bulk states for the two spin directions (for details on the form of the distribution function,

see [27]). The Boltzmann equation then provides the evolution of f. It can be used to describe both, the ballistic as well as the diffusive limit, in which the electrons scatter multiple times when propagating from one interface to another. In general, however, it has to be solved numerically [48]. To obtain analytical expressions, different approximations to the Boltzmann equation were employed. Slonczewski used circuit theory in connection with an approximate Boltzmann equation [49]. He found an analytical expression for the case that the structure is symmetric, i.e. with the two magnetic layers being identical. The assumption was to treat the spacer in the ballistic limit and to include diffusive transport in the magnetic layers only. In this approximation g takes the form [48, 49]

$$g^{\text{partly}}_{\text{diffusive}}(P, \eta, \Lambda) = \frac{P\Lambda^2}{(\Lambda^2+1)+(\Lambda^2-1)\cos\eta}, \tag{18}$$

where $\Lambda = GR$ with the overall resistance $R = 1/2(R_\uparrow + R_\downarrow)$ and the conductivity G of the spacer material (for a parabolic band $G = Ae^2k_F^2/\pi^2\hbar$ with the Fermi wave vector k_F and the cross-sectional area A of the structure). In the symmetric case, $\Lambda = 1$, $g^{\text{partly}}_{\text{diffusive}}$ becomes a constant and the torque is equal at both interfaces as for the simple model discussed before (see Fig. 3a). For $\Lambda \neq 1$, the torque exhibits skew as in the fully ballistic case of Fig. 3b. However, while in the fully ballistic case it is the spin polarization P that governs both, torque and angular dependence, in the case of diffusive transport within the magnets, P affects the amplitude of the torque, while there is another parameter (Λ) that influences both, amplitude and angular dependence. For $\Lambda < 1$ the skew becomes even opposite to the fully ballistic case, i.e. larger torque amplitudes for $\eta < 90°$.

Xiao et al. have solved Slonczewski's equations for the general asymmetric case of two different ferromagnetic layers [48]. In this case there are two different torques acting at the left and right interfaces between the spacer and the adjacent ferromagnetic layers. Denoting the interface to the polarizing ferromagnet by the subscript L and the one to the free ferromagnetic layer by R, the efficiency function for the torque acting on the interface between spacer and free layer becomes

$$g^{\text{partly}}_{\text{diffusive}}(P_i, \eta, \Lambda_i) = \frac{q_+}{A + B\cos\eta} + \frac{q_-}{A - B\cos\eta}. \tag{19}$$

with

$$\begin{aligned} q_\pm &= \frac{1}{2}\left[P_L\Lambda_L^2\sqrt{\frac{\Lambda_R^2+1}{\Lambda_L^2+1}} \pm P_R\Lambda_R^2\sqrt{\frac{\Lambda_L^2-1}{\Lambda_R^2-1}}\right] \\ A &= \sqrt{(\Lambda_L^2+1)(\Lambda_R^2+1)} \\ B &= \sqrt{(\Lambda_L^2-1)(\Lambda_R^2-1)}. \end{aligned} \tag{20}$$

For the asymmetric case there are different Λ_i $(i = L, R)$ values and spin polarization factors P_i $(i = L, R)$ for the two interfaces. In the symmetric case $\Lambda_L = \Lambda_R = \Lambda$ and $P_L = P_R = P$, which yields $q_- = 0$. The equations reduce to Slonczewski's form for the symmetric system given by Eq. (18) [49].

In Fig. 3c the typical angular variation of the torque according to the solution of the Boltzmann equation for an asymmetric case is plotted. The most prominent difference between the ballistic approach by Slonczewski (Fig. 3b) and the result from using the Boltzmann equation (Fig. 3c) is given by the non-vanishing q_- term resulting in a small bump in the angular range $0 < \eta < 45°$ (as mentioned before note that the bump results only in case of an asymmetric structure). This bump was shown to play a key role for current induced magnetization oscillations in spin valve systems [48].

The study of Xiao et al. [48] clearly shows that diffusive transport plays the key role for most of the experimental structures with layer thicknesses of several nanometers. Therefore, the so-called drift-diffusion approximation that ignores the details of the scattering near interfaces and, thus, describes transport in the diffusive limit, was introduced [50, 51]. In this model which can be directly derived from the Boltzmann equation the electron current density is expressed as a sum of two components: The drift component which is driven by the electric field and the diffusion component caused by the gradient of the electron concentration. The typical angular dependence resulting from this approach is shown in Fig. 3d. It can be seen that it reproduces all main features obtained by solving the full Boltzmann equation which indicates that scattering at the interfaces is negligible unless very thin layers are considered.

Finally, we mention that in special cases the efficiency function can adopt more complex shapes including "wavy" behavior with zero crossings for non-collinear alignment of the magnetizations. Examples include asymmetric spin valves due to different materials with different spin diffusion lengths for the two magnetic layers [31, 52] and the 90°-state of symmetric trilayers discussed in detail in Sects. 3.1.3 and 3.1.4.

3 Influence of Magnetic Anisotropy on Spin-Torque Systems

The general expression for the critical current [Eq. (15)] derived in section "Macrospin Description: Landau–Lifshitz–Gilbert Equation" shows a direct influence of magnetic anisotropies via B_{eff} on the current-driven magnetization switching. This also holds for the general case of spin-torque driven magnetization dynamics describing the motion of magnetization under the action of spin-transfer torque in an energy landscape, which to a large extent is shaped by magnetic anisotropies. Below we distinguish two cases with either dominant in-plane anisotropy forcing the static magnetization in the plane of the sample (Sect. 3.1) or dominant out-of-plane anisotropy in perpendicularly magnetized structures (Sect. 3.2).

3.1 Spin Transfer Torque and In-Plane Anisotropy

In this section we consider a pillar stucture with in-plane magnetized magnetic layers in an external field, which is applied in the plane of the layers. For thin films shape anisotropy favors the in-plane magnetized state, if we assume that the intrinsic out-of-plane field $B_\perp$, e.g. due to perpendicular interface anisotropy, is much weaker than $\mu_0 M$. In the remainder of this section we neglect $B_\perp$ to keep notation short. If needed, $B_\perp$ can be accounted for by an effective magnetization M_{eff} in the shape anisotropy term.

3.1.1 Critical Switching Current for In-Plane Magnetized Structures

We rewrite Eq. (15) for I_c taking into account the external field B_0, the dipolar coupling field between the layers B_{dip}, the total in-plane anisotropy field B_{ip}, and the shape anisotropy:

$$I_c^{\text{P}\to\text{AP}} = \frac{2e}{\hbar}\frac{\alpha M V}{g(P,\eta=0)}\left(B_0 - B_{\text{dip}} + B_{\text{ip}} + \frac{\mu_0}{2}M\right) \tag{21}$$

$$I_c^{\text{AP}\to\text{P}} = -\frac{2e}{\hbar}\frac{\alpha M V}{g(P,\eta=\pi)}\left(B_{\text{dip}} - B_0 + B_{\text{ip}} + \frac{\mu_0}{2}M\right). \tag{22}$$

The effective field expressions for parallel and antiparallel configurations are different for two reasons: (i) the external field always favors the parallel state and thus increases(decreases) $I_c^{\text{P}\to\text{AP}}(I_c^{\text{AP}\to\text{P}})$. The dipolar interaction via the stray field favors antiparallel alignment and thus acts opposite to B_0. Note, that even for free layers with in-plane anisotropy the demagnetizing field appears in the expression for the critical current. This results from the fact that the magnetization reversal or excitations involve a significant out-of-plane component of the magnetization. Once the magnetization rotates out of the plane due to spin-torque, the demagnetizing field is added to the effective field in the LLG equation.

The stability of the switching layer (typically a nanoscale disk-shaped magnet) against thermal excitation giving rise to unwanted changes of the magnetization state is given by the energy barrier $U = K_{\text{ip}} V = (M V B_{\text{ip}})/2$, where $B_{\text{ip}} = 2K_{\text{ip}}/M$. This barrier has also to be overcome to switch the magnetization within the film plane by spin-torque [17]. Therefore, the critical current for switching from the parallel to the antiparallel configuration (for $B_0 = 0$) can be written as

$$I_c^{\text{P}\to\text{AP}} = \frac{2e}{\hbar}\frac{2\alpha}{g(P,\eta=0)}\left(U + \frac{\mu_0}{4}M^2 V\right). \tag{23}$$

The basic result of Eq. (23) is that the critical current scales linearly with the thermal stability energy but includes a large additive term resulting from shape anisotropy ($\propto M^2$) that increases I_c, but does not contribute to thermal stability.

This behavior will be contrasted with the situation for out-of-plane magnetized structures in Sect. 3.2.

3.1.2 Magnetocrystalline Anisotropy in Spin-Torque Pillars

In the context of spin-torque pillars, there are three main origins for an in-plane anisotropy field B_{ip}: Magnetocrystalline anisotropy, shape anisotropy, e.g. in an elliptically shaped nanodisk [53], and exchange anisotropy due to direct exchange of the ferromagnetic layer with an antiferromagnet. Exchange bias is unidirectional and frequently used to stabilize the polarizer in spin-torque systems [54–56]. Here, we are interested in anisotropies acting on the free layer, in particular magnetocrystalline anisotropy with higher symmetry than the uniaxial shape anisotropy of elliptical nanodisks.

Our model system is an epitaxial, singlecrystalline Fe(2 nm)/Ag(6 nm)/Fe(20 nm) multilayer that we grow by thermal evaporation on a Ag(001) buffer layer on a GaAs(001) wafer. All layers grow with (001) orientation with low lattice mismatch. The epitaxial relationships are confirmed by low-energy electron diffraction (LEED). We then employ photo and e-beam lithography in combination with ion-beam etching to pattern nanopillars with a diameter of 70 nm [26, 57]. The etching is timed such that only the top 2-nm-thick Fe layer is structured, while the 20-nm-thick bottom Fe layer remains extended over the width of the bottom electrode (several tens of micrometers, see inset of Fig. 4b). Although it is well established that Fe/Ag/Fe(001) multilayers grown according to this recipe are of high crystalline quality with sharp interfaces and well developed magnetocrystalline anisotropy, it is not obvious that these properties are still present after nanofabrication of the 2-nm-thick circular disk with a diameter of 70 nm. In particular the ion-beam etching process could impair the crystalline order and thus the magnetocrystalline anisotropy. However, we find from CPP-GMR measurements and the respective Stoner-Wohlfarth fits (Fig. 4a) that both Fe layers remain in-plane magnetized and exhibit clear four-fold in-plane anisotropy of magnetocrystalline origin. The fit yields an anisotropy constant of the free layer $K_{\mathrm{MC}} = 63\,\mathrm{kJ/m^3}$, which basically corresponds to the value of bulk Fe. An interesting magnetic configuration occurs after decreasing the field to zero, where the two magnetizations rest in two different easy axes and, thus, include an angle of $\eta = 90°$. For a standard, symmetric angular dependence of the normalized resistance $r(\eta) = \frac{R(\eta)-R(0°)}{R(180°)-R(0°)}$ would be $r(90°) = 0.5$. Instead we find a much lower value of 0.3 (dashed line). This deviation originates from enhanced spin accumulation at the Fe/Ag(001) interfaces and yields in Slonczewski's model [49] introduced in Sect. 2.5 an asymmetry parameter $\Lambda_{GMR} = 1.6$. The definition of the parameter Λ is given in the context of Eq. (18). The subscript GMR indicates that this Λ value is determined from a GMR measurement. $\Lambda_{GMR} > 1$ suggests an angular dependence of the spin-torque magnitude as shown in the top right panel of Fig. 3.

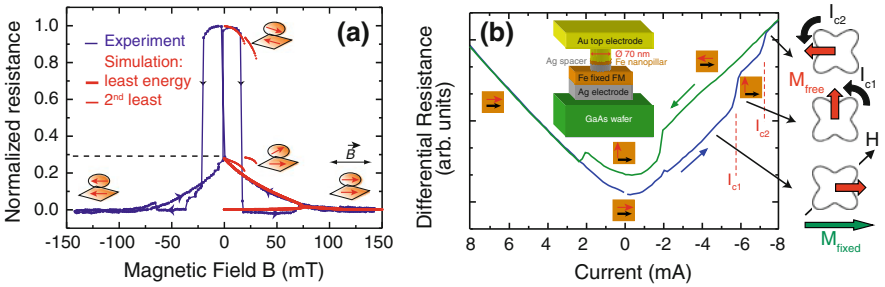

Fig. 4 **a** CPP-GMR data (*blue*) measured at 5 K with the magnetic field applied along a hard axis of the single-crystalline Fe(001) layers. *Thick* and *thin red* lines are least and second least energy solutions of a Stoner-Wohlfarth fit, respectively. Pairs of red arrows indicate the relative alignment of magnetizations as derived from the fit. **b** Two-step current-induced magnetization switching of a single-crystalline Fe/Ag/Fe(001) nanopillar measured at 5 K. $\mathbf{M}_{\text{free}}$ switches first from parallel to perpendicular and then to antiparallel alignment relative to $\mathbf{M}_{\text{fixed}}$ and vice versa for the decreasing current branch (*green*). The diagrams on the right-hand side represent the in-plane anisotropy energy landscape. The four minima correspond to easy axis directions. Taken from [57]

3.1.3 Two-Step Switching Process

Figure 4b shows the differential resistance through the pillar versus DC current taken at a magnetic field of 7.9 mT applied along a hard axis. This field is much weaker than the anisotropy field of about 40 mT. Therefore, both magnetizations are aligned along an easy axis and the measurement starts at zero DC current in a low resistive state. In contrast to the usually observed behavior [5] the switching occurs here in two steps via an intermediate resistance level. Note that the abscissa is scaled from positive to negative currents to conform to the (arbitrary) convention of this chapter that a positive current corresponds to an electron flow from the polarizer to the free layer. At a negative current I_{c1} the free layer starts to rotate with respect to the fixed layer. The anisotropy energy minimum at 90° stabilizes the orthogonal state. Only at an even higher current I_{c2} the local energy minimum is overcome and the free layer switches to the antiparallel alignment. Upon reversing the current, a similar behavior is observed.

At first glance, it is surprising that there are two switching events at different critical currents, because the anisotropy energy barriers to overcome are in both cases the same. The macrospin simulations in Fig. 5 show that the different critical current densities arise from the angular dependence of the spin-torque efficiency function $g(\eta)$. For the analysis of the data we use Slonczewski's model [49] and the efficiency function $g^{\text{partly}}_{\text{diffusive}}(P, \eta, \Lambda)$ [Eq. (18)], for details see [58]. Figure 5a shows the trajectory of the first switching step from parallel to perpendicular with respect to the fixed magnetization. The direction of the damping torque (red) and the spin-torque (blue) during the switching are shown in Fig. 5c. The viewing direction is along the $-x$-direction. As expected, the spin-torque always points outward and, thus, acts as an excitation. Therefore, the cone angle of the precession around the

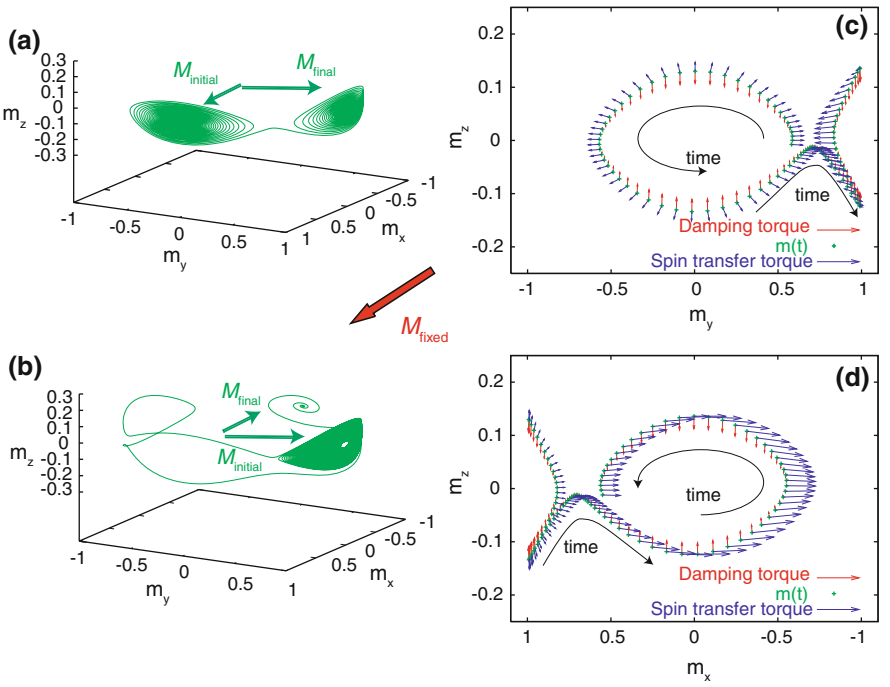

Fig. 5 Spin-torque induced switching of a macrospin in the presence of cubic magnetocrystalline anisotropy and demagnetizing field. $\mathbf{M}_{\text{free}}$ switches under the influence of a persistent DC current first from parallel ($+x$-direction) to a 90°-orientation ($+y$-direction) with respect to $\mathbf{M}_{\text{fixed}}$ and then from the 90°-orientation to the antiparallel alignment ($-x$-direction). (**a**, **b**) Trajectories of the two switching events. (**c**, **d**) representation of the spin-torque (*blue arrows*) and damping torque (*red arrows*) viewed along (**b**) the initial, parallel and (**c**) the 90°-orientation of the macrospin. Only a fraction of the trajectory in the immediate vicinity of the switching event (**a**) is shown in (**c**) and (**d**). Taken from [58]

initial state increases, until the anisotropy energy barrier between the initial and the 90°-state is overcome. Figure 5d shows the torques after the switching; now with the viewing direction in $-y$-direction (note the different abscissae of Fig. 5c and d). The symmetry of the spin-torque after switching is completely different. For $m_x < 0$ (right half of Fig. 5d) the spin-torque is still pointing outward and is an exciting torque. For $m_x > 0$ (left half of Fig. 5d), however, the spin-torque points towards the precession axis and damps the oscillatory motion. The total action of the spin-torque along one revolution tends to cancel out. Therefore, the magnetization relaxes towards the $+x$-direction after the first switching step as can also be seen in Fig. 5a. The simulation also reproduces the second switching step at a higher DC current from the 90°-state to the antiparallel state (Fig. 5b). Again, the angle of the precession around the initial state increases until the switching occurs. (In this specific simulation the switching is a bit more complicated, because the magnetization overcomes the energy barrier on the 'wrong' side of the trajectory, which requires it to reach the final

state via a 'detour'.) But how can the spin-torque in Fig. 5d excite the magnetization at a higher current and induce the switching? The answer is found by looking at the efficiency function $g(\eta)$ in Fig. 3b. The magnitude of the spin-torque is not constant along the trajectory. In fact, for $m_x < 0$ (right half of Fig. 5d) it is stronger than for $m_x > 0$ (left half of Fig. 5d). Therefore, the total action along one revolution does not completely cancel out and a small exciting net torque remains. For a large enough critical current I_{c2} this net torque is sufficient to overcome the damping torque and induces the second switching step.

The comparison between the experimentally determined ratio of the critical currents I_{c2}/I_{c1} with corresponding values extracted from simulations with varying asymmetry parameter Λ yields –this time based on spin-transfer torque experiments– $\Lambda_{STT} = 3.4$ [57]. This experiment and the GMR data of the previous section represent the first direct determination of the asymmetry parameter Λ for GMR and spin-torque in the same sample. Using spin-dependent interface area resistances calculated by Stiles and Penn [59] we obtain a theoretical value $\Lambda = 4$. The deviations between the theoretically expected value of Λ (4.0) and those determined from GMR and spin-torque data (1.6 and 3.4, respectively) most likely arise from imprecise knowledge of material parameters and from simplifying assumptions of the Slonczewski model, such as the complete neglect of the minority channel, which is only approximately fulfilled for Fe/Ag(001) [57].

3.1.4 Zero-Field Excitations in the 90 °-State

The simulations in Fig. 5 suggest that a steady-state oscillatory mode can be excited at a low external field, if the system is prepared in the 90 °-state and a DC current between I_{c1} and I_{c2} is applied. Figure 6a shows microwave spectra measured under these conditions [58]. The frequencies of the observed modes slightly shift with increasing current strength to higher frequencies. A corresponding macrospin simulation is shown in Fig. 7a and b. We indeed find a precessional trajectory around the $+y$-direction, which is the static direction of the free magnetization in the 90 °-state. The analysis of the torques in Fig. 7b yields a similar picture as for the second switching step in Fig. 5: The excitation of the spin-torque on the right hand part of the trajectory is larger than the damping on the left hand part due to the asymmetry of $g(\eta)$. The integrated action of the spin-torque along one revolution almost cancels out. Only a relatively small net excitation remains.

Figure 6b shows for comparison microwave spectra measured in a saturating field of 120 mT. We observe the "normal" in-plane precession that mainly results from the counteraction of spin-torque and externally applied magnetic field. The high-frequency modes show a dependence on the field direction since we need to apply higher currents to excite microwaves when the field is applied parallel to an easy axis of the Fe layers. The observed frequencies also differ for the two cases. The magnetocrystalline anisotropy increases(decreases) the effective field when the external field is applied along an easy(hard) axis yielding higher(lower) frequencies. The difference of 0.5 GHz at 10.4 mA can be translated to a difference of the mean

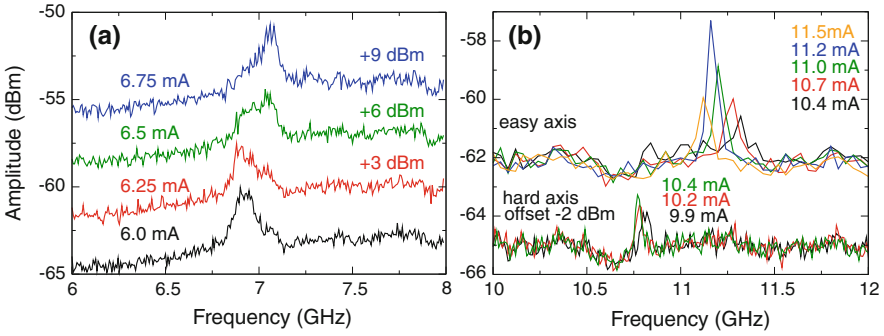

Fig. 6 Comparison of high-frequency excitations under low and high field conditions. **a** Low-field precession recorded in a weak field of 5 mT applied at an angle of 15° relative to an easy axis. Curves are taken in the 90°-state, i.e. at DC currents between I_{c1} and I_{c2} in Fig. 4b. **b** High-field precessions recorded in a saturating field of 120 mT applied along an easy or hard axis and for different DC currents as indicated. Taken from [58]

effective field of 19 mT. The estimated maximum anisotropy field contribution to the effective field is 40 mT. In contrast to FMR experiments the precession frequencies of the current-driven large-angle precessions are determined by the average over one trajectory and, thus, many different directions with respect to the crystalline axes. Therefore, the frequency shift is smaller than expected for FMR-like small-angle precessions. Figure 7b and d shows corresponding simulations of excitation in a saturating field of 120 mT. In this typical situation for current-driven magnetization dynamics, the spin-torque acts as an excitation everywhere along the trajectory and therefore leads to much larger excitation angles. The shape anisotropy flattens the precessional motion in z-direction to the so-called clamshell-type trajectory.

The observation of a steady-state precession at low external or even zero field is of importance from the application point of view, because the usual need for an external field exceeding the coercivity of the oscillating layer (see for instance the phase diagram in Fig. 9) is disadvantageous as it increases the complexity and cost of STNOs. There are different ways to circumvent the necessity of an external field. One recently presented possibility is to shape the angular dependence of the spin-transfer torque by using different magnetic materials as free and fixed layer [52]. If these provide complementary spin scattering parameters, a reversal of the sign (direction) of the spin-torque between the parallel and the antiparallel alignment of the magnetizations can be achieved. Both alignments are therefore destabilized/stabilized by the given current polarity and can cause a steady oscillatory motion at zero applied magnetic field [52]. A second possibility is to pin $\mathbf{M}_{\text{fixed}}$ in a 90° orientation with respect to the easy axis of the shape anisotropy of the free layer magnetization, i.e., the long axis of the elliptically shaped free layer [53]. In this geometry the in-plane demagnetizing field counteracts the spin-torque in such a way that no hysteretic switching, but only precessional motion of the magnetization is enabled. In our case shown in Figs. 6a and 7a, b, the role of the external field is taken by an internal field, namely

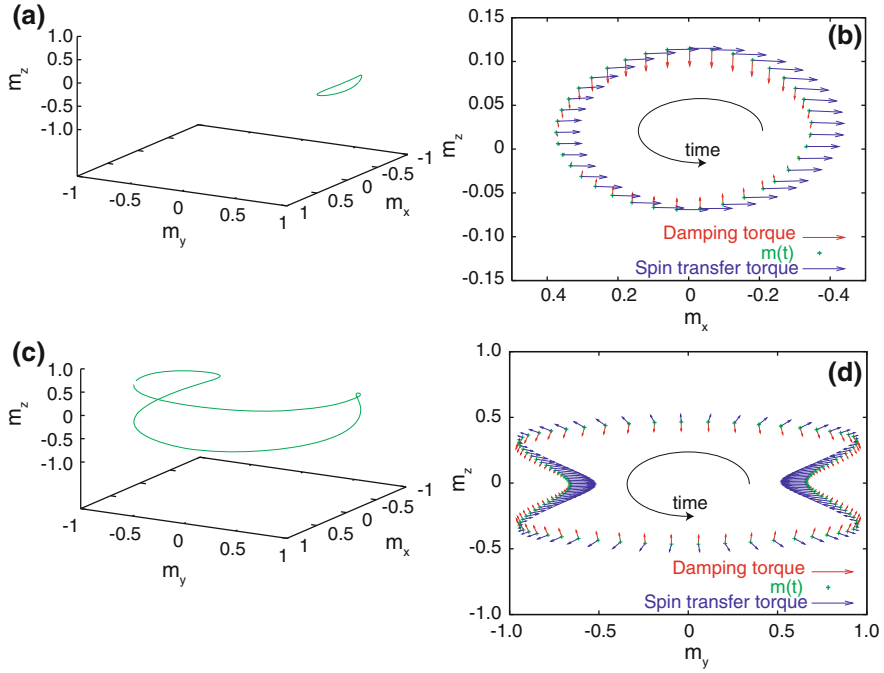

Fig. 7 Comparison of spin-torque induced excitation of low-field precession in the 90°-state (**a**, **b**) and in the saturated, parallel state (**c**, **d**) in the presence of cubic magnetocrystalline anisotropy and demagnetizing field. (**a**, **c**) Simulated trajectories and (**b**, **d**) representations of the spin-torque (*blue arrows*) and damping torque (*red arrows*) viewed along $-y$-direction (**b**) and $-x$-direction (**c**). Taken from [58]

the magnetocrystalline anisotropy field [58]. Therefore, the observation of low-field excitations in the 90°-state is—as is the case for the two-step switching process presented in Fig. 4b—a direct consequence of the interplay between magnetocrystalline anisotropy and the spin-transfer torque.

3.2 Switching Layer with Out-of-Plane Anisotropy

For switching layers with intrinsic out-of-plane anisotropy the effective anisotropy field is given by $B_{\mathrm{oop}} = B_{\mathrm{shape}} - B_{\perp} = \mu_0 M - B_{\perp}$ and the critical current [Eq. (15)] thus becomes

$$I_c^{\mathrm{P(AP)}\rightarrow\mathrm{AP(P)}} = +(-)\frac{2e}{\hbar}\frac{\alpha M V}{g(P,\eta=0(\pi))}\left[+(-)B_0 + (-)B_{\mathrm{dip}} + (\mu_0 M - B_{\perp})\right]. \tag{24}$$

This case yields the possibility to influence the effective out-of-plane anisotropy, i.e. to reduce shape anisotropy. Note that in this geometry the stray field tends to stabilize the parallel alignment of switching layer and polarizer. The thermal stability barrier is now given by $U = (MVB_{\mathrm{oop}})/2$, yielding the following critical current for switching from parallel to antiparallel alignment

$$I_c^{\mathrm{P}\to\mathrm{AP}} = \frac{2e}{\hbar}\frac{2\alpha}{g(P,\eta=0)}U. \tag{25}$$

In contrast to the in-plane case [Eq. (22)] the critical current scales linearly with U without additive term. This difference makes perpendicularly magnetized pillars attractive for applications requiring low critical current densities for switching in combination with a large thermal stability, such as MRAM memory cells.

Several studies have been performed using layers with perpendicular anisotropy to investigate spin-transfer torque, see e.g. [44, 60–66]. It is a critical issue to develop new magnetic memories based on this effect [17]. Indeed, the efficiency for magnetization reversal of a spin-valve with out-of-plane anisotropy is larger than with in-plane anisotropy. Thanks to this perpendicular anisotropy, the critical switching current can be reduced by one order of magnitude, while keeping enough thermal stability for applications [67, 68]. Figure 8 shows a current-swept measurement obtained for a nanopillar with elliptical cross section of $50 \times 300\,\mathrm{nm}^2$ based on a perpendicularly magnetized (CoNi)-multilayer as switching layer and a (magnetically harder and also perpendicularly magnetized) composite (Co/Pt)/(CoNi)-multilayer as polarizer. The DC current was swept at constant magnetic field, given by the sum of the dipolar stray field from the polarizer and the external magnetic field. One observes two distinct jumps in the resistance, which correspond to the switching from parallel (P) to antiparallel (AP) alignment or vice versa. Clearly, the switching field from the AP to the P orientation occurs for smaller current values. This is a direct consequence of the larger torque close to the AP alignment given by the function $g(P, \eta = \pi)$ (see Fig. 3b). First experiments on the (CoNi)-system revealed an average switching current density of $6.4 \times 10^7\,\mathrm{A/cm}^2$ for a $50 \times 100\,\mathrm{nm}^2$ pillar [44]. By optimizing the magnitude of the out-of-plane anisotropy, magnetization reversal for a CoNi pillar with 45 nm diameter at critical currents as low as $120\,\mu\mathrm{A}$ (corresponding to about $7 \times 10^6\,\mathrm{A/cm}^2$) was reported [67]. This shows that out-of-plane systems indeed are promising candidates for reducing the critical current for magnetization reversal. As can be already seen from the expression for the switching current [see Eq. (24)] the intrinsic anisotropy in this case reduces the overall out-of-plane anisotropy, which is given by the sum of intrinsic and shape anisotropy.

Note, that in perpendicular anisotropy structures with composite free layers it should be possible to further decrease the critical switching current while maintaining a good thermal stability [24].

In Table 1 we have given an overview about different systems that have been used in spin-torque experiments. We provide the effective out-of-plane uniaxial anisotropy energy density $K_{\mathrm{eff}} = M_S B_{\mathrm{oop}}/2 = \frac{\mu_0}{2} M_S^2 - K_\perp$, the magnetocrystalline

Table 1 Overview of material parameters and switching currents in materials used for spin-torque experiments

Material	$K_{\text{eff}}\left[\frac{\text{kJ}}{\text{m}^3}\right]$	$K_{\perp}\left[\frac{\text{kJ}}{\text{m}^3}\right]$	$M_{\text{S}}\left[\frac{\text{kA}}{\text{m}}\right]$	$U[k_B \cdot 300\text{K}]$	$I_c^{\text{AP}\rightarrow\text{P}}$[mA]	$J_c^{\text{AP}\rightarrow\text{P}}\left[10^{11}\frac{\text{A}}{\text{m}^2}\right]$	Structure	Reference
FePt-alloy	−340	1080†	1084	3×10^4 †	40*	10*(460)†	$L1_0$-structure (tetragonal)	[60]
GdFe-alloy	un (OOP)	un	un	75	7.3†	4.3	sputtered, amorphous	[71]
[CoFe/Pt] multilayer	−5†	155†	500†	100†	45	10**	polycryst. with (111) texture	[61]
[Co/Pt] multilayer	−475	586†	425	60†	5.5	6.4	polycryst. with (111) texture	[72]
[Fe/Pt] multilayer	< -3500†	>5000	1100†	60	1.6	1.1	$L1_0$-structure (tetragonal)	[73]
[Co/Ni] multilayer	−84 (OOP)†	350†	650†	45	0.12	0.7	polycryst. with (111) texture	[67]
Co	un (IP)	un	1420	250†	13	10	sputtered on Si/Cu	[5]
$Ni_{81}Fe_{19}$	260 (IP)	0	645	66	0.39	0.8	sputtered Py	[21]
$Co_{74}Gd_{26}$	un (IP)	un	0-un	un	2	2	sputtered, amorphous	[74]
$Co_2FeAl_{0.5}Si_{0.5}$	un	un	960	36	2	1.2	epitaxial (001) orientation	[75]
(Ga, Mn)As	un	un	32	52(520)†	0.8	0.02	epitaxial MTJ $T_C = 50\text{K}$	[20]

Data was either taken from cited references or calculated from data given in the references (†). Listed are materials with magnetic moments perpendicular to the sample plane (OOP) and with an in-plane magnetization (IP). Unknown parameters are marked with the letters 'un'

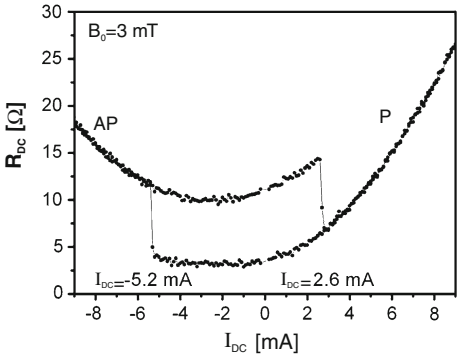

Fig. 8 Current-swept measurement on an elliptical 50 $\times$ 300 nm^2 nanopillar system with free layer based on a (Co/Ni)-multilayer exhibiting out-of-plane easy axis of magnetization. Taken from [76]

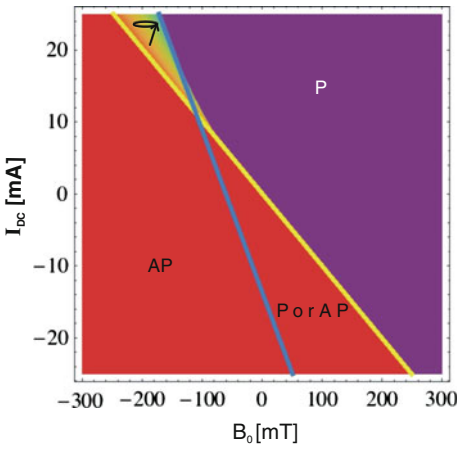

Fig. 9 Theoretical I_{DC}/B_0 phase diagram calculated for an elliptical 50 $\times$ 300 nm^2 nanopillar system with free layer based on a (Co/Ni)-multilayer exhibiting out-of-plane easy axis of magnetization. For the calculations an uniaxial macrospin model at $T = 0$ was assumed [76]

out-of-plane anisotropy energy density $K_\perp$, the magnetization M_S, the critical switching currents $I_c^{AP\to P}$ and current densities $J_c^{AP\to P}$ as well as the stability barriers U.

3.2.1 Theoretical I_{DC}/B_0 Phase Diagram

A useful plot to get an overview about stable configurations of a spin-torque system is provided by the I_{DC}/B_0 phase diagram which can be derived from solving the LLG equation. Such theoretical phase diagrams have been described in the literature by different methods [44, 69, 70]. Figure 9 shows an example of a calculated phase diagram of an elliptical 50 $\times$ 300 nm^2 nanopillar with perpendicular anisotropy. The magnetically hard layer acting as a spin polarizer is given by a (Co/Pt)/(Co/Ni)-multilayer, while the free (switching) layer is a (Co/Ni)-multilayer. Both layers are separated from each other by a copper spacer layer. For details on the (Co/Ni) system we refer to [44].

The calculated I_{DC}/B_0 phase diagram (see [76] for details) clearly shows regions for which the parallel (antiparallel) alignment (labelled P and AP, respectively) being the stable configuration. In this case positive (negative) currents stabilize parallel (antiparallel) alignment of polarizer and free layer. Since the spin-transfer torque is more efficient in the antiparallel configuration than in the parallel one, the slopes of the two borders, which depend on the efficiency function $g(P, \eta)$ see (Sect. 2.5) are different [76]. Note, that the stray field originating from the perpendicular polarizer and acting on the free layer as additive field $\mathbf{B}_{\text{dip}}$ has been included in the calculation and shifts the whole phase diagram towards negative fields. This can be seen when looking to the switching fields for the field hysteresis at $I_{DC} = 0$ for which the stray field leads to a shift towards negative magnetic field values by about 30 mT. For positive currents (which according to the definition in [76] refer to electrons flowing from the polarizer to the free layer) and negative fields a precessional state is expected in the macrospin approximation, which was assumed for the calculations.

3.2.2 Experimental I_{DC}/B_0 Phase Diagram

While Fig. 9 showed the *calculated* I_{DC}/B_0 phase diagram of an elliptical 50 × 300 nm^2 nanopillar spin-valve, in Fig. 10 the *measured* phase diagram is plotted. The three experimental curves shown around the phase diagram in Fig. 10 represent measurements along the respective solid lines. A useful way to present a state diagram is to plot the half sum of resistances between the increasing and the decreasing parts of the hysteresis loop, that is to say $R_{sum}(B_0) = 1/2[R_{inc}(B_0) + R_{dec}(B_0)]$. This method transforms the hysteresis loop into a step curve where each step corresponds to a specific region of the phase diagram. State diagrams obtained from the half sum highlight non-hysteretic behavior as the one obtained in the high field and current regions. Note that the measurements were recorded at constant DC current while the external magnetic field was swept. These field-swept measurements have the advantage of not producing a parabolic background signal, which is present in the current-swept measurements due to Joule heating (see Fig. 8). There are lots of similarities between the theoretical state diagram shown in Fig. 9 and the experimental result. Both of them are composed of two borders dividing the (I_{DC}, B_0) plane into four regions. At high positive fields and currents, the spin-valve is in the parallel state, whereas at high negative fields and currents it is in the antiparallel state. At high positive fields and negative currents, it can be either parallel or antiparallel, this is the bistable region characterized by hysteresis loops. Finally, at high negative fields and positive currents it is neither parallel nor antiparallel. When the two borders cross, the hysteresis loops give rise to series of peaks or dips in the differential resistance $R_{\text{AC}} = \mathrm{d}U/\mathrm{d}I$ in the experimental phase diagrams. The differential resistance can be detected by measuring the response of the system to the DC current on top of which an AC current with small amplitude is added by means of a Lock-in amplifier. In general the voltage drop across the nanopillar is a function of the resistance and the current, i.e. $U = U(R_{\text{DC}}, I)$. The differential resistance thus is given by

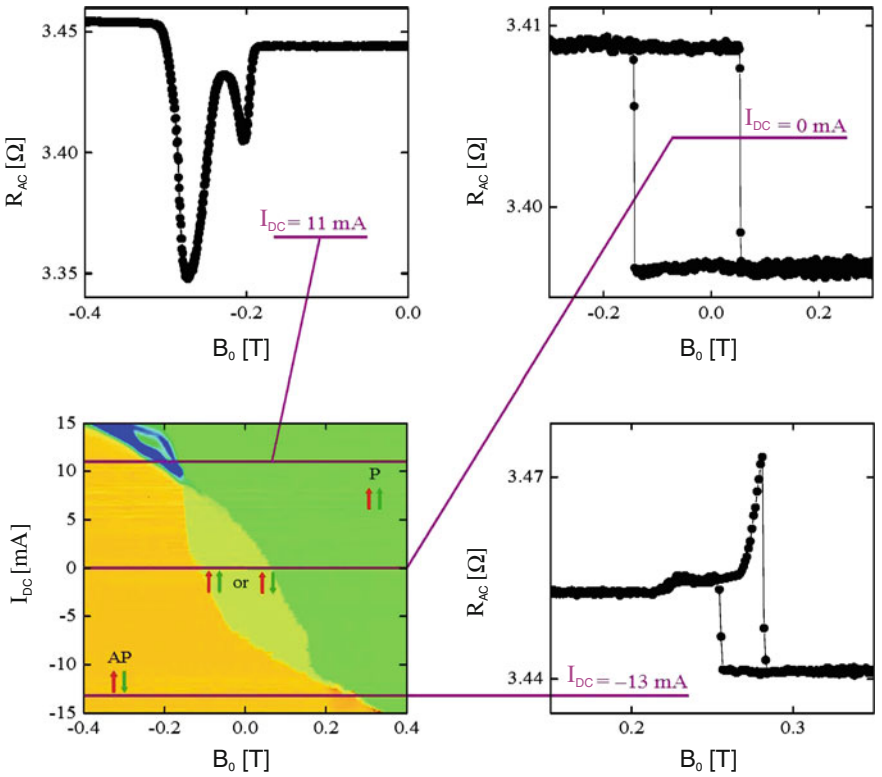

Fig. 10 Experimentally measured I_{DC}/B_0 phase diagram of an elliptical $50 \times 300\,\mathrm{nm}^2$ nanopillar spin-valve with a hard layer made of (Co/Pt)/(Co/Ni) and a free layer made of (Co/Ni) obtained from the half sum method ($R_{sum}(B_0) = 1/2[R_{inc}(B_0) + R_{dec}(B_0)]$, see also explanation in the text) along with three characteristic hysteresis loops at $I_{DC} = -13\,\mathrm{mA}$, $I_{DC} = 0\,\mathrm{mA}$ and $I_{DC} = 11\,\mathrm{mA}$

$$\frac{\mathrm{d}U}{\mathrm{d}I} = R_{\mathrm{DC}} + I \cdot \frac{\mathrm{d}R_{\mathrm{DC}}}{\mathrm{d}I} \tag{26}$$

Assuming that the system is ohmic such that $\mathrm{d}R_{\mathrm{DC}}/\mathrm{d}I = 0$, then $\mathrm{d}U/\mathrm{d}I = R_{\mathrm{DC}}$. If, however, there are current-induced changes in the resistance that are reversible with the AC current, we need to include the second term, $I\mathrm{d}R_{\mathrm{DC}}/\mathrm{d}I$, in $\mathrm{d}U/\mathrm{d}I = R_{\mathrm{DC}}$. This second term can add or subtract to R_{DC} depending on the sign of the slope of $\mathrm{d}R_{\mathrm{DC}}/\mathrm{d}I$ at $I = 0$ and the sign of I. Thus, peaks and dips observed in the phase diagramm are compatible with magnetization precessions as predicted by theory (see the theoretical phase diagram of Fig. 9 and Ref. [77]). One should note that besides using Lock-In detection of the differential resistance such precessions in spin-valves are commonly recorded with at least one magnetization in-plane because they generate an alternating voltage thanks to the angular dependence of the giant magnetoresistance. However, in *all perpendicular* spin-valves, a uniform precession

of the magnetization of the free layer around the out-of-plane axis does not affect the angle between the magnetizations of the free layer and of the polarizer. As a consequence, no alternating voltage is generated in first approximation, so that in this case the precessions have to be detected indirectly by means of differential measurements and Lock-in technique [44]. It should, however, be noted that these methods cannot guarantee that every measured peak is a consequence of magnetization precession. Note, that a method using GHz microwave irradiation has been developed to enhance and detect spin-torque driven magnetization precession in nanopillars with magnetic perpendicular anisotropy [76].

The borders determined by the switching fields or currents evolve linearly in a large range of current and field, however around the zero current switching fields a strong deviation from this linearity occurs. Experimentally it seems that the magnetization reversal becomes virtually independent of the injected current around these two fields and the current has to reach a critical value before the linear evolution appears. This observation seems paradoxical contrary to the theoretical predictions because the spin-transfer effect is expected to always modify the damping by increasing or decreasing the impact of the damping torque. The experimental state diagrams in this perpendicular geometry are actually much closer to the state diagrams in the planar geometry, see [70, 78–81]. It has been shown that this discrepancy is mainly due to a break in the uniaxial symmetry [82]. Indeed, it shows that above a critical angle of application of the magnetic field, the injected current has no impact on the magnetization reversal [83].

Nevertheless, it is clear that non-uniform magnetization reversal plays an important role in the magnetization reversal processes. Indeed, it was shown that the formation of domains and domain walls could be observed even for nanopillars as small as $50 \times 100\ \mathrm{nm}^2$ [84–86].

3.2.3 Magnetization Dynamics

Magnetization reversal dynamics has also been studied in samples with perpendicular anisotropy. Perpendicular anisotropy was shown to influence the fast dynamics, see [87, 88], as well as the slow magnetization switching dynamics. The reversal dynamics was determined by measuring the switching probability P as a function of time for a $50 \times 100\ \mathrm{nm}^2$ square (Co/Pt)/(Co/Ni)-(Co/Ni)-nanopillar exhibiting perpendicular anisotropy. Current pulses of variable amplitude and duration have been applied and the sample state was determined by measuring the device resistance using an AC-current. The same pulse amplitude and duration was repeated 100 to 10,000 times to determine the switching probability. Figure 11 shows the switching behavior from the antiparallel to the parallel state over nine orders of magnitude in current pulse duration. The pulse amplitude I for $P = 0.5$ corresponding to the observation of switching for half of the events is plotted versus pulse duration τ on a logarithmic scale. For short pulse durations ($\tau < 10\,\mathrm{ns}$) the pulse amplitude required to switch the nanomagnet increases dramatically. For long pulses the pulse amplitude depends weakly on pulse duration, varying logarithmically for $\tau > 10\,\mu\mathrm{s}$.

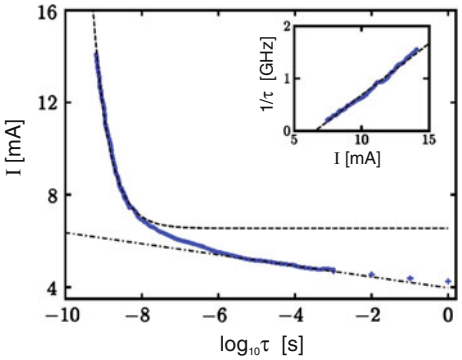

Fig. 11 Pulse switching results for pulses of duration 0.3 ns to 1 s: Pulse amplitude for P=0.5 vs pulse duration measured for a 50 × 100 nm^2 square (Co/Pt)/(Co/Ni)-(Co/Ni)-nanopillar with perpendicular anisotropy. Inset: switching rate $1/\tau$ vs pulse amplitude for short pulses showing behavior $\propto (I - I_{c0})$. The intercept at $1/\tau = 0$ is I_{c0}. The dashed line in the main figure shows this behavior on a logarithmic scale. The dash-dotted line is a fit to the long-time data using Eq. (27). Taken from [88]

The short- and long-time switching characteristics are thus quite distinct. The inset of Fig. 11 shows $1/\tau$ plotted versus pulse amplitude at short pulse durations. This regime follows the form $1/\tau = A(I - I_{c0})$, which is expected based on the conservation of angular momentum [89]. The zero temperature critical current I_{c0} in this expression reflects the portion of the spin-angular momentum that is needed to overcome the magnetization damping. The dashed line in the main part of Fig. 11 shows this same fit to the short-time data on a logarithmic pulse duration scale, showing that this form describes the data up to pulse durations of 5 ns. At longer times the switching boundary was fit (dash-dotted line) to the form given in [90, 91]

$$I = I_{c0}\left[1 - \frac{k_B T}{U_0} \ln\left(\frac{\tau}{\tau_0 \ln(1-P)}\right)\right] \tag{27}$$

where U_0 is the energy barrier in the absence of the spin current. And τ_0 is the Arrhenius prefactor. This expression fits the data for $\tau > 6\,\mu$s well, as seen by the dashed-dotted line in Fig. 11. The slope of the curve gives the ratio $U_0/k_B T = 63$ and the intercept of this curve with I_{c0} yields the Arrhenius prefactor, $\tau_0 = 24$ ps. Figure 11 also shows that at intermediate time scales, from 10 ns to 6 μs, the switching boundary follows neither the short- or long-time forms, i.e., this is a crossover regime.

The results demonstrate that there is an optimal pulse length that minimizes the energy required to reverse the magnetization. Non-uniform magnetization is found to play an important role in the switching dynamics. Time-resolved scanning transmission X-ray microscopy measurements were performed to study the current induced magnetization switching mechanism. Direct imaging of the magnetization demonstrates that, after an incubation time of about 1 ns, an ellipsoidal device switches via domain nucleation and propagation. Domain-wall velocities on the order of 100 m/s

were reported [92]. In the thermally activated regime domain walls nucleate and propagate leading to telegraph noise that may be studied in the light of the Néel-Brown model [93].

4 Conclusions

We have discussed spin-transfer torque effects in nanopillars. The transfer of spin angular momentum from a spin-polarized current to the local magnetization is described by an additional torque acting on the magnetization, which has to be taken into account when solving (in the macrospin approximation or in full-scale micromagnetic simulations) the equation of motion of the magnetization (Landau-Lifshitz-Gilbert equation) to describe current-driven magnetization dynamics. Magnetic anisotropies of various origins (shape, magnetocrystalline, interface) enter this term on equal footing with the external field and, thus, have a strong influence on the current-driven magnetization dynamics.

For current-induced magnetization switching the critical current densities strongly depend on the total anisotropy, which favors either the in-plane or out-of-plane orientation of the static magnetization of the free layer. In terms of the application of spin-transfer torque as a writing scheme in MRAM cells, the perpendicular magnetized switching layer yields the better combination of low switching current and high thermal stability.

For current-driven magnetization excitations the shape and symmetry of the total anisotropy function determine the excitation trajectories, which can involve large excitation angles and thus strongly deviate from simple circles, in clear contrast to the small angle precessions in FMR. Anisotropies with higher symmetry enable fundamental studies addressing the angular dependence of the spin-torque efficiency function $g(\eta)$, e.g. the determination of the spin-torque asymmetry parameter Λ. Furthermore, they allow for steady magnetization oscillations in zero external field, which is a favorable condition for the application of spin-transfer torque in STNOs.

Acknowledgments We thank all our former and present coworkers who have contributed to the results presented here. This work was supported by the DFG, SFB 491, in parts by the Friends contract of the French National Research Agency (ANR) and by the NSF Award #1008654.

Appendix

In the following we show that Eq. (13) and Eq. (16) are indeed eqvivalent. We start from Eq. (13),

$$\frac{\mathrm{d}\mathbf{M}}{\mathrm{d}t} = -|\gamma|\,\mathbf{M}\times\mathbf{B}_{\mathrm{eff}} + \frac{\alpha}{M}\mathbf{M}\times\frac{\mathrm{d}\mathbf{M}}{\mathrm{d}t} - |\gamma|\,\frac{a_J}{M}\mathbf{M}\times\left(\mathbf{M}\times\mathbf{m}_p\right). \qquad (28)$$

Inserting $\mathrm{d}\mathbf{M}/\mathrm{d}t$ on the right hand side yields:

$$\frac{\mathrm{d}\mathbf{M}}{\mathrm{d}t} = -|\gamma|\,\mathbf{M}\times\mathbf{B}_{\mathrm{eff}} - |\gamma|\,\frac{a_J}{M}\mathbf{M}\times\left(\mathbf{M}\times\mathbf{m}_p\right) + \frac{\alpha}{M}\mathbf{M} \times\left[-|\gamma|\,\mathbf{M}\times\mathbf{B}_{\mathrm{eff}} + \frac{\alpha}{M}\mathbf{M}\times\frac{\mathrm{d}\mathbf{M}}{\mathrm{d}t} - |\gamma|\,\frac{a_J}{M}\mathbf{M}\times\left(\mathbf{M}\times\mathbf{m}_p\right)\right]. \quad (29)$$

Using the relation $\mathbf{a}\times(\mathbf{b}\times\mathbf{c}) = \mathbf{b}(\mathbf{a}\cdot\mathbf{c}) - \mathbf{c}(\mathbf{a}\cdot\mathbf{b})$ and considering that $\mathbf{M}\perp\dot{\mathbf{M}}$ one easily derives

$$\begin{aligned}\mathbf{M}\times\left(\mathbf{M}\times\frac{\mathrm{d}\mathbf{M}}{\mathrm{d}t}\right) &= \mathbf{M}\left(\mathbf{M}\cdot\frac{\mathrm{d}\mathbf{M}}{\mathrm{d}t}\right) - \frac{\mathrm{d}\mathbf{M}}{\mathrm{d}t}\cdot\mathbf{M}^2 = -\frac{\mathrm{d}\mathbf{M}}{\mathrm{d}t}\cdot M^2\\ \mathbf{M}\times\left(\mathbf{M}\times\mathbf{m}_p\right) &= \mathbf{M}\left(\mathbf{M}\cdot\mathbf{m}_p\right) - \mathbf{m}_p\cdot M^2\\ \mathbf{M}\times\left[\mathbf{M}\times\left(\mathbf{M}\times\mathbf{m}_p\right)\right] &= -\mathbf{M}\times\mathbf{m}_p\cdot M^2. \end{aligned} \quad (30)$$

This in turn yields:

$$\frac{\mathrm{d}\mathbf{M}}{\mathrm{d}t} = -|\gamma|\,\mathbf{M}\times\mathbf{B}_{\mathrm{eff}} - |\gamma|\,\frac{\alpha}{M}\mathbf{M}\times(\mathbf{M}\times\mathbf{B}_{\mathrm{eff}}) - \alpha^2\frac{\mathrm{d}\mathbf{M}}{\mathrm{d}t} + |\gamma|\,\alpha a_J\mathbf{M}\times\mathbf{m}_p - |\gamma|\,\frac{a_J}{M}\mathbf{M}\times\left(\mathbf{M}\times\mathbf{m}_p\right). \quad (31)$$

Reorganizing the terms finally leads to

$$\frac{1}{|\gamma|}\frac{\mathrm{d}\mathbf{M}}{\mathrm{d}t} = -A\cdot\mathbf{M}\times\left(\mathbf{B}_{\mathrm{eff}} - \alpha a_J\mathbf{m}_p\right) - A\cdot\frac{\mathbf{M}}{M}\times\left[\mathbf{M}\times\left(\alpha\mathbf{B}_{\mathrm{eff}} + a_J\mathbf{m}_p\right)\right], \quad (32)$$

which is Eq. (16).

References

1. L. Berger, J. Appl. Phys. **50**, 2137 (1979)
2. P.P. Freitas, L. Berger, J. Appl. Phys. **57**, 1266 (1985)
3. J.C. Slonczewski, J. Magn. Magn. Mater. **159**, L1 (1996)
4. L. Berger, Phys. Rev. B **54**, 9353 (1996)
5. J.A. Katine, F.J. Albert, R.A. Buhrman, E.B. Myers, D.C. Ralph, Phys. Rev. Lett. **84**, 3149 (2000)
6. M.D. Stiles, J. Miltat, in Spin Dynamics in Confined Magnetic Structures III, ed. by B. Hillebrands, A. Thiaville. Topics in Applied Physics, vol 101 (Springer, Berlin, 2006), p. 225
7. D.C. Ralph, M.D. Stiles, Series of review articles. J. Magn. Magn. Mater. **320**, 1190 (2008)
8. J.A. Katine, E.E. Fullerton, ibid, p. 1217
9. J.Z. Sun, D.C. Ralph, ibid, p. 1227
10. D.V. Berkov, J. Miltat, ibid, p. 1238

11. T.J. Silva, W.H. Rippard, ibid, p. 1260
12. G.S.D. Beach, M. Tsoi, J.L. Erskine, ibid, p. 1272
13. Y. Tserkovnyak, A. Brataas, G.E.W. Bauer, ibid, p. 1282
14. H. Ohno, T. Dietl, ibid, p. 1293
15. P.M. Haney, R.A. Duine, A.S.Núñez, A.H. MacDonald, ibid, p. 1300
16. C.H. Marrows, Adv. Phys. **54**, 585 (2005)
17. J.A. Katine, E.E. Fullerton, J. Magn. Magn. Mater. **320**, 1217 (2008)
18. D.C. Ralph, M.D. Stiles, J. Magn. Magn. Mater. **320**, 1190 (2008)
19. K. Inomata, IEICE Trans. Electron. E**84C**, 740 (2001)
20. D. Chiba, Y. Sato, T. Kita, F. Matsukura, H. Ohno, Phys. Rev. Lett. **93**, 216602 (2004)
21. P.M. Braganca, I.N. Krivorotov, O. Ozatay, A.G.F. Garcia, N.C. Emley, J.C. Sankey, D.C. Ralph, R.A. Buhrman, Appl. Phys. Lett. **87**, 112507 (2005)
22. O. Ozatay, P.G. Gowtham, K.W. Tan, J.C. Read, K.A. Mkhoyan, M.G. Thomas, G.D. Fuchs, P.M. Braganca, E.M. Ryan, K.V. Thadani, J. Silcox, D.C. Ralph, R.A. Buhrman, Nat. Mater. **7**, 567 (2008)
23. J. Lindner, Superlattices Microstruct. **47**, 497 (2010)
24. I. Yulaev, M. Lubarda, S. Mangin, V. Lomakin, E.E. Fullerton Appl, Phys. Lett. **99**, 132502 (2011)
25. M. AlHajDarwish, H. Kurt, S. Urazhdin, A. Fert, R. Loloee, W.P. Pratt Jr, J. Bass, Phys. Rev. Lett. **93**, 157203 (2004)
26. H. Dassow, R. Lehndorff, D.E. Bürgler, M. Buchmeier, P.A. Grünberg, C.M. Schneider, A. van der Hart, Appl. Phys. Lett. **89**, 222511 (2006)
27. T. Valet, A. Fert, Phys. Rev. B **48**, 7099 (1993)
28. R. Meservey, P.M. Tedrow, Phys. Rep. **238**, 174 (1994)
29. T. Taniguchi, S. Yakata, H. Imamura, Y. Ando, Appl. Phys. Express **1**, 031302 (2008)
30. T. Kimura, J. Hamrle, Y. Otani, Phys. Rev. B **72**, 014461 (2005)
31. M. Gmitra, J. Barnas. Phys. Rev. Lett. **96**, 207205 (2006)
32. M.D. Stiles, A. Zangwill, Phys. Rev. B **66**, 014407 (2002)
33. W.H. Butler, X.-G. Zhang, T.C. Schulthess, J.M. MacLaren, Phys. Rev. B **63**, 054416 (2001)
34. J. Mathon, A. Umerski, Phys. Rev. B **63**, 220403 (2001)
35. J.C. Slonczewski, Phys. Rev. B **39**, 6995 (1989)
36. T. Yang, T. Kimura, Y. Otani, Nat. Phys. **4**, 851 (2008)
37. S. Zhang, P.M. Levy, A. Fert, Phys. Rev. Lett. **88**, 236601 (2002)
38. M.D. Stiles, W.M. Saslow, M.J. Donahue, A. Zangwill, Phys. Rev. B **75**, 214423 (2007)
39. R. Lehndorff, D.E. Bürgler, A. Kakay, R. Hertel, C.M. Schneider, IEEE Trans. Mag. **44**, 1951 (2008)
40. E. Martinez, L. Torres, L. Lopez-Diaz, M. Carpentieri, G. Finocchio, J. Appl. Phys. **97**, 10E302 (2005)
41. M. Tsoi, A.G.M. Jansen, J. Bass, W-C. Chiang, M. Seck, V. Tsoi, P. Wyder, Phys. Rev. Lett. **80**, (1998)
42. S.I. Kiselev, J.C. Sankey, I.N. Krivorotov, N.E. Emley, R.J. Schoelkopf, R.A. Buhrman, D.C. Ralph, Nature **425**, 380 (2003)
43. W.H. Rippard, M.R. Pufall, S. Kaka, S.E. Russek, T.J. Silva, Phys. Rev. Lett. **92**, 027201 (2004)
44. S. Mangin, D. Ravelosona, J.A. Katine, M.J. Carey, B.D. Terris, E.E. Fullerton, Nat. Mater. **5**, 210 (2006)
45. S. Bonetti, P. Muduli, F. Mancoff, J. Åkerman, Appl. Phys. Lett. **94**, 102507 (2009)
46. Haiwen Xi, Kai-Zhong Gao, Yiming Shi, Appl. Phys. Lett. **84**, 4977 (2004)
47. A. Slavin, V. Tiberkevich, IEEE Trans. Magn. **45**, 1875 (2009)
48. J. Xiao, A. Zangwill, M.D. Stiles, Phys. Rev. B **70**, 172405 (2004)
49. J.C. Slonczewski, J. Magn. Magn. Mater. **247**, 324 (2002)
50. L. Berger, J. Appl. Phys. **89**, 5521 (2001)
51. M.D. Stiles, J. Xiao, A. Zangwill, Phys. Rev B **69**, 54408 (2004)

52. O. Boulle, V. Cros, J. Grollier, L.G. Pereira, C. Deranlot, F. Petroff, G. Faini, J. Barnas, A. Fert, Nat. Phys. **3**, 492 (2007)
53. T. Devolder, A. Meftah, K. Ito, J.A. Katine, P. Crozat, C. Chappert, J. Appl. Phys. **101**, 063916 (2007)
54. Y. Jiang, T. Nizake, S. Abe, T. Ochiai, A. Hirohata, N. Tezuka, K. Inomata, Nat. Mater. **3**, 361 (2004)
55. Y. Jiang, S. Abe, T. Ochiai, T. Nozaki, A. Hirohata, N. Tezuka, K. Inomata, Phys. Rev. Lett. **92**, 167204 (2004)
56. Hoang Yen Thi Nguyen, Hyunjung Yi, Sung-Jung Joo, Kyung-Ho Shin, Kyung-Jin Lee, Bernard Dieny, Appl. Phys. Lett. **89**, 094103 (2006)
57. R. Lehndorff, D.E. Bürgler, A. Kakay, R. Hertel, C.M. Schneider, Phys. Rev. B **76**, 214420 (2007)
58. R. Lehndorff, D.E. Bürgler, A. Kakay, R. Hertel, C.M. Schneider, IEEE Trans. Magn. **44**, 1951 (2008)
59. M.D. Stiles, D.R. Penn, Phys. Rev. B **61**, 3200 (2000)
60. T. Seki, S. Mitani, K. Yakushiji, K. Takanashi, Appl. Phys. Lett. **88**, 172504 (2006)
61. H. Meng, J.P. Wang Appl, Phys. Lett. **88**, 172506 (2006)
62. A. Kent, B. Ozyilmaz, E. del Barco, Appl. Phys. Lett. **84**, 3897 (2004)
63. A.D. Kent, Nat. Mater. **6**, 399 (2007)
64. K.J. Lee, O. Redon, B. Dieny, Appl. Phys. Lett. **86**, 022505 (2005)
65. D. Houssameddine, U. Ebels, B. Delaët, B. Rodmacq, I. Firastrau, F. Ponthenier, M. Brunet, C. Thirion, J.-P. Michel, L. Prejbeanu-Buda, M.-C. Cyrille, O. Redon, B. Dieny, Nat. Mater. **6**, 447 (2007)
66. Y. Zhou, J. Åkerman, Appl. Phys. Lett. **94**, 112503 (2009)
67. S. Mangin, Y. Henry, D. Ravelosona, J.A. Katine, E.E. Fullerton, Appl. Phys. Lett. **94**, 012502 (2009)
68. H. Yoda, T. Kishi, T. Nagase, M. Yoshikawa, K. Nishiyama, E. Kitagawa, T. Daibou, M. Amano, N. Shimomura., S. Takahashi, T. Kai, M. Nakayama, H. Aikawa, S. Ikegawa, M. Nagamine, J. Ozeki, S. Mizukami, M. Oogane, Y. Ando, S. Yuasa, K. Yakushiji, H. Kubota, Y. Suzuki, Y. Nakatani, T. Miyazaki, K. Ando. Curr. Appl. Phys. **10**, e87 (2010)
69. Y.B. Bazaliy, B.A. Jones, S.C. Zhang, J. Appl. Phys. **89**, 6793 (2001)
70. Y.B. Bazaliy, B.A. Jones, S.C. Zhang, Phys. Rev. B **69**, 094421 (2004)
71. K. Aoshima, N. Funabashi, K. Machida, Y. Miyamoto, N. Kawamura, K. Kuga, N. Shimidzu, T. Kimura, Y. Otani, F. Sato, IEEE Trans. Magn. **44**, 2491 (2008)
72. J.H. Park, M.T. Moneck, C. Park, J.G. Zhu, J. Appl. Phys. 105, 07D129 (2009)
73. Y.S. Yuasa, T. Nagahama, A. Fukushima, H. Kubota, T. Katayama, K. Ando, Appl. Phys. Express **1**, 041302 (2008)
74. X. Jiang, L. Gao, J.Z. Sun, S.S.P. Parkin, Phys. Rev. Lett. **97**, 217202 (2006)
75. H. Sukegawa, S. Kasai, T. Furubayashi, S. Mitani, K. Inomata, Appl. Phys. Lett. **96**, 042508 (2010)
76. N. Reckers, J. Cucchiara, O. Posth, C. Hassel, F.M. Römer, R. Narkowicz, R.A. Gallardo, P. Landeros, H. Zähres, S. Mangin, J.A. Katine, E.E. Fullerton, G. Dumpich, R. Meckenstock, J. Lindner, M. Farle, Phys. Rev. B **83**, 184427 (2011)
77. W. Lin, J. Cucchiara, C. Berthelot, T. Hauet, Y. Henry, J.A. Katine, E.E. Fullerton, S. Mangin, Appl. Phys. Lett **96**, 252503 (2010)
78. S.I. Kiselev, J.C. Sankey, I.N. Krivorotov, N.C. Emley, R.J. Schoelkopf, R.A. Buhrman, D.C. Ralph, Nature **425**, 380 (2003)
79. J. Grollier, V. Cros, A. Hamzi, J.M. Georges, G. Faini, J. Ben Youssef, H. Le Gall, A. Fert, Phys. Rev. B **67**, 174402 (2003)
80. H. Morise, S. Nakamura, Phys. Rev. B **71**, 014439 (2005)
81. J. Xiao, A. Zangwill, M.D. Stiles, Phys. Rev. B **72**, 014446 (2005)
82. J. Cucchiara, E.E. Fullerton, A.D. Kent, J.Z. Sun, Y. Henry, S. Mangin, Phys. Rev. B **84**, 100405 (2011)
83. Y. Henry, S. Mangin, J. Cucchiara, J.A. Katine, E.E Fullerton, Phys. Rev. B **79**, 214422 (2009)

84. D. Ravelosona, S. Mangin, Y. Lemaho, J. Katine, B. Terris, E.E. Fullerton, Phys. Rev. Lett. **96**, 186604 (2006)
85. D. Ravelosona, S. Mangin, J.A. Katine, E.E. Fullerton, B.D. Terris, Appl. Phys. Lett. **90**, 072508 (2007)
86. C. Burrowes, D. Ravelosona, C. Chappert, S. Mangin, E.E. Fullerton, J.A. Katine, B.D. Terris, Appl. Phys. Lett **93**, 172513 (2008)
87. D. Bedau, H. Liu, J-J. Bouzaglou, A.D. Kent J.Z. Sun, J.A. Katine, E.E Fullerton, S. Mangin, Appl. Phys. Lett **96**, 022514 (2010)
88. D. Bedau, H. Liu, J.Z. Sun, J.A. Katine, E.E. Fullerton, S. Mangin, A.D. Kent, Appl. Phys. Lett **97**, 262502 (2010)
89. J.Z. Sun, Phys. Rev. B **62**, 570 (2000)
90. Z. Li, S. Zhang, Phys. Rev. B **69**, 134416 (2004)
91. M. Apalkov, P.B. Visscher, Phys. Rev. B **72**, 180405 (2005)
92. D.P. Bernstein, B. Bräuer, R. Kukreja, J. Stöhr, T. Hauet, J. Cucchiara, S. Mangin, J.A. Katine, T. Tyliszczak, K.W. Chou, Y. Acremann, Phys. Rev. B **83**, 180410 (2011)
93. J. Cucchiara, Y. Henry, D. Ravelosona, D. Lacour, E.E. Fullerton, J.A. Katine, S. Mangin, Appl. Phys. Lett **94**, 102503 (2009)

Spin Dynamics in the Time and Frequency Domain

Michael Farle, Tom Silva and Georg Woltersdorf

Abstract The current status of experimental approaches to analyze the spin wave dynamics in ferromagnetic nanoscale structures is reviewed. Recent developments in frequency- and field swept spectroscopy to determine the resonant response of nanoscale ferromagnets are described together with time-resolved measurements in the GHz frequency and pico second time domain, respectively. Examples for the analysis and manipulation of different mechanisms for the relaxation of the magnetization after microwave excitation into its ground state are presented.

1 Introduction

Dynamics (from Greek—dynamikos "powerful") in general refers to the time evolution of physical properties. In magnetism the term "spin dynamics" refers to the time evolution of the static macroscopic magnetization after thermal, electromagnetic (e.g. microwave) or matter wave/particle (e.g. neutron, electron or phonon) excitations. As the magnetization is the vector sum of all atomic magnetic moments—each containing an orbital and spin magnetic moment—(neglecting here the small nuclear magnetic moment which however is easily detected in magnetic resonance

M. Farle (✉)
Fakultät für Physik and Center for NanoIntegration Duisburg-Essen (CENIDE),
Universität Duisburg-Essen, Lotharstr. 1, 47057 Duisburg, Germany
e-mail: farle@uni-due.de

T. Silva
National Institute of Standards and Technology, Boulder, Colorado, USA
e-mail: silva@boulder.nist.gov

G. Woltersdorf
Department of Physics/ Magnetism Group, Universität Regensburg,
Universitätsstraße 31, 93040 Regensburg, Germany
e-mail: georg.woltersdorf@ur.de

H. Zabel and M. Farle (eds.), *Magnetic Nanostructures,*
Springer Tracts in Modern Physics 246, DOI: 10.1007/978-3-642-32042-2_2,

experiments, see for example [1]), one has to keep in mind that *orbital* dynamics which couples the spin moment to the crystal lattice is an important ingredient in spin dynamics. The orbital contribution is often hidden in a so-called effective spin model [2] or neglected due to its small contribution ($<10\,\%$) to the overall magnetization for example in 3d ferromagnets. In nanoscale structures, however, the contribution of orbital magnetism to spin dynamics may become important due to the increased percentage of magnetic moments which are located at surfaces and interfaces where they experience a low-symmetry electrostatic potential (crystal field) causing an enhanced orbital magnetic moment. Here, we will restrict our discussion to the model of effective spins or effective magnetization, respectively.

This chapter is organized as follows. We will begin with a short reminder on at first sight different manifestations of "spin dynamics" in ferromagnetic materials followed by a short overview of experimental techniques to record ferromagnetic resonance phenomena in materials with sub-micron dimensions. Magnetoresistive, microwave resonance, and optical detection schemes will be presented in a more detailed form in respective sections. This experimental part is preceded by a general discussion of the current understanding of how a magnetization relaxes to its ground state after resonant microwave or spin current excitation.

In spin dynamics—like in any other type of time evolution of a physical quantity—one has to consider the magnetic response in relation to the type (i.e. vector or scalar), amplitude and energy spectrum of the excitation as well as the relaxation rates and likely different dissipation channels allowing the stored energy to dissipate to the lattice. A wide energetic range of excitations produced by time varying magnetic fields has been investigated in the frequency and time domain of spin dynamics. Depending on the amplitude of the excitation linear- and non-linear magnetic responses which are described by the field- and frequency-dependent magnetic susceptibility tensor χ can be monitored. The phenomena can be subdivided into ultrafast magnetization processes (few tens to hundreds of femtoseconds) and processes evolving on the ps to ns timescale [3]. We will restrict our discussion to the later, that is resonant processes at $1 - 100\,\mathrm{GHz}$ frequencies.

The temperature dependence of the magnetization is governed by the thermally excited energy spectrum of elementary excitations of the magnetization called spin waves or magnons [4]—which are always present at finite temperatures (at 295 K there are app. $10^{21}-10^{22}$ cm^{-3} magnons). Spin waves follow dispersion relations [5] which depend on crystallographic orientation, size and shape of the ferromagnet [6, 7]. The dispersion relations for the spin wave vector ($\mathbf{q}$) covering momentum transfers over the full Brillouin zone and the energy range from μeV to several tens of meV (Stoner excitations), or that is in wavelength covering the range of tens of micrometers to nearest neighbor atomic distances, have been confirmed by experimental techniques like Brillouin Light Scattering (BLS) (see for example [8]), inelastic neutron scattering and energy loss spectrocopy (see for example [9]).

The term spin dynamics also covers the research areas of thermally induced "spin fluctuations" and "spin excitations" which for example become visible in the temperature dependence of the interlayer exchange coupling of two ferromagnetic layers coupled across a normal metal spacer layer like Cu [10], the temperature

dependence of the macroscopic magnetic anisotropy energy density (MAE) or at the para-ferromagnetic phase transition in form of the so-called critical broadening of the magnetic resonance linewidth at the Curie temperature (see for example [11]). A very straight forward way to see the effect of spin excitations is the temperature dependence of the magnetization at low temperatures ($T^{3/2}$ law). As evidenced in cubic nanoparticles the changes of the magnon excitation spectrum due to confinement are readily reflected in a modified temperature dependence of the macroscopic magnetization [12]. Also, it has been shown by scanning tunneling spectroscopy that the lifetime of a localized excited spin state of an Fe atom [13], which is a sensitive measure of magnetic dipole-dipole and exchange interactions with its local and distant environment, varies between 50 and 250 ns depending on its local coordination.

Available techniques cover the non-linear (large excitation amplitudes) and linear response regime. In the latter case the exciting microwave power is limited to a few tens of mW and the precession angle of the magnetization is only a few degrees. Ideally, only coherent precession of the magnetization is excited, that is to say we consider dispersion relations in the long spin wavelength (λ) limit that is $2\pi/\lambda = q \mapsto 0$. The discussion will be restricted to recent advances in modeling and experimental techniques, since the state of the art of measuring and modeling magnetization dynamics in confined magnetic structures has been described up to the year 2006 in three excellent books edited by B. Hillebrands and K. Ounadjela [14].

In recent years a number of time-resolved techniques have been developed with the aim to measure and image magnetization dynamics in magnetic micro and nanostructures. The magnetization state is probed using X-rays or light in the visible range. The contrast mechanism is X-ray magnetic circular dichroism or the magneto-optical Kerr effect respectively. While X-ray based techniques such a X-ray photoemission microscopy (XPEEM) or scanning transmission X-ray microscopy (STXM) [15] can have a spatial resolution as high as 20 nm, their time resolution is limited by the electron bunch length of the synchrotron to about 30 ps, i.e. a few GHz. Brillouin light scattering (BLS) (see for example [8, 16]) and time resolved Kerr microscopy (TRMOKE) [17] on the other hand can achieve only a moderate spatial resolution of 200–300 nm. The sub picosecond time resolution, however, allows to follow magnetization dynamics well into the THz regime [18]. Recent developments also include element-resolved spectroscopies in alloyed or composite ferromagnetic materials like X-ray Detected Magnetic Resonance (XDMR) [19] in which X-ray Magnetic Circular Dichroism (XMCD) [20, 21] can be used to probe the resonant precession of local magnetization components in a strong microwave pump field up to the THz regime and X-ray Resonant Magnetic Scattering (XRMS) which probes the motion of the magnetization stroboscopically as a function of time after magnetic field pulse excitation [22, 23].

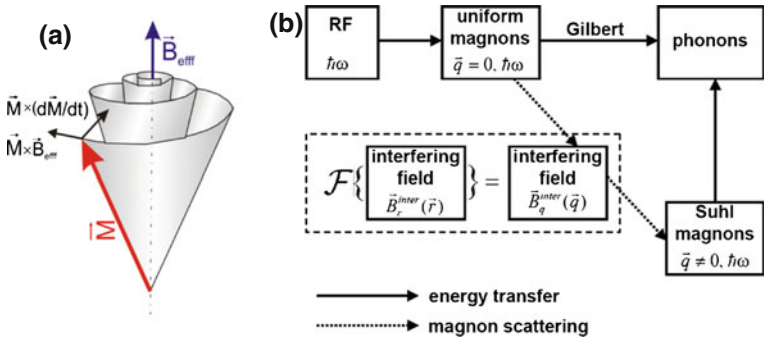

Fig. 1 **a** Simplified scheme showing the relaxation of the magnetization vector after microwave excitation. Restoring torques according to the Landau-Lifshitz-Gilbert equation are indicated. **b** Block diagram of the two most simple relaxation channels after microwave excitation. q is the wavevector of a magnon. Adapted from [24]

2 Energy Dissipation Channels for Reversal and Relaxation of the Magnetization

In general, one can say that the understanding of spin dynamics in nanomagnets requires a detailed knowledge of the precessional motion of the magnetization vector, involving the conditions for spin wave generation and dispersions and different relaxation channels after excitation. It involves various research areas in theory as well as in experiment (resonance, spin-torque, spin-injection, magnetic reversal, non-linear dynamics) to interpret the different modes of magnetic damping, relaxation and magnon scattering. Topics which will be touched upon involve linear versus non-linear processes, spin-spin versus spin-orbit driven mechanisms, frequency- versus time-domain measurements, ground state magnetism versus magnetism in an excited state. For all these mechanisms characteristic differences between metallic and insulating ferromagnets exist. Another interesting problem is the classification in dissipative and non-dissipative mechanisms in regard to the energy of the spin system.

We start very simply with the discussion of the relaxation of the magnetization by considering the phenomenological model of a precessing macroscopic magnetization of a ferromagnetic material Fig. 1a. In this model one considers a homogeneous magnetization which is the vectorial sum of initially collinear magnetic moments. The Larmor frequency of the precessional motion is well described by the Landau-Lifshitz equation from which the static magnetic properties appearing in the equation can be determined by angular- and frequency dependent FMR measurements. As discussed in [25] the resonance frequency ω is calculated by:

$$\left(\frac{\omega}{\mu_B g/\hbar}\right)^2 = \frac{1}{M^2 \sin^2(\theta)}\left[\frac{\partial^2 F}{\partial\theta^2}\frac{\partial^2 F}{\partial\phi^2} - \left(\frac{\partial^2 F}{\partial\theta\partial\phi}\right)^2\right] \tag{1}$$

where ω is the microwave frequency, g—the g-factor, ϕ and θ—azimuthal and polar equilibrium angles of the vector of magnetization M. Different forms of the free energy density functional F can be used. The following exemplary expression is valid for the geometry of an ultrathin film [25]:

$$F = -\mu_0 \mathbf{M} \cdot \mathbf{H}_{ext} - \mu_0 M\, H_\perp \cos^2\theta + K_2^{||} \sin^2\theta\ \sin^2\left(\phi - \phi_{K_2}\right) + K_4 \sin^2\theta - \frac{K_4}{8}\left(7 + \cos 4\phi\right)\sin^4\theta \tag{2}$$

that includes the Zeeman term, the perpendicular anisotropy field $H_\perp$, the in-plane uniaxial anisotropy $K_2^{||}$ with its easy axis defined by the in-plane angle ϕ_{K_2} and the cubic magneto-crystalline anisotropy K_4. The anisotropy fields K_i/M can be obtained with an accuracy of $<1\,\%$. The error of the anisotropy constants is dominated by the uncertainty of the saturation magnetization of $\leq 10\,\%$, evaluated from magnetometry measurements.

This analysis determines only the eigenfrequency of the uniform precession of the macroscopic magnetization, that is only the magnons with $\mathbf{q} = 0$. If one considers regionally non-collinear or in other words in time and space varying (out-of-phase) excited states, one can derive dispersion relations $\omega(q)$ for magnons which in the case of a thin film are for example given by [26] :

$$\omega = \gamma \left[\left(\mu_0 H + \mu_0 M_s \left(1 - \frac{1 - e^{-qd}}{qd}\right)\sin^2\phi_q + Dq^2 + H_{\mathrm{MAE1}}\right) \times \left(\mu_0(H + H_\perp) - \mu_0 M_s \left(1 - \frac{1 - e^{-qd}}{qd}\right) + Dq^2 + H_{\mathrm{MAE2}}\right)\right]^{1/2} \tag{3}$$

ω is a function not only of the wave vector q, but also of the external magnetic field H and sample parameters such as saturation magnetization M_s, effective perpendicular field $H_\perp$, spin wave stiffness D, film thickness d, the spectroscopic splitting factor $\gamma = \mu_B g/\hbar$, and parameters H_{MAE1} and H_{MAE2}, which are functions of very small anisotropy fields. Here, ϕ_q describes the angle between the magnetization and the spin wave vector. As explained in detail in Ref. [26] ϕ_q is very small, so that $\sin\phi_q \approx 0$.

The dynamic response of the magnetization is described by the equation of motion given by Landau and Lifshitz and the damping term suggested by Gilbert.

$$\frac{d\mathbf{M}}{dt} = -\gamma\left(\mathbf{M} \times \mu_0 \mathbf{H}_{\mathrm{eff}}\right) + \frac{\alpha}{M}\left(\mathbf{M} \times \frac{d\mathbf{M}}{dt}\right) \tag{4}$$

where $\mathbf{M}$ is the magnetization. The damping parameter α in SI units is related to the commonly used Gilbert damping factor G in CGS units by $\alpha = G4\pi/\mu_0 M\gamma$.

In a recent review by Fähnle et al. (see [3] and references therein) it was summarized that this phenomenological picture can be also understood in terms of electron-magnon scattering. It was calculated that the dominant contributions to the dissipative part of the dynamics in metallic ferromagnets arise from the creation of

electron-hole pairs and from their subsequent relaxation by spin-dependent scattering processes which transfer angular momentum to the lattice. Effective field theories (generalized breathing and bubbling Fermi-surface models) have been developed [3] which show that the Landau-Lifshitz-Gilbert equation of motion should be extended for the description of ultrafast magnetization processes, but in general provides an quantitatively excellent approach for the description of spin dynamics. Recently, Barsukov et al. [28] established by detailed frequency dependent FMR measurements and *ab initio* electronic structure calculations using the fully relativistic Korringa-Kohn-Rostoker Green's function method within spin-density-functional theory that the damping factor α is isotropic and depends on the composition in $Fe_{1-x}Si_x$ thin films. These films show for all compositions $0 < x < 40$ a very small composition dependent anisotropy K_4 (Fig. 2a). This may explain the observed and calculated isotropic behavior of α which in general should reflect the anisotropy of the orbital magnetic moment μ_l. As already pointed out by Kambersky (see [29] and references therein), for magnetic metallic systems two processes Eq. (5) for the relaxation of the net magnetization dominate the Gilbert damping factor G. Both *ordinary* and *spin-flip scattering* processes depend on the density of states at the Fermi level $N(E_F)$ and on the electron scattering time τ. They are directly proportional to the square of the deviation of the g-factor from its free spin-value [29]:

$$Spin - flip - scattering : G = \left(\frac{\gamma\hbar}{2}\right)^2 N(E_F)(g-2)^2/\tau \tag{5}$$

$$Ordinary - scattering : G = \left(\frac{\gamma}{2}\right)^2 N(E_F)\lambda_{SO}^2(g-2)^2/\tau \tag{6}$$

Since the magnetic anisotropy energy density is related to the anisotropy of the orbital magnetic moment $\delta\mu_l$ and since the g-factor measured in FMR (see for example [30]) is a measure of the orbital-to-spin magnetic moment ratio, one could hope to identify *anisotropic* Gilbert-type (spin-orbit) damping only in materials with large magnetic (uniaxial) anisotropy [31]. It must be noted, however, that the identification of such a intrinsic *anisotropic* Gilbert damping may be impossible due to the presence of the so-called two-magnon scattering which can also cause an angular dependent relaxation rate.

In a very simple scheme the relaxation channels of the excited magnetization can be described by the cartoon in Fig. 1b which dates back to discussions by H. Suhl recently reviewed in [32, 33]. The scheme indicates that uniform magnons with $\mathbf{q} = 0$—that is the uniformly precessing magnetization in Fig. 1a—are excited by microwave (RF) excitation. The uniform magnons can relax either via spin-orbit coupling and phonon-magnon interaction directly to the lattice or by dissipationless magnon-magnon scattering into non-zero wave vector magnon states followed by relaxation to the lattice. The intrinsic Gilbert damping path leads to heating of the lattice which for example can be used to detect magnetic resonance in a nanomagnet [34]. The other route indicated by the dashed arrow represents an initially dissipation free channel. Uniform magnons scatter into magnons with $\mathbf{q} \neq 0$ but with the same

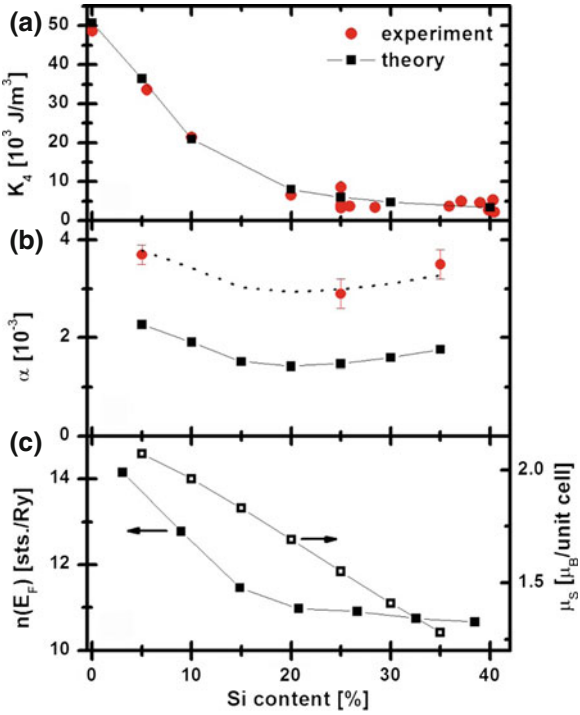

Fig. 2 Magnetic anisotropy energy and magnetic damping constant of Fe_{1-x} Si_x as a function of Si concentration. **a** Magneto-crystalline anisotropy constant K_4. Red dots show experimental data extracted from combined SQuID and FMR measurements on thin films grown on MgO(001). Error bars are 10 % due to the error in determining the magnetic volume. *Black dots* show the results of the DFT calculations for Fe-Si bulk-systems at 0 K. **b** Gilbert-damping parameter: *black squares* are results of the DFT calculation showing a minimum at $x \cong 20\,\%$. *Red dots* are experimental data obtained by frequency-dependent FMR measurements. *Dashed line* is a guide to the eye according to the theoretical data. **c** Average spin magnetic moment μ_s and electron density of states at the Fermi edge $n(E_F)$. The dependence on Si concentration correlates with the dependence of the Gilbert parameter. From [27]

energy $\hbar\omega$ as the $\mathbf{q} = 0$ state. Such a process is only feasible if the momentum transfer $\mathbf{q} = 0 \mapsto \mathbf{q} \neq 0$ is negligible and degenerate states in energy are available (compare Fig. 1b). The Suhl ($\mathbf{q} \neq 0$) magnons eventually lose their energy to the lattice. In the literature these two principally different relaxation channels are either referred to as intrinsic versus extrinsinc or Gilbert-type versus dissipation free channels. They are associated with different relaxation times T_1 and T_2 or in other words a longitudinal and transverse relaxation time as can be described by the Bloch-Bloembergen form of the Landau-Lifshitz equation:

$$\frac{dm_z}{dt} = -\gamma\,(\mathbf{m} \times \mu_0 \mathbf{H}_{\text{eff}})_z - \frac{m_z - M_S}{T_1} \tag{7}$$

$$\frac{dm_{x,y}}{dt} = -\gamma\,(\mathbf{m} \times \mu_0 \mathbf{H}_{\text{eff}})_{x,y} - \frac{m_{x,y} - M_S}{T_2} \tag{8}$$

In regard to the simple relaxation scheme of Fig. 1a one realizes that the dissipation free relaxation channel (dashed arrow) in the Scheme 1b results in a temporary decrease of the length of the magnetization vector associated with the transverse relaxation time T_2 or in other words a dephasing of the coherently precessing magnetic moments. A pure Gilbert type of relaxation would not lead to a change of the magnitude of the magnetization, and the tip of the vector would spiral along the surface of a sphere to its ground state. Finally, by annihilation of the Suhl magnons the system recovers its full magnetization given by the longitudinal relaxation time T_1.

The two-magnon scattering mechanism has been described theoretically by Arias and Mills [26, 35] based on the linear response theory and experimentally confirmed by several groups. In a two-magnon process a uniform magnon ($q_\parallel = 0$) initially created in a thin film with the magnetization lying in plane is scattered into a non-uniform state with the same energy and different wave vector $q_{\parallel S} \neq 0$, as shown in Fig. 3 (straight dotted line). Due to the local nature of this scattering process the momentum conservation can be violated [36]. In Fig. 3 the magnon dispersion for an ultrathin film magnetized in-plane including dipole-dipole interaction is shown. For the spin wave vector in-plane and parallel to the magnetization ($\phi = 0 < \phi_C$) the blue dispersion relation is obtained. Energetically degenerate states $q_{\parallel S}$ and $q_{\parallel 0}$ exist which can be coupled via the scattering potential F_{SCAT}. Usually, F_{SCAT} is given by randomly distributed defects in a thin film. If the angle ϕ between the in-plane direction of the magnetization and the wave vector increases beyond a critical angle ϕ_C, the degeneracy of the $q_{\parallel 0}$ and $q_{\parallel S}$ states is lifted, and the two-magnon scattering process becomes inoperative- allowing a straight forward identification in the experiment.

For applications that require certain relaxation times one wants to control the relaxation rate while maintaining the desired static magnetic properties of a material such as its magnetic anisotropy energy density, the saturation magnetization and interlayer exchange coupling. Some concepts for modifying the local damping in metallic ferromagnets, which unfortunately involve the risk of altering the static magnetic properties are:

- Doping with different elements [37–39]
- Ion mixing [40]
- Ion-induced segregation [41]
- Surface patterning of metallic layers by ion implantation [28]
- Formation of a regular defect pattern by oblique deposition in binary alloy films (e.g. Fe_3Si [42]).

An interesting possibility to minimize the unwanted changes of the static parameters of a ferromagnetic layer is the so-called spin-pumping effect [43]. By adding

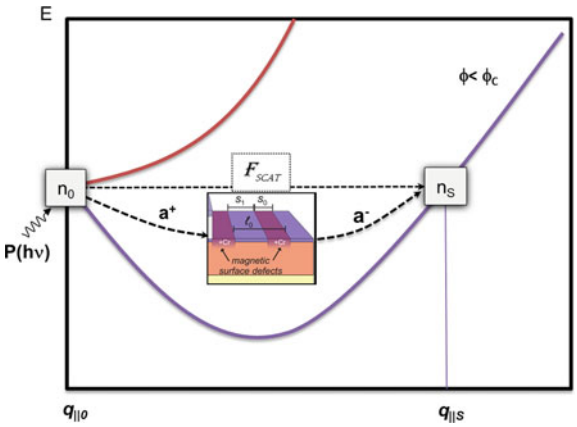

Fig. 3 Dispersion relation (including dipolar interaction) for magnons in a thin film. A number of uniform ($q_{||0}$) magnons are annihilated (a^-) and a number non-uniform magnons (n_S) with $q_{||S} \neq 0$ are created (a^+). This process is mediated by the scattering field F_{SCAT} which couples both magnon states. The number of uniform magnons (n_0) is increased by the microwave excitation and reduced by relaxation processes like the two-magnon scattering

a non-ferromagnetic metallic layer a spin-sink for a diffusive spin-current generated by the precessing magnetization after microwave excitation across the ferromagnetic/normal metal interface is created. Here, one has to be aware that this is a non-localized form of magnetic relaxation. The spin current carries away angular momentum from the ferromagnet into the normal metal where it is dissipated. Considerable effects have been seen in multilayered structures in which the relative orientation of two ferromagnetic layers separated by a normal metal layer determines the magnitude of the additional spin-pumping contribution to the intrinsic Gilbert damping [44]. The addition of the normal metal layer, however, may also modify the local crystalline structure by strain relief or creation [45] and thereby modify the static magnetic parameters like the magnetic anisotropy energy density.

Recently, a new approach for mesoscopically sized magnetic structures has been suggested based on the control of the two-magnon scattering mechanism. This approach realizes one possible route to extrinsically influence the longitudinal relaxation time—as indicated by the box of 'interfering fields" or scattering potentials for magnons in Fig. 1b. By artificially designing a periodic potential whose periodicity is adapted to the dominating magnon excitations the scattering rate can be enhanced and thereby the extrinsic or longitudinal relaxation time shortened. This is indicated in Fig. 3 by the scattering field F_{scat}.

The analysis of experimental FMR linewidths should at least include four different contributions ([46] and references therein):

$$\Delta B(\omega, \psi_B) = \Delta B^{\text{Gilbert}}(\omega, \psi_B) + \Delta B^{\text{mosaic}}(\omega, \psi_B) + \Delta B^{\text{2mag}}(\omega, \psi_B)\Delta B^{\text{inhom}} \tag{9}$$

Here ΔB denotes the peak-to-peak linewidth of the FMR signal. ψ_B denotes the two angles θ_B and ϕ_B, the first being the polar angle of the external field measured with respect to the film normal and the latter the azimuthal angle of **B** measured with respect to the in-plane [100]-direction.

The four different contributions to the FMR linewidth of Eq. (9) are:

(i) The Gilbert contribution $\Delta B^{\text{Gilbert}}$.
In various magnetic systems, the damping can be described by the phenomenological Gilbert damping parameter G. If the Gilbert damping represents the entire intrinsic damping, then it follows from the Landau-Lifshitz-Gilbert equation of motion that the FMR linewidth should depend linearly on the microwave frequency [31]. In order to determine G or α, frequency-dependent FMR measurements over a large range of microwave frequencies are needed. Note, that the linear frequency dependence of FMR linewidth is valid *only* when the magnetization and external magnetic field are parallel to each other. Otherwise the so-called field dragging contribution has to be included. If one wants to express relaxation rates in terms of linewidths, i.e. to convert from frequency-swept to the field-swept linewidth measured by FMR one can use the following conversion:

$$\Delta B(\omega, \psi_B) = \gamma \frac{dB_{\text{res}}(\omega, \psi_B)}{d\omega} \cdot \Delta\left(\frac{\omega}{\gamma}\right). \tag{10}$$

Here $\Delta(\frac{\omega}{\gamma})$ is the frequency-swept linewidth written in magnetic field units. The suffix 'res' indicates that $dB_{\text{res}}(\omega, \psi_B)/d\omega$ has to be calculated at the resonance condition. In Eq. (10) ω is a function of B and $\psi_B(B)$, therefore Eq. (10) can be written as

$$\begin{aligned}\Delta B(\omega, \psi_B) = {} & \gamma \frac{\partial B_{\text{res}}(\omega, \psi_B \equiv \text{constant})}{\partial \omega} \cdot \Delta\left(\frac{\omega}{\gamma}\right) \\ & + \gamma \frac{\partial B_{\text{res}}(\omega \equiv \text{constant}, \psi_B)}{\partial \psi_B} \cdot \frac{d\psi_B}{d\omega} \cdot \Delta\left(\frac{\omega}{\gamma}\right).\end{aligned} \tag{11}$$

The second term in Eq. (11) is commonly called the field-dragging contribution, because the partial derivative gets large at angles for which the magnetization **M** is dragged behind $\mathbf{B} = \mu_0 \mathbf{H}$ due to magnetic anisotropy effects. Along the hard and easy axes of magnetization, for which **M** and $\boldsymbol{\mu}_0 H$ are parallel, this dragging contribution vanishes. The Gilbert damping contribution in Eq. (9) is therefore given by:

$$\Delta B^{\text{Gilbert}}(\omega, \psi_B \equiv \beta) \approx \frac{2}{\sqrt{3}} \frac{\alpha}{\gamma} \frac{\omega}{\cos\beta} \tag{12}$$

where β is the angle between the magnetization $\mathbf{M}$ and external field $\mu_0\mathbf{H}$. For the in-plane configuration $\beta = \phi_{eq} - \phi_H$ and for the out-of-plane configuration $\beta = \theta_{eq} - \theta_H$.

(ii) Line broadening due to mosaicity (ΔB^{mosaic}).
The second term in Eq. (9) is the so called mosaicity term. It is caused by a small spread of sample parameters on a very large scale. This variation can be found in the internal fields, thickness, or orientation of crystallites within the sample. The individual regions thus have slightly different resonance fields. The overall signal will be a superposition of these local FMR lines yielding a broader linewidth. We consider the fluctuations of the *directions* of the anisotropy fields by the mosaicity contribution given by:

$$\Delta B^{\text{mosaic}}(\omega, \psi_B) = \frac{\partial B_{\text{res}}(\omega, \psi_B)}{\partial \phi_B}\Delta\phi_B + \frac{\partial B_{\text{res}}(\omega, \psi_B)}{\partial \theta_B}\Delta\theta_B \qquad (13)$$

where $\Delta\phi_B$ and $\Delta\theta_B$ represent the average spread of the direction of the easy axes in the film plane and normal to the film, respectively. Note that for frequency dependent measurements along the easy and hard axes the partial derivatives are zero and thus the mosaicity contribution vanishes.

(iii) The two-magnon scattering contribution $\Delta B^{2\text{mag}}$.
The two-magnon scattering is a process, where the $q = 0$ magnon excited by FMR scatters into degenerate states of magnons having wave vectors $q \neq 0$. This process requires that the spin-wave dispersion allows for degenerate states, and that there are scattering centers in the sample. The geometrical separation of the scattering centers is connected to the extension of the final magnon states in real space. If long wavelength spin-waves are involved in the relaxation process, defects of the order of several 100 nm rather than atomic defects act as scattering centers. The existence of two-magnon scattering has been demonstrated in many systems of ferrites.

The linewidth $\Delta B^{2\text{mag}}$ caused by the two-magnon scattering mechanism is a measure of the scattering rate of the uniform ($q = 0$) magnons into other spin-wave modes ($q \neq 0$). For a homogenously magnetized thin film, $\Delta B^{2\text{mag}}$ can be expressed as [47]:

$$\Delta B^{2\text{mag}}(\omega, \psi_B) \propto \sum_{\langle x_i \rangle} \Gamma_{\langle x_i \rangle} f(\phi_B - \phi_{\langle x_i \rangle}) \times \arcsin\left(\sqrt{\frac{\sqrt{\omega^2 + (\omega_0/2)^2} - \omega_0/2}{\sqrt{\omega^2 + (\omega_0/2)^2} + \omega_0/2}}\right) U\left(\theta_{eq} - \theta_c\right) \qquad (14)$$

with $\omega_0 = \gamma\mu_0 M_{\text{eff}} = \gamma\,(\mu_0 M - 2K_{2\perp}/M)$ and $\mu_0 M_{\text{eff}}$ being the effective magnetization that consists of $\mu_0 M$ and the intrinsic out-of-plane anisotropy field $2K_{2\perp}/M$. $\mu_0 M_{\text{eff}}$ can be determined by analyzing the angle dependent FMR resonance field. The factor $\Gamma_{\langle x_i \rangle}$ denotes the strength of the two-magnon scattering along the

principal in-plane crystallographic direction $\langle x_i \rangle$. This parameter will be fitted to the experimental data. The $f(\phi_H - \phi_{\langle x_i \rangle})$-term allows for the two-magnon contribution to depend on the in-plane direction of $\mu_0 \mathbf{H}$ relative to the principal in-plane crystallographic directions $\langle x_i \rangle$ given by the angles $\phi_{\langle x_i \rangle}$. An angle dependent two-magnon scattering may occur when the scattering centers are not isotropic within the sample. In the case that the centers are given by lattice defects, the angular dependence should reflect this lattice symmetry. In the case that different contributions of two-magnon scattering along the principal crystallographic directions $\langle x_i \rangle$ occur, one has to sum up these contributions weighted by their angular dependence given by f. The step function $U\left(\theta_{\mathrm{eq}} - \theta_c\right)$ in Eq. (14) is equal to 1 for $\theta_{\mathrm{eq}} > \theta_c$ and zero for $\theta_{\mathrm{eq}} < \theta_c$. It is used to describe the 'switching off' of the two-magnon scattering at a critical out-of-plane angle of the magnetization. Theoretically, it is shown that in oblique configuration, when the magnetization is tipped out of the film plane, finite wave vector modes are degenerate with the FMR mode for $|\theta_{\mathrm{eq}}| > |\theta_c| = 45°$. Thus the two-magnon scattering should be operative in this regime of the tipping angle, but it should shut off for $|\theta_{\mathrm{eq}}| < |\theta_c| = 45°$. It has been shown that the angular dependence of the two-magnon scattering can be approximated by a step function.

3 Ferromagnetic Resonance Detection in the Frequency Domain

3.1 Cavity Ferromagnetic Resonance

For macroscopic bulk samples Ferromagnetic Resonance has been measured using standard microwave technology based on microwave cavities working at fixed frequencies in a narrow band of about 1, 2, 4, 9, 26.5, 35 and 75 GHz (so called L-,S-, C-, X-, K-, Q- and W-band). The magnetic field part of the microwave field is perpendicular with respect to the external magnetic field which can be swept from 0 to 2.3 Tesla using electromagnets. The appearance of the resonance is observed by monitoring the reflected rectified microwave power from the microwave cavity. Setups for measurements of the Ferromagnetic Resonance (FMR) (or Electron Spin Resonance (ESR) for paramagnetic molecules) in ultrahigh vacuum have been developed (see [25] and references therein). For example, the temperature dependence of the magnetic properties of ferromagnetic monolayers under ultrahigh vacuum conditions, surface states (dangling bonds) at silica surfaces, and sub-monolayer coverages of paramagnetic molecules/atoms at low temperatures has been successfully analyzed [1, 48]. Standard cavity based spectrometers offer a detection limit of 10^{10} to 10^{14} paramagnetic moments with spin $S = 1/2$ provided the resonance linewidth is narrower than 10 mT [49]. This corresponds to a coverage of paramagnetic atoms or molecules on a cm^2 surface of 10^{-4} to 1 monolayer. Recently, the "cavity" concept was successfully miniaturized to the micron scale [50]. Due to the increased filling factor different spin wave modes in a single permalloy micron-sized stripe could be detected and quantitatively compared to the results of micromagnetic simulations.

This new approach offers currently an ultimate sensitivity of 10^6 magnetic moments corresponding to a nanoparticle of less than 100 nm diameter.

In the FMR experiment the presence of different relaxation channels (Fig. 1b) as discussed in the previous section is identified by the frequency dependence of the linewidth (ΔB) of the resonant spin precession [45, 46, 51]: The Gilbert damping exhibits a linear frequency dependence, whereas the two-magnon scattering follows the curved $arcsin$-like Eq. (14) behavior [26]. Although non-monotonous linewidth behavior had been considered for disordered polycrystalline systems previously [36], only recently (see for example references in [35, 52, 53]) systematic investigations on how to unambiguously identify and eventually control the two magnon relaxation mechanism have been published. Here we will discuss two examples beginning with the effects of a network of defects created in Fe_3Si ultrathin films by oblique deposition of the constituents. In the following chapter the frequency-selective enhancement of the magnetic relaxation rate by designing the periodicity of the defect structure will be demonstrated.

In [42] oblique angle deposition of Si during the deposition of 40 nm thick Fe_3Si epitaxial thin films on MgO(001) was used to create a network of defects with a preferential orientation. It could be demonstrated that this procedure created an effective scattering field for two-magnon scattering with 2-fold symmetry, whose preferential direction can be chosen by the deposition angle during film growth and whose scattering rate $\Gamma = 0.2$ GHz is comparable with the Gilbert damping of Fe_3Si in X-band. In Fig. 4 the experimental data which were extensively discussed and compared to theory in [42] are reproduced. By the uniaxial symmetry of the oblique deposition process an additional twofold contribution to the two-magnon scattering process can be controlled in magnitude and orientation by creating chemical disorder with a symmetry axis along any given in-plane direction and thus independently of the fourfold contribution from the network of unavoidable defects reflecting the cubic symmetry of the crystal lattice. The Si is deposited under an oblique angle of approximately 15° with respect to the film normal and the projection of the incident Si stream on the film plane is referred to as axis β (Fig. 4a). Such growth conditions are known to provoke so-called shadow effects.

Figure 4b shows the in-plane angular dependence of the resonance field B_{res} of a 40 nm thick film measured at 9.3 GHz and 295 K (Sample #2). Using the saturation magnetization $M_S = 0.96(8)10^6$ A/m measured by SQuID magnetometry, the effective perpendicular anisotropy field is $B_\perp \approx 1$ T and the in-plane magnetocrystalline anisotropy constant $K_{\parallel 4} \approx (3.3 \leftrightarrow 4.3)10^3$ J/m^3 can be calculated from the fit (solid line) to the data (red circles). The in-plane uniaxial anisotropy constant is small and amounts to $K_{\parallel 2}(0.1 \leftrightarrow 0.5)10^3$ J/m^3. Except for this small uniaxial anisotropy, a comparison with anisotropy values of the samples grown by non-oblique deposition reveals that the modified growth conditions do not considerably change the static magnetic parameters. However, there is a correlation of the in-plane uniaxial anisotropy $K_{\parallel 2}$ and the sample preparation. The hard axis of $K_{\parallel 2}$ is aligned parallel to the in-plane projection β of the Si flow. Indeed, stripelike defects caused by the shadow effect are known to induce such magnetic anisotropy in thin films by means

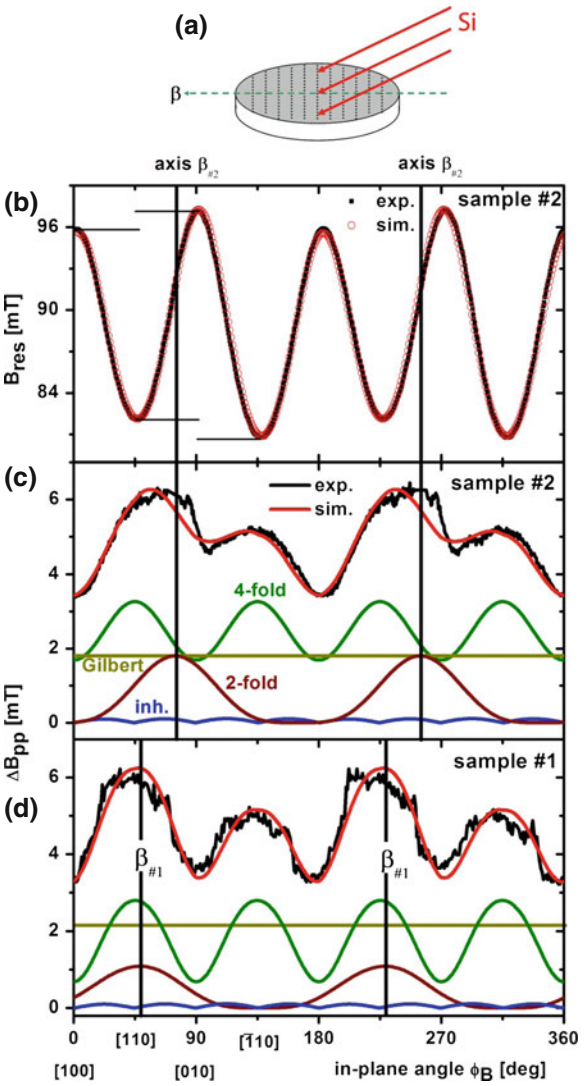

Fig. 4 **a** Sketch of the film deposition geometry. Oblique deposition of Si causes stripe-like defects with the symmetry axis perpendicular to the projection of the Si-flow β. **b–d**: 40 nm Fe_3Si/MgO(001) FMR data at 9.3 GHz. **b** In-plane angular dependence of FMR resonance fields, revealing the 4-fold crystalline anisotropy $K_{\parallel 4}$ and the small uniaxial anisotropy $K_{\parallel 2}$. FMR linewidth: **c** The native 4-fold contribution $\Gamma_{4\text{-}fold}$ caused by crystalline defects is superimposed by the 2-fold contribution $\Gamma_{2\text{-}fold}$. The maximum of the latter one is parallel to the hard axis of the uniaxial anisotropy and corresponds to the in-plane projection of the Si-flow: $\phi_{2\text{-}fold} = \phi_{uniax} = \beta$. **d** Linewidth of the sample #1, for which the axis β was set close to the [110] direction. From [42]

of the dipolar interactions among the defects. The low value of $K_{\parallel 2}$ suggests a low density of these defects.

The FMR linewidth ΔB_{pp} allows to identify the relaxation processes in the sample. In Fig. 4c the experimental linewidth (black line) is shown as a function of in-plane angle ϕ_B of the magnetic field. This in-plane angular dependence exhibits a behavior remarkably different from that of a regular film grown with a non-tilted Si evaporator [46]. While it has the typical fourfold symmetry of Fe_3Si/MgO(001) films, one also finds an additional *twofold* contribution superimposed. The latter

Table 1 Static and dynamic magnetic parameters (at X-band) of Fe_3Si/MgO(001) prepared under different growth conditions

Sample, Si deposition and film thickness	$K_4^{\|\|}$ (10^3 J/m^3)	$K_2^{\|\|}$ (10^3 J/m^3)	$\Gamma^{max}_{\langle 100\rangle}$ (10^7 Hz)	$\Gamma^{max}_{\langle 110\rangle}$ (10^7 Hz)	$\Gamma^{max}_{twofold}$ (10^7 Hz)	$\phi_{twofold}$ (deg)
#1 Oblique, 40 nm	4.0	0.2	51	13	20	49
#2 Oblique, 40 nm	3.8	0.5	58	30	33	74
#3 Oblique, 40 nm, not annealed	2.7	0.25	269	95	33	74
#5 normal, 40 nm (from Ref. [46])	3.3	–	53	26	–	–

Error bar of anisotropy constants: <10 %, of Γ^{max}_{ζ}: ~30 %, of $\Gamma^{max}_{twofold}$: <10 %, and of $\phi_{twofold}$: <5°

turns out to be of the same order of magnitude as the *fourfold* contribution and the Gilbert contribution. The simulation (red line) of the experimental ΔB_{pp} is the same as of the afore mentioned contributions to the FMR linewidth whose fitted angular dependences are shown by the green (*fourfold* two-magnon, extrinsic), brown (*twofold* extrinsic), blue (*inh* mosaicity, extrinsic) and yellowgreen (isotropic *Gilbert*, intrinsic) solid lines. The corresponding equations have been given in [42] and are not reproduced here. This angular dependence can be compared with the one of a nearly identical sample (#1) which was deposited with a change of the plane of incidence of the oblique Si stream. The angular dependence of ΔB_{pp} reveals the change of the plane of incidence from $\beta_{\#2}$ to $\beta_{\#1}$ (Fig. 4d). The calculated fit parameters for the magnetic anisotropy constants and two-fold and four-fold scattering rates are given in Table 1 in comparison to a non-annealed film and a film deposited with normal incidence of Si.

As shown in the Table 1, the modified growth conditions do also not affect the 4-fold two-magnon scattering process $\Gamma_{fourfold}$. Its intensity is comparable with results presented in [46]. The effective size of the rectangular, randomly located defects assumed for the fitting procedure lies in the range of few hundreds of nanometers—being plausible for the distance between crystalline defects in this system. Comparing the results of samples #1 and #3 reveals, that despite the modified growth the $\Gamma_{fourfold}$ intensity can be decreased by means of sample annealing.

3.2 Non-Cavity Approaches to FMR Detection

In this section we will briefly refer the reader to a selection of detection schemes of Ferromagnetic Resonance in the frequency domain which do not require the classical microwave cavity approach. The following list gives a few examples of such schemes.

- Ferromagnetic Resonance Force Microscopy [54]
- Photothermally Modulated Ferromagnetic Resonance (PM-FMR) for locally resolved and depth dependent measurements [55]

- Scanning Thermal Microscopy Ferromagnetic Resonance (SThM-FMR) [56], offering a lateral resolution of <100 nm and a sensitivity of 10^6 spins
- High-sensitivity broadband microwave spectroscopy with small non resonant coils [57]
- Broadband bolometric detection of resonant absorption in ferromagnetic nanoparticles [34]
- Broadband resonance detection of paramagnetic inclusions in weak links of Josephson junctions [58]
- Micro-resonators at fixed frequencies [50])
- Stripline and shorted wave guide based FMR techniques (see [51] and references therein).

Each of these schemes has certain advantages for specific materials and applications. Some of these techniques allow to sweep the frequency in a range of 1 to 10 GHz or even higher microwave frequencies, while in others the magnetic field is swept at constant microwave frequency. Also, one has to consider if one needs to characterize materials under ultrahigh vacuum (UHV) conditions, as a function of temperature, frequency and/or applied magnetic field strength/angle (see for example [25]). It is worthwhile to note that Kalarickal et al. [51] showed experimentally for three methods that frequency or field swept techniques yield the same FMR linewidth.

In the following we present a recent experimental result (Fig. 5) showing the possibility of manipulating the relaxation rate of permalloy films by introducing an artificial periodic scattering field F_{SCAT}. As described in detail in [28] a well-defined periodically modulated surface magnetization (scattering field F_{SCAT}, Fig. 3) of a permalloy film was prepared by low-dosage Cr implantation along stripes of width s_0 and separation s_1. In regard to the schematics in Fig. 3 one may expect to see characteristic changes in the relaxation rates due to extrinsic (*two magnon*) damping contributions. According to the theory developed by Landeros and Mills [59] increases of the FMR linewidth as a function of frequency are expected at characteristic spin wave vectors q_p reflecting the periodicity of the magnetization modulation. In Fig. 5 the first experimental observation [28] of this effect is shown. Using a newly developed shortened-coaxial-waveguide setup [60], which is UHV compatible, the FMR linewidth was determined in a quasi-continuous frequency range of 2 – 26 GHz. In Fig. 5a the experimental frequency dependence of the linewidth for the magnetic field applied parallel to the stripes with periodicity $l = s_1 + s_0 = 250$ nm is shown. The general behavior of the linewidth frequency dependence is not affected by the direction of the external magnetic field. The convex curvature is related to the high modulation field used to increase the signal-to-noise ratio. Additional measurements showed no isotropic two-magnon relaxation channel due to, e.g., grain-grain effects [61] in these polycrystalline samples. When the external magnetic field is applied perpendicular to the stripes, the behavior of the linewidth-frequency dependence becomes non-monotonous and is related to the two-magnon scattering process, which is known to be activated in such a configuration. One finds a large peak at 12.7 GHz and two smaller ones at 5.4 and 21.2 GHz. These appear only for the direction

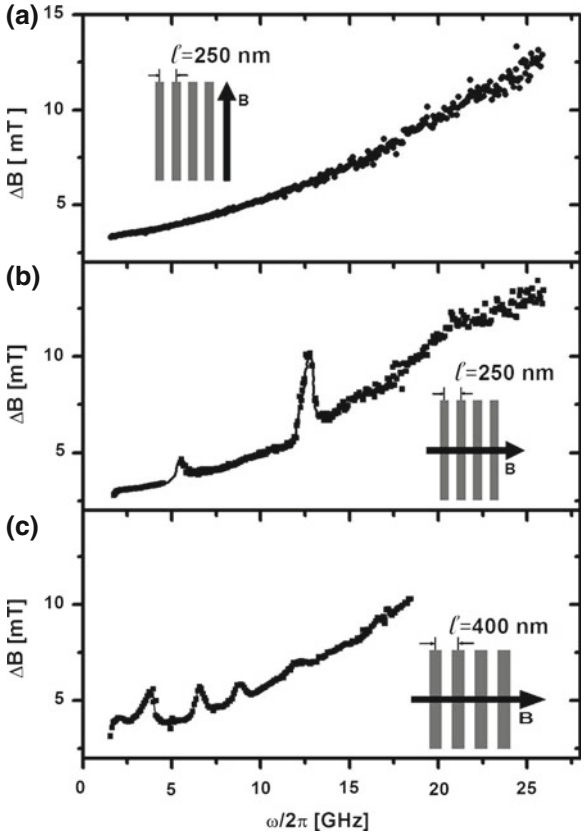

Fig. 5 Frequency dependence of the FMR linewidth of two samples structured with stripelike defects. While the general behavior is the same within one single sample for B parallel to the stripes (**a**) and B perpendicular to the stripes (**b**), for the latter configuration additional peaks due to the two-magnon scattering occur. Increasing the defects periodicity l from 250 to 400 nm in the second sample changes the position of the peaks and therefore the frequency dependence of the overall spin relaxation. In (**c**) the frequency range is limited due to technical reasons. *Solid lines* are guides for the eye

perpendicular to the stripes. Upon changing the periodicity to $l = 400\,\text{nm}$ the spacing of the relaxation rate (linewidth) peaks becomes smaller. This behavior is clearly distinct from the original monotonous arcsin-like Eq. (14) frequency dependence. In order to understand the appearance of these peaks one has to consider the dispersion relation of magnons parallel to the magnetization of a thin film Eq. (3). In a two-magnon process a uniform magnon with $q_{||_0}$ is scattered into a nonuniform state with the same energy and different wave vector $q_{||_S}$, as shown in Fig. 3. In order to find the wave vector of such a final-state magnon one needs to solve the equation $\omega(q_{||} = 0) = \omega(q_{||_S})$. The wave vector of the final-state magnons $q_S(\omega)$ can be calculated using the values of the effective perpendicular field, anisotropy fields, and

g factor. The scattering process itself is enabled by the scattering field, which couples the uniform with the final-state magnons. The coupling strength and consequently the FMR linewidth scale with the square of the Fourier transform of the scattering field for $q = q_S$. Using this model a very good qualitative agreement with the theory has been achieved [28].

3.3 Spin-Torque Ferromagnetic Resonance

Spin-torque ferromagnetic resonance (ST-FMR) is an alternative approach to measure spin dynamics in magnetic nanostructures [62–72]. The general approach is quite straightforward; an ac current is applied to a magnetic nanodevice that exhibits either giant magnetoresistance or tunneling magnetoresistance, and a dc voltage is generated that has a resonant structure when the ac frequency matches the resonance condition for FMR. The physical mechanism that gives rise to the dc voltage may be understood as follows. In a process commonly referred to as spin-momentum-transfer, or spin-torque, the non-equilibrium spin currents generated in such a device due to charge current flow between the different magnetic layers necessarily impart angular momentum to the magnetic layers in the device due to the sharp gradient in the spin current at the surface of a magnetic conductor.[1] The resultant ac torque at the surface of the magnetic layer gives rise to motion of the magnetization, thereby causing an ac variation in the device resistance. If the device resistance has a component that is in-phase with the ac current, rectification gives rise to a dc voltage. As will be shown below, the rectification is maximized when the excitation frequency approaches the FMR frequency, though the details of the voltage signal near resonance are strongly dependent on the symmetry of the spin torque in the structure.

Let U be the magnetic free energy for a rigid magnetic body. The equation of motion for magnetization $\mathbf{M}$ in a field $\mathbf{H} = -|\gamma|\left[\left(dU/dm_x\right)\hat{x} + \left(dU/dm_y\right)\hat{y}\right]$ is given by

$$\frac{d\mathbf{M}}{dt} = -|\gamma|\left[\mu_0\left(1+\alpha\hat{m}\times\right)\mathbf{M}\times\mathbf{H} - \frac{J_s}{\delta}\left(\varepsilon_\perp + \varepsilon_{||}\hat{m}\times\right)\hat{m}\times\hat{s}\right] \qquad (15)$$

where γ is the gyromagnetic ratio, μ_0 is the permeability of free space, α is the Landau-Lifshitz damping parameter, J_s is the transverse spin-current-density incident upon the magnet, δ is the thickness of the magnetic layer, $\varepsilon_\perp$ is the efficiency of the perpendicular, or "field-like" spin-torque, $\varepsilon_{||}$ is the efficiency for the parallel, or "damping-like" spin-torque, and $\hat{s}$ is the polarization direction of the spin-current.[2] The spin-current density has units of energy density, $\mathrm{J/m^3}$. For all-metal systems, it

[1] For a more detailed description of spin torque, see Chap. 2 by J. Lindner et al. in this book.

[2] A similar equation is presented in Chap. 2 by J. Lindner et al, though in terms of the Landau-Lifshitz-Gilbert damping phenomenology rather than the Landau-Lifshitz formulation employed here. In the limit of small damping, both equations are equivalent.

is generally understood that $\varepsilon_{\perp} \ll \varepsilon_{||}$. However, both data and theory indicate that $\varepsilon_{\perp}$ and $\varepsilon_{||}$ are of comparable scale for magnetic tunnel junctions (MTJs), though they have very different dependencies on the bias voltage applied across the tunnel barrier [69].

For the case of field-driven FMR (FD-FMR) with $J_s = 0$, an ac field $\mathbf{h}_{ac} = h_0 e^{-i\omega t}\hat{y}$, and $\mathbf{M} \cong m_x\hat{x} + m_y\hat{y} + M_s\hat{z}$, where $m_x, m_y \ll M_s$, the excitation torque-density $\mathbf{N}_{FMR} = \mu_0\mathbf{M} \times \mathbf{h}_{ac}$ is

$$\mathbf{N}_{FMR} \cong -\mu_0 M_s h_0 e^{i\omega t}\hat{x} \tag{16}$$

Thus, the excitation torque is necessarily at right angles to the excitation field. To understand the relationship of the magnetization to the excitation torque, we need to consider the small-amplitude motion of the magnetization as a function of excitation frequency, which can be easily derived from the Polder susceptibility tensor for the Landau-Lifshitz equation of motion,

$$\begin{pmatrix} m_x \\ m_y \end{pmatrix} = \chi \begin{pmatrix} h_x \\ h_y \end{pmatrix} \tag{17}$$

where

$$\chi \cong \frac{f_M}{f_0^2 - f^2 - if\Delta f} \begin{pmatrix} f_y + i\alpha f & -if \\ if_x & f_x + i\alpha f \end{pmatrix} \tag{18}$$

with $f = \omega/2\pi$, $f_M = |\gamma|\,\mu_0 M_s/2\pi$, $f_0^2 = f_x f_y$, $\Delta f = \alpha\left(f_x + f_y\right)$,

$f_{x,y} = |\gamma|\,M_s\left(d^2U'/dm_{x,y}^2\right)$, and U' does not include the excitation field.[3] If we consider the simplest high symmetry case with $f_x = f_y = f_0$ and $\alpha \ll f_{x,y}/f$, the equation of motion for the component of magnetization parallel to the applied ac field becomes

$$m_y = \frac{f_0 f_M h_0}{f_0^2 - f^2 - i2\alpha f f_0} \tag{19}$$

In the limit of $f \ll f_0$, we have $m_y = \left(f_M/f_0\right)h_0$; m_y is 180° out-of-phase with the excitation torque $\mathbf{N}_{FMR}$ along the x-axis, as depicted in Fig. 6. At resonance with $f = f_0$, we have $m_y = \left(i/2\alpha\right)\left(f_M/f_0\right)h_0$; m_y is 90° advanced relative to $\mathbf{N}_{FMR}$ and 90° retarded relative to $\mathbf{h}_{ac}$, but m_x is now 180° out-of-phase with N_{FMR}. The resonance condition is shown schematically in Fig. 6. This is an important general result of ferromagnetic resonance that is independent of the excitation source: $\mathbf{m}\cdot\hat{x}$ and $\mathbf{N}_{FMR}\cdot\hat{x}$ are anti-phased on resonance such that the excitation torque acts purely to counteract the damping torque, thereby maintaining a steady-state precessional

[3] This particular form of the susceptibility tensor presumes that $d^2U'/\left(dm_x dm_y\right) = 0$, i.e. the x and y coordinates have been chosen to lie along principal axes of the anisotropy, and the applied field is perpendicular to the $x - y$ plane.

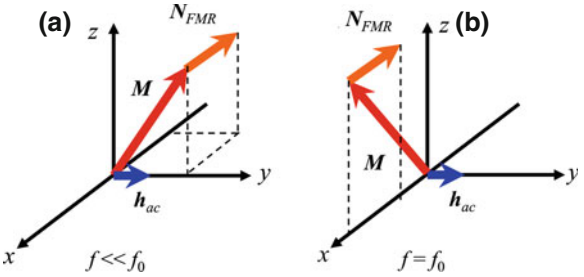

Fig. 6 Sketch of excitation torque acting on magnetization in field-driven FMR

orbit of maximum amplitude.[4] We will return to this point when we discuss the case of spin-torque FMR below.

The output signal for a field-driven FMR measurement depends on the type of detection method. If the detection is based upon an inductive measurement, then we have

$$V = i2\pi\mu_0 f A m_y \tag{20}$$

Now we will consider the case of spin-torque FMR (ST-FMR) with $\mathbf{h}_{ac} = 0$. The device structure now consists of two magnetic layers: A fixed reference layer that sets the direction of the spin current polarization, and an excited layer. Let us again assume small-amplitude magnetization motion of the excited layer about the saturation direction along $\hat{z}$. Let the polarization of the absorbed spin current $\hat{s}$ lie in the y-z plane, as depicted in Fig. 7. When the ac spin current is $J_{ac} = J_0 e^{-i\omega t}$, the excitation torque density $\mathbf{N}_{ST}$ is

$$\mathbf{N}_{ST} \cong \frac{J_0}{\delta}\left(\varepsilon_\perp \hat{x} + \varepsilon_{||}\hat{y}\right) e^{i\omega t} \tag{21}$$

This allows us to define an effective ac excitation field $\mathbf{h}_{ST}$ for the purposes of calculating the magnetization response, where

$$\mathbf{h}_{ST} = \frac{|\gamma| J_0 e^{i\omega t}}{2\pi f_M \delta}\left(\varepsilon_{||}\hat{x} - \varepsilon_\perp \hat{y}\right) \tag{22}$$

The relationship between the spin-current polarization vector $\hat{s}$ and the effective spin torque ac field $\mathbf{h}_{ST}$ is shown in Fig. 7. Let us now examine the signal produced by the spin-torque excitation. The output signal $V(t)$ due to giant magnetoresistance

[4] One must remember that the magnetization and angular momentum are antiparallel for electrons. Thus, a torque that is antiparallel to the magnetization will act to increase the magnetization along the torque.

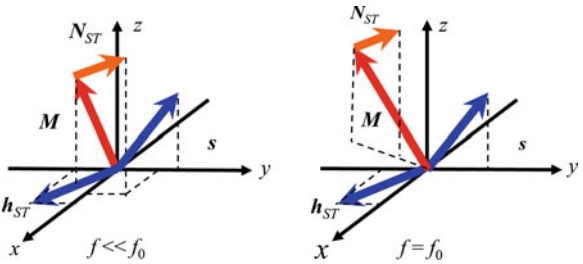

Fig. 7 Cartoon sketch of excitation torque acting on magnetization in spin-torque FMR

is given by

$$\begin{aligned} V(t) &= \left[\frac{Re\left[I(t)\right]\Delta R}{M_s}\right] Re\left[\mathbf{m}(t)\right]\cdot\hat{s} \\ &= \frac{1}{4}\frac{\Delta R}{M_s}\left[I(t)+I^*(t)\right]\left[m_y(t)+m_y^*(t)\right]\sin(\theta) \\ &= \frac{1}{2}\left(\frac{|\gamma|J_0 e^{i\omega t}}{2\pi f_M \delta}\cdot\frac{I_0\Delta R}{M_s}\right)\cos(\omega t)\left[\frac{f_M(if\varepsilon_{||}-f_x\varepsilon_\perp)}{f_0^2-f^2-if\Delta f}e^{i\omega t}+cc\right]\sin(\theta) \end{aligned} \tag{23}$$

where θ is the angle between the magnetizations of the reference layer (the presumptive source reservoir for the spin current) and the excited layer. The resultant voltage has a dc component V_{dc} given by

$$\begin{aligned} V_{dc} &= \frac{1}{2}\left(\frac{|\gamma|J_0}{2\pi F_M\delta}\cdot\frac{I_0\Delta R}{M_s}\right)\left[\frac{f_M(if\varepsilon_{||}-f_x\varepsilon_\perp)}{f_0^2-f^2-if\Delta f}+\frac{f_M(if\varepsilon_{||}-f_x\varepsilon_\perp)}{f_0^2-f^2+if\Delta f}\right]\sin(\theta) \\ &= \left(\frac{|\gamma|J_0}{2\pi\delta}\cdot\frac{I_0\Delta R}{M_s}\right)\left[\frac{\varepsilon_\perp f_x(f_0^2-f^2)+\varepsilon_{||}f_2\Delta f}{(f_0^2-f^2)+(f^2\Delta f)^2}\right]\sin(\theta) \end{aligned} \tag{24}$$

We immediately see that the parallel spin torque gives rise to an even-symmetry resonance response, whereas the perpendicular spin torque results in an odd-symmetry resonance spectrum. We can understand this quite easily since we know that the time-varying effective resistance is proportional to $\mathbf{m}\cdot\hat{y}$, and $\mathbf{N}_{ST}\cdot\hat{y}$ is 180° out-of-phase with m_y when on resonance. Thus, only the y-component of the spin torque contributes to the output signal when on resonance, resulting in a peak amplitude that is proportional to $\varepsilon_{||}$. Conversely, $\mathbf{N}_{ST}\cdot\hat{x}$ due to the perpendicular component of spin torque is 180° out-of-phase with m_x when on resonance, but any voltage signal due to $\mathbf{N}_{ST}\cdot\hat{x}$ is necessarily 90° out-of-phase with the excitation spin current, resulting in an odd-symmetry response curve.

An important prerequisite for the measurement of ST-FMR, as seen in the Eq. (24), is the mis-orientation of the active and reference layers. To accomplish this, various

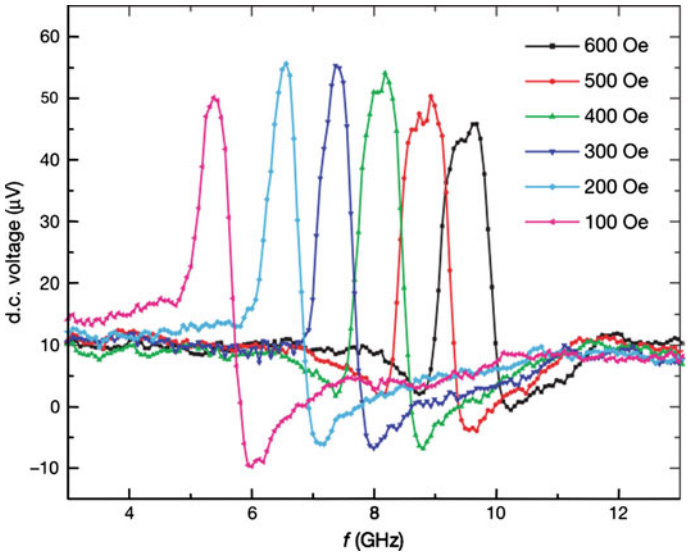

Fig. 8 Examples of the first ST-FMR spectra obtained with a magnetic tunnel junction device. The data show how the resonance frequency depends on an in-plane applied magnetic field, as expected for FMR. From Ref. [62]

approaches have been successfully used. For example, use of materials with greatly differing magnetic moment for the active and reference layers can result in strong misalignment of the magnetization orientation for the case of a perpendicular applied field.

While ST-FMR has yielded some of the first data for FMR in individual nanoscale magnetic structures, it suffers from inflexibility with regard to the thickness of the structure in question. This is immediately apparent in Eq. (24), where we see that the ST-FMR signal scales inversely with device thickness as a result of the interfacial nature of the spin-torque effect. Thus, only very thin devices are amenable to such measurements, leaving unanswered questions as to the role of phenomena such as spin-pumping in determining the overall damping in nanomagnets.

Spin-torque FMR was first demonstrated by Tulapurkar et al., by use of a 100×200 nm MgO-based magnetic tunnel junction (MTJ) device with a TMR ratio 100 % and a zero-bias, low-resistance of 150 ohms [62]. The applied magnetic field was in the film plane of the device. The device was excited at room temperature by ac currents ranging from 200 to 640 μA. The output dc voltage scaled quadratically with excitation current as expected for a rectification effect, and output signals as large as 35 μV were reported. Spectra were obtained by sweeping the excitation frequency, an example of which is shown in Fig. 8. The presented spectra exhibited a single peak at the resonance frequency with both even and odd symmetries, indicative of both the in-plane and perpendicular components of spin torque in the MTJ, as theoretically predicted for such devices [12]. The resonance frequency scaled with

applied dc magnetic field, and fitting of the data with the Kittel equation yielded an in-plane anisotropy of 176 Oe and an effective magnetization of 12.8 kOe. However, a dc bias voltage was not applied to the device, thus precluding any determination of the bias dependence for the different spin torque components in this particular device.

The first demonstration of ST-FMR in an all-metallic current-perpendicular-to-plane giant-magnetoresistive (CPP-GMR) device was reported by Sankey et al., for a 30×90 nm device with a 20 nm-thick Permalloy reference layer and a 5.5 nm-thick $Py_{65}Cu_{35}$ active layer [2]. The measurements were performed at cryogenic temperatures (<10 K), presumably to enhance the signal-to-noise ratio of the measurement. The applied magnetic field was out of the film plane and of sufficient strength to saturate the active layer magnetization out of the plane, while insufficient to do the same for the reference layer. The excitation currents ranged from 12 to 990 μA, and the maximum output signal was approximately 5 μV. Spectra were obtained by sweeping the excitation frequency, and multiple peaks were reported, indicative of multiple excitation modes in both the active and reference layers. In the absence of a dc bias current, the resultant spectra exhibited even symmetry about the resonance frequency at low ac currents. However, at high ac currents, the spectra acquired a distinct asymmetry that suggests nonlinear magnetization dynamics [9]. For these measurements, a dc current was also applied to modify the effective damping of the active layer, as shown in Fig. 9, which also includes an exemplary spectrum for zero dc current. Analysis of the data for linewidth vs. dc current yielded a zero-current damping of $\alpha = 0.04$ and a critical current ($\alpha = 0$) of $I_c = 0.4$ mA at an applied field of 0.535 T. Conventional room-temperature FMR measurements of unpatterned blanket films of the same composition as the active layer yielded a $= 0.021$. It was conjectured by the authors that the discrepancy in damping could be attributed to exchange coupling between the patterned active layer and an antiferromagnet oxide on the edges of the device that is below its blocking temperature for such cryogenic measurements. The absence of such extreme damping enhancement in subsequent room temperature measurements, as discussed below, corroborated this conjecture. However, an erroneous formulation for the dependence of the frequency-swept linewidth on damping was used for the data analysis. This was addressed in a subsequent publication from the same group, discussed below [66].

A theoretical treatment of ST-FMR in CPP-GMR devices was initially presented by Kupferschmidt et al. [64]. Their approach was to find a self-consistent solution of the charge- and spin-current propagation through a one-dimensional structure subject to appropriate boundary conditions. The methodology included an accounting for the reactive emission of spins from precessing ferromagnets into the nonmagnetic spacers, also known as spin pumping [43]. An important finding from the theoretical analysis was the contribution of the non-equilibrium spin accumulation in the nonmagnetic spacer layer to the dc voltage signal due to the generation of a nonzero dc chemical potential at the various ferromagnet/conductor interfaces within the device. It was determined that the contribution of the spin emission component to the net dc voltage signal was comparable to that due to simple rectification when the spin pumping component of the damping was of the same scale as the intrinsic damping.

To date, however, an experimental confirmation of this result remains lacking. A subsequent theoretical analysis by Kovalev et al., using similar methods, arrived at the same conclusion [65]. Another important result shared by both theories is the manifestation of an odd-symmetry component of the resonance even if $\varepsilon_{\perp} = 0$. The origin of the odd-symmetry is purely geometrical in origin, stemming from the possible misalignment of the effective spin-torque ac field $\mathbf{h}_{ST}$ with respect to the principle anisotropy axes of the device [64].

Fuchs, et al. first reported room temperature measurements for 50×10 nm all-metal CPP-GMR nanopillars [66]. An in-plane applied magnetic field was used. As was presented in the first work by the same group [63], the damping was inferred by measuring frequency-swept linewidth as a function of dc current, then using a linear fit to determine the zero-current linewidth. Since the dependence of frequency-swept linewidth on damping is proportional to the sum of the stiffness frequencies f_x and f_y, it is necessary to determine the effective anisotropy that establishes the FMR frequency. To see this, we consider the dependence of frequency-swept linewidth on damping,

$$\Delta f = \alpha(f_x + f_y) \tag{25}$$

where f_x and f_y are defined earlier in this chapter. Let us now consider the derivative of resonance frequency with respect to applied field,

$$\frac{df_0}{dH} = \frac{\gamma\mu_0}{4\pi f}(f_x + f_y) \tag{26}$$

Thus,

$$\alpha = \frac{\gamma\mu_0}{4\pi f_0}\frac{\Delta f}{\left(\frac{df_0}{dH}\right)} \tag{27}$$

We clearly see that determination of the damping from frequency-swept data is facilitated by a commensurate determination of the resonance frequency dependence on applied field. However, such data were not forthcoming in Ref. [66] which required an estimation of the stiffness frequencies by modeling the active elements as uniformly magnetized elliptical cylinders. The systematic errors associated with such an estimate were not determined. Nevertheless, the authors concluded that the extracted values for the zero-current damping were essentially identical (with 50 % error bars) to the measured values for unpatterned blanket films presented elsewhere in the literature.

A more accurate determination of damping in nanostructured CPP-GMR devices was presented by Chen et al. [67, 68]. This work used a Co/Ni multilayer active layer with perpendicular anisotropy, although the interfacial anisotropy was insufficient to overcome the intrinsic shape anisotropy for a thin film. The applied magnetic field was perpendicular to the film plane. The large difference in the net anisotropy

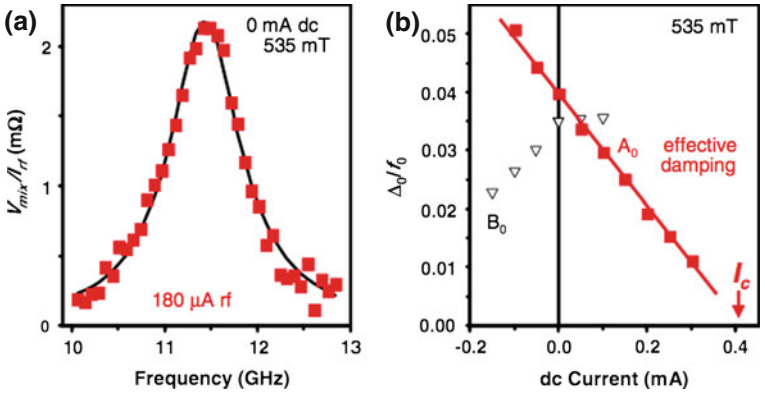

Fig. 9 Example of ST-FMR spectrum and dependence of spectral linewidth on dc current for metallic GMR device. **a** An example of a ST-FMR spectrum without any additional dc current. The applied field of slightly more than 0.5 T is oriented out of the film plane and is sufficient to saturate the excited layer out of the film plane. **b** The dependence of the ST-FMR linewidth on dc current. The observed linear dependence is in agreement with theoretical predictions (see Eq. 15). The critical current I_c for self-oscillations is extrapolated from a linear fit to the data. From Ref. [63]

of the active and reference layers allowed for the requisite misalignment of the magnetization angles over a wide range of applied magnetic field. Here, the field-swept linewidth was determined as a function of excitation frequency, permitting an unambiguous determination of the damping parameter as $\alpha = 0.033 \pm 0.003$, which was within error bars of a conventional FMR measurement for an unpatterned multilayer film with $\alpha = 0.036 \pm 0.002$. The linewidth vs. frequency data for both ST-FMR and FD-FMR are presented in Fig. 10. Similar to Fuchs et al., the authors concluded that patterning of the active layer nanomagnet did not cause a detectable change in the intrinsic damping. While micromagnetic simulations predict [73] and data have shown [74, 75] that multiple modes should be present in such finite-sized active layers, the experimental signal-to-noise was not sufficient to clearly determine the presence of such higher order modes. In addition, the shift of the device resonance frequency from that of the unpatterned film was approximately a factor of two less than what simulations predicted for the lowest order normal mode. The discrepancy between modeling and experiment was not explained, though it was conjectured that the actual device size may have been substantially different from the nominal dimensions of 50×150 nm.

The use of ST-FMR to study tunnel junction devices was revisited by Sankey et al. in an IBM/Cornell collaboration [69]. The devices under study (500×100 nm and 50×150 nm) utilized a CoFeB (3 nm)/MgO (1.25 nm)/CoFeB (2.5 nm) stack. In this case, the authors were less concerned with the damping of the active layer. Instead, the intention was to determine the dependence of the spin torque on bias voltage. It was observed that the ST-FMR lineshape exhibited both even and odd symmetry

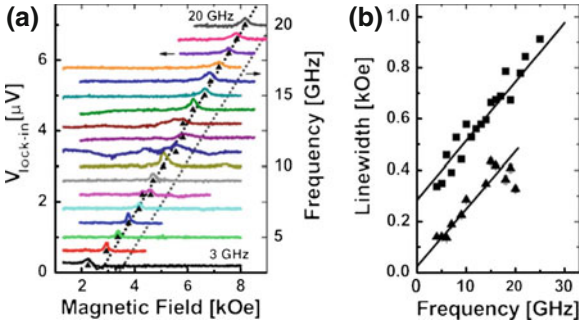

Fig. 10 Dependence of ST-FMR spectral peak position (**a**) and linewidth (**b**) on microwave frequency. The applied field is perpendicular to the plane of the device. The linewidth for FD-FMR is also shown in (**b**) with the filled square data points. The linewidth exhibits classic linear dependence on frequency, as expected for Landau-Lifshitz damping processes. From Ref. [67]

components Eq. (24) that had different dependencies on bias voltage. It was found that the parallel, or "damping-like", torque (referred to as the "in-plane" torque in Ref. [69]) only displayed a weak dependence on bias voltage for voltages as large as 0.4 V, even though the TMR ratio was reduced by a factor of two at such a bias voltage. In addition, the perpendicular, or "field-like", torque was comparable in magnitude to the parallel torque over the range of bias voltages, although its dependence on bias voltage appeared linear with a zero-intercept at zero bias.

Nonlinear resonance effects were indicated by Chen, et al. in another work from the NYU group that utilized CPP-GMR structures with Co/Ni active layers [70]. It was found that the field-swept resonance lineshape took on a distinctive "saw-tooth" shape with increasing microwave current excitation, as shown in Fig. 11. Such a lineshape results in a shift of the peak resonance frequency to lower applied magnetic fields with increasing microwave excitation. The saw-tooth shape is a tell-tale signature of nonlinear bistability in FMR measurements [76–78]. However, hysteresis of the lineshape, another essential feature of bistability, was very weak in comparison to macrospin simulation results. The authors speculate that thermally driven fluctuations might obscure the observation of such hysteretic effects.

ST-FMR has also been demonstrated with point-contact spin-torque devices, where the active layer is not lithographically patterned [71]. Instead, the current is injected into a blanket spin-valve stack using a lithographically defined point contact [79]. Again, the extracted value of damping was found to be in rough agreement with previously published results for the same material as the active layer, a Co/Ni multilayer with a net perpendicular anisotropy of only 64 mT. In addition, the determined ST-FMR resonance frequency dependence on applied field at zero bias current was found to coincide with the onset frequency of auto-oscillations at the critical current, demonstrating that the excitation generated by dc current in this particular device was of small amplitude at threshold.

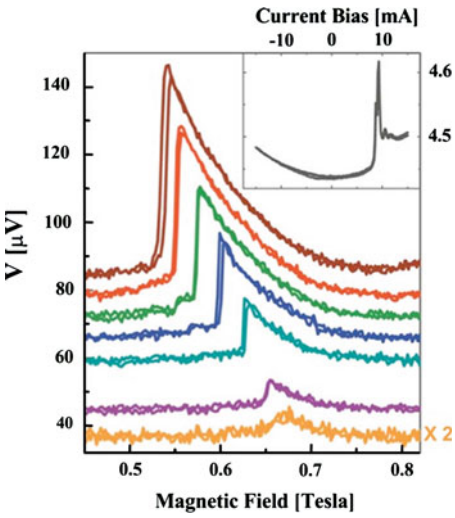

Fig. 11 ST-FMR spectra versus ac current amplitude for metallic GMR device. From *bottom* to *top*, the rf current amplitude was 1.4, 2.1, 3.3, 4.6, 6.2, 7.8, and 9.0 mA. The saw-tooth shape for large excitation amplitudes is evidence for large amplitude precession of the active layer magnetization. The shift in the peak resonance frequency from that for small excitation amplitude is linearly proportional to the decrease in the z-component of the magnetization at the maximum precession amplitude. From Ref. [70]

4 Ferromagnetic Resonance Detection in the Time Domain

4.1 Time Resolved Kerr Microscopy

Time resolved Kerr microscopy is a very convenient technique to study the magnetization dynamics in the time domain. In this method light from a pulsed laser is coupled into an optical microscope with polarization analysis. Due to the magneto-optic Kerr effect (MOKE) the polarization of light that is reflected from a magnetic sample is altered as a function of the orientation of the magnetization vector. Here this effect is used to study the dynamics of the magnetization vector in the sample. Time Resolved (TR)-MOKE is a pump-probe technique where the sample is periodically excited by an external stimulus (e.g. optical pulse or magnetic field pulse) which is synchronized to the laser pulses. The time resolution of such experiments is only limited by the duration of pump and probe events. For the experiments discussed in the following a Ti:sapphire laser is used to generate light pulses of 150 fs duration at a repetition rate of 80 MHz and at a central wavelength 800 nm. The laser light is split into two parts, which are referred to as pump and probe beams. The pump pulses are used to trigger magnetic field pulses which excite magnetization dynamics in the sample. The probe pulses sample the state of the system at a delay time Δt which is determined by the time delay between pump and probe pulse. In the present experimental setup the detection of the magneto optic Kerr effect is such that only the polar component of the magnetization vector contributes to the measured signal. However in principle it is possible to detect all components of magnetization vector in TR-MOKE experiments using a more sophisticated detection scheme [80]. In order to measure the time dependence of the magnetization an opto-mechanical

delay stage can be used to scan the optical path of the pump pulses with respect to probe events.

It is necessary to perform TR-MOKE measurements in a stroboscopic fashion since the signal of a single pump-probe event is too small to be detected. In order to obtain a sufficient signal to noise ratio the same experiment is typically repeated many million times at a fixed delay time while the pumping is modulated at a frequency of a few kHz. This modulation allows lock-in detection of the small dynamic Kerr signal. In addition, for experiments with pulsed excitation two conditions should be fulfilled. First, the relaxation of the system back into its ground state should be completed before the next pump pulse arrives. For the experiments discussed here the repetition rate of the laser is 80 MHz, i.e. this relaxation should take place within 12.5 ns. Second, the response of the system to the pump event has to be reproducible. All stochastic processes, such as variations of the response due to slightly different experimental conditions or thermal magnon excitation average out.

In the experimental setup the fundamental near infrared beam of the Ti:Sapphire laser ($\lambda \sim 800\,\text{nm}$) is focused into a lithium-borate (LBO) crystal, where the light is partly frequency doubled to $\lambda \sim 400\,\text{nm}$ by second harmonic generation. The spatial resolution $x_{\min}$ is obtained by scanning the sample laterally under the objective lens of a microscope using a piezo-mechanical stage. The resolution is diffraction-limited and determined by the numerical aperture of the objective lens and the wavelength of the light. The objective lens that is used has a numerical aperture of $\text{NA} = 0.90$. Therefore a spatial resolution of $x_{\min} = \frac{\lambda}{2\text{NA}} \approx 230\,\text{nm}$ can be achieved. The the polarization state of the reflected light is analyzed by means of a Wollaston polarizer and the difference signal is measured by two photo diodes. This difference signal is fed into a lock-in amplifier and sensitive to the time dependent magnetization state of the sample. In addition the intensity i.e. the sum signal of both photo diodes represents the reflectivity of the sample at the laser spot position. This signal allows to record the topography of the sample simultaneously with the magneto-optic response.

In the following sections experiments with pulsed and continuous wave (cw) excitation are discussed with the aim to illustrate the potential of the TR-MOKE technique.

4.2 Pulsed Experiments

In this section two experiments with pulsed excitation will be discussed. In the first experiment short current pulses are generated by optical pump pulses in a photoconductive switch. In a second experiment microwave bursts are generated by a signal generator. These rf-currents are coupled into a micro structured transmission line and the corresponding rf-magnetic field excites magnetization dynamics in the magnetic sample. The pump-probe experiments allow to record the ring down of the excitation by measuring the Kerr signal as a function of the delay time between pump and probe pulses. In the first experiment the interaction between a magnetic vortex

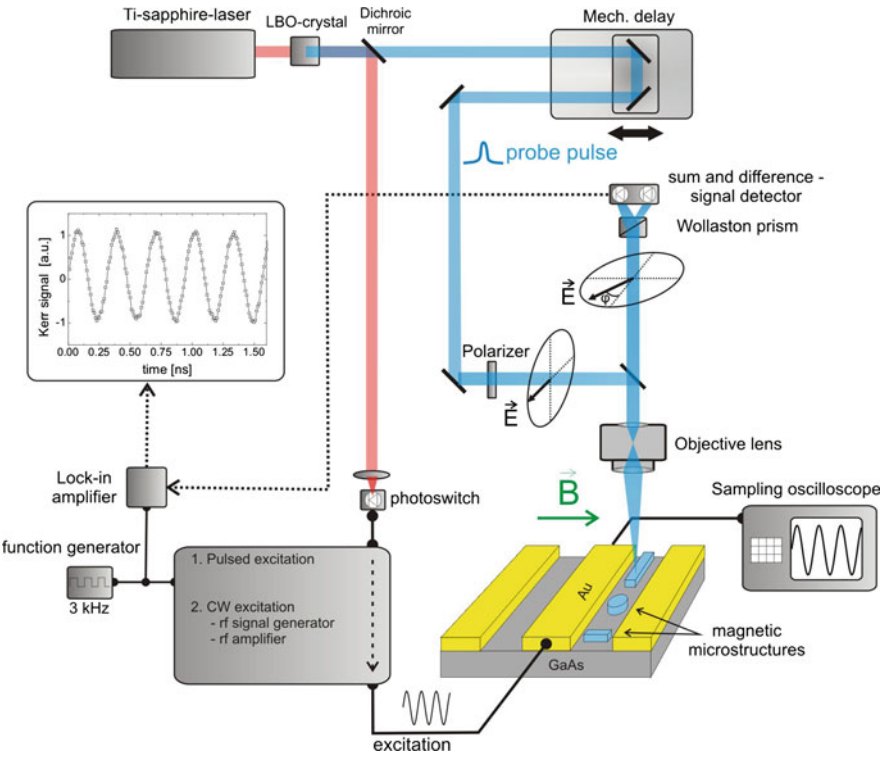

Fig. 12 Illustration of the time resolved Kerr microscopy setup. Part of the fundamental infrared beam of the Ti-Sapphire laser (∼800 nm) is frequency doubled using a LBO crystal. This frequency doubled blue beam (∼400 nm) probes the perpendicular magnetization component by means of the polar magneto-optic Kerr effect. The red laser pulses are delayed by means of a mechanical delay stage and focused onto a fast photo diode which triggers the generation of phase-synchronized microwaves. The microwave current passes through the coplanar waveguide structure of the sample, leading to an rf-magnetic field **h** which excites the precession of the magnetization. The sample is placed on a piezo scanning stage which is used to scan the sample laterally under the fixed laser focus. Static magnetic fields **H** can be applied in any direction in the sample plane by a rotatable electromagnet

core and spin wave eigenmodes in a magnetic disk will be examined. In the second experiment the propagation of spin-wave pulses which are excited by microwave bursts is studied.

4.2.1 Interaction Between Spin-Waves and a Vortex Core

In this experiment the magnetization in a disk of $Ni_{80}Fe_{20}$ with a diameter of 1.5 μm and a thickness of 15 nm is excited by in-plane magnetic field pulses. The current pulses which create an in-plane magnetic rf pumping field are generated by pulsed

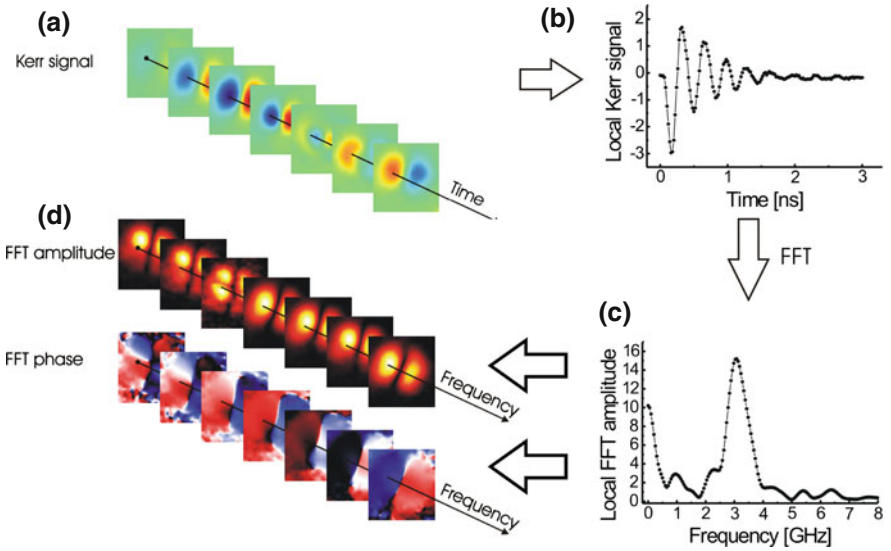

Fig. 13 Principle of imaging of eigenmodes by local Fourier transformations. **a** first a series of images of the Kerr contrast is recorded by TR-MOKE at various delay times after pulsed excitation of a $Ni_{80}Fe_{20}$ disk with a diameter of 1.5 μm and a thickness of 15 nm. Second the time dependence in each pixel of these images (shown in **b**) is Fourier transformed (**c**). **d** shows the amplitude and phase of the Fourier transformation (FFT) visualized as a function of frequency. Adapted from [82]

illumination of a photo-conductive switch as illustrated in Fig. 12 and the magnetic disk is placed on top of the signal line of a coplanar waveguide. The magnetization dynamics is recorded by TR-MOKE. For a given time delay between pump and probe pulses snapshots of the magnetic excitation as shown in Fig. 13a can be recorded. For each pixel of the snapshot the time evolution of the magnetic excitation can be plotted as can be seen in Fig. 13b. The application of a Fourier transformation to these time dependent data allows to identify the spin-wave eigenmodes [81]. In the frequency domain one can identify peaks corresponding to the excited eigenmodes (Fig. 13c). The amplitude and phase of the Fourier transformed spectra can be reassembled to form images as a function of frequency (see Fig. 13d). The eigenmodes are clearly visible. An in-plane field pulse applied to vortex state with its circulating magnetization mostly excites the first azimuthal mode $(1, \pm 1)$ as the $\mathbf{M} \times \mathbf{h}_{\mathrm{rf}}$ term has the opposite sign on both sides of the disk [82]. In addition also the magnetic vortex core is excited to gyrate around the center of the disk.

From the Fourier transformed data that were spatially averaged over one half of the disk as shown in Fig. 14a one can see that the intrinsic degeneracy of the clockwise and counter clockwise rotating first azimuthal modes $(1, +1)$ and $(1, -1)$ is lifted. In the amplitude and phase images at both peaks one can see that they correspond to the first azimuthal mode. However the phase of the lower peak rotates clockwise while the phase of the higher frequency peak rotates counterclockwise. This splitting is a

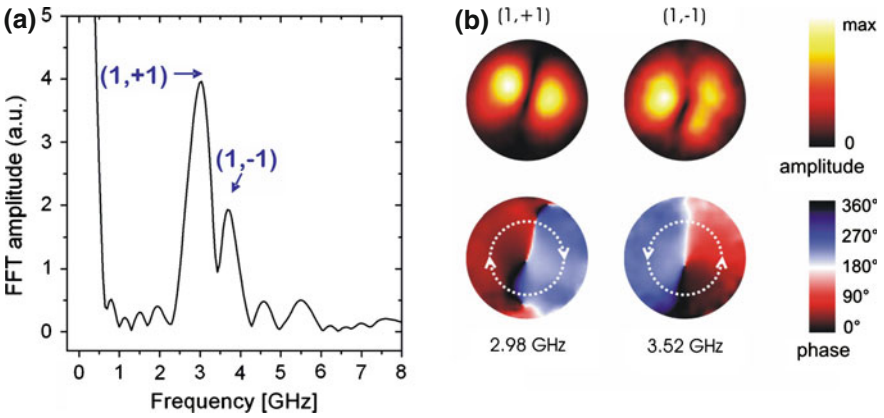

Fig. 14 **a** Fourier spectrum of measured dynamics averaged over one half of a $Ni_{80}Fe_{20}$ disk with a diameter of 1.5 μm and a thickness of 15 nm. **b** Spectral amplitude and phase images of the two azimuthal modes (1, +1) and (1, −1) measured by TR-MOKE. Adapted from [82]

consequence of the interaction of the spin-wave eigenmodes with the vortex core. We have demonstrated in [82] that the removal of the magnetic vortex core (by etching a hole in the center of the disk) results in a disappearance of the splitting. Guslienko et al. have shown theoretically that the dynamic interaction between the rotating spin-waves and the vortex core motion is responsible for the mode splitting [83].

4.2.2 Spin-wave Propagation

In order to study the propagation of spin-waves extended magnetic structures are needed. For this purpose this section discusses the propagation of spin-wave packets in large $Ni_{80}Fe_{20}$ film structures upon pulsed microwave excitation. Traditionally the spin-wave propagation and the propagation of non-linear spin-wave packets (bullets or spin-wave solitons) has been investigated mostly for the ferrimagnetic insulator Yttrium Iron Garnet due to its small intrinsic damping. In experiments employing inductive detection the propagation of spin-waves in ferromagnetic thin $Ni_{80}Fe_{20}$ films was observed over distances of up to 50 μm [84]. Here the direct TR-MOKE observation of the propagation of spin-waves in a 20 nm thick continuous $Ni_{80}Fe_{20}$ film is demonstrated.

The sample considered in the following consists of a 20 nm thick $Ni_{80}Fe_{20}$ film with lateral dimensions of 200 × 200 μm^2 patterned onto a GaAs substrate. Subsequently a coplanar stripline (CPS) is patterned over one edge of the $Ni_{80}Fe_{20}$ film using optical lithography (see Fig. 15a). A microwave generator is synchronized to the 80 MHz repetition rate of the Ti:Sapphire laser system in order to provide a phase-stable correlation between microwave excitation and the laser probe pulses. In addition a frequency mixer is added into the microwave circuit in order to generate

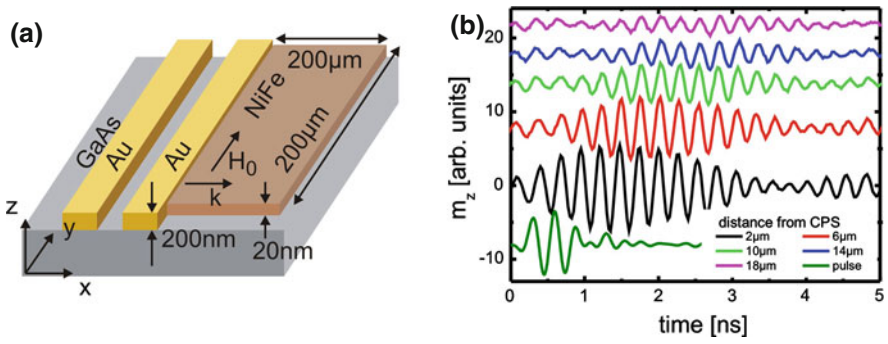

Fig. 15 **a** Sample layout. The 200 nm thick CPS fabricated from Au is placed over one edge of the $Ni_{80}Fe_{20}$ film. **b** Propagation of spin wave packets. Profile of the 4 GHz microwave pulse with a duration of 1 ns (*lowest line*) and scans in time of the spin wave packet at various distances from the CPS (the distance in microns is indicated above the individual lines). The curves have been offset for clarity. Adapted from [85]

microwave field pulses as short as 1 ns at a carrier frequency given by a multiple of the 80 MHz repetition rate of the laser. By measuring the Kerr signal as a function of delay time at various distances from the excitation source (waveguide) one can follow the propagation of a spin-wave packet directly. This allows one to observe the propagation of spin-wave packets in space and time as shown in Fig. 15b.

For a continously applied microwave excitation the response of the magnetization is given by the product of the q-dependent excitation and the q-dependent susceptibility. The q-vector where this product has a maximum is determined by the waveguide and the direction and magnitude of the applied magnetic field. This means that the magnetic film 'picks' the wave vector with the largest susceptibility from the Fourier spectrum of the CPS at a given driving frequency. By measuring line scans as a function of time the phase velocity v_{Ph} of the spin-waves can be directly determined from the slope $\triangle x/\triangle t$ of the oscillatory signal. The phase velocity can easily be converted into a q-vector: $q = \frac{2\pi f}{v_{Ph}}$. By performing such measurements as a function of frequency one can experimentally determine the dispersion relation for spin-waves [85].

When only short bursts of microwave excitation are applied to the sample one can study the propagation and dispersion of spin-wave pulses. Delay scans recorded at various distances from the CPS are shown in Fig. 15b. It can clearly be observed how the microwave burst triggers a spin-wave packet that propagates along the x-direction and broadens considerably as a function of time due to dispersion. In addition, the signal is damped according to the intrinsic damping parameter of the $Ni_{80}Fe_{20}$ film. Nevertheless, we are able to detect a response at distances up to 80 μm from the CPS. From these data of the pulsed excitation the group velocities of the spin-wave packets are readily determined. The measured group velocities $v_G = \frac{\partial \omega}{\partial q}$ are highest (up to 17 km/s) when the wave vector of the spin-wave and magnetic field are orthogonal (Damon Eshbach geometry), while they are smaller for intermediate field directions

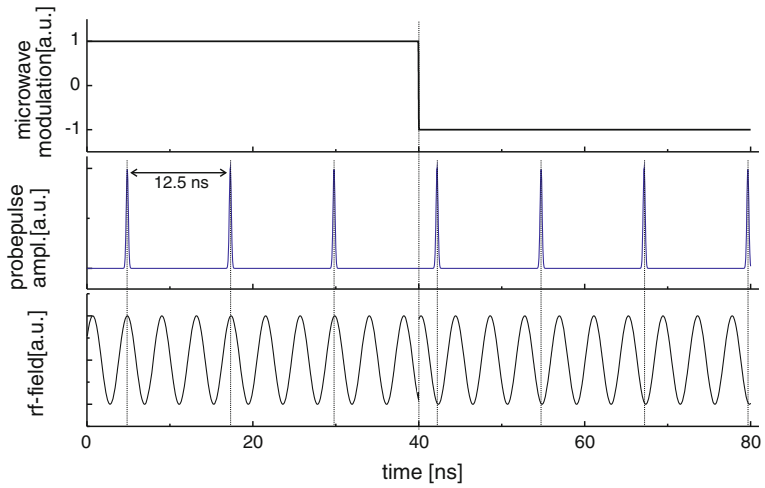

Fig. 16 Synchronization between continuous microwave excitation and laser probe pulses. Due to the repetition rate of the laser, the magnetization is probed every 12.5 ns. The microwave phase is the same for each probe event. 180° phase modulation of the microwaves is performed with a low frequency in the kHz-range. Note that at $t = 40$ ns, the phase of the excitation field is switched by 180°

and close to zero when q-vector and applied magnetic field are parallel (backward volume geometry).

4.3 CW Experiments: Ferromagnetic Resonance

Instead of applying a short magnetic field pulse or a microwave burst to the magnetic system the sample can be excited by means of a cw rf-field which is phase-locked to the laser pulses [86]. By measuring the TR-MOKE signal as a function of the time delay between microwave signal and optical probe one obtains the amplitude of the oscillating out-of-plane component of the precession. In addition, the phase of the response can be measured by comparing the phase of the Kerr signal to the phase of the microwave signal measured by a sampling oscilloscope.

For a fixed microwave frequency one can also measure ferromagnetic resonance (FMR) spectra by sweeping the external field. Depending on the relative phase between the probe pulses and microwave field, such FMR-TR-MOKE spectra are a combination or real and imaginary parts of the rf-susceptibility. The expected line shapes for real (in-phase) part χ' and imaginary (out-of-phase) part χ'' of the susceptibility are shown in Fig. 17. The static magnetization is assumed to point along the x-direction and the tip of the precessing magnetization is assumed to precess on a circular path in the y-z-plane due to the microwave excitation. The dots label the position of the tip of **M** at the point in time when the probe pulse samples the

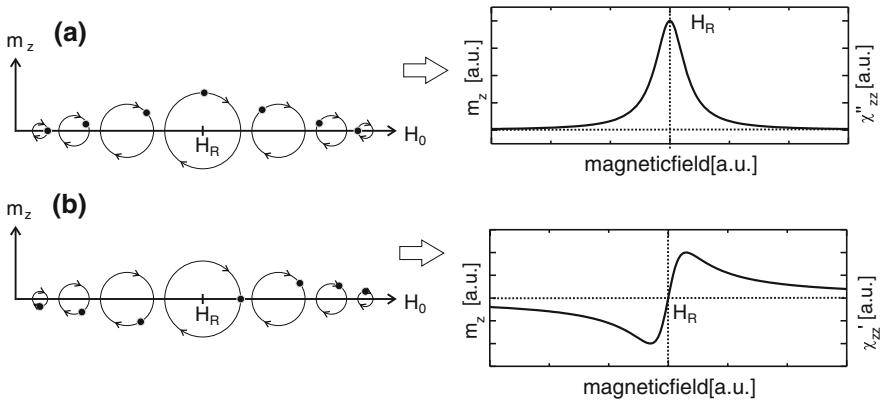

Fig. 17 Illustration of the different line shapes in Kerr-FMR measurements. (*Left side*) z-components of the magnetization m_z versus external magnetic field H for two different microwave phases. The static magnetization lies along the x-direction. The circles represent the precessing magnetization in the y-z-plane. The dots label the position of the tip of the magnetization vector for different field values at the moment when the probe pulses sample the polar component (m_z). (*Right side*) Depending on the phase correlation, the resulting spectra can have a symmetric (**a**) or an asymmetric line shape (**b**)

z-component of **M**. Far away from resonance ($H \ll H_R$ and $H \gg H_R$), the precession amplitudes are small, expressed by the smaller circles. At resonance ($H = H_R$), the precession amplitude is maximum. In addition, the phase between excitation field $\mathbf{h}_{\mathrm{rf}}$ and the precessing magnetization **M** has to be considered. For high magnetic fields, $\mathbf{h}_{\mathrm{rf}}$ and **M** move in phase ($\varphi = 0$), since the frequency of the microwave field excitation is much lower than the resonance frequency. The phase changes gradually from 0 to $\pi/2$ when the external field is decreased. At resonance, the phase lag of the precessing magnetization behind the excitation field is exactly $\pi/2$. In order to perform such measurements a microwave generator is synchronized with the laser pulses and an electronic line stretcher allows precise adjustment of the microwave phase. The rf-signal is delivered to the sample by a coplanar waveguide. In order to ensure both the excitation of the sample and the phase synchronization of the microwave signal with the probe laser pulses the microwave signal is monitored using a sampling oscilloscope. The synchronization between excitation and probe pulses is shown schematically in Fig. 16. Since the microwave phase is modulated by 180° (cf. Fig. 16), the output signal from the lock-in amplifier represents the difference signal of magnetization vector from opposite sides of the precession cone (cf. Fig. 17). TR-MOKE with cw excitation allows to combine two experimental techniques: ferromagnetic resonance (FMR) and time-resolved scanning Kerr microscopy. FMR-TR-MOKE allows one to perform spatially resolved resonance measurements. Thus this technique can be used to image magnetic modes in confined magnetic structures or to visualize local variations of the internal fields [87].

In the following the capabilities of this technique will be demonstrated by two examples. First this technique is used to measure the dynamics due to pure spin currents in metallic multilayers. In the second example local magnetic resonance spectroscopy is used to obtain the magnetic anisotropies in stained nano-structures of a magnetic semiconductor.

4.3.1 Spin Pumping in Magnetic Bilayers

In this section the FMR-TR-MOKE technique is used to study the magnetization dynamics due to pure spin currents. Spin polarized currents offer the possibility to exert a large torque on nano-magnets [88, 89]. In recent years current induced magnetization dynamics was successfully demonstrated in magnetic nanostructures [79, 90, 91]. Such current induced dynamics is mostly studied in spin valve structures using columnar nano-magnets. In a nonlocal crossed wire geometry even the switching of a magnetic nano-particle by a spin current was demonstrated [92]. In all these experiments the spin polarized currents are driven by charge currents. The precession of the magnetization in a ferromagnet which is in contact with a normal metal layer leads to the emission of a pure spin current into the normal metal [93]. This effect is known as spin pumping and leads to an increased damping for the magnetization dynamics in the layer that emits the spin current [94, 95].

In the FMR-TR-MOKE experiment that is discussed in the following it is shown that rf-precession can be excited by the absorption of a pure spin current which is generated by spin pumping. For this an epitaxial stack of layers consisting of Fe and Au grown on GaAs(001) is investigated. It is known that the magnetic layers in Au/Fe/Au/Fe/GaAs structures are dynamically coupled via spin pump and spin sink effects [17, 95]. In such a magnetic bilayer the magnetization dynamics in the presence of spin pump and spin sink effects can be described by the following coupled set of modified Landau-Lifshitz-Gilbert equations [95]:

$$\frac{d\mathbf{m}_i}{dt} = -\gamma_{\mu_0}\left[\mathbf{m}_i \times \mathbf{H}_{\text{eff}}\right] + \alpha_i\left[\mathbf{m_i} \times \frac{d\mathbf{m}_i}{dt}\right] + \alpha_i{}^{\text{SP}}\left[\mathbf{m}_i \times \frac{d\mathbf{m}_i}{dt} - \mathbf{m}_j \times \frac{d\mathbf{m}_j}{dt}\right] \tag{28}$$

where $\mathbf{m}_{1,2}$ are unit vectors along the instantaneous magnetization directions of the two ferromagnetic layers F1 and F2. The strength of the spin pump and spin sink effects is given by the parameter $\alpha^{\text{SP}} = g\mu_B \frac{g^{\uparrow\downarrow}}{M_s}\frac{1}{t_1}$, where t_1 is the thickness of F1, $g^{\uparrow\downarrow}$ (in units of e^2/h) is the real part of the spin mixing conductance [95] and μ_B is the Bohr magneton. The exchange of spin currents is a symmetric concept and the equation of motion for layer F2 can be obtained by interchanging the indices $i \rightleftarrows j$ in Eq. (28). The net spin current generated by layer F1 propagates away from the F1/N interface [93] and is absorbed at the N/F2 interface if N is thinner or comparable to the spin diffusion length (spin-sink effect) [96]. Conservation of angular momentum requires that layer F1 looses spin momentum which leads to an increase of the Gilbert damping parameter of layer F1. Subsequently, the spin current absorbed at the N/F2

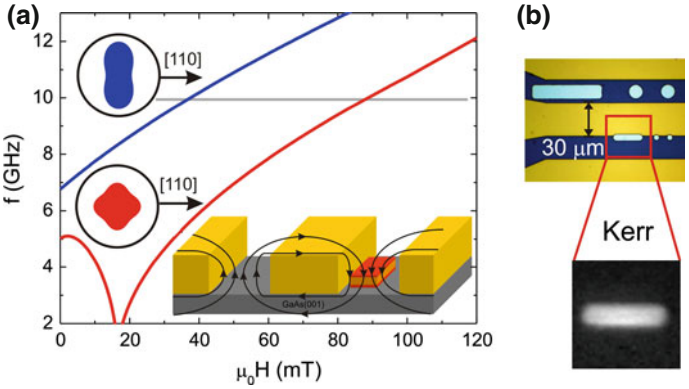

Fig. 18 **a** Calculated resonance frequency vs. applied field for 20Au/10Fe/250Au/16Fe/GaAs(001) (*numbers are in monolayers*) with the magnetic field applied along the [110] direction of Fe. The FMR frequencies for the 10Fe(F2) and 16Fe(F1) layers are shown in the *red* and *blue lines*, respectively. Note, that the *blue line* is shifted upwards compared to the *red line*. This shift is caused by the in-plane uniaxial interface anisotropy at the Fe/GaAs interface with the easy axis along the [110] direction. Layer F2 has a weak cubic anisotropy with easy ⟨100⟩ directions. Above 20 mT both layers are aligned parallel with their resonance frequencies separated by several GHz. The inset shows the experimental configuration. **b** Optical image of the actual sample. The signal line has a width of 30 μm. The magnification shows the Kerr signal of the 25 × 8 μm^2 rectangle in a bias field of 65 mT at a frequency of 8.08 GHz. From [17]

interface creates an rf-torque on the magnetic moment in F2. Since F2 is an ultrathin ferromagnet the interface torque results in a homogeneous precession of the layer F2 at the resonance frequency of F1. In an inductive FMR experiment this effect cannot be observed directly since the rf-response is dominated by the FMR signal from F1.

The single crystalline magnetic double layer structures that are used in the experiment are grown by molecular beam epitaxy in ultra high vacuum on GaAs(001) substrates, further details can be found in [94]. The different interface anisotropies of the two ferromagnetic layers can be used to split the resonance frequencies of F1 and F2 by several GHz. The expected resonance frequencies for F1 and F2 as a function of bias field applied along the [110] direction are shown in Fig. 18a. As shown in Fig. 18, for fields above 40 mT the magnetic moments of layers F1 and F2 and the dc field are collinear and parallel to the [110] direction of Fe.

A cw-signal of 10 GHz was applied to the micro structured coplanar transmission line (shown in Fig. 18b) and as expected from Fig. 18a the FMR-TR-MOKE signal for the layer F2 occurs at a field of 96 mT, as can be seen in Fig. 19a. At the resonance field of layer F1 a typical antisymmetric line (corresponding to the real part of the rf-susceptibility χ') and a symmetric line (corresponding to the imaginary part of the rf-susceptibility χ'') are found in the tails of the out-phase and in-phase rf-response, respectively. These signals at the F1 resonance field are in agreement with the spin pumping theory. F2 is driven by the spin current generated by F1, see Eq. (28), which is proportional to the time derivative of the rf-magnetization of layer F1.

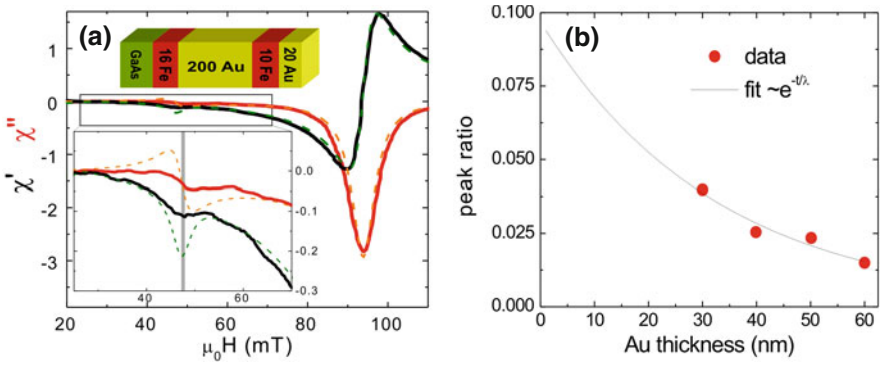

Fig. 19 **a** Measured real (*red line*) and imaginary (*black line*) parts of the perpendicular rf-susceptibility of layer F2. A frequency of 10 GHz was used and the magnetic dc-field was swept parallel to the [110] direction of Fe. The corresponding calculations using Eq. (28) are shown as *dotted lines*. The inset magnifies the region of interest. **b** The ratio of the signal amplitudes (FMR signal/ spin pumping signal) is plotted for a series of samples with Au spacer layer thicknesses between 30 and 60 nm. These data allow one to estimate of the spin diffusion length for Gold to be $\lambda_{sd} = 34$ nm. [97]

Therefore this driving is phase shifted by about $\pi/2$ with respect to the applied rf-field. Consequently, the additional driving due to spin pumping exchanges the resonance line shapes for the real and imaginary parts in the rf-susceptibility. I.e. in the imaginary (real) part of the F2 susceptibility has a contribution at the F1 resonance which has the line shape of the real (imaginary) part of the susceptibility of F1, see Fig. 19a. All these experimental features are well reproduced by the spin pumping theory using Eq. (28). The measured signal agrees with the calculations in its shape, however due to spin relaxation in the Gold spacer layer the amplitude is reduced by 70 % compared to ballistic spin transport, (c.f. dashed lines in Fig. 19a).

In the measurements the direct Kerr signal from the bottom layer is suppressed using an optical compensator [17]. In addition one should point out that dipolar coupling between the ferromagnetic layers e.g. caused by roughness would always lead to a symmetric line at the F1 resonance but cannot result in the observed antisymmetric line shape. Therefore one can firmly conclude that the signal measured at the F1 resonance in Fig. 19a is a sole consequence of the absorbed spin current in F2.

It is worthwhile to point out that the technique presented here can be used to estimate the spin diffusion length in the metallic spacer layer [17, 97]. For this the decay of the signal due to spin pumping is measured as a function of spacer thickness and compared to theory. This is shown in Fig. 19b. For the interpretation it is important to take spin diffusion effects into account [97]. The value one obtains for the spin diffusion length from these data at room temperature in Gold is $\lambda_{sd} = 34$ nm [97].

4.3.2 Local Magnetic Anisotropies

In this section it is shown that the FMR-TRMOKE technique can be used to determine the magnetic anisotropies with high spatial resolution. For this purpose measurements of the magnetic anisotropy of are performed in a spatially resolved manner on nanostructures of the magnetic semiconductor (Ga, Mn)As.

Due to the low Curie temperature of the diluted magnetic semiconductor, the experiments are carried out low temperature in a microscope cryostat. The magnetic properties of the diluted magnetic semiconductor (Ga, Mn)As have been studied previously using ferromagnetic resonance, SQUID, magnetotransport or Hall-effect measurements. In (Ga, Mn)As the magnetic anisotropies depend on temperature and hole concentration [98]. It was shown that the magnetic anisotropies can be manipulated by applying mechanical stress to the sample [99]. It has also been demonstrated that the easy axis of the magnetization can be rotated by varying the hole concentration using a strong electric field [100]. However, these techniques do not resolve magnetic anisotropies in (Ga, Mn)As micro-and nanostructures locally.

The experiments presented in the following show spatially resolved measurements of the magnetic anisotropy with a resolution of 500 nm. A (Ga, Mn)As film grown on GaAs(001) was investigated. Due to the lattice mismatch between (Ga, Mn)As and GaAs this sample is compressively strained. The strain gives rise to a strong perpendicular magnetic anisotropy with a hard axis along the film normal. By patterning a (Ga, Mn)As film into small structures this strain can be partially relieved, strongly affecting the magnetic anisotropies. The FMR-TR-MOKE approach combines the advantages of two experimental techniques: angle-dependent FMR provides direct access to the energy landscape and the magnetic anisotropies and TRMOKE microscopy allows spatially resolved measurements. Thus these experiments can serve to visualize local variations of the magnetic anisotropy.

In the following a 50 nm thick $Ga_{1-x}Mn_xAs$ film with a nominal Mn content $x = 0.06$ grown on a GaAs(001) substrate is studied. This sample has a Curie temperature of 170 K. Further details concerning the sample preparation can be found in [101]. The magnetic elements are defined by electron beam lithography and dry etching steps. The etch depth into the GaAs substrate is approximately 30 nm. Stripes having a width ranging from 200 nm up to 4 μm patterned along different crystallographic directions ([100], [110], [010]) and disks with different diameters were prepared. For the excitation of the magnetization with microwaves in the GHz-range a coplanar waveguide was defined in a subsequent lithography step. The magnetic elements are placed in the gap between the 30 μm wide signal line and the ground plane resulting in a out-of-plane rf-excitation, cf. Fig. 20a.

In order to determine the magnetic anisotropies FMR spectra are recorded for a series of applied field angles. Fig. 20b shows angle dependent FMR spectra for a large 60×60 μm^2 (Ga, Mn)As reference sample which represents the response of on an isotropically strained 'unpatterned' film. The individual TR-MOKE spectra are fitted to Lorentzian line shapes in order to determine the resonance fields. The resulting angular dependence of the resonance fields is shown in Fig. 20. By fitting this angular dependence the magnetic anisotropy constants in the free energy density can

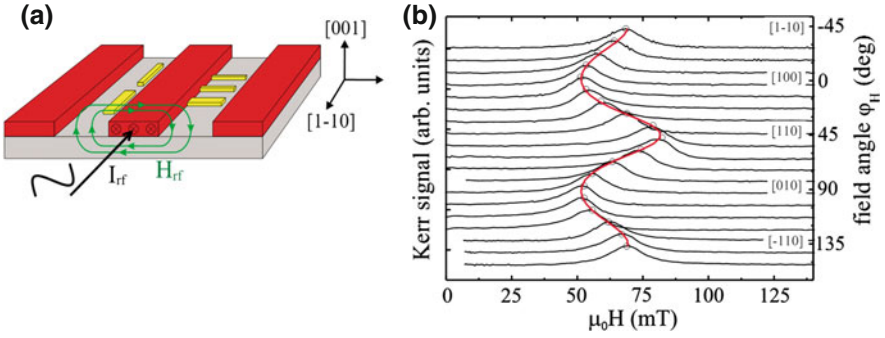

Fig. 20 **a** Sketch illustrating the waveguide and the rf excitation of the magnetic elements. **b** FMR spectra for various angles φ_H of the magnetic field in the film plane (001) for $f = 3.84\,\text{GHz}$ and $T = 7\,\text{K}$ for the reference structure. The resonance fields are obtained by fitting the experimental data to an asymmetric Lorentz function and are indicated by *open dots*. The *red solid line* represents the fit which is used to extract the anisotropy constants. From [101]

be determined [25, 101] : $F = -\mu_0 MH\,(\cos(\varphi_\text{M} - \varphi_H)) - \frac{1}{8}K_{4\parallel}(3 + \cos 4\varphi_\text{M}) - K_{2\parallel}\sin^2\left(\varphi_\text{M} - \frac{\pi}{4}\right)$, where M is the magnetization and φ_M and φ_H are the angles of the magnetization and the external magnetic field H with respect to the [100]-direction. $K_{2\parallel}$ and $K_{4\parallel}$ are the uniaxial and cubic in-plane anisotropy constants.

The angular dependence shown in Fig. 20b (isotopically strained film) is dominated by the intrinsic cubic anisotropy K_4. The difference in resonance field observed along the [110] and [1$\bar{1}$0]-directions is due to the in-plane uniaxial anisotropy $K_{2\parallel}$. The experimental data can be fitted well using the above energy density. The resulting anisotropy constants are $K_{4\parallel} = 2.2 \times 10^2 \frac{\text{J}}{\text{m}^3}$, $K_{2\parallel} = -1.1 \times 10^2 \frac{\text{J}}{\text{m}^3}$ and $K_{2\perp} = -3.0 \times 10^3 \frac{\text{J}}{\text{m}^3}$.

Next, the patterned (Ga, Mn)As structures are addressed. First we focus on narrow stripes. The four-fold symmetry of the reference sample shown in Fig. 20b changes into a pronounced two-fold symmetry when the (Ga, Mn)As film is patterned into a narrow stripe with a width of a few hundred nm (Fig. 21a). As the lattice can relax partially only along the side of the stripe for all three orientations of the stripes ([100], [010], [110]) the easy axis always coincides with the long axis of the stripe; in agreement with earlier studies using SQUID and magneto-transport measurements [102]. From these measurements we estimate the magnitude of the strain induced anisotropy $K_U = 1.8 \times 10^3 \frac{\text{J}}{\text{m}^3}$ for the 400 nm wide stripe. For narrow stripes (below a width of 500 nm) the induced anisotropy saturates since the strain can be fully relaxed across the stripe width. These results clearly demonstrate that the magnitude of the induced uniaxial anisotropy can be well adjusted by using stripe widths ranging between 500 nm and 1.5 μm.

In the following disk-shaped elements are addressed. The angular dependence of the resonance fields for a disk with a large diameter ($d = 10\,\mu$m, black symbols) and a small diameter ($d = 1.5\,\mu$m, red symbols) is shown in Fig. 22a. The experimental data for the 10 μm-diameter disk were obtained at the disk center where the strain

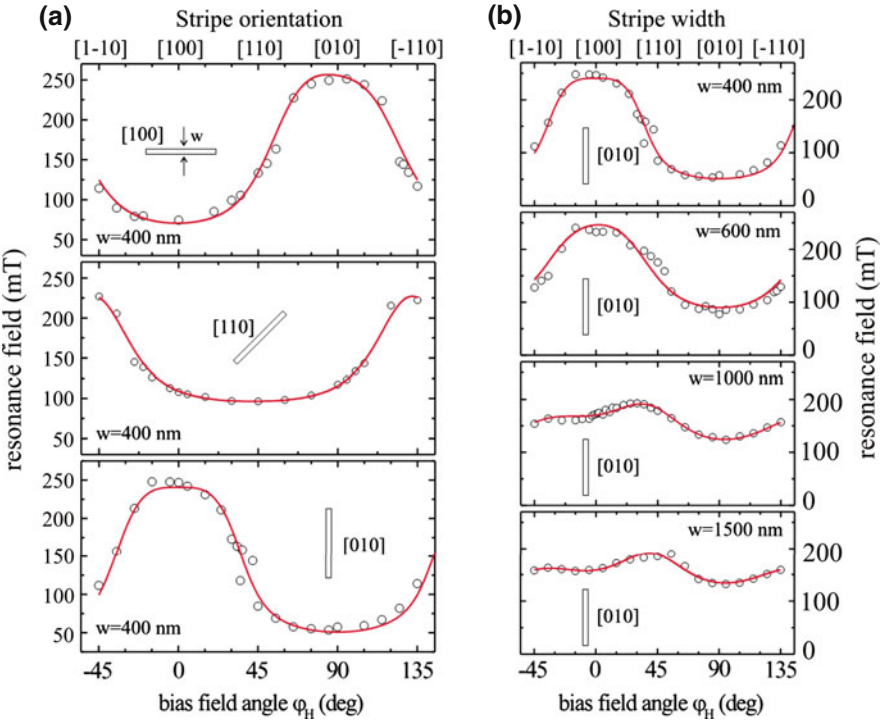

Fig. 21 Resonance field as a function of the external field angle φ_H for stripes patterned along different crystallographic axes (**a**) and different stripe width w (**b**). All data was obtained at $f = 7.2\,\text{GHz}$ and $T = 7\,\text{K}$. The solid lines are fits to the experimental data. From [101]

relaxation is almost zero. It should be emphasized that for a narrow rectangular structure the strain can only relax in one direction giving rise to a strong uniaxial anisotropy (Fig. 21a). For a disk-shaped element we expect isotropic strain relaxation. For this reason the in-plane anisotropies $K_{2\parallel}$ and $K_{4\parallel}$ should remain constant while the strain-induced perpendicular anisotropy $K_{2\perp}$ should be reduced. This reduction is indeed observed (Fig. 22a) as the resonance fields are only shifted to higher field values. The fits to the experimental data show that $K_{2\parallel}$ and $K_{4\parallel}$ remain almost constant while $K_{2\perp}$ is reduced by approximately 20 % for the disk with 1.5 μm diameter.

Finally we demonstrate the ability to visualize the local variations of the magnetic anisotropies for both the disk-shaped and the rectangular (Ga, Mn)As structures. Figure 22c–e show spatially resolved images of the Kerr signal obtained at a fixed excitation frequency f and applied field H. One finds laterally isotropic strain relaxation (indicated by the thick arrows in Fig. 22b). Furthermore one can distinguish two regions as illustrated in the figures: (i) the boundary of the structure where the strain relaxation takes place and a strong uniaxial strain induced magnetic anisotropy can be expected. And (ii) the central region of the structure where the (Ga, Mn)As

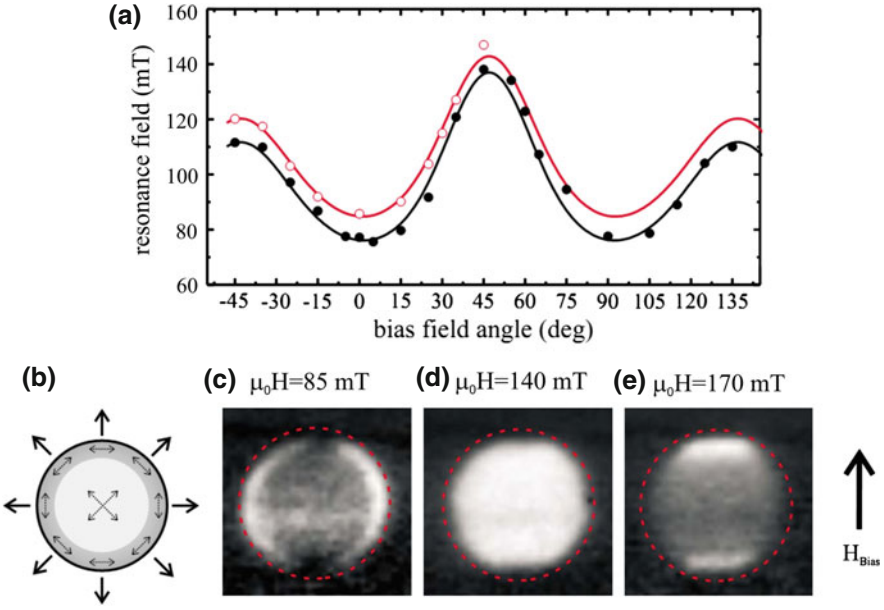

Fig. 22 **a** Angular dependence of the resonance field for disk-shaped (Ga, Mn)As elements for $f = 5.8\,\text{GHz}$ and $T = 7\,\text{K}$. The full *black* and the *open red dots* represent the experimental data for a disk with a diameter $d = 10\,\mu\text{m}$ and $d = 1.5\,\mu\text{m}$, respectively. The solid lines are obtained by fitting the experimental data. **c–e** Images of the polar Kerr signal for a disk-shaped element with a diameter of $10\,\mu\text{m}$ at a microwave frequency of $f = 5.8\,\text{GHz}$. From [101]

lattice remains fully strained and the magnetic anisotropy is unchanged compared to the extended (Ga, Mn)As film. As a consequence the magnetic anisotropies and the direction of the easy axes of the magnetization are varying locally. Based on previous results we expect the local easy axes (shown by the thin arrows) to be parallel to the boundary of the elements, whereas in the central region we expect the film-like behavior with easy axes along the ⟨100⟩-directions [101].

Spatially non-uniform magnetic anisotropies lead to a non-uniform magnetic response for uniform excitation. This behavior is clearly observed in Fig. 22c and e. The resonance field measured at the disk center (which for $\varphi_H = 45°$ is approximately $\mu_0 H_U = 140\,\text{mT}$, see Fig. 22a) leads to a uniform magnetic response (Fig. 22d). However for $H < H_U$ two ring shaped modes at the disk boundary (Fig. 22c) and for $H > H_U$ two modes localized at the edges are found (Fig. 22e). Note that while for $H < H_U$ these ring shaped modes are aligned along the field direction, for $H > H_U$ the modes are aligned perpendicular to H. The ring-shaped modes can be explained in the following way: Due to the lattice relaxation at the disk boundary the easy axis follows the circumference. Based on the results for narrow stripes where the easy axis of the magnetization prefers alignment along the long axis of the stripe we expect that the local easy axis is aligned tangentially to the boundary for curved elements like disks. For the ring shaped areas the external field

is aligned along the local easy axes which means that the resonance is observed at a lower bias field than the main resonance. In contrast for the areas located at the bottom and top of the image the bias field is aligned along a local hard axis, which results in a higher resonance field.

Acknowledgments This chapter is dedicated to the memory of Douglas L. Mills who lost his long battle with leukemia during the writing of this chapter. We thank all former and present co-workers—many of them appearing as co-authors of our publications—who have contributed to the results presented here. This work was supported by the DFG, Sfb 491. G.W. acknowledges financial support from the DFG through SFB 689 and project WO1422/2-1.

References

1. M. Zomack, K. Baberschke, Submonolayers of paramagnetic NO_2 adsorbed on Argon and Xenon films. Phys. Rev. B **36**, 5756 (1987)
2. A. Abragam, B. Bleaney, *Electron Paramagnetic Resonance of Transition Ions* (Oxford University Press, USA, 2012). ISBN 978-0-19-965152-8
3. M. Faehnle, C. Illg, Electron theory of fast and ultrafast dissipative magnetization dynamics. J. Phys. Condens. Matter **23**, 493201 (2011)
4. T.G. Phillips, H.M. Rosenberg, Spin waves in ferromagnets. Rep. Progr. Phys. **29**, 285 (1966)
5. A.I. Achiezer, V.G. Barjachtar, M.I. Kaganov, Spinwellen in ferromagnetika und antiferromagnetika. Fortschritte der Physik **10**, 471 (1962)
6. S.-K. Kim, Micromagnetic computer simulations of spin waves in nanometre-scale patterned magnetic elements. J. Phys. D Appl. Phys. **43**, 264004 (2010)
7. H. Puszkarski, Theory of surface states in spin wave resonance. Progr. Surf. Sci. **9**, 191–247 (1979)
8. B. Hillebrands, in *Brillouin Light Scattering from Layered Magnetic Structures*. vol. 75, ed. by M. Cardona, G. Gntherodt, Light Scattering in Solids VII, Topics in Applied Physics, (Springer, Berlin 2000), pp. 174–289. 10.1007/BFb0103386
9. Y. Zhang, P.A. Ignatiev, J. Prokop, I. Tudosa, T.R.F. Peixoto, W.X. Tang, Kh Zakeri, V.S. Stepanyuk, J. Kirschner, Elementary excitations at magnetic surfaces and their spin dependence. Phys. Rev. Lett. **106**, 127201 (2011)
10. S. Schwieger, J. Kienert, K. Lenz, J. Lindner, K. Baberschke, W. Nolting, Spin-wave excitations: The main source of the temperature dependence of interlayer exchange coupling in nanostructures. Phys. Rev. Lett. **98**, 057205 (2007)
11. Yi. Li, M. Farle, K. Baberschke, Critical spin fluctuations and Curie temperatures of ultrathin ni(111)/w(110): A magnetic-resonance study in ultrahigh vacuum. Phys. Rev. B **41**, 9596 (1990)
12. O. Margeat, M. Tran, M. Spasova, M. Farle, Magnetism and structure of chemically disordered $FePt_3$ nanocubes. Phys. Rev. B **75**, 134410 (2007)
13. S. Loth, M. Etzkorn, C.P. Lutz, D.M. Eigler, A.J. Heinrich, Measurement of fast electron spin relaxation times with atomic resolution. Science **329**, 1628 (2010)
14. K. Ounadjela, B. Hillebrands (ed.), in *Spin Dynamics in Confined Magnetic Structures I, II and III*. Topics in Applied Physics, (Springer, Berlin, 2002, 2004 and 2006)
15. A. Vansteenkiste, K.W. Chou, M. Weigand, M. Curcic, V. Sackmann, H. Stoll, T. Tyliszczak, G. Woltersdorf, C.H. Back, G. Schütz, B. van Waeyenberge, X-ray imaging of the dynamic magnetic vortex core deformation. Nat. Phys. **5**, 332 (2009)
16. V.E. Demidov, S. Urazhdin, S.O. Demokritov, Direct observation and mapping of spin waves emitted by spin-torque nano-oscillators. Nat. Mater. **9**, 984 (2010)

17. G. Woltersdorf, O. Mosendz, B. Heinrich, C.H. Back, Magnetization Dynamics due to Pure Spin Currents in Magnetic Double Layers. Phys. Rev. Lett. **99**, 246603 (2007)
18. A. Mekonnen, M. Cormier, A.V. Kimel, A. Kirilyuk, A. Hrabec, L. Ranno, T. Rasing, Femtosecond Laser Excitation of Spin Resonances in Amorphous Ferrimagnetic $Gd_{1-x}Co_x$ Alloys. Phys. Rev. Lett. **107**, 117202 (2011)
19. J. Goulon, A. Rogalev, G. Goujon, F. Wilhelm, J.B. Youssef, C. Gros, J.-M. Barbe, R. Guilard, X-ray detected magnetic resonance: a unique probe of the precession dynamics of orbital magnetization components. Int. J. Mol. Sci. **12**, 8797 (2011)
20. S. Pizzini, J. Vogel, M. Bonfim, A. Fontaine, in *Time-Resolved x-ray Magnetic Circular Dichroism : A Selective Probe of Magnetization Dynamics on Nanosecond Timescales*. vol. 87, ed. by B. Hillebrands, K. Ounadjela, Spin Dynamics in Confined Magnetic Structures II, Topics in Applied Physics, (Springer, Berlin 2003), pp. 157–187
21. H. Wende, Recent advances in x-ray absorption spectroscopy. Rep. Progr. Phys. **67**, 2105 (2004)
22. S. Buschhorn, F. Brüssing, R. Abrudan, H. Zabel, Precessional damping of fe magnetic moments in a feni film. J. Phys. D Appl. Phys. **44**, 165001 (2011)
23. R. Salikhov, R. Abrudan, F. Brüssing, St. Buschhorn, M. Ewerlin, F. Radu, I.A. Garifullin, H. Zabel, Precessional dynamics and damping in Co/Cu/Py spin valves. Appl. Phys. Lett. **99**, 092509 (2011)
24. I. Barsukov, R. Meckenstock, J. Lindner, M. Möller, C. Hassel, O. Posth, M. Farle, H. Wende, Tailoring spin relaxation in thin films by tuning extrinsic relaxation channels. IEEE Trans. Magn. **46**, 2252 (2010)
25. M. Farle, Ferromagnetic resonance of ultrathin metallic layers. Rep. Progr. Phys. **61**, 755 (1998)
26. R. Arias, D.L. Mills, Extrinsic contributions to the ferromagnetic resonance response of ultrathin films. Phys. Rev. B **60**, 7395 (1999)
27. I. Barsukov, S. Mankovsky, A. Rubacheva, R. Meckenstock, D. Spoddig, J. Lindner, N. Melnichak, B. Krumme, S.I. Makarov, H. Wende, H. Ebert, M. Farle, Magnetocrystalline anisotropy and gilbert damping in iron-rich $fe_{1-x}si_x$ thin films. Phys. Rev. B **84**, 180405 (2011)
28. I. Barsukov, F.M. Römer, R. Meckenstock, K. Lenz, J. Lindner, S. Hemken to Krax, A. Banholzer, M. Körner, J. Grebing, J. Fassbender, M. Farle, Frequency dependence of spin relaxation in periodic systems. Phys. Rev. B **84**, 140410 (2011)
29. V. Kamberský, Spin-orbital gilbert damping in common magnetic metals. Phys. Rev. B **76**, 134416 (2007)
30. A.N. Anisimov, M. Farle, P. Poulopoulos, W. Platow, K. Baberschke, P. Isberg, R. Wäppling, A.M.N. Niklasson, O. Eriksson, Orbital magnetism and magnetic anisotropy probed with ferromagnetic resonance. Phys. Rev. Lett. **82**, 2390 (1999)
31. W. Platow, A.N. Anisimov, G.L. Dunifer, M. Farle, K. Baberschke, Correlations between ferromagnetic-resonance linewidths and sample quality in the study of metallic ultrathin films. Phys. Rev. B **58**, 5611 (1998)
32. H. Suhl, Theory of the magnetic damping constant. IEEE Trans. Mag. **34**(4, Part 1), 1834–1838 (1998). 7th Joint MMM-Intermag Conference. (San Francisco, California, 1998), Jan. 06–09
33. K. Baberschke, in *Investigation of Ultrathin Ferromagnetic Films by Magnetic Resonance*. vol. 3, ed. by H. Kronmüller, S.S. Parkin, Handbook of Magnetism and Advanced Magnetic Materials, (Wiley, 2007), p. 1617. ISBN: 978-0-470-02217-7
34. I. Rod, O. Kazakova, D.C. Cox, M. Spasova, M. Farle, The route to single magnetic particle detection: a carbon nanotube decorated with a finite number of nanocubes. Nanotechnology, **20**, 19 (2009)
35. J. Lindner, I. Barsukov, C. Raeder, C. Hassel, O. Posth, R. Meckenstock, P. Landeros, D.L. Mills, Two-magnon damping in thin films in case of canted magnetization: theory versus experiment. Phys. Rev. B **80**, 224421 (2009)
36. C.W. Haas, H.B. Callen, *Magnetism*, vol. I (Academic Press, New York and London, 1963)
37. W. Bailey, P. Kabos, F. Mancoff, S. Russek. Control of magnetization dynamics in $Ni_{81}Fe_{19}$ thin films through the use of rare-earth dopants. IEEE Trans. Mag. **37**, 1749 (2001)

38. J.O. Rantschler, R.D. McMichael, A. Castillo, A.J. Shapiro Jr, W.F. Egelhoff, B.B. Maranville, D. Pulugurtha, A.P. Chen, L.M. Connors, Effect of 3d, 4d, and 5d transition metal doping on damping in permalloy thin films. J. Appl. Phys. **101**, 033911 (2007)
39. G. Woltersdorf, M. Kiessling, G. Meyer, J.-U. Thiele, C.H. Back, Damping by slow relaxing rare earth impurities in ni80fe20. Phys. Rev. Lett. **102**, 257602 (2009)
40. J.-M.L. Beaujour, A.D. Kent, D. Ravelosona, I. Tudosa, E.E. Fullerton, Ferromagnetic resonance study of Co/Pd/Co/Ni multilayers with perpendicular anisotropy irradiated with helium ions. J. Appl. Phys. **109** (2011)
41. C. Bilzer, T. Devolder, C. Chappert, O. Plantevin, A.K. Suszka, B.J. Hickey, A. Lamperti, B.K. Tanner, B. Mahrov, S.O. Demokritov, Ferromagnetic resonance linewidth reduction in feau multilayers using ion beams. J. Appl. Phys. **103**, 07B518 (2008)
42. I. Barsukov, P. Landeros, R. Meckenstock, J. Lindner, D. Spoddig, Z.-A. Li, B. Krumme, H. Wende, D. L. Mills, M. Farle, Tuning magnetic relaxation by oblique deposition. Phys. Rev. B **85**, 014420 (2012)
43. Y. Tserkovnyak, A. Brataas, G.E.W. Bauer, Spin pumping and magnetization dynamics in metallic multilayers. Phys. Rev. B **66**, 224403 (2002)
44. X. Joyeux, T. Devolder, J.-V. Kim, Y. Gomez De La Torre, S. Eimer, C. Chappert, Configuration and temperature dependence of magnetic damping in spin valves. J. Appl. Phys. **110** (2011)
45. J. Lindner, K. Baberschke, Ferromagnetic resonance in coupled ultrathin films. J. Phys. C **15**, S465 (2002)
46. Kh. Zakeri, J. Lindner, I. Barsukov, R. Meckenstock, M. Farle, U. von Hörsten, H. Wende, W. Keune, J. Rocker, S.S. Kalarickal, K. Lenz, W. Kuch, K. Baberschke, Z. Frait, Spin dynamics in ferromagnets: Gilbert damping and two-magnon scattering. Phys. Rev. B **76**, 104416 (2007)
47. Kh. Zakeri, J. Lindner, I. Barsukov, R. Meckenstock, M. Farle, U. von Hörsten, H. Wende, W. Keune, J. Rocker, S.S. Kalarickal, K. Lenz, W. Kuch, K. Baberschke, Z. Frait, Erratum: Spin dynamics in ferromagnets: Gilbert damping and two-magnon scattering [phys. rev. b 76, 104416 (2007)]. Phys. Rev. B **80**, 059901 (2009)
48. M. Yulikov, M. Sterrer, T. Risse, H.-J. Freund, Gold atoms and clusters on MgO(100) films; an epr and iras study. Surf. Sci. **603**(10–12), 1622–1628 (2009)
49. M. Farle, M. Zomack, K. Baberschke, ESR of adsorbates on single crystal metal surfaces under UHV conditions. Surf. Sci. **160**(1), 205–216 (1985)
50. A. Banholzer, R. Narkowicz, C. Hassel, R. Meckenstock, S. Stienen, O. Posth, D. Suter, M. Farle, J. Lindner, Visualization of spin dynamics in single nanosized magnetic elements. Nanotechnology **22**, 295713 (2011)
51. S.S. Kalarickal, P. Krivosik, M. Wu, C.E. Patton, M.L. Patton, M.L. Schneider, P. Kabos, T.J. Silva, J.P. Nibarger, Ferromagnetic resonance linewidth in metallic thin films: comparison of measurement methods. J. Appl. Phys. **99**, 093909 (2006)
52. G. Woltersdorf, B. Heinrich, Two-magnon scattering in a self-assembled nanoscale network of misfit dislocations. Phys. Rev. B **69**, 188417 (2004)
53. L. Lei, J. Young, W. Mingzhong, C. Mathieu, M. Hadley, P. Krivosik, N. Mo, Tuning of magnetization relaxation in ferromagnetic thin films through seed layers. Appl. Phys. Lett. **100**(2), 022403 (2012)
54. P. Wigen, M. Roukes, P. Hammel, in *Ferromagnetic Resonance Force Microscopy*. vol 101, ed. by B. Hillebrands, A. Thiaville, Spin Dynamics in Confined Magnetic Structures III, Topics in Applied Physics, (Springer, Berlin, 2006), pp. 105–136
55. F. Schreiber, M. Hoffmann, O. Geisau, J. Pelzl, Investigation of the photothermally modulated ferromagnetic resonance signal from magnetostatic modes in yttrium iron garnet films. Appl. Phys. A Mater. Sci. Process. **57**, 545 (1993)
56. R. Meckenstock, Invited review article: Microwave spectroscopy based on scanning thermal microscopy: resolution in the nanometer range. Rev. Sci. Instrum. **79**, 041101 (2008)
57. H. Mahdjour, W.G. Clark, K. Baberschke, High-sensitivity broad-band microwave spectroscopy with small nonresonant coils. Rev. Sci. Instrum. **57**, 1100 (1986)
58. K.D. Bures, K. Baberschke, S.E. Barnes, Electron-Spin-Resonance insitu with a Josephson tunnel jucnction. J. Magnetism Magn. Mater. **54**(Part 3), 1415 (1986)

59. P. Landeros, D.L. Mills, Spin waves in periodically perturbed films. Phys. Rev. B **85**, 054424 (2012)
60. F.M. Romer, M. Moller, K. Wagner, L. Gathmann, R. Narkowicz, H. Zahres, B.R. Salles, P. Torelli, R. Meckenstock, J. Lindner, M. Farle, In situ multifrequency ferromagnetic resonance and x-ray magnetic circular dichroism investigations on Fe/GaAs(110): Enhanced g-factor. Appl. Phys. Lett. **100**, 092402 (2012)
61. S.S. Kalarickal, M. Nan, P. Krivosik, C.E. Patton, Ferromagnetic resonance linewidth mechanisms in polycrystalline ferrites: Role of grain-to-grain and grain-boundary two-magnon scattering processes. Phys. Rev. B **79**, 094427 (2009)
62. A.A. Tulapurkar, Y. Suzuki, A. Fukushima, H. Kubota, H. Maehara, K. Tsunekawa, D.D. Djayaprawira, N. Watanabe, S. Yuasa, Spin-torque diode effect in magnetic tunnel junctions. Nature **438**(7066), 339–342 (2005)
63. J.C. Sankey, P.M. Braganca, A.G.F. Garcia, I.N. Krivorotov, R.A. Buhrman, D.C. Ralph, Spin-transfer-driven ferromagnetic resonance of individual nanomagnets. Phys Rev Lett **96**, 227601 (2006)
64. J.N. Kupferschmidt, S. Adam, P.W. Brouwer, Theory of the spin-torque-driven ferromagnetic resonance in a ferromagnet/normal-metal/ferromagnet structure. Phys. Rev. B **74**(13), 134416 (2006)
65. A. Alexey, Gerrit E. W. Bauer, A. Brataas, Current-driven ferromagnetic resonance, mechanical torques, and rotary motion in magnetic nanostructures. Phys. Rev. B **75**, 014430 (2007)
66. G.D. Fuchs, J.C. Sankey, V.S. Pribiag, L. Qian, P.M. Braganca, A.G.F. Garcia, E.M. Ryan, Z.-P. Li, O. Ozatay, D.C. Ralph, R.A. Buhrman, Spin-torque ferromagnetic resonance measurements of damping in nanomagnets. Appl. Phys. Lett. **91**, 062507 (2007)
67. W. Chen, J.-M.L. Beaujour, G. de Loubens, A.D. Kent, J.Z. Sun, Spin-torque driven ferromagnetic resonance of co/ni synthetic layers in spin valves. Appl. Phys. Lett. **92**, 012507 (2008)
68. W. Chen, G. de Loubens, J.-M. L. Beaujour, A.D. Kent, J.Z. Sun, Finite size effects on spin-torque driven ferromagnetic resonance in spin valves with a Co/Ni synthetic free layer. J. Appl. Phys. **103**(7), 07A502 (2008)
69. J.C. Sankey, Y.-T. Cui, J.Z. Sun, J.C. Slonczewski, R.A. Buhrman, D.C. Ralph, Measurement of the spin-transfer-torque vector in magnetic tunnel junctions. Nat. Phys. **4**, 67–71 (2008)
70. W. Chen, G. de Loubens, J.-M.L. Beaujour, J.Z. Sun, A.D. Kent, Spin-torque driven ferromagnetic resonance in a nonlinear regime. Appl. Phys. Lett. **95**, 172513 (2009)
71. W.H. Rippard, A.M. Deac, M.R. Pufall, J.M. Shaw, M.W. Keller, S.E. Russek, G.E.W. Bauer, C. Serpico, Spin-transfer dynamics in spin valves with out-of-plane magnetized CoNi free layers. Phys. Rev. B **81**, 014426 (2010)
72. C. Wang, Y.-T. Cui, J.A. Katine, R.A. Buhrman, D.C. Ralph, Time-resolved measurement of spin-transfer-driven ferromagnetic resonance and spin torque in magnetic tunnel junctions. Nat. Phys. **7**, 496 (2011)
73. R.D. McMichael, M.D. Stiles, Magnetic normal modes of nanoelements. J. Appl. Phys. **97**, 10J901 (2005)
74. J.M. Shaw, T.J. Silva, M.L. Schneider, R.D. McMichael, Spin dynamics and mode structure in nanomagnet arrays: effects of size and thickness on linewidth and damping. Phys. Rev. B **79**, 184404 (2009)
75. H.T. Nembach, J.M. Shaw, T.J. Silva, W.L. Johnson, S.A. Kim, R.D. McMichael, P. Kabos, Effects of shape distortions and imperfections on mode frequencies and collective linewidths in nanomagnets. Phys. Rev. B **83**, 094427 (2011)
76. P.W. Anderson, H. Suhl, Instability in the motion of ferromagnets at high microwave power levels. Phys. Rev. **100**, 1788 (1955)
77. Y.K. Fetisov, C.E. Patton, V.T. Synogach, Nonlinear ferromagnetic resonance and foldover in yttrium iron garnet thin films-inadequacy of the classical model. IEEE Trans. Magn. **35**, 4511–4521 (1999)
78. M.T. Weiss, Microwave and low-frequency oscillation due to resonance instabilities in ferrites. Phys. Rev. Lett. **1**, 239–241 (1958)

79. W.H. Rippard, M.R. Pufall, S. Kaka, S.E. Russek, T.J. Silva, Direct-current induced dynamics in $Co_{90}Fe_{10}/Ni_{80}Fe_{20}$ point contacts. Phys. Rev. Lett. **92**, 027201 (2004)
80. W.K. Hiebert, L. Lagae, J. De Boeck, Spatially resolved ultrafast precessional magnetization reversal. Phys. Rev. B **68**, 020402(R) (2003)
81. M. Buess, R. Hoellinger, T. Haug, K. Perzlmaier, U. Krey, D. Pescia, M.R. Scheinfein, D. Weiss, C.H. Back, Fourier transform imaging of spin vortex eigenmodes. Phys. Rev. Lett. **93**, 077207 (2004)
82. F. Hoffmann, G. Woltersdorf, K. Perzlmaier, A.N. Slavin, V.S. Tiberkevich, A. Bischof, D. Weiss, C.H. Back, Mode degeneracy due to vortex core removal in magnetic disks. Phys. Rev. B **76**, 014416 (2007)
83. K.Y. Guslienko, A.N. Slavin, V. Tiberkevich, S.-K. Kim, Dynamic origin of azimuthal modes splitting in vortex-state magnetic dots. Phys. Rev. Lett. **101**, 247203 (2008)
84. M. Covington, T.M. Crawford, G.J. Parker, Time-resolved measurement of propagating spin waves in ferromagnetic thin films. Phys. Rev. Lett. **89**, 237202 (2002)
85. K. Perzlmaier, G. Woltersdorf, C.H. Back, Observation of the propagation and interference of spin waves in ferromagnetic thin films. Phys. Rev. B **77**, 054425 (2008)
86. I. Neudecker, G. Woltersdorf, B. Heinrich, T. Okuno, G. Gubbiotti, C.H. Back, Comparison of frequency, field, and time domain ferromagnetic resonance methods. J. Mag. Mag. Mat. **307**, 148–156 (2006)
87. I. Neudecker, K. Perzlmaier, F. Hoffmann, G. Woltersdorf, M. Buess, D. Weiss, C.H. Back, Modal spectrum of permalloy disks excited by in-plane magnetic fields. Phys. Rev. B **73**, 134426 (2006)
88. L. Berger, Emission of spin waves by a magnetic multilayer traversed by a current. Phys. Rev. B **54**, 9353 (1996)
89. J.C. Slonczewski, Current-driven excitation of magnetic multilayers. J. Magn. Magn. Mater. **159**, 1 (1996)
90. S.I. Kiselev, J.C. Sankey, I.N. Krivorotov, N.C. Emley, R.J. Schoelkopf, R.A. Buhrman, D.C. Ralph, Microwave oscillations of a nanomagnet driven by a spin-polarized current. Nature **425**, 380 (2003)
91. I.N. Krivorotov, N.C. Emley, J.C. Sankey, S.I. Kiselev, D.C. Ralph, R.A. Buhrman, Time-domain measurements of nanomagnet dynamics driven by spin-transfer torques. Science **307**, 228 (2005)
92. T. Kimura, Y. Otani, J. Hamrle, Switching magnetization of a nanoscale ferromagnetic particle using nonlocal spin injection. Phys. Rev. Lett. **96**, 037201 (2006)
93. Y. Tserkovnyak, A. Brataas, G.E.W. Bauer, Enhanced gilbert daming in thin ferromagnetic films. Phys. Rev. Lett. **88**, 117601 (2002)
94. R. Urban, G. Woltersdorf, B. Heinrich, Gilbert damping in single and multilayer ultrathin films: Role of interfaces in nonlocal spin dynamics. Phys. Rev. Lett. **87**, 217204 (2001)
95. B. Heinrich, Y. Tserkovnyak, G. Woltersdorf, A. Brataas, R. Urban, G.E. Bauer, Dynamic exchange coupling in magnetic bilayers. Phys. Rev. Lett. **90**, 187601 (2003)
96. M.D. Stiles, A. Zangwill, Anatomy of spin-transfer torque. Phys. Rev. B **66**(1), 014407 (2002)
97. O. Mosendz, G. Woltersdorf, B. Kardasz, B. Heinrich, C.H. Back, Magnetization dynamics in the presence of pure spin currents in magnetic single and double layers in spin ballistic and diffusive regimes. Phys. Rev. B **79**, 224412 (2009)
98. K. Khazen, H.J. von Bardeleben, J.L. Cantin, L. Thevenard, L. Largeau, O. Mauguin, A. Lemaître, Ferromagnetic resonance of $Ga_{0.93}Mn_{0.07}As$ thin films with constant Mn and variable free-hole concentrations. Phys. Rev. B **77**, 165204 (2008)
99. C. Bihler, M. Althammer, A. Brandlmaier, S. Geprägs, M. Weiler, M. Opel, W. Schoch, W. Limmer, R. Gross, M.S. Brandt, S.T.B. Goennenwein, $Ga_{1-x}Mn_xAs$ /piezoelectric actuator hybrids: A model system for magnetoelastic magnetization manipulation. Phys. Rev. B **78**, 045203 (2008)
100. D. Chiba, M. Sawicki, Y. Nishitani, Y. Nakatani, F. Matsukura, H. Ohno, Magnetization vector manipulation by electric fields. Nature **455**, 515 (2008)

101. F. Hoffmann, G. Woltersdorf, W. Wegscheider, A. Einwanger, D. Weiss, C.H. Back, Mapping the magnetic anisotropy in (Ga, Mn)As nanostructures. Phys. Rev. B **80**, 054417 (2009)
102. J. Wenisch, C. Gould, L. Ebel, J. Storz, K. Pappert, M.J. Schmidt, C. Kumpf, G. Schmidt, K. Brunner, L.W. Molenkamp, Control of magnetic anisotropy in (Ga, Mn)As by lithography-induced strain relaxation. Phys. Rev. Lett. **99**, 077201 (2007)

Spin-Polarized Electrons in Superconductor/Ferromagnet Hybrid Structures

Konstantin B. Efetov, Ilgiz A. Garifullin, Anatoly F. Volkov and Kurt Westerholt

Abstract We review recent experimental and theoretical progress in the physics of the proximity effect in thin film structures combined of superconducting (S) and ferromagnetic (F) layers with special emphasis on the occurrence of odd triplet superconductivity. In the theoretical works it has been shown that a long range odd triplet component (LRTC) of the superconducting condensate function can appear at S/F interfaces, if the magnetization of F is inhomogeneous. In Josephson junctions of the type S/F/S the ferromagnetic barriers must have an internal $F'/S/F'$ structure with the magnetization direction of F' rotated with respect to the magnetization direction of F in order to create a superconducting LRTC current. Recent experiments are in accord with these predictions. The experimental progress concerning the realization of superconducting spin valves and recent experiments proving the existence of the inverse proximity effect are also reviewed.

1 Introduction

The mutual influence of magnetism and superconductivity in superconductor/ferromagnet (S/F) thin film hybrid structures has been an exciting topic in solid state physics during the last 15 years (see, e.g., the reviews [1–5]). The interplay between

K. B. Efetov (✉) · A. F. Volkov
Institut für Theoretische Physik III, Ruhr-Universität Bochum,
D-44780 Bochum, Germany
e-mail: efetov@tp3.rub.de

I. A. Garifullin
Zavoisky Physical-Technical Institute RAS, 420029 Kazan, Russia
e-mail: ilgiz_garifullin@yahoo.com

K. Westerholt
Institut für Experimentalphysik/Festkörperphysik, Ruhr-Universität Bochum,
D-44780 Bochum, Germany
e-mail: kurt.westerholt@rub.de

H. Zabel and M. Farle (eds.), *Magnetic Nanostructures,*
Springer Tracts in Modern Physics 246, DOI: 10.1007/978-3-642-32042-2_3,

the superconducting and the ferromagnetic order in systems such as an S/F bilayer or an S/F/I/S Josephson junction (I denotes an insulating interlayer) is due to the proximity effect (PE), i.e. due to Cooper pairs penetrating into the ferromagnetic layer (direct PE) and/or due to a ferromagnetic magnetization induced in the superconductor (inverse PE).

Superconductivity and ferromagnetism are antagonistic phenomena, since ferromagnetism requires a parallel alignment of the spins whereas conventional singlet superconductivity requires an antiparallel alignment. The exchange splitting of the conduction bands in typical transition metal ferromagnets is larger than the pairing energy of the electrons in the Cooper pairs by orders of magnitude. Therefore singlet pairing is strongly suppressed by the exchange field and Cooper pairs can penetrate into a diffusive F layer only over the small distance given by the superconducting penetration depth $\xi_F = (4\hbar D_F/I)^{1/2}$ (where D_F is the diffusion coefficient of the conduction electrons in the F layer and I is the exchange splitting) [6]. For strong ferromagnets like Fe, Ni or Co ξ_F is typically of the order of 1 nm or smaller (see, e.g., [7]).

The coexistence of superconductivity and ferromagnetism close to the interfaces in S/F systems leads to unusual and interesting phenomena, part of which are well established in the literature now, others being under current debate. One of the first intriguing properties for S/F structures is the spatial oscillation of the Cooper pair wave function within the F-layer [1–5]. This leads to a non monotonic dependence of the critical temperature on the thickness of the F layer in S/F bilayers and to an oscillatory dependence of the critical Josephson current in S/F/S Josephson junctions. These oscillations were first predicted in Ref. [8, 9] and later observed experimentally [10–17]. Nowadays S/F/S Josephson junctions with negative critical current, so-called $\pi-$junctions, are used for the realization of Qubits, the basic operating units of future quantum computing [18].

A particularly interesting phenomenon at S/F interfaces is the occurrence of a new type of superconducting pairing function, the so-called odd triplet pairing, first predicted theoretically in Ref. [3, 5, 19]. This pairing can arise due to the proximity effect in an F layer with a nonhomogeneous magnetization. In case of an uniform magnetization, the pair wave function in F consists of the singlet component $f_{sng} \sim \langle\psi_\uparrow(t)\psi_\downarrow(0) - \psi_\downarrow(0)\psi_\uparrow(t)\rangle$ and the ordinary triplet component with zero projection of the total spin of the Cooper pairs in the direction of the magnetization M, $f_0 \sim \langle\psi_\uparrow(t)\psi_\downarrow(0) + \psi_\downarrow(0)\psi_\uparrow(t)\rangle$. Both components oscillate in space and decay on a short length scale of the order of ξ_F.

In the case of a nonuniform magnetization in F not only the components f_{sng} and f_0 may arise in the F layer, but also the odd triplet component $f_1(t) \sim \langle\psi_\uparrow(t)\psi_\uparrow(0) + \psi_\uparrow(0)\psi_\uparrow(t)\rangle$ with a nonzero projection of the total Cooper pair spin in the direction of M. This component is insensitive to the exchange field and can penetrate into the F layer over a distance much larger than ξ_F. Without spin-orbit interaction and scattering by magnetic impurities this distance may be comparable to the penetration length of the superconducting condensate into a normal (nonmagnetic) metal, which is given by $\xi_N = (\hbar D_F/2\pi T)^{1/2}$. This is the reason why the

superconducting odd triplet component is sometimes referred to as the long-range triplet component (LRTC).

It is important to realize that the odd triplet component of the superconducting condensate function is symmetric in momentum space and, as a consequence, is insensitive to scattering by ordinary (nonmagnetic) impurities. In this respect the LRTC differs drastically from the ordinary triplet component f_{tr} which describes superconductivity in Sr_2RuO_4, e.g., [3, 5, 20]. The ordinary triplet component is antisymmetric in momentum space and therefore is destroyed by nonmagnetic impurity scattering. It changes sign by permutation of the operators $\psi_\uparrow(t)$ and $\psi_\uparrow(0)$ as it should be according to the Pauli principle. The Pauli principle claims that the Fermi operators $\psi_\uparrow(t)$ and $\psi_\uparrow(0)$ anticommute at equal times. This means that $f_1(0) \sim \langle \psi_\uparrow(0)\psi_\uparrow(0) + \psi_\uparrow(0)\psi_\uparrow(0)\rangle = 0$, i. e., the function $f_1(t)$ is an odd function of time t, or, in other words, it is an odd function of the frequency ω in the Fourier representation. This is the origin of the term *odd triplet component* for f_{tr}. As will be detailed in the main part of this paper, the occurrence of LRTC does not arise in any system with a nonuniform magnetization, but requires a specific symmetry of the magnetization vector with respect to the interface plane. On the experimental side, in recent years an increasing number systems corroborating the existence of LRTC have been detected [21–27].

An interesting new phenomenon in S/F-layer systems is the so called *inverse proximity effect*. As predicted theoretically in Refs. [28–30] first, besides the ordinary PE (penetration of the superconducting pair wave function from the superconductor into the ferromagnet) the inverse PE (penetration of the magnetic moment from the ferromagnet into the superconductor) should also arise at S/F interfaces. In the diffusive limit, which is realized in most experimental systems, the magnetic moment induced in the superconductor has a direction opposite to the magnetization direction in the ferromagnet, thus the superconducting condensate has the tendency to screen the ferromagnetic moments. Therefore the inverse PE has also been called the *spin screening effect* [28–30]. As will be discussed in the main part of this paper, first experimental evidence using nuclear magnetic resonance (NMR) techniques [31, 32], the magneto optical Kerr effect [33] and scanning tunnelling spectroscopy [34] has been reported in the recent literature.

There is an interesting thin film device based on the proximity effect, the so-called superconducting spin valve, where in recent years essential experimental progress was achieved, as will also be reported below. This device combines two ferromagnetic layers F1 and F2 with a superconducting layer S. The basic idea of the device is to change the superconducting transition temperature T_c by switching the relative magnetization direction of F1 and F2 from parallel to antiparallel. The first theoretical prediction dates back to 1997 [35], where the authors proposed a F1/F2/S layer sequence, i.e. an S layer deposited on top of two F layers. Two years later an F1/S/F2 layer sequence combining the spin valve was proposed theoretically by Tagirov [36] and Buzdin et al. [37, 38]. Subsequent experimental work confirmed these predictions [39–42]), however, the difference in T_c accompanying the switching of F1 and F2 from parallel to antiparallel was quite small, actually smaller than the width of the resistive superconducting transition. Only quite recently an experimental

superconducting spin valve with a full switching effect was successfully designed. [43, 44].

A device similar to the superconducting spin valve but based on the Josephson effect in S/F1/I/F2/S junctions has also been under theoretical investigation recently. As first shown in Ref. [45] and later in Ref. [46, 47], the critical current $I_c(\uparrow\downarrow)$ for the antiparallel orientation of F1 and F1 can by far exceed the critical current $I_c(\uparrow\uparrow)$ for the case of parallel orientation of F1 and F2 and even may be larger than the critical current of a comparable S/I/S tunnel junction. First experimental confirmation of this effect has been reported recently in Ref. [48].

In the following sections we will review the recent theoretical and experimental progress on different S/F systems. In section "Josephson Effect in Multilayered S/F/S Junctions" we summarize a theoretical study of the dc Josephson effect in an S/F1/F2/F3/S junction [49], mimicking closely the experimental system investigated in Ref. [23] which gave the clearest evidence for the existence of LRTC until now. In section "Long-Range Proximity Effect in High-T_c Superconductors" we describe the theory of a huge PE in multilayered S/F/S/F structures with high-T_c, d-wave superconductors, which is caused by the LRTC arising at magnetic domains in the ferromagnetic layers [50].

In section "Experimental Evidence for Triplet Superconductivity in S/F Hybrid Structures" the experimental situation concerning the evidence for triplet superconductivity in S/F/S Josephson junctions will be reviewed, followed by a summary of the recent experimental observations on the spin screening effect (inverse PE) in S/F structures in section "Spin Screening Effect" [31–34]. In the final experimental section "Superconducting Spin Valve Effect" we review the recent achievements concerning the experimental realization of the superconducting spin valve [43, 44, 51], and finally, in section "Summary and Conclusions", we summarize, draw some conclusions and discuss the perspectives.

2 Josephson Effect in Multilayered S/F/S Junctions

2.1 Theoretical Studies of Long-Range Triplet Superconductivity

In this subsection we briefly describe recent theoretical studies of the LRTC in S/F structures with nonhomogeneous magnetization. Most predictions in these works still need experimental verification.

In Ref. [19] the LRTC in a diffusive S/F bilayer was predicted. It was assumed that a domain wall with a width w much larger than the electron mean free path is located at the S/F interface. A more general case of a DW with of arbitrary width with respect to the mean free path and an arbitrary impurity concentration was studied in Ref. [52]. The LRTC in diffusive S/F structures with a Neel-type DW has been analyzed in Ref. [53, 54]. The case of a half-metallic ferromagnet in S/F or S/F/S structures was investigated in Refs. [55–57]. Braude and Nazarov [58] studied the

LRTC in S/F structures with highly transparent interfaces so that the amplitude of the condensate functions induced in the ferromagnet was not small (strong proximity effect). Ballistic S/F structures with a nonhomogeneous magnetization were studied in Refs. [56, 59–61] and it was shown that the LRTC could be created. The papers [62–64] were devoted to the study of the LRTC in spiral ferromagnets attached to superconductors.

In other papers [55, 56, 65–67] the LRTC was investigated in S/F structures with so-called spin-active interfaces. In this approach the properties of the S/F interface are characterized by a scattering matrix with elements treated as phenomenological parameters. One does not need to know the detailed structure of the S/F interface, but proceeds calculating the physical quantities using these parameters. From the physical point of view the region with a narrow DW considered in Ref. [52] can be regarded as a spin-active S/F interface. If the width w is comparable to the Fermi wave length, one has to go beyond the quasi-classical theory and derive the boundary conditions from first principles (see [68] as well as [66, 69] and references therein).

The possibility to create the LRTC in an S/F structure with a nonhomogeneous magnetization in the form of a magnetic vortex in the F layer was put forward in Ref. [70]. The dc Josephson effect in S/F/S junctions with a magnetic vortex in F was studied in Refs. [71]. Bobkova and Bobkov [72] suggested to control the critical Josephson current I_c in an S/F/S junction by injection of spin polarized electrons into the F layer with an nonuniform magnetization. The current I_c is caused by the LRTC and the amplitude depends on concentration of the spin-polarized electrons. The spin current was discussed in Refs. [71, 73].

Theoretically the dc Josephson effect in S/F/S junctions with a non-collinear magnetization has been studied in several works. In Refs. [59, 74] the Josephson current in ballistic S/F/S junctions was calculated. Diffusive S/F/F/S junctions with two F layers were considered in Refs. [75, 76]. However, it was found that the long-range Josephson effect in these junctions does not occur. The Josephson critical current I_c is exponentially small, unless the total thickness of the ferromagnetic layer, $L_F + L_{F'}$, is comparable to the short length ξ_F: $I_c \sim \exp(-(L_F + L_{F'})/\xi_F)$.

The reason for the absence of the long-range Josephson effect in Josephson junctions with only two F layers is the following: Obviously, at least one of the F layer should be thin enough ($L_{F'} \leq \xi_F$); otherwise Cooper pairs do not penetrate through the F layers. If $L_{F'} \leq \xi_F$ and the magnetization in the F and F′ layers is not collinear, the LRTC may arise on the left side of the S‘/F/F′/S junction and spread through the F′ film. However, the Josephson current due to the LRTC is zero because it stems from the overlapping of the condensate functions of the same symmetry penetrating the junction from the left and right side. The symmetry of the singlet and short-range triplet component arising at the right differs from the symmetry of the LRTC penetrating from the left, and thus its product is zero. In order to establish the long-range Josephson effect, one needs two LRTCs arising at the left and right sides of the junction simultaneously, as is possible in an S/F/F′/F/S junction with non-collinear magnetizations.

Diffusive Josephson junctions with three ferromagnetic layers with non-collinear magnetization have been analyzed in Refs. [77, 78] and in a recent paper [49].

The authors of Ref. [77] considered the F′/S/F/S/F′structure with different magnetization directions in the F and F′ layers. In Ref. [78] a slightly different S/F′/F/F′/S layer structure with different M directions in the F and F′ layers was analyzed, this structure seems more suitable for an experimental realization. In both papers the exchange energy in F and F' was assumed to be equal.

The amplitude of the LRTC, f_1, and the Josephson critical current due to this component I_{cLR} have been calculated in both works. Although the layer sequence studied in Refs. [77, 78] are different, the results obtained are similar. The final formula for the critical current can be written in both cases as

$$I_{cLR} = F(L_h) \sin \alpha_l \sin \alpha_r \tag{1}$$

In Eq. (1), $\alpha_{l,r}$ are the angles between the z-axis and the magnetization vectors in the left (right) F′ layers, while the magnetization M in the F layer is assumed to be parallel to the z-axis. The function $F(L_h)$ is a non-monotonic function with a maximum at $L_h \sim \xi_h$. This function vanishes at small and large thickness L_h of the F′ layers (see Eq. (12) in Ref. [77] and Fig. 2 in Ref. [78]). Qualitatively, this prediction agrees with the observations in Ref. [23]. However, the experimental parameters presented in this publication are well defined and this makes a more detailed comparison of the theoretical predictions for the LTRC with the experimental results quite interesting.

In the next subsection, we discuss theoretical results on the Josephson effect in a multilayered Josephson junction in more detail. Our analysis is based on the results of Ref. [49] where the critical Josephson current was calculated for a SF′/F(↑)/F(↓/)F′/S junction. The middle F(↑)/F(↓) layers are assumed to be magnetized in antiparallel directions.

2.2 Long-Range Josephson Effect in S/F′/F/F′/S Junctions

We consider the multi-layer S/F Josephson junction drawn schematically in Fig. 1. It consists of two superconductors, S, and three ferromagnetic layers F, $F'_{r,l}$. The middle F layer may consist of two domains or layers with parallel or antiparallel orientations of the magnetization M. This structure is more similar to the experimental one of Ref. [23] than those analyzed theoretically in Refs. [77, 78] before. We assume that the exchange energies in the F′ and F layers (h an H respectively) are different and that the S/F′ interface is not perfect and the proximity effect weak. This assumption allows one to linearize the Usadel equation and to calculate the critical Josephson current I_c at any temperatures T. We also analyze the situation where the F layer consists of two domains with parallel and antiparallel orientations of the magnetization, as in the experimental realization in Ref. [23].

The presence of the normal N layers in the experimental S/N/F_l/N/F/N/F_r/N/S structures cannot change qualitatively the results for the S/F'_l/F/F'_r/S structure considered here, because the scattering in the N layers does not depend on the spin

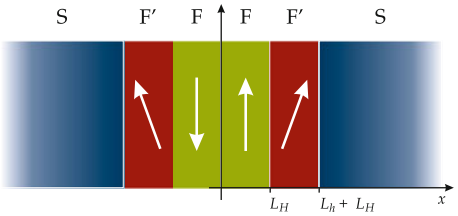

Fig. 1 (color online) Josephson structure under consideration. The F′(F) layers are weak (strong) ferromagnets. The middle F layer consists of two layers with parallel or antiparallel (shown in figure) magnetization orientation. The arrows denote the directions of the magnetization in the F′ and F layers

(we assume that spin-orbit scattering is weak and can be neglected). Therefore, all the superconducting components, singlet and triplet, decay in the N layers in a similar way over a large distance of the order ξ_N. The exchange fields acting on the electron spins are h in the F′ layers and H in the middle F layer. The magnetization vector $\mathbf{M}$ in F is supposed to be aligned along the z-axis and to have the components $M(0, \sin\alpha_{l,r}, \cos\alpha_{l,r})$ in the $\mathrm{F}'_{\mathrm{l,r}}$ layers. The magnetization in the F layer is oriented along the z-axis, but may have parallel or antiparallel orientations in the regions $(-L_H < x < 0)$ and $(0 < x < L_H)$.

For the calculations the quasiclassical Green's function technique is exploited, which is the most efficient tool for studying S/F structures (see reviews [1–3, 79–82]), and it is assumed that all ferromagnetic layers are in the diffusive regime, so that the Usadel equation can be used. The amplitude of the condensate wave function in the ferromagnetic layers is assumed to be small (weak proximity effect) and therefore the Usadel equation can be linearized. The small amplitude of the condensate wave function may be either due to a mismatch of the Fermi velocities in S and F, or due to the presence of a tunnel barrier at the S/F interfaces.

The anomalous (Gor'kov) quasiclassical Green's function in the considered case of a spin-dependent interaction is a 4×4 matrix $\check{f}$. We are interested in the dc Josephson current I_c, i.e. in a thermodynamical quantity. Therefore we can use the Matsubara representation for the matrix $\check{f}$ and consider $\check{f}$ as a function of the Matsubara frequency $\omega = \pi T(2n+1)$ and coordinate x normal to the interfaces: $\check{f} = \check{f}(\omega, x)$. The linearized Usadel equation for $\check{f}$ has the form (see [3], Eq. (3.15))

$$\partial^2 \check{f}/\partial x^2 - \kappa_\omega^2 \check{f} - i(\kappa_F^2/2)\cos\alpha(x) \times \{\tan\alpha(x)\hat{\tau}_3 \otimes [\hat{\sigma}_2, \check{f}] + [\hat{\sigma}_3, \check{f}]_+\} = 0 \tag{2}$$

where $\kappa_\omega^2 = 2|\omega|/D$, $\kappa_F^2 = 2sgn\omega \cdot h/D$ in the $\mathrm{F}'_{\mathrm{l,r}}$ layers and $\kappa_F^2 = 2sgn\omega \cdot H/D$ in the F layer, the Pauli matrices $\hat{\tau}_i, \hat{\sigma}_i$ operate in the particle-hole and spin space respectively**.** The angle α is equal to $\alpha_{l,r}$ in the $\mathrm{F}'_{\mathrm{l,r}}$ layers and to zero in the F layer in the case of the parallel orientation of the magnetization M in the domains. In the case of the antiparallel orientation $\alpha(x) = \pi$ in the interval $(-L_H < x < 0)$ and

$\alpha(x) = 0$ in the interval $(0 < x < L_H)$. The diffusion coefficient D is assumed to be the same in all the ferromagnetic layers.

The matrix $\check{f}$ can be represented for the system under consideration in form of an expansion in the spin matrices $\hat{\sigma}_i$ as

$$\check{f} = \hat{f}_0 \otimes \hat{\sigma}_0 + \hat{f}_1 \otimes \hat{\sigma}_1 + \hat{f}_3 \otimes \hat{\sigma}_3 \tag{3}$$

The matrices $\hat{\sigma}_0$ and $\hat{\sigma}_{1,3}$ are the unit matrix and the $\hat{\sigma}_{x,z}$ Pauli matrices, respectively. The $\hat{f}_{0,1,3}$ matrices are matrices in the particle-hole space. The first term is the short range triplet component with the zero projection of the total spin on the z-axis, the second term is the LRTC with the non-zero projection of the total spin, and the third term is the singlet component of the condensate Green's function (see [3, 77]).

Equation (2) should be complemented by boundary conditions. We consider the simplest model of the S/F heterostructures assuming that the interfaces have no effect on spins (spin-passive interface). These boundary conditions have the form [83, 84]

$$\partial \check{f}/\partial x|_{x=\pm L} = \pm \gamma_B \check{f}_S|_{x=\pm L}, \tag{4}$$

where $\gamma_B = 1/(R_B \sigma)$, R_B is the S/F interface resistance per unit area, σ is the conductivity of the ferromagnet. The matrix $\check{f}_S$ is the Gor'kov's quasiclassical Green's function in the left and right superconductors. It has the form

$$\check{f}_S|_{x=\pm L} = f_S \hat{\sigma}_3 \otimes (\hat{\tau}_2 \cos\varphi \pm \hat{\tau}_1 \sin\varphi), \tag{5}$$

where $f_S = \Delta/\sqrt{\omega^2 + \Delta^2}$, $\pm\varphi$ is the phase in the right (left) superconductor, so that the phase difference is 2φ.

If there is a spin-dependent interaction in a thin layer at the interface (exchange field, spin-dependent scattering etc.), the boundary condition acquires a more complicated form. In particular, the coefficient γ_B becomes a matrix with matrix elements containing very often unknown phenomenological parameters. Such interfaces are called spin-active interfaces. In many papers the LRTC is studied in S/F systems with spin-active interfaces [55–57, 66, 67].

The F/F$'_{l,r}$ interfaces are assumed to be ideal and therefore the function $\check{f}(x)$ and its derivative $\partial \check{f}/\partial x$ must be continuous at these interfaces. Solving the linear equation (2) with the boundary conditions (4) one can calculate the dc Josephson current using the formula [2, 3]

$$j_J = (\sigma/8) 2\pi T \sum_{\omega \geq 0} Tr\{\hat{\sigma}_0 \otimes \hat{\tau}_3 \check{f} \partial \check{f}/\partial x\}, \tag{6}$$

This problem can be solved in the general case of an arbitrary thicknesses of the F and F$'$ layers (L_H and L_h) and angles $\alpha_{l,r}$.

However, these general results seem too cumbersome. In order to present analytical formulas in a more or less compact form, we present here the results for

two limiting cases: a) thin $F'_{l,r}$ layers ($L_h \ll \xi_h, \xi_N$) and arbitrary angles $\alpha_{r,l}$, b) arbitrary thicknesses L_H, L_h, but small angles $\alpha_{r,l}$ ($\alpha \ll 1$). First, we consider the case a).

a) Thin F' layers

Assume that the $F'_{l,r}$ layers (or h-layers) are very thin, so that the inequality $|\kappa_h|L_h \ll 1$ is satisfied, where $\kappa_h^2 = 2sgn\omega(h/D)$ (usually $\kappa_h \gg \kappa_N = \sqrt{\pi T/D}$ and therefore the condition $\kappa_N L_h \ll 1$ is also fulfilled). Then we can easily obtain the form of the short-range and singlet components, $f_{0,3}$, neglecting their variations in the thin F layers. These components are 4×4 matrices $\check{f}$ and obey the Usadel equation

$$\partial^2 \check{f}/\partial x^2 - \kappa_\omega^2 \check{f} - i\kappa_H^2 \cos\alpha(x)\hat{\sigma}_3 \otimes \check{f} = 0, \tag{7}$$

where $\kappa_H^2 = 2sgn\omega(H/D)$ and $\alpha(x) = 0$ in the case of parallel orientation of magnetizations in the middle layer and $\alpha(x) = \pi$ in the interval $(-L_H < x < 0)$ and $\alpha(x) = 0$ in the interval $(0 < x < L_H)$ in the case of the antiparallel orientation.

In zero order approximation in the parameter $|\kappa_h|L_h$ a solution of Eq. (7) consists of only short-range components $\hat{f}_{0,3}$ that can be easily found [49]. Having found these components, one can obtain effective boundary conditions for the LRTC f_1 at the F/F′interface. In the considered limit of thin F layers, $L_h \ll \xi_h$, one can integrate the Usadel equation for the $f_{0,3}$ components over the thickness of the F′-layers and come to effective boundary conditions for the triplet component

$$\partial \hat{F}_1/\partial x|_{x=\pm L_H} = \pm\gamma_1 \hat{f}_3(\pm L_H)\sin\alpha_{r,l}, \tag{8}$$

where $\gamma_1 \equiv \kappa_h^2 L_h$. We have introduced in Eq. (8) a matrix $\hat{F}_1 = \hat{\tau}_3 \otimes \hat{f}_1$ describing the LRTC. This matrix $\hat{F}_1$ satisfies an equation that directly follows from Eq. (2)

$$\partial^2 \hat{F}_1/\partial x^2 - \kappa_\omega^2 \hat{F}_1 = 0. \tag{9}$$

The solution for the matrix $\hat{F}_1$ can be written as

$$\hat{F}_1 = \hat{A}_1 \cosh(\kappa_\omega x) + \hat{B}_1 \sinh(\kappa_\omega x) \tag{10}$$

From the effective boundary conditions (8) we find

$$\begin{aligned} \hat{A}_1 &= \frac{\gamma_1}{2\kappa_\omega \sinh\theta_\omega}[\hat{f}_3(L_H)\sin\alpha_r + \hat{f}_3(-L_H)\sin\alpha_l], \\ \hat{B}_1 &= \frac{\gamma_1}{2\kappa_\omega \cosh\theta_\omega}[\hat{f}_3(L_H)\sin\alpha_r - \hat{f}_3(-L_H)\sin\alpha_l]. \end{aligned} \tag{11}$$

where $\gamma_1 = 2sgn\omega(h/D)L_h$, i.e. the matrix $\hat{F}_1$ is an odd function of the Matsubara frequency.

The solution for $\hat{F}_1$, Eq. (10), demonstrates that the LRTC described by the function $\hat{F}_1$ decays slowly at a large distance of the order $\kappa_\omega^{-1} \sim \xi_N$. Its amplitude is

related to the amplitudes of the singlet component $\hat{f}_3$ penetrating the ferromagnet F due to the PE in the vicinity of the F′ layers. As it should be, the function $\hat{F}_1(x)$ turns to zero in the absence the exchange field or in the case of collinear magnetization because $\gamma_1 = \kappa_h^2 L_h \sim h$ and $\sin\alpha_{r,l} = 0$ in the case of collinear M orientations.

Equations (10–11) determine the LRTC. Using these functions and formulas for the short-range components [49], we calculate the Josephson current in subsection *c). b) Arbitrary thicknesses of ferromagnetic layers at weak non-collinearity*.

Consider now a more interesting case of an arbitrary thicknesses of the ferromagnetic layers F′, F (or h, H-layers). We restrict ourselves with the case of the parallel M orientations in the F layer because there is no qualitative difference between the behavior of the LRTC in the P and AP magnetic configurations. For simplicity we assume that the angle α is small, $\alpha \ll 1$. In this case the amplitude of the LRTC is proportional to the small parameter α. In the zero order approximation only the singlet component, $\hat{f}_3$, and the short range triplet component, $\hat{f}_0$, with zero projection of the total spin of Cooper pairs on the z-axis are not zero. Indeed, we will look for a solution of Eq. (2) in the form $\hat{f}_3(x) \sim \hat{f}_0(x) \sim \hat{f}_1(x) \sim \{\cosh(\kappa x), \sinh(\kappa x)\}$, where κ is the eigenvalue.

In the ferromagnetic layers we obtain the following equations for the eigenvectors

$$\hat{f}_0(\kappa^2 - \kappa_\omega^2) - \hat{f}_3 i\kappa_F^2 \cos\alpha = 0 \tag{12}$$

$$\hat{f}_3(\kappa^2 - \kappa_\omega^2) - \hat{f}_0 i\kappa_F^2 \cos\alpha - \hat{F}_1\kappa_F^2 \sin\alpha = 0 \tag{13}$$

$$\hat{F}_1(\kappa^2 - \kappa_\omega^2) + \hat{f}_3\kappa_F^2 \sin\alpha = 0 \tag{14}$$

where the matrix $\hat{F}_1$ introduced in Eq. (8) describes the LRTC. This set of equations has three eigenvalues

$$\kappa_{1,2}^2 \equiv \kappa_{F\pm}^2 = \kappa_\omega^2 \pm i\kappa_F^2,\ \kappa_3^2 = \kappa_\omega^2 \tag{15}$$

Two of them, $\kappa_{F\pm}$, describe a sharp decay of the density of Cooper pairs in the ferromagnet (in the case $\{H, h\} \gg T, \Delta$) and the latter one, κ_ω ($\kappa_\omega = 1/\xi_{LR}$), is an inverse characteristic length of decay of the LRTC in the ferromagnet. By order of magnitude it is equal to $\kappa_\omega^2 \approx \pi T/D$, which shows that the length ξ_{LR} is rather large and does not depend on the exchange energies h, H. Spin-orbit interaction or a spin-dependent impurity scattering make this length shorter [71, 85, 86]

$$\kappa_3^2 = \kappa_\omega^2 + \kappa_m^2 \tag{16}$$

where $\kappa_m^{-2} \approx \min\{D\tau_m, D\tau_{sp-orb}\}$, τ_m and τ_{sp-orb} are characteristic times related to the spin-dependent impurity scattering or spin-orbit interaction. The lengths $\kappa_{F\pm}^{-1}$ also depend on κ_m^2 and can be found by shifting $\kappa_{F\pm}^2 \Rightarrow \kappa_{F\pm}^2 + \kappa_{mF}^2$.

It is seen from Eqs. (12–14) that the LRTC arises only at non-zero α when $\hat{F}_1 \neq 0$. In the zero-order approximation ($\alpha = 0$) we should find the matrices $\hat{f}_{0,3}$ in each

ferromagnetic layer. As follows from Eqs. (12–13), at $\alpha = 0$ only the eigenvectors $\hat{f}_{0\pm} = \pm\hat{f}_{3\pm}$ corresponding to the eigenvalues $\kappa_\pm$ can be finite and found easily [49].

Again, as in the previous subsection, the LRTC can be expressed in terms of the short-range components. We write the equation for the matrix $\hat{F}_1$ in the h-region projecting of Eq. (2) on the $\hat{\sigma}_1$ matrix in the spin space

$$\partial^2 \hat{F}_1(x)/\partial x^2 - \kappa_\omega^2 \hat{F}_1(x) = -\kappa_h^2 \sin\alpha \cdot \hat{f}_3(x), \tag{17}$$

where the function $\hat{f}_3(x)$ is the singlet component.

The solution of Eq. (17) can readily be obtained (see Ref. [49]).

c) Josephson current.

Using the Green's functions, $\hat{f}_{0,1,3}$ obtained in section "Long-Range Josephson Effect in S/F′/F/F′/S Junctions" one can now calculate the dc Josephson current. Substituting the expansion (3) into Eq. (6), we obtain for the Josephson current density

$$j_J = i\sigma\pi T \sum_{\omega\geq 0} Tr\{\hat{\tau}_3[\hat{f}_0\partial\hat{f}_0/\partial x + \hat{f}_3\partial\hat{f}_3/\partial x + \hat{f}_1\partial\hat{f}_1/\partial x]\}, \tag{18}$$

The first two terms in Eq. (18) are the contribution from the short-range components ($\hat{f}_{0,3}$) and the third term is due to the LRTC ($\hat{f}_1 = \hat{\tau}_3\hat{F}_1$). Using this equation and formulas for the amplitudes of the short-range, $\hat{f}_{0,3}$ (triplet and singlet), and of the LRTC, $\hat{f}_1$, one can calculate the Josephson current j_J in an analytical form [49]. We present here the results of these calculations in Figs. 2 and 3.

In Figs. 2a, b we show the dependence of the normalized total current, $I_c = Sj_J$,(solid thin line) on the thickness of the middle F layer as well as the partial currents I_{cSR} and I_{cLR} caused by the short-range (point line) and long-range (solid thick line) components (here S is the area of the junction). The exchange energy in the F layer H is chosen equal to $H = 70\Delta_0$ (Fig. 2a) and $H = 170\Delta_0$ (Fig. 2b). It is clearly seen that if the width of the F layer L_F exceeds $0.6\sqrt{D/\Delta_0}$ (Fig. 2a) or $0.4\sqrt{D/\Delta_0}$ (Fig. 2b), the total critical current is caused by the LRTC and decays rather slowly with increasing L_F.

The curves shown in Fig. 2 correspond to the case of a thin F′ layers. In Fig. 3a, b we present the dependence of the total critical current I_c on $L_{F'}$ using the formulas for the amplitudes $\hat{f}_{0,1,3}$ in the case of arbitrary thickness of the F′ layers. It is seen from Fig. 3a that the current I_c reaches a maximum at some thickness $L_{F'}$ the magnitude of which depends on the exchange energy h in these layers. On the other hand, the position of the maxima is weakly dependent on the exchange energy H in the F layer (Fig. 3b).

The dependencies shown in Figs. 2 and 3 are in semi-quantitative agreement with experimental data obtained by Khaire et al. [23]. The exact quantitative comparison can not be carried out because it was assumed in a theoretical model [49] that the

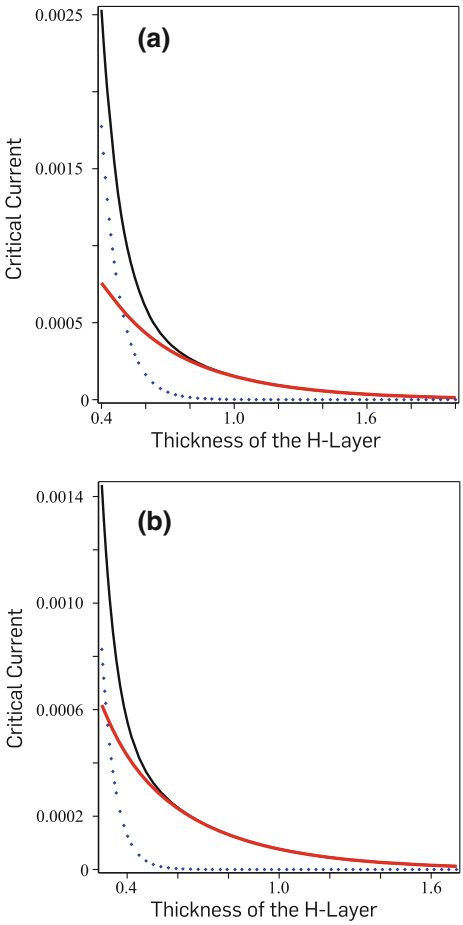

Fig. 2 (Color online) The dependence of the normalized critical current due to the SR component (*point line*), LRTC (*solid thick line*) and the total critical current (*solid thin line*) on the thickness of the H-layer for $\tilde{H} = 70$ (A) and $\tilde{H} = 170$ (B). The normalized temperature is equal to 0.1. Other parameters are the same as in Ref. [49]

diffusion coefficients for minority and majority electrons in F and F′ layers are equal. In fact they are different.

3 Long-Range Proximity Effect in High-T_c Superconductors

In this section we consider the possibility of the appearance of the LRTC in high-T_c layered superconductors [50]. We will see that the LRTC leads to an anomalous, or long-range, proximity effect (PE). The long range PE was usually studied in S/F heterostructures with conventional superconductors (s-wave singlet superconductivity). At the same time, S/F heterostructures can be fabricated using high temperature

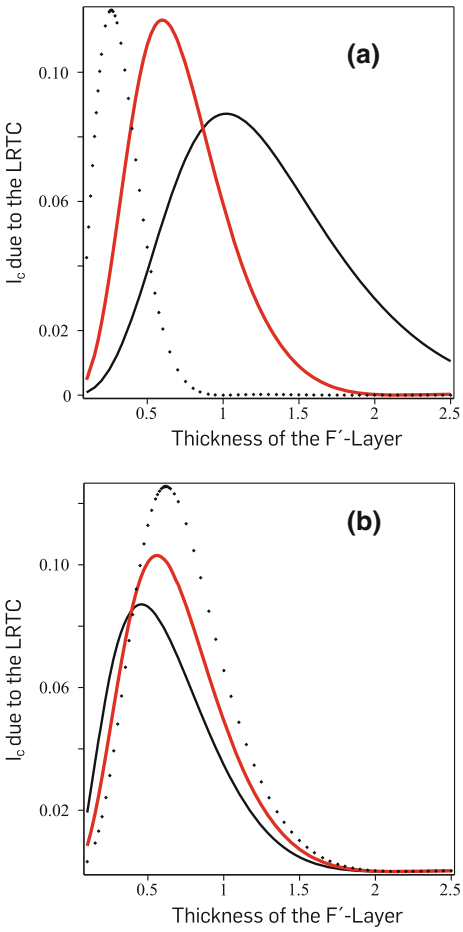

Fig. 3 (Color online) **a** Normalized critical current due to the LRTC as a function of the thickness of the h-layer for different exchange energies h for the P orientation. The parameters are: $\tilde{h} = 2, 5, 20$ (*solid thin*, *solid thick* and *point lines*, respectively). The other parameters are $\tilde{H} = 50$, $\tilde{T} = 0.25$, $\tau_m \Delta = 0.1$, $\tilde{L}_H = 0.5$. B) The same dependence for different $\tilde{H}$: $\tilde{H} = 5$ (*thin solid curve*), $\tilde{H} = 20$ (*thick solid curve*) and $\tilde{H} = 100$ (*point curve*). The parameter $\tilde{h} = 5$. Other parameters are the same as in Ref. [49]. All the curves correspond to the P orientation

superconductors (HTS) [87, 88], and study of PE in such systems is also important and interesting.

In a recent work, the authors of Ref. [88, 89] using the scanning tunnelling spectroscopy measured the density of states (DOS) $\nu(\epsilon)$ at the outer surface of the ferromagnet in a bilayer YBCO/F (a magnetic material SrRuO was used as the ferromagnet). They found a dip in $\nu(\epsilon)$ at energies $\epsilon = eV \leq 10\,\text{meV}$ in bi-layers with the thickness of the ferromagnet $\leq 26\,\text{nm}$, whereas the "magnetic" length ξ_h was estimated to be $\sim 3\,\text{nm}$, that is, much shorter than the thickness of the F layer. Another interesting finding was that the change of DOS occured only in the vicinity of DW. As a possible reason for the observed effects, the authors of Ref. [88, 89] considered LRTC. However, believing that this component had to spread all over the sample rather than to be located near DW, they finally ruled out this possibility.

Although the superconducting pairing in both conventional superconductors and HTS cuprates is singlet, one cannot just use for HTS the theory developed previously for the conventional superconductors because of a special symmetry of the order parameter Δ in these materials.

The HTS cuprates are layered compounds with a weak coupling between the layers. The symmetry of the order parameter in HTS differs from that in the BSC superconductors [90, 91]. In the simplest version the order parameter Δ in HTS has the structure: $\Delta(p) = \Delta_0(p_a^2 - p_b^2)/p^2 = \Delta_0 \cos 2(\phi - \phi_0)$, where ϕ is the azimuthal angle in the (a, b) plane normal to the c crystallographic axis, p_a and p_b are projections of the momentum on the axes a and b. Such a dependence of the order parameter in HTS leads to many interesting phenomena specific to HTS. For example, the gap in the excitation spectrum turns to zero for certain directions. In addition, the sign-variable angular dependence of Δ is the reason for the sign change of the Josephson current in tunnel junctions composed of two HTS with different orientations of crystallographic axes [90, 91].

In this section we analyze proximity effects of the HTS in contact with disordered ferromagnets containing domain walls. We concentrate on the most interesting situation when the c-axis is perpendicular to the interface, such that the layers of the HTS are parallel to the interface. This geometry corresponds to the experiment [88, 89] and is special because, in cases when c-axis is not orthogonal to the interface, PE is similar to the one in an s-wave S/N (or S/F) bi-layer.

We will see below that in the geometry considered the superconducting d-wave condensate penetrates a normal metal with the mean free path l over a distance of order l, which is much shorter than the length ξ_N, characterizing the penetration of the s-wave superconductivity. One can say that PE is almost absent in this case but, as we will show, it is restored if one replaces the normal metal by a ferromagnet with domain walls perpendicular to the interface. In this case an *odd triplet* s-wave component is induced near DW and this is just the LRTC predicted in Ref. [19] for S/F heterostructures with conventional superconductors. It penetrates over much longer distances of order ξ_N. Previously, inhomogeneities of the exchange field lead to generation of the odd triplet s-wave condensate from the conventional s-wave singlet superconductor. Now the presence of DW leads to formation of the same s-wave component but starting from the d-wave singlet superconductivity.

As in the previous section, we will use the method of quasiclassical Green's functions. These functions obey the Eilenberger equation. In order to simplify the problem we assume a weak PE, which corresponds to a small transmission through the HTS/F interface. In this case the amplitude of the condensate function f in the ferromagnet is small and the Eilenberger equation can be linearized. As a result, this equation takes in the ferromagnet the following form (see, e.g., [3, 52])

$$sgn\omega \cdot l(\mathbf{n} \cdot \nabla)\hat{\tau}_3 \otimes \check{f} + \kappa_\omega \check{f} - i\lambda_h \{\cos\alpha(y)[\hat{\sigma}_3, \check{f}]_+ + \sin\alpha(y)\hat{\tau}_3 \otimes [\hat{\sigma}_2, \check{f}]\} = \langle \check{f}(\mathbf{n}, \mathbf{r}) \rangle, \tag{19}$$

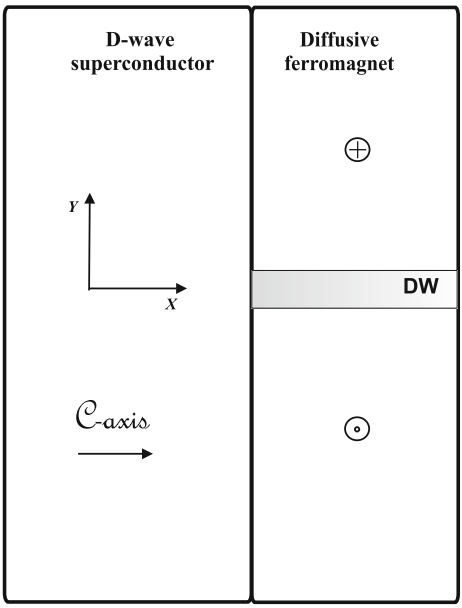

Fig. 4 Schematic picture of a HTS/F bi-layer with a domain wall DW of the Bloch type (*the shadowed stripe*). The signs in the circles denote the direction of the magnetization in domains

where $\kappa_\omega = 1 + 2|\omega|\tau$, $\lambda_h = h\tau sgn\omega$, $\omega = \pi T(2n+1)$ and $\mathbf{n} = \mathbf{p}/p$ is the unit vector parallel to momentum. The products $h\tau$, $|\omega|\tau$ are assumed to be small. The angle brackets mean the angle average, $[\hat{\sigma}_3, \check{f}]_+$ and $[\hat{\sigma}_2, \check{f}]$ denote anticommutator and commutator (Figs. 4, 5).

We consider the case when the magnetization is oriented along the z-axis far away from the DW and rotates in the DW in the $\{y, z\}$ plane changing asymptotically its sign (see Fig. 1). This rotation is described by the angle $\alpha(y)$. The c-axis is assumed to be orthogonal to the interface.

The quasiclassical Gor'kov function $\check{f}$ entering Eq. (19) is a 4×4 matrix in spin ($\hat{\sigma}_i$) and particle-hole ($\hat{\tau}_i$) spaces and it depends on coordinates $\mathbf{r} = \{x, y\}$ (here the subindex $i = 0, x, y, z$ and $\hat{\sigma}_0$, $\hat{\tau}_0$ are the unit matrices). This matrix is off-diagonal in the particle-hole space and contains both the diagonal ($f_\pm$) and off-diagonal elements in spin space. We use the boundary conditions derived in Refs. [83] (a particular dependence of the order parameter on the momentum $\mathbf{p}$ is not essential for their derivation)

$$sgn(\omega \cdot n_x)(\check{f}(n_x, n_y) - \check{f}(-n_x, n_y)) = T(n_x)\hat{\tau}_3 \otimes \check{f}_S \tag{20}$$

where $T(n_x)$ is the transmission coefficient, and $\check{f}_S = \hat{\sigma}_3 \otimes \hat{f}_S$, $\hat{f}_S = \hat{\tau}_2 f_S$ is the quasiclassical Gor'kov function in the HTS. We assume that this function is not perturbed by the PE due to the smallness of the coefficient $T(n_x)$ and write it in the form $f_S = \Delta(\mathbf{n})/\sqrt{\omega^2 + \Delta^2(\mathbf{n})}$ with $\Delta(\mathbf{n}) = \Delta_0(p_a^2 - p_b^2)/p^2$.

Solving Eq. (19) for f with the boundary conditions, Eq. (20), one can write the condensate contribution $\delta\nu(\epsilon)$ to the DOS at the outer surface of the F film as

$$\delta\nu(\epsilon) = -\frac{1}{8} Tr(\hat{\tau}_0 \otimes \hat{\sigma}_0 \langle \check{f}^2(\mathbf{n}, x)\rangle)|_{\omega=-i\epsilon, x=d} \tag{21}$$

The solution of Eq. (19) can be found in a way similar to the one used in Ref. [50]. First, we make a transformation introducing a new matrix $\check{f} = \check{U}\check{f}_U\check{U}^+$, where the transformation matrix $\check{U} = \exp(i\hat{\tau}_3\hat{\sigma}_1\alpha(y)/2)$ describes a rotation in the spin space. Then, we represent the matrix $\check{f}_U$ as a sum of symmetric and antisymmetric in momentum space parts: $\check{f}_U = \check{s} + \check{a}$. Substituting the matrices $\check{s}$ and $\check{a}$ into Eq. (19), one can express the antisymmetric matrix in terms of the symmetric one.

$$-l^2(\mathbf{n}\cdot\nabla)^2\hat{s}_1 + \kappa_\omega^2\hat{s}_1 = \kappa_\omega\langle\hat{s}_1\rangle + in_y[l^2(\mathbf{n}\cdot\nabla)(Q\hat{\tau}_3\otimes\hat{s}_0) - ilQ\kappa_\omega sgn\omega\hat{a}_0], \tag{22}$$

It is seen that the component s_1 can be easily found from this equation and expressed in terms of the short-range components $\hat{a}_0$ and $\hat{s}_0$ [50].

Now we come to the demonstration that the presence of the ferromagnetism and DW restores the long range penetration of the superconducting condensate. This phenomenon occurs because such an inhomogeneous configuration of the exchange field induces the odd triplet s-wave component of the superconducting condensate with the projections of the spin $S_z = \pm 1$.

Substituting the matrices $\hat{s}_0$ and $\hat{a}_0$ into Eq. (22) (see [52]), one can obtain the equation for the triplet, $S_z = \pm 1$, component, $\hat{s}_1$. We represent $\hat{s}_1$ in the form: $\hat{s}_1 = \hat{s}_{1av} + \hat{s}_{1\sim}$ with $\hat{s}_{1av} \equiv \langle\hat{s}_1\rangle$, such that, $\hat{s}_{1av}$ does not depend on angles and $\langle\hat{s}_{1\sim}\rangle = 0$. Equations describing $\hat{s}_{1av}$ and $\hat{s}_{1\sim}$ have quite different forms. Since $\langle\hat{s}_{1\sim}\rangle = 0$, one can see from the left-hand side of the equation for $\hat{s}_{1\sim}$ that the characteristic scale for decay of $\hat{s}_{1\sim}$ is the mean free path l (in the considered dirty limit $\kappa_\omega^2 \approx 1$). In the equation for $\hat{s}_{1av}$ the second term on the left hand side and the first term on the right hand side almost compensate each other and one has: $\kappa_\omega^2\hat{s}_{1av} - \kappa_\omega\langle\hat{s}_1\rangle \approx (2|\omega|\tau)\hat{s}_{1av}$. Therefore the angular averaged part of $\hat{s}_1$ decays over a large distance of the order of $l/\sqrt{|\omega|\tau} \sim \sqrt{D/T}$ and this is just the $S_z = \pm 1$ odd frequency triplet component.

In the main approximation the equation for $\hat{s}_{1av}$ reads

$$-l^2\frac{\partial^2\hat{s}_{1av}(q)}{\partial x^2} + \kappa_q^2\hat{s}_{1av}(q) = 3il^2(\partial Q/\partial y)_q\langle n_y^2\hat{s}_0(x)\rangle, \tag{23}$$

$\hat{s}_{1av}(q) = \int dy\hat{s}_{1av}(y)\exp(iqy)$ and $\kappa_q^2 = 6|\omega|\tau + q^2l^2$.

The function $\hat{s}_0(x)$ decays over a distance of the order l, whereas the characteristic scale for $\hat{s}_{1av}(x, y)$ is much longer: $l/\sqrt{6\omega\tau} \approx \sqrt{D/2\pi T}$. Therefore, the term on the right hand side can be replaced by $B\delta(x)$, where B does not depend on x. Solving Eq. (23) in this approximation and Fourier transforming back to y, one can obtain the function $\hat{s}_{1av}(d, y)$ that determines the contribution $\delta\nu(\epsilon)$ of the superconducting

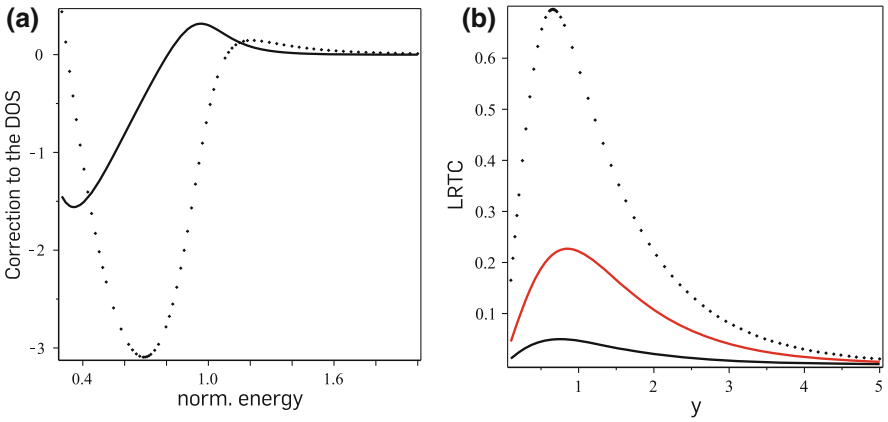

Fig. 5 **a** Normalized correction to the DOS versus normalized energy ϵ/Δ_0 for $d = 2\xi_\Delta, m = \Delta_0\tau_m 0.3$ (*solid curve*) and $d = \xi_\Delta, m = 0.6$ (*point curve*), where $\xi_\Delta^2 = D/(2\Delta_0)$; **b** Dependence of LRTC amplitude on the normalized y-coordinate at $x = d$ for $w = \xi_\omega, d = 0.5\xi_\omega$ (*point curve*); $w = \xi_\omega, d = \xi_\omega$ (*upper solid curve*) and $w = 0.2\xi_\omega, d = \xi_\omega$ (*lower solid curve*). The y-coordinate is measured in units ξ_ω

condensate to the density of states on the outer side of the ferromagnet. The solution for the LRTC $\hat{s}_{1av}(x, y)$ at the $x = d$ can be presented in the form

$$\hat{s}_{1av}(d, y) = (3/4)i\hat{\tau}_1\lambda_h \cos(2\varphi_0)T_{av} f_{Sav} S(y) \tag{24}$$

where T_{av} and f_{Sav} are the angle-averaged transmission coefficient and condensate function in S and the Fourier component of the function $S(y)$ is equal to: $S(q) = l^2(\partial Q/\partial y)_q[\kappa_q \sinh(\kappa_q d/l)]^{-1}$.

We emphasize that, in contrast to the singlet component $\hat{f}_S$, the LRTC, $\hat{s}_{1av}$, is an odd function of the Matsubara frequency because $\lambda_h \sim sgn\omega$ (see Eq. (19)). Thus, the odd-frequency triplet s-wave component $\hat{s}_{1av}$ arises as a result of the influence of the non-homogenous magnetization in the DW on the d-wave singlet component. One can see that the LRTC is zero if the nodes in the spectrum of the d-wave superconductor lie in the plane of the DW.

One can express the spatial dependence of this component in an explicit form in limiting cases. If DW is broader than the LRTC penetration depth we write, using Eq. (21), the correction $\delta\nu(\epsilon) = \nu(\epsilon) - 1$ to the density of states

$$\delta\nu_{eff}(\epsilon) = \delta\nu(\epsilon)[(3/2)l^2\lambda_h T_{av}(\partial Q/\partial y)]^{-2} \tag{25}$$

The function $\nu_{eff}(\epsilon)$ is calculated numerically and represented in Fig. 2a an effective local correction to the DOS $\delta\nu_{eff}(\epsilon)$ at $x = d$ caused by the LRTC.

In the opposite limiting case a simple form for the LRTC can be obtained if the DW is approximated by a step-like function ($Q = \pi/w$ for $|y| < w/2$ and

$Q = 0$ for $|y| > w/2$). In this approximation we calculate the spatial dependence of $S_{eff}(y) = -(w/l)S(y)$, for various values of w and d (Fig. 2b). We see that the LRTC decays exponentially from DW over a long distance of order ξ_N.

Note that spin-dependent scattering makes the characteristic length of the LRTC decay shorter [3, 52]. In this case the effective decay length equals $\xi_{Neff} = 1/\sqrt{\xi_\omega^{-2} + \xi_m^{-2}}$, where $\xi_m = \sqrt{D\tau_m}$, τ_m is the spin-dependent scattering time. The amplitude of LRTC contains a small parameter (l^2/wd). If this parameter is not small, the formulas given above are valid qualitatively.

These results can help to explain the experimental data on the density of states in a setup analogous to that considered here [88, 89], but more information about the DW, barrier transparency $T(n_x)$ etc., is needed for a detailed comparison.

Therefore, the presence of a domain wall at the interface of a high temperature, d-wave superconductor/ferromagnet bi-layer leads to the generation of an odd frequency triplet s-wave component of the condensate. As a result, the superconducting condensate penetrates the ferromagnet along DW over distances by far exceeding the penetration depth of the d-wave condensate into a normal metal. This explicitly demonstrates the enhancement of the proximity effect by an inhomogeneous exchange field.

4 Experimental Evidence for Triplet Superconductivity in S/F Hybrid Structures

In recent years one notices an increasing number of different experimental systems giving clear indications in favor of the existence of LRTC in S/F hybrid structures. [21–27]. The first experimental evidence came from Keizer et al. [21], who studied the Josephson current in an S/F/S Josephson junctions with the ferromagnetic half metal CrO_2. They observed a superconducting dc current through such junctions with the F layers being much thicker than the penetration depth ξ_F. This current cannot be carried by singlet Cooper pairs, because the spins of the conduction electrons in this material are perfectly polarized in one direction (the exchange splitting of the conduction band in this material is larger than the Fermi energy). Later-on these results were reproduced in a similar experiment [27]. The LRTC in CrO_2 may be created at the interfaces (spin active interface) [55, 92] and penetrate into the F layer over a long distance.

In a different work Sosnin et al. [22] measured the conductance of a ferromagnetic wire (Ho) attached to a superconducting layer. The conductance variations below T_c was too large to be explained by a short-range component of the condensate function penetrating into the F wire from the superconductor. Since the Ho ferromagnet has a spiral magnetic structure, it is reasonable to assume that the conductance variations are caused by the LRTC predicted theoretically [62–64, 93].

Probably the most convincing experimental results in favor of the LRTC penetration in a ferromagnet until now have been presented in experiments on multilayered Josephson junctions [23, 26]. In Ref. [23], a multilayered S/N/F/N/F′/N/F/N/S

Josephson junction is used in which F and F′ are weak (PdNi or CuNi) and strong (Co) ferromagnets, respectively. The middle F layer was a trilayer structure consisting of two F layers with antiparallel orientation of the magnetization M and of a thin layer (Ru) providing an antiferromagnetic interlayer exchange coupling between the F layers. For different thicknesses L of the F′ and F layers (we denote the thicknesses of the F′ and F layers as L_h and L_H layers, respectively) the authors measured the critical current.

It was demonstrated that in the absence of the F′ layers ($L_h = 0$) the critical current I_c was negligible, if the thickness of the F layer L_H essentially exceeded the small length $\xi_H = \sqrt{D/H}$, where H is the exchange energy in the F layer. This is what one expects for conventional singlet superconductivity. However, adding the F′ layers resulted in an increase of the critical current I_c by several orders of magnitude. thus these F layers, in which the magnetization vectors are not collinear with F′, are essential for the appearance of LRTC. The dependence of $I_c(L_h)$ is non-monotonous: the critical current is small at small and large L_h, reaching a maximum at $L_h \sim \xi_h$. The authors of Ref. [23] suggested an explanation of these results in terms of the LRTC.

In Ref. [26] the ferromagnetic layer F in the multilayered S/F/S junction was designed as a combination of two spiral Rare earth magnets (Ho) with a strong ferromagnet (Co) in the middle. The LRTC was created in Ho layers and could penetrate the rather thick Co layer, the critical current caused by the LRTC decayed very slowly with increasing thickness of the Co layer

4.1 Triplet Superconductivity in Josephson Junctions with Ferromagnetic Cu_2MnAl Heusler Barriers

In a recent paper Josephson junctions of the type S/F/I/S with Nb as the superconducting layers, a thin isolating layer I, and one single Cu_2MnAl-Heusler layer as the ferromagnetic layer F were studied [24] and strong evidence for the existence of a LRTC was reported. The results could be modelled closely in a recent theoretical paper assuming LRTC [93]. The ternary metallic alloy Cu_2MnAl has very peculiar magnetic properties unknown for conventional transition metal ferromagnets and responsible for the formation of an intrinsic F/F′/F structure.

When prepared at room temperature, the Cu layers are non ferromagnetic (Fig. 6). At room temperature Cu grows in the A2-structure with a random distribution of all atoms on a bcc lattice [94–96]. In the A2-structure nearest neighbor Mn atoms are coupled by strong antiferromagnetic exchange interactions, whereas Mn-next nearest neighbors with an Al-atom in-between are coupled ferromagnetically via a superexchange type of interaction [97]. The competition of these two interactions and the randomness of the atomic distribution in the A2 structure gives rise to spin glass type of magnetic order with a freezing temperature of 240 K [98]. Upon annealing at 240 °C the unit cell symmetry transforms to the ordered $L2_1$ Heusler structure,

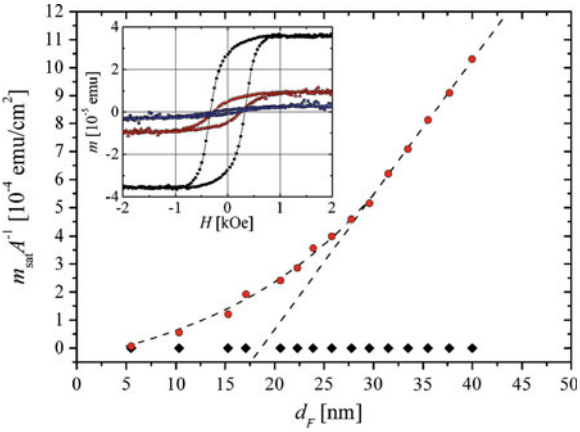

Fig. 6 (Color online) Magnetic moment (measured at 1 kOe and 15 K) divided by the sample area versus the thickness of the Heusler layer in the as-prepared state (*diamonds*) and after annealing at 240 °C for 24 h (*dots*). The *dashed linear slope* corresponds to a magnetic moment of 2.9 μ_B/Mn-atom. The *inset* shows hysteresis loops measured at 15 K for samples in the annealed state with the Heusler layer thickness $d_F = 5.4$ nm (*inner loop*, *blue*), $d_F = 10.2$ nm (*middle loop*, *red*) and $d_F = 17$ nm (*outer loop*, *black*) (Data taken from [24])

which is combined of four interpenetrating fcc-sublattices occupied by Mn, Cu and Al, exclusively [99]. With this symmetry in Cu there are no Mn-Mn nearest neighbors and the ferromagnetic Mn-Al-Mn exchange interactions leads to ferromagnetic order with a magnetic moment of about 3.2 μ_B per Mn-atom and a ferromagnetic Curie temperature above 600 K [98].

In the inset of Fig. 6 we show examples of ferromagnetic hysteresis loops of Cu-layers in the Josephson junctions for different thicknesses of the Heusler layers after annealing at 240 °C for 24 h. A ferromagnetic hysteresis loop is only observed above a critical thickness $d_F = 5$ nm. For $d_F < 5$ nm the spin glass state still exists. Above $d_F = 5$ nm the saturation magnetic moment increases gradually over a very broad thickness range, up to about $d_F = 30$ nm where it reaches a constant slope corresponding to a value of 2.9 μ_B/Mn-atom. This behavior of the Heusler layers indicates a gradual transition of the magnetic order from pure spin glass to high moment ferromagnetism across intermediate phases with coexisting spin glass order and low moment ferromagnetism. The magnetization profile inside each Heusler layer also reflects these different phases: there is a low moment spin glass type of order close both interfaces and larger moment, ferromagnetic type of order at the core of the Heusler film. The microscopic origin of this behavior is an intrinsic gradient of the degree of $L2_1$-type atomic order inside the Heusler layer with a low degree of order at the interfaces and a higher degree of order in the interior of the film. [100, 101].

The thickness dependence of the normalized critical current density (normalized to the junction area and the junction resistance in the normal state) in the as-prepared

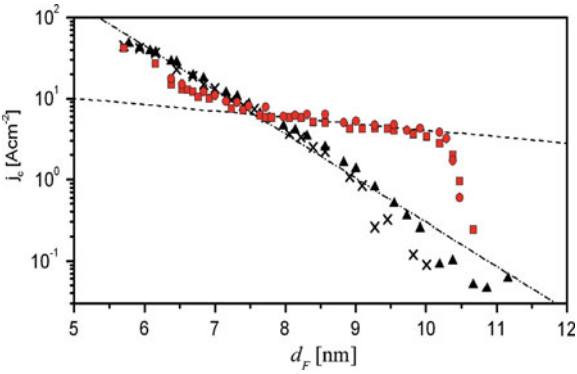

Fig. 7 (Color online) Critical current density versus the Heusler layer thickness in the as-prepared state (*black crosses* and *triangles*) and the annealed state (*red circles* and *squares*). Measurement done at 4.2 K. *Dashed line* $\xi = 5.7$ nm; *dash-dotted line* $\xi = 0.8$ nm. (Data taken from [24])

state is plotted in Fig. 7. One observes an exponentially damped curve with a decay length $\xi = 0.8$ nm. The decay length of a dirty metal with inelastic pair breaking scattering is given by $\xi = \sqrt{D_F/E_{ie}}$ with the diffusion constant D_F and the scattering energy $E_{ie} = \hbar/\tau_{ie}$ (scattering time τ_{ie}). With the electrical resistivity measured on separate samples and the other parameters taken from the literature one can estimate D_F and get $E_{ie} = 45$ meV for the inelastic scattering energy.

After annealing the junctions at 240 °C for 24 h, the Heusler layers develop ferromagnetic order (see Fig. 6). Whereas below a thickness of about $d_F = 8$ nm in Fig. 7, the critical current in the annealed state is slightly smaller than in the as-prepared state, there is an strong increase above, up to a thickness of $d_F = 10.5$ nm. Above 10.5 nm there is a sharp drop-off and the critical current approaches the value for the as-prepared state again.

The theory for singlet pairing of a Josephson junctions with a ferromagnetic barrier of variable thickness d_F in the dirty limit predicts the functional dependence

$$j_c(d_F) = j_0 \left| \cos\left(\frac{d_F}{\xi_{F2}}\right) \right| \exp\left(-\frac{d_F}{\xi_{F1}}\right) \tag{26}$$

with the decay length ξ_{F1} and the oscillation length ξ_{F2} [2]. Without pair breaking scattering both lengths are given by the penetration depth in a ferromagnet $\xi_{F1} = \xi_{F2} = \xi_F$. With pair breaking scattering the decay length decreases and the oscillation length increases compared to ξ_F [2]. The first term in the equation describes the transition from a 0-junction to a π-junction and leads to a deviation of the current density from an exponentially damped curve towards smaller values when approaching the transition range, in sharp contrast to what is observed for the annealed state in Fig. 6. In the plateau region in Fig. 7 the decay length has a value of $\xi_F = 5.7$ nm, which in the framework of singlet superconductivity cannot be interpreted in any reasonable way, thus leading to the conclusion that in the plateau region a LRTC shows up.

The appearance of a LRTC is due to the intrinsic magnetization profile inside very thin single Heusler layers. In the thickness range just above the onset of ferromagnetism, where the LRTC appears (see Fig. 7), ferromagnetic order already exists in the core of the Heusler layers, whereas at the interfaces spin glass order still prevails. The coupling between the two types of magnetic order parameters induces a small ferromagnetic magnetization close to the interfaces, however, with some canting of the local magnetization with respect to the magnetization direction of the core, because of the coupling to the coexisting spin glass type of order. Essentially, the interface layers with canted moments play the role of the F′ layers in an artificial F′/F/F′ trilayer structure, which, according to the theory, presents the minimum requirement for the generation of LRTC. With the development of full ferromagnetic order in the Heusler layers at larger thicknesses, the canting and thus the LRTC of the superconducting condensate function vanishes [93]. This gives rise to the sharp drop-off of the critical current density above $d_F = 10.5\,\mathrm{nm}$.

5 Spin Screening Effect

Qualitatively the physical origin of the spin screening effect in S/F layer systems can be understood as follows: Assuming an S/F bilayer with highly transparent interfaces and with the F layer very thin compared to the superconducting penetration depth ξ_F, the Cooper pairs penetrate freely from the S-layer into the F-layer. Due to the exchange field in F the conduction electron spins at the Fermi level combining the Cooper pairs are polarized in one direction, predominantly. These electrons have their Cooper partners deep in the S layer, at a distance of the order ξ_s, the superconducting coherence length in the S-layer. Thus, due to the superconducting correlations, a spin polarization with a direction antiparallel to the magnetization direction in F is induced. Theoretically it has been shown that for this ideal model the induced magnetic moment in the S layer should exactly compensate the magnetic moment in the F layer [30], i.e. one should have perfect so-called spin screening.

For a real experimental S/F bilayer system with low transparency of the interface and a finite thickness, the amplitude of the magnetization induced by the spin screening effect is expected to be very small. Thus for an experimental proof of the spin screening effect one needs a method which can sensitively probe small changes of the spin polarization in the S layer below T_c. In the literature the measurement of the Knight shift by nuclear magnetic resonance (NMR) techniques [31, 32], the magneto-optical Kerr effect (MOKE) [33] and scanning tunnelling spectroscopy (STM) [34] has been applied to prove the existence of the spin screening effect.

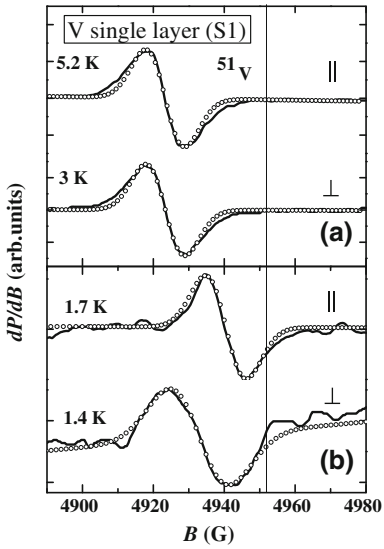

Fig. 8 NMR spectra for a single V layer (thickness d = 30 nm; $T_c = 4.7$ K) in the normal **a** and superconducting **b** states for the parallel (∥) and the perpendicular (⊥) orientation of the magnetic field. The NMR spectra are fitted by the Gaussian line shape (*circles*). The vertical line shows the NMR line position for ^{51}V nuclei in an insulator. (Data taken from [31])

5.1 Observation of the Spin Screening Effect by NMR

In the investigation of Ref. [31, 32] the Knight shift of the ^{51}V nuclei of a superconducting V film as part of F/S/F trilayers was analyzed using an ultra sensitive NMR spectrometer especially designed for this study. Conventional NMR spectrometers can hardly detect the small changes of the Knight shift occurring below T_c. The reason for the high sensitivity needed is the small number of the V nuclei in the sample and the rather thick V-layer one must use. Since the spin screening effect is expected to occur on a length scale of the order of ξ_s, which for V films is about 10 nm, typically, it would be best to limit the thickness of the V-layer to $d_V < 20$ nm. However, V layers of this thickness in F/S/F trilayers are not superconducting any more (see, e.g., [7], thus the minimum thickness d_s needed is limited to about $4\xi_s$.

The experimental evidence for the spin screening effect by NMR is based on the expected change of the spin susceptibility in the superconducting V layer caused by the spin polarization in V below T_c. The spin polarization of the conduction electrons is part of the Knight shift of the NMR resonance line.

In Fig. 8 we present the NMR signals for a single V layer above and below T_c. These spectra provide a reference for a comparison with the subtle changes of the resonance line observed for F/S/F trilayers. In the normal state (Fig. 8a) the resonance line shape is well described by the derivative of a Gaussian absorption curve for the parallel as well as for the perpendicular orientation of the dc magnetic field relative to the film plane. For the Knight shift in the normal state of V, which is defined as the ratio of the NMR line shift relative to its position in an insulator to the position of the NMR line in an insulator, 0.59 ± 0.01 % results from these measurements, in good agreement with previous work [102–104].

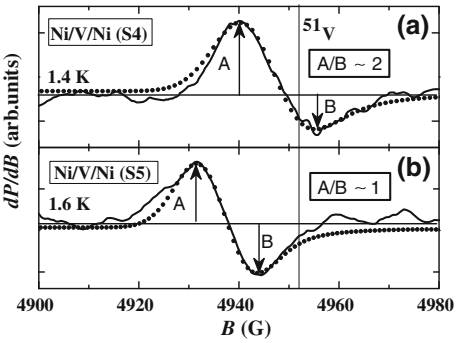

Fig. 9 NMR spectra for Ni/V/Ni trilayers (**a** $d_V = 44\,\text{nm}$, $d_{Ni} = 5\,\text{nm}$, $T_c = 4.1\,\text{K}$ and **b** $d_V = 70\,\text{nm}$, $d_{Ni} = 5\,\text{nm}$, $T_c = 4.4\,\text{K}$) in the superconducting state (parallel magnetic field). The *dotted line* is a theoretical fits taking the spin screening effect into account. (Data taken from [31])

In Fig. 8b the NMR spectrum for the single V layer below T_c for both field orientations is depicted. Compared to the normal state (Fig. 8a) the resonance line is shifted towards higher magnetic fields and definitely broadened in case of the perpendicular orientation ($\Delta B = 15.5$ G). The broadening of the NMR line is caused by the inhomogeneous magnetic field distribution in the vortex state for the perpendicular orientation of the field [105–107]), the line shift is due to the change of the spin susceptibility below T_c.

For a Ni/V/Ni trilayer in the normal state above T_c, the NMR resonance line position and the line width observed was virtually identical to that observed for the single V layer in Fig. 8a. In the superconducting state in Fig. 9, however, the NMR spectra are characteristically different. There also is a shift of the resonance line to higher magnetic fields, but, simultaneously, the line shape is markedly changed with the high-field wing of the NMR line strongly distorted.

The change of the NMR line shape of the F/S/F trilayers on the transition to the superconducting state is a clear indication of the spin screening effect. Taking the spatial distribution of the spin polarization in the S layer into account, the NMR line shape was calculated quantitatively and good agreement was found (see Fig. 9). A careful inspection of all data leads to an exclusion of other possible explanations for the change of the line shape, such as quadrupole effects or local field distributions in the vortex state [31, 32]. The same anomalous change of the NMR line shape below T_c was also observed for the NMR spectra of $Pd_{1-x}Fe_x$/V/$Pd_{1-x}Fe_x$ trilayers with $x = 0.02$ and 0.03 in the superconducting state [31, 32].

5.2 Other Experiments on the Spin Screening Effect

Measurements of the magnetization using the polar magneto-optical Kerr effect on S/F bilayers above and below the superconducting transition temperature T_c have also been employed to search for the spin screening effect [33]. Using Pb/Ni and Al/CoPd bilayers, a slight change of the magneto-optical response across T_c gave indication of an induced magnetization in S. Making use of the possibility to have the

optical penetration depth of the light much smaller than the thickness of the S layer, the Kerr effect from the F-layer was suppressed to a large extend, thus enhancing the sensitivity for small magnetization changes in S. For the Pb/Ni bilayer system, with a superconducting coherence length ξ_s of about one half of the thickness of the S layer, the amplitude of the signal was very small. For the Al/CoPd bilayer system with a much larger ξ_s the effect was more distinct and the signal was found to increases in amplitude when lowering the temperature below T_c. This is in accordance with predictions within the framework of the theory of the inverse proximity effect in Ref. [28, 29].

Another interesting recent experiment using scanning tunnelling electron spectroscopy has also been tentatively interpreted as giving evidence for the spin screening effect [34]. The authors have grown islands of ferromagnetic $SrRuO_3$ on a c-axis oriented thin film of the high T_c superconductor $YBa_2Cu_3O_{7-\delta}$. When measuring the tunnelling current on the ferromagnetic islands, the density of states was found to exhibit a small gap like feature, consistent with the expected short range penetration of the superconducting order into the ferromagnet. On the superconducting film in the vicinity of ferromagnetic islands the authors found anomalous split-gap structures, possibly providing evidence of the inverse proximity effect. However, the length scale of this effect inside the superconductor was found to be an order of magnitude larger than ξ_s, inconsistent with the theoretical prediction of a penetration depth of the order of ξ_s [28, 29]. As discussed in Sect. 4 above, the effect should better be associated with triplet superconductivity close to an S/F interface.

6 Superconducting Spin Valve Effect

As mentioned in the Introduction, in recent years there has been essential progress in the experimental realization of the superconducting spin valve based on the S/F proximity effect. As proposed in the theoretical papers [35–38] there are two possible designs for a spin valve, the F1/F2/S layer scheme with two ferromagnetic layers on one side of the S layer, or the F/S/F trilayer with the superconducting layer interleaved between two ferromagnetic layers. The difference ΔT_c between the transition temperature with the parallel and antiparallel orientation of the two F layers in F/S/F type spin valves turned out to be quite small [39–42].

6.1 Superconducting Spin Valve Effect in Epitaxial Fe/V Layer Structures

In a recent systematic study of superconducting spin valves based on the Fe/V layer system grown epitaxially on MgO substrates [51], the maximum shift $\Delta T_c = 20\,\mathrm{mK}$ could be achieved using FeV alloys as the ferromagnetic layers (Fig. 10). In these

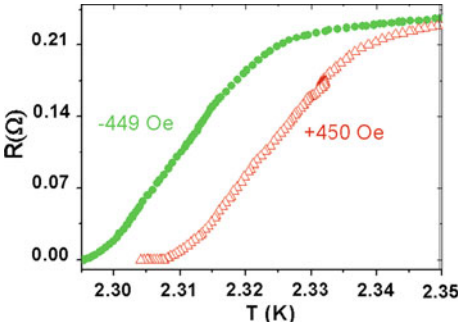

Fig. 10 Resistive superconducting transition of a spin valve with the layer sequence CoO(3 nm)/Co(7 nm)/$Fe_{24}V_{76}$(3.7 nm)/V(24 nm)/ $[Fe_{24}V_{76}$(2.4 nm)/Fe(0.44 nm)$]_8$ in an applied magnetic of +450 Oe and −450 Oe. In the positive field the ferromagnetic layers are oriented in antiparallel direction, in the negative field in parallel direction. (Data taken from [51])

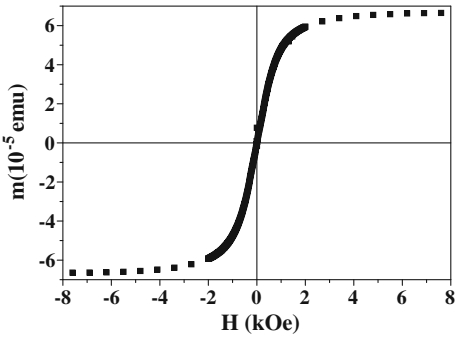

Fig. 11 Magnetic moment versus magnetic field measured at 10 K for the sample Pd(5 nm)/V(24 nm)/[Fe(3Ml)/V(12Ml)]$_{25}$ (Ml denotes a monolayer). (Data taken from [51])

spin valves the top ferromagnetic layer is pinned by the exchange bias effect from an antiferromagnetic CoO layer so that the magnetization direction of the bottom ferromagnetic layer can be reversed without affecting the pinned top ferromagnetic layer. One sees that the shift of the superconducting transition is definitely smaller than the transition width, so that the there is no real switching behavior between the normal and superconducting state, as would be desirable for a superconducting switch.

The second possible spin valve design, the layer scheme S/F1/F2, found much less attention in the literature until now, but has possibly superior potential for exhibiting larger ΔT_c shifts. This was demonstrated using a superconducting V-film grown epitaxially on an epitaxial $[Fe/V]_n$ superlattice with antiferromagnetic interlayer exchange coupling between the Fe layers [108].

In Fig. 11 a magnetization curve for one of the $[Fe/V]_n$ superlattices studied is shown. The magnetization curve reveals an antiferromagnetic interlayer exchange coupling between successive Fe-layers. With increasing magnetic field the magnetization direction of subsequent Fe layers is gradually rotated from an

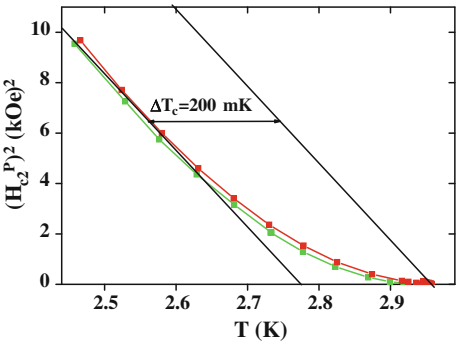

Fig. 12 Squared parallel upper critical magnetic field versus temperature for the same sample as in Fig. 11. The *solid straight line* describes the temperature dependence for $(H_{c2}^P)^2$ above 5 kOe^2. Another *straight line* shows the $(H_{c2}^P)^2$ versus temperature for unchanged mutual orientation of magnetizations of the subsequent Fe layers in the multilayer. (Data taken from [51])

antiparallel alignment in zero field to a parallel alignment for the saturation field above 2 kOe.

In Fig. 12 the square of the upper critical magnetic field for the same sample has been plotted. For the field direction in-plane the upper critical field of the V-layer is in the two-dimensional limit, thus the upper critical field is given by [109]:

$$H_{c2}^P(T) = \frac{\Phi_0}{2\pi\xi^2(0)} \frac{\sqrt{12}}{d_S} \sqrt{\left(1 - \frac{T}{T_c}\right)} \tag{27}$$

with the flux quantum Φ_0, the thickness of the film d_S and the Ginzburg-Landau correlation length ξ,

As shown in Fig. 12, the straight line describes the temperature dependence of the upper critical field for the field range above the saturation field of 2 kOe perfectly. At lower fields there is an increasing deviation. From the extrapolation of the straight line one gets a superconducting transition temperature ΔT_c which is more than 200 mK below the true transition temperature measured at zero field. This difference in T_c of 200 mK is due to the superconducting spin valve effect i.e. due to the rotation of the sublattice magnetization from antiparallel to parallel orientation. The amplitude of the spin valve effect is about one order of magnitude larger than typically observed in F/S/F-type spin valves, thus indicating the superior potential of the F1/F2/S spin valve design.

6.2 Full Switching in F1/F2/S-Type Superconducting Spin Valves

In the following we reproduce the essential findings of Ref. [43, 44] on spin valves of the F1/F2/S-type, following the design originally proposed in Ref. [35]. The layer sequence is CoO_x/Fe(1)/Cu/Fe(2)/In, prepared on a high quality single crystalline

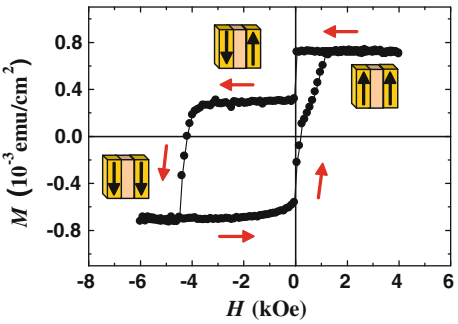

Fig. 13 Magnetic hysteresis loop measured at 10 K for a spin valve CoO_x/Fe(1)/Cu/Fe(2)/In with the thickness $d_{Fe(1)} = 2.4$ nm and $d_{Fe(2)} = 0.5$ nm. (Data taken from [43])

MgO(001) substrate. In this spin valve a 4 nm thick antiferromagnetic CoO layer pins the first ferromagnetic Fe(1) layer by an exchange bias field, a 4 nm thick Cu-layer magnetically separates the second Fe layer Fe(2) from Fe(1). The superconducting layer is an In-layer of 230 nm thickness. The Fe(1) layer has a thickness of typically 2.3 nm, the Fe(2) layer is thinner, in order to allow a penetration of the superconducting pairing function into Fe(1).

The magnetic hysteresis loop of one of the spin valves, measured at 10 K after field-cooling in a field of 4 kOe, is shown in Fig. 13. One sees two well defined magnetic states with parallel and antiparallel magnetization orientation of Fe(1) and Fe(2), respectively.

The sample was cooled down in a magnetic field of 4 kOe applied parallel to the sample plane and measured at 4 K. The magnetic field was varied from 4 to −6 kOe and back again to the value of 4 kOe. Both limits correspond to the orientation of the magnetization of the Fe(1) and Fe(2) layers parallel to the applied field.

Minor hysteresis loops and parameters of the corresponding resistive superconducting transition are plotted in Fig. 14. The resistive transition was measured at positive and negative fields $+H_0$ and $-H_0$, respectively, during re-magnetization of the Fe(2) layer. The resistive transition is strongly broadened in the multidomain state and very sharp in magnetic saturation of Fe(2) in the parallel (P) as well as the antiparallel (AP) orientation of the magnetization of Fe(2) with respect to Fe(1).

In magnetic saturation one notices a sizable difference $\Delta T_c = T_c^{AP} - T_c^P$ for the two orientation of the magnetization of Fe(2), this is the superconducting spin valve effect, which for the sample in Fig. 15 amounts to $\Delta T_c = 19$ mK. Actually this shift is not the largest one among the data published before (see, e.g., Ref. [41], where $\Delta T_c \simeq 41$ mK at $\delta T_c \sim 100$ mK). However, most important, it is substantially larger than δT_c which is of the order of 7 mK at the saturation field $H_0 = 110$ Oe. Thus one can switch the superconducting current off and on by reversing the magnetic field, as required for the operation of a superconducting switch (see details of Fig. 15).

Remarkably it was found that the sign of ΔT_c depends sensitively on the thickness of the layer Fe(2) and is positive for $d_{Fe(2)} < 1$ nm and turns negative for $d_{Fe(2)} \geq 1$ nm. This dependence of the spin valve effect ΔT_c on the thickness of the Fe(2)-layer is shown in Fig. 16.

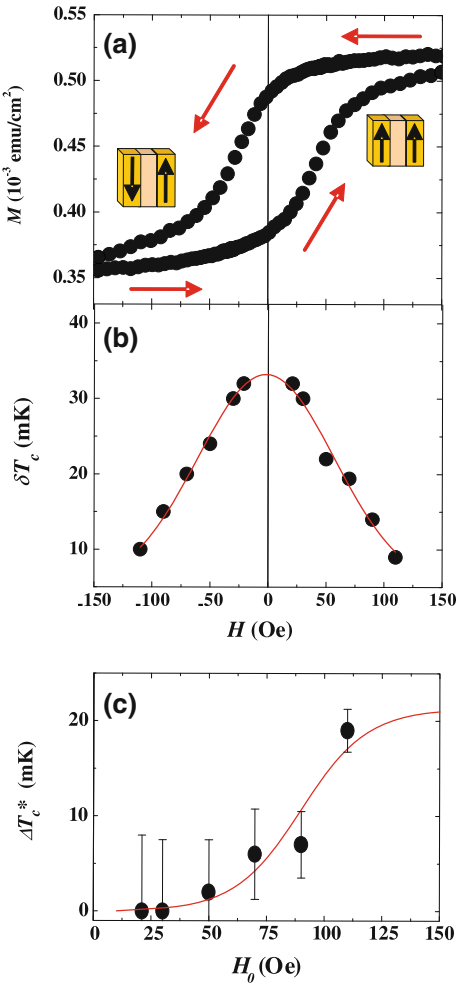

Fig. 14 Minor hysteresis loops (**a**) width of the resistive superconducting transition δT_c (**b**) and the shift of the superconducting transition temperature ΔT_c^* (**c**) for the same sample as in Fig. 13. $\Delta T_c^* = T_c(-H_0) - T_c(+H_0) = \delta T_c$ at the saturation field. (Data taken from [44])

One sees that the $\Delta T_c(d_{Fe(2)})$-dependence exhibits an oscillating character in the thickness range $0.5\,\text{nm} \leq d_{Fe(2)} \leq 2.6\,\text{nm}$. The origin of this interesting behavior is under intense discussion in the literature, since it reveals that the superconducting spin valve effect obviously is more complex than assumed in the previous theoretical work [35], which only predicts $\Delta T_c > 0$. In Ref. [43, 44] different possible scenarios were discussed: (i) occurrence of magnetic domains in the Fe layers; (ii) a spin accumulation in the S layer; (iii) quantum mechanical interference of the Cooper pair wave function in the S/F multilayer. The authors argued in favor of the possibility (iii) and excluded (i) and (ii).

In a recent theoretical treatment by Fominov et al. [110] modelling the experimental spin switch scheme, an oscillating $\Delta T_c(d_{Fe2})$ was reproduced, and although

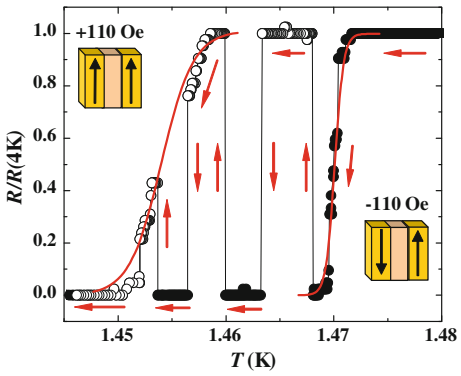

Fig. 15 (Color online) Switching between normal and superconducting states in a spin valve sample during a slow temperature sweep by applying the magnetic field $H_0 = -110$ Oe (*closed circles*) and $H_0 = +110$ Oe (*opened circles*) in the sample plane. (Data taken from [44])

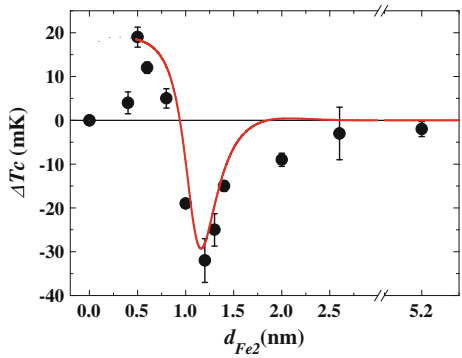

Fig. 16 The dependence of the T_c shift ΔT_c on $d_{Fe(2)}$. The theoretical curve (*solid line*) corresponds to the calculated function $[W(0) - W(\pi)]/W(0)$ (see Fominov et al. [110]) normalized to our experimental data. This fit gives $\xi_F = 0.9$ nm, $l_F = 1.5$ nm and a rough estimate of the quantum mechanical transparency of the S/F interface for the electrons $T = 0.7$. (Data taken from [43])

the assumptions in the theory seem oversimplified compared to the experimental situation, it was possible to fit the experimental curve with reasonable set of parameters using this theory (see Fig. 16) which basically assumes quantum interference at the boundaries as the origin for the oscillations.

7 Summary and Conclusions

In this review we have discussed results of recent theoretical and experimental studies of S/F thin film heterostructures. We summarized the experimental situation concerning the inverse proximity effect, i.e. the spin polarization of the Cooper pairs in a superconducting layer. Experimentally, a partial screening of the magnetic moment of the ferromagnetic layer in S/F systems has clearly been observed recently [31, 32].

We also have reviewed the recent progress in the experimental realization of the superconducting spin valve effect. The absolute value of the shift in the

superconducting transition temperature T_c between the two magnetic states (magnetization of the two F layers either parallel or antiparallel) in the F/S/F- as well as F1/F2/S-type valves is still quite small. However, recently it was at least possible to design an F1/F2/S spin valve with complete switching behavior, i.e. with the resistive transition width smaller than the shift in T_c.

The main attention of the present review has been paid to a new type of superconducting correlations, the so-called long range triplet component LRTC of the superconducting condensate function. Theoretically it has been shown that these triplet correlations, odd in frequency, even in spin and even in momentum, may occur in S/F thin film heterostructures with a nonhomogeneous magnetization. The superconductor S can be a conventional singlet BCS- or an d-wave high-T_c superconductor.

The superconducting order parameter Δ is determined by electron-electron interactions in the superconductor and has either ordinary BCS or d-wave symmetry. The singlet component penetrates from the superconductor S into the ferromagnet F over the short length ξ_F. In the ferromagnet it creates different triplet components: the component f_0 with zero projection of the total spin of the Cooper pair with respect to the magnetization vector and the component f_1 ($f_{\uparrow\uparrow}$ or $f_{\downarrow\downarrow}$) with nonzero projection. The latter component (LRTC) penetrates the ferromagnet on a distance large compared to ξ_F. The ratio of the penetration length of the LRTC and the singlet component is of the order $\sim\sqrt{I/2\pi T} \gg 1$. It spreads also into the superconductor over the length of the order of ξ_S.

The existence of the LRTC in S/F structures with a nonhomogeneous magnetization $M(x)$ has been predicted theoretically a decade ago already [19]. Experimentally, however, it has been detected only very recently [21–23, 25, 26, 24, 27]. In experimental systems the magnetic inhomogeneity can be realized in different manners, e.g. in multilayered S/F structures by non collinear M vectors in subsequent F layers, in a single F layer by a domain wall at the S/F interface, or in Rare Earth ferromagnets by the intrinsic spiral magnetic structure. An intrinsic inhomogeneity with canted spins at the interfaces also can be established in Cu_2MnAl Heusler layers. The main experimental evidence of a LRTC is a long range penetration of the superconducting condensate into the ferromagnetic layer, because only the LRTC is insensitive to the exchange field and to non magnetic scattering.

We also discussed the LRTC in an S/F structure combining a high-T_c superconductor $S_{d\text{-wave}}$ with singlet d-wave pairing and a diffusive ferromagnet with a domain wall (DW) [50]. It turns out that in case of the c-axis normal to the S/F interface the LRTC arises near the DW and spreads into F over a distance much larger than ξ_F and the mean free path l. Therefore the highly anisotropic, singlet d-wave condensate in the $S_{d\text{-wave}}$ superconductor leads to the creation of a triplet, isotropic condensate (LRTC) in the ferromagnetic layer. On the other hand, in the case of a contact of a $S_{d\text{-wave}}$ and a diffusive normal (nonmagnetic) metal N_{dif}, the condensate penetrates from the $S_{d\text{-wave}}$ into N_{dif} over a rather short distance of the order of l and has the same structure as in the $S_{d\text{-wave}}$ i.e. is also of d-wave symmetry. Thus an anomalous PE arises in the case of a contact between a $S_{d\text{-wave}}$ and a diffusive F layer with a DW. This effect has possibly been observed in experiments, already [87, 88].

As noted in the review [5] "an order parameter such as the LRTC has never been observed in nature before". This effect is important not only from the point of view of fundamental physics, but also from a technical point of view, because multilayered S/F/S Josephson junctions with the LRTC may be applied in future spintronic devices [5].

Acknowledgments The authors are grateful for support by the (DFG) within SFB 491. One of us (IAG) would like to acknowledge partial financial support from the Russian Foundation for Basic Research (Grant No. 11-02-01063à).

References

1. A.A. Golubov, MYu. Kupriyanov, E. Il'ichev, Rev. Mod. Phys. **76**, 411 (2004)
2. A. Buzdin, Rev. Mod. Phys. **77**, 935 (2005)
3. F.S. Bergeret, A.F. Volkov, K.B. Efetov, Rev. Mod. Phys. **77**, 1321 (2005)
4. K.B. Efetov, I.A. Garifullin, A.F. Volkov, K. Westerholt, Magnetic Heterostructures, Advances and Perspectives in Spinstructures and Spintransport. ed. by H. Zabel, S.D. Bader, Series. Springer Tracts in Modern Physics, vol 227 (Springer, New York, 2007), P. 252
5. M. Eschrig, Phys. Today **64**, 43 (2011)
6. Z. Radović, L. Dobrosavljevic-Grujić, A.I. Buzdin, J.A. Klem. Phys. Rev. B **38**, 2388 (1988)
7. L. Lazar, K. Westerholt, H. Zabel, L.R. Tagirov, YuV Goryunov, N.N. Garif'yanov, I.A. Garifullin, Phys. Rev. B **61**, 3711 (2000)
8. L.N. Bulaevskii, V.V. Kuzii, A.A. Sobyanin, JETP Lett. **25**, 290 (1977)
9. A.I. Buzdin, L.N. Bulaevskii, S.V. Panyukov, JETP Lett. **35**, 178 (1982)
10. V.V. Ryazanov, V.A. Oboznov, AYu. Rusanov, A.V. Veretennikov, A.A. Golubov, J. Aarts, Phys. Rev. Lett. **86**, 2427 (2001)
11. V.A. Oboznov, V.V. Bolginov, A.K. Feofanov, V.V. Ryazanov, A.I. Buzdin, ibid 96, 197003 (2006)
12. T. Kontos, M. Aprili, J. Lesueur, X. Grison, Phys. Rev. Lett. **89**, 137007 (2002)
13. Y. Blum, A. Tsukernik, M. Karpovski, A. Palevski, Phys. Rev. Lett. **89**, 187004 (2002)
14. A. Bauer, J. Bentner, M. Aprili, M.L. Della Rocca, M. Reinwald, W. Wegscheider, C. Strunk, Phys. Rev. Lett. **92**, 217001 (2004)
15. H. Sellier, C. Baraduc, F. Lefloch, R. Calemczuk, Phys. Rev. Lett. **92**, 257005 (2004)
16. V. Shelukhin, A. Tsukernik, M. Karpovski, Y. Blum, K.B. Efetov, A.F. Volkov, T. Champel, M. Eschrig, T. Lofwander, G. Schon, A. Palevski, Phys. Rev. B **73**, 1 (2006)
17. A.A. Bannykh, J. Pfeiffer, V.S. Stolyarov, I.E. Batov, V.V. Ryazanov, M. Weides, Phys. Rev. B **79**, 054501 (2009)
18. Y. Makhlin, G. Schoen, A. Shnirman, Rev. Mod. Phys. **73**, 357 (2001)
19. F.S. Bergeret, A.F. Volkov, K.B. Efetov, Phys. Rev. Lett. **86**, 4096 (2001)
20. A.P. Mackenzie, Y. Maeno, Rev. Mod. Phys. **75**, 657 (2003)
21. R.S. Keizer, S.T.B. Goennenwein, T.M. Klapwijk, G. Miao, G. Xiao, A. Gupta, Nature **439**, 825 (2006)
22. I. Sosnin, H. Cho, V.T. Petrashov, A.F. Volkov, Phys. Rev. Lett. **96**, 157002 (2006)
23. T.S. Khaire, M.A. Khasawneh, W.P. Pratt Jr, N.O. Birge, Phys. Rev. Lett. **104**, 137002 (2010)
24. D. Sprungmann, K. Westerholt, H. Zabel, M. Weides, H. Kohlstedt, Phys. Rev. B **82**, 060505 (2010)
25. J. Wang, M. Singh, M. Tian, N. Kumar, B. Liu, C. Shi, J.K. Jain, N. Samarth, T.E. Mallouk, M.H.W. Chan, Nat. Phys. **6**, 389 (2010)
26. J.W.A. Robinson, J.D.S. Witt, M.G. Blamire, Science **329**, 59 (2010)
27. M.S. Anwar, M. Hesselberth, M. Porcu, J. Aarts, Phys. Rev. B **82**, 100501 (2010)

28. F.S. Bergeret, A.F. Volkov, K.B. Efetov, Phys. Rev. B **69**, 174504 (2004)
29. F.S. Bergeret, A.F. Volkov, K.B. Efetov, Europhys. Lett. **66**, 111 (2004)
30. MYu. Kharitonov, A.F. Volkov, K.B. Efetov, Phys. Rev. B **73**, 054511 (2006)
31. R.I. Salikhov, I.A. Garifullin, N.N. Garif'yanov, L.R. Tagirov, K. Theis-Bröhl, K. Westerholt, H. Zabel, Phys. Rev. Lett. **102**, 087003 (2009)
32. R.I. Salikhov, N.N. Garif'yanov, I.A. Garifullin, L.R. Tagirov, K. Westerholt, H. Zabel, Phys. Rev. B **80**, 214523 (2009)
33. J. Xia, V. Shelukhin, M. Karpovski, A. Kapitulnik, A. Palevski, Phys. Rev. Lett. **102**, 087004 (2009)
34. I. Asulin, O. Yuli, G. Koren, O. Milo, Phys. Rev. B **79**, 174524 (2009)
35. S. Oh, D. Youm, M.R. Beasley, Appl. Phys. Lett. **71**, 2376 (1997)
36. L.R. Tagirov, Phys. Rev. Lett. **83**, 2058 (1999)
37. A.I. Buzdin, A.V. Vedyaev, N.N. Ryzhanova, Europhys. Lett. **48**, 686 (1999)
38. I. Baladié, A. Buzdin, N. Ryzhanova, A. Vedyayev, Phys. Rev. B **64**, 054518 (2001)
39. J.Y. Gu, C.Y. You, J.S. Jiang, J. Pearson, Y.B. Bazaliy, S.D. Bader, Phys. Rev. Lett. **89**, 267001 (2002)
40. A. Potenza, C.H. Marrows, Phys. Rev. B **71**, 180503(R) (2005)
41. I.C. Moraru Jr, W.P. Pratt, N.O. Birge, Phys. Rev. Lett. **96**, 037004 (2006)
42. G-X. Miao, A.V. Ramos, J. Moodera, Phys. Rev. Lett. **101**, 137001 (2008)
43. P.V. Leksin, N.N. Garif'yanov, I.A. Garifullin, J. Schumann, H. Vinzelberg, V. Kataev, R. Klingeler, O.G. Schmidt, B. Büchner, Appl. Phys. Lett. **97**, 10505 (2010)
44. P.V. Leksin, N.N. Garif'yanov, I.A. Garifullin, J. Schumann, V. Kataev, O.G. Schmidt, B. Büchner, Phys. Rev. Lett. **106**, 067005 (2011)
45. F.S. Bergeret, A.F. Volkov, K.B. Efetov, Phys. Rev. Lett. **86**, 3140 (2001)
46. Y.M. Blanter, F.W.J. Hekking, Phys. Rev. B **69**, 024525 (2004)
47. A.V. Zaitsev, JETP Lett. **90**, 475 (2009)
48. J.W.A. Robinson, G. Halasz, A.I. Buzdin, M.G. Blamire, Phys. Rev. Lett. **104**, 207001 (2010)
49. A.F. Volkov, K.B. Efetov, Phys. Rev. B **81**, 144522 (2010)
50. A.F. Volkov, K.B. Efetov, Phys. Rev. Lett. **102**, 077002 (2009)
51. G. Nowak, H. Zabel, K. Westerholt, I. Garifullin, M. Marcellini, A. Liebig, B. Hjörvarsson, Phys. Rev. B **78**, 134520 (2008)
52. A.F. Volkov, K.B. Efetov, Phys. Rev. B **72**, 184504 (2008)
53. A.F. Volkov, Y.V. Fominov, K.B. Efetov, Phys. Rev. B **72**, 184504 (2005)
54. Y.V. Fominov, A.F. Volkov, K.B. Efetov, Phys. Rev. B **75**, 104509 (2007)
55. M. Eschrig, J. Kopu, J.C. Cuevas, G. Schön, Phys. Rev. Lett. **90**, 137003 (2003)
56. Y. Asano, Y. Sawa, Y. Tanaka, A.A. Golubov, Phys. Rev. B **76**, 224525 (2007)
57. A.V. Galaktionov, M.S. Kalenkov, A.D. Zaikin, Phys. Rev. B **77**, 094520 (2008)
58. V. Braude, YuV Nazarov, Phys. Rev. Lett. **98**, 077003 (2007)
59. Z. Pajović, M. Bozović, Z. Radović, J. Cayssol, A. Buzdin, Phys. Rev. B **74**, 184509 (2006)
60. K. Halterman, O.T. Valls, Physica C **420**, 111 (2005)
61. B. Béri, J.N. Kupferschmidt, C.W.J. Beenakker, P.W. Brouwer, Phys. Rev. B **79**, 024517 (2009)
62. A.F. Volkov, A. Anishchanka, K.B Efetov, Phys. Rev. B **73**, 104412 (2006)
63. T. Champel, T. Löfwander, M. Eschrig, Phys. Rev. Lett. **100**, 077003 (2008)
64. G.B. Halász, J.W.A. Robinson, M.G. Blamire, J.F. Annett, Phys. Rev. B **79**, 224505 (2009)
65. M.S. Kalenkov, A.V. Galaktionov, A.D. Zaikin, Phys. Rev. B **79**, 014521 (2009)
66. A. Cottet, D. Huertas-Hernando, W. Belzig, YuV Nazarov, Phys. Rev. B **80**, 184511 (2009)
67. M. Alidoust, J. Linder, G. Rashedi, T. Yokoyama, A. Sudbo, Phys. Rev. B **81**, 014512 (2010)
68. A. Millis, D. Rainer, J.A. Sauls, Phys. Rev. B **38**, 4504 (1988)
69. M. Eschrig, Phys. Rev. B **80**, 134511 (2009)
70. M.A. Silaev, Phys. Rev. B **79**, 184505 (2009)
71. M.S. Kalenkov, A.D. Zaikin, V.T. Petrashov, Phys. Rev. Lett. **107**, 087003 (2011)
72. I.V. Bobkova, A.M. Bobkov, Phys. Rev. B **82**, 024515 (2010)
73. R. Grein, M. Eschrig, G. Metalidis, G. Schön, Phys. Rev. Lett. **102**, 227005 (2009)

74. Y.S. Barash, I.V. Bobkova, T. Kopp, Phys. Rev. B **66**, 140503(R) (2002)
75. B. Crouzy, S. Tollis, D.A. Ivanov, Phys. Rev. B **75**, 054503 (2007)
76. I. Sperstad, J. Linder, A. Sudbo, Phys. Rev. B **78**, 104509 (2008)
77. A.F. Volkov, F.S. Bergeret, K.B. Efetov, Phys. Rev. Lett. **90**, 117006 (2003)
78. M. Houzet, A.I. Buzdin, Phys. Rev. B **76**, 060504(R) (2007)
79. A.I. Larkin, Y.N. Ovchinnikov, in Nonequilibrium Superconductivity, ed. by D.N. Langenberg, A.I. Larkin (Elsevier, Amsterdam, 1984)
80. J. Rammer, H. Smith, Rev. Mod. Phys. **58**, 323 (1986)
81. W. Belzig, G. Schoen, C. Bruder, A.D. Zaikin, Superlattices Microstruct. **25**, 1251 (1999)
82. N.B. Kopnin, *Theory of Nonequilibrium Superconductivity* (Clarendon Press, Oxford, 2001)
83. A.V. Zaitsev, JETP **59**, 1015 (1984)
84. M.Y. Kupriyanov, V.F. Lukichev, JETP **67**, 1163 (1988)
85. E.A. Demler, G.B. Arnold, M.R. Beasley, Phys. Rev. B **55**, 15174 (1997)
86. L.D. Landau, E.M. Lifshitz, *Electrodynamics of Continuous Media* (Butterworth-Heinemann, Oxford, 1982), p. 107
87. V. Peńa, Z. Sefrioni, D. Arias, C. Leon, J. Santamria, M. Varela, S.J. Pennycook, J.L. Martinec, Phys. Rev. B **69**, 224502 (2004)
88. I. Asulin, O. Yuli, G. Koren, O. Millo, Phys. Rev. B **74**, 092501 (2006)
89. I. Asulin, O. Yuli, I. Felner, G. Koren, O. Millo, Phys. Rev. B **76**, 064507 (2007)
90. D.J. Van Harlingen, Rev. Mod. Phys. **67**, 515 (1995)
91. C.C. Tsuei, J.R. Kirtley, ibid. 72, 969 (2000)
92. M. Eschrig, T. Lofwander, T. Champel, J.C. Cuevas, J. Kopu, G. Schön, J. Low Temp. Phys. **147**, 457, (2007)
93. M. Alidoust, J. Linder. Phys. Rev. B **82**, 224504 (2010)
94. P.J. Webster, K.R.A. Ziebeck, Landolt-Brnstein New Series III/19c (1986)
95. S. Picozzi, A. Continenza, A.J. Freemanet, Phys. Rev. B **69**, 094423 (2004)
96. I. Galanakis, P.H. Dederichs, N. Papanikolaou. Phys. Rev. B **66**, 134428 (2002)
97. S. Picozzi, A. Continenza, A.J. Freemanet, Phys. Rev. B **69**, 094423 (2004)
98. D. Erb, G. Nowak, K. Westerholt, H. Zabel, J. Phys. D: Appl. Phys. **43**, 285001 (2010)
99. A. Deb, Y. Sakurai, J. Phys. Condens. Matter **12**, 2997 (2000)
100. J. Grabis, A. Bergmann, A. Nefedov, K. Westerholt, H. Zabel, Phys. Rev. B **72**, 024438 (2005)
101. A. Bergmann, J. Grabis, B.P. Toperverg, V. Leiner, M. Wolff, H. Zabel, K. Westerholt, Phys. Rev. B **72**, 214403 (2005)
102. B.J. Noer, W.D. Knight, Rev. Mod. Phys. **36**, 177 (1964)
103. I.A. Garifullin, N.N. Garif'yanov, R.I. Salikhov, L.R. Tagirov, Pis'ma v Zh. Eksp. Teor. Fiz. **87**, 367 (2008)
104. I.A. Garifullin, N.N. Garif'yanov, R.I. Salikhov, L.R. Tagirov, JETP Lett. **87**, 317 (2008)
105. D. Rossier, D.E. MacLaughlin, Phys. Kondens. Materie **11**, 66 (1970)
106. J.-M. Delriew, Solid State Commun. **8**, 61 (1970)
107. L. Dobrosavljević, C.R. Acad, Sci. Paris **263**, 502 (1966)
108. K. Westerholt, D. Sprungmann, H. Zabel, R. Brucas, B. Hjörvarsson, D.A. Tikhonov, I.A. Garifullin. Phys. Rev. Lett. **95**, 097003 (2005)
109. P.G. de Gennes, M. Tinkham, Physics **1**, 107 (1964)
110. Y.V. Fominov, A.A. Golubov, T.Y. Karminskaya, Y. Kupriyanov, R.G. Deminov, L.R. Tagirov, JETP Lett. **91**, 308 (2010)

Ferromagnetic Heusler Alloy Thin Films: Electronic Properties and Magnetic Moment Formation

Heike C. Herper, Peter Kratzer, Heiko Wende, Bernhard Krumme, Kurt Westerholt and Peter Entel

Abstract Heusler alloys have attracted huge interest due to their outstanding magnetic properties which make them suitable for various applications. Bulk Heusler alloys are applied in magnetic shape memory and magneto-caloric devices. Here, we focus on thin films of Heusler alloys as needed for magneto-electronic applications. Especially, Co- or Fe-based systems such as Co_2MnSi are known to be half-metallic or have at least a high spin polarization and a high Curie temperature making them appropriate as spintronic materials. In the present paper the influence of composition, disorder, and structural deformation on the magnetic properties is discussed from experimental as well as theoretical point of view. Since the quality of a spintronic device crucially depends on the interplay between the ferromagnet and the substrate the influence of different substrates (GaAs, MgO) on the electronic and magnetic properties is studied.

1 Introduction

In modern technology magnetic materials play an important role, prominent examples being data recording, magnetic field sensors, and biomedical applications [1–4]. The development of magnetic devices is achieved by theoretical and experimental work, searching for new materials and explaining the experimental observations on the atomic level [5–8].

Heike C. Herper (✉) · Peter Kratzer · Heiko Wende · Bernhard Krumme · Peter Entel
Faculty of Physics, University of Duisburg-Essen, Lotharstraße 1,
47048 Duisburg, Germany
e-mail: Heike.Herper@uni-due.de

Kurt Westerholt
Institute of Physics, Ruhr-University of Bochum, Universitätsstraße 150,
44780 Bochum, Germany
e-mail: Kurt.Westerholt@rub.de

H. Zabel and M. Farle (eds.), *Magnetic Nanostructures,*
Springer Tracts in Modern Physics 246, DOI: 10.1007/978-3-642-32042-2_4,

One class of materials which has attracted considerable interest in recent years because of its outstanding magnetic properties are Heusler-type alloys. In bulk their magnetic properties can be relatively easily controlled by composition and stoichiometry [9–11] which renders them interesting as functional materials for different applications such as magnetic shape memory alloys (MSMA) [12, 13], magnetic tunnel junctions (MTJ) [14–16], magneto-caloric devices [17, 18], and topological insulators [19]. Using one and the same material class for different applications opens up a wide field for future multifunctional applications. Heusler alloy thin films which are the subject of the present chapter, find their major application in magnetoelectronics, e.g. MTJs. Hence we discuss their properties with respect to these applications, while keeping the other two areas in mind.

The magnetic shape memory effect (MSME) [20] is related to the observation of a magnetic field driven shape change below the martensitic phase transformation temperature, which is different from the temperature driven change in conventional shape memory materials. In Heusler type shape memory alloys the shape change reaches meanwhile 10 % in an external magnetic field of less than 1 T, which actually is about 100 times larger than in conventional piezoceramics. Small effects have already been observed in thin Ni_2MnGa films [21, 22]. Unfortunately, the prototype MSMA Heusler materials such as Ni_2MnGa are too brittle for practical applications. In order to overcome the problem, intensive studies have been started by changing also the composition and stoichiometry of the Heusler alloy [23, 24].

Similar problems also arise for magneto-caloric Heusler alloys. Here the temperature T of a sample is increased (conventional magneto-caloric effect) or reduced (inverse effect) adiabatically by an amount of ΔT if a magnetic field is switched on. The inverse magnetocaloric effect has become popular as a possible environmental friendly refrigerator tool for local cooling [25]. However, the effect is relatively small and similar to the MSMA, material design by variation of composition is a topical task. Both, the MSME and the magnetocalorics are intensively studied especially by theoretical groups in order to find new and better compositions for applications [26–28].

Here, the focus is on the most advanced application for Heusler alloys namely magnetoelectronics whereby a combination with the above mentioned features is desirable as a long term perspective for multifunctional materials. Regarding to magneto-electronic applications a new aspect enters the search for suitable materials. While magnetic shape memory and magneto-caloric devices are usually built of bulk materials, MTJs are naturally layered thin film systems consisting of two ferromagnetic electrodes and an insulating tunneling barrier such as GaAs(001), MgO(001), AlO_x or TiO_x [29], see Fig. 1. Accordingly, it is not sufficient to optimize the properties of the ferromagnet (FM), the interface between the FM and insulating barrier is important as well [30–32]. In case of GaAs(001) the lattice mismatch between Fe-Co-Si Heusler alloys and the insulator is rather small (<1 %), but due to the complex surface structure of GaAs(001), diffusion is likely to occur at the interface deteriorating the quality of the heterostructure [33]. This effect could be suppressed by using MgO(001) which shows no significant surface reconstruction, see Sects. 2.2 and 3.1.2. Alternatively, AlO_x or similar amorphous oxides are used,

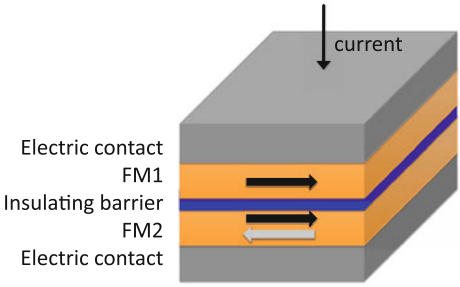

Fig. 1 Schematic drawing of a magnetic tunnel junction (MTJ). In this case the magnetization of the FM is in-plane. The electric current is always oriented perpendicular to the plane of layers. The magnetization direction of FM2 is changed from antiparallel (*gray arrow*) to parallel (*black arrow*) by applying a magnetic field

however, the quality of the hybrid system strongly depends of the fabrication of the AlO_x layer [34].

The efficiency of a MTJ is expressed by the tunnel magnetoresistance (TMR) ratio. The TMR measures the change of the resistance when a small magnetic field is applied to the sample, which is sufficient to switch the magnetization direction of FM2 in Fig. 1 from antiparallel to parallel alignment compared to FM1. Usually the resistance in the parallel arrangement is smaller than in the antiparallel configuration. The change of the resistance is usually defined by

$$\mathrm{TMR} = \frac{R_a - R_p}{R_p} = \frac{G_p - G_a}{G_a} \tag{1}$$

where R_p and R_a are the resistances for parallel and anti-parallel alignment of the ferromagnetic layers FM1 and FM2, respectively, with the corresponding conductances named G_p and G_a. This so called positive definition of the TMR diverges if only electrons of one spin orientation exist at the Fermi level. The TMR effect was already discovered in 1975 by Jullière [35], but due to the lack of an appropriate thin film technology and suitable materials it took until 1995 when the TMR experiences its *Indian summer* [36]. Henceforce, an relentless search for new ferromagnets has started to maximize the TMR value and Heusler alloys seem to fulfill the prerequisites for huge TMR values.

Heusler alloys with the generic formula X_2YZ crystallize in $L2_1$ structure with $Fm\bar{3}m$ symmetry which consists of four interpenetrating fcc lattices, see Fig. 2 whereby in the ideal stoichiometric case sublattices A and B are occupied by the same species (X). In some cases the so called inverse Heusler structure (prototype Hg_2CuTi) occurs in which X occupies sublattices A and C. Depending on the application high Curie temperatures and spin polarizations are necessary (magnetoetronics, TMR) or the system has to undergo a shape change in the low temperature phase (MSMA). Designing materials with the desired magnetic properties can be achieved, for example, by varying the composition of the constituents X, Y, and Z,

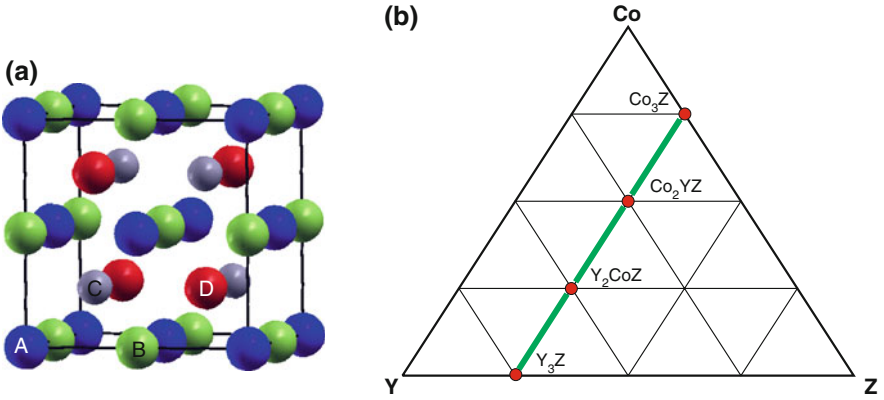

Fig. 2 **a** Sketch of a Heusler type structure. Different colors indicate the four interpenetrating sublattices. The ordinary $L2_1$ ordered Heusler structure is achieved if sublattice *A* and *B* are occupied by the same species. In case that the same type of atoms sits on *A* and *C*, the system is in the so-called inverse Heusler structure with $F\bar{4}3m$ symmetry. When three sublattices are occupied by the same material, as in Fe_3Si, this leads to $D0_3$ symmetry. **b** Sketch of phase diagram of a ternary Co-based Heusler alloy $Co_{3-x}Y_xZ$, with Y being a magnetic transition metal, i.e., Fe or Mn. In case of Heusler systems being interesting for spintronic applications Z is usually a half metal such as Ge and Si or poor metal like Al

off-stoichiometric composition or impurities which means changing the number of valence electrons in the system. The focus of the present article is on systems being possible candidates for spintronics applications, i.e., materials which provide a high T_C and large spin polarization P. Halfmetallic systems (100 % spin polarization) such as Co_2MnSi or Co_2FeSi are the most attractive candidates.Theoretically, for half metals the expected TMR ratio is infinite, since the conductance for the case of antiparallel magnetization goes to zero (see Eq. 1). Since there are no appropriate states at the Fermi level of FM2 which could be occupied by electrons tunneling from FM1 [1, 37]. Unfortunately, these promising predictions are not always confirmed by experiments and the measured TMR values may fall behind the theoretical predictions, especially at elevated temperatures [38]. However, there are very promising experimental results which have been measured for $Co_2Fe_{0.5}Al_{0.5}Si$ with a TMR = 386 % and Co_2MnSi 217 % on MgO(001) at room temperature [14, 39]. An overview of the experimental properties such as anisotropy, polarization etc. can be found in Ref. [40].

The key point for the quality of ferromagnet-insulator hybrid structures is the design of the ferromagnet-insulator interface. It is quite challenging to build a perfect interface, because diffusion processes or alloy formation, which may occur at the interface, can destroy the ideal magnetic properties of the Heusler alloy or in the words of Swagten "The use of these [Heusler] materials in ferromagnetic-insulator junctions is obviously extremely tedious due to the crucial role of two barrier interfaces." [41].

Depending on the fabrication technique the samples are not or at least not fully $L2_1$ ordered but show partially B2 order, which also reduces the spin polarization and

the TMR [42]. Furthermore, it has been argued that the composition of the Heusler alloys grown on an insulating substrate may not be completely homogeneous and deviations from the ideal stoichiometry can influence the magnetic properties as well [43].

Since there exists a quite large amount of literature dealing with Heusler alloys and TMR, the aim of the present review is to focus on the mechanisms which are essentially responsible for the magnitude of the spin polarization and the influence of the interface. The important aspects are exemplarily discussed for selected systems, which embrace the quasi-Heusler alloy Fe_3Si as a kind of prototype for magnetic Heusler alloys and the high-T_C compounds Co-Fe-Si, and Co-Mn-Si(Ge). The systems, or in fact their magnetic properties, will be illuminated from two sides: Using element-specific magnetic methods such as X-ray magnetic dichroism (XMCD) and density functional theory (DFT). Here, experiment and theory can be viewed to complement each other, which is demonstrated in Sect. 2 where the induced magnetism in Cu_2MnAl and Fe_3Si is studied. The main part of the paper is dedicated to Co-Fe-Si (Sect. 3.1) and Co-Mn-Si(Ge) (Sects. 3.2 and 3.3) Heusler alloys, whereby the discussion covers both bulk systems (as model for thick films) and thin films. In Sect. 4 a brief overview of transport through junctions with Heusler alloys as electrodes is given.

2 Induced Magnetic Moments

2.1 The Primary Heusler Alloy: Cu_2MnAl

One of the most characteristic features of the ferromagnetic Heusler alloys is the intimate relationship between structural and magnetic order. The desired crystallographic structure with the best magnetic properties for the spintronic compounds such as Co_2MnSi is the perfectly ordered $L2_1$ structure. However, less well ordered states such as the B2 structure and the A2 structure and mixtures between those compete with the $L2_1$ structure, with important consequences for the magnetism of the system.

One focal point of this review is the study of the magnetic properties of Heusler compounds on a microscopic level. This goal can be achieved by utilizing the element specificity of the X-ray magnetic circular dichroism (XMCD) technique. Thereby, the local spin and orbital moments of the magnetic elements can be determined experimentally and compared to the spin-resolved electronic structure as revealed by DFT calculations. A detailed analysis can be carried out by directly comparing the calculated X-ray absorption spectra (XAS) and XMCD spectra with the experimental results. Since the structural ordering is closely connected to the magnetic properties of the Heusler compound, the investigation of the magnetism is a sensitive tool to achieve a more complete understanding of the system. A very delicate 'detector' of an accurate description of the electronic structure is the analysis of induced magnetism

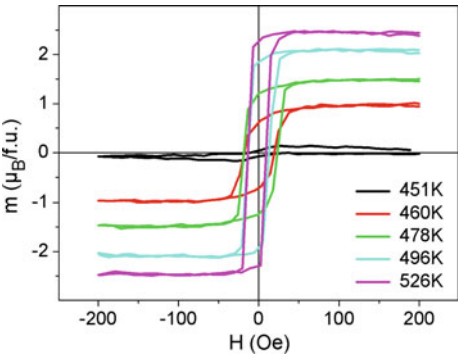

Fig. 3 Magnetic hysteresis loops of a Cu_2MnAl-film measured at room temperature after annealing for 1 h at the annealing temperature given inside the figure (data taken from [46])

by hybridization effects. The hybridization of the 'non-magnetic' elements like Cu or Si with the magnetic elements as e.g. Mn or Fe can lead to small induced magnetic moments in Cu or Si, for example in the systems Cu_2MnAl or Fe_3Si. The element specificity of the XMCD technique and the advances of the synchrotron radiation facilities allows to measure even tiny induced magnetic moments. This shall be demonstrated here for Cu_2MnAl and Fe_3Si.

We start with an illustrative example which is provided by the original Heusler compound Cu_2MnAl [44]. The magnetism of this compound is exceptionally simple, because there is only one magnetic atom per formula unit. In the perfectly ordered $L2_1$ structure there are no Mn-Mn nearest neighbors and the strongest exchange interaction in the unit cell is a ferromagnetic next nearest neighbor superexchange across the Al-orbitals, giving rise to ferromagnetism with a ferromagnetic Curie temperature of 630 K [45]. In contrast, in the B2 and A2-structure in Cu_2MnAl Mn-Mn nearest neighbors exist and very strong nearest neighbor Mn-Mn antiferromagnetic exchange interactions competing with the ferromagnetic superexchange interactions come into play. The magnetic ground state then changes drastically to a spin glass state with a freezing temperature below room temperature [46]. Even for Cu_2MnAl bulk samples after optimum preparation perfect $L2_1$ order cannot be achieved [47, 48], there is always some remnant B2-type site disorder. This implies that Mn-Mn nearest neighbors always exist and the magnetic ground state even in bulk Cu_2MnAl is not purely ferromagnetic but contains some static spin disorder.

When prepared by sputtering at room temperature Cu_2MnAl grows in the completely disordered A2 structure with nanocrystalline grains [46]. Figure 3 shows the development of the ferromagnetic magnetization of a Cu_2MnAl film of 50 nm thickness grown on MgO(100) after annealing for one hour at successively higher maximum annealing temperatures T_{ann}, starting from the as-prepared, low moment state. The magnetic moment gradually increases with T_{ann}. The development of the magnetic moment is accompanied by a continuous change of the crystallographic structure from A2 order to $L2_1$ order. The corresponding X-ray Bragg scans in the

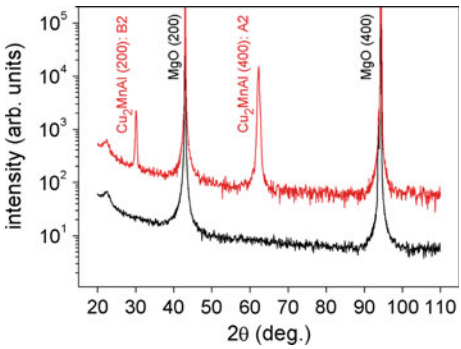

Fig. 4 X-ray Bragg scan using Cu-K_α radiation of a Cu_2MnAl film grown on MgO (100) in the as-prepared state (*lower curve*) and after annealing at 526 K for 1 h (*upper curve*) (data taken from [46])

as-grown state and in the state with the maximum magnetic moment are shown in Fig. 4. In the as-grown sample state there are no resolvable Bragg peaks, since the film is nanocrystalline with very small structural coherence length. After annealing the (200) and the (400) Heusler Bragg reflections show up, indicating a crystalline state with the expected (100) out-of-plane texture of the Heusler films induced by the MgO(100) substrate [49].

For an element-specific determination of the magnetic moments the samples were studied by means of XMCD spectra at BESSY II, the synchrotron radiation facility in Berlin, Germany. To achieve well ordered films the samples were annealed at 600 K for 1 h [50]. The experimental results measured at the Mn and Cu $L_{2,3}$-edges are presented in Fig. 5. As expected, the magnetic properties of this Heusler compound are determined by the Mn moments, however, the high sensitivity of the XMCD technique even allows for the identification of an induced moment in Cu. As can be seen in Fig. 5d a pronounced XMCD signal is measured at the Mn $L_{2,3}$-edges whereas a quite small XMCD signal is detected at the Cu $L_{2,3}$-edges (Fig. 5b). We first turn to the analysis of the large magnetic moment of Mn. The usual analysis of XMCD spectra is carried out by means of the so-called sum rule analysis to determine the spin and orbital moments μ_S and μ_L. However, because of core hole correlation effects this analysis procedure must be corrected for light 3*d* elements like Mn (see e.g. [51] and references therein). For the case of Mn a correction factor of 1.5 for the spin moment has been used following Ref. [52]. The experimental spin and orbital moments of Mn are presented in Table 1 and are compared to ab initio calculations using the Korringa-Kohn-Rostoker (KKR) Green's functions technique with the SPR-KKR code [50]. Interestingly, the calculated spin moment μ_S for the ordered case $\mu_S^{\mathrm{Mn}}(\mathrm{theory}) = 3.387\mu_B$ is quite similar as compared to the experimental result $\mu_S^{\mathrm{Mn}}(\mathrm{exp.}) = (3.36 \pm 0.50)\mu_B$ which is determined with the correction factor of 1.5. Using this code it is possible to determine the theoretical XAS and XMCD spectra on the same footing that were used to calculate the spin and orbital magnetic moments. As can be seen in Fig. 5c, d there is a clear discrepancy between experiment and theory

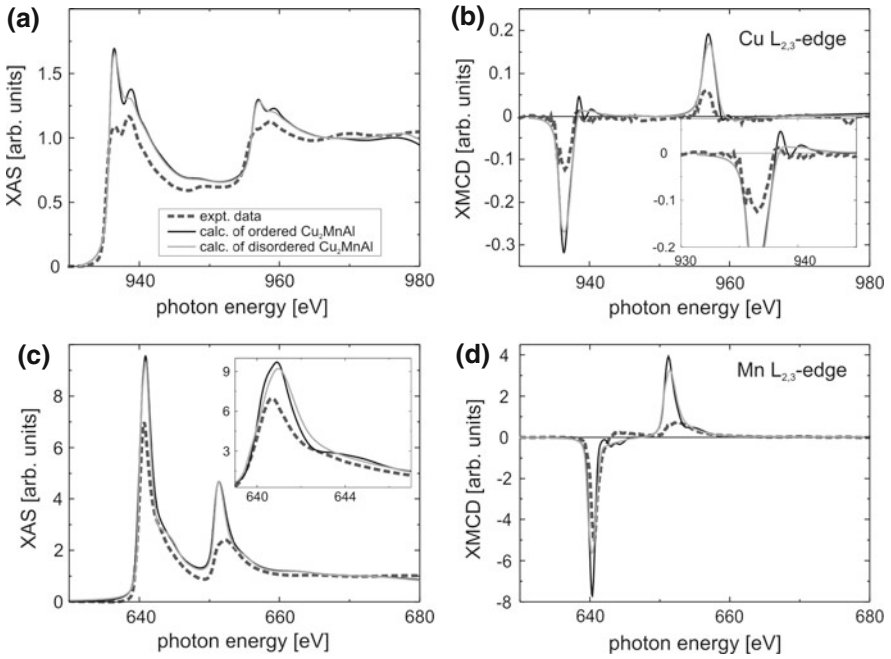

Fig. 5 Calculated (*black and light grey curve*) and experimental (*dashed curve*) XAS (*left*) and XMCD (*right*) spectra of Cu_2MnAl films at the Cu (*top*) and Mn (*bottom*) $L_{2,3}$-edges (data taken from [50]). For the calculations of disordered Cu_2MnAl an exchange of 12.5 % of the Mn- atoms with Al-atoms has been assumed

for the spectral shape at the Mn $L_{2,3}$-edges. The intensity of the calculated white line (Fig. 5c) is obviously larger as compared to the experiment. This is also directly reflected in a larger theoretical XMCD intensity. A possible explanation for this discrepancy could be atomic disorder. This might be expected because the annealing of the sample could lead to an intermixing at the interface to the Al capping layer. To test this, the effect of an intermixing of the Mn and Al sublattices was modeled in the framework of the coherent potential approximation (CPA) by exchanging 12.5 and 25 % of the Mn atoms with Al atoms, respectively. However, this intermixing only results in minor changes in the spin and orbital moments of Mn and the corresponding spectra (see Fig. 5). Hence, there must be other reasons for the deviation of the calculated XAS and XMCD spectra from the experimental ones. Since the branching ratio seen in the experimental Mn spectra clearly differ from the statistical value (white line intensities at L_3 to L_2-edge $=$ 2:1), the theoretical description has to go beyond the local spin-density approximation (LSDA) in future calculations e.g. by applying the dynamical mean-field theory (DMFT) and by treating the core hole beyond the final-state approximation, as it is discussed e.g. in Ref. [53].

Now we turn to the analysis of the induced moments in Cu in the Cu_2MnAl Heusler compound. The experimental XMCD spectra at the Cu $L_{2,3}$-edges (Fig. 5b)

Table 1 Experimental and theoretical magnetic moments of Cu_2MnAl obtained from SPR-KKR calculations and XMCD measurements given in μ_B per atom [50]

Technique	Element	m_S/μ_B	m_L/μ_B	m_{tot}/μ_B
SPR-KKR ordered	Cu	0.038	0.005	0.043
12.5 % disorder	Cu	0.034	0.005	0.039
25 % disorder	Cu	0.032	0.005	0.037
XMCD	Cu	0.033 ± 0.01	0.009 ± 0.001	0.042 ± 0.01
SPR-KKR ordered	Mn	3.387	0.008	3.395
12.5 % disorder	Mn	3.390	0.008	3.398
25 % disorder	Mn	3.402	0.008	3.410
XMCD	Mn	3.36 ± 0.5	0.21 ± 0.02	3.57 ± 0.5
SQUID				2.95 ± 0.3

The magnetization measured by SQUID is given in μ_B per unit cell. An error of 15 % is assumed for m_S and 10 % for m_L

demonstrate the existence of these induced moments. Since induced moments originate from subtle hybridization effects these features represent an interesting benchmark for the accuracy of the theoretical description of the relevant details in the band structure. Therefore, the absolute values of the induced spin and orbital moments in Cu and the corresponding XAS and XMCD spectra at the Cu $L_{2,3}$-edges determined using the SPR-KKR code. Although the induced spin moment is quite small (in the regime of a few hundredth of a Bohr magneton) the agreement between experiment and theory is astonishingly good. As can be seen in Table 1 the theoretical result for the ordered system of $\mu_S^{\mathrm{Cu}}(\mathrm{theory}) = 0.038\mu_B$ agrees nicely with the experimental result of the XMCD sum rule analysis of $\mu_S^{\mathrm{Cu}}(\mathrm{exp.}) = (0.033 \pm 0.01)\mu_B$. The calculated Cu $L_{2,3}$-edge spectra reveal all the experimental fine structures. Their origin can be understood from a direct comparison with the density of the (unoccupied) states above the Fermi level, cf. Fig. 6. The band structure calculations show that the first peak at the Cu L_3-edge stems from a hybridization of the Cu spin-down d-states (minority states) with the Mn spin-down d-states (minority states), see Fig. 6 left. Because of this hybridization, the first peak is also responsible for the dichroic signal detected at the Cu L_3-edge. The second peak located at a photon energy slightly below 940 eV originates from a hybridization of the Cu s- and d-states with the ones from Al. Consequently, hardly any XMCD signal is seen that correlates with this second feature. Since the theoretical intensities of the first and second peak at the Cu L_3-edge clearly deviate from the experimental result, we also studied the effect of atomic disorder on the induced moments and the corresponding XAS and XMCD spectra. It turns out that the introduction of disorder leads to a smearing of the two peaks at the Cu L_3-edge. However, the obviously smaller intensity of the first peak compared to the second peak seen in the experimental data cannot be reproduced by the calculation. The introduction of disorder leads to a small decrease of the induced spin moment, however, as can be seen in Table 1, the induced moment in Cu is actually relatively insensitive to disorder.

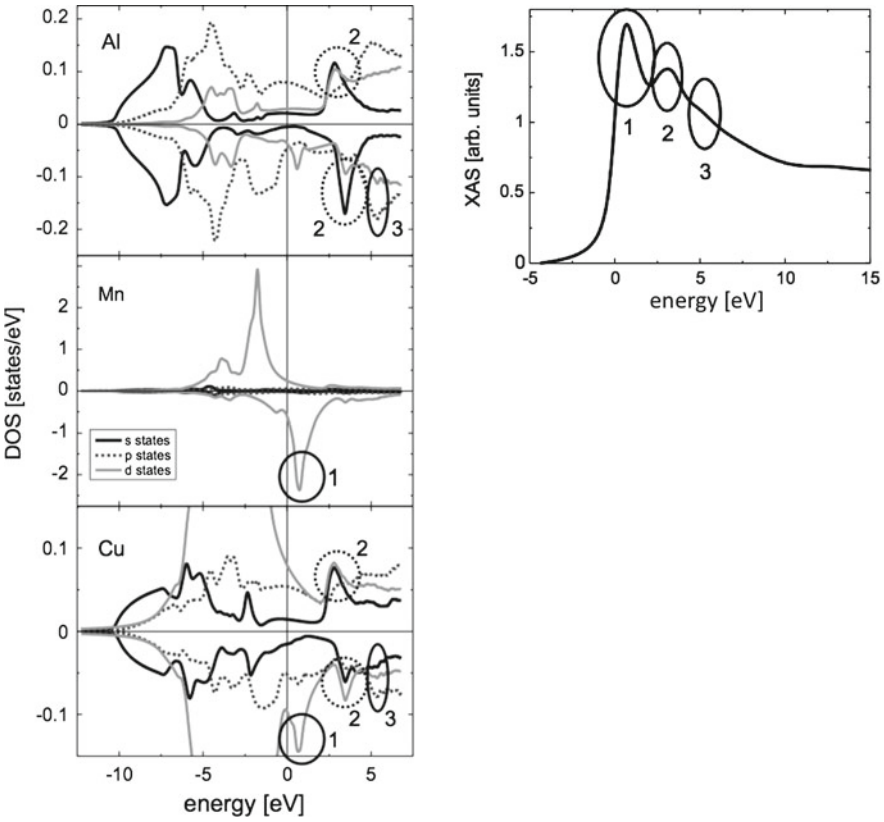

Fig. 6 Enlargement of the Cu L_3-edge calculated for perfectly ordered Cu_2MnAl (*right side*) and the corresponding DOS of Al (*top left*), Mn (*middle*) and Cu (*bottom*). For details see text (data taken from [50])

We have seen in this chapter that the magnetism of the Cu_2MnAl Heusler compound is determined by only one element, namely Mn, whereas a small induced moment can be identified for the element Cu. The magnetic properties crucially depend on the structural ordering since the magnetization of the samples evolves when the samples are transformed from A2 order to $L2_1$ order by annealing.

We now want to turn to the binary system of Fe_3Si which can be viewed as a quasi-Heusler system that can be considered as a prototype for a possible spin injector material for future spintronic devices. According to Fig. 2b the Fe_3Si system can be taken as the starting point to discuss more complex ternary Heusler systems, as e.g. Fe_2CoSi and Co_2FeSi which will be presented in Sect. 3.1. In the following chapter we will see in which way the ordering at the interface determines the magnetic properties of the system Fe_3Si which is crucial for testing the applicability of Heusler films for spintronic devices. Furthermore, a tiny induced moment can also

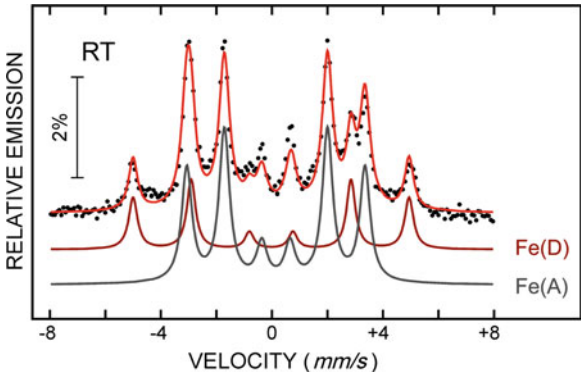

Fig. 7 CEMS of bulklike $Fe_3Si(001)$ film (57 monolayers (ML)) on MgO(001) described by two sextets corresponding to the inequivalent Fe sites Fe(A) and Fe(D)

be identified in Si that serves as a test case for the description of the hybridization effects in this system by means of DFT methods.

2.2 The Binary Prototype: Fe_3Si

The binary system Fe_3Si is of interest for (room temperature) spintronic applications, since it exhibits a relatively high Curie temperature of 840 K [54] and experimentally a spin polarization of 45 % is reported [55]. In layered systems the magnetic moment and the spin polarization may be smaller compared to the bulk values. The interplay of the ordering at the interface and the magnetic properties will be addressed below.

At first, we will describe the ideally ordered structure: the Fe_3Si system can also be discussed as Fe_2FeSi. As can be seen in Fig. 2a, in the perfectly ordered $D0_3$ structure two equivalent Fe atoms are located at the A and the B sites, respectively, which are surrounded by 4 Si atoms (located at the C sites) and 4 Fe atoms. Since the Fe atoms at the A and B sites are equivalent, we will refer to them as Fe(A). The Fe atoms located at the D sites (Fe(D)) are surrounded by 8 Fe atoms only. This different local structure results in different magnetic moments for the Fe(A) and Fe(D) atoms. Because of the hybridization of the Fe(A) d-states with the Si states, a smaller total magnetic moment of $\mu_{\mathrm{tot}}(\mathrm{Fe(A)}) = 1.42\mu_B$ is determined by our SPR-KKR calculations [56] whereas a total moment of $\mu_{\mathrm{tot}}(\mathrm{Fe(D)}) = 2.72\mu_B$ is found for the Fe(D) sites. Since these two moments directly lead to different hyperfine fields, Mössbauer spectroscopy can be used to identify these inequivalent Fe sites.

The Fe_3Si films are prepared by molecular beam epitaxy under UHV conditions utilizing Fe and Si coevaporation on the substrates at 520 K. We found that well ordered Fe_3Si films can be grown on a MgO(001) substrate. This can be demonstrated by analyzing the conversion electron Mössbauer spectrum (CEMS) of a 57 monolayer

(ML) Fe_3Si film on MgO(001) which is presented in Fig. 7. This spectrum can be described quite well by the sum of two sextets. The larger moment of the Fe(D) atoms leads to a hyperfine field of B_{hf}(Fe(D))$\approx$ 30 T whereas the smaller moment of the Fe(A) corresponds to B_{hf}(Fe(A)) $\approx$ 20 T. Consequently, the energy splitting seen in the CEMS spectra (Fig. 7) is clearly larger for the Fe(D) sites compared to the Fe(A) sites, as can be seen easily for the outer lines of the sextets. However, this facile identification of the in-equivalent Fe sites is only possible if the structure is well ordered. In the case of larger disorder the Fe atoms can have 0-8 Si neighbours leading to serious broadening of the Mössbauer spectrum.

So far, we only discussed Fe_3Si films grown on the insulator MgO(001) where the lattice mismatch is 5.2 % when the Fe_3Si grows rotated by 45°. However, for possible spintronic applications the Fe_3Si films need to be grown on semiconductors as e.g. GaAs in order to serve as spin injectors. Since the lattice mismatch of Fe_3Si on GaAs(001) is only 0.1% this systems appears to be quite promising for this kind of applications. We studied the magnetic properties of Fe_3Si films grown on two GaAs(001) surfaces, namely the Ga-terminated GaAs(001)-(4×6) and the As-terminated GaAs(001)-(2×2) surfaces. The growth of the films was studied by reflection high-energy electron diffraction (RHEED) measurements. In contrast to the MgO(001) surface, where we find epitaxial growth from the very beginning of the film growth, the RHEED pattern vanishes for the first few Fe_3Si monolayers (ML) [6]. The Fe_3Si reflections start to reappear around 6 ML for faster growth rates [6], whereas the pattern is immediately detected when lower deposition rates (0.01–0.02 Å/s) are used [57]. The Mössbauer spectra of 57 ML Fe_3Si films on the different substrates are shown in Fig. 8. Even without a detailed fitting analysis of the spectra it is obvious that the ordering of the Fe_3Si film on MgO is more perfect compared to the two GaAs substrates. The spectrum for the MgO substrate is very similar to the one discussed in Fig. 7 which could be modeled by two sextets. In contrast, the two spectra for the GaAs substrate shown in Fig. 8 are very broad. We interpret this by a larger disorder on the GaAs substrates as an indication for interdiffusion at the Fe_3Si/GaAs(001) interface. This is supported by our Mössbauer studies utilizing ^{57}Fe-enriched Fe_3Si tracer layers grown directly at the crucial interfaces as presented in Ref. [57]. The spectra shown in Fig. 8 for the GaAs substrates were fitted with two subspectra (for details see [6]): The blue subsectrum (1) is determined following a fitting routine described by Arita et al. [58]. This model starts from a perfectly ordered $D0_3$ structure and then the atoms are randomly replaced. From this procedure long range ordering parameters can be determined [6]. The green subspectrum (2) is calculated from a hyperfine field distribution that we assign to the interdiffused interface. The question is in which way this interdiffusion affects the magnetic moments of this system. The determination of the magnetic moments by Mössbauer spectroscopy is problematic, as it can be seen by comparing the ratio of the hyperfine fields for the two inequivalent Fe sites B_{hf}(Fe(D))/B_{hf}(Fe(A))$\approx$ 30 T/20 T = 3/2 to the calculated bulk-like moments for the two sites μ_{tot}(Fe(D))/μ_{tot}(Fe(A)) = $2.72\mu_B/1.42\mu_B \approx 2/1$. This deviation indicates that the hyperfine fields cannot be scaled linearly to determine the magnetic moments. Therefore, we made use of the XMCD technique to analyze

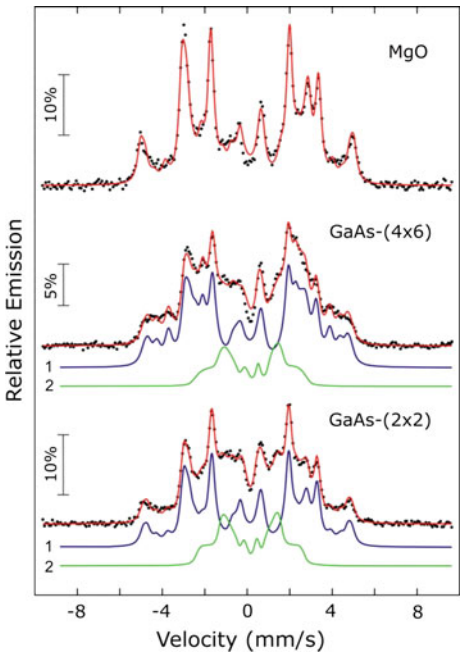

Fig. 8 Measured CEMS (*solid circles*) of 57 ML Fe_3Si on different substrates at RT together with *fitting curves* (*lines*) as described in the text (data taken from Ref. [6])

the Fe magnetic moments. As we will show below, we can even identify induced magnetic moments in Si with this highly sensitive technique.

The experimental XAS and XMCD results for 57 ML Fe_3Si films on the two substrates MgO(001) and GaAs(001)-(4×6) are shown in Fig. 9. For comparison the spectra of a bulk-like Fe film are also presented as a reference. At first, it should be noted that the two inequivalent Fe sites cannot be disentangled by the XMCD spectroscopy. The reason is that for this metallic system the $L_{2,3}$-edge features are very broad. Hence, from the sum rule analysis only the averaged moment per Fe atom can be calculated. From this analysis the following averaged Fe total magnetic moments for the Fe_3Si films are determined: μ_{tot}^{Fe}(on MgO)=$(1.60\pm0.15)\mu_B$, μ_{tot}^{Fe}(on GaAs-(4×6))=$(1.50\pm0.15)\mu_B$ and μ_{tot}^{Fe}(on GaAs-(2×2))=$(1.30\pm01.5)\mu_B$ (spectra not shown). Hence, there is a trend of a slightly reduced magnetic moment for the GaAs substrates. We have seen before, that the Mössbauer spectra indicate a worse ordering for these GaAs substrates which we have taken as an effect of interdiffusion at the interface. Combining these results, disorder leads to a small decrease of the averaged moment. This trend is confirmed by our DFT calculations which show that placing Ga or As impurities in Fe_3Si leads to a reduction of the averaged Fe moment (for details see Ref. [6]).

Although the two inequivalent Fe sites cannot be disentangled in the experimental XMCD spectra, some specific fine structures can be identified in the XAS and XMCD

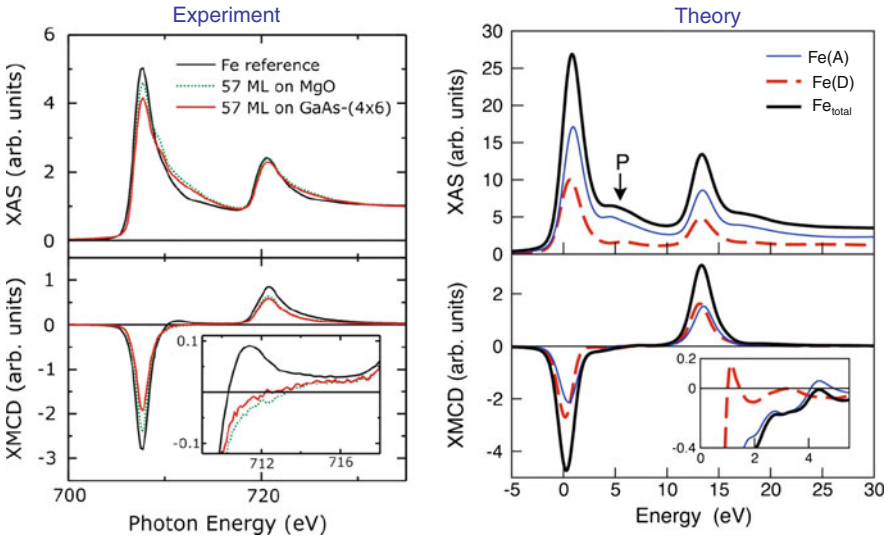

Fig. 9 *Left* normalized XAS (*top*) and XMCD (*bottom*) spectra measured at the Fe $L_{2,3}$-edges of 57 ML Fe_3Si on MgO(001) and GaAs(001)-(4×6) compared to the spectra of a bulk-like Fe sample as a reference (data taken from Ref. [6]). The spectra were measured at RT. *Right* calculated XAS (*top*) and XMCD (*bottom*) spectra of the different Fe-sites (Fe(A) and Fe(D)) in bulk Fe_3Si ($E_F = 0$). The insets present an enhancement of the energy region between the L_3 and L_2 peak. In order to make these tiny features visible we disclaim smoothing of the theoretical data

spectra: in the experimental XAS spectra of the Fe_3Si films a shoulder can be seen at the L_3-edge which is not detectable in the Fe reference spectra. Furthermore, in the inset of Fig. 9 the enlarged XMCD spectra in the energy region between the L_3 and L_2-edge are presented. Also here, clear differences can be seen between the Fe reference and the Fe_3Si films. To understand the origin of these features, we used the possibility to calculate the XMCD spectra with the SPR-KKR code as presented on the right side of Fig. 9. The theoretical calculation has the advantage, that the individual contributions of the Fe atoms at the A and the D sites can be determined. The shoulder labeled P stems from the Fe(A) atoms which indicates that this feature might be due to a hybridization of Fe states with Si states. Furthermore, the "overshoot" (positive contribution in the XMCD signal seen in the inset) originates from the Fe(D) atoms with the larger magnetic moment. This feature is quite similar to the one of the Fe reference. This is reasonable, since the Fe(D) atom has 8 Fe nearest neighbors and no Si nearest neighbors. However, the calculations reveal that the region between the $L_{2,3}$-edges is dominated by the Fe(A) atom contributions, since no "overshoot" is seen in the total contribution (black line in Fig. 9 (right)). This means that hybridization effects with the Si neighbor are crucial in this energy regime.

For a closer look at these features we analyzed the calculated density of states (DOS) which is presented in the vicinity of the Fermi level in Fig. 10. Pronounced

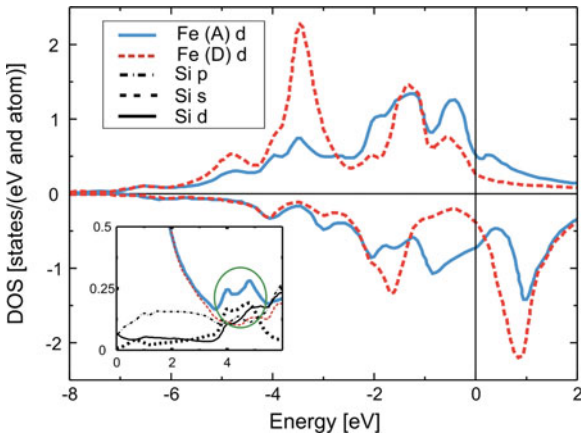

Fig. 10 Calculated spin-resolved density of states of Fe_3Si (data taken from Ref. [6]). The inset shows the total (not spin-resolved) DOS of the region above the Fermi energy ($E_F = 0$) being relevant for the calculation of XMCD spectra

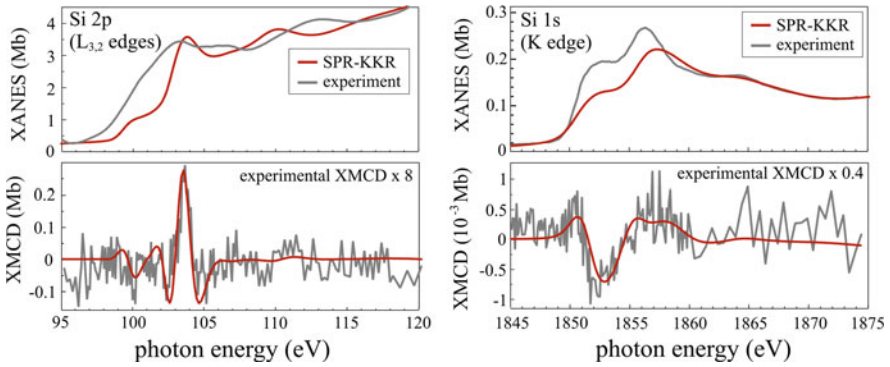

Fig. 11 Experimentally obtained and calculated XANES and XMCD at the Si $L_{3,2}$ absorption edges and the Si K-edge, respectively (data taken from Ref. [56]). The experimental data were normalized to fit the calculated XANES intensity in the pre- and post-edge region. To fit the intensity of the calculated dichroism, experimental XMCD data have been scaled by an additional factor that is used for an estimation of the magnetic moments of Si in the Fe_3Si sample

differences can be seen between the DOS of the Fe d-states at the A and the D sites. The Fe(D) d DOS is very similar to the DOS of bulk Fe. However, the hybridization of the Fe(A) atoms with Si strongly alters the DOS, as can be seen for the light blue solid line in Fig. 10. To understand the origin of the specific features in the experimental XAS and XMCD spectra, the empty states have to be inspected. The feature P arises from the hybridization of the Fe(A) d-states with the Si s-states as it can be seen in the inset of Fig. 10. Hence, the shoulder at the L_3-edge in the

XAS data is a characteristic feature of the (quasi) Heusler system. Furthermore, the features in the XMCD signal between the $L_{2,3}$-edges are also dominated by this Fe-Si hybridization.

A subtle indicator for this hybridization is the induced magnetic moment in Si. Indeed, an induced magnetic moment in Si can be detected experimentally, as can be seen in Fig. 11. Here we use again the element specificity and the high sensitivity of the XMCD technique. The experimental dichroic signal is clearly above the noise level, as can be seen both at the Si $L_{2,3}$ as well as at the Si K-edge (Fig. 11). Interestingly, various fine structures can be identified in the Si XAS and XMCD spectra. For a more detailed analysis we compare the experimental results to SPR-KKR calculations which are also presented in Fig. 11. It is striking that the agreement of the line shape, especially for the XMCD, is quite reasonable. For the case of the Si $L_{2,3}$-edge XAS spectra the agreement is less good. A reason could be that only initial state effects are considered in the calculation. However, the splitting of the L_3-and the L_2-edge is very small and therefore a strong overlap of the contributions can be expected. The SPR-KKR calculations predict an induced Si spin moment of $\mu_S^{Si}(\text{theo.}) = -0.121\mu_B$ and an orbital moment of $\mu_L^{Si}(\text{theo.}) = -0.0019\mu_B$. The negative signs indicate that these moments are aligned antiparallel to the Fe moments. This means that the Si $L_{2,3}$-edge XMCD is dominated by the spin moment. Therefore, the experimental spin moment can be determined by scaling the experimental $L_{2,3}$-edge XMCD results to the theory. As is shown in Fig. 11 the experimental data have to be scaled up by a factor eight. Consequently the experimental moment is $\mu_S^{\text{Si}}(\text{exp.}) = -0.121/8\mu_B = -0.015\mu_B$. Since transitions from the $1s$-state to final p-states are investigated at the K-edge, the initial state does not exhibit a spin-orbit interaction. Hence, the K-edge XMCD originates from the orbital moment only. This provides the possibility to determine the experimental orbital moment by investigating the K-edge XMCD. As the experimental K-edge XMCD spectrum has to be scaled down by a factor of 0.4 to match the theoretical results (Fig. 11) the experimental orbital moment can be calculated to $\mu_L^{\text{Si}}(\text{exp.}) = -0.0047\mu_B$. Obviously, detailed fine structures can be seen in the XAS and XMCD. For a closer inspection of these features we show the spectra at the Si $L_{2,3}$, the Si K and the Fe $L_{2,3}$-edge, as calculated by the SPR-KKR code, in Fig. 12. In this figure the spectra are arranged according to the photon energy. Two prominent structures can be identified at the Si absorption edges which are labeled a and b. The indices refer to the respective absorption edges, i.e. K or L. As we have discussed above, the Si $L_{2,3}$ egde signal mostly stems from the induced spin moment. At the Si $L_{2,3}$-edges predominately $2p \rightarrow 2d$ transitions contribute to the signal. Therefore, the empty Si d-states have to be analyzed to relate the feature a_L and b_L in Fig. 12 to the calculated spin resolved density of states (DOS). The spin and orbital resolved DOS as calculated from the SPR-KKR code is presented in Fig. 13. The strongest XMCD signal at the Si $L_{2,3}$-edges can be assigned to feature b_L. As we have seen before, the induced moment in Si originates from the hybridization of the Fe(A) atoms with the Si atoms. The Si s-states exhibit a clear spin polarization in the region marked 'b' in Fig. 13. Via an intra-atomic hybridization in Si, this polarization is also reflected in a spin polarization of Si d-states (grey line in Fig. 13) which is responsible for feature b_L in

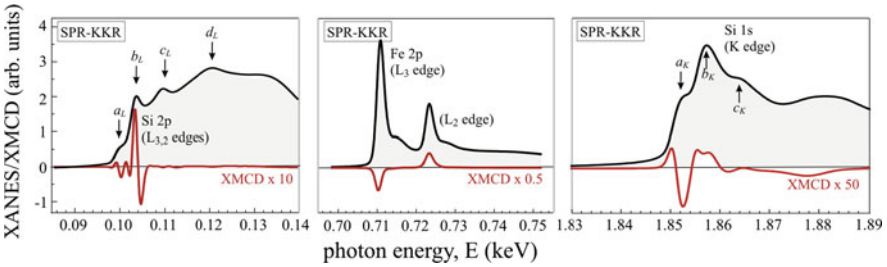

Fig. 12 Calculated XANES and XMCD spectra of Fe_3Si at the Si $L_{3,2}-$, Fe $L_{3,2}-$ and Si K-edges by means of SPR-KKR (*upper panel*) (data taken from Ref. [56])

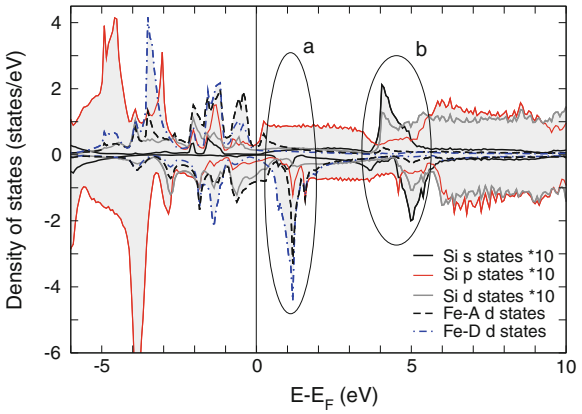

Fig. 13 The spin and orbital resolved density of states of Fe_3Si. Positive and negative sides are for the spin up and spin-down parts, respectively. The amplitude for Si s-, p-, and d-states are rescaled by a factor of 10

Fig. 12. The tiny dichroic structure a_L originates from the small spin polarization of the d-states about 1 eV above the Fermi level as can be seen in the DOS in Fig. 13. Interestingly, the feature a_K is much more pronounced in the K-edge XMCD in Fig. 12. The reason is that $1s \rightarrow 2p$ transitions contribute to this X-ray absorption signal. The empty p-states (red solid line) show a clear spin polarization in the area marked 'a' in Fig. 13 which is responsible for this feature. The smaller contribution b_K can be linked to the smaller spin polarization of the Si p-states in the regime of 4–5 eV above the Fermi level.

The discussion above demonstrates that element-specific spectroscopies can provide a detailed insight into the magnetism and the electronic structure of this binary compound Fe_3Si. Since the inequivalent Fe sites lead to different magnetic properties of Fe at the A and Fe at the D sites, this system can serve as a starting point for the discussion of more complex ternary systems. Furthermore, the importance of interface effects was illustrated by comparing the effect of different substrates

(MgO and GaAs) on the magnetic properties. Various similarities will be seen when discussing more complex Heusler systems in the following sections.

3 Magnetism and Interface Properties in Transition Metal-Based Bulk Heusler Alloys and Heusler Thin Films

3.1 Co-Fe-Si: Bulk and Thin Films

The discussion of magnetic properties of hybrid structures consisting of ferromagnetic (FM) films—Heusler alloys in our case—and insulating or semiconducting surfaces such as MgO and GaAs can be viewed from different perspectives: direct interface effects such as interface states and matching of the band structures of the two materials [7, 59] and indirect influence of the interface, e.g., changes due to diffusion, lattice deformation, and strain which effects also layers far away from the interface. Since thicker films (>15 nm) often behave bulk-like in the sense that the measured XAS and XMCD spectra agree well with theoretical findings for the bulk Heusler system [60], the influence of the direct Heusler/substrate interface may be of secondary importance. Therefore, in literature the magnetic properties of the actual hybrid systems are modeled using bulk Heusler compounds by investigating the influence of lattice strain, volume, and disorder on the magnetic properties [6, 61, 62]. However, local features of the contact cannot be understood from bulk investigations and also for very thin Heusler films this assumption may be too simplifying and multilayers have to be used for a proper theoretical description.

3.1.1 Bulk Properties

Here, the $Fe_{3-x}Co_xSi$ system is discussed as an example of Heusler systems with high Curie temperature T_C and large spin polarization P. The focus is on the influence of concentration fluctuations on the magnetic properties, because half-metallicity is only achieved for particular (stoichiometric) compounds such as Co_2FeSi [63]. Deviations from the ideal stoichiometry destroy the half-metallic character and therefore, lower the TMR ratio which can be achieved, see Sect. 1.

In case of $Fe_{3-x}Co_xSi$ an additional problem arises from the fact that the system undergoes a structural phase transition. The half metallic FM Co_2FeSi crystallizes in $L2_1$ structure, whereas the inverse Heusler structure (see Fig. 2) is realized for Fe_2CoSi. The calculated heat of formation ΔH reveals that the transition takes place at $x = 1.5$, whereby the other structure would decompose into Fe_3Si and Co_3Si, see Fig. 14. The heat of formation is here given by

$$\Delta H^s = E^s_{\text{alloy}} - \frac{1}{3}\left((3-x)E_{Fe_3Si} + xE_{Co_3Si}\right) \tag{2}$$

with s indicating $L2_1$ or inverse order. Only $x = 1.75$ provides a metastable inverse Heusler structure besides the $L2_1$ ordered system, i.e., $\Delta H < 0$ for both structures. The change of the local neighborhood, which takes place from $L2_1$ to inverse order, has a huge impact on the magnetic properties, for example on T_C or P. Although, the Curie temperature of Co_2FeSi and Fe_2CoSi differ only by about 80 K, i.e. $T_C = 1,100$ K ($x = 1$) and $T_C = 1,023$ K ($x = 2$) [62, 64], deviations from stoichiometry can cause drastic changes of T_C. This is shown in Fig. 16, where T_C is shown together with the magnetization curves resulting from Monte Carlo simulations. The finite temperature behavior is obtained from a combined calculation of ab initio exchange parameters J_{ij} and Monte Carlo simulation by mapping the actual system onto a classical Heisenberg model

$$\mathscr{H} = -\frac{1}{2}\sum_{i \neq j} J_{ij}\, \mathbf{e}_i \mathbf{e}_j \tag{3}$$

with $\mathbf{e}_i$ representing the orientation of the local magnetic moment on site i. Lichtenstein's formula, as implemented in the SPR-KKR code [65–67], has been employed to determine the ab initio exchange parameters J_{ij},

$$J_{ij} = \frac{1}{4\pi}\int^{E_F} dE \Im \mathrm{Tr}_L(\Delta_i T_\sigma^{ij} \Delta_j T_\sigma^{ji}) \tag{4}$$

in which σ corresponds to the spin index and Δ_i is the difference of the inverse single-site scattering matrices for spin-up and spin-down. The scattering path operator is denoted by T and the trace runs over the orbital index L.

The largest calculated moment ($m = 5.42\,\mu_B$) and the highest T_C (898 K) are obtained for Co_2FeSi, however, additional Co by replacing Fe, the Curie temperature is drastically reduced by about 240 K, see Fig. 16. As expected in case of inverse ordered systems, the T_C values are smaller, but in contrast to the $L2_1$ ordered compounds the composition dependence seems to be smaller. The absolute values of T_C given in Table 2 tend to be too small compared to experiment, because the calculations have been performed within the generalized gradient approximation (GGA) for the exchange correlation functional. Taking into account the localized character of the d electrons by employing the GGA+U method [69, 70] the absolute values could be improved [71]. However, the size of U may depend on the Co concentration x and the structure, which makes it difficult to determine a proper U for arbitrary compositions. Apart from the underestimation of the absolute values, the GGA description is sufficient to illustrate chemical trends. For this kind of Heusler alloys the magnetization and Curie temperature show a significant composition dependence, however, T_C stays well above room temperature. Though the magnetic properties vary with composition in the cubic phase the changes become even more drastic in presence of lattice distortions.

When Co-Fe-Si or similar Heusler alloys are grown on a substrate such as MgO(001), the relatively large lattice mismatch (∼5 %) causes a strained growth

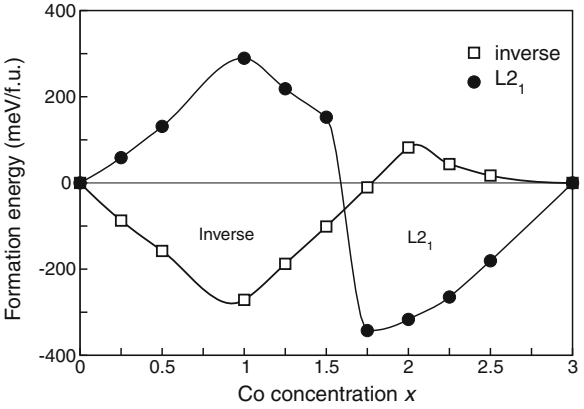

Fig. 14 Heat of formation of $Fe_{3-x}Co_xSi$. Negative energies indicate the relative stability of the alloy against decomposition into the two binary alloys Fe_3Si and Co_3Si. The inverse Heusler structure is preferred for Fe rich systems up to $x < 1.5$. Systems with larger Co concentration have $L2_1$ structure. Except in a small region close to $x = 1.75$ only one structure is stable in each case. Data taken from Ref. [68]

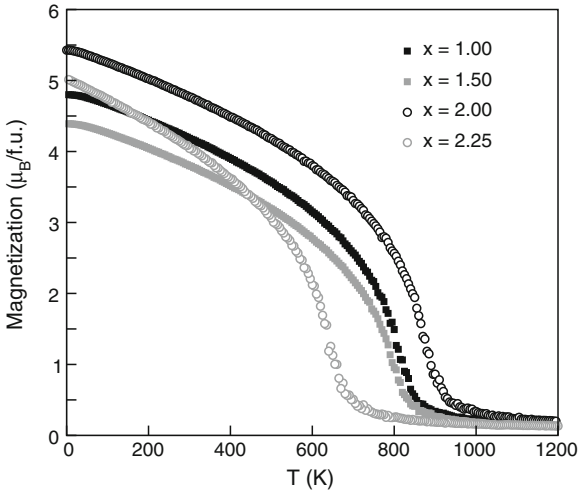

Fig. 15 Density of states (DOS) of bulk Fe_2CoSi for the cubic inverse Heusler phase and a tetragonal distortion of $c/a = 1.2$. The data have been obtained from VASP calculations. Both calculations have been performed using the calculated ground state volume ($V = 5.61^3$ a.u.^{3})

of the ferromagnet which can drastically influence the magnetic properties. Furthermore, it has been pointed out by Hongzhi et al. that the spin polarization of inverse ordered Heusler alloys such as Fe_2CoSi or Fe_2NiSi is very sensitive to volume changes due to the lattice mismatch [62]. Their calculations show that slight volume changes (lattice constant varies from 5 to 7 %), which are reasonable if grown on

MgO(001) can lead to sign changes in the spin polarization. This is definitely undesirable with regard to spintronics [62]. In their work the authors have investigated only stoichiometric compositions and their polarization dependence on the volume. Instead of changing the lattice constant, it seems more appropriate to study the influence of the tetragonal distortion which occurs if the Heusler film is grown on an insulator. This can be modeled by bulk calculations keeping the volume constant and changing the ratio between the in-plane and out-of-plane lattice constant c/a from 0.8 to 1.5, see Fig. 17. Except for $Co_2Fe_{0.5}Si_{1.5}$ the cubic structure was found to be the ground state. However, with increasing Co concentration the systems develop a structural instability and a second metastable state occurs close to $c/a = 1.2$. For Co_2FeSi ($x = 2$) the energy difference amounts only to 25 meV per formula unit (f.u.). In case that Fe is partially replaced by Si, i.e., $Co_2Fe_{0.5}Si_{1.5}$, the tetragonal phase becomes the ground state, whereas in the opposite case the cubic phase is stabilized (triangles in Fig. 17). No metastable state was found for the inverse ordered systems. As an example, the result for Fe_2CoSi is shown in Fig. 17.

An impression how or whether strain influences the magnetic properties can be gained from the calculation of the spin polarization depending on the homogenous lattice strain c/a. Results for the cubic structure and $c/a = 1.2$ are given in Fig. 15. The polarization has been obtained from the density of states at the Fermi level for majority $N_\uparrow$ and minority $N_\downarrow$ spins

$$P = \frac{N_\uparrow(E_F) - N\downarrow(E_F)}{N_\uparrow(E_F) + N\downarrow(E_F)}. \tag{5}$$

The polarization strongly depends on structure and c/a. As expected the $L2_1$ ordered systems close to $x = 2$ show a relatively large P in the cubic phase, however, moving away from $c/a = 1.0$ leads to a drastic decrease of the polarization, i.e., about 50 % reduction. There is only one exception for $x = 1.25$ in which already the cubic phase has a very tiny polarization. That means small concentration fluctuations in the sample can already reduce the effective polarization. In case of inverse ordered systems the situation seems to be more complex, because tetragonal distortions do not only influence the size of P but may also change its sign. For example Fe_2CoSi shows a large spin polarization in both cases but with opposite sign, because the strain leads to a shift of the density of states of the d levels, see Fig. 15 which confirms the findings in Ref. [62]. This effect seems to be located to the region of $x = 1.0$. All other concentrations show occasionally strong fluctuations of the size of the polarization, but no sign change. The polarization of the quasi-Heusler alloy Fe_3Si is not much affected by the lattice strain and together with the high T_C it appears to be a suitable system for magnetoelectronics.

Summarizing this section, lattice distortions can have a huge impact on the polarization, but only in the vicinity of Fe_2CoSi a sign change of P, i.e., minority and majority electrons change their role, could be observed. The reason for the often reported too small TMR values can be twofold: reduction of the polarization due to strain and due to small deviations from stoichiometry in the ferromagnet.

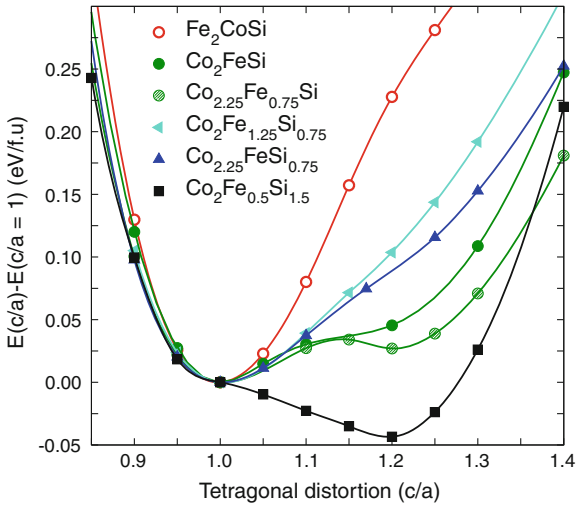

Fig. 16 Magnetization curves of $Fe_{3-x}Co_xSi$ obtained from Monte Carlo simulations of the Heisenberg model. Exchange parameters were derived from Lichtenstein's formula (see text). Data partially published in [75]

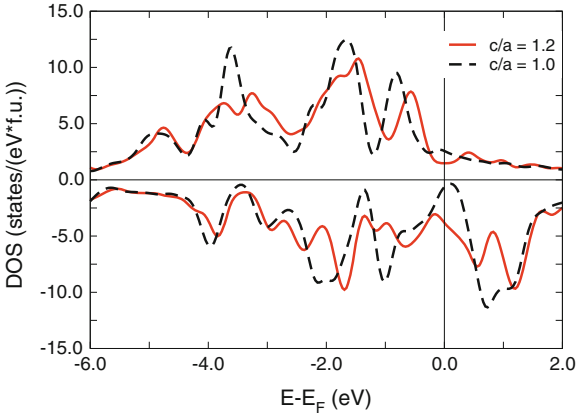

Fig. 17 Tetragonal distortion c/a of $Fe_{3-x}Co_xSi$ alloys. Calculations have been performed in a 16 atom supercell using VASP [74]. *Triangles* mark systems in which Si has been partially replaced by Fe or Co. The *black squares* denote a system with strong Si excess which leads to a tetragonal distorted ground state. The inverse ordered Fe_2CoSi system is marked by *open circles*. The volume is kept constant during the c/a variation using the corresponding value for $c/a = 1.0$

3.1.2 Heterostructures: Influence of the Substrate

Bulk calculations as discussed in the previous section include lattice distortions and diffusion in a kind of averaging manner. However, they do not reveal detailed information of atomic arrangements at the interface and neglect the changes which

arise from the variation of the coordination at the interface. In this section the interplay between ferromagnet and insulator in heterostructures will be discussed for particular examples, starting with the quasi-Heusler system Fe_3Si, which crystallizes in $D0_3$ structure, see Fig. 2.

Fe_3Si/GaAs(001) and Fe_3Si/GaAs(110)

Due to the perfect matching of the lattice constants of GaAs and Fe_3Si (and other Fe-Co-Si Heusler alloys as well) it seemed to be a promising combination for heterostructures and epitaxial film growth has been reported for Fe_3Si/GaAs(001) [77]. However, GaAs(001) is known to show complex surface reconstructions [78, 79] which may hinder epitaxial growth depending on the preparation technique, see also Sect. 2.2. This can cause diffusion or alloy formation which leads in each case to a degradation of the magnetic properties in the vicinity of the interface or, in the worst case, to so-called magnetic dead layers [80]. An attempt to figure out the diffusion processes, which are expected for the highly reactive GaAs(001) surface, has been undertaken by Mirbt et al. They investigated the interface structure for a model system in which reconstruction is neglected and the adatoms are Fe [81]. Obviously, Fe placed on a GaAs(001) surface occupies most likely the substitutional place of Ga such that massive segregation effects must be expected. However, assuming that segregation could be suppressed by using Fe_3Si instead of bcc Fe, multilayers consisting of 7 ML Fe_3Si and 9 ML GaAs(001) (neglecting surface reconstruction) have been studied as a model system. Despite the simplifications, this calculation gives already an impression of the difficulties arising from the complex GaAs(001) surface. The results shown in Fig. 18 were obtained from DFT supercell calculations employing VASP [74] and the GGA. A detailed description of the method can be found in Ref. [68]. The ferromagnet and insulator interfaces are terminated by Fe and As, respectively. As has been chosen, because in experiment additional evaporation of As on the GaAs(001) wafer seem to abet epitaxial growth [83]. The resulting spin polarization at the Fe_3Si/GaAs(001) interface is of the same size as for bulk Fe_3Si ($\sim -40\,\%$). But with increasing distance from the interface the polarization decreases, especially in the Fe-Si layers. For the 7 ML system shown in Fig. 18 the polarization of the center layer is only about 15 %. In view of TMR elements it is also essential that energy gap of the insulating layer remains finite. Unfortunately, at the interface the energy gap is closed and the DOS slowly decreases with the distance from the interface. At the interface the polarization amounts to $P = 28\,\%$, which indeed decreases with the distance from the ferromagnet, however, after 5 ML the polarization is still finite and the band gap is closed. Even if this may partially result from the underestimation of the band gap (theory: 0.6 eV, experiment: 1.5 eV) and the artificially flat interface, it shows that the GaAs(001) surface is not the optimal choice for tunneling devices. This may also explain that despite the larger spin polarization of the bulk system only a spin injection of 10 % was observed [77].

In view of the small TMR effect and the specific problems due to the complex surface, GaAs(110) has been discussed as an alternative [84, 85]. The advantage to

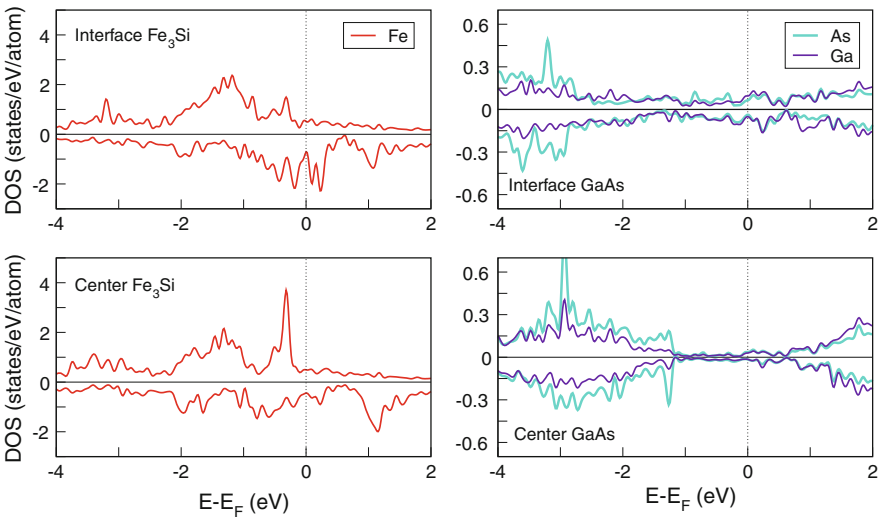

Fig. 18 Layer resolved density of states (DOS) of a (7ML)Fe_3Si/(9ML)GaAs(001) multilayer assuming Fe termination of the ferromagnet. *Top row* shows DOS of the interface layers. The polarization of Fe is similar to bulk Fe_3Si. A strong induced polarization is also observed on the GaAs side. With increasing distance from the interface, the polarization of Fe is reduced. It is about 15 % in the center of the ferromagnet and the band gap of GaAs is still closed after 5 ML (*bottom row*)

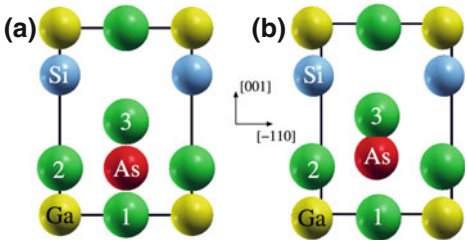

Fig. 19 Schematic view of the Fe_3Si/GaAs(110) interface without atomic relaxation (**a**) and including relaxation (**b**). The relaxation mainly effects the As atom. Fe atoms are labeled by numbers. Published in Ref. [82]

use this surface is that it does not form complex surface reconstruction, but shows only a small buckling which vanishes after 1 or 2 layers away from the surface when, for example, overgrown with Fe [85]. In order to investigate the interface structure in case of $(Fe_3Si)_n$ ($n = 1,2,3$) films on GaAs(110) (Fig. 19), total energy calculations have been performed using density functional theory (VASP), whereby the position of the Fe_3Si film is rigidly shifted on the substrate surface. The energy surfaces for different film thicknesses are shown in Fig. 20. For all n the minimum corresponds to the configuration shown in Fig. 19a with Fe and Si atoms sitting on the hollow positions of the GaAs(110) surface. Relaxation effects on this surface are small and mainly affect the As atoms, c.f. Fig. 19b. From theoretical investigations it turns out that the magnetic moments of the quasi-Heusler on GaAs(110) should be close to the calculated bulk values ($\bar{m} = 1.76\mu_B$ per Fe atom), c.f. bars in Fig. 21.

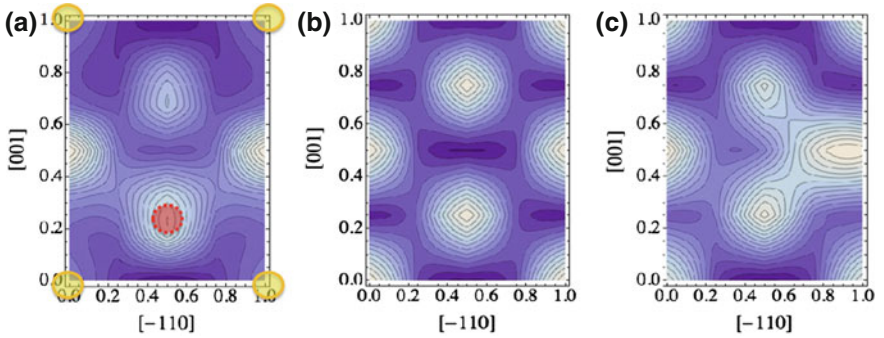

Fig. 20 Calculated energy surfaces of $(Fe_3Si)_n$/GaAs(110) for $n = 1$ (**a**), 2 (**b**), 3 (**c**). The *circles* mark the underlying GaAs(110) layer, c.f. Fig. 19 and the FM film is rigidly shifted on the surface such that the energy is given relative to the position of the Fe atom marked by "1" in Fig. 19. The energy increases with the brightness of the color, i.e., *dark colors* denote low energies. The distance of the contour lines is 0.4 eV. The minimum ($E = 0$ eV) appears when Fe "1" occupies the center of the [−110] axis. Data taken from [82]

However, experimental realization of Fe_3Si/GaAs(110) heterostructures seems to be difficult, because the thermal stability of the interface is low and the estimated magnetic moment lies in the region of $1.3\mu_B$ [86]. So what is the problem? From DFT calculations (T = 0 K) for thin Fe_3Si films on GaAs(110) (Figs. 19 and 20) the ideally ordered interface is found to be stable but configurations with Ga interdiffusion are only 30 meV/atom higher in energy which corresponds to approximately 350 K. Due to interdiffusion the magnetic moment is also reduced to $1.26\,\mu_B$ which agrees with the experimental observations. This suggests the conclusion that an ordered structure could only be achieved in case of an infinitesimal slow growth process. However, from calculations for $(Fe_3Si)_n$/GaAs(110) multilayers (periodic cell, no free surface) it turns out that even in case of ideal interfaces the system does not justifies the high expectations. The magnetic moments are indeed large, 1.8–2.0 μ_B per Fe atom in case of $n = 3$–7, but the spin polarization strongly varies from layer to layer within the ferromagnetic film (see Fig. 21) and the average polarization per layer (20 %) is small compared to the bulk value. Unfortunately, this effect does not vanish with increasing layer thickness. In case of $n = 7$ the polarization at the interface and in the center of the film is about $P = -30\,\%$, however, the layer next to the interfaces provides a small but positive polarization, cf. Fig. 21. Hence, GaAs(110) is suitable to only a limited extent.

$Fe_{3-x}Co_xSi$/MgO(001)

Besides amorphous oxides such as AlO_x [39], MgO(001) is quite frequently discussed as tunneling barrier for TMR junctions [88, 89]. MgO crystallizes in rocksalt structure with lattice constant $a = 4.21$ Å and has a direct band gap of $E_g \sim 8$ eV

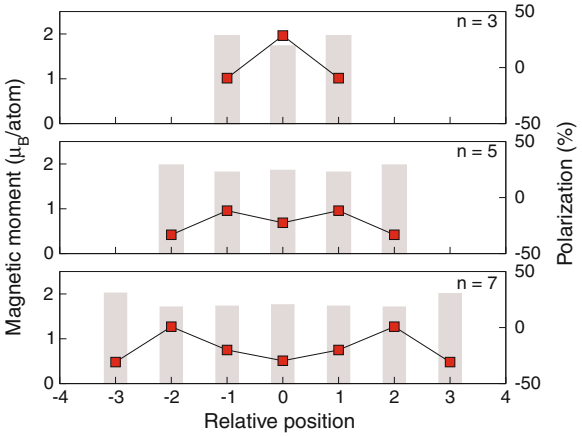

Fig. 21 Calculated magnetic moments (*bar*) and spin polarization (*symbols*) of $(Fe_3Si)_n$/GaAs(110) multilayers with $n = 3, 5, 7$. Data taken from Ref. [87]

Table 2 Calculated Curie temperatures T_C^{MC} for $Fe_{3-x}Co_xSi$ obtained from Monte Carlo calculations using ab initio calculated exchange parameters

x	T_C^{MC} (K)	T_C^{MF} (K)	$T_C^{exp.}$ (K)
0.00	838	1113	838 [72]
1.00	827	1036	1023 [62]
1.50	812	691	
2.00	898	1168	1100 [64]
2.25	657	857	

For comparison the mean field values T_C^{MF} are given. They have been obtained using the method of the largest eigenvalue [73]

[90, 91]. The mismatch of the lattice constants between MgO(001) and Fe-Co-Si (or similar) Heusler compounds is $\sim 5\,\%$ and leads to a 45° rotated growth pattern [92, 93]. In case of MgO(001) epitaxial growth has been reported for Heusler films [94]. In the as-prepared state the films usually have B2 structure, but after annealing they show L21 order; the degree of ordering essentially determines the quality of the magnetic properties [94] as much as stoichiometry [60]. In order to discuss the influence of structure ($L2_1$ or inverse) and stoichiometry on the magnetic properties, we focus here on F_3Si, Fe_2CoSi, and Co-rich $L2_1$ ordered $Fe_{3-x}Co_xSi$ compounds. The subsequent results have been obtained from calculations of periodic supercells consisting of 5 ML of Heusler compound on 5 ML MgO(001). A detailed description of the computational method can be found in Refs. [68, 60]. In Fig. 22 the layer resolved density of states is given for Fe_3Si/MgO(001), whereby both interfaces are terminated with Fe such that the actual amount of Fe in the sample is larger than in the stoichiometric bulk sample (4 Fe to 1 Si). In contrast to the observations at the (ideal) GaAs(001) interface (Fig. 18), the majority spin channel is almost filled and mostly minority states are present at the Fermi level. The spin polarization amounts

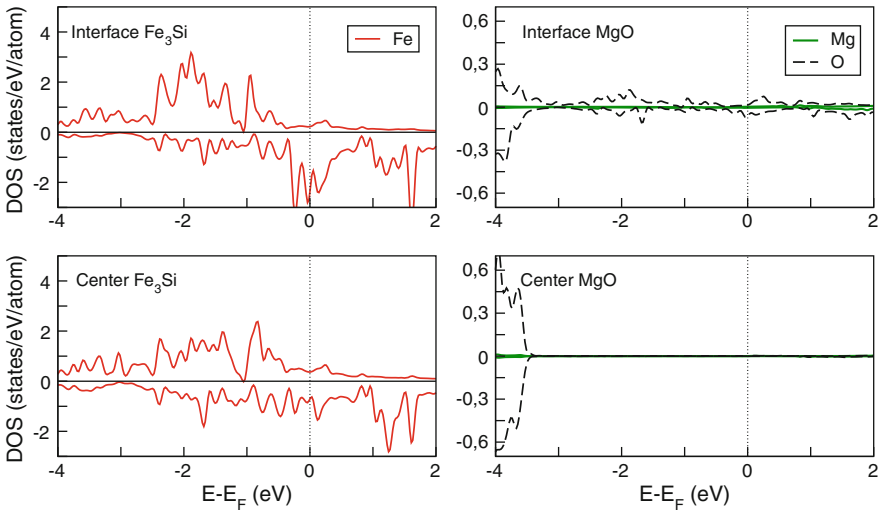

Fig. 22 Layer resolved density of states (DOS) of a (5 ML)Fe_3Si/(5 ML)MgO(001) multilayer. The interfaces are terminated with Fe

to $-85.7\,\%$ decreasing to the bulk value for Fe_3Si with increasing distance from the interface. Unfortunately, there are still oscillations in polarization and the local polarization of the Fe-Si layers amounts only to half of the bulk value, see Table 3. However, the total polarization of the film is about $-38\,\%$ which is considerably higher compared to the GaAs(110) case, cf. Fig. 21. Similar to the previously discussed GaAs(001), there are induced surface states in the interface layer of MgO(001), see Fig. 22. The polarization at the direct interface is about $-70\,\%$, but in contrast to GaAs(001) the energy gap (necessary for a tunneling barrier) opens again in the 3rd ML. Together with the larger spin polarization of the ferromagnetic layer, the use of the inert MgO(001) surface improves considerably the magnetic properties compared to GaAs. This corroborates the experimental findings from X-ray absorption measurements shown in Sect. 2.2.

From a theoretical point of view the drawback of the binary Fe_3Si system is related to the small spin polarization in the pure Fe-Si layers, c.f. Table 3. It has been shown that addition of Co cures this problem. In the present case, half of the Fe atoms in the pure Fe layers are replaced by Co which leads to an inverse ordered Heusler structure of composition $Fe_2Co_{1.2}Si_{0.8}$, see also Sect. 3.1.

Due to the additional Co, the average moment per Fe atom is mostly unchanged compared to the pure Fe_3Si film, namely $\bar{m}_{Fe} = 2.10\,\mu_B$. The average Co moment amounts to $\bar{m}_{Co} = 0.97\,\mu_B$. The values are close to moments obtained for Fe_2CoSi bulk ($\bar{m}_{Fe} = 2.02\,\mu_B$, $\bar{m}_{Co} = 1.00\,\mu_B$) and Ref. [62]. Although the magnetic moments do not change much, the overall magnetic properties improve through Co, especially the fluctuations of the spin polarization are removed, see Fig. 23. Obviously, the density of states for the interface and central layer are very similar

Table 3 Influence of the tetragonal distortion c/a on the spin polarization of $Fe_{3-x}Co_xSi$ Heusler alloys obtained from ab initio calculations using the GGA [68]

Structure	Composition	Polarization (%)		
		$c/a = 1.0$	$c/a = 1.2$	$c/a = 1.0$ (others)
$D0_3$	Fe_3Si	−37.6	−44.4	12.5[a]
	$Fe_{2.5}Co_{0.5}Si$	−20.3	−15.5	
Inverse	Fe_2CoSi	+70.0	−45.0	47.0[a]
	$Fe_{1.5}Co_{1.5}Si$	−16.0	−66.2	
	$Co_{1.75}Fe_{1.25}Si$	−7.0	−27.0	
$L2_1$	Co_2FeSi	−68.9	−29.4	100.0[b], −65.0[c]
	$Co_{2.25}Fe_{1.75}Si$	−50.8	−29.4	
	$Co_2Fe_{0.5}Si_{1.5}$	−78.9	−18.9	

[a]LDA, expt. lattice constant [62]
[b]LDA+U [71]
[c]GGA, calc. lattice constant [76]

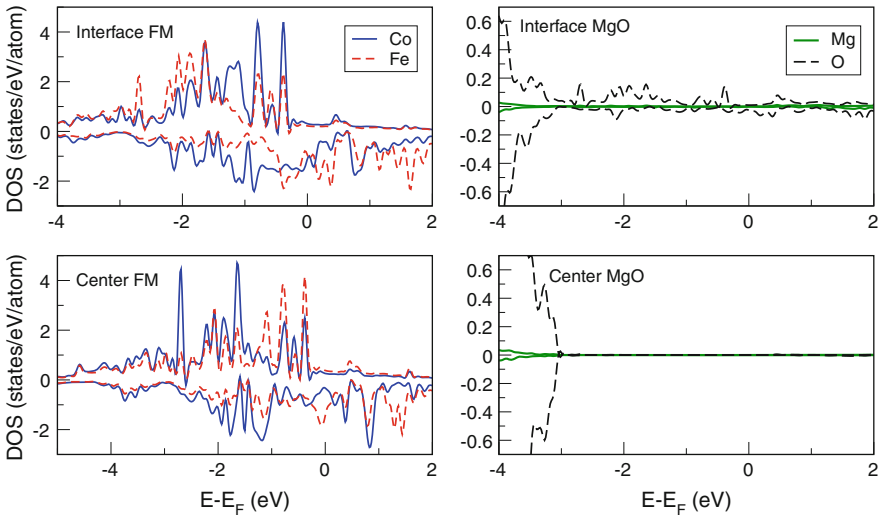

Fig. 23 Layer resolved density of states of a (5 ML)Fe_2CoSi/(5 ML)MgO(001) multilayer. Both interfaces are terminated with Fe, accordingly the actual composition is $Fe_2Co_{1.2}Si_{0.8}$. Data taken from Ref. [68]

and the calculated spin polarization was found to range between −63 and −73 %, cf. Table 4.

In view of the observations for inverse ordered bulk Heusler compounds, the high spin polarization is quite surprising. Inverse ordered bulk Heusler alloys showed significant changes of the spin polarization with tetragonal strain to the point of sign changes (see Sect. 3.1). But note that, the actual composition of the multilayer does not correspond to the stoichiometric case, since it has a slightly enhanced Co

Table 4 Calculated spin polarization P for multilayers consisting of 5 ML Fe_3Si or $Fe_2Co_{1.2}Si_{0.8}$ and 5 ML MgO(001)

System	Interface FM	2nd (Fe-Si)	Center FM	Interface MgO	Center MgO
Fe_3Si + Fe ($D0_3$)	−85.7	−15.9	−38.6	−69.9	0.0
$Fe_2Co_{1.2}Si_{0.8}$ (inverse)	−66.0	−73.1	−62.8	−52.8	0.0

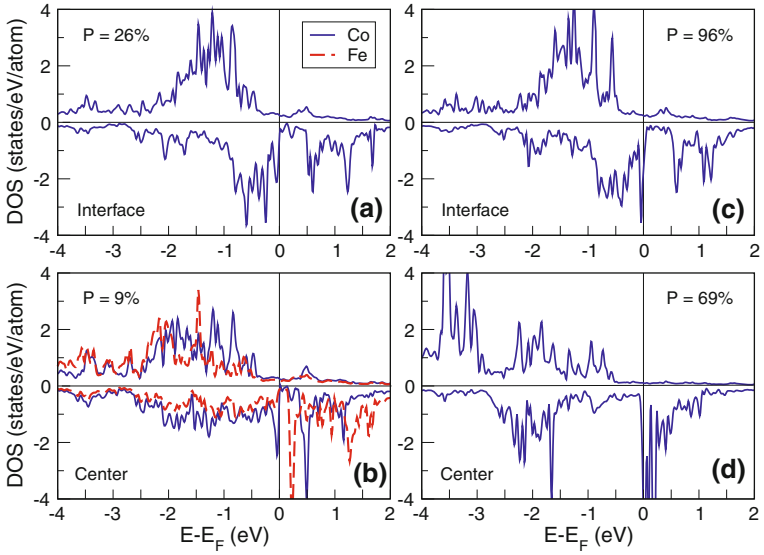

Fig. 24 Layer resolved density of states of multilayers consisting of (5 ML) $Co_{1.75}Fe_{1.25}Si$ (**a**), (**b**) and $Co_{2.25}Fe_{0.75}Si$ (**c**), (**d**) on (5 ML)MgO(001). The interfaces are terminated with Co such that the actual composition corresponds to $Co_{2.2}FeSi_{0.8}$ (**a**), (**b**) and $Co_{2.6}Fe_{0.6}Si_{0.8}$ (**c**), (**d**). Data taken from Ref. [60]

concentration (the number of valence electrons per atom is $e/a = 7.5$, being the same as for Co_2FeSi).

Following the Slater-Pauling rule, the magnetic moment per formula unit is expected to be 6 μ_B and the system should be half-metallic [95]. However, Fe-rich alloys obey less strictly the Slater-Pauling rule [96] and the investigated multilayer is not half-metallic but provides a high spin polarization which can be understood from the valence electron argument. Furthermore, in contrast to the homogeneous distortion discussed in Sect. 3.1.1 here an inhomogeneous strain occurs, which leads to different layer distances ranging from 1.97 (interface) to 1.20 Å (1st layer of the Heusler film). In the center layer of the FM the layer distances are close to the bulk value (1.35 Å, bulk: 1.40 Å). This has additional impact on the magnetic properties. Obviously, conclusions from bulk calculations are somewhat limited, because the actual spin polarization depends crucially on the composition and lattice distortions.

Co-Rich Systems: $L2_1$ Ordered

With increasing amount of Co, the order of the Heusler films changes from inverse to $L2_1$ order, see Fig. 2. Many of those $L2_1$ ordered Heusler alloys such as Co_2YSi (Y = Fe, Mn) are halfmetals in their bulk phase. If grown on an insulating or semiconducting substrate depending on the growth technique the magnetic properties appear less promising [94]: the lack of full spin polarization has been ascribed to anti-site disorder, i.e., Co and Y changing their sites [97]. This leads to a peak in the previously empty minority spin channel. The investigations are based on bulk calculations, where the influence of the surface is not included. However, it has been shown in Sect. 3.1 that deviations from cubic symmetry may strongly influence the magnetic properties. Therefore, Co-rich $L2_1$ ordered multilayers of $Fe_{3-x}Co_{1-x}Si$/MgO(001) consisting of 5 ML Heusler compound and 5 ML MgO have been investigated. The interfaces are Co terminated. Local concentration changes are simulated by replacing a Fe atom by Co and vice versa, i.e., the actual compositions are $Co_{2.2}FeSi_{0.8}$ and $Co_{2.6}Fe_{0.6}Si_{0.8}$, respectively. As expected, the average Fe and Co moments vary with composition, see Table 5, whereby the atoms sitting on the sublattice of the other species experience the largest change. In case of Fe on the Co site the average Fe-moment decreases to 2.38 μ_B compared to 2.80 μ_B for bulk Co_2FeSi, because the moment of Fe atom on the Co sublattice is only 1.48 μ_B. Also the Co moments are by 0.5 μ_B smaller compared to the ideal bulk value. Placing Co onto the Fe sublattice ($Co_{2.6}Fe_{0.6}Si_{0.8}$) causes less drastic changes. The moments are quite similar to the values obtained for Co_2FeSi, only Co on the Fe site has a strongly enhanced moment of $1.9\mu_B$. The reduction of the magnetic moment due to local deviations from the stoichiometry and/or order is in agreement with the experimental findings, see Table 5; partial disorder reduces the Fe and Co spin moments compared to higher ordered bulk like samples. Co on the Fe site is an exception, because the average Fe moment remains almost unchanged compared to its value in bulk Co_2FeSi.

Picozzi et al. have shown that Co anti-site disorder, which means the local change of the atomic environment, has also significant influence on spin polarization [97]. Therefore, it is expected that similar changes can be observed when the composition of the film slightly deviates from the stoichiometric case. The density of states unveil clear differences between $Co_{2.2}FeSi_{0.8}$ and $Co_{2.6}Fe_{0.6}Si_{0.8}$, see Fig. 24. Since Co excess leads to a high spin polarization all over the FM film, Fe replacing Co is less favorable. In the latter case the spin polarization at the interface is about $-26\,\%$, however in the center of the Heusler layer only $-9\,\%$ polarization survives. This confirms the previous observations for bulk Fe-Co-Si Heusler alloys with similar configurations. $Co_{2.25}Fe_{0.75}Si$ has a high spin polarization ($-50.8\,\%$) at least in the cubic phase, whereas the one for $Co_{1.75}Fe_{1.25}Si$ is tiny ($-7.0\,\%$). Here, the additional Co layer at the interfaces, which increases the actual Co concentration compared to bulk, seems to be of minor importance. The magnetic properties are determined by the local atomic arrangements in the central part of the Heusler film and the increase of number of valence electrons per atom (e/a) leads to higher spin polarization.

In summary, it has been demonstrated for the quasi-Heusler Fe_3Si that the inert MgO(001) substrate is preferable compared to GaAs surfaces, independent of the

Table 5 Average magnetic spin moments for Co_2FeSi-type/MgO(001) multilayers

Magnetic moment	Excess Fe	Excess Co	Co_2FeSi (bulk)	exp. 1[a]	exp. 2[b]
$\bar{m}_{Fe}(\mu_B)$	2.38	2.82	2.80	2.46	2.74
$\bar{m}_{Co}(\mu_B)$	0.84	1.16	1.33	1.07/1.28	1.38

Excess Co ($Co_{2.6}Fe_{0.6}Si_{0.8}$) and Fe ($Co_{2.2}FeSi_{0.8}$) mean additional Co atoms sit on Fe sites or vice versa. The experimental values belong to samples with different degree of ordering: Sample 1 is slightly disordered and not half metallic, whereas sample 2 shows a total moment of 6 μ_B (Remind: Here, only the spin moments are given)
[a]Taken from Ref. [94]
[b]Data published in Ref. [60]

orientation. Regarding magnetic properties of the Heusler film Co improves the spin polarization, which is expected from the Slater-Pauling rule. However, one should keep in mind the rule works properly only in case of Co_2YZ alloys [96]. In view of magnetoelectronics and TMR $L2_1$ ordered systems are preferable, because they provide a more stable spin polarization in presence of lattice distortions and small changes in composition. However, a reduction of e/a by placing Fe on Co sites worsens the magnetic properties. Recently, Co_2FeSi has been used successfully as top electrode in a tunnel junction with crystalline MgO(001) tunnel barrier [88]. Despite a lattice distortion due to MgO and the bottom electrode, a TMR of 120 % has been measured. Inverse ordered Fe-Co-Si Heusler alloys are more sensitive to lattice strain and composition, but apart from the region close to the stoichiometric compound Fe_2CoSi they provide also reasonable spin polarization. From experimental side, systematic investigations of composition dependence of the TMR are still lacking.

3.2 Co-Mn-Si: Bulk and Thin Films

Perfectly ordered Co_2MnSi in the $L2_1$ crystal structure is found to be a magnetic half-metal in scalar-relativistic DFT calculations. However, even in carefully prepared bulk samples (and even more so in thin films, where preparation conditions are more restrictive), site disorder may have a detrimental effect on the half-metallicity. In particular, DFT calculations (WIEN2k code) have revealed that Co atoms sitting on the 'wrong' sublattice positions tend to induce electronic states in the half-metallic gap. As an example, the total density of states (DOS) of the Co–Si swap, is compared to the ideal case in Fig. 25. There are two defect states close to the Fermi energy that are solely derived from the Co atom at Si site. One of them is occupied and lies slightly below E_F, the other one is unoccupied. Due to these states the remaining spin gap is very small. The DOS of the Co_{Si} antisite is similar to that of the Co–Si swap showing also the two defect states. In particular, Co-rich $Co_{2-x}Mn_{1+x}Si$ alloys, i.e. with $x < 0$, are therefore not useful for TMR electrodes.

For Mn-rich alloys, $x > 0$, however, the calculations predict a different behavior: Mn atoms successively replacing Co atom do *not* introduce gap states up to $x \sim 1.7$.

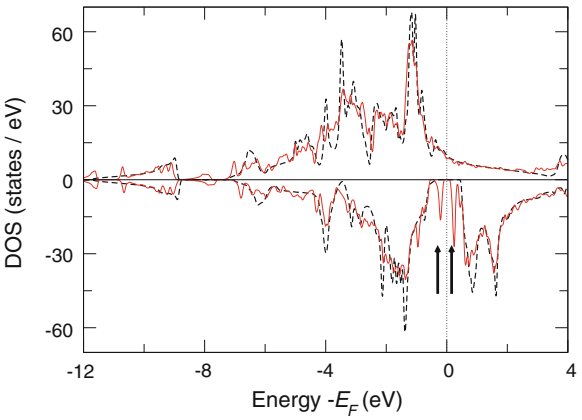

Fig. 25 The total density of states of ideal Co_2MnSi (*black dotted line*) and the Co–Si swap (*red line*). The crucial difference lies in the states in the band gap, i.e. between -0.5 eV and $+0.35$ eV, indicated by the *two arrows*, that are derived solely from the Co atoms at Si sites (data taken from [98])

While the gap in the minority spin channel becomes smaller with increasing x, only close to the composition Mn_3Si an energetic overlap of the valence and conduction bands occurs. To monitor the half-metallic property for $x > 0$ in the DFT calculations, we sample a large supercell with random occupations of the Co and Mn sublattices by Mn atoms and use a cluster expansion of the magnetic moment of the supercell [98].

Since a magnetic half-metal has an integer magnetic moment (an integer number of electrons in the minority spin channel that displays the energy gap), the magnetic moment serves as a necessary (although not sufficient) indicator of alloy compositions that possibly show half-metallicity. We find that the exchange of Co by Mn atoms in the alloy most likely preserves the half-metallic property in a range of compositions. This is concluded from the results shown in Fig. 26, where the light gray data points indicate the formation energies of 27 million different configurations screened by the cluster expansion, while the black data points indicate those configurations for which the cluster expansion predicts an integer magnetic moment. It is remarkable that the region of black points has a certain width on the energy scale, indicating that even a configuration different from the ground state, that could result from a thermally excited atomic configuration or from imperfect annealing of the sample, might still preserve the half-metallicity for some Mn-enriched Heusler alloys. Since the integer magnetic moment is just a first indicator of half-metallicity, additional DFT calculations have been performed to test some selected configurations (circles in Fig. 26). Indeed an energy gap in the Kohn-Sham eigenvalue spectra of the minority spin channel has been found in all cases. In summary, Fig. 26 establishes that adding more Mn in the synthesis of $Co_{2-x}Mn_{1+x}Si$ may even enhance its

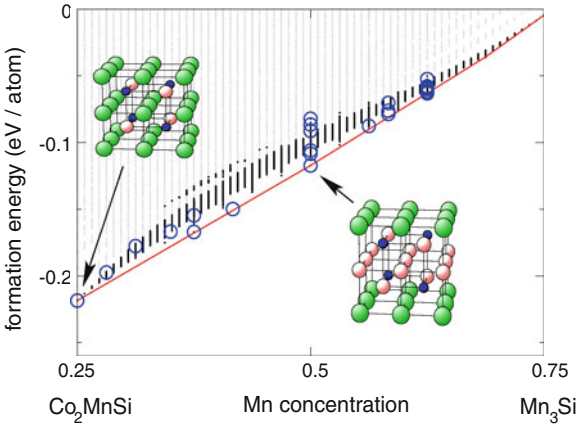

Fig. 26 Formation energies of 27 million structures obtained from the cluster expansion by direct enumeration (*light grey points*). For the *black points*, the cluster expansion of the magnetic moments predicts an integer value. Both the integer magnetic moment and the existence of a spin gap has been confirmed by DFT calculations for the structures indicated by the *circles*

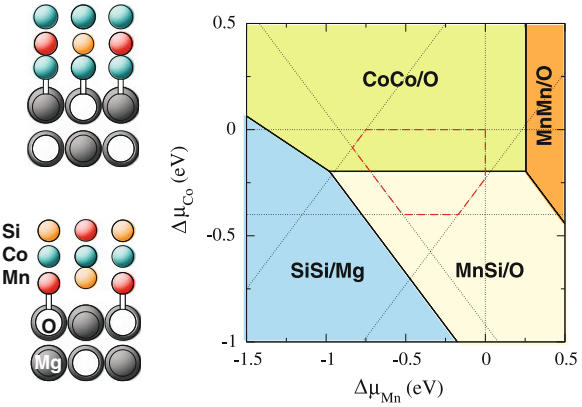

Fig. 27 *Left* ball-and-stick models of the relaxed atomic structures of the CoCo/O interface (*top*), and the MnSi/O interface (*bottom*). *Right* phase diagram for the epitaxial $Co_2MnSi(001)/MgO(001)$ interface. The colored regions correspond to different interface terminations being stable under the conditions described by the chemical potentials $\Delta\mu_i = \mu_i - g_i$, where g_i (i = Co, Mn) is the total energy of one unit cell of the stable bulk phase of the elements (hcp Co and α-Mn). The polygon bounded by the *red dashed lines* indicates the region accessible in thermodynamic equilibrium with the bulk phases of Mn, Co, Mn_3Si or Co_3Si (data taken from [102])

half-metallic properties. The robustness of Mn-enriched Co_2MnSi alloys for spintronics applications has been confirmed in a recent experimental study [99].

By combining an MgO barrier with Co_2MnSi electrodes, TMR ratios as high as 192 % [100] and even 753 % [14] have been achieved. DFT calculations give important information about the energetically most favorable atomic structure of the

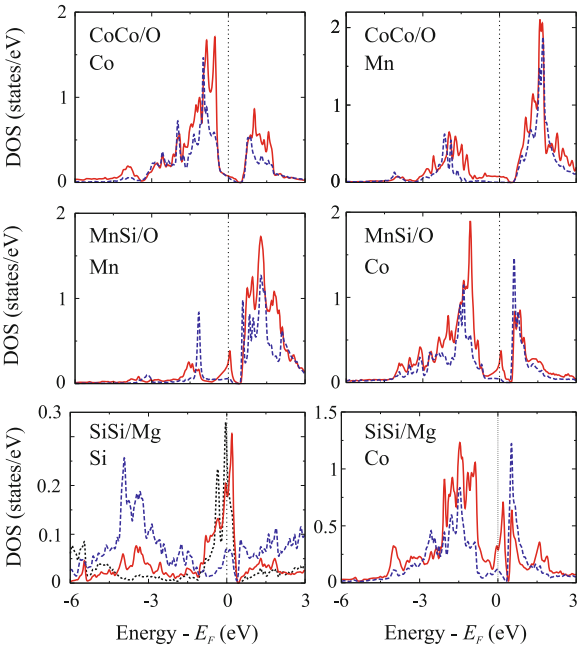

Fig. 28 The orbital-resolved DOS of the atoms at the interface (*left column*) and in the first sublayer (*right column*) of the Heusler alloy for the three non half-metallic heterostructures CoCo/O, MnSi/O and SiSi/Mg (*rows*). The second label in each sub-plot denotes the species that is projected out. *Red* (*full*) *lines* show the projected DOS for the 'out-of-plane' orbitals ($d_{3z^2-r^2} + d_{xz} + d_{yz}$ for Co and Mn, p_z for Si). *Blue* (*dashed*) *lines* show the projected DOS for the 'in-plane' orbitals ($d_{x^2-y^2} + d_{xy}$ and $p_x + p_y$). The *black* (*dotted*) *line* is a projection onto the Si-*s* orbital (data taken from [102])

$Co_2MnSi(001)/MgO(001)$ interface. In order to compare the stability of the various terminations of the Heusler structure that could possibly occur at real interfaces, we use the method of ab initio atomistic thermodynamics [101]. Depending on the conditions under which the Heusler electrodes are prepared, i.e., if there is a surplus of Co or Mn, we find that the alloy will be terminated at the interface either by a Co layer (Co-rich conditions) or by a mixed MnSi layer (Co-poor conditions), as evident from the structures within the red dashed polygon in Fig. 27 [102]. For both terminations, the structure where the transition metal atoms sit on top of the oxygen atoms is found to be most stable. The interplay between the atomic and the electronic structure of the interfaces is best analyzed by inspecting the orbital-resolved densities of states (DOS). Only if the Co_2MnSi electrode is terminated by a full Mn layer, which is not stable in thermodynamic equilibrium, we find that the gap remains free of interface states. For the other cases, the orbital-resolved DOS in the minority spin channel is shown in Fig. 28. It is observed that the CoCo/O interface has only a small DOS at E_F which involves both in-plane and out-of-plane Co orbitals, as well as out-of-plane orbitals of the sublayer Mn atoms. The MnSi/O interface shows a sharp peak of the DOS at E_F arising from the out-of-plane orbitals of the sublayer Co

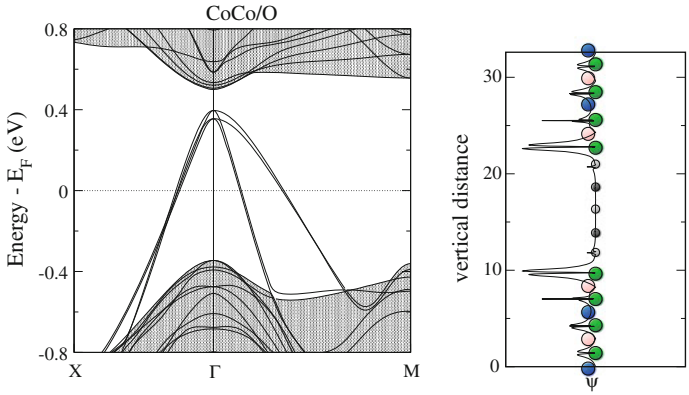

Fig. 29 Kohn-Sham band structure projected onto the Brillouin zone of the interface in a $Co_2MnSi(001)/MgO(001)/Co_2MnSi(001)$ heterostructure terminated by Co layers. The gap region in the minority spin channel is shown. The shaded regions correspond to projected bulk bands of Co_2MnSi. The highly dispersive bands inside the gap are Co-induced interface states. The *right panel shows* the wavefunction belonging to the interface band at E_F. The *vertical axis* is a spatial coordinate normal of the interface. The *small balls* in the middle of the picture symbolize the Mg and O atoms of the barrier

atoms that hybridize with out-of-plane Mn orbitals in the interface layer, similar to the surface states studied previously [103]. In case of the SiSi/Mg interface, the half-metallic gap is completely filled with interface states originating from Si orbitals. These interface states may drastically reduce the spin polarization of the DOS at the Fermi level, in particular for the MnSi/O and SiSi/Mg interfaces. For the CoCo/O interface, a rather high degree of spin polarization, $P_{\text{int}} = 67\,\%$, is retained despite the interface state.

By calculating the Kohn-Sham band structure, we can access the dispersion of the electronic interface states in the minority spin channel. As an example, Fig. 29 shows the band structure for the interface layer of Co atoms bonding to the oxygen atoms in the top-most MgO layer. The electrons in this state may contribute to the tunneling current through the MgO barrier only at finite crystal momentum parallel to the interface, because the interface band crosses the Fermi level amid the ΓM and ΓX lines in the Brillouin zone (see Fig. 29, left panel). Moreover, there is a mismatch in orbital character between the oxygen $2p$-states and interface state that has mostly Co $3d$-character. For both reasons, the wave function amplitude of the interface state is suppressed inside the MgO barrier (Fig. 29, right panel). This is important for the functioning of the TMR device in the 'closed' state, at opposite magnetization of the electrodes.

3.3 Co-Mn-Ge: Bulk and Thin Films—Interface Magnetism

One characteristic phenomenon of ferromagnetic Heusler alloys in thin film heterostructures is the reduction of ferromagnetism by intermixing, alloying or disorder at the interfaces with other materials. Examples of devices where the interface magnetism is of utmost importance are TMR elements with Heusler/insulator interfaces, GMR elements with Heusler/normal metal interfaces and spin injection devices with Heusler/semiconductor interfaces. For all these spintronic devices the reduction of ferromagnetism even in the range of a few monolayers close to the interfaces is detrimental, since it is necessarily accompanied by a reduction or even complete loss of the conduction electron spin polarization. This is the main reason why the ferromagnetic Heusler half metals with a theoretically predicted full spin polarization at the Fermi level in most spintronic devices do not exhibit the performance expected for a perfect ferromagnetic half metal. Only very recently it seems that in TMR elements it was possible to avoid this problem by choosing special preparation conditions and material combinations [14].

The experimental analysis of the magnetization or the spin polarization close to internal interfaces, which is needed for the characterization of the magnetic quality of an electrode, is a difficult task. The surface sensitivity of XMCD when measured by the total electron yield in comparison to the X-ray absorption measured in transmission on the same film has been used to unveil the magnetic moment density close to the surface of Heusler compounds compared to the bulk [104, 105]. Details of the magnetization profile at buried interfaces, however, cannot be resolved by this method.

The only available direct experimental methods for studying the magnetization profile at internal interfaces of the Heusler alloys is magnetic neutron scattering and synchrotron radiation based magnetic soft X-ray scattering [106–108]. Using these methods, the magnetization profile can principally be determined by a comparison of the experimental X-ray or neutron reflectivity with model calculations assuming a certain shape for the internal magnetization profile. Principally the methods can be applied even to single magnetic layers. In practice, however, when a resolution in the range of a few monolayers is needed, the study of multilayers with very thin magnetic layers is superior. High quality multilayers of the spintronic Heusler compound Co_2MnGe with Au-interlayers [106], V-interlayers [108] and Al_2O_3 [107] have been prepared and studied using X-ray and neutron reflectivity. As an example in Fig. 30 we show the hard X-ray reflectivity of a $[CoMn_2Ge(3\,nm)/Au(3\,nm)]_{25}$ superlattice (3 nm thickness, 25 periods) showing superlattice reflections up to 9th order.

For the analysis of the magnetic moment density soft X-ray reflectivity spectra with the X-ray energy close to the $L_{2,3}$ absorption edges of the Co and Mn atoms were taken. As an example, in Fig. 31 we show an energy scan of the reflectivity at the $L_{2,3}$-edges of Co in the $[CoMn_2Ge(3\,nm)/Au(3\,nm)]_{25}$ superlattice using left hand and right hand circularly polarized light with the scattering angle fixed at the position of the first superlattice Bragg reflection. Taking the difference of the two spectra

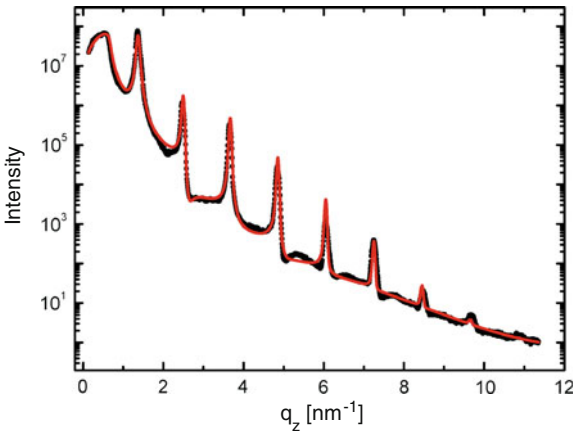

Fig. 30 Small angle X-ray reflectivity scan using Cu-K_α radiation of a [$CoMn_2Ge$(3 nm)/Au(3 nm)]$_{25}$ multilayer (data taken from [108])

(lower panel in Fig. 31) one derives the magnetic part of the reflectivity spectrum, which is a very sensitive function of the Co magnetic moment distribution inside the Heusler layers. Sophisticated data analysis [106] with the magnetic moment profile as the fitting parameter then leads to the moment distribution profile inside a single Heusler layer shown in Fig. 32. Since the soft X-ray reflectivity is element-specific the same procedure was also applied to derive a magnetic moment density profile of Mn (Fig. 32). The essential finding is that at the Co_2MnGe/Au interface there exists an interlayer of about 0.5 nm thickness with strongly reduced Co-moment. For Mn this interlayer is even thicker, namely about 1 nm. Similar moment profiles have also been observed at the Co_2MnGe/V interface [108] and at the interface of Co_2MnGe with amorphous Al_2O_3. Only for the case of the Co_2MnGe/MgO interface the Heusler layer keeps its high moment with only a very slight reduction until very close to the interface [107].

4 Electronic Transport Through Heusler Alloys

One important application of half-metallic Heusler compounds is the TMR, where two magnetic electrodes are separated by a very thin (only a few nanometer thick) oxide barrier, see Fig. 1. The relative magnetization of both electrodes is used to represent the bit of information stored in the TMR element, while the electrical conductivity of the tunnel junction serves as the read-out signal. The figure of merit is the TMR ratio, i.e. the difference of the conductance through the TMR device in the two states where the electrodes are magnetized either parallel or antiparallel to each other, divided by the smaller of the two values, cf. Eq. 1. Controlling the half-metallicity in the bulk of the electrodes by suitable alloy composition and materials processing

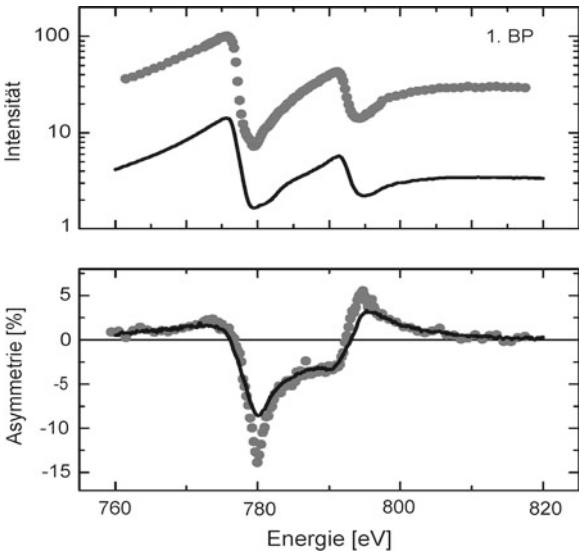

Fig. 31 *Upper panel* soft X-ray reflectivity scan for *left*- and *right hand* circularly polarized light for the $[CoMn_2Ge(3\,nm)/Au(3nm)]_{25}$ of Fig. 30 close to the $L_{2,3}$ absorption edge of Co. The *bottom* figure depicts the normalized difference of the two spectra (data taken from [108])

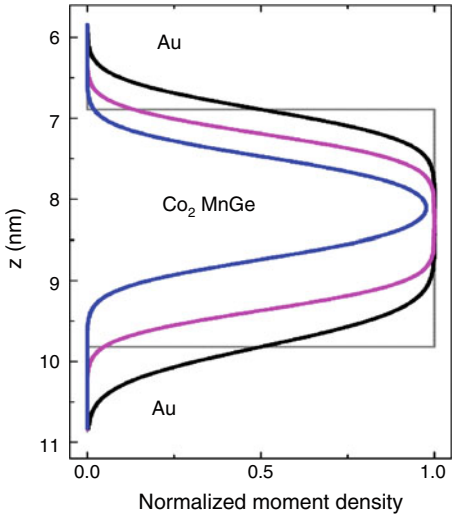

Fig. 32 Density profiles inside a Heusler layer of a $[CoMn_2Ge(3\,nm)/Au(3\,nm)]_{25}$ multilayer. *Black line* chemical density profile, *red line* Co-magnetic moment density profile; *blue line* Mn-magnetic moment density profile (data taken from [108])

(deposition and tempering steps) is prerequisite for achieving a high figure of merit. However, electronic states inside the gap in the minority spin channel at the interface between electrode and oxide barrier could act as centers for spin-flip scattering and could thus significantly diminish the figure of merit. In order to control and possibly eliminate this detrimental effect, one needs to know whether these interface states

are localized at only one side of the oxide barrier (in the case of antiparallel magnetization of the electrodes), or if they extend through the barrier, and how much they contribute to the transmission of electrical current. The electronic properties of the interface states depend on their energetic position relative to the Fermi energy in the electrodes and on their orbital symmetry. The latter aspect is important for epitaxial, highly crystalline barriers made of MgO: An s-like character of the interface state allows for hybridization between the transition metal orbitals and the states derived from the conduction band in MgO, leading to metal-induced gap states, while a $3d$-like character of these states prevents their hybridization with any states near the fundamental band gap in the MgO. Which of these alternatives is realized is a question that can be answered by DFT calculations of the interface electronic structure. The role of interface states for TMR is also discussed by Mavropoulos et al. [109].

In order to calculate the transport properties of a heterostructure from ab initio methods one can make use of the Boltzmann equation [110] or use linear response theory (Kubo method) [111]. However, in view of tunneling magnetoresistance it is common to employ the Landauer-Büttiker formula [112, 113], which describes the conductance G of a mesoscopic system by incoming and outgoing Bloch states

$$G = \frac{e^2}{h} \sum_{k_\parallel, k'_\parallel} \left| T_{k_\parallel, k'_\parallel} \right|^2 \tag{6}$$

where $k_\parallel$ is the in-plane component of the incoming Bloch vector; the prime denote the Bloch vector of the outgoing mode (current flows perpendicular to the plane) and $\left| T_{k_\parallel, k'_\parallel} \right|^2$ is the transmission coefficient [114]. In case of Fe/MgO(001)/Fe Butler et al. reported as a result of their calculation a TMR effect of 6,000 % for ideal interfaces and monocrystalline MgO layers [115]. These calculations show that the symmetry of states propagating from the FM Heusler electrode match with the decaying states of the insulator, which is an important criteria for high transmission coefficients. But note that, this is strictly valid only in case of ideal structures and at $T = 0\,\mathrm{K}$. Large values of the TMR ratio were also obtained experimentally for Co_2MnSi Heusler films on MgO(001) [14, 116]. From experiment it is known that the TMR is strongly temperature dependent and decreases with increasing temperature [117]. Possible reasons are structural disorder and spin-flip processes. In a real TMR device, spin-flip processes related to electronic interface states could invalidate the advantages of half-metallic electrodes [109]. Even so, spin-selective tunneling may help to operate these devices with high TMR ratio. Recently, it has been shown that the temperature dependence can be improved by adding a thin film of a 2nd Heusler material [118].

5 Summary and Outlook

In the field of solid state magnetism the past decade experienced an unprecedented surge of interest in ferromagnetic Heusler alloys. This huge class of ternary ferromagnetic alloys provides unparalleled examples exhibiting, e.g. the magnetic shape memory effect, the magneto-caloric effect or, last not least, half metallicity, the key feature for spintronic materials. In the present review we summarize part of our recent work on the ferromagnetic Heusler half metals and related compounds with the main interest on their electronic properties. We focus on non-ideal situations such as off-stoichiometry, site disorder, mechanical strain and interfaces of the Heusler alloy with insulators and semiconductors. The technological relevance is obvious, since experimentally it is known that the half metallicity of the Heusler compounds sensitively depends on deviations from the ideal, fully ordered bulk crystal structure and in real spintronic devices these features easily lead to a loss of half metallicity which leads to smaller TMR values compared to the theoretically predicted ones.

The main part of this review is based on the results of modern electronic energy band structure methods using the DFT, which reveal in great detail the modifications of the electronic states induced by deviations from the ideal composition, atomic site order or by nearby interfaces. The calculations clearly demonstrate the sensitivity of the electronic structure of the Heusler alloys at the Fermi level. Slight changes of the stoichiometry, changes of the terminations of the Heusler layers and/or the substrate can induce drastic changes of the electronic states and the degree of spin polarization. Experimentally it is very difficult to resolve these detailed electronic features, especially if buried interfaces of the Heusler alloys with other materials are involved. However, the theoretical calculations can serve as a valuable guideline for optimizing spintronic devices.

In the experimental sections of this review we have shown that element specific X-ray absorption or X-ray reflectivity techniques and, with some limitations, also Mössbauer spectroscopy and polarized neutron reflectivity can e.g. reveal modifications of the atomic magnetic moments close to interfaces and in off-stoichiometric samples. These moments are directly related to the electronic structure and can favorably be compared with the theoretical calculations, as demonstrated in several sections of this review.

References

1. S. Maekawa, T. Shinjo (eds.), *Spin Dependent Transport in Magnetic Nanostructures, Advances in Condensed Matter Science* (Taylor & Francis, London, 2002)
2. N. Tran, T.J. Webster, J. Mater. Chem. **20**, 8760 (2010)
3. A. Ayuela, J. Enkovaara, K. Ullakko, R.M. Nieminen, J. Phys.: Condens. Matter. 11, 2017 (1999)
4. T. Mizuno, Y. Tsuchiya, T. Machita, S. Hara, D. Miyauchi, K. Shimazawa, T. Chou, K. Noguchi, K. Tagami, IEEE Trans. Magn. **44**, 3584 (2008)

5. A. Kalitsov, M. Chshiev, I. Theodonis, M. Kioussis, W.H. Butler, Phys. Rev. B **79**, 174416 (2009)
6. B. Krumme et al., Phys. Rev. B **80**, 144403 (2009)
7. P. Mavropoulos, N. Papanikolaou, P.H. Dederichs, Phys. Rev. Lett. **85**, 1088 (2000)
8. S. Chadov, G.H. Fecher, C. Felser, J. Minár, J. Braun, H. Ebert, J. Phys. D: Appl. Phys. **42**, 084002 (2009)
9. P. Klaer, M. Kallmayer, C.G.F. Blum, T. Graf, J. Barth, B. Balke, G.H. Fecher, C. Felser, H.J. Elmers, Phys. Rev. B **80**, 144405 (2009)
10. K. Tsuchiya, H. Nakamura, D. Ohtoyo, H. Nakayama, H. Ohtsuka, M. Umemoto, Int. J. Mater. Prod. Technol. **SPM1**, 409 (2001)
11. G. Wu, C. Yu, L. Meng, J. Chen, F. Yang, S. Qi, W. Zhan, Z. Wang, Y. Zheng, C. Zhao, Appl. Phys. Lett. **75**, 2990 (1999)
12. P. Entel, M.E. Gruner, A. Dannenberg, M. Siewert, S.K. Nayak, H.C. Herper, V.D. Buchelnikov, Mater. Sci. Forum **635**, 3 (2010)
13. A.N. Vasil'ev, A.D. Bozhko, V.V. Khovailo, I.E. Dikshtein, V.G. Shavrov, V.D. Buchelnikov, M. Matsumoto, S. Suzuki, T. Takagi, J. Tani, Phys. Rev. B **59**, 1113 (1999)
14. S. Tsunegi, Y. Sakuraba, M. Oogane, K. Takanashi, Y. Ando, Appl. Phys. Lett. **93**, 112506 (2008)
15. G.Q. Yu, L. Chen, S. Rizwan, J.H. Zhao, K. Xu, X.F. Han, Appl. Phys. Lett. **98**, 262501 (2011)
16. K. Inomata, S. Okamura, A. Miyazaki, N. Tezuka, M. Wojcik, E. Jedryka, J. Phys. D: Appl. Phys. **39**, 816 (2006)
17. X. Moya, L. Mañosa, A. Planes, S. Aksoy, M. Acet, E.F. Wassermann, T. Krenke, Phys. Rev. B **75**, 184412 (2007)
18. J. Marcos, L. Mañosa, A. Planes, F. Casanova, X. Batlle, A. Labarta, B. Matínez, J. Phys. IV France **115**, 105 (2004)
19. S. Chadov, X.L. Qi, J. Kübler, G.H. Fecher, C. Felser, S.C. Zhang, Nat. Mater. **9**, 541 (2010)
20. K. Ullakko, J. Huang, C. Kantner, R. O'Handley, V. Kokorin, Appl. Phys. Lett. **69**, 1966 (1996)
21. O. Heczko, M. Thomas, R. Niemann, L. Schultz, S. Fähler, Appl. Phys. Lett. **94**, 152513 (2009)
22. C.A. Jenkins, R. Ramesh, M. Huth, T. Eichhorn, P. Pörsch, H.J. Elmers, G. Jakob, Appl. Phys. Lett. **93**, 234101 (2008)
23. S. Ghosh, B. Sanyal, J. Phys. Condens. Matter **22**, 346001 (2010)
24. S. Hamann et al., Acta Materialia **58**, 5949 (2010)
25. A. Planes, L. Mañosa, M. Acet, J. Phys.: Condens. Matter **21**, 233201 (2009)
26. P. Entel, V.D. Buchelnikov, V.V. Khovailo, A.T. Zayak, W.A. Adeagbo, M.E. Gruner, H.C. Herper, E.F. Wassermann, J. Phys. D: Appl. Phys. **39**, 865 (2006)
27. M. Gilleßen, R. Dronskowski, J. Comput. Chem. **30**, 1290 (2008)
28. A. Dannenberg, M. Siewert, M.E. Gruner, M. Wuttig, P. Entel, Phys. Rev. B **82**, 214421 (2010)
29. J.-G. Zhu, C. Park, Mater. Today **9**, 36 (2006)
30. M. Kallmayer et al., Appl. Phys. Lett. **91**, 192501 (2007)
31. J. Schmalhorst, A. Thomas, G. Reiss, X. Kou, E. Arenholz, J. Appl. Phys. **102**, 053907 (2007)
32. A. Vedyayev, N. Ryzhanova, R. Vlutters, B. Dieny, Europhys. Lett. **46**, 808 (1999)
33. C. Gusenbauer, T. Ashraf, J. Stangl, G. Hesser, T. Plach, A. Meingast, G. Kothleitner, R. Koch, Phys. Rev. B **83**, 035319 (2011)
34. X.W. Zhou, H.N. Wagley, Phys. Rev. B **71**, 054418 (2005)
35. M. Julliere, Phys. Lett. **54**, 225 (1975)
36. T. Miyazaki, N. Tezuka, J. Magn. Magn. Mater. **139**, 231 (1995)
37. J.P. Velev, P.A. Dowben, E. Tsymbal, S.J. Jenkins, A.N. Caruso, Surf. Sci. Rep. **63**, 400 (2008)
38. M. Hattori, Y. Sakuraba, M. Oogane, Y. Ando, T. Miyazaki, Appl. Phys. Express **1**, 021301 (2008)
39. N. Tezuka, N. Ikeda, F. Mitsuhashi, S. Sugimoto, Appl. Phys. Lett. **94**, 162504 (2009)
40. S. Trudel, O. Gaier, J. Hamrle, B. Hillebrands, J. Phys. D: Appl. Phys. **43**, 193001 (2010)

41. K.J. Buschow (ed.), *Handbook of Magnetic Materials*, vol. 17 (North-Holland, Amsterdam, 2007)
42. M. Oogane, Y. Sakuraba, J. Nakata, H. Kubota, Y. Ando, A. Sakuma, T. Miyazaki, J. Phys. D: Appl. Phys. **39**, 834 (2006)
43. P. Pörsch, M. Kallmayer, T. Eichhorn, G. Jakob, H.J. Elmers, C.A. Jenkins, C. Felser, R. Ramesh, M. Huth, Appl. Phys. Lett. **93**, 022501 (2008)
44. F. Heusler, Verh. Deutsch. Phys. Ges. **5**, 219 (1903)
45. J. Kübler, Phys. Rev. B **28**, 1745 (1983)
46. D. Erb, G. Nowak, K. Westerholt, H. Zabel, J. Phys. D: Appl. Phys. **43**, 285001 (2010)
47. L. Krusin-Elbaum, A.P. Malozemoff, R.C. Taylor, Phys. Rev. B **27**, 562 (1983)
48. P.J. Webster, J. Phys. Chem. Solids **32**, 1221 (1983)
49. U. Geiersbach, A. Bergmann, K. Westerholt, J. Magn. Magn. Mater. **240**, 546 (2002)
50. B. Krumme, H. Herper, D. Erb, C. Weis, C. Antoniak, A. Warland, K. Westerholt, P. Entel, H. Wende, J. Phys. D: Appl. Phys. **44**, 415004 (2011)
51. H. Wende, Rep. Prog. Phys. **67**, 2105 (2004)
52. H. Dürr, G. van der Laan, D. Spanke, F. Hillebrecht, N. Brookes, Phys. Rev. B **56**, 8156 (1997)
53. O. Šipr, J. Minár, A. Scherz, H. Wende, H. Ebert, Phys. Rev. B **84**, 115102 (2011)
54. H. Landolt, R. Börnstein (eds.), *New Series Landolt-Börnstein*, vol. III/19c (Springer, Berlin, 1988)
55. A. Ionescu et al., Phys. Rev. B **71**, 094401 (2005)
56. C. Antoniak, H.C. Herper, Y.N. Zhang, A. Warland, T. Kachel, F. Stromberg, B. Krumme, C. Weis, K. Fauth, W. Keune, P. Entel, R.Q. Wu, J. Lindner, H. Wende, Phys. Rev. B **85**, 214432 (2012)
57. S.I. Makarov, B. Krumme, F. Stromberg, C. Weis, W. Keune, H. Wende, Appl. Phys. Lett. **99**, 141910 (2011)
58. M. Arita, S. Nasu, F. Fujita, Trans. Jpn. Inst. Met. **26**, 710 (1985)
59. V. Ko, J. Qiu, P. Luo, G.C. Han, Y.P. Feng, J. Appl. Phys. **109**, 07B103 (2011)
60. H.C. Herper, B. Krumme, D. Ebke, C. Antoniak, C. Weis, A. Warland, A. Hütten, H. Wende, P. Entel, J. Appl. Phys. **109**, 07E128 (2011)
61. V. Jung, G.H. Fecher, B. Balke, V. Ksenofontov, C. Felser, J. Phys. D: Appl. Phys. **42**, 084007 (2009)
62. L. Hongzhi, Z. Zhiyong, M. Li, X. Shifeng, L. Heyan, Q. Jingping, L. Yangxian, W. Guangheng, J. Phys. D: Appl. Phys. **40**, 7121 (2007)
63. J. Kübler, G. Fecher, C. Felser, Phys. Rev. B **76**, 024414 (2007)
64. S. Wurmehl, G.H. Fecher, H.C. Kandpal, V. Ksenofontov, C. Felser, H.-J. Lin, J. Morais, Phys. Rev. B **72**, 184434 (2005)
65. H. Ebert et al., The Munich SPR-KKR package, version 3.6, http://olymp.cup.uni-muenchen.de/ak/ebert/SPRKKR
66. H. Ebert, Fully relativistic band structure calculations for magnetic solids—formalism and application, in *Electronic Structure and Physical Properties of Solids*, Lecture Notes in Physics, vol. 535, ed. by H. Dreyssé (Springer, Berlin, 2000), p. 191
67. H. Ebert, Rep. Prog. Phys. **59**, 1665 (1996)
68. H.C. Herper, to be published
69. A.I. Liechtenstein, V.I. Anisimov, J. Zaanen, Phys. Rev. B **52**, R5467 (1995)
70. S.L. Dudarev, G.A. Botton, S.Y. Savrasov, C.J. Humphreys, A.P. Sutton, Phys. Rev. B **57**, 1505 (1998)
71. J. Thoene, S. Chadov, G. Fecher, C. Felser, J. Kübler, J. Phys. D: Appl. Phys. **42**, 084013 (2009)
72. Y. Nakamura, *Landolt-Börnstein, New Series*, vol. III/19c (Springer, Berlin, 1988)
73. P.W. Anderson, in *Solid State Physics*, Chap. Theory of magnetic exchange interactions: exchange in insulators and, semiconductors, vol. 14, ed. by F. Seitz, D. Turnbull (Academic, New York, 1993), p. 99
74. G. Kresse, J. Furthmüller, Comput. Mater. Sci. **6**, 15 (1996)

75. P. Entel, A. Dannenberg, M. Siewert, H.C. Herper, M.E. Gruner, V.D. Buchelnikov, V.A. Chernenko, Mater. Sci. Forum **684**, 1 (2011)
76. X.-Q. Chen, R. Podloucky, P. Rogl, J. Appl. Phys. **100**, 113901 (2006)
77. J. Herfort, H.-P. Schönherr, A. Kawaharazuka, M. Ramsteiner, K.H. Ploog, J. Cryst. Growth **278**, 666 (2005)
78. V.P. LaBella, M.R. Krause, Z. Ding, P.M. Thibado, Surf. Sci. Rep. **60**, 1 (2005)
79. Q. Xue, T. Hashizume, J.M. Zhou, T. Sakata, T. Ohno, T. Sakurai, Phys. Rev. Lett. **74**, 3177 (1995)
80. R.A. Gordon, E.D. Crozier, D.-T. Jiang, T.L. Monchesky, B. Heinrich, Phys. Rev. B **62**, 2151 (2005)
81. S. Mirbt, B. Sanyal, C. Isheden, B. Johansson, Phys. Rev. B **67**, 155421 (2003)
82. H.C. Herper, P. Entel, Philos. Mag. **88**, 2699 (2008)
83. J. Herfort, H.-P. Schönherr, K. Ploog, Appl. Phys. Lett. **83**, 3912 (2003)
84. L. Wining, M. Wenderoth, J. Homoth, A. Siewers, R. Ulbrich, Appl. Phys. Lett. **92**, 193102 (2008)
85. A. Grünebohm, H.C. Herper, P. Entel, Phys. Rev. B **80**, 064417 (2009)
86. H. Wende, unpublished
87. A. Grünebohm, M. Siewert, H.C. Herper, M.E. Gruner, P. Entel, J. Phys.: Conf. Ser. **200**, 072038 (2009)
88. W.C. Lim, G.M. Choi, T.D. Lee, S. Seo, IEEE **44**, 2595 (2008)
89. S. Hakamata, T. Ishikawa, T. Marukame, K. Matsuda, T. Uemura, M. Arita, M. Yamamoto, J. Appl. Phys. **101**, 09J513 (2007)
90. D.M. Roessler, W.C. Walker, Phys. Rev. **159**, 733 (1967)
91. O. Taurian, M. Springborg, N. Christensen, Sol. States Commun. **55**, 351 (1985)
92. D. Kmiec, B. Sepiol, M. Sladecek, M. Rennhofer, S. Stankov, G. Vogl, B. Laenens, J. Meersschaut, T. Slezak, M. Zajkac, Phys. Rev. B **75**, 054306 (2007)
93. K. Zakeri et al., Phys. Rev. B **76**, 214421 (2007)
94. H. Schneider, G. Jakob, M. Kallmayer, H. Elmers, B. Balke, S. Wurmehl, C. Felser, M. Aeschlimann, H. Adrian, Phys. Rev. B **74**, 174426 (2006)
95. I. Galanakis, P. Dederichs (eds.), *Half-Metallic Alloys, Lecture Notes in Physics* (Springer, Berlin, 2005)
96. G.H. Fecher, H.C. Kandpal, S. Wurmehl, C. Felser, G. Schönhense, J. Appl. Phys. **99**, 08J106 (2006)
97. S. Picozzi, A. Continenza, A.J. Freeman, Phys. Rev. B **69**, 094423 (2004)
98. B. Hülsen, M. Scheffler, P. Kratzer, Phys. Rev. B **79**, 094407 (2009)
99. T. Ishikawa, H. Liu, T. Tairo, K.-I. Matsuda, T. Uemura, M. Yamamoto, Appl. Phys. Lett. **95**, 232512 (2009)
100. T. Ishikawa, T. Marukame, H. Kijima, K.-I. Matsuda, T. Uemura, M. Arita, M. Yamamoto, Appl. Phys. Lett. **89**, 192505 (2006)
101. K. Reuter, C. Stampfl, M. Scheffler, in *Handbook of Materials Modeling*, Chap. Ab initio thermodynamics and statistical mechanics of surface properties and functions, edited by S. Yip (Springer, Berlin, 2005), p. 149
102. B. Hülsen, M. Scheffler, P. Kratzer, Phys. Rev. Lett. **103**, 046802 (2009)
103. S.J. Hashemifar, P. Kratzer, M. Scheffler, Phys. Rev. Lett. **94**, 096402 (2005)
104. M. Kallmayer, H. Schneider, G. Jakob, H.J. Elmers, B. Balke, S. Cramm, J. Phys. D: Appl. Phys. **40**, 1552 (2007)
105. M. Jourdan, E.A. Jorge, C. Herbort, M. Kallmayer, P. Klaer, H.J. Elmers, Appl. Phys. Lett. **95**, 172504 (2009)
106. J. Grabis, A. Bergmann, A. Nefedov, K. Westerholt, H. Zabel, Phys. Rev. B **72**, 024438 (2005)
107. M. Vadalá, A. Nefedov, M. Wolff, K.N. Zhernenkov, K. Westerholt, H. Zabel, J. Phys. D: Appl. Phys. **40**, 1289 (2007)
108. A. Bergmann, J. Grabis, A. Nefedov, K. Westerholt, H. Zabel, J. Phys. D: Appl. Phys. **39**, 842 (2006)
109. P. Mavropoulos, M. Ležaić, S. Blügel, Phys. Rev. B **72**, 174428 (2005)

110. I. Mertig, Rep. Prog. Phys. **62**, 237 (1999)
111. H.C. Herper, P. Weinberger, L. Szunyogh, C. Sommers, Phys. Rev. B **66**, 064426 (2002)
112. J.S. Moodera, J. Nassar, G. Mathon, Annu. Rev. Mater. Sci. **29**, 381 (1999)
113. J. Mathon, A. Umerski, Phys. Rev. B **63**, 220403 (2001)
114. R. Landauer, IBM Res. J. Dev. **1**, 223 (1957)
115. W.H. Butler, X.-G. Zhang, T. Schulthess, J.M. MacLaren, Phys. Rev. B **63**, 054416 (2001)
116. M. Oogane, S. Mizukami, Trans. R. Soc. **369**, 3037 (2011)
117. Y. Sakuraba, M. Hattori, M. Oogane, Y. Ando, H. Kato, A. Sakuma, T. Miyazaki, H. Kubota, Appl. Phys. Lett. **88**, 192508 (2006)
118. E. Ozawa, S. Tsunegi, M. Oogane, H. Naganum, Y. Ando, J. Phys, Conf. Ser. **266**, 012104 (2011)

Multiferroic and Magnetoelectric Materials

Wolfgang Kleemann and Christian Binek

Abstract Magnetoelectric (*ME*) materials are of utmost interest in view of both fundamental understanding and novel desirable applications. Despite its smallness the linear *ME* effect has been shown to control spintronic devices very efficiently, e.g. by using the classic *ME* antiferromagnet Cr_2O_3. An electric field can switch its ferromagnetic surface magnetization and thus control exchange bias based spin valve devices. Similar nano-engineering concepts exist also for *type-I multiferroic* single phase materials like $BiFeO_3$ and $BiMnO_3$. *ME* response has been realized in stress-strain coupled *multiphase magnetoelectric* composites like $BaTiO_3$/Fe and—record high—in PZT/ FeBSiC, just right for sensorics applications. In *type-II multiferroics*, whose ferroelectricity is due to modulated magnetic ordering, the *ME* coupling is of fundamental interest. Higher order *ME* response characterizes disordered *type-III multiferroics* and extends the conventional multiferroic scenario toward *ME multiglass* (e.g. $Sr_{1-x}Mn_xTiO_3$) or *relaxor spin glass* (e.g. $PbFe_{0.5}Nb_{0.5}O_3$).

1 Introduction

In the beginning of this century, Hill (now: Spaldin) posed the provocative question 'Why are there so few magnetic ferroelectrics?' [1]. No doubt, she knew the answer, at least for the case of oxidic perovskites with the chemical formula ABO_3, where magnetism becomes established via transition metal ions such as Ni^{2+}, Fe^{3+}, Mn^{4+}. They have partially filled d shells. while virtually all ferroelectric (*FE*) perovskites contain transition metal ions with empty d shells, such as Ti^{4+}, Ta^{5+}, W^{6+}.

Wolfgang Kleemann (✉)
Angewandte Physik, Universität Duisburg-Essen, 47048 Duisburg, Germany
e-mail: wolfgang.kleemann@uni-due.de

Christian Binek
Department of Physics and Astronomy, University of Nebraska, Lincoln,
NE 68588-0299, USA
e-mail: cbinek@unl.edu

H. Zabel and M. Farle (eds.), *Magnetic Nanostructures,*
Springer Tracts in Modern Physics 246, DOI: 10.1007/978-3-642-32042-2_5,

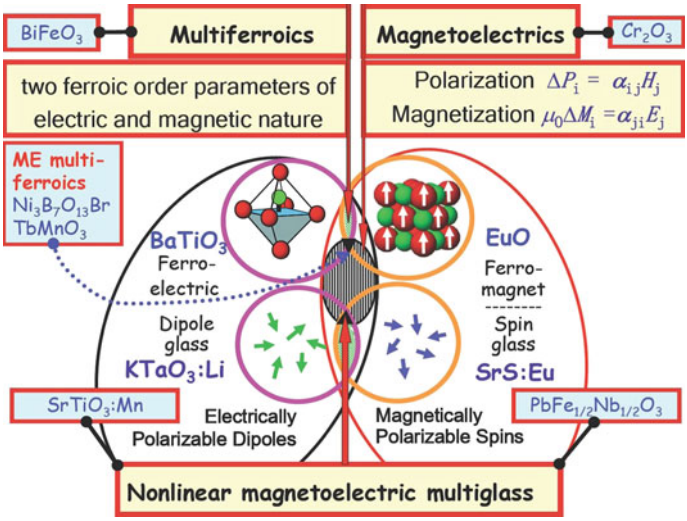

Fig. 1 The 'world of electrically and magnetically polarizable materials' including bare ferroics, multiferroics and linear magnetoelectrics [13], as well as dipole-, spin-, and non-linear *ME* multiglasses [14]

The latter favor off-centrality due to their ability to form covalent bonds with neighboring
oxygen ions. This process is strongly suppressed with d electrons present, which strongly discourage multiferroicity, i.e. the coexistence of magnetic and electric long-range order [2]. Nevertheless, many research groups became involved studying the rare situation of coexisting order parameters and their coupling. In particular, the magnetoelectric (*ME*) effect, *viz*. the cross coupling of the order parameters, magnetization $\boldsymbol{M}$ and polarization $\boldsymbol{P}$, to their conjugate fields, $\boldsymbol{E}$ and $\boldsymbol{H}$, was newly brought into focus because of its possible maximization in multiferroics [3]. Independently, however, the possible usefulness of *ME* antiferromagnets such as the "classic" α-Cr_2O_3 [4], had been acknowledged in the emerging field of spintronics. On the occasion of ICM-2003 at Rome/Italy we proposed a novel control mechanism for the exchange bias effect in magnetic heterostructures [5]. It takes advantage of the *ME* effect which occurs in the antiferromagnetic (*AF*) pinning layer. The contribution of the field-induced surface magnetization and its impact on the exchange bias effect was estimated and prompted us to propose several *ME* spintronic devices and memory concepts [6–10].

Also in other fields of application the *ME* effect enjoyed a breathtaking revival [11]. Upcoming visions were challenging and promising, e.g., switching magnetism with bare electric fields and thus getting rid of overheating in microelectronic devices [12]. Today we encounter a rich variety of multiferroics and magnetoelectrics. More than 400 papers were published in 2010 in both of these fields, many of them being mutually linked. The world of electrically and magnetically polarizable materials [13] is depicted in an updated version in Fig. 1. Its still growing complexity, which

we recently extended toward multiglass materials with non-linear *ME* interactions [14], will be subject to this overview.

2 Magnetoelectrics

2.1 ME Effect

The linear *ME* effect was first verified on the rhombohedral antiferromagnet chromia, α-Cr_2O_3, [4] and theoretically explored by Landau and Lifshitz [15]. They found that quite stringent symmetry properties must be fulfilled, namely time and spatial inversion symmetry, $\boldsymbol{T}$ and $\boldsymbol{I}$, respectively, have to be broken. This property is found in 69 magnetic point groups, out of which only 58 allow the *ME* effect because of additional restrictions [11]. In this case the free energy density $\boldsymbol{F}$ of the system contains a contribution, $W_{ME} = -\alpha\, \boldsymbol{HE}$, which is bilinearly coupled to $\boldsymbol{H}$ and $\boldsymbol{E}$ via the linear *ME* susceptibility tensor α. In the axial system Cr_2O_3 this term enables the formation of single *AF* domains by so-called '*ME* cooling' to below the *AF* ordering temperature, $T_N = 308\,\mathrm{K}$, [16] in simultaneously applied parallel or antiparallel magnetic and electric fields, respectively.

If a system with polar and magnetic properties does not fulfil the above symmetry conditions, it may still be a candidate for higher order *ME* effects. They emerge systematically from a series expansion of the free energy density under Einstein summation [2],

$$F(\mathbf{E},\mathbf{H}) = F_0 - \frac{1}{2}\varepsilon_0\chi^e_{ij}E_iE_j - \frac{1}{2}\mu_0\chi^m_{ij}H_iH_j - \alpha_{ij}H_iE_j - \frac{\beta_{ijk}}{2}E_iH_jH_k - \frac{\gamma_{ijk}}{2}H_iE_jE_k - \frac{\delta_{ijkl}}{2}E_iE_jH_kH_l \quad (1)$$

Apart from the field-induced terms coupled to bilinear functions E^2, H^2 and EH via linear susceptibility tensors χ^e_{ij}, χ^m_{ij} and α_{ij}, respectively, increased interest has recently arisen in second-order EH^2 and E^2H, and third-order E^2H^2 effects, synonymously referred to as α, β, γ, and δ effects, respectively. They are very precisely measured, e.g., by *ME* Superconducting Quantum Interference Device (SQUID) susceptometry [17] via the electric field-induced components of the magnetization

$$\mu_0 M_i = -\partial F/\partial H_i = \mu_0\chi^m_{ij}H_j + \alpha_{ij}E_j + \beta_{jki}E_jH_k + \frac{\gamma_{ijk}}{2}E_jE_k + \delta_{jkli}H_jE_kE_l \quad (2)$$

It involves external *ac* and *dc* electric and magnetic fields, $E = E_{ac}\cos\omega\,\mathrm{t} + E_{dc}$ and H_{dc}, and records the complex first harmonic *ac* magnetic moment, $m(t) = (m' - im'')\exp(-i\omega t)$. Frequencies low enough as to minimize the loss component, m'',

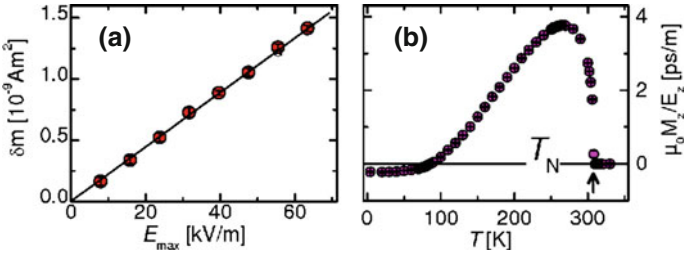

Fig. 2 Linear *ME* response of *AF* single domained single crystalline α-Cr_2O_3 measured according to Eq. (3) at the ac frequency $f = 1\,\text{Hz}$ as functions **a** of the ac field amplitude E_{max} at $T = 260\,\text{K}$ and **b** of the temperature T at $E_{max} = 63.4\,\text{kV/m}$. Adapted from [18]

e.g. $\omega/2\pi \approx 1\,\text{Hz}$, are routinely employed. Under well-defined protocols involving appropriate field amplitudes and directions with respect to the crystal coordinates, the full variety of susceptibility tensor components can be determined. In case of a polycrystalline sample with volume V the response

$$m' = (\alpha E_{ac} + \beta E_{ac} H_{dc} + \gamma E_{ac} E_{dc} + 2\delta E_{ac} E_{dc} H_{dc})(V/\mu_0) \tag{3}$$

allows determining orientation averaged coupling parameters α, β, γ, and δ.

As an example, Fig. 2 shows the *ME* response of an *AF* single domained (*ME* cooled in $E_{fr} = 300\,\text{kV/m}$ and $\mu_0 H_{fr} = 0.6\,\text{T}$) single crystal of α-Cr_2O_3 measured along the trigonal c axis [18]. In Fig. 2a the linearity with the electric field amplitude, $0 \le E_{\max} \le 63.4\,\text{kV/m}$, confirms linear *ME* coupling, where the slope yields the coupling constant $\alpha_{33}\,(T = 260\,\text{K}) = 3.8 \times 10^{-12}\,\text{sm}^{-1}$. The peak value of $\alpha_{33} = \mu_0 \delta m_z / V_{Ez}$, V = sample volume, is found to appear at $T = 266\,\text{K}$ as shown in Fig. 2b, while a steep descent toward $\alpha_{33} = 0$ is realized as $T \to T_N = 308.5\,\text{K}$. The gradual descent and change of sign at low temperatures is a consequence of competing single- and two-ion (exchange) effects [19].

These experiments show that the linear *ME* effect is usually very small. The above peak value of α-Cr_2O_3, denotes an average spin-flip rate of merely $\approx 5 \times 10^{-7}(\text{kV/cm})^{-1}$ [16].

However, owing to the particular boundary magnetism of *ME* antiferromagnets [20–23], which in the case of chromia is accompanied by temperature dependent surface reconstructions of its (0001) plane [24], the *ME* effect of Cr_2O_3 can be extremely efficient in composites with an adjacent *FM* layer. As shown in Fig. 3, even a rough surface of an *AF* single domained crystal retains a net magnetization, which can be switched magnetoelectrically [6, 23], and thus paves the way to pertinent spintronics applications. Details will be discussed in Sect. 1.2.2.

Particularly large *ME* effects are expected in the vicinity of the ferroic phase transitions, where suitable components of the χ^e and χ^m tensors diverge and $(\alpha_{ij})^2 \le \chi^e_{ii} \chi^m_{jj} c^{-2}$ maximizes [3]. Unfortunately no really existing material

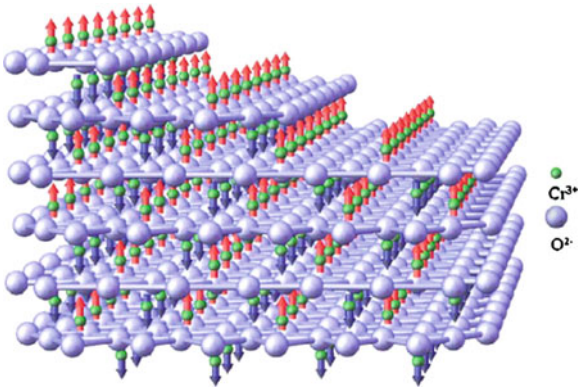

Fig. 3 The spin structure of a α-Cr_2O_3 single crystal with a stepped (0001) surface is shown for one of its two antiferromagnetic single domain states. *Up* (*red*) and *down* (*blue*) spins of the Cr^{3+} ions (*green spheres*) point along the *c*-axis. Adapted from [23]

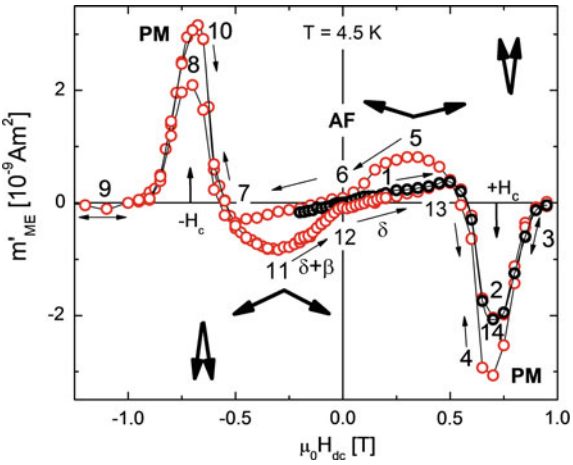

Fig. 4 *ME* response of polycrystalline $EuTiO_3$ at $T = 4.5\,\mathrm{K}$ under external fields E_{ac}, E_{dc}, and $\mu_0 H_{dc}$ (on cycling between $\pm 1.2\,\mathrm{T}$) as indicated by numbering from 1 to 14. The initial and final slopes δ and $\delta + \beta$, respectively, the critical fields $\pm\mu_0 H_c$ of the *AF*-to-*PM* phase transitions and the *AF* spin orientations are marked. Adapted from [26]

even roughly fulfills the condition of two simultaneous ferroic transitions. However, recently we have proposed a 'second-best' choice for achieving 'giant' *ME* response, namely the fluctuation regime (large χ^e_{jj}) of a quantum paraelectric material coming close to *FM* instability (large χ^m_{jj}). To this end we experienced $EuTiO_3$, which is a *G*-type *AF* below $T_N = 5.4\,\mathrm{K}$, where $\chi^e_{ii} \approx 400$ and $\chi^m_{ii} \approx 100$ due to strong *FM* next-nearest neighbor exchange interaction [25]. Figure 4 shows the *ME* moment m'_{ME} of a polycrystalline sample of $EuTiO_3$ excited at $T = 4.5\,\mathrm{K}$ with $E_{ac} = 8\,\mathrm{kV/m}$ under '*ME* annealing' [16] in constant $E_{dc} = 80\,\mathrm{kV/m}$ and cycling $|\mu_0 H_{dc}| \leq 1.2\,\mathrm{T}$.

When returning from saturation, e.g. $\mu_0 H_{dc} = -1.2\,\mathrm{T}$, and approaching $\mu_0 H_{dc} \to 0$, linear behavior with slope, $\delta_{eff} = 2.1 \times 10^{-21}$ sm/VA (Fig. 4, Sect. 11–12), indicates a large third order δ-effect, which is about 200× larger than that of the pioneering example of third order *ME* coupling, $Sr_{0.98}Mn_{0.02}TiO_3$ [14]. Closer inspection shows [26] that δ_{eff} contains contributions due to a second order β-effect, $\delta_{\mathrm{eff}} = \delta + \beta$, which becomes allowed due to the formation of an *AF* single domain in the presence of net electric polarization after *ME* annealing [16]. After crossing $\mu_0 H_{dc} = 0$, however, the memory of the *AF* single domain gets lost and the smaller slope δ (Fig. 4, section 12–13) indicates mere third order *ME* coupling.

Most surprisingly, however, the initial *ME* response suddenly changes sign at $\pm 0.6\,\mathrm{T}$ and develops a sharp peak with 'giant' $\left|m'_{ME}\right| \approx 3 \times 10^{-9}\ \mathrm{Am}^2$ at $\mu_0 H_c = \pm 0.68\,\mathrm{T}$. At these critical fields the system undergoes a phase transition from an *AF* spin-flop to (saturated) paramagnetic phases. The *ME* response is taking advantage of the critical fluctuations of the (*AF* ordered) transverse magnetization components, $\pm S_x$, and thus fulfills the prediction [3] in an impressive way. Very probably the peak is due to electric field-induced Dzyaloshinskii-Moriya exchange interaction, which gives rise to near-divergent non-diagonal third order *ME* response as $\pm S_x \to 0$ [26].

2.2 Magnetoelectronics with Magnetoelectrics

Gauge invariant quantum field theories [27] provide a conceptually unifying view on modern physics. Gauge coupling constants, which determine interaction strengths, are key elements in these field theories. In classical electromagnetism, the gauge coupling constant is the allegedly familiar electric charge, a degree of freedom controlling the coupling between charged matter and the electromagnetic field. Virtually all of today's electronic device applications utilize coupling between electron charge and electromagnetic field thus enabling control over the flow of electric current, e.g. in transistors, or the accumulation of charge in capacitors.

Pioneering experiments of Stern and Gerlach [28] in 1922 followed by the electron spin hypothesis of Uhlenbeck and Goudsmit [29] found a solid theoretical framework in Dirac's relativistic quantum theory of electrons [30]. Finally, spin as an additional, purely quantum mechanical internal degree of freedom of the electron was established.

From this point on, it seemed conceptually straightforward to take advantage of this additional degree of freedom for novel functionalities of electronic devices. However, the absence of direct coupling between spin and electric field makes the technologically most desirable electric control of the spin degree of freedom a scientific challenge.

Modern spintronics faces this challenge when striving to exploit the spin degree of freedom of electrons in addition to their charge for an advanced generation of electronic devices [31, 32]. In particular, voltage-controlled spin electronics is of vital importance to continue progress in information technology. The electric power

consumption and its accompanying production of Joule heat in present day complementary metal-oxide semiconductor (CMOS) integrated electronics is a major bottleneck. It limits further progress anticipated in Moore's law [33] through scaling of device structures. Ever decreasing structure sizes and increasing clock rates are ultimately limited by the possibility to efficiently manage power dissipation. Therefore, the major objective of an advanced spin-based technology is to reduce power consumption while enhancing processing speed, integration density, and functionality [8, 12, 34–36].

The first realizations of spintronic devices fall into the category of passive spintronics. Here electron currents are driven by electric fields without discriminating their spin states. Spin-polarization [37] of electric currents is internally produced and passively exploited via spin-selective transmission or scattering of electrons. Prototypical examples are giant magnetoresistance (*GMR*) and tunneling magnetoresistance (*TMR*) trilayer structures, which are utilized in magnetic field sensors and modern magnetic read heads fuelling a multi-billion dollar information industry [38, 39].

In contrast to passive spintronics there are additional attempts to exploit the full potential of the spin degree of freedom via active electric control [31]. A conceptual starting point for this approach is the celebrated Datta and Das spin transistor [40]. Here a *FM* source injects a spin-polarized current into a two-dimensional electron gas. A gate electrode allows for voltage-controlled precession of the electron spin. The latter control is envisioned with the help of the Rashba effect [41]. Subsequently the spin state is analyzed by a *FM* drain, where—depending on the spin state of the incoming electron—reflection or transmission takes place. The Rashba effect originates from spin-orbit coupling in two dimensional electron gases. It gives rise to a spin-dependent energy splitting proportional to the electron's crystal momentum and thus suggesting the possibility to control the spin orientation with the help of an applied electric field [41]. Many of today's challenges in the realization of spintronic devices, especially those which rely on spin-polarized currents, have been first encountered in the architecture of the spin-transistor proposed by Datta and Das [40]. Here, spin injection, lifetime and manipulation are among the major obstacles towards spintronic applications [31].

Recently, spin-polarized currents carrying net spin and, hence, angular momentum, have been successfully exploited for spin-torque transfer. The latter can result in current induced magnetization switching. Record-low current densities achieving complete magnetization switching are today in the order of only $1\,\mathrm{MA/m^2}$ [42]. As promising as these results are, those achievements are still a domain of low temperature physics and not yet suitable for applications.

Considering the difficulties which spintronics based on spin-polarized currents faces, it appears desirable to eliminate currents, e.g. for magnetization switching, in first place. Controlling magnetism at thin-film interfaces at room temperature by purely electrical means is therefore a key challenge to better spintronics [43–46].

As mentioned above, the linear *ME* susceptibility of *ME* antiferromagnets with long-range order near room temperature is discouragingly small owing to its relativistic origin [16]. Despite this obstacle, in particular chromia, α-Cr_2O_3, revived

among the most promising materials for voltage-controlled spintronics. The key to success in overcoming the smallness of the linear *ME* bulk susceptibility of at most $\approx$4 ps/m (Fig. 2) lies in utilizing the recently discovered isothermally controllable boundary magnetization at the (0001) surface or interface of antiferromagnetically ordered chromia, which turns out to be roughness-insensitive [20, 23], thanks to the unique symmetry conditions in *ME* antiferromagnets allowing for robust boundary magnetization in the *AF* single domain state [20–22]. The realm of linear *ME* response is clearly left, when the *AF* spin structure is magnetoelectrically switched between two time-reversed single domain states. The boundary magnetization, a generic property of all *ME* antiferromagnets [22], couples to the three-dimensional *AF* long-range order parameter, η, and thus follows the latter on its electrically controlled reversal. Since the pioneering work of Martin and Anderson [47] it is known that electrically controlled switching of an *AF* single domain state in bulk chromia between $\eta = \pm 1$ is possible in a non-linear isothermal process. It requires overcoming a critical threshold given by the temperature dependent product $|E \cdot H|_c$, where $\boldsymbol{E}$ and $\boldsymbol{H}$ are isothermally applied axial electric and magnetic fields. When the boundary magnetization of a *ME* antiferromagnet such as chromia is exchange coupled to an adjacent ferromagnetic thin film, a variety of spintronic applications can be envisioned.

The investigation of chromia-based exchange bias systems, which aim at electric control of the exchange bias field has been pioneered by the authors of this review chapter [5–7]. Our suggested spintronic applications have been acknowledged as ground-breaking proposals which

> triggered much activity in the search for exchange bias using multiferroics . . . and ultimately its electrical control [48].

All of those spintronic applications exploit exchange bias and its electric control as the basic building block of a potential spintronic device. Quantum mechanical exchange coupling at the interface between chromia and a perpendicularly anisotropic *FM* heterolayer such as Co/Pt or Co/Pd induces unidirectional magnetic anisotropy in the *FM* film. The electric control of the resulting exchange bias effect allows shifting the global magnetic hysteresis loop of the Co/Pt or Co/Pd film isothermally and reversibly along the magnetic field axis back and forth between negative to positive field values.

Recently we evidenced the intimate coupling between surface magnetization and bulk *AF* registration via the crossover behavior of the exchange bias field $\mu_0 H_{eb}$ versus temperature T of a crystalline sample of Cr_2O_3(0001) attached to a trilayer Pt0.5nm/Co0.35nm/Pt3nm grown under UHV conditions after *ME* field-cooling in $\mu_0 H_{fr} = 0.3$T and $E_{fr} = -500$ kV/m (Fig. 5) [49]. Solid red and dot-dashed black lines indicate best fits of all data points, respectively, to the power law $C(1-T/T_N)^{\beta}$ with $\beta = 0.30$ and, slightly worse, to the mean value of the Cr^{3+} spins within mean field theory, $\langle S \rangle_T = S B_{S=3/2}(T_N/T)$, where $B_{S=3/2}$ is the Brillouin function to $S = 3/2$ and $T_N = 308.5$ K. Alternatively and much better fitting, a sequential scenario is pursued from 3*D*-Heisenberg bulk (double-dot dashed blue) to surface critical

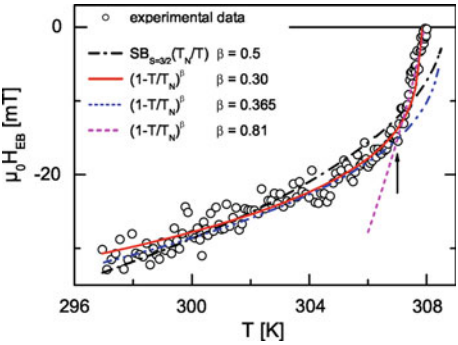

Fig. 5 Exchange bias field $\mu_0 H_{eb}$ versus T of a *ME* field-cooled ($\mu_0 H_{fr} = 0.3\,\mathrm{T}$ and $E_{fr} = -500\,\mathrm{kV/m}$) heterostructure Cr_2O_3(0001)/Pt 0.5nm/Co 0.35nm/Pt3nm with best-fits to power laws $C(1 - T/T_N)^{\beta}$ of all data points (*solid red line*), to mean field Brillouin function $SB_{S=3/2}(T_N/T)$ (*dot-dashed black line*), and as crossover between 3*D*-Heisenberg bulk ($\beta = 0.365$; *dotted blue line*) and surface critical behavior ($\beta = 0.81$; *dashed magenta line*), respectively. Adapted from [49]

behavior (dashed magenta) with $\beta = 0.365$ changing into 0.81 at the crossover temperature $T_{cr} = 0.996\,T_N$ (vertical arrow in Fig. 5).

The control of exchange bias, either isothermally or via *ME* annealing, is at the center of the functionality of spintronic applications where interface magnetization can be switched without the need of spin-polarized currents. Figure 6 shows an example of a proposed device which is based on spin-valve architecture. The device was originally envisioned [8] on the basis of the linear *ME* effect. As outlined above, the linear *ME* effect of chromia is small for fundamental reasons. Hence, its impact on electrically controlled exchange bias is small [50] and might only become sizable in the presence of electric fields with significant strength exploring the stability limits close to dielectric breakdown. Currently, there are no chromia thin films, which come close to bulk dielectric properties, however, the boundary magnetization of *AF* magnetoelectrics may virtually 'shield' the interface from being affected by the electrically induced magnetization in the bulk. Therefore, isothermally operating spintronic devices become better feasible in the framework of the demonstrated electrically switchable boundary magnetization, where the smallness of the linear *ME* susceptibility is of no concern and the boundary magnetization is actively exploited. The spin-valve heterostructure, when pinned through a *ME* antiferromagnet such as chromia, enables functionality of a logic device with additional magnetic storage capability. Exchange coupling between chromia's boundary magnetization (see ensemble of small, parallel arrows in the left and right panels of Fig. 6) and the interface magnetization of the bottom *FM* layer (*FM*1) gives rise to isothermally switchable exchange bias fields, $\pm\mu_0 H_{EB}$.

Temperature assisted switching through *ME* annealing was first shown on the hysteresis cycles of a *FM* multilayer Pt 0.5nm/[Co 0.3nm/Pt 1.5nm]$_3$/Pt 1.5nm on top of a (0001) oriented single crystal of Cr_2O_3 by switching $\mu_0 H_{EB}$ between -32.1

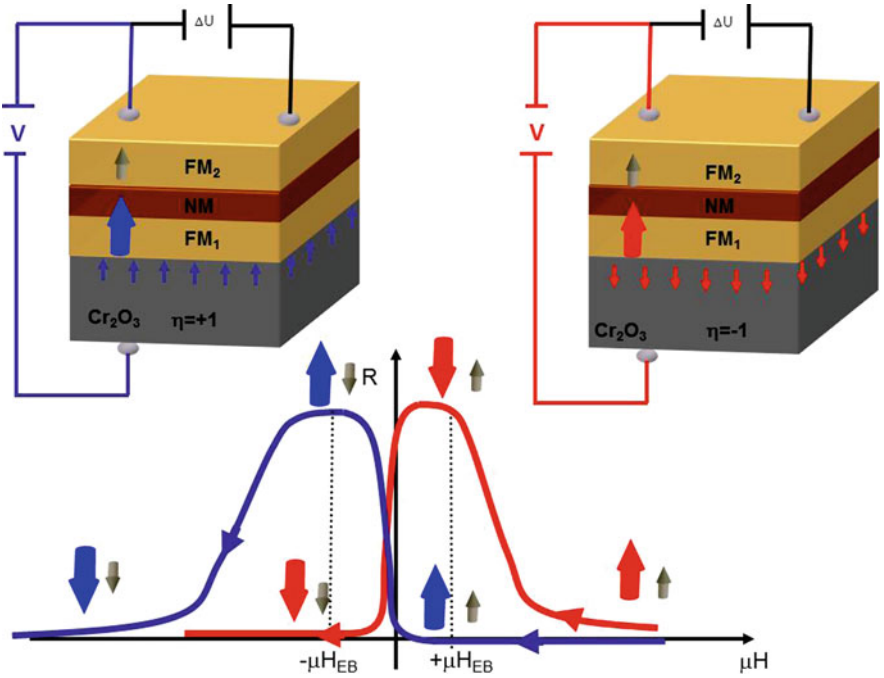

Fig. 6 Schematics of a GMR device based on the antiferromagnet chromia as *ME* pinning layer voltage-controlling the *FM* state of the adjacent ferromagnet *FM*1 [8]. A nonmagnetic spacer, *NM*, builds together with the free *FM* layer *FM*2 the remaining components of a GMR-type device. ΔU measures the resistance in current-in-plane geometry. Idealized hysteresis-free magnetosresistance curves are shown for positive and negative exchange bias fields originating from switchable states of the chromia boundary magnetization coupling to the *AF* single domain states with either positive ($\eta = +1$) or time reversed negative ($\eta = -1$) order parameter. η and the boundary magnetization (*small arrows*) are isothermally controlled by the applied voltage V in the presence of an axial magnetic field

and +30.3 mT [6]. Complete temperature assisted switching of the entire hysteresis curves free from superpositions, with similar values of $\mu_0 H_{EB}$ was successful with a *FM* trilayer Pt 0.5nm/Co 0.35nm/Pt 3nm attached to $Cr_2O_3(0001)$ [51] as shown in Fig. 7. The normalized hysteresis curves were measured at $T = 297$ K after cooling the sample from $T = 350$ to 297 K in the two freezing fields, $\mu_0 H_{fr} = 0.3$ T and $E_{fr} = -500$ kV/m (blue open circles) or $E_{fr} = +500$ kV/m (red solid circles), respectively. The broken vertical arrow mimics isothermal switching of the magnetization under constant magnetic bias, $\mu_0 H_0 \approx 20$ mT, and sufficiently large electric fields satisfying the Martin-Anderson limit, $|\mu_0 H_0 E_0|_{cr} \approx 500$ mT kV/mm [47].

The pioneering device architecture [8] depicted in Fig. 6 relies on isothermal control of the pinning of the *FM* layer1. The voltage-controlled pinning is realized through the exchange bias mechanism. It is a major leap, both conceptually and experimentally, to progress from thermally assisted switching to isothermal switching.

The achievement of the latter could finally be stated in Ref. [23], 5 years after the pioneering work reported in Ref. [6] and even 7 years after we introduced the idea of isothermal voltage-controlled exchange bias [5]. A conceptual difficulty for isothermal device functionality originates from the fact that constant temperature control of the exchange bias field exploits switching between two degenerate *AF* single domain states of chromia. A sophisticated consideration of the exchange bias phenomenon acknowledges that the unavoidable presence of roughness at the *AF*/*FM* interface should eliminate exchange bias for a conventional uncompensated *AF* pinning system if the latter is in a perfect single domain state. Hence, one might expect, that isothermal switching between *AF* single domain states of chromia does not give rise to sizable voltage-controlled exchange bias. In order to overcome this conceptual difficulty one has to realize the key role which our newly discovered boundary magnetization plays for isothermal switching of exchange bias [20–23] in addition to the established switchability of the *AF* domain state via the Martin-Anderson mechanism [47]. Boundary magnetization is a thermodynamic equilibrium property of *ME* single domain antiferromagnets based on rigorous symmetry considerations. The equilibrium properties include the entropy driven equilibrium roughness at surfaces and interfaces [22].

In the *ME* chromia, the *AF* single domain state gives rise to sizable roughness-insensitive equilibrium boundary magnetization. Its strong coupling with the *AF* order parameter (Fig. 5) ensures that the *AF* interface magnetization follows the isothermal switching of the *AF* single domain state thus giving rise to isothermal switching of exchange bias. The uniqueness of this exchange bias phenomenon as a consequence of the particular role of boundary magnetization is confirmed by the absence of training or aging effects [23] which are a hallmark of regular exchange bias systems [52, 53]. It is this inherent potential of *ME* antiferromagnets for isothermal switching of boundary magnetization making the device architecture of the example shown in Fig. 6, and described together with additional isothermal device concepts in Ref. [8], feasible.

In the example displayed in Fig. 6, the pinned ferromagnet *FM*1 (large arrow) and the magnetization of the free top layer *FM*2 (small arrow) are separated by a nonmagnetic (*NM*) spacer and form a GMR-type device. A voltage ΔU is used to measure the magnetoresistance, R versus H, of the *FM*1/*NM*/*FM*2 trilayer in current-in-plane geometry. A voltage difference V applied in the presence of a symmetry breaking magnetic field of arbitrary strength can provide control over chromia's *AF* spin registration, $\eta = 1$. Therefore, electric control over the boundary magnetization is achieved when overcoming the product field threshold $|\boldsymbol{E} \cdot \boldsymbol{H}|_c$, where $E = V/d$ is the electric field across the chromia film of thickness d. The orientation of the boundary magnetization follows the sign of $(\boldsymbol{E} \cdot \boldsymbol{H})_c$ thus controlling in turn the sign of the exchange bias field [6, 23]. From numerous investigations of chromia-pinned exchange bias heterostructures [6, 23, 51, 54] it is evident that exchange bias fields can be realized, which overcome the intrinsic coercive field of a soft pinned *FM* film (*FM*1). Inverting the critical voltage V provides the electric field which, in the presence of an arbitrarily small magnetic field, allows changing the pinning direction. Depending on the orientation of the boundary magnetization we obtain two

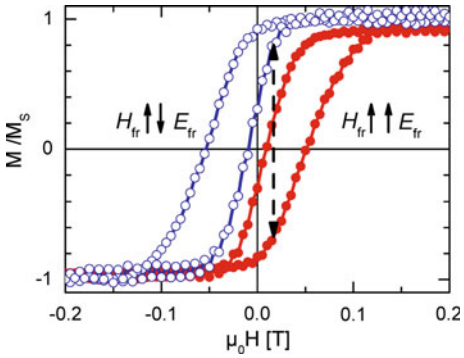

Fig. 7 Normalized hysteresis curves of the heterostructure Cr_2O_3(0001)/Pt 0.5nm/Co 0.35nm/Pt 3nm measured at T = 297 K after field cooling from T = 350 to 297 K in $\mu_0 H_{fr} = 0.3$ T and $E_{fr} = -500$ kV/m (*blue open circles*), and $E_{fr} = 500$ kV/m (*red solid circles*), respectively. The *vertical arrow* indicates isothermal ME switching of the magnetization at finite $\mu_0 H$ (see text). Adapted from [51]

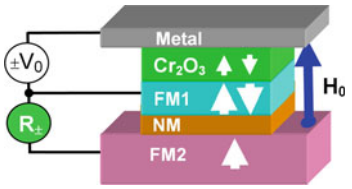

Fig. 8 Schematic view of a MERAM cell [9, 10] based on *ME* Cr_2O_3(0001) controlling the magnetization of the Pt/Co/Pt trilayer *FM*1 via voltages $\pm V_0$ and constant magnetic stray field H_0 of NdFeB thick film *FM*2. $R_\pm$ is the corresponding giant (or tunneling) magnetoresistance along *FM*1/*NM*(Cu or MgO)/*FM*2. Adapted from [9, 10]

distinct magnetoresistance curves, R versus H, shown in the lower panel of Fig. 6. For simplicity the sketch neglects *FM* hysteresis. Pairs of large and small arrows assigned to specific positions in the R versus H curves illustrate the successive order of magnetization switching of the layers when lowering the magnetic field strength from positive saturation. The parallel or antiparallel magnetic configurations at low field values are of particular interest for the functionality of the device. Here, the relative orientation of *FM*1 with respect to *FM*2 depends on the sign of the exchange bias field. For small applied magnetic fields, which control the magnetization state of the free layer *FM*2, it is possible to control the relative orientation between *FM*1 and *FM*2 purely through the polarity of V.

Alternatively, the 'free' layer *FM*2 may be replaced by a hard magnetic thick film (of e.g. NdFeB), which provides a constant stray field H_0 as shown in the *ME* random access memory cell MERAM [9, 10] of Fig. 8. In conjunction with the switchable electric field $E_0 = \pm V_0/d$ it determines the polarity of η in the Cr_2O_3 layer, and thus the sign of the magnetization in the 'slave' layer *FM*1 (e.g. ultrathin Pt/Co/Pt [9, 10]). The serial resistance R of *FM*1 and *FM*2 embedding a non-magnetic (*NM*)

Table 1 Physical and logical input and output parameters of a ME XOR device [8]

Phys. in 1	Phys. in 2	Logic in 1	Logic in 2	Phys. out	Logic out
$(EH)_C > 0$	$H < 0$	0	0	R_{high}	0
$(EH)_C > 0$	$H > 0$	0	1	R_{low}	1
$(EH)_C < 0$	$H < 0$	1	0	R_{low}	1
$(EH)_C < 0$	$H > 0$	1	1	R_{high}	0

conducting (e.g. Cu) or insulating tunneling (*e.g.* MgO) layer thus encounters two different values due to *GMR* or tunneling magnetoresistance (*TMR*) corresponding to logical "0" and "1", respectively.

Combining logical and magnetic storage function is a very attractive use of magnetic storage elements, with speed, information retention, and flexibility advantages [55, 56]. Next we outline in some detail how such the device of Fig. 6 can provide, e.g., the logical functionality of an exclusive OR gate (XOR) [8]. The polarity of the voltage V controls the sign of the field product EH which can be used as one logical input. The direction of a subsequently applied external magnetic field is the other logical input. The various combinations of the input variables result in a high or low value of the resistance as logical output. For example, we assign a logical input "0" to $(EH)_C > 0$ (blue R vs. H curve in Fig. 6), and logical input value "1" to $(EH)_C < 0$ (red R vs. H curve in Fig. 6). A positive applied field, $H > 0$, is identified with a logical "1" input, and $H < 0$ corresponds to a logical "0". If both inputs are "0", or "1" the resistance value, R, is high due to antiparallel alignment of the *FM* layers. We assign the logical output "0" to a state of high resistance and correspondingly a logical output "1" to a configuration of low resistance. The two other logical input configurations result in a low resistance output, assigned to output "1". Table 1 summarizes the physical as well as logical input and output parameters of the device in accordance with the truth table of an exclusive disjunction.

When giving up on the advantage of virtually powerless switching, even more functionality can be envisioned [8] when combining current-induced switching due to a voltage ΔU in a perpendicular geometry with the *ME* control due to V.

3 Multiferroics

3.1 Single Phase Multiferroics

Multiferroics (*MF*s) are classified single or multiphase, if the order parameters involved occur either in one single compound or in different components of a composite material [57]. Since recently [58] one further distinguishes *type-I* and *type-II single phase MF*s. *Type-I MF*s like $Fe_3B_7O_{13}Cl$, $BiMnO_3$, $BiFeO_3$, $Fe_{2-x}Ga_xO_3$, $LuFe_2O_4$, Fe_3O_4 etc. have independent origins of the spontaneous order parameters,

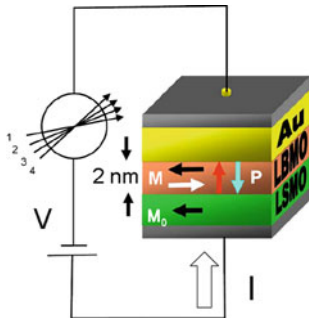

Fig. 9 Schematics of a multiferroic 4-bit memory spin-valve involving a non-*ME FM-FE* LBMO tunneling barrier, a LSMO fixed magnetization layer, and an Au sink electrode. Four different currents *1*, *2*, *3*, and *4* are due to independently field-switchable *TMR* and *TER* values. Adapted from [61]

P_s and M_s (or *AF* L_s). Contrastingly, in *type-II MF*s like $LiCu_2O_2$, $CuFeO_2$, $Ni_3V_2O_8$, $TbMnO_3$, $TbMn_2O_5$, $MnWO_4$, $CoCr_2O_4$, Ca_3CoMnO_6 etc. the ferroelectricity is primordially due to non-collinear magnetism (see below).

The increased variety of internal degrees of freedom opens new possibilities for making use of multiferroics in information technology. Increased data storage may be realized by exploiting both magnetic and electric switching. In particular multiple-valued *magnetoresistance* cells are a promising route to further increase the storage density, e.g. in magnetic random access memory (*MRAM*) technology.

Multiferroic tunnel junctions (*MFTJ*) promise just that. They are magnetic tunnel junctions exploiting resistance control through ferromagnetic switching and simultaneously resistance control through switchability of the polarization of the ferroelectric tunneling barrier. *MFTJs* are envisioned as the next logical step towards four-state non-volatile memory devices with functionality beyond today's conventional *MRAM* technology [59, 60].

An impressive step toward this end has been made by Gajek et al. [61], who investigated a spin valve with the layer sequence $La_{0.7}Sr_{0.3}MnO_3$(LSMO) / $La_{0.1}Bi_{0.9}MnO_3$ (LBMO)/Au (Fig. 9), where the halfmetallic *FM* LSMO defines the fixed magnetization, $\boldsymbol{M}_0$, against which that of the multiferroic LBMO, $\pm M$, is switched by a magnetic field. The *FE* polarization, $\pm P$, of LBMO (Curie temperature $T_c^e \approx 400\,\mathrm{K}$) is switched by the voltage V across the Au top electrode and the LSMO bottom layer. It was shown [61] that four different tunnelling currents, *1*, *2*, *3*, and *4*, due to *TMR* and Tunneling Electro-Resistance (*TER*) [44] arise under the different mutual orientations of the order parameters, $\boldsymbol{M}$ and $\boldsymbol{P}$, in the 2 nm thick LBMO layer, as desired for quaternary logic. It should be stressed that in this novel non-volatile memory cell the vanishing linear *ME* coupling within LBMO is imperative and highly welcome. Unfortunately, its too low magnetic transition temperature, $T_c^m \approx 90\,\mathrm{K}$, rules out technological applications, but its idea will continue fueling future search for more suitable *MF* materials. Another step to higher performance might be to thin-down the *FM* LSMO electrode in the spin valve of Fig. 9 to a few

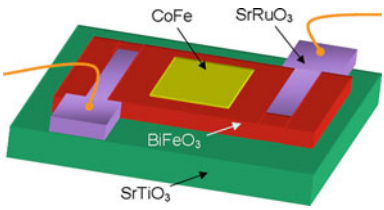

Fig. 10 Schematics of the electric control of the easy axis of CoFe magnetization via multiferroic domain switching of $BiFeO_3$. Adapted from [64]

lattice spacings, which is expected to substantially increase the *TER* in the *FE* (*MF*) tunneling barrier [62].

Quite often *type-I MF*s reveal high ordering temperatures, but their theory—including the *ME* coupling—can be very complex. Probably the most popular *type-I* single phase *MF* is $BiFeO_3$ with record high ordering temperatures, $AF\ T_N = 643\,\mathrm{K}$ and $FE\ T_c = 1103\,\mathrm{K}$, which makes it the '*holy grail*' in the world of multiferroics [63]. Despite or—since recently—because of its large variety of different *FE*-ferroelastic and *AF* domains it has ever since been considered a hot favorite for applications in sensorics or spintronics [64, 65].

As an example, Fig. 10 shows the schematics of the electric control of the easy axis of CoFe magnetization via multiferroic domain switching of $BiFeO_3$ [64]. It is an attempt to make use of the multidomain nature of $BiFeO_3$ in a device, which comes close to the technological break-even of switching magnetism with an electric field. Chu et al. [64] switched the magnetic anisotropy of a thin *FM* CoFe layer attached to an $AF + FE$ film of $BiFeO_3$ (Fig. 10). By lateral application of an electric field the *FE* polarisation is switched together with the elastically coupled *AF* domains. As a result of exchange coupling the *FM* anisotropy axis is switched by 90°, which might be useful for information storage in spintronic devices. Another important step toward *ME* control of a spintronic device was taken by Lebeugle et al. [65], who demonstrated electric field switching of the magnetic anisotropy of a soft magnetic layer of $Ni_{0.78}Fe_{0.22}$ (NiFe) attached to a single crystal of ferroelectric (*FE*) and *AF* $BiFeO_3$. It was shown that an electric field-induced change of the *FE* polarization of the BFO substrate is able to toggle the easy direction of the magnetization in the NiFe layer by use of the *ME* effect. In fact, two successive coupling mechanisms are exploited. The first is the *ME* coupling within BFO between the *AF* and the *FE* order. As a matter of fact, it is found that the *FE* domains, i.e. regions with different collective polarization, go perfectly with the *AF* ones due to the accompanying differently oriented lattice strain. The second coupling process is based on exchange interactions at the interface between the *AF* BFO and the *FM* NiFe. More precisely, it is the projection of the *AF* order which couples to the *FM* magnetization. Unfortunately, the magnetization of the NiFe layer could not completely be switched along the directions of the anisotropy axes as it is impossible to form a ferroelectric single domain in the (001) plane of BFO. Out of the manifold

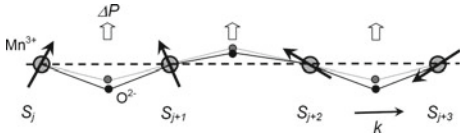

Fig. 11 Counterclockwise spin spiral of $TbMnO_3$ promoting an upward directed electric polarization by forced oxygen displacements. Adapted from [66]

of eight differently poled domains only four of them can be selected by a uniform intraplanar field.

On the other hand, the theory of *type-II MF*s is symmetry based and straightforward, albeit often quite sophisticated. In most cases the ordering temperatures are very low and the order parameter amplitudes ridiculously (from an application point of view) small. E.g., in the orthorhombic perovskite system $TbMnO_3$ it was found that spiral spin ordering due to Dzyaloshinskii-Moriya exchange interaction breaks both $\boldsymbol{T}$ and $\boldsymbol{I}$, such that a net polarization $\boldsymbol{P} = \gamma \left(\boldsymbol{r}_{\mathrm{j}} - \boldsymbol{r}_{\mathrm{j+1}}\right) \times \left(\boldsymbol{S}_{\mathrm{j}} \times \boldsymbol{S}_{\mathrm{j+1}}\right)$ becomes induced as depicted in Fig. 11 [66]. In the Ising chain magnet Ca_3CoMnO_6 [67] alternating Co^{2+}/Mn^{4+} ionic order creates competing *FM* nearest neighbor and *AF* next-nearest neighbor exchange interactions. As a consequence, up-up-down-down ('ANNNI-type') spin ordering arises below $T_N \approx 16\,\mathrm{K}$. It is accompanied by asymmetric exchange striction, which breaks $\boldsymbol{I}$ and, hence, induces electric polarization below T_N [68].

3.2 Composite Multiferroics

Composites or core-shell structures consisting of a *FE* and a *FM* material represent an alternative to intrinsic *MF* materials [69]. These multiphase *MF*s are usually based on stress-strain coupling between the order parameters of *FE*-piezoelectric and *FM*-magnetostrictive components like $BaTiO_3$ and $CoFe_2O_4$, respectively [70]. This pioneering self-assembled ceramic material has become famous for its large *ME* voltage coefficient $\alpha_{ME}(BaTiO_3/CoFe_2O_4) = dE/dH = 130\,\mathrm{mV/cmOe}$. This corresponds to a linear *ME* coefficient $\alpha = \varepsilon_0 \varepsilon_r \alpha_{ME} \approx 720\,\mathrm{ps/m}$ (assuming $\varepsilon_r \approx 500$), which exceeds that of Cr_2O_3 at 260 K (Fig. 2) [4] and even that of the record holding single phase *type-I MF* material $TbPO_4$ [71, 72] by factors of about 180 and 20, respectively.

Among the *ME* coupled multiferroic oxide composites [73] also hybrid oxide-metal composites such as $BaTiO_3$-Fe have successfully been tested [74]. Figure 12a shows magnetic properties of a thin Fe film evaporated onto the (001) face of a *FE* $BaTiO_3$ crystal under thermal cycling between the different crystalline phases of the substrate, which are (on cooling): cubic → tetragonal → orthorhombic → rhombohedral. Both the coercivity, $\mu_0 H_c$, and the scaled remanence, M_r/M_s, reveal net kinks at the phase boundaries, which are related to typical changes of substrate morphology

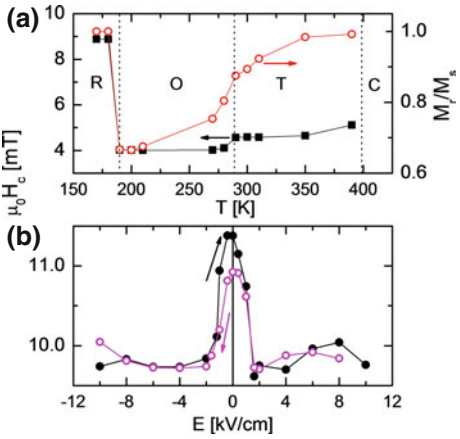

Fig. 12 Strain controlled magnetism of a $BaTiO_3$(001)/Fe(10 nm) composite: **a** coercivity, $\mu_0 H_c$ (*squares*), and scaled remanence, M_r/M (*circles*), under rhombohedral (R)-orthorhombic (O)-tetragonal (T) phase changes of the $BaTiO_3$ substrate within 170 K$\leq T \leq$ 390 K; **b** coercivity $\mu_0 H_c$ at $T = 300$ K under ascending and descending (*arrows*) electric fields, respectively. Adapted from [74]

and FE domain pattern. Figure 12b demonstrates the converse piezoelectric effect of $BaTiO_3$ exerted onto the coercivity of Fe, $\mu_0 H_c$, under ascending and descending electric fields, respectively. Single domaining of the *FE* substrate under large electric fields (e.g. $\approx \pm 10$ kV/cm) diminishes the coercive field by ≈ 10 %, large enough to be useful in spintronic devices. A first obvious step into this direction is the piezoelectric control of exchange bias. To this end we exploit piezoelectrically tuned magnetostriction in a $BaTiO_3$/Co/CoO heterostructure [75]. Here, piezoelectrically controlled exchange bias originates to a large extent from the magnetostrictive contribution to the magnetic anisotropy of the Co film. When cooling the strained heterostructure to below its blocking temperature, stress-induced changes in the magnetic anisotropy alter the relative orientation of the *FM* and *AF* interface magnetization thus allowing to electrically tune the exchange bias field [75]. Recent progress in epitaxial growth of multiferroic $BaTiO_3$/Fe(001) heterojunctions [76] gives hope that such elementary material combinations might become candidates of spintronics applications in the near future. Note, however, that isothermal electric control of exchange bias near room temperature remains unique for the chromia based exchange bias system [9, 10, 23].

ME oxide-metal composites have meanwhile achieved the highest conversion rates and are now considered for applications in transducer, filter and sensor devices [69]. Record high *ME* response can be achieved by taking advantage of resonance effects. One possible design is shown in Fig. 13, where amorphous *FM* METGLAS (=FeBSiC) layers are excited by a longitudinal magnetic *ac* field and laterally coupled to a periodically poled *FE* PZT [=Pb(Zr,Ti)O_3] piezofiber layer. The voltage

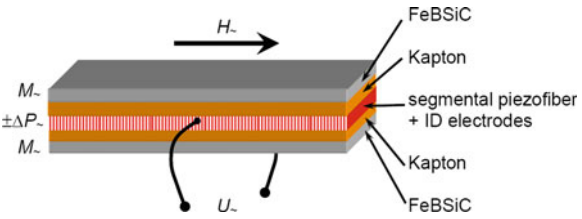

Fig. 13 Schematics of an *ME* composite consisting of two magnetostrictive FeBSiC layers and a piezoelectric periodically poled PZT piezofiber layer intercalated by Kapton films [69]. Adapted from [77]

conversion factor $\alpha_{ME} = 0.8\,\mathrm{kV/cm\,Oe}$ (corresponding to $\alpha \approx 5 \times 10^{-6}$ s/m assuming $\varepsilon_r \approx 600$) at the resonance frequency $f \approx 2\,\mathrm{kHz}$ [77] exceeds that of archetypical Cr_2O_3 by six orders of magnitude.

3.3 Disordered Multiferroics

The nature of glassy states in disordered materials has long been controversially discussed. In the magnetic community generic spin glasses [78] are meanwhile accepted to undergo phase transitions at a static freezing temperature T_g (=glass temperature), where they exhibit criticality and originate well-defined order parameters. Widely accepted, albeit still under debate [79], also polar systems may undergo a transition into a generic 'dipolar' or 'orientational glass' state [80], which fulfils similar criteria as the spin glass state. Hence, it appears quite natural to coin the term 'multiglass' for a new kind of *MF* material revealing both polar and spin glass properties, which we discovered in ceramic solid solutions of $Sr_{0.98}Mn_{0.02}TiO_3$ [14]. On one hand, the Mn^{2+} ions being randomly distributed and off-centered from their Sr^{2+}-sites [81] form nanopolar clusters with frustrated dipolar interaction and give rise to a dipolar glass state below $T_g^e \approx 38\,\mathrm{K}$ [14, 82]. This can easily be judged from the asymptotic shift of the dynamic dielectric susceptibility peak, $T_m(f)$, for frequencies within the range $10^{-3} \le f \le 10^6\,\mathrm{Hz}$ in Fig. 14a. It follows glassy critical behaviour, i.e. $f(T_m) \propto (T_m - T_g^e)^{z\nu}$ with the dynamic critical exponent $z\nu = 8.5$.

On the other hand, frustrated and random Mn^{2+}–O^{2-}–Mn^{2+} (supported by spurious Mn^{4+}–O^{2-}–Mn^{2+} bonds [83]) superexchange is at the origin of spin glass formation below $T_g^m \approx 34\,\mathrm{K}$. This temperature marks the confluence of three characteristic magnetization curves recorded upon zero-field cooling/field heating (*ZFC*), field cooling (*FC*), and subsequent zero-field heating (thermoremanence, *TRM*) as shown in Fig. 14c. It should be noticed that both glassy states have unanimously been confirmed by clear-cut aging and rejuvenation effects in their respective *dc* susceptibilities [14]. The 'holes' burnt into the electric and magnetic susceptibilities by waiting in zero field for 10.5 h at 32.8 K and for 2.8 h at 33 K, respectively, and subsequent heating with weak electric and magnetic probing fields are shown in

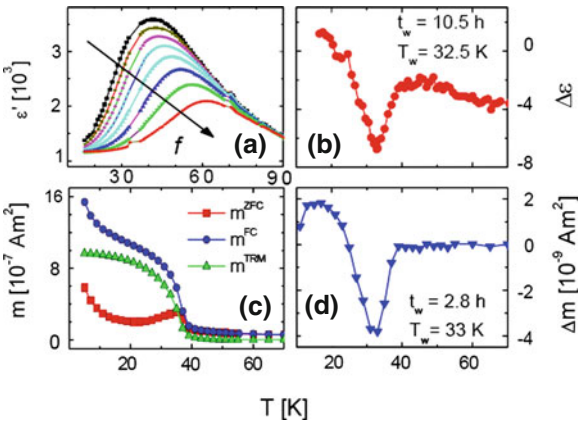

Fig. 14 Dielectric susceptibility $\varepsilon(T)$ of $Sr_{0.98}Mn_{0.02}TiO_3$ ceramics recorded at frequencies $10^{-3} \leq f \leq 10^6$ Hz (**a**) and magnetization measured on *ZFC-FH, FC* and subsequent *ZFH* (*TRM*) (**c**). Holes $\Delta\varepsilon(T)$ and $\Delta m(T)$ burnt in zero fields at $T_{wait} = 32.5$ K for 10.5 h (**b**) and $T_{wait} = 33$ K for 2.8 h (**d**) corroborate memory and rejuvenation, respectively, of both dielectric and magnetic glassy subsystems. Adapted from [14]

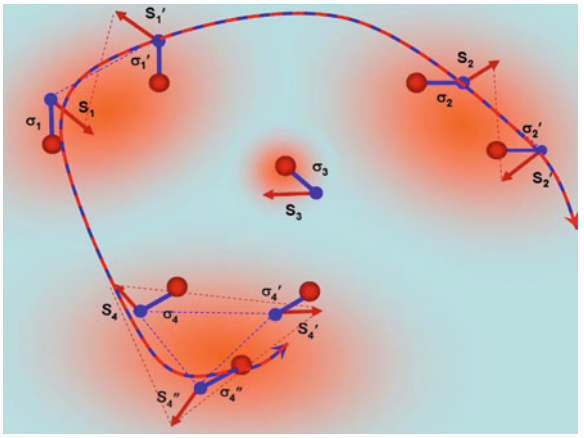

Fig. 15 Multiglass formation in $SrTiO_3$ doped with Mn^{2+} impurities involving *FE* polar clusters (pseudospins σ_j, σ_j', σ_j'') and superantiferromagnetic spin clusters (S_j, S_j', S_j''). Adapted from [82]

Fig. 14b and d. They corroborate the glassy ground states of both the polar and the magnetic subsystem and their compatibility with spin glass theory [78, 79]. Observation of biquadratic (δ-type) *ME* interaction—see Eq. 3 [14]—is fully compatible with the low symmetry of the compound and supposed to crucially reinforce the spin glass 'ordering' as schematically depicted in Fig. 15 [82]. Both glassy systems are assumed to occupy the same spatial network.

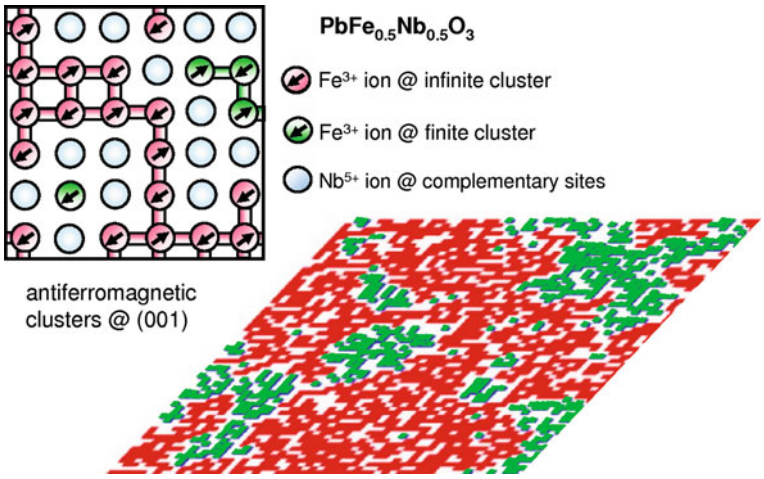

Fig. 16 *AF* Fe^{3+} clusters with projections of ⟨111⟩ oriented spins viewed in (001) cross sections of PFN at different scales. Adapted from [87]

In the *MF* perovskite $PbFe_{0.5}Nb_{0.5}O_3$ (PFN), both Fe^{3+} and Nb^{5+} ions are randomly distributed at *B* sites [84]. This enables the establishment of two different orderings—a soft-mode driven *FE* one as in $PbTiO_3$, and a super-exchange driven *AF* one in the percolating Fe^{3+} subspace. Owing to the inherent disorder, however, unconventional phases emerge. The polar phase transforms into a so-called relaxor *FE* below $T_c^e \approx 385\,\mathrm{K}$ due to quenched random electric fields emerging from the cationic charge disorder. It decays into a polar domain state as known from the related prototype compound $PbMg_{1/3}Nb_{2/3}O_3$ (PMN) [85]. Even more unusual is the coexistence of two magnetic phases both of which fulfill the requirements of the thermodynamic limit. Infinitely large numbers of finite-sized Fe^{3+} clusters without mutual overlap make up a spin glass (*SG*) coexisting with an *AF* phase of exchange coupled Fe^{3+} ions. The phase coexistence resides on percolation theory. While the *AF* phase transition at $T_N \approx 153\,\mathrm{K}$ is permitted on the bond-percolated infinite cluster of super-exchange coupled Fe^{3+} spins, the *SG* transition at $T_g \approx 10\,\mathrm{K}$ is restricted to the complementary space accommodating isolated and small clusters of Fe^{3+} ions, where magnetic dipolar and super-exchange interaction via oxygen and lead ions [86] warrant spin glassy bond coherence (Fig. 16 [87]).

Secured [87] signatures of long-range glassy order are critical slowing-down, memory and rejuvenation after aging, *de Almeida-Thouless-type* phase boundary, and stretched exponential relaxation of remanence. The independent nature of both phases is corroborated by their different magnetic point group symmetries, being *3m* with quadratic *ME* response on the infinite *AF* cluster, but m' with linear *ME* response on the *SG* subspace. Figure 17 shows the magnetic and *ME* responses as functions of the temperature and measured under different external field conditions (see caption). The magnetization, m versus T, marks the *AF* Néel temperature and

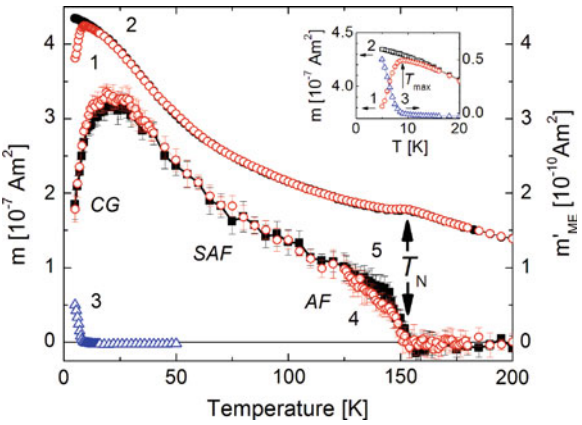

Fig. 17 Magnetic moment m versus T of PFN(001) obtained on *ZFC/FH* (curve *1*), on *FC* (*2*) with $\mu_0 H = 0.1\,\mathrm{T}$, and on *ZFH* as *TRM* (*3*) (inset: low-T data magnified) (*lefthand ordinate*). *ME* moment m'_{ME} versus T obtained with $E_{ac} = 12.5\,\mathrm{kV/m}$ on *ZFC/FH* in $\mu_0 H_{dc} = 0.2\,\mathrm{T}$ and $E_{dc} = 0$ (*4*, *open circles*) or 50 kV/m (*5*, *solid squares*) (*righthand ordinate*). T_N and dominance of 'phases' *AF*, *SAF* and CG are indicated. Adapted from [87]

the spin-glass-typical non-ergodic behavior below T_g. *ZFC* (curve 1) and *FC* (2) as well as the thermoremanent magnetization (3) (emphasized in the inset to Fig. 17) are typical of the spin glass phase. Signatures of the *AF* Néel temperature T_N, of superantiferromagnetic (*SAF*) clusters and of the spin cluster glass (*CG*) below T_g are well pronounced in the β-type *ME* signal, m'_{ME} versus T, induced by E_{ac} and H_{dc} [87]. The δ-effect induced by additional E_{dc} is comparably small and becomes visible only in the critical regions of the *AF* and the *CG* transitions at $T \approx 140$ and 25 K, respectively.

It should be noticed that the coexistence of two magnetic phases in the same solid system has often been matter of controversy in past decades. In the case of PFN, we are convinced that percolation theory allows both the *AF* and the *SG* phase to coexist without spatial overlap, but nevertheless fulfilling the requirements of the thermodynamic limit. Recently we encountered a similar situation with another single phase type-I multiferroic, namely the dilute lamellar antiferromagnet $CuCr_{1-x}In_xP_2S_6$ ($T_N \approx 32\,\mathrm{K}$) [88]. It rapidly loses magnetic percolation upon diamagnetically diluting the triangular Cu-Cr-P_2 planar network with In^{3+} ions (Fig. 18a and b). For $0 \leq x < 0.3$ antiferroelectricity ($T_c \leq 150\,\mathrm{K}$) and *AF* spin order ($T_N \approx 32\,\mathrm{K}$) coexist. Both orders are superposed by ferroic fluctuations. For $x > 0.3$ pseudo-critical planar 2D *FM* fluctuations of the Cr^{3+} spins ($S = 3/2$) are encountered. They give rise to Langevin-type magnetization saturation and, surprisingly, large quasi-molecular magnetic anisotropy.

In the polar subsystem of $CuCr_{1-x}In_xP_2S_6$, which involves off-centered Cu^+ ions (Fig. 18a and b), dynamic polar clustering with glass-like polydispersive dielectric susceptibility emerges for $x > 0$ at $T \leq T_c$. Figure 18c shows the dielectric losses measured on a single crystal with moderate dilution, $x = 0.2$, via ε'' versus T for

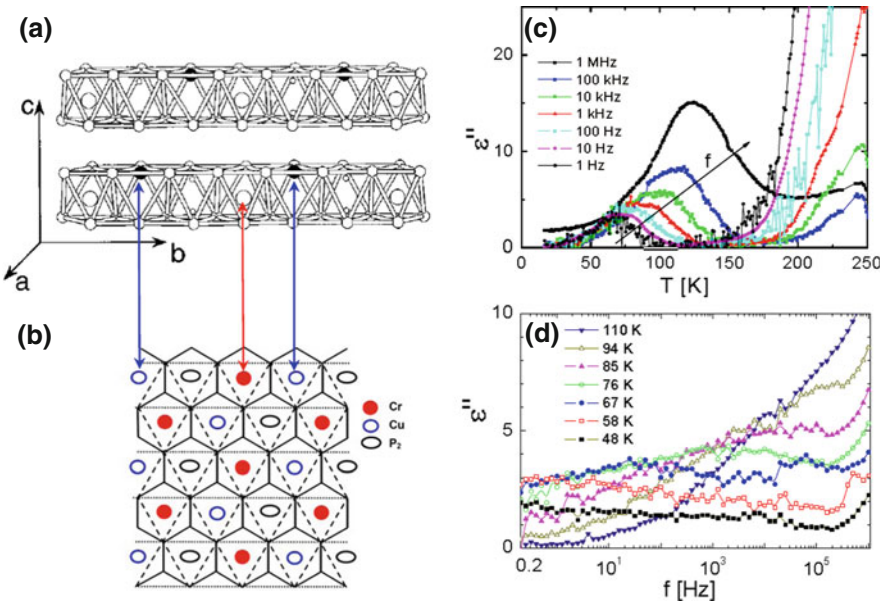

Fig. 18 Ordered distribution of Cr, Cu, and P_2 pairs in the lamellar network (**a**) and in the *ab* plane of $(CuCr)P_2S_6$ (**b**). Dielectric permittivity component (**c**) ε'' versus T, and (**d**) ε'' versus f measured along the c^* axis of the magnetically dilute compound $(CuCr_{0.8}In_{0.2})P_2S_6$ at frequencies $10^0 \leq f \leq 10^6$ Hz and temperatures $20 \leq T \leq 250$ K. Adapted from [88]

various frequencies within $10^0 \leq f \leq 10^6$ Hz. They arise below $T \approx 150$ K and shift toward lower T as f decreases in an Arrhenius-like fashion, $f_m = 1.4 \cdot 10^{12}$ Hz $\cdot$ $\exp(-1{,}400\,\mathrm{K}/T)$. This law seems to exclude glassiness, which would rather be expected to obey, e.g., Vogel-Fulcher-type 'criticality' by replacing the denominator T by $T - T_g^e$ with some finite glass temperature, $T_g^e > 0$. However, in order to finally exclude glassy asymptotic behaviour more data are needed at lower frequency and lower temperature. Preliminarily, however, a strong hint at dipolar glassy dynamics is offered by the huge dipolar polydispersivity as shown by the extremely broad and flat spectra, ε'' versus f, in Fig. 18d [88]. Apparently they have tendency to diverge toward $f \to 0$ as T falls below 50 K. This clearly hints at dipolar glassiness, which seems to coexist with the ferrielectric long-range order residing on the percolating cluster—a rare event, probably for the first time observed in a disordered polar system.

4 Perspectives

From a fundamental point of view both *type-II multiferroics* and *ME multiglasses* are clearly most challenging because of their fascinating interplay between different ordering schemes. New horizons are opened in particular by their nonlinear *ME* effects, which are not as small as hitherto presumed.

On the other hand applications have entered the agenda from the beginning [7–11]. To begin with, *ME* composites are meanwhile established as magnetic field and current sensors, transformers, gyrators, tunable microwave devices, resonators, filters, phase shifters, delay lines etc [69].

Single phase magnetoelectrics promise to realize low-power electric control of magnetic order [12, 23], while the magnetic control of electric order is much less attractive for obvious reasons. As an example, our *ME* Random Access Memory (*MERAM*) [9, 10] (Fig. 8) is based on the electric control of the exchange bias exerted by a *ME* antiferromagnet like Cr_2O_3 onto an attached *FM* (multi)layer such as $(Pt/Co)_n$, $n \geq 1$. However, for practical applications one should finally be able to extend functionality significantly above room temperature. One way out of the present tight situation given by $T_N(Cr_2O_3) = 308\,K$ might be alloying Cr_2O_3 with α-Fe_2O_3 in order to increase the ordering temperature.

Single phase multiferroics open possibilities of double action involving two order parameters. For their 4-bit memory (Fig. 9), Gajek et al. [61] proposed a thin film of the *MF* ferro-electromagnet $La_{0.1}Bi_{0.9}MnO_3$ to serve as a tunneling layer in a magnetoresistance element showing four different tunnel magneto- and electro resistances (*TMR* and *TER*, respectively) when setting the various magnetic and electric states, $\pm\boldsymbol{M}$ and $\pm\boldsymbol{P}$. Unfortunately the search for suitable materials fully functional above room temperature has not yet been successful. Presently still the only room temperature *type-I MF* material $BiFeO_3$ appears promising for future spintronics applications, which is probably bound to exploit the various couplings of domain switching [64, 65].

In the very near future the ongoing research on the large variety of multiferroic and/or magnetoelectric materials and their novel device structures will certainly bring improved understanding of the physical interrelations and, hopefully, also the often proclaimed breakthrough solving current technological challenges.

Acknowledgments Fruitful cooperation with S. Bedanta, K. D. Belashchenko, P. Borisov, X. Chen, P. D. Dowben, X. He, A. Hochstrat, S. Sahoo, and V. V. Shvartsman, and financial support by DFG (SFB 491, KL306/38), EU (STREP MULTICERAL), NSF through Career DMR-0547887, MRSEC Program, and by NRC/NRI supplement to MRSEC are gratefully acknowledged.

References

1. N.A. Hill, J. Phys. Chem. B **104**, 6694 (2000)
2. H. Schmid, Ferroelectrics **162**, 317 (1994)
3. W.F. Brown, R.M. Hornreich, S. Shtrikman, Phys. Rev. B **168**, 574 (1968)
4. D.N. Astrov, Sov. Phys. JETP **11**, 708 (1960)
5. A. Hochstrat, Ch. Binek, X. Chen, W. Kleemann, J. Magn. Magn. Mater. **272–276**, 325 (2004)
6. P. Borisov, A. Hochstrat, X. Chen, W. Kleemann, Ch. Binek, Phys. Rev. Lett. **94**, 117203 (2005)
7. Ch. Binek, A. Hochstrat, X. Chen, P. Borisov, W. Kleemann, B. Doudin, J. Appl. Phys. **97**, 10C514 (2005)
8. Ch. Binek, B. Doudin, J. Phys.: Condens. Matter **17**, L39 (2005)
9. X. Chen, A. Hochstrat, P. Borisov, W. Kleemann, Appl. Phys. Lett. **89**, 202508 (2006)

10. X. Chen, A. Hochstrat, P. Borisov, W. Kleemann, US Patent 7,719,883 B2, May 2010
11. M. Fiebig, J. Phys. D **38**, R123 (2005)
12. W. Kleemann, Physics **2**, 105 (2009)
13. W. Eerenstein, N. Mathur, J.F. Scott, Nature **442**, 759 (2006)
14. V.V. Shvartsman, S. Bedanta, P. Borisov, W. Kleemann, A. Tkach, P.M. Vilarinho, Phys. Rev. Lett. **101**, 165704 (2008)
15. L.D. Landau, E.M. Lifshitz, *Electrodynamics of Continuous Media* (Pergamon, Cambridge, 1960)
16. T.H. O'Dell, *The Electrodynamics of Magneto-Electric Media* (North-Holland, Amsterdam, 1970)
17. P. Borisov, A. Hochstrat, V.V. Shvartsman, W. Kleemann, Rev. Sci. Instr. **78**, 106105 (2007)
18. P. Borisov, Ph.D. Thesis, Universität Duisburg-Essen, Duisburg, 2009 p. 72
19. R. Hornreich, S. Shtrikman, Phys. Rev. **161**, 506 (1967)
20. N. Wu, X. He, A.L. Wysocki, U. Lanke, T. Komesu, K.D. Belashchenko, Ch. Binek, P.A. Dowben, Phys. Rev. Lett. **106**, 087202 (2011)
21. A.F. Andreev, JETP Lett. **63**, 758 (1996)
22. K.D. Belashchenko, Phys. Rev. Lett. **105**, 147204 (2010)
23. X. He, Y. Wang, N. Wu, A. Caruso, E. Vescovo, K.D. Belashchenko, P.A. Dowben, Ch. Binek, Nat. Mater. **9**, 579 (2010)
24. H.-J. Freund, H. Kuhlenbeck, V. Staemmler, Rep. Prog. Phys. **59**, 283 (1996)
25. T.R. Mc Guire, M.W. Shafer, R.J. Joenk, H.A. Alperin, S.J. Pickart, J. Appl. Phys. **37**, 981 (1966)
26. V.V. Shvartsman, P. Borisov, W. Kleemann, S. Kamba, T. Katsufuji, Phys. Rev. B **81**, 064426 (2010)
27. D.E. Neuenschwander, *Emmy Noether's Wonderful Theorem* (The Johns Hopkins University Press, Baltimore, 2011)
28. W. Gerlach, O. Stern, Z. Physik **9**, 353 (1922)
29. G.E. Uhlenbeck, S. Goudsmit, Naturwissenschaften **47**, 953 (1925)
30. P.A.M. Dirac, Proc. Roy. Soc. A **117**, 610 (1928)
31. S.A. Wolf, D.D. Awschalom, R.A. Buhrman, J.M. Daughton, S. von Molnár, M.L. Roukes, A.Y. Chtchelkanova, D.M. Treger, Science **294**, 1488 (2001)
32. I. Žutić, J. Fabian, S. Das Sarma, Rev. Mod. Phys. **76**, 323 (2004)
33. G.E. Moore, Electronics **38**, 114 (1965)
34. V.V. Zhirnov, J.A. Hutchby, G.I. Bourianoff, J.E. Brewer, IEEE Circ. Dev. Mag. **21**, 37 (2005)
35. A. Ney, C. Pampuch, R. Koch, K.H. Ploog, Nature **425**, 485 (2003)
36. H. Dery, P. Dalal, Ł. Cywiński, L.J. Sham, Nature **447**, 573 (2007)
37. P.A. Dowben, N. Wu, Ch. Binek, J. Phys.: Condens. Matter **23**, 171001 (2011)
38. G. Prinz, Science **282**, 1660 (1998)
39. C. Chappert, A. Fert, F.N. Van Dau, Nat. Mater. **6**, 813 (2007)
40. S. Datta, B. Das, Appl. Phys. Lett. **56**, 665 (1990)
41. G. Feve, W.D. Oliver, M. Aranzana, Y. Yamamoto, Phys. Rev. B **66**, 155328 (2002)
42. F. Jonietz, S. Mühlbauer, C. Pfleiderer, A. Neubauer, W. Münzer, A. Bauer, T. Adams, R. Georgii, P. Böni, R.A. Duine, K. Everschor, M. Garst, A. Rosch, Science **330**, 1648 (2010)
43. F. Zavaliche, T. Zhao, H. Zheng, F. Straub, M.P. Cruz, P.L. Yang, D. Hao, R. Ramesh, Nano Lett. **7**, 1586 (2007)
44. E.Y. Tsymbal, H. Kohlstedt, Science **313**, 181 (2006)
45. T. Maruyama, Y. Shiota, T. Nozaki, K. Ohta, N. Toda, M. Mizuguchi, A.A. Tulapurkar, T. Shinjo, M. Shiraishi, S. Mizukami, Y. Ando, Y. Suzuki, Nat. Nanotech. **4**, 158 (2008)
46. J.P. Velev, P. Dowben, E.Y. Tsymbal, S.J. Jenkins, A.N. Caruso, Surf. Sci. Rep. **63**, 400 (2008)
47. T.J. Martin, J.C. Anderson, IEEE Trans. Mag. **2**, 446 (1966)
48. M. Bibes, A. Barthélémy, Nat. Mater. **7**, 425 (2008)
49. P. Borisov, W. Kleemann, J. Appl. Phys. **110**, 033917 (2011)
50. J.P. Liu, E. Fullerton, O. Gutfleisch, D.J. Sellmyer (eds.) *Nanoscale Magnetic Materials and Applications, Chapter 6* (Springer, Berlin, 2009)

51. P. Borisov, A. Hochstrat, X. Chen, W. Kleemann, Phase Trans. **79**, 1123 (2006)
52. Ch. Binek, Phys. Rev. B. **70**, 014421 (2004)
53. Ch. Binek, S. Polisetty, X. He, A. Berger, Phys. Rev. Lett. **96**, 067201 (2006)
54. S.-H. Lim, M. Murakami, S.E. Lofland, A.J. Zambano, L.G. Salamanca-Riba, I. Takeuchi, J. Magn. Magn. Mater. **321**, 1955 (2009)
55. C.Y. You, S.D. Bader, J. Appl. Phys. **87**, 5215 (2000)
56. C. Pampuch, A.K. Das, A. Ney, L. Däweritz, R. Koch, K.H. Ploog, Phys. Rev. Lett. **91**, 14720 (2003)
57. K.F. Wang, J.-M. Liu, Z.F. Ren, Adv. Phys. **58**, 321 (2009)
58. D. Khomskii, Physics **2**, 20 (2009)
59. J.P. Velev, C.-G. Duan, J.D. Burton, A. Smogunov, M.K. Niranjan, E. Tosatti, S.S. Jaswal, E.Y. Tsymbal, Nano Lett. **9**, 427 (2009)
60. J.P. Velev, S.S. Jaswal, E.Y. Tsymbal, Philos. Trans. R. Soc. A **369**, 3069 (2011)
61. M. Gajek, M. Bibes, S. Fusil, K. Bouzehouane, J. Fontcuberta, A. Barthélémy, A. Fert, Nat. Mater. **6**, 206 (2007)
62. J.D. Burton, E.Y. Tsymbal, Phys. Rev. Lett. **106**, 157203 (2011)
63. A.M. Kadomtseva, Yu.F. Popov, A.P. Pyatakov, G.P. Vorob'ev, A.K. Zvezdin, D. Viehland, Phase Trans. **79**, 1019 (2006)
64. Y.H. Chu, L.W. Martin, M.B. Holcomb, M. Gajek, S.-J. Han, Q. He, N. Balke, C.-H. Yang, D. Lee, W. Hu, Q. Zhan, P.-L. Yang, A. Fraile-Rodriguez, A. Scholl, S.X. Wang, R. Ramesh, Nat. Mater. **7**, 478 (2008)
65. D. Lebeugle, A. Mougin, M. Viret, D. Colson, L. Ranno, Phys. Rev. Lett. **103**, 257601 (2009)
66. T. Kimura, Y. Tokura, J. Phys.: Condens. Matter **20**, 434204 (2008)
67. Y.J. Choi 1, H.T. Yi, S. Lee, Q. Huang, V. Kiryukhin, S.-W. Cheong, Phys. Rev. Lett. **100**, 047601 (2008)
68. H. Wu, T. Burnus, Z. Hu, C. Martin, A. Maignan, J.C. Cezar, A. Tanaka, N.B. Brookes, D.I. Khomskii, L.H. Tjeng, Phys. Rev. Lett. **102**, 026404 (2009)
69. C.-W. Nan, M.I. Bichurin, S.X. Dong, D. Viehland, G. Srinivasan, J. Appl. Phys. **103**, 031101 (2008)
70. J. van Suchtelen, Philips Res. Rep. **27**, 26 (1972)
71. G.T. Rado, J.M. Ferrari, W.G. Maisch, Phys. Rev. B **29**, 4041 (1984)
72. J.-P. Rivera, Eur. Phys. **71**, 299 (2009)
73. C.A.F. Vaz, J. Hoffman, C.H. Ahn, R. Ramesh, Adv. Mater. **22**, 2900 (2010)
74. S. Sahoo, S. Polisetty, C.-G. Duan, S.S. Jaswal, E.Y. Tsymbal, Ch. Binek, Phys. Rev. B **76**, 092108 (2007)
75. S. Polisetty, W. Echtenkamp, K. Jones, X. He, S. Sahoo, Ch. Binek, Phys. Rev. B **82**, 134419 (2010)
76. H.L. Meyerheim, F. Klimenta, A. Ernst, K. Mohseni, S. Ostanin, M. Fechner, S. Parihar, V. Maznichenko, I. Mertig, J. Kirschner, Phys. Rev. Lett. **106**, 087203 (2011)
77. S.X. Dong, J. Zhai, J.-F. Li, D. Viehland, Appl. Phys. Lett. **88**, 082907 (2006)
78. K. Binder, A.P. Young, Rev. Mod. Phys. **58**, 801 (1986)
79. K. Binder, J.D. Reger, Adv. Phys. **41**, 547 (1992)
80. U.T. Höchli, K. Knorr, A. Loidl, Adv. Phys. **39**, 405 (1990)
81. A.I. Lebedev, I.A. Sluchinskaya, A. Erko, V.F. Kozlovskii, JETP Lett. **89**, 457 (2009)
82. W. Kleemann, S. Bedanta, P. Borisov, V.V. Shvartsman, S. Miga, J. Dec, A. Tkach, P.M. Vilarinho, Eur. Phys. B **71**, 407 (2009)
83. R.O. Kuzian, V.V. Laguta, A.-M. Daré, I.V. Kondakova, M. Marysko, L. Raymond, E.P. Garmash, V.N. Pavlikov, A. Tkach, P.M. Vilarinho, R. Hayn, Europhys. Lett. **92**, 17007 (2010)
84. S.A. Ivanov, R. Tellgren, H. Rundlof, N.W. Thomas, S. Ananta, J. Phys.: Condens. Matter **12**, 2393 (2000)
85. V. Westphal, W. Kleemann, M.D. Glinchuk, Phys. Rev. Lett. **68**, 847 (1992)
86. I.P. Raevski, S.P. Kubrin, S.I. Raevskaya, V.V. Titov, D.A. Sarychev, M.A. Malitskaya, I.N. Zakharchenko, S.A. Prosandeev, Phys. Rev. B **80**, 024108 (2009)
87. W. Kleemann, V.V. Shvartsman, P. Borisov, A. Kania, Phys. Rev. Lett. **105**, 257202 (2010)
88. W. Kleemann, V.V. Shvartsman, P. Borisov, J. Banys, M. Yu, Vysochanskii, Phys. Rev. B **84**, 094411 (2011)

Competing Interactions in Patterned and Self-Assembled Magnetic Nanostructures

Olav Hellwig, Laura J. Heyderman, Oleg Petracic and Hartmut Zabel

Abstract In this chapter we describe the static properties of different nanomagnetic systems, which have one thread in common: they consist of arrays of structures each containing a macrospin or a magnetic dipole interacting with its neighbors. We start with a general overview on rectangular and circular islands, their domain structures and interactions. In the second part we discuss the competing interactions and geometric frustration of magnetic dipoles arranged on square and honeycomb lattices, a new field that has become known as artificial spin-ice. The third part covers a technologically very important aspect of densely packed magnetic nanostructures with perpendicular anisotropy for use in hard disk drives in the form of bit patterned media. Here the interaction with neighboring islands may increase or decrease the switching field of an individual target island in the patterned array. The fourth part discusses magnetic clusters, which are arranged by self-organization rather than by lithography, providing further possibilities for investigating magnetic ordering and phase transitions.

Olav Hellwig (✉)
San Jose Research Center, HGST, a Western Digital Company,
3403 Yerba Buena Road, San Jose CA 95135, USA
e-mail: Olav.Hellwig@HGST.com

Laura J. Heyderman
Paul Scherrer Institute, CH-5232 Villigen PSI, Villigen, Switzerland
e-mail: laura.heyderman@psi.ch

Oleg Petracic
Jülich Centre for Neutron Science JCNS and Peter Grünberg Institute PGI,
Forschungszentrum Jülich GmbH, 52425 Julich, Germany
e-mail: o.petracic@fz-juelich.de

Hartmut Zabel
Institut für Experimentalphysik/Festkörperphysik, Ruhr-Universität Bochum,
44780 Bochum, Germany
e-mail: hartmut.zabel@ruhr-uni-bochum.de

H. Zabel and M. Farle (eds.), *Magnetic Nanostructures,*
Springer Tracts in Modern Physics 246, DOI: 10.1007/978-3-642-32042-2_6,

1 Lateral Magnetic Nanostructures and Competing Interactions

1.1 Overview

Competing interactions in magnetic nanostructures have been at the center of interest from the very beginning of magnetic thin film and superlattice research. Competing interactions occur, for instance, between bulk anisotropy and surface (interface) anisotropy in thin films, between ferromagnetic and antiferromagnetic interlayer exchange coupling, or between ferromagnetic and antiferromagnetic exchange interactions in exchange bias systems. Many reviews are devoted to these topics and shall not be repeated here, but we refer to the following reviews and further references quoted therein: Refs. [1–3]. Since about the turn of the century an additional artificial structuring in the lateral direction started to move into the center of interest. Reducing the film extension within the plane requires experimental tools in addition to the usual film deposition techniques. They imply some kind of lithography or self-organization and usually these methods are quite demanding. Some of the fabrication methods are detailed in Refs. [4–6]. Lateral structures can be shaped into different forms, sizes, periodic patterns, obeying different symmetries. There is a myriad of possibilities to arrange islands in the plane.

Isolated islands can be characterized by their shape and aspect ratio, ranging from needle like bars to circular islands. These islands can be periodically arranged in the plane or stacked on top of each other to yield a columnar and stratified type structure as sketched in Fig. 1. The new twist that these lateral patterns provide is the manipulation of the magnetic domain structure on the one hand and the strength of the intra- and interisland interaction on the other hand.

Bringing the islands closer together, they start to interact via their dipolar stray fields. It is this range which is of interest in the present chapter. In one case the interaction is desirable and leads to new order or frustration, such as in the spin ice patterns discussed in Sect. 2, in the other case dipolar stray fields are to be avoided in order to guarantee independent switching in perpendicular magnetic storage media (bit patterned media), as discussed in Sect. 3. The temperature dependence of lateral magnetic nanostructures is still an open issues. Only in rare cases the temperature dependence and intrinsic phase transitions have been taken into account [7].

This chapter contains four parts, which illustrate the current research and developments in magnetic nanostructures. Starting with a general overview on lateral rectangular and circular islands in the first part, the second part contains a discussion of recent work on lateral arrangements of magnetic dipoles on lattices with square or triangular symmetry, leading to intrinsic frustration. The next part covers the topic of closely packed square islands with perpendicular anisotropy known as bit patterns, which are being developed for future high density magnetic storage media. In the fourth and last part magnetic clusters are considered, which are arranged by self-organization rather than by lithography, providing further possibilities for the investigation of competing interactions.

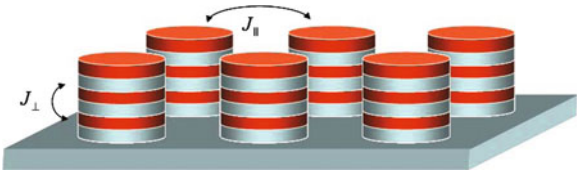

Fig. 1 Schematics of lateral magnetic patterns of islands. Each islands contains a multilayer of alternating magnetic and non-magnetic layers mediating an interlayer coupling $J_\perp$. The islands may interact via a dipolar stray field $J_\parallel$

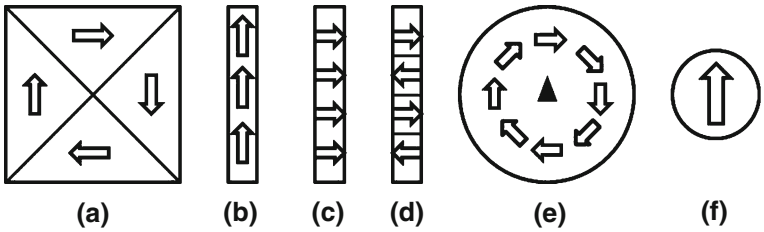

Fig. 2 Sketch of magnetic domain structures in nanopatterns. **a** Landau pattern in a square islands; **b** single domain dipole state in an elongated stripe with magnetization parallel to the long axis of the island; **c** single domain pattern as in **b** but with perpendicular orientation of the magnetization; **d** multidomain state separated by 180° domain walls; **e** magnetic vortex state in a circular island, characterized by a chirality and a core polarity; **f** single domain dipole state upon reducing the island size

1.2 Single Islands, Stacks, and Lateral Patterns

When reducing the lateral extension of a film down to nanometer size, multidomain states collapse to a single domain (SD) state [8, 9], which is sketched in Fig. 2b and f. In circular islands a vortex state is encountered below a critical diameter characterized by a chirality of the in-plane spins and a polarity of the vortex core (Fig. 2e). In rectangular bars multidomain states (Fig. 2a) are reduced to SD dipoles (Fig. 2b) if the aspect ratio $m = l/w$ of length l to width w exceeds a critical value. The critical diameter or critical aspect ratio is a function of the ferromagnetic material used and it is different for Py or Co, meaning that the exchange interaction, the magnetocrystalline anisotropy, and the shape anisotropy are the controlling factors. Vortex systems and SD dipoles are particularly appealing as these magnetic islands can either be stacked on top of each other or they can be periodically arranged in the plane forming patterns of selected symmetry.

Let us first consider a single rectangular island. The multidomain state of a rectangular islands as shown in Fig. 2a goes into a SD state (Fig. 2b), when the demagnetization energy E_D becomes smaller than the domain wall energy E_W, which is required to create domain walls. The demagnetization energy density is given by $E_D = 1/2\mu_0 H_D M_S$, where M_S is the saturation magnetization and H_D is the demagnetization field. The demagnetization field depends on the shape and

the aspect ratio. For rectangular islands of the alloy $Ni_{80}Fe_{20}$ (Py) a phase diagram for the domain state as a function of aspect ratio was established by Last et al. [10]. This phase diagram shows that a single domain state is reached with an aspect ratio $m \leq 10$. Although the global state at remanence is SD, the domain structure at both ends is usually much more complex, as micromagnetic simulations [11] and imaging experiments show [12].

As mentioned, a rectangular bar with $m \leq 10$ will exhibit a SD state at remanence with the magnetization axis pointing parallel to the long axis. A SD state in the direction perpendicular to the long axis is excluded because of the much higher demagnetization energy which is produced in that direction. Thus in a long thin bar with an aspect ratio $m = l/w > 10$ the magnetic state is controlled by the shape anisotropy, which dictates the magnetization vector to form a dipole parallel to the wire axis. A SD state perpendicular to the wire axis as shown in case Fig. 2c would be highly unstable at remanence, but can be realized in a high saturating field.

In some cases competition between the shape anisotropy of the SD state and a substrate induced uniaxial anisotropy may occur leading to surprising results. If the uniaxial anisotropy becomes larger than the shape anisotropy, the actual domain state observed depends on the relative orientation to each other. As long as the uniaxial anisotropy is parallel to the long side of the rectangular island axis (bar), there is no change to the already discussed situation presented in Fig. 2b. However, if the uniaxial anisotropy, i.e. the easy axis, is oriented perpendicular to the long axis of the bar, a domain state may be become favorable as sketched in Fig. 2c, i.e. if the anisotropy energy E_a exceeds the domain wall energy E_w. This situation has been encountered in Co_2MnGe Heusler alloy stripes prepared by lithographic means in the work by Gross et al. [13]. Here the domain state becomes the real ground state and is reached at remanence independent of the magnetization protocol (see Fig. 3). Furthermore the width of the domains scales with the square root width of the bars, as predicted by theory [15] and confirmed in [13] for the first time. Similar domain states have also been observed for Co stripes [16, 17] and for Fe stripes [14, 18, 19].

Having established magnetic dipoles by virtue of their aspect ratio, they can be arranged parallel to each other within the plane at different distances and angles in order to control their interaction via dipole fields. An illustrative example is shown in Fig. 4 where Py magnetic dipoles are placed next to each other forming an antiparallel magnetic state at remanence. In this X-ray magnetic circular dichroism (XMCD) picture the gray scale is determined by the direction of the incident circular polarized X-ray beam with respect to the magnetization direction. Highest intensity is coded black for parallel orientation and lowest intensity is coded white for antiparallel orientation. Any angle in between assumes a gray color.

Clearly there are many possibilities to arrange nanostructured SD magnetic dipoles within the plane. Particular exciting is the arrangement of these dipoles on square or honeycomb lattices, which are frustrated forming square or kagome spin ice, as discussed in more detail in Sect. 2.

At the other extreme of in-plane aspect ratios are circular islands with $m = 1$. As already mentioned, below a critical aspect ratio $n = R/L$ (R = radius, L = thickness) the magnetization distribution in islands assumes a vortex state [20]. The

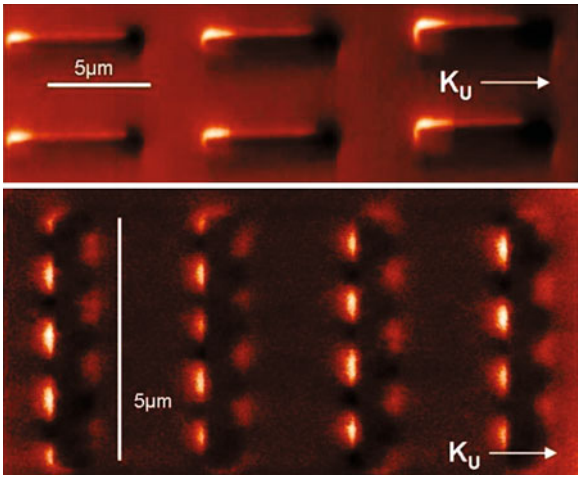

Fig. 3 Domain structure in Co_2MnGe Heusler alloy bars grown on a sapphire substrate. In the *top panel* the *bars* are aligned parallel to a uniaxial anisotropy K_U provided by the substrate. In the bottom panel the bars a aligned perpendicular to the unaxial anisotropy axis K_U (Reprinted with permission from Ref. [13]. Copyright (2011) by the American Physical Society)

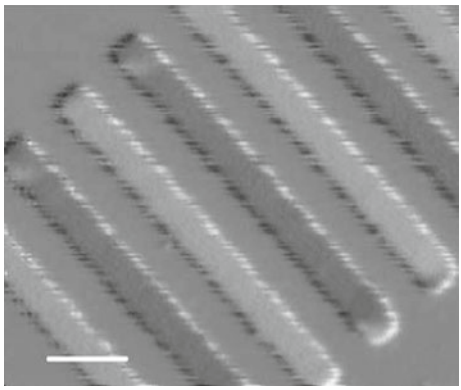

Fig. 4 XMCD image of parallel oriented Py rectangular bars interacting via stray fields. The image was taken with incident left and right circular polarized light tuned to the L-absorption edge of Fe, providing magnetic contrast. The *gray scale* contrast indicates that in this periodic array parallel bars have antiparallel magnetization at remanence. The *scale bar* indicates 1 μm (courtesy to T. Eimüller)

phase diagram from SD to vortex state has been analyzed in much detail, including the nucleation and annihilation fields of the vortex [21, 22], the slow vortex dynamics close to the nucleation point [23], the gyration of the center vortex core [24], and the flipping fields of the core in external static and rf-fields [25]. Micromagnetic simulations and analytic analysis have shown that a vortex state forms if the magnetostatic energy dominates over the exchange energy, i.e. if the dipolar energy

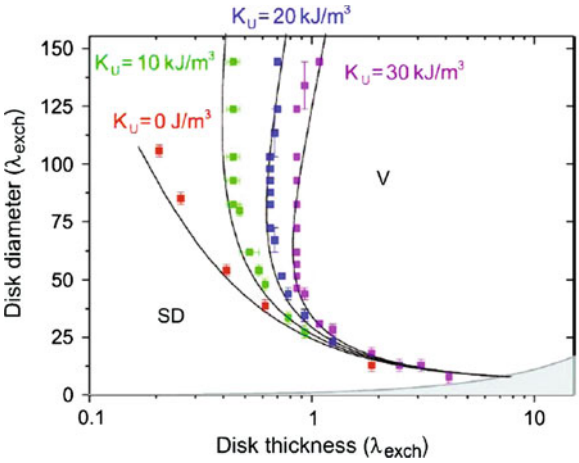

Fig. 5 Phase diagram for a single domain state (SD) versus a vortex state (V) in circular islands as function of disk diameter and disk thickness for different uniaxial anisotropy constants. Diameter and thickness are given in unity of exchange lengths. *Lines* correspond to the analytical model, dots to micromagnetic simulations (Reprinted with permission from Ref. [22]. Copyright (2004) by the American Physical Society)

can be reduced by the formation of a vortex state in spite of an enhanced exchange energy. The competition between the dipolar field in the single domain state and the exchange energy in the vortex state leads to a well defined phase diagram depending on disk diameter and disk thickness, as shown in Fig. 5 [22]. If the islands in lateral patterns come closer together, they start to interact affecting their chirality [26, 27]. The dipolar coupling of vortices in close proximity is also expressed in the dynamics of their vortex cores, as impressively shown by Jung et al. [28, 29].

Considering a pattern of highly symmetric circular islands in a saturating field, on the descending magnetization branch a vortex occurs at the nucleation field either with clockwise or anticlockwise chirality (clockwise chirality is sketched in Fig. 2e). Furthermore, during magnetization reversal the vortices nucleating along the ascending branch and descending branch of the hysteresis will exhibit opposite chiralities. In an array of identical islands and neglecting interaction between them there will be as many vortices with clockwise chirality as with anticlockwise chirality along the descending branch. However, if the islands are flattened at the top, nucleation in the descending field will always occur close to the flat top in an anticlockwise fashion, whereas in an ascending field the nucleation will occur at the bottom of the island in a clockwise fashion. This birefringence of nucleation and annihilation of the vortex state is spatially separated and can indeed be observed either by magnetic force microscopy (MFM) [30, 31] or by using a combination of vector MOKE and Bragg-MOKE [32, 33]. Vector MOKE resolves the x- and y- components of the magnetization vector. Bragg-MOKE, in addition, is sensitive to the magnetization distribution inside of islands by taking the Fourier-transform in the diffraction mode.

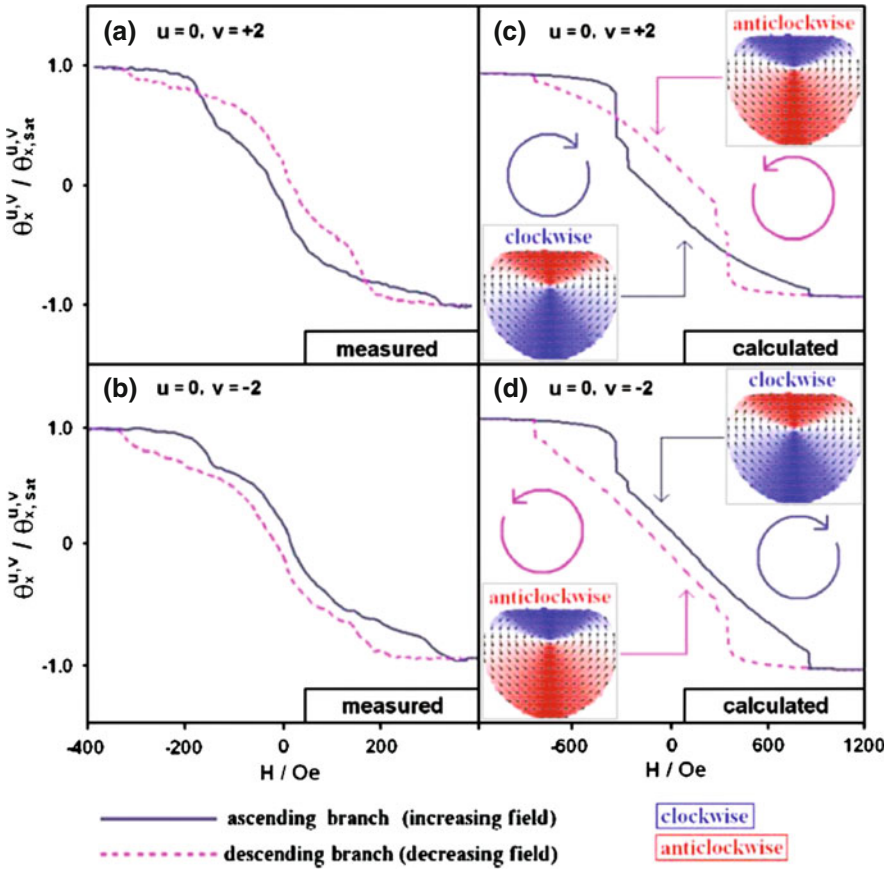

Fig. 6 Vortex state and reversal in islands with a flat *top*. The flat breaks the symmetry such that the vortices nucleate with an anticlockwise chirality at the top in a field descending from saturation. Vice versa, starting from negative saturation the vortex nucleates at the *bottom* in a clockwise fashion. *Left panels* the chirality can be distinguished in magnetooptical Kerr-effect experiments when the magnetic hysteresis is recorded at higher orders of diffraction, in this case at the diffraction spots $(0, +2)$ and $(0, -2)$, which refers to diffraction spots above and below the scattering plane respectively. *Right panels* micromagnetic simulations confirm the characteristic hysteresis loops being different for clock- and anticlockwise chirality (Reprinted with permission from Ref. [34]. Copyright (2008) by the American Institute of Physics)

Using this method, the chirality during vortex formation can indeed be distinguished by their characteristic hysteresis at higher order diffraction spots [34] as shown in Fig. 6.

The next step of complexity is a stack of ferromagnetic (F) circular dots on top of each other, separated by non-magnetic material (N) in a sequence F/N/F. The obvious question is how the vortices may interact with each other either via dipolar stray fields and/or via interlayer exchange interaction, depending on the material

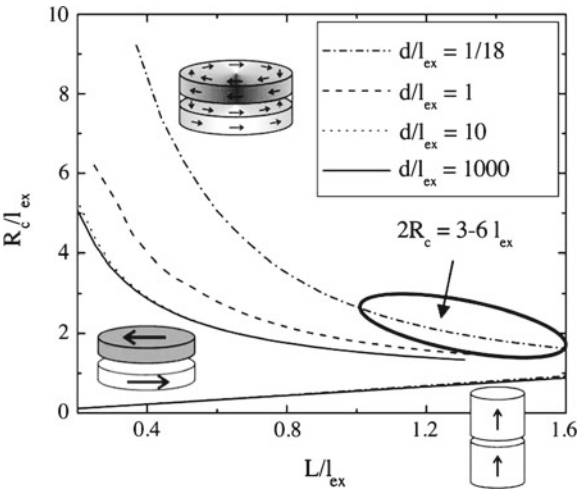

Fig. 7 Magnetic phase diagram of trilayer circular islands separated by non-magnetic spacer of thickness d. L is the thickness of the island normalized to the exchange length l_{ex} and R_c is the critical dot radius for a vortex state, also normalized to l_{ex} (Reprinted with permission from Ref. [35]. Copyright (2005) by the American Physical Society)

chosen for the interlayer. In single circular islands vortices form in order to reduce the magnetostatic energy. However, in a triple stack F/N/F it is not *a priori* clear whether the magnetic domains will arrange in a vortex or in a dipole type fashion. Micromagnetic simulation have indicated that for a large part of the phase diagram vortices form in both disks with opposite chirality and with vortex cores that avoid each other from nucleation until annihilation (Fig. 7) [35]. The question of vortex stability and reversal mechanism in triple stacks F/N/F was investigated by Buchanan et al. [35] using Py islands in the form of Py/Cu/Py. They used XMCD contrast for imaging the top island and MOKE for characterizing the hysteresis. The experimental results yield evidence that both Py disks form vortices. Whether the chirality of these vortices are oriented in opposite directions and whether the vortex cores avoid each other as indicated by micromagnetic simulations, could not be decided from the experimental results.

Szary et al. [36] have performed similar experiments, but combining soft and hard magnetic dots in a triple stack of Co/N/Py (Fig. 8). Here N was an insulating aluminum-oxide layer in order to avoid direct interlayer exchange coupling. The spin structure and the magnetization reversal in this triple stack were investigated both via micromagnetic simulations and experimentally by magneto-optical Kerr effect measurements. In this work the authors found that depending on the diameter, isolated Py dots show either a vortex state or a SD state during magnetization reversal, in agreement with well known phase diagrams. However, in the triple stack Co/N/Py the reversal process is governed by dipolar coupling between the soft and the hard F layer. Then, a stabilization and triggering of the vortex state or various types of

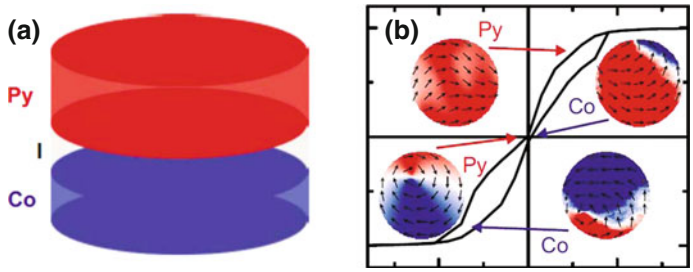

Fig. 8 **a** Sketch of a triple layer stack of Co/AlO_x/Py; **b** magnetic hysteresis of the triple layer stack for a diameter of 300 nm, 21 nm thickness of Py disk and 6 nm thickness of Co disk. *Color* coding refers to the x-axis of the magnetization (Reprinted with permission from Ref. [36]. Copyright (2010) by the American Institute of Physics)

buckling states may occur. In case of a high uniaxial anisotropy of the hard Co layer, only the Py layer undergoes a magnetization reversal via a vortex state whereas the Co layer stays in a SD state upon minor loops. On the other hand, for Co with a random anisotropy axis as is the case in polycrystalline Co films, both, the Co and the Py dot undergo a magnetization reversal. Surprisingly the authors find a stabilization and even a triggering of the vortex state due to the dipolar coupling of both disks in agreement with micromagnetic simulations. Similar experiments were performed by Rose et al. and Wu et al. [37, 38]. While Rose et al. find experimentally a vortex type coupling in triple layer rings of Co/Cu/Py [37], Wu et al. distinguished between ferro- and antiferromagnetic coupling in single crystalline Co/Cu/Py/Cu(001) trilayer disks. In the ferromagnetic case they find a vortex state, which becomes suppressed in the antiferromagnetic case [38].

Upon decreasing the diameter of a single magnetic disk the spin structure goes from a multidomain state through a vortex state to finally a SD dipole state. Two dots in a SD dipole state stacked on top of each other according to F_1/N/F_2 will naturally go into an antiparallel configuration in order to minimize their stray fields. However, three F layers with equal saturation magnetization M_s in the sequence F_1/N/F_2/N/F_3 may be frustrated assuming that the in-plane anisotropy can be neglected. Then the first disk will interact with the second layer by a strength e_{12} and the first with the third layer with a strength of e_{23}. If e_{23} is sufficiently strong, then a compromise can be reached by a non-collinear angle between the layer magnetization vectors as indicated in Fig. 9. The criterion is that $2\ e_{23} \geq e_{12}$, a criterion which depends strongly on the distance between the layers.

Fraerman et al. have indeed observed via magnetic force microscopy a non-collinear orientation of a Co layer stack in good agreement with the prediction [39]. The frustration between the dipolar interaction of layer 1, 2 and 1, 3 as compared to layers 2,3 only occurs for an odd number of layers. For an even number of layers the layer magnetization is expected to be entirely collinear, as has been shown in the work of van Kampen et al. [40]. The hysteresis for a stack of 10 double Py layers with diameters of 300 and 500 nm shows no sign of a vortex state or non-collinear

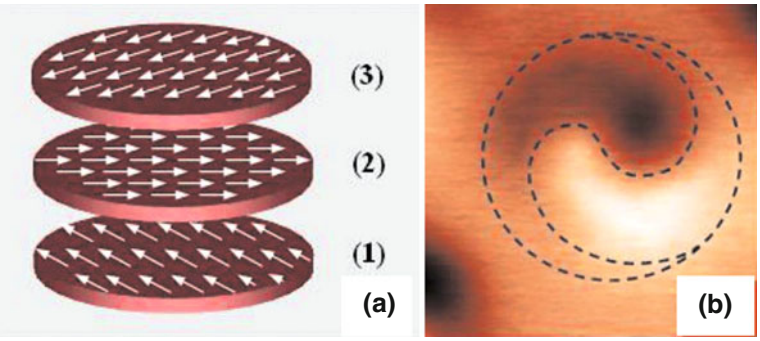

Fig. 9 **a** Sketch of triple layer sequence of disks in a SD dipole state. Depending on the mutual interactions, a non-collinear spin structure from layer to layer is expected. **b** MFM image of the magnetization distribution in the top layer reveals a spiral symmetry, which is suggestive for a non-collinear spin structure in the triple stack of Co disks (Reprinted with permission from Ref. [39]. Copyright (2008) by the American Institute of Physics)

coupling, although the hysteresis goes perfectly through a zero remanent magnetization. This is typical for a complete antiparallel compensation, while the in-plane anisotropy is negligible.

Stacks of disks are playgrounds for the investigation of inter- and intra-dipolar interactions. At zero field the demagnetization fields of the individual layers are completely compensated and there is no interaction in an array of these stacks. As the field increases, the magnetization rotates into the field direction, increasing the dipolar stray fields. Then the multilayer stacks start to interact at some critical field value. When the stacks are arranged on a triangular lattice, the interaction may cause frustration and disorder in an intermediate field range before they go into saturation. This scenario has, however, not been analyzed yet.

Before closing it should be mentioned that the circular islands with vortex state are also fascinating objects with respect to their dynamical response in an external field. As already mentioned in Sect. 1.2, a vortex always consists of a flux closed circular magnetization characterized by clockwise or counterclockwise chirality and a center vortex core of a few exchange length wide and with a polarity, which is either pointing up or down. If the center core could be switched in a controlled fashion, it would be useful for encoding and storing information. Indeed the vortex core can be excited and flipped over by excitation of a gyrotropic mode in the sub GHz frequency range, which eventually distorts the vortex core by the creation and subsequent annihilation of a vortex-antivortex pair. The vortex flip can either be excited via a pulsed field [41, 42], alternating magnetic field [24, 25], or a spin polarized current [43]. A completely different vortex reversal mechanism was discovered recently by Kammerer et al. by excitation of spin wave eigenmodes at higher frequencies in the GHz regime [44]. These azimuthal eigenmodes are due to the magneto-static interaction and characteristic for the circular boundary condition. They are, however, distorted by the presence of vortex cores, lifting the degeneracy for clockwise and

counterclockwise eigenmodes, which, in turn, allows to selectively excite them in a rotating magnetic field. Simultaneously by excitation of these azimuthal modes the vortex core is being reversed.

2 Artificial Spin Ice

2.1 Introduction

The term 'spin ice' was introduced as a result of the discovery of geometrical frustration similar to that in water ice in the rare earth titanate pyrochlore $Ho_2Ti_2O_7$ [45]. Frustration refers to the inability of a system to satisfy all interactions simultaneously and can be found in a wide variety of physical systems, [46–50] with some of the earliest references to frustration in magnetic systems found in the work of Toulouse [51, 52] and Kirkpatrick [53]. Geometrical frustration, which is a consequence of the lattice geometry, can be most easily understood by considering the classical example of spins on a triangular lattice with antiferromagnetic interactions as shown in Fig. 10a. If two spins are aligned antiparallel, the third spin has a favourable antiparallel alignment with one of the nearest neighbour spins but an unfavourable parallel alignment to the other nearest neighbour spin. The spin in question is therefore frustrated since it does not know which way to point. In infinite spin systems, frustration leads to a large degeneracy of low energy states and a non-zero entropy at absolute zero. The spins are thus unable to freeze and there are spontaneous transitions between the low energy states.

At this point, it should be mentioned that there is also a class of frustrated magnets, the spin glasses [54, 55], where the frustration arises from the disorder in the system. For example in the spin glass CuMn, diluted Mn atoms sit at random sites in the Cu and the Mn atoms interact via an RKKY coupling that is oscillatory in nature, with the sign depending on the Mn–Mn distance. Therefore the Mn–Mn interaction is both random in sign and magnitude, and has competing interactions resulting in frustration. An analogous scenario is found in dipolar coupled magnetic nanoparticles, where the frustrated interaction, site disorder and/or randomly oriented anisotropy axes give rise to a so-called superspin glass state as described in Sect. 4.

Returning now to water ice, the frustration comes about because of an incompatibility in the bonding distances between the protons and oxygen ions, leading to the 'ice rule' at a tetrahedron for a given oxygen ion where two protons are closer to the oxygen ion and two are further away (Fig. 10b). In spin ice, an equivalent situation occurs due the presence of both the interactions between the spins on the corners of the pyrochlore tetrahedra, and the crystal field that results in an Ising anisotropy along the 111-type directions constraining the spins to point either towards the centre or away from the centre of each tetrahedron. This results in an energy minimum when the 'two-spins-in/two-spins-out' ice rule is obeyed (Fig. 10c). Since the tetrahedra are corner sharing, a large assembly of equivalent spin configurations are required in order to achieve the ground state. The spin ice crystals display a range of fascinating

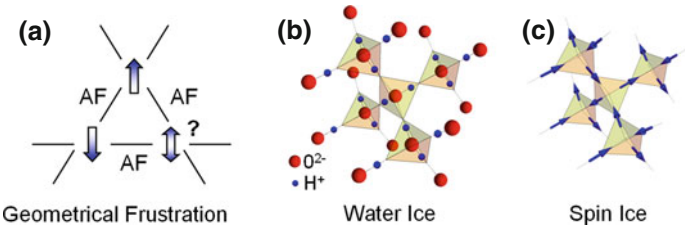

Fig. 10 **a** Model for geometrical frustration: part of a triangular lattice with antiferromagnetic interactions. While one interspin interaction is satisfied, the third spin is frustrated since it can not satisfy the other two spin interactions simultaneously. **b** Schematic representation of frustration in water ice. Each oxygen ion has two protons closer to it and two further away and **c** spin ice [45] with each tetrahedron having two spins pointing towards and two spins pointing away from the centre

behaviour arising from the geometrical frustration [45, 56–59], but tuning the crystal lattice is somewhat difficult and direct observation of the spin configurations is not possible.

In 2006, pioneering work was carried out on an artificial square ice, where the three dimensional spin ice was recreated as a two dimensional array of single domain magnetic elements [60], which can be patterned from a ferromagnetic thin film of, for example, permalloy or cobalt with electron beam lithography. In such artificial spin systems, the geometry (including the island shape and size, the lattice type and interaction strength) can be fully controlled by design, and the magnetic configurations can be directly determined with various magnetic imaging methods [60–63]. The artificial square ice consists of elongated ferromagnetic islands placed on a square lattice as shown in Fig. 11a [60]. The shape and size of the islands is chosen so that they are single domain at remanence, and the role of the Ising spins is taken on by the island moments that, due to the shape anisotropy, point in one of two directions along the long axis of the islands. The dipolar interactions dictate that the moments in pairs of elements prefer to arrange themselves head-to-tail (north pole facing south pole), and there is a corresponding two-in/two-out ice rule for the moments at each vertex where four islands meet. The 16 different possible moment configurations are shown in Fig. 11b together with the expected percentage of a given vertex type if the resulting configurations were random and, since it is never possible to minimise all of the local dipolar interactions, the system is frustrated. An equivalent procedure to a thermal annealing of the sample can be performed by rotating the sample in a magnetic field, decreasing the field from a value above saturation down to zero. Employing such a demagnetization procedure, it was found that nearest neighbour correlations were important, so mimicking the characteristics of the bulk spin ice, although it was not possible to achieve the ground state [60, 64].

It turns out that there is a fundamental issue with the square ice system, in that not all of the dipolar interactions between the magnetic islands at a vertex are equivalent, simply because the distance between the islands on the opposite sides of the vertex is larger than that of the neighbouring islands (see Fig. 11a). One way to get around this would be to modify the height of the different sub-lattices so that all interaction

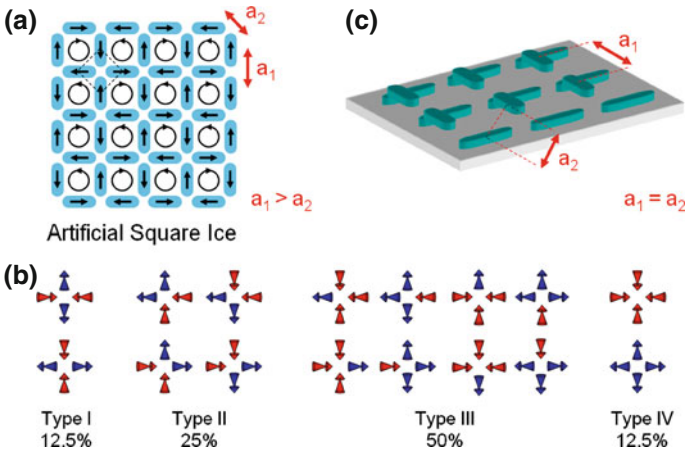

Fig. 11 **a** Artificial square ice in the ground state with a checkerboard pattern of vortices [60, 93]. Here the island interactions at a vertex are not equal since $a_1 > a_2$. **b** The sixteen possible moment configurations at an island vertex, sorted into the four different types. The *percentages* indicate the expected percentage of each type if the individual moment orientations in an array were completely random. **c** Raising one island sublattice compared to the other gives an artificial square ice with $a_1 = a_2$

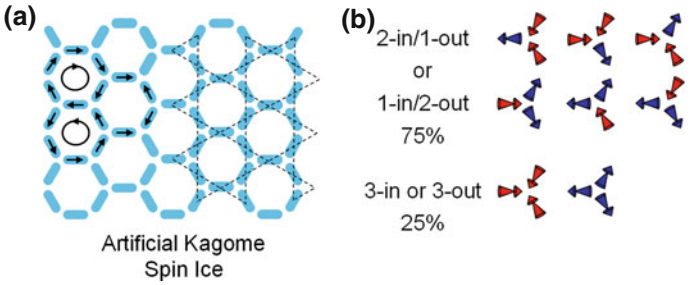

Fig. 12 Artificial kagome spin ice [65, 67, 72]. **a** Hexagonal array of elongated ferromagnetic islands placed on the sites of the kagome lattice, with a ground state configuration indicated [69, 70]. **b** The eight possible moment configurations at an island vertex, sorted into the two different types. The *percentages* indicate the expected fraction of each type if the individual moment orientations in an array were completely random

distances are the same (see Fig. 11c) [65, 66]. Another possibility is to consider instead the kagome (or hexagonal) spin ice [65, 67, 72] where the elongated ferromagnetic islands are placed on the sites of the kagome lattice so forming the links of a honeycomb (see Fig. 12a) and all island interactions at a vertex are the same. For the three island vertices where the moments meet, there are eight possible configurations, six of them obeying the ice rule, which becomes two-in/one-out or one-in/two-out (see Fig. 12b). Such a kagome spin ice phase arises in three dimensional pyrochlore spin ice when a magnetic field is applied along the [111] direction [68]. The ground

state of the square ice (Fig. 11a) is a series of vortices with alternating chirality [93]. The ground state in a kagome spin system is a little harder to imagine but, using a long range dipolar calculation, it has been found to be a tessellation of the three ring configuration containing a double vortex and a hexagonal ring with all head-to-tail moments [69, 70] as shown in Fig. 12a. Indeed, while the short range moment correlations are dominant in artificial spin ice, it is necessary to consider long range interactions to fully understand the moment configurations [71].

The final states observed in an artificial spin ice, either experimentally or theoretically, are dependent on the magnetic field or thermal history of the sample and on the detailed geometry, which determines the extent of frustration and therefore the degree of ordering. In particular, the behaviour of such artificial spin systems depends intimately on the island length, width and the lattice parameter. For example, in artificial kagome spin ice, the ice rule is very robust occurring at every vertex following demagnetization [61, 72], as long as the dipolar coupling is strong enough. However, the ice rule can be broken on application of a magnetic field [62, 74], forming an ordered array of ice rule defects at reduced dipolar coupling [73]. The final magnetic configuration is also highly dependent on the orientation of the applied magnetic field. For example, in the square ice the magnetic configuration depends on whether the field is applied parallel to one of the island rows or along the lattice diagonal [75].

While the square and kagome spin ice geometries are the most investigated to date, one could imagine other frustrated artificial spin geometries, which display different behaviours. For example, placing the magnetic islands on a triangular lattice results experimentally in areas of ordered moments [76]. Other arrangements include islands placed on the links of the kagome lattice [78], or modifications to the basic spin ice geometries [79, 77], and one could even imagine other more exotic designs, for example, placing the magnetic islands on a quasiperiodic lattice [80]. It should also be pointed out that, rather than considering an arrangement of isolated ferromagnetic islands, one can construct hexagonal (or honeycomb) networks comprising joined nanowires [61, 62, 81, 82]. Such connected systems have the advantage of allowing magnetoresistance measurements, [62] although they are fundamentally different to the arrays of dipolar coupled single domain magnets since there is a magnetic link between the 'artificial spins' and, in contrast to magnetization reversal of individual magnetic islands, the reversal in connected systems is mediated by movement of domain walls through the system [82]. Here the domain walls can be thought of as magnetic charge carriers. It should also be pointed out that a connected square ice system is part of a class of patterned thin film systems referred to as antidot arrays [83], which are also of interest in the field of magnonic crystals [84] and for the generation of antivortices [85].

While the focus of the current section is on artificial spin ice systems fabricated from two dimensional arrangements of nanomagnets with in-plane anisotropy, it should be pointed out there are other systems that can mimic the behaviour of spins on a crystal lattice. Such systems make use, for example, of colloids [86–88] or trapped superconducting vortices, [89] or dipolar coupled magnetic islands with out-of-plane magnetization that represent the up-down Ising spins on a triangular

lattice, with the dipolar interaction replacing the interspin antiferromagnetic exchange interaction [90].

2.2 Artificial Spin Ice Building Blocks

In order to address the physics of frustration in artificial spin ice, it is advantageous to break the problem down into its constituent parts, considering the building blocks of an infinite system, in other words finite clusters of magnetic islands [72, 91]. For the artificial kagome spin ice, one can therefore consider the building blocks with one, two and three hexagonal rings [72], as shown in Fig. 13. Since the building blocks are finite, it is possible to calculate the dipolar energy of every possible state, assuming a macrospin associated with each island and using the standard expression for the dipolar energy for two interacting islands:

$$E(\mathbf{r}_1, \mathbf{r}_2, \mathbf{m}_1, \mathbf{m}_2) = \frac{\mu_0}{4\pi} \frac{1}{|\mathbf{r}|^3} \left[(\mathbf{m}_1 \cdot \mathbf{m}_2) - \frac{3}{|\mathbf{r}|^2} (\mathbf{m}_1 \cdot \mathbf{r})(\mathbf{m}_2 \cdot \mathbf{r}) \right] \quad (1)$$

where $\mathbf{m}_1$ and $\mathbf{m}_2$ are the magnetic moments of two islands and $\mathbf{r}$ is the distance vector between the centres of the islands.

For a single hexagonal ring, the presence of six islands gives a total of $2^6 = 64$ possible states. From the above expression, one can then determine the ground state to be the vortex state with neighbouring moments pointing head-to-tail (see Fig. 13) and with a two-fold degeneracy since the moments can circulate clockwise or anticlockwise around the ring. For a two-ring building block, the two lowest energy states are the double-vortex ground state, consisting of two vortices with opposite chirality, and the external flux closure state with moments circulating in a given sense around the rim of the structure as shown in Fig. 13. For the three-ring building block, the ground state has a double-vortex with the third ring not quite being able to form a vortex since it shares islands with the other two rings and the next highest energy state is also an external flux closure state (Fig. 13).

On demagnetizing arrays of the kagome building block structures by rotating in a magnetic field, it was found that as the number of rings increased, the percentage of structures that fell into the lowest energy states shown in Fig. 13 significantly dropped from more than 90 % for the one-ring structures down to less than 40 % for the three-ring structures [72]. This carries the important implication that it will be impossible to achieve the ground state in an infinite system using such a demagnetization protocol. One might, however, ask whether this increasing inability to attain the ground state is really a result of the increasing number of three-island vertices and therefore increasing frustration, or is simply because of the increasing number of islands resulting in a longer and more complex path to the ground state through many more magnetic configurations. In order to address this question, Li et al. [91], studied different island clusters based on the square ice. All of the clusters contained four elongated islands that either included or did not include a vertex where more than two islands meet, and therefore included or did not include frustration.

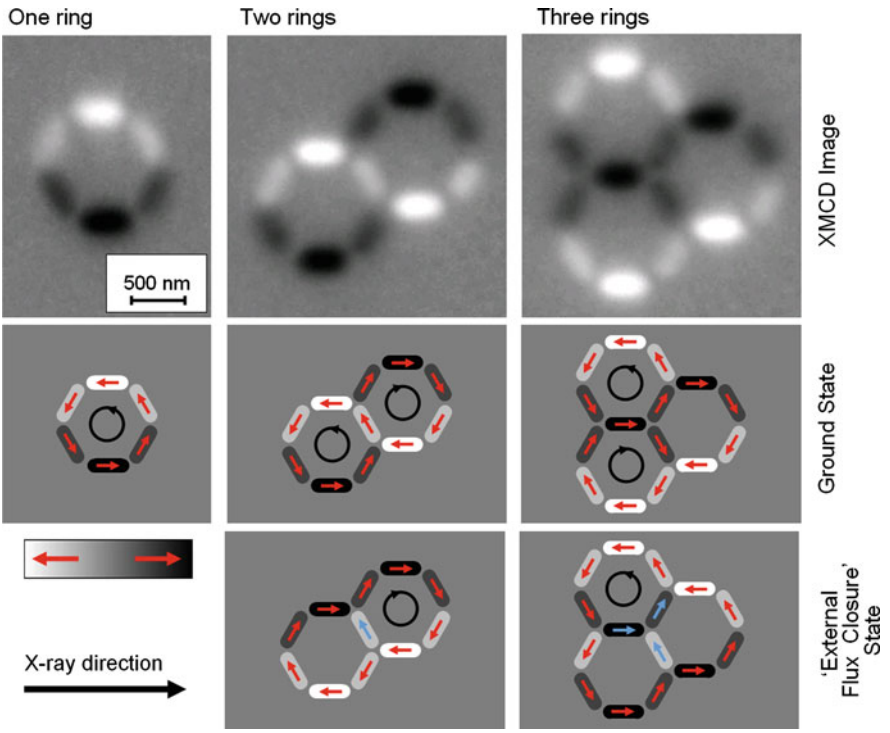

Fig. 13 X-ray magnetic circular dichroism (XMCD) images of the ground states of the artificial kagome spin ice building blocks [72]. The single contrast associated with each island indicates that they are monodomain with the magnetic moment aligned parallel to the island long axis. Islands with moments parallel (antiparallel) to the X-ray direction, i.e., pointing to the right (*left*), have a black (*white*) contrast. Islands with moments at $\pm 60°$ or $\pm 120°$ to the X-ray polarization direction have one of two intermediate contrasts: *dark grey* or *light grey*, respectively. The four contrast levels in a single XMCD image allow the determination of the magnetic states given schematically below each image. The next highest 'external flux closure' energy states are given for the two- and three-ring building blocks

On demagnetization in a rotating field, the cluster geometries where the interactions were not frustrated were found to more easily reach the ground states than those with frustrated geometries. Therefore one can conclude that it is indeed the frustration that hinders energy minimization.

2.3 Achieving the Ground State

One might expect that a modification of the way in which the field is applied during demagnetization would improve the likelihood of achieving the ground state in artificial spin ice systems. While it was found that the geometry of the demagnetization setup, i.e. rotating the sample about an in-plane or out-of-plane axis, did not make a

difference to the ability to achieve the ground state [72], the use of finer field steps during the demagnetization did indeed lead to a higher frequency of low energy states and a successful demagnetization with zero residual moment [64]. However, extrapolation of the dipolar energies indicated that the energy would still be well above that of the ground state as the field step is reduced to zero.

Theoretical modeling has indicated that a rotating field of constant strength applied to finite square ice arrays [92] can lead to an optimization of the number of ground state vertices when the applied magnetic field is set to a particular value. When the magnitude of the field is too low, the island magnetic moments will not react to the field at all and when the field is very high, the moments will simply follow it. For an intermediate field strength, just above the minimum value needed to give a dynamic response, a maximum number of ground state vertices is achieved. One could imagine experimental implementation of such a procedure with monitoring of the magnetic response during demagnetization to identify and control the required applied magnetic field strength.

Although the moment configuration in such artificial spin ice systems is athermal, i.e. the energy barrier to flipping of moments in the absence of thermal fluctuations is of the order of 10^5 K, it is possible to describe the magnetic configurations following demagnetization in an alternating magnetic field as a thermal ensemble with an effective temperature [93, 94] and calculate the entropy by considering the configurations of clusters of islands within the array [95]. However, the deterministic behaviour of the moments in an applied magnetic field is very different to the stochastic behaviour when the system undergoes a thermal annealing. As the amplitude of the applied alternating magnetic field is decreased, each of the island moments freezes into a particular configuration, given by the local dipolar energy and the instantaneous field magnitude and direction. This deterministic setting of states is seen most clearly at low dipolar coupling strengths where states are favoured with the moments oriented towards the same direction, given by the direction of the field as the moments are frozen in [72].

Therefore non-deterministic methods, using for example a real thermal annealing, need to be implemented in order to achieve the ground state [96]. A first indication that thermal annealing will indeed provide a route to the low energy states has been discovered in an as-grown artificial square ice comprising permalloy islands [97]. Here it appears that the ground state was formed in the first stages of film growth when the layer was thin enough (sub-1 nm) to support thermal fluctuations and the moments froze in as the layer became thicker. The ground state consisted of vortices of alternating chirality as shown in Fig. 11a, with boundaries separating domains of opposite chirality. Local excitations consisting of clusters of islands with moments flipped compared to the background were also present and the frequency of these excitations decreased exponentially with their excitation energy above the ground state. This followed a Boltzmann distribution, so providing a signature for thermal excitations and therefore ‘true thermodynamics’.

2.4 Emergent Magnetic Monopoles

In 2008, it was predicted that emergent magnetic monopoles would appear in pyrochlore spin ice systems as charge excitations resulting from the collective behaviour of the spins [98]. Such quasi-particles occur in monopole–antimonopole pairs of opposite charge, and are connected by a so-called 'Dirac String', which refers to an arbitrarily narrow flux tube transporting magnetic flux between them, an idea that Dirac used in his original work to take account of Maxwell's equations ($\nabla \cdot \mathbf{B} = 0$) [99]. It is important at this stage to note that emergent magnetic monopoles in a condensed matter system should be differentiated from their elementary counterparts [100], which may or may not have string-like singularities, but have not yet been discovered. The prediction of emergent magnetic monopoles resulted in a series of experimental demonstrations in reciprocal space with neutron scattering of the signatures of monopoles and classical versions of Dirac strings in $Ho_2Ti_2O_7$ and $Dy_2Ti_2O_7$ bulk spin ice [101–103]. Motivated by this work in the bulk crystals, the next step was to look for monopoles in quasi-infinite artificial spin ice systems [74, 81].

In order to be able to identify the magnetic monopoles, one can imagine that each dipole of magnetic moment, m, is stretched into a charge dumbbell with a $+q$ and $-q$ charge at each end [98]. Considering the net charge at each vertex for a fully saturated configuration, gives zero charge at every vertex for the artificial square ice and an ordered charge state of $(+1q, -1q)$ at every neighbouring vertex pair in the kagome spin ice (see Fig. 14a). When a magnetic field is applied in the reverse direction, an island moment will flip and the net charges at a vertex will change. One can then define a change in the charge of $\Delta Q = +2q(-2q)$ as a monopole (antimonopole) as shown schematically for the artificial kagome spin ice in Fig. 14b. It should be noted that, while for a square ice the monopoles correspond to the position of ice rule defects, i.e. where the net charge $Q = \pm 2q$, for the artificial kagome spin ice the monopoles do not necessarily occur where there is an ice rule defect, since the net charge can be either $\pm 1q$ (ice rule preserved) or $\pm 3q$ (ice rule broken).

It has been shown in an artificial kagome spin ice how, on application of a magnetic field, monopole–antimonopole pairs nucleate and separate, and move through the two dimensional system along one dimensional paths [74]. A snapshot of the magnetization reversal in a quasi-infinite artificial kagome spin ice is shown in the XMCD image of Fig. 15. Here, the islands in the initial state (moments pointing towards the left) have a bright contrast and islands where the moments have reversed (moments pointing towards the right) have a dark contrast. The magnetization reversal starts via the creation of monopole–antimonopole pairs at specific islands. After creation, these monopole–antimonopole pairs separate and the path followed by the monopoles, i.e. the history of their displacement, can be seen as a dark chain of islands with reverse moments which corresponds to the Dirac string. The Dirac strings are indicated in the neighbouring schematic in Fig. 15 by a continuous line connecting a red-blue monopole–antimonopole pair corresponding to vertices with $\Delta Q = +2q$ and $-2q$ as described above. In order to confirm the presence of monopoles, one can

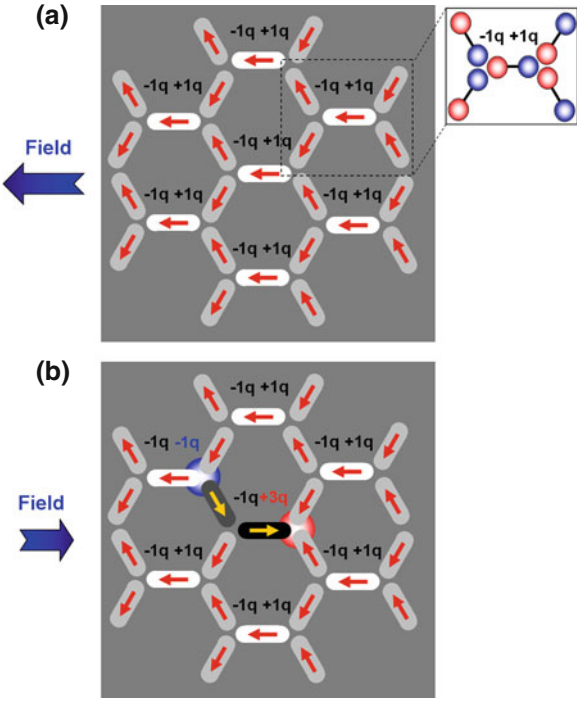

Fig. 14 Schematic representation of emergent monopoles and Dirac strings in an infinite artificial kagome spin ice. The schematic in **a** represents the XMCD contrast (see Fig. 13) corresponding to the moments pointing to the left following the application of a magnetic field pointing to the left. The inset shows how the magnetic moments can be considered as dumbbells carrying charge $+q$ and $-q$ (in *red* and *blue*). The net charge results in an alternating $(+q, -q)$ charge ordering at the vertices. **b** On application of a magnetic field to the right, moments are reversed and the corresponding charge dumbbells are overturned along the Dirac string (*dark contrast*), resulting in two charge defects with $\Delta Q = +2q$ and $-2q$ at the ends of the string as indicated by the large *red* and *blue spheres*

consider the coarse grained charge density, ρ_m, defined as the discrete distribution of total charges Q convoluted with a Gaussian [98]. In the right hand panel of Fig. 15, it can be seen that the dimensionless charge density, ρ_m, is indeed consistent with the position of the charge defects $\Delta Q/q = \pm 2$. From Monte Carlo simulations that directly mimic the experimental behaviour [74], it could be observed that when an island moment flips on application of a particular field, this causes the moments of the neighbouring islands to flip sequentially until an island with a higher switching field is met. When delving into the details of avalanche behaviour, it turns out that the power law normally expected with avalanche behaviour is not obeyed. Instead, the probability $P(s)$ for the occurrence of a Dirac string avalanche decays exponentially with its length s. This reflects the one dimensional growth of the Dirac strings, which is very different to the two-dimensional domain growth that occurs in

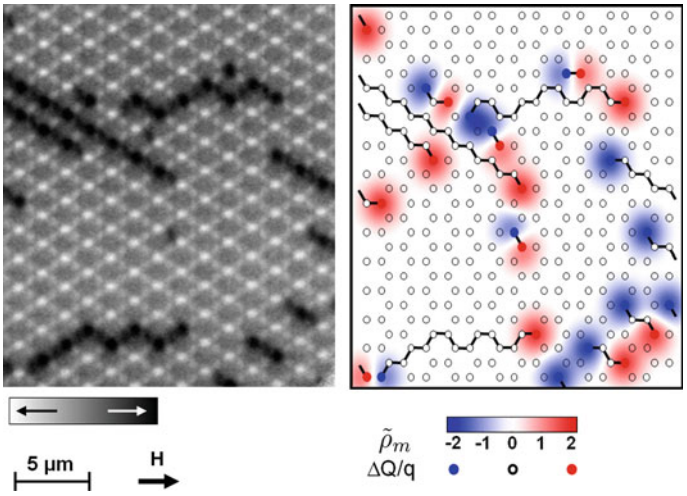

Fig. 15 Experimental observation of emergent monopoles and Dirac strings in a quasi-infinite artificial kagome spin ice [74]. XMCD image of an artificial kagome spin ice consisting of permalloy islands (thickness 20 nm, length 470 nm and width 160 nm, lattice parameter 500 nm) together with the associated ΔQ map. The Dirac strings connect monopole–antimonopole pairs, with $\Delta Q = +2q$ and $-2q$ indicated with *red* and *blue dots*. The ΔQ map is shown together with the dimensionless coarse grained magnetic charge density, ρ_m, both of which give signatures for nonzero charge density

continuous magnetic thin films. The reversal behaviour is highly dependent on the detailed geometry of the artificial spin ice system. In an artificial kagome spin ice with low interisland coupling compared with the shape anisotropy [73], an ordered array of $\pm 3q$ magnetic charges can be obtained on application of a magnetic field along the relevant direction. The displacement of monopoles can also be observed in square ice arrays [63] but, in order to allow them to be free to move, the relative heights of the sublattices should be increased [66] as shown in Fig. 11c.

Considering the charge model in artificial kagome spin ice, the phases as a function of temperature have been theoretically predicted [69, 70]. Cooling down from the highest temperature paramagnetic phase, corresponding to a gas of magnetic charges ($\pm 1q$ or $\pm 3q$), there is a transition to a gas of $\pm 1q$ charges, followed by an NaCl ordering of the magnetic charges at lower temperature, i.e. alternating $+1q$ and $-1q$ vertices, so that the ice rule is obeyed at every vertex. The lowest temperature phase then has both charge order and spin order as shown in Fig. 12a. This breaking of degeneracy only occurs when not only the nearest neighbour exchange interactions are considered but also the longer range dipolar interactions. In other words, when considering nearest-neighbour interactions only, neither charge nor spin order is displayed [67, 70].

Since the original work on artificial spin ice in 2006 [60], artificial spin systems have provided a new research focus in the scientific community, with several groups employing arrangements of dipolar coupled magnets to study the physics of

frustration in systems with tunable geometries. The work reported to date has revealed some fascinating phenomena and has also raised several interesting questions, providing the foundations for future scientific discoveries with a view to novel device applications.

One important future direction will be to identify quasi-particle interactions, where monopoles with like charges should repel and oppositely charged monopoles should attract. A first hint of such interactions in artificial square ice has been seen by Morgan et al. [97] who observed that for local excitations in their as-grown sample in the ground state, closed loop configurations such as a ring of four flipped moments is preferable to open chains of flipped moments, minimizing the number of monopole–antimonopole pairs.

While it is envisaged that arrays of dipolar coupled magnetic islands could be exploited in data storage and spintronics applications [90, 104], in order to successfully implement the artificial spin ice systems in devices, the magnetic configurations will need to be well-defined and accessible. One route to gain this control would be to modify the behaviour of particular islands. One possibility is to decrease (increase) the width of particular islands, so that the shape anisotropy is increased (decreased) and the switching field is increased (reduced). Indeed, it has been shown that on introducing islands with modified switching fields in an artificial spin ice, one can generate sites for the creation of monopole–antimonopole pairs and for halting their movement (supplementary information of Ref. [74]).

3 Magnetic Nanostructures for Data Storage in Hard Disk Drives

While the previous chapter captured fundamental issues of magnetic islands, their interaction in frustrated lattices, and excitations above the ground state, the present chapter is devoted to applications, in particular to the technology of patterned magnetic hard disks using ordered arrays of perpendicular anisotropy magnetic islands. One does not exaggerate when stating that the physics of magnetic nanostructures is at the heart of magnetic hard disk drive (HDD) technology [105, 106]. This will be even more so the case in the future, when new technologies, such as bit patterned media (BPM) or heat assisted magnetic recording (HAMR) have to be introduced in order to increase areal densities well beyond 1 Terabit/inch^2 (1 Tb/in^2) [107, 108].

The current section is divided into five subunits: (i) Current state of the art granular perpendicular magnetic recording (PMR), (ii) Introduction to bit patterned media (BPM), (iii) Importance of a narrow magnetic switching field distribution (SFD) in BPM, (vi) Importance of media architecture and pattern uniformity in BPM, (v) Different fabrication approaches for BPM.

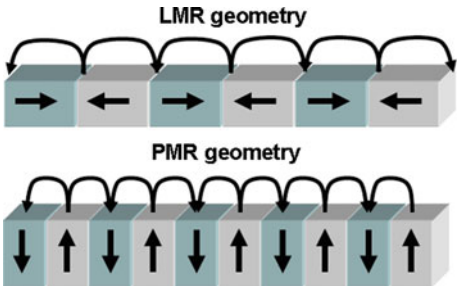

Fig. 16 Longitudinal magnetic recording (LMR) versus perpendicular magnetic recording (PMR) bit geometry. *Thick arrows* indicate the two different magnetization directions along the easy anisotropy axis, while *thin arrows* represent stray fields outside the bits at the surface of the disk

3.1 Current State of the Art Granular Perpendicular Magnetic Recording

Currently HDD media technology is built upon phase-segregated CoCrPt-based granular magnetic thin films that consist of Co-rich magnetic grains and oxide based non-magnetic grain boundaries (see also Fig. 17) [106]. Up until about 2006 the magnetization of the grains, i.e. the easy anisotropy axis, was confined within the thin film plane (oriented as much as possible in circumferential down track direction) for so-called longitudinal magnetic recording (LMR) media. After extending LMR via antiferromagnetically coupled (AFC) media [109] to densities of about 100 Gigabit/inch^2 (Gb/in^2), continuous improvements in deposition technology combined with successful research and development efforts led to the introduction of high quality CoCrPt+oxide based granular recording media with the magnetization (easy axis) aligned perpendicular to the film plane. This was a crucial technology breakthrough that enabled areal densities well beyond 100 Gb/in^2.

Traditionally for LMR media grain size reduction was the major pathway for increasing areal density, while after the introduction of perpendicular magnetic recording (PMR) the grain size has remained more or less constant or if at all increased slightly over time from 2006 until today. In PMR media gains in areal density were achieved due to various other effects. On the one hand bit transitions can be packed closer together in a PMR geometry as compared to a LMR geometry, since in PMR adjacent bits with opposite magnetization form a magnetic flux closure at the bit transitions, while in LMR identical polarities face each other at the position of the bit transitions as illustrated in Fig. 16. Therefore bits packed at high density in PMR geometry are less exposed to demagnetization fields and thermal decay than bits packed at the same density in LMR geometry. Furthermore the introduction of a soft magnetic underlayer (SUL) below the granular recording media as part of the magnetic recording head structure allowed achieving higher magnetic write fields aligned perpendicular to the film plane as previously available in LMR. Thus it was possible to use higher write fields with higher write field gradients and produce better

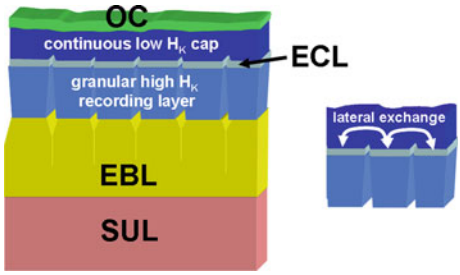

Fig. 17 Modern PMR media structure with soft underlayer (SUL), exchange break layer (EBL), which contains the seed- and underlayers for the magnetic media, high anisotropy granular recording layer, which consists of laterally decoupled magnetic grains and a more continuous low anisotropy cap layer with strong lateral exchange. In order to control the vertical exchange between the granular recording layer and the continuous cap layer for the reversal assist, an exchange coupling layer (ECL) may be introduced in between the high anisotropy recording layer and low anisotropy cap. The degree of lateral exchange for the composite recording system can now be mainly controlled by the thickness of the cap layer [113] as illustrated on the right. An overcoat (OC) layer is finally deposited to protect the media from oxidation and other damage

defined bit transitions. Moreover once it was possible to align the Co c-axis of the CoCrPt grains, i.e. the easy axis of magnetization perpendicular to the film plane the grain to grain variation in easy axis orientation could be reduced significantly [110] as compared to LMR media, where the easy axes had to be aligned circumferentially by mechanically orienting the ellipsoidal shaped grains with the long axis in track direction [106]. The better easy axis alignment of the columnar shaped grains down to about 3° in today's PMR media increased signal to noise ratio at the bit transitions significantly as compared to LMR media. Furthermore, the introduction of a continuous magnetic cap layer with lower anisotropy that assists the switching of the high anisotropy granular recording layer allows using even harder materials in recording media. Such a hard granular/soft continuous media bilayer architecture also provides a better control and uniformity of the inter-granular lateral exchange in the media [110, 111]. With this improvement it was possible to fabricate laterally completely de-coupled grain structures within the high anisotropy recording layer and then fine tune the degree of lateral exchange from grain to grain by varying the thickness of the laterally continuous and laterally highly exchange coupled low anisotropy reversal assist layer as illustrated schematically in Fig. 17 on the right. The possible introduction of an additional non-magnetic exchange coupling layer (ECL) in between the high anisotropy granular and low anisotropy continuous layer enables an even better control of the overall magnetic performance of the media stack via a more incoherent reversal mode of the composite media structure. In such exchange spring layer (ESL) or exchange coupled composite (ECC) media structures [111–113] lateral inter-granular exchange is separately optimized via the degree of vertical exchange through the non-magnetic or low moment ECL as well as via the thickness of the lower anisotropy reversal assist layer (see also for illustration Fig. 17).

Today PMR media has paved the way to achieve densities that approach 1 Tb/in^2. However magnetic layer structures have become increasingly complex and areal density gain factors are getting smaller as PMR media evolve to higher and higher levels of sophistication and complexity, as described in the previous paragraph [114–116]. Scaling the lateral grain size further down from the current grain to grain spacing of about 8–10 nm is most essential in order to push PMR technology beyond 1 Tb/in^2. Alternatively (i.e. without further grain size reduction) with the down track bit period approaching about twice the current grain size, significant additional areal density gains can only be achieved by packing the tracks tighter together, which, with a current bit aspect ratio of 4–5, are still on the order of 80 nm wide in today's HDDs.

Shingled magnetic recording (SMR) is one pathway for extending PMR granular media performance based on current grain dimensions into the future. In SMR subsequently written neighbor tracks are overlapping like shingles on a roof and thus allow reducing the bit aspect ratio significantly from current values of 4–6 towards lower values of 2–3 [117]. In return, single tracks cannot be written independently any more. Instead whole larger bit blocks (sectors) have to be addressed at a time due to the overlapping architecture of the tracks during the write process, which also implies some trade off between higher areal density and fast read/write data access time. Today it is projected that SMR may take granular PMR media up to densities of about 1.5 Tb/in^2.

More dramatic future HDD technology approaches that would allow densities beyond 1.5 Tb/in^2 are energy assisted magnetic recording (EAMR) and bit patterned recording (BPR). The most prominent candidates for EAMR considered today are heat assisted magnetic recording (HAMR) and microwave assisted magnetic recording (MAMR) that use additional energy sources in the form of heat and microwaves for lowering the magnetic reversal field in ultra-high anisotropy granular PMR media. One crucial assumption for exploiting EAMR based on granular media structures is that a significant reduction of the current grain size down to the 3–4 nm level is possible. Even though such small grains require very high magnetic anisotropy in order to maintain thermal stability over the lifetime of a HDD, the reversal assist in the form of heat or microwaves allows lowering the reversal field to currently available magnetic write field levels. Some of the most critical challenges that still have to be addressed in HAMR are the fabrication of small, columnar grain media with tight grain size distribution based on high anisotropy materials [118, 119], such as $L1_0$ FePt and the control of thermal fluctuations during the write process when the media cools down and the magnetic state is "frozen in". Such thermal fluctuations during media cool down have to be consistent with achieving bit error rates (BER) of below 10^{-3} in order to support a stable recording system [120]. The only media technology currently explored that does not rely heavily on small grain media with tight size distributions is bit patterned recording (BPR).

3.2 Introduction to Bit Patterned Media

In bit patterned media (BPM) the bits no longer consist of an assembly of chemically segregated random grains, but are pre-defined lithographically as single magnetic units that we also refer to as islands [121, 122]. Thus BPM does not rely on any grain/grain-boundary segregation process. Moreover the thermal stability requirement for single grains $K_U V_{grain} > 70\, k_B T$ is replaced by the much more relaxed thermal stability requirement for single bits $K_U V_{bit} > 70\, k_B T$ (see Fig. 18).

With today's media consisting of only 15–20 grains per bit and a 2-dimensional BPM island area filling factor of about 50 % (i.e. island diameter is about 0.7 times island pitch) one can expect a 7–8 fold increase in areal density based on the same magnetic anisotropy K_U, i.e. the same magnetic media material system. Thus it would be possible to increase densities from today's granular media of around 500 Gb/in^2 to about 3–4 Tbit/in^2, when moving to a BPM-based recording scheme. An additional gain in areal density may be possible by moving to higher anisotropy materials, such as $L1_0$ FePt [123, 124] in combination with lower anisotropy reversal assist layers [125, 126] or by ultimately combining BPR with EAMR [127].

Besides the general mass fabrication challenges that have to be faced with the introduction of any new recording technology, moving to a BPR system requires also some very specific changes with respect to the recording system architecture itself that represent additional barriers. Such changes include write synchronization with the pre-defined bits as well as servo integration into the master pattern fabrication process. Furthermore the recording system has to correct so called "written in errors" that occur during the write process. Such "written in errors" are not present in current granular PMR systems, where only some small fraction of the 15–20 grains that contribute to the final signal of the bit may end up being magnetized in the wrong direction. Thus the averaged signal to noise ratio (SNR) usually still allows recovering the correct bit polarity in granular PMR media. In BPR there is no such gradual loss in SNR due to the fact that the bit signal is statistically averaged over many grains. Instead entire bits (or islands) magnetized in the wrong direction may occur as "written in" hard errors. In order to limit the probability of such hard write errors to below 10^{-3} the island array requires a very narrow magnetic switching field distribution (SFD), such that the magnetically hardest islands can still be written by the head without overwriting a neighbor island that may be part of the magnetically softest islands in the array.

3.3 Importance of a Narrow Magnetic SFD in BPM

We distinguish multiple contributions to the magnetic SFD of a BPM island array. First there is the long-range dipolar interaction due to the stray fields of the islands that act upon each other. We call this the dipolar part or dipolar broadening of the SFD. Such dipolar interactions within the island array during a magnetic field reversal are illustrated in Fig. 19, where we also show Magnetic Force Microscopy (MFM) images

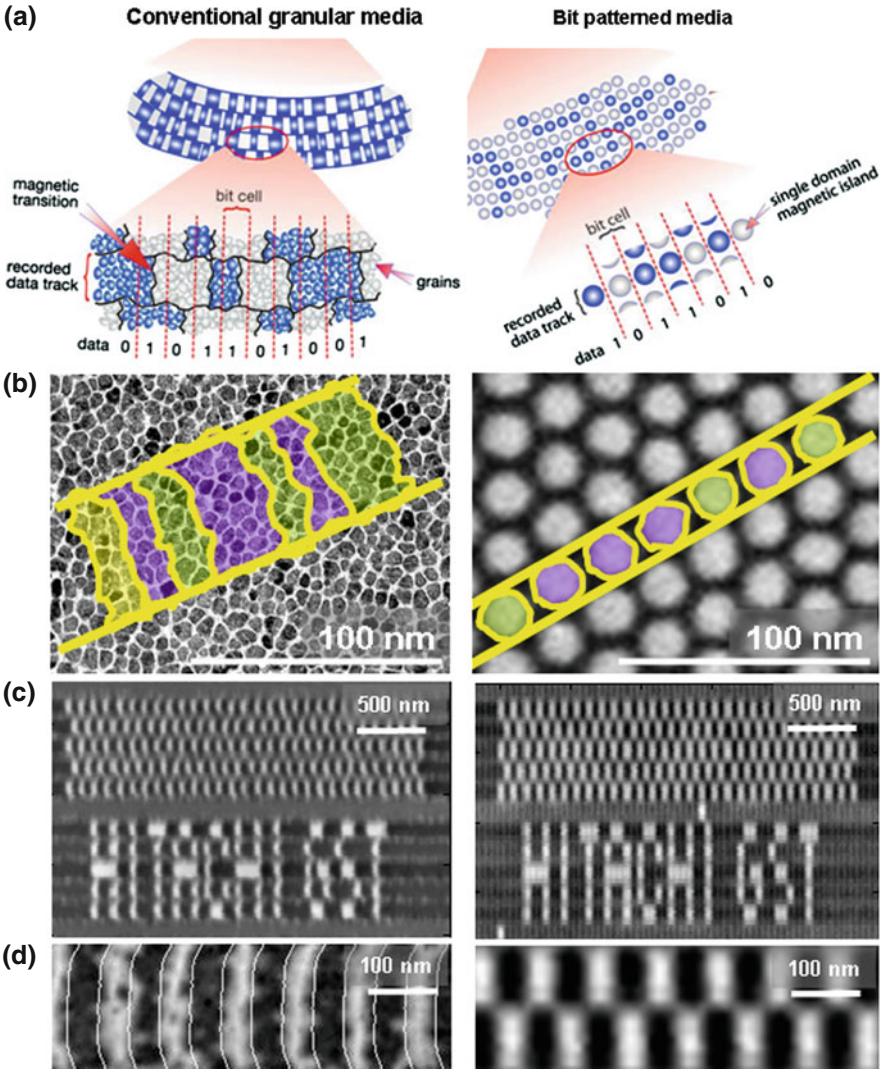

Fig. 18 Comparison of granular PMR (*left*) and BPR (*right*) media systems. **a** Illustration of the bit scheme on the disk for both recording systems. **b** Illustration of how the bits are defined within the lateral recording media microstructure. **c** Comparison of static read/write testing on both media systems. **d** High resolution images with alternating up-down bit structure for both recording systems obtained from the static read write tester [128]. For both, PMR and BPR, bit dimensions in **c** and **d** are 145 nm cross track and 45 nm down track, which corresponds to an areal density of about 100 Gb/in^2

of AC demagnetized samples that exhibit typical magnetic patterns that represents the lowest energy magneto-static configurations in corresponding island arrays with a square or hexagonal lattice for 50 % up and 50 % down states.

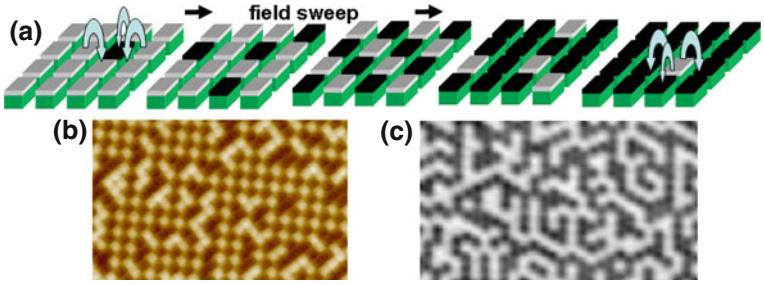

Fig. 19 **a** Illustration of the different states in a BPM island array during an external magnetic field sweep. Initially the dipolar fields from neighboring islands add to the externally applied field and help reversing the intrinsically easy to switch islands at even lower external fields. When finally the intrinsically hardest to switch islands are reversed, the dipolar fields from neighbor islands delay the reversal to higher external fields. Thus overall the island reversal is uniformly broadened by the dipolar interactions. **b** For a square island lattice at the coercive point when 50 % of the islands are magnetized up and 50 % are magnetized down, a checkerboard state is the lowest energy magnetostatic configuration as observed in this MFM image of a squared BPM island array with 100 nm pitch (64 Gb/in^2). **c** For a hexagonal island lattice the formation of a checkerboard state is not possible due to its geometry. Instead one observes a labyrinth stripe like domain pattern (similar as in full film perpendicular anisotropy systems) as displayed in this MFM image of a hexagonal BPM island array with 38 nm pitch (500 Gb/in^2)

Of more fundamental nature than dipolar interactions however is the intrinsic part of the magnetic SFD, which originates on the one hand from the intrinsic distributions of the magnetic material properties, such as size and angular orientation of the anisotropy and on the other hand from fabrication induced distributions, such as size and shape of the magnetic islands that form the bits as well as magnetic damage that has been introduced during the fabrication process. Using minor magnetic hysteresis loop measurements it is possible to separate both, dipolar and intrinsic part from each other and determine their relative and absolute contributions to the total SFD, which is for Gaussian profiles often defined as the standard deviation of the derivative of the magnetic reversal curve (or hysteresis loop branch). A simple separation method between dipolar and intrinsic SFD as derived from the 50 % island reversal curve following the method of Tagawa [129] is illustrated in Fig. 20. When comparing the (red) 50 % reversal curve (i.e. the reversal of the easy to switch 50 % of the islands, with the hard to switch 50 % of the islands already magnetized into the external field direction) with the first half of the (blue) full reversal curve (i.e. the reversal of the easy to switch 50 % of the islands, but with the hard to switch 50 % of the islands still magnetized opposite to the external field direction), then the shift $\Delta H_{C,ext}$ between both curves at the 25 % reversal level provides a measure for the dipolar part of the SFD, since we switch the identical subset of islands, but with different dipolar mean field from the harder to switch 50 % of the islands. Similarly when comparing the loop shift of the (red) 50 % reversal curve with the second half of the (blue) full reversal curve, then the shift $\Delta H_{C,int}$ between both curves at the 75 % reversal level provides a measure for the intrinsic part of the SFD, since we

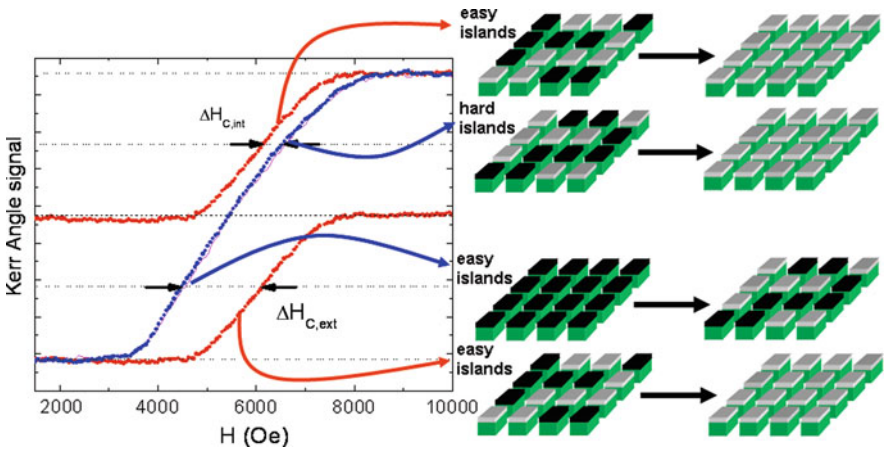

Fig. 20 **a** Illustration of the H_C-method for separating the dipolar and intrinsic part of the magnetic SFD. The *red curve* is the 50 % island reversal curve after returning from the negative coercive point back to positive saturation, while the *blue curve* is the increasing branch of the full hysteresis loop. The field shift $\Delta H_{C,int}$ of the 50 % (*red*) island reversal curve at the 50 % reversal point with respect to the complete 100 % (*blue*) island reversal curve at the 75 % reversal point provides a measure for the intrinsic portion of the SFD. Different subsets of islands are reversed with the same mean dipolar interactions acting upon them. The field shift $\Delta H_{C,ext}$ of the 50 % (*red*) island reversal curve at the 50 % reversal point with respect to the complete 100 % (*blue*) island reversal curve at the 25 % reversal point provides a measure for the dipolar portion of the SFD. The same subset of islands is reversed with different mean dipolar interactions acting upon it

switch different subsets of islands (easy to switch 50 % versus hard to switch 50 % of the islands) in the same dipolar mean field. So in average dipolar interactions are the same and the shift is purely due to intrinsic distributions in island properties. A more sophisticated method developed by Berger et al. [130–132] that also includes the possibility of lateral exchange in between islands (or grains for granular PMR), uses a complete set of minor loops in order to extract intrinsic SFDs of arbitrary functional form.

Obviously the dipolar interactions within an island array depend on the magnetic moment of the media, its thickness and the island area filling factor within the array. In a magnetometry experiment as shown in Fig. 20, many shells of neighbor islands contribute to the overall dipolar field acting on a target island, since the fields are commonly not shielded by anything else. The significance of dipolar interactions may however change in a real magnetic recording write scenario, where head shields are in close proximity to the write pole and thus absorb the majority of stray fields from neighboring islands. Furthermore recording experiments will generally be performed on an AC-demagnetized media (i.e. on a pattern with 50% up and 50% down island states similar as shown in Figs. 19b and c) in order to minimize dipolar interactions. These effects can reduce the effective dipolar interactions by a factor of 3–5 [133] and thus dipolar interactions may not be the major concern for the actual write process in BPR. Further mechanisms for reduction of dipolar interactions have been proposed

in the literature, such as AF-coupled BPM structures [134, 135] or the introduction of weak lateral exchange in between islands that still allows independent reversal and addressability of islands, but compensates some of the dipolar interactions from neighbors [136–138]. However these suggestions are mainly based on modeling and do not address the immense fabrication challenges that are usually connected with such thin and complex layered media structures and the necessity to have very tight distributions also in all additionally introduced magnetic properties, such as lateral inter-island exchange or antiferromagnetic interlayer exchange coupling.

From the above considerations it becomes apparent that distributions of the intrinsic island properties (anisotropy strength, direction of easy anisotropy axis, island size, island shape, etc) [139] are the most important contributions to the overall magnetic SFD that affects the bit error rate (BER) during the write process. Thus a narrow intrinsic magnetic SFD is of great importance in order to design a successful BPR system [140]. Several studies from the literature address the various origins of intrinsic magnetic SFD. Thus Shaw et al. compared the SFD in perpendicular anisotropy Co/Pd multilayer with different crystalline microstructure, namely single crystalline, i.e. epitaxial, textured granular, i.e. with a well-defined out-of-plane crystalline direction, but a random in-plane crystalline structure and polycrystalline granular [141]. Surprisingly the textured granular structure revealed the lowest SFD after patterning, confirming that the introduction of grains and grain boundaries is not the main source of the intrinsic SFD, but rather that the statistical averaging over different strongly exchange coupled grains within one island may help achieving a narrow SFD.

In general multilayers allow easy control of magnetic properties via tuning individual layer thicknesses within the multilayer as well as the number of multilayer repeats [142]. Therefore such c-axis out-of-plane oriented perpendicular anisotropy Co/Pd or Co/Pt multilayers that can easily be deposited onto glass substrates, SiN membranes or oxidized Si-wafers are often used as model systems for SFD-studies in BPM. In a second study Shaw et al. show that the reversal field of individual islands is highly dependent on the applied field direction, the position of a possible defect within the structure, and the defect anisotropy axis orientation [143]. Subsequent TEM studies of the microstructure of islands with the lowest magnetic switching fields in the array reveal that characteristic misaligned “trigger” grains within the island core are responsible for the lowered reversal fields [144, 145] and thus need to be avoided in order to achieve tight magnetic SFD.

3.4 Importance of Media Architecture and Pattern Uniformity in BPM

Using more complex layered BPM multilayer structures, it was shown that the combination of different hard and soft magnetic materials may yield a lower SFD than similar homogeneous single layer systems [146]. In laminated BPM structures the

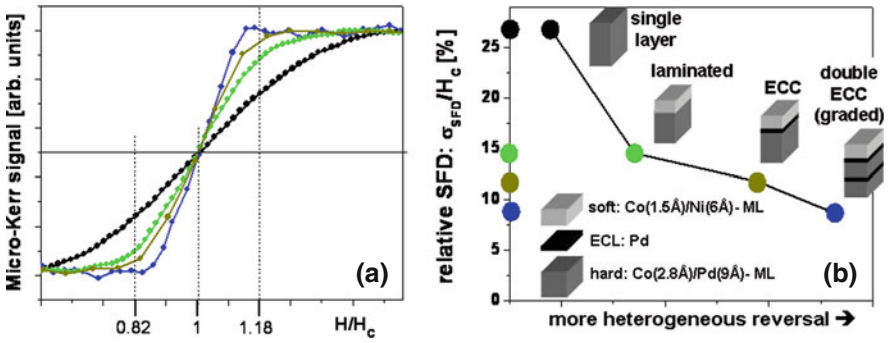

Fig. 21 Evolution of the relative SFD (SFD/H_C) from a standard multilayer media via a laminated hard Co/Pd multilayer-soft Co/Ni multilayer media via a single ECL hard/soft media to a double ECL hard/hard/soft media. The magnetization and overall thickness of the media was kept about constant, such that dipolar interactions are about the same for all four media structures. Thus the reduction in relative SFD can be attributed to reductions in the intrinsic part of the SFD. All data was obtained on 320 Gb/in^2 density arrays with 30 nm island size and 45 nm island pitch. In part (**a**) we show the reversal curves for the four different samples plotted versus the re-scaled external field H/H_C. H_C values for these four samples were all in the range between 5.2 and 6.2 kOe in agreement with currently available write head fields. In part (**b**) we display the extracted relative SFD values (in %) and illustrate the evolution of the sample structure towards more complex layer designs

magnetic defects and distributions of switching fields may be uncorrelated in the various layers that form the media stack and thus provide a statistical advantage over single layer media that leads to a narrowing of the SFD [146, 147]. Furthermore the introduction of an exchange coupling layer (ECL) in between different media layers is able to alter the reversal process from uniform rotation to a more heterogeneous type of reversal, where the switching field of a higher anisotropy storage layer is reduced via a lower anisotropy reversal assist layer. Such exchange coupled composite (ECC) BPM systems do not only allow using higher anisotropy materials for better thermal stability at higher areal densities, but are also able to lower the SFD [126, 148, 149]. Recent results based on Co/Pd multilayer hard layers and Co/Ni multilayer soft layers are summarized in Fig. 21, where the relative SFD (SFD/H_C) could be lowered from more than 25 % down to less than 10 % by moving from a single multilayer media to a laminated hard/soft structure and then subsequently introducing initially one and then two ECL layers in order to create more heterogeneous 2-coupled-layer and 3-coupled-layer structures.

The intrinsic part of the SFD is not only influenced by the intrinsic magnetic material variations as outlined above, but also depends on the pattern uniformity itself. In order to obtain tight island size, shape and placement distributions top-down lithography and bottom-up self-assembly have been successfully combined in a guided self-assembly patterning approach [150]. Thus it has been shown that a better pattern quality due to guided self-assembly yields a lower SFD than conventional e-beam patterning alone for otherwise identical media materials [151]. Self assembly and guided patterning is discussed in more detail in Sect. 4.

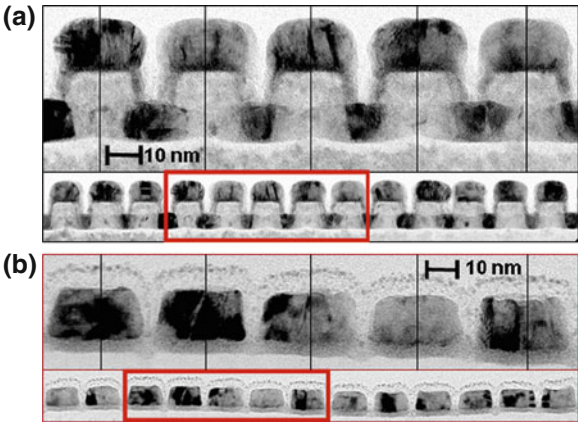

Fig. 22 Cross-sectional transmission electron microscopy (TEM) comparison of the two most common fabrication approaches for BPM at 500 Gb/in^2 density (35 nm pitch). **a** Fabrication of BPM via blanket deposition of the magnetic material onto pre-patterned pillar substrates. **b** Fabrication of BPM from initially continuous magnetic thin films via ion milling or reactive ion etching. In both cases the magnetic media used were high perpendicular anisotropy Co/Pd multilayer structures

3.5 Different Fabrication Approaches for BPM

The fabrication of BPM can be based on different approaches. Early studies were mostly utilizing blanket deposition of the magnetic media layers onto pre-patterned pillar structures [128, 152–155] as shown in cross sectional TEM images in Fig. 22a. The advantage of this approach is that all pattern fabrication can be done prior to the media deposition, such that the magnetic properties of the media are not directly affected by the actual patterning process. Pattern fabrication thus can be optimized independently from the media materials and deposition process. Originally at lower areal densities media damage was not an issue for this approach and results looked quite promising. However there are also severe disadvantages that come with this approach, such as limited under- and seed layer thicknesses due to finite pre-patterned pillar height, deposition of undesired magnetic trench material [156] that acts as a noise source in between the elevated islands forming the bits, side wall deposition of magnetic material that may lead to lateral exchange as well as overgrowth and curvature effects due to media growth on non-perfect pre-patterned pillar shapes. The pre-patterned substrate approach worked particularly well in combination with Co/Pd and Co/Pt multilayer media, since such systems do not require thick seed layer systems as their perpendicular anisotropy originates from the chemical layering during the deposition process.

The alternative approach to using pre-patterned substrates is patterning of an initially continuous magnetic media layer into isolated islands via reactive ion etching (RIE) or ion milling as shown in the TEM images of Fig. 22b. Here the magnetic media is deposited onto a flat substrate, which allows thick seed layers for media

materials that obtain their perpendicular anisotropy from a well-defined out-of-plane crystallite alignment, such as CoCrPt, CoPt and FePt alloys. The biggest challenge for this fabrication approach is media damage during the patterning process due to intermixing of interfaces, damage of the microstructure and crystallite alignment, oxidation and edge roughness, side wall tapering and uncontrolled re-deposition of magnetic material. In that sense the patterning process has to be optimized with respect to the chosen magnetic media material and its specific challenges. Corresponding island edge damage has to be minimized in order to scale the island size to areal densities of more than 1 Tb/in^2 as is necessary for the introduction of BPM [157].

A third proposed fabrication approach that should at least be mentioned here entirely avoids the removal of magnetic material and instead employs ion irradiation of the "trench regions" through a corresponding hard mask in order to transform this portion of the media layer into a non-magnetic phase and thus create isolated magnetic dots [158–160]. Controlling the lateral resolution of the ion irradiation process itself within the media layer and thus creating sharp boundaries between the magnetic and non-magnetic phases is the biggest challenge for this otherwise quite attractive approach that does not require any additional planarization steps.

4 Self-Organized Lateral Magnetic Nanostructures and Assisted Self-Assembly

Magnetic nanostructures can alternatively be prepared by so-called 'self-organization' or equivalently 'self-assembly' or 'bottom-up' techniques. They have in common that the order is not achieved by direct writing, imprinting or exposing, but by intrinsic ordering forces between individual building blocks. The building blocks discussed here are magnetic nanoparticles (NPs).[1] Self-organized NP arrangements are investigated in the context of e.g. next-generation magnetic data storage media [121, 161, 162], NP spintronic devices [163, 164] or as building blocks of novel materials with tunable magnetic, electronic and optical properties [165].

Self-organization techniques can be subdivided into four approaches, i.e., (i) 'simple' self-organization of NPs, (ii) self-organization involving several types of NPs, (iii) directed self-organization of NPs, and (iv) templated or guided self-organization of NPs. In the following sections the various types are discussed.

4.1 'Simple' Self-Organization of Nanoparticles

'Simple' self-organization of NPs describes the case, when only one type of NPs is involved and when the forces between the particles are basically spherically

[1] Or equivalently: 'nanocrystals', 'fine particles', 'nanobeads' or 'nanoclusters'.

symmetric. To obtain well-ordered arrangements of reasonable long-range order the size distribution of the NPs should be less than 10 %, ideally 5 % or lower.

The underlying self-organization processes are well understood from the field of colloidal systems. Several review articles exist on this topic [166–171]. Self-organized arrangements of NPs are the consequence of the presence and the competition of various interaction energies, i.e. [167],

- *van der Waals energy*, which is the consequence of all integrated van der Waals interactions between pairs of polarizable atoms or molecules in each NP.
- *electrostatic energy*, due to charged NPs. It can be controlled by the choice of e.g. the solvent and the concentration of surrounding counterions.
- *molecular crosslinking*, i.e. using specific 'linker' molecules.
- *steric repulsion*, meaning the repulsive interaction between hard spheres or between particles being surrounded by a soft shell of ligands.
- *depletion effects*, i.e. an attractive force due to the presence of smaller particles or molecules (e.g. of the solvent) between the NPs. One can describe it in terms of a net osmotic pressure forcing the NPs together.
- *effective magnetic dipole energy* between fluctuating moments. The magnetic dipole–dipole interaction is a non-isotropic coupling, unless it acts as an effective averaged energy between fluctuating moments. Otherwise the dipole–dipole interaction can lead to more complex arrangements like chain or ring formation [172–174].

Reference [167] provides a detailed list of all relevant interaction energies and example values of interaction strengths. Moreover, also the influence of entropy is discussed in self-organized arrangements [167].

These energies are effective between the particles and between particles and the substrate. A vast number of investigations exist on how to control these energies to (a) achieve long range order over as large as possible areas or to (b) manipulate the particular type of arrangement [167, 169]. Figure 23 shows examples of self-organized NPs on planar substrates. Such systems show closed-packed so-called superlattices[2] either with cubic or hexagonal symmetry.

Another completely different type of self-organization is found in NPs prepared by physical vapour deposition methods, e.g. when sputtering a metal on top of an oxide like Al_2O_3 or SiO_2. In that case NPs are formed spontaneously due to non-wetting behavior [198–202]. The advantage is that one deals with a full 'solid-state' process. However, the disadvantage is that no long-range order of self-organization beyond only few particles has been achieved so far. A third possibility is the self-organization of NPs on step edges of crystalline substrates. This occurs when depositing a metal under conditions of molecular beam epitaxy (MBE) on top of a clean crystalline surface [203, 204].

The magnetic behavior of self-organized arrays of NPs depends on (1) the individual and general magnetic behavior of NPs [176, 177, 181, 186, 189]. And it depends on (2) the type and strength of magnetic interactions between the particles in the

[2] Or: 'supracrystals'.

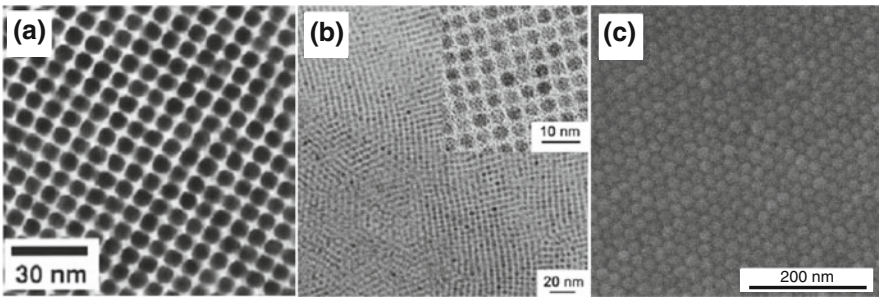

Fig. 23 Examples of self-organized NPs on planar substrates. **a** TEM image of 6 nm FePt NPs [161] (reprinted with permission from Adv. Mater. Copyright 2006 John Wiley and Sons), **b** TEM image of 4 nm Iron oxide NPs [175] (reprinted with permission from J. Am. Chem. Soc. Copyright 2009 American Chemical Society.) and **c** SEM image of 20 nm iron oxide NPs [176] (Reprinted with permission from Ref. [176]. Copyright (2011) by the Institute of Physics)

array [171, 177–180, 182–185, 187, 188, 190]. Considering only the model case of single-domain NPs and considering only NPs from a ferromagnetic or ferrimagnetic material, one can distinguish between the following behaviors:

- *superparamagnetism (SPM)*,
- *modified SPM or interacting SPM (ISP)*,
- *superspin glass (SSG) or correlated superspin glass (CSSG)*,
- *superferromagnetism (SFM)*, or
- *correlated granular ferromagnetism (CFM)*.

SPM behavior of the entire array is observed, when inter-particle interactions are negligible. In most cases the interaction is of dipolar type. The dipolar energy scales as m^2/a^3 (with m being the magnetic moment of the NP and a the inter-particle distance). For a complete expression refer to Eq. 1. Thus, the only way to achieve SPM behavior is to (1) increase the distance a between particles or (2) decrease the magnetic moment m. The latter can be realized by either reducing the size of the NP or by choosing materials with a low saturation magnetization. Furthermore, another possibility is to (3) increase the anisotropy energy of each NP so that the dipolar energy becomes negligible.

In self-organized NP arrays the pure SPM case is hard to realize. A simple estimate for 20 nm Fe_3O_4 NPs at distances of 25 nm yields for $E_{dd}/k_B = (\mu_0/4\pi k_B)(m^2/a^3) \approx 3800$ K. Another example of 5 nm Co-NPs at distances of 10 nm yields 16 K, which is still not negligible. Therefore, SPM behavior can be realized only either by increasing the interparticle distances artificially via templating (see below) or in frozen ferrofluids using a low concentration of NPs [191].

Modified SPM is characterized by individual blocking of NPs, where the interactions enter as an additional effective energy term into the single-NP energy barrier [177, 187, 190, 191]. No collective behavior is found here.

SSG or CSSG behavior is observed for sufficiently strong interactions *and* when frustration and disorder is present. In this case the particle moments freeze

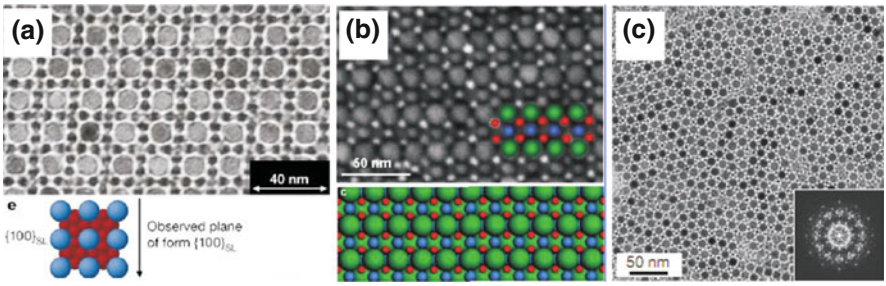

Fig. 24 Examples of complex self-organized NP superlattices composed of two or three different types of NPs. **a** TEM image and corresponding schematic of an AB_{13} type binary superlattice of 11 nm γ-Fe_2O_3 and 6 nm PbSe NPs (Reprinted by permission from Macmillan Publishers Ltd: Nature Journal [205], copyright (2003)), **b** HRSEM image and schematic of an ABC_2 type superlattice of 16.5 nm Fe_3O_4, 7.0 nm Fe_3O_4 and 5.0 nm FePt NPs (Reprinted with permission from Ref. [211]. Copyright 2011 American Chemical Society.) and **c** Quasicristalline superlattice from 9 nm PbS and 3 nm Pd NPs. The inset shows a fast Fourier transform pattern (Reprinted by permission from Macmillan Publishers Ltd: Nature Journal [208], copyright (2009))

collectively into a state analoguous to the spin glass state below a critical temperature T_g [193]. This state has been demonstrated by a multitude of experiments [177, 180, 185, 188, 190, 192].

For even larger interactions and less disorder a SFM state can be encountered, which is characterized by ferromagnetic-like correlations and the presence of SFM domains [179, 180, 190, 194]. One should note that there is still no consensus whether a true ferromagnetic ground state is expected for pure dipolar systems [195, 196]. However, when additional exchange-like interactions are present a true ferromagnetic collective state can be observed. E.g. Co-NPs covered by a Pt-network yield ferromagnetic behavior termed CFM [197].

4.2 Self-Organization Involving Several Types of Nanoparticles

Analogous to crystals composed of different types of atoms like NaCl, CsCl, ZnS etc. also NP superlattices from different NP types can be fabricated. Fascinating examples are found of binary and even ternary superlattices [205–211]. As in atomic cystals the order is the consequence of close packing, interaction energies and entropy. Figure 24 shows various examples. Even quasicrystalline order has been reported recently [208].

Binary superlattice crystals also exist in natural opals or have previously been prepared with hard sphere colloidal particles [212, 213]. It has been claimed that for particles with negligible interactions the only driving force for superlattice formation might be merely the entropy of the system [212, 214, 217]. This is, on the first glance, counter-intuitive. However, one has to consider two parts of the total entropy, i.e.:

firstly, the 'configurational entropy'. This is the entropy associated with the degree of spatial ordering. And, secondly, one has to consider the entropy associated with the space available to each sphere for local free motion [217]. When the space of the spheres is confined (e.g. for NPs it means, when they start to self-assemble onto a surface) the configurational entropy is decreased. But since the particles in an ordered superlattice have more 'local free volume' compared to the fluid, the 'free-volume entropy' is increased [217]. For high concentrations of particles the second entropy term dominates and thus superlattice formation is favored. In contrast, binary superlattices have also been found in systems of oppositely charged colloidal particles [215, 216]. In this case the driving force for ordering is the electrostatic interaction analogous to usual ionic crystals.

The magnetic behavior of binary or ternary superlattices is basically unexplored. The emphasis so far has been on the fabrication and structural characterization only.

4.3 Directed Self-Organization of Nanoparticles

Directed self-organization occurs, when the process of self-organization is deliberately influenced or 'directed' by proper choice of inter-particle interactions [218–224].

In particular two strategies are employed:

- *Tailoring of inter-particle interactions*,
- *Use of DNA-molecules as programmed NP-links*.

In the first approach, one introduces artificially non-isotropic interactions between particles similar to covalent bonding in atomic crystals. One group realized this idea recently by depositing capping layers on two opposite sides of the particles [220]. The particles then have two 'polar caps' with a different material than the core of the NP itself. This breaks the spherical symmetry of e.g. the van-der-Waals interactions and thus favors the formation of more complex superlattices compared to the cases described above. This study used non-magnetic particles, but one could in principle transfer this idea also to magnetic NPs.

By using DNA the inter-particle links can be even 'programmed'. It is possible to achieve various supercystal structures by the proper choice of DNA strands [221–224]. Thus fabricated systems are usually 3-dimensional supercrystals. Their structure is investigated using e.g. grazing incidence X-ray scattering (GISAXS) and electron microscopy. Or, one can direct the self-assembly to obtain regular patterns on a substrate [219], which is analogous to 'templated self-organization' (see next section).

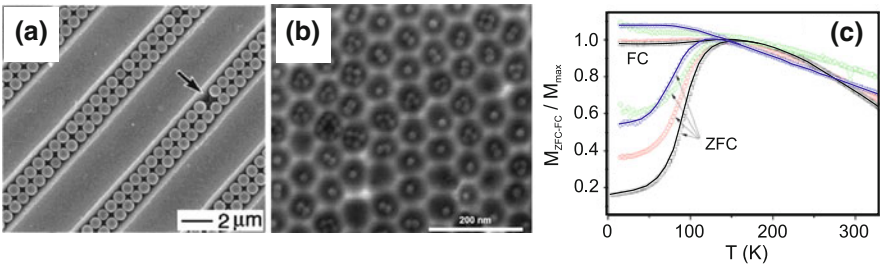

Fig. 25 **a** SEM image of 800 nm polystyrene beads in lithographically patterned grooves [225] (Reprinted with permission of the American Chemical Society, Copyright 2001). **b** SEM image of 20 nm Iron Oxide NPs in alumina membrane pores [232] and **c** measured magnetization data on 20 nm Iron Oxide NPs in various alumina membrane templates [232] (Reprinted with permission from Ref. [232]. Copyright (2011) by the Institute of Physics)

4.4 Templated Self-Organization of Nanoparticles

In this section the case of templated or guided self-organization is discussed. This approach implies that first a 'template' is fabricated and subsequently this template is 'filled' with NPs. In the literature one can find four different methods for templating [225–233]:

- *patterning*,
- *block-copolymers*,
- *alumina pores*, and
- *micelles*.

In the first case predefined structures are patterend e.g. using lithography or nanoimprint methods. These structures are then filled with NPs [225–228]. Figure 25a shows an example of such a structure. The advantage of these systems is the combination of top-down and bottom-techniques. The advantages of self-organization (viz. order on very small scales) and those of patterning (viz. controlled order even on large scales) could be used e.g. for magnetic recording media or matter with specifically tuned optical properties. Only very few studies exist on the influence of the patterning on the magnetic properties of NP ensembles [226].

The second case involves the combination of two self-organization steps. In the first step a regular pattern is fabricated using block-copolymer self-organization [229–231]. The result is analoguous to that of patterning, however no complete control can be gained since the process is based on intrinsic ordering forces. Therefore, most studies involving block-copolymers report about long-range order on mesoscopic scales only, whereas wafer-sized control still seems difficult to achieve. The second step is again filling the structures with NPs as in the case above.

The third case involves first the fabrication of a template structure in an alumina membrane [234]. Again by a self-organization a well-ordered array of pores is formed during the electro-chemical etching process. These pores can then be filled with NPs

analoguous to the previous two cases. In this approach, however, one is confined to pores only. No trenches, grooves or other patterns could be achieved so far.

Concerning the magnetic properties such structures offer the unique possibility to study the inter-particle coupling systematically. I.e. when the pores are of sizes comparable to the NP diameter one can isolate individual particles and hence reduce the magnetic dipolar interactions. Such an example is shown in Fig. 25b, where either only one or small clusters with few NPs are localized inside each pore [232]. This sample shows basically SPM behavior due to negligible inter-particle interactions. This can be evidenced from zero-field cooling (ZFC)/field cooling (FC) curves of the magnetization (Fig. 25c) and from measurements of the so-called memory-effect [185, 188, 190, 232]. The memory-effect is an unambiguous probe for the presence of coupled dipolar behavior [185].

In contrast, a simple self-organized monolayer of particles shows strong dipolar coupling, i.e. both the ZFC-FC curves and the memory effect evidence a SSG state.

Another possibility of templated self-organization is the utilization of micelle structures [233]. In this case, macromolecular 'reverse' micelles are prepared in a first step. These micelles are loaded with a metal precursor salt. In the second step the micelles self-organize on top of a surface in a regular fashion. Eventually, metallic NPs result after plasma processing. By this technique high-quality FePt particles have been achieved [233].

To summarize, despite apparent successes to fabricate magnetic systems by self-assembly, still many goals are not reached yet. Key challenges of the self-organization methods are presently

- *achieve macroscopic long-range order, e.g. for magnetic recording media*,
- *arbitrary programming of the order, e.g. for the study of novel magnetic materials with specific properties*,
- *fabrication of NPs with well-defined structural, magnetic, electronic and optical properties for the preparation of novel composite and functional materials*.

The methods mentioned above constitute first steps toward realizing true long-range order, e.g. using templating [225–228]. However, well-defined and practical routes to fabricate self-organized arrays on wafer scale areas for industrial purposes seem still far away nowadays. Regarding the second goal, viz. to be able to arbitrarily 'program' the order, interesting studies have been performed so far [218–224]. However, to fabricate complicated or even non-periodic structures (e.g. single devices) seems also still far away. Moreover, much efforts are undertaken worldwide to e.g. control the size, the shape, the size-distribution, the crystallographic composition, the crystallographic orientation with respect to the NP array, the magnetic, electronic, and optical properties.

Eventually the aim is to be able to fabricate any arbitrary structure, array, material, device or even machine by self-organization alone (e.g. the 'computer from the test tube') [235].

5 Summary and Outlook

In this chapter we presented a spectrum of current topics in the field of magnetic nanostructures. Here, the focus has been in particular on the role of *competing* energies or, in other words, the competition between intra-island and inter-island interactions. This is highlighted using several examples from both fundamental research and technological applications. The examples range from cases where competing interactions are essential, so leading to complex ordering phenomena, to cases where it is preferable to avoid interactions for a better signal-to-noise ratio.

Competing contributions, for example of different anisotropies, can lead to various domain states inside magnetic nanostructures as shown in Heusler-nanostripes or circular dots. In addition, a competition between the energy contributions inside each layer and the dipolar interactions between the layers in a stack can lead to an interesting interplay between the domain structures (Sect. 1).

If the competing interactions lead to frustration, fascinating magnetic ground-states can be observed as shown in artificial spin-ice. Its intriguing properties, such as the complex ground-state, emergent magnetic monopoles and Dirac-strings, makes it another fundamental model system in magnetism (Sect. 2).

Another example of frustration is found in self-organized arrays of nanoparticles. Here the competing interactions lead to a collective state, called a superspin glass, which is simply the 'superspin' version of the classical spin-glass (Sect. 4).

A completely different focus is given to lateral arrays of magnetic nanoislands with large perpendicular anisotropy. This so-called bit patterned media has the potential to be used as next generation recording media in magnetic hard disk drives. To this end, the stray field interactions between the individual islands should be avoided, because any interaction leads to a cross-talk between individual stored bits. Consequently, the requirements on the anisotropy, the switching field distribution and the geometry of the dots is a major topic (Sect. 3).

From these examples one finds that the field of research into magnetic nanostructures is full of challenges and opportunities. Of course, most discoveries cannot be predicted and they unexpectedly arise. Therefore this field will continue to generate numerous breakthroughs and findings. Nevertheless, several extrapolations into the future can be made. For example, it is clear that soon the difference between top-down and bottom-up approaches to fabrication will gradually vanish. Top-down approaches provide structures that are well-defined but they are associated with a lower size limit. While lithographic machines and processes are becoming increasingly better, and structure sizes down to 10 nm are possible with the most modern equipment, typical structure sizes achieved using regular university laboratory equipment are of the order of 100 nm. Hence, the scale of nanoparticles and clusters, i.e. $\sim$5 nm, is still out of reach with top-down lithography. In contrast, bottom-up approaches open up the possibility to achieve length scales as far down as 3 nm. However, the control over the lateral ordering is still far from perfect.

As the gap between top-down and bottom-up approaches closes, lithographic processes become more and more powerful, while self-assembly techniques become

increasingly better defined. Moreover, combined techniques of lithographic structuring and self-assembly might become increasingly important. The new developments in fabrication of magnetic nanostructures will lead to new scientific discoveries in magnetism at the nanoscale. This in turn will lead to the invention of revolutionary devices, such as novel sensors and actuators, or for data storage, processing and transfer, providing advantages in terms of footprint, speed, cost and energy consumption.

References

1. P. Grünberg, Phys. Today **54**, 31 (2001)
2. I.K. Schuller, S. Kim, C. Leighton, J. Magn. Magn. Mater. **200**, 571 (1999)
3. B. Heinrich, Exchange coupling in magnetic multilayers. Springer Tracts Mod. Phys. **227**, 185 (2007)
4. J.I. Martin, J. Nogues, K. Liu, J.L. Vincent, I.K. Schuller, J. Magn. Magn. Mater. **256**, 449 (2003)
5. A.O. Adeyeye, N. Singh, J. Phys. D: Appl. Phys. **41**, 153001 (2008)
6. A. Remhof, A. Westphalen, H. Zabel, in *Handbook of Nanophysics: Nanoelectronics and Nanophotonics*, ed. by K.D. Sattler (CRC Press, Boca Raton, 2010)
7. B. Hjörvarsson, Private communication and to be published
8. A. Aharoni, J. Appl. Phys. **83**, 3432 (1998)
9. A. Hubert, R. Schäfer, *Magnetic Domains* (Springer, New York, 1998) (and references therein)
10. T. Last, S. Hacia, M. Wahle, S.F. Fischer, U. Kunze, J. Appl. Phys. **96**, 6706 (2004)
11. D. Hinzke, U. Nowak, J. Magn. Magn. Mater. **221**, 365 (2000)
12. M. Kläui, J. Phys.: Condens. Matter **20**, 313001 (2008)
13. K. Gross, P. Szary, O. Petracic, F. Brüssing, K. Westerholt, H. Zabel, Phys. Rev. B **84**, 054456 (2011)
14. C. Hassel, F.M. Römer, R. Meckenstock, G. Dumpich, J. Lindner, Phys. Rev. B **77**, 224439 (2008)
15. C. Kittel, Phys. Rev. **70**, 965 (1946)
16. I.L. Prejbeanu, L.D. Buda, U. Ebels, M. Viret, C. Fermon, K. Ounadjela, IEEE Trans. Magn. **37**, 2108 (2001)
17. S. Cherifi, R. Hertel, A. Locatelli, Y. Watanabe, G. Potdevin, A. Ballestrazzi, M. Balboni, S. Heun, Appl. Phys. Lett. **91**, 092502 (2007)
18. J. Yu, U. Rüdiger, L. Thomas, S.S.P. Parkin, A.D. Kent, J. Appl. Phys. **85**, 5501 (1999)
19. R. Pulwey, M. Zölfl, G. Bayreuther, D. Weiss, J. Appl. Phys. **91**, 7995 (2002)
20. R.P. Cowburn, D.K. Koltsov, A.O. Adeyeye, M.E. Welland, D.M. Tricker, Phys. Rev. Lett. **83**, 1042 (1999)
21. K.Y. Guslienko, V. Novosad, Y. Otani, H. Shima, K. Fukamichi, Phys. Rev. B **65**, 024414 (2001)
22. P.-O. Jubert, R. Allenspach, Phys. Rev. B **70**, 144402 (2004)
23. G.N. Kakazei, M. Ilyn, O. Chubykalo-Fesenko, J. Gonzalez, A.A. Serga, A.V. Chumak, P.A. Beck, B. Laegel, B. Hillebrands, K.Y. Guslienko, Appl. Phys. Lett. **99**, 052512 (2011)
24. B. Van Waeyenberge, A. Puzic, H. Stoll, K.W. Chou, T. Tyliszczak, R. Hertel, M. Fahnle, H. Brueckl, K. Rott, G. Reiss, I. Neudecker, D. Weiss, C.H. Back, G. Schütz, Nature **444**, 461 (2006)
25. T. Kamionka, M. Martens, K.W. Chou, M. Curcic, A. Drews, G. Schütz, T. Tyliszczak, H. Stoll, B. Van Waeyenberge, G. Meier, Phys. Rev. Lett. **105**, 137204 (2010)

26. M. Natali, I.L. Prejbeanu, A. Lebib, L.D. Buda, K. Ounadjela, Y. Chen, Phys. Rev. Lett. **88**, 57203 (2002)
27. M. Natalia, A. Popa, U. Ebels, Y. Chen, S. Li, M.E. Welland, J. Appl. Phys. **96**, 4334 (2004)
28. H. Jung, Y.-S. Yu, K.-S. Lee, M.-Y. Im, P. Fischer, L. Bocklage, A. Vogel, M. Bolte, G. Meier, S.-K. Kim, Appl. Phys. Lett. **97**, 222502 (2010)
29. H. Jung, K.-S. Lee, D.-E. Jeong, Y.-S. Choi, Y.-S. Yu, D.-S. Han, A. Vogel, L. Bocklage, G. Meier, M.-Y. Im, P. Fischer, S.-K. Kim, Sci. Rep. **1**, 59 (2011)
30. T. Shinjo, T. Okuno, R. Hassdorf, K. Shigeto, T. Ono, Science **289**, 930 (2000)
31. J. Raabe, R. Pulwey, R. Sattler, T. Schweinböck, J. Zweck, D. Weiss, J. Appl. Phys. **88**, 4437 (2000)
32. M. Grimsditch, P. Vavassori, J. Phys.: Condens. Matter **16**, R275 (2004)
33. A. Westphalen, M.-S. Lee, A. Remhof, H. Zabel, Rev. Sci. Instrum. **78**, 121301 (2007)
34. M.-S. Lee, A. Westphalen, A. Remhof, A. Schumann, H. Zabel, J. Appl. Phys. **103**, 093913 (2008)
35. S. Buchanan, KYu. Guslienko, A. Doran, A. Scholl, S.D. Bader, V. Novosad, Phys. Rev. B **72**, 134415 (2005)
36. P. Szary, O. Petracic, F. Brüssing, M. Ewerlin, H. Zabel, J. Appl. Phys. **107**, 113922 (2010)
37. V. Rose, X.M. Cheng, D.J. Keavney, J.W. Freeland, K.S. Buchanan, B. Ilic, V. Metlushko, Appl. Phys. Lett. **91**, 132501 (2007)
38. J. Wu, D. Carlton, E. Oelker, J.S. Park, E. Jin, E. Arenholz, A. Scholl, C. Hwang, J. Bokor, Z.Q. Qiu, J. Phys.: Condens. Matter **22**, 342001 (2010)
39. A.A. Fraerman, B.A. Gribkov, S.A. Gusev, B. Hjörvarsson, AYu. Klimov, V.L. Mironov, D.S. Nikitushkin, V.V. Rogov, S.N. Vdovichev, H. Zabel, J. Appl. Phys. **103**, 073916 (2008)
40. M. van Kampen, I. Sorroka, R. Brucas, B. Hjörvarsson, R. Wieser, K.D. Usadel, M. Hansson, C. Josza, B. Koopmans, J. Grabis, H. Zabel, J. Phys. Condens. Matter **17**, L27 (2005)
41. Q. Xiao, J. Rudge, B. Choi, Y. Hong, G. Donohoe, Appl. Phys. Lett. **89**, 262507 (2006)
42. R. Hertel, S. Gliga, M. Fahnle, C.M. Schneider, Phys. Rev. Lett. **98**, 117201 (2007)
43. K. Yamada, S. Kasai, Y. Nakatani, K. Kobayashi, T. Ono, Appl. Phys. Lett. **93**, 152502 (2008)
44. M. Kammerer, M. Weigand, M. Curcic, M. Noske, M. Sproll, A. Vansteenkiste, B. Van Waeyenberge, H. Stoll, G. Woltersdorf, C.H. Back, G. Schuetz, Nat. Comm. doi:10.1038/ncomms1277 (2011)
45. M.J. Harris, S.T. Bramwell, D.F. McMorrow, T. Zeiske, K.W. Godfrey, Phys. Rev. Lett. **79**, 2554 (1997)
46. J.E. Shea, J.N. Onuchic, C.L. Brooks, Proc. Natl. Acad. Sci. U S A **96**, 12512 (1999)
47. T. Matsumoto, A. Fukuda, M. Johno, Y. Motoyama, T. Yui, S.S. Seomun, M. Yamashita, J. Mater. Chem. **9**, 2051 (1999)
48. G.J. Kellogg, D.G. Walton, A.M. Mayes, P. Lambooy, T.P. Russell, P.D. Gallagher, S.K. Satija, Phys. Rev. Lett. **76**, 2503 (1996)
49. W.L. Luo, S.R. Nagel, T.F. Rosenbaum, R.E. Rosensweig, Phys. Rev. Lett. **67**, 2721 (1991)
50. H. Bersini, Neural Networks **11**, 1017 (1998)
51. G. Toulouse, Comm. Phys. **2**, 115 (1977)
52. J. Vannimenus, G. Toulouse, J. Phys. C: Sol. State Phys. **10**, L537 (1977)
53. S. Kirkpatrick, Phys. Rev. B **16**, 4630 (1977)
54. K. Binder, A.P. Young, Rev. Mod. Phys. **58**, 801 (1986)
55. J.E. Greedan, J. Mater. Chem. **11**, 37 (2001)
56. J. Snyder, J.S. Slusky, R.J. Cava, P. Schiffer, Nature **413**, 48 (2001)
57. J.S. Gardner, A. Keren, G. Ehlers, C. Stock, E. Segal, J.M. Roper, B. Fak, M.B. Stone, P.R. Hammar, D.H. Reich, B.D. Gaulin, Phys. Rev. B **68**, 180401 (2003)
58. A.P. Ramirez, A. Hayashi, R.J. Cava, R. Siddharthan, B.S. Shastry, Nature **399**, 333 (1999)
59. I. Mirebeau, H. Mutka, P. Bonville, A. Apetrei, A. Forget, Phys. Rev. B **78**, 174416 (2008)
60. R.F. Wang, C. Nisoli, R.S. Freitas, J. Li, W. McConville, B.J. Cooley, M.S. Lund, N. Samarth, C. Leighton, V.H. Crespi, P. Schiffer, Nature **439**, 303 (2006)
61. Y. Qi, T. Brintlinger, J. Cumings, Phys. Rev. B **77**, 094418 (2008)
62. M. Tanaka, E. Saitoh, H. Miyajima, T. Yamaoka, Y. Iye, Phys. Rev. B **73**, 052411 (2006)

63. C. Phatak, A.K. Petford-Long, O. Heinonen, M. Tanase, M. De Graef, Phys. Rev. B **83**, 174431 (2011)
64. X. Ke, J. Li, C. Nisoli, P.E. Lammert, W. McConville, R.F. Wang, V.H. Crespi, P. Schiffer, Phys. Rev. Lett. **101**, 037205 (2008)
65. G. Möller, R. Moessner, Phys. Rev. Lett. **96**, 237202 (2006)
66. L.A.S. Mól, W.A. Moura-Melo, A.R. Pereira, Phys. Rev. B **82**, 054434 (2010)
67. A.S. Wills, R. Ballou, C. Lacroix, Phys. Rev. B **66**, 144407 (2002)
68. T. Fennell, S.T. Bramwell, D.F. McMorrow, P. Manuel, A.R. Wildes, Nat. Phys. **3**, 566 (2007)
69. G. Möller, R. Moessner, Phys. Rev. B **80**, 140409(R) (2009)
70. G.W. Chern, P. Mellado, O. Tchernyshyov, Phys. Rev. Lett. **106**, 207202 (2011)
71. N. Rougemaille, F. Montaigne, B. Canals, A. Duluard, D. Lacour, M. Hehn, R. Belkhou, O. Fruchart, S. El Moussaoui, A. Bendounan, F. Maccherozzi, Phys. Rev. Lett. **106**, 057209 (2011)
72. E. Mengotti, L.J. Heyderman, A. Fraile Rodríguez, A. Bisig, L. Le Guyader, F. Nolting, H.B. Braun, Phys. Rev. B **78**, 144402 (2008)
73. A. Schumann, B. Sothmann, P. Szary, H. Zabel, Appl. Phys. Lett. **97**, 022509 (2010)
74. E. Mengotti, L.J. Heyderman, A.F. Rodríguez, F. Nolting, R.V. Hügli, H.B. Braun, Nat. Phys. **7**, 68 (2011)
75. A. Remhof, A. Schumann, A. Westphalen, H. Zabel, N. Mikuszeit, E.Y. Vedmedenko, T. Last, U. Kunze, Phys. Rev. B **77**, 134409 (2008)
76. X.L. Ke, J. Li, S. Zhang, C. Nisoli, V.H. Crespi, P. Schiffer, Appl. Phys. Lett. **93**, 252504 (2008)
77. J. Li, X. Ke, S. Zhang, D. Garand, C. Nisoli, P. Lammert, V.H. Crespi, P. Schiffer, Phys. Rev. B **81**, 092406 (2010)
78. A. Westphalen, A. Schumann, A. Remhol, H. Zabel, M. Karolak, B. Baxevanis, E.Y. Vedmedenko, T. Last, U. Kunze, T. Eimuller, Phys. Rev. B **77**, 174407 (2008)
79. Y. Li, T.X. Wang, H.Y. Liu, X.F. Dai, G.D. Liu, Phys. Lett. A **375**, 1548 (2011)
80. E.Y. Vedmedenko, H.P. Oepen, J. Kirschner, Phys. Rev. Lett. **90**, 137203 (2003)
81. S. Ladak, D.E. Read, G.K. Perkins, L.F. Cohen, W.R. Branford, Nat. Phys. **6**, 359 (2010)
82. P. Mellado, O. Petrova, Y.C. Shen, O. Tchernyshyov, Phys. Rev. Lett. **105**, 187206 (2010)
83. L.J. Heyderman, F. Nolting, D. Backes, S. Czekaj, L. Lopez-Diaz, M. Kläui, U. Rüdiger, C.A.F. Vaz, J.A.C. Bland, R.J. Matelon, U.G. Volkmann, P. Fischer, Phys. Rev. B **73**, 214429 (2006)
84. S. Neusser, D. Grundler, Adv. Mater. **21**, 2927 (2009)
85. S. Gliga, M. Yan, R. Hertel, C.M. Schneider, Phys. Rev. B **77**, 060404 (2008)
86. A. Libal, C. Reichhardt, C.J.O. Reichhardt, Phys. Rev. Lett. **97**, 228302 (2006)
87. Y.L. Han, Y. Shokef, A.M. Alsayed, P. Yunker, T.C. Lubensky, A.G. Yodh, Nature **456**, 898 (2008)
88. L. Baraban, D. Makarov, M. Albrecht, N. Rivier, P. Leiderer, A. Erbe, Phys. Rev. E **77**, 031407 (2008)
89. A. Libal, C.J.O. Reichhardt, C. Reichhardt, Phys. Rev. Lett. **102**, 237004 (2009)
90. E. Mengotti, L.J. Heyderman, A. Bisig, A.F. Rodríguez, L. Le Guyader, F. Nolting, H.B. Braun, J. Appl. Phys. **105**, 113113 (2009)
91. J. Li, S. Zhang, J. Bartell, C. Nisoli, X. Ke, P.E. Lammert, V.H. Crespi, P. Schiffer, Phys. Rev. B **82**, 134407 (2010)
92. Z. Budrikis, P. Politi, R.L. Stamps, Phys. Rev. Lett. **105**, 017201 (2010)
93. C. Nisoli, R.F. Wang, J. Li, W.F. McConville, P.E. Lammert, P. Schiffer, V.H. Crespi, Phys. Rev. Lett. **98**, 217203 (2007)
94. C. Nisoli, J. Li, X.L. Ke, D. Garand, P. Schiffer, V.H. Crespi, Phys. Rev. Lett. **105**, 047205 (2010)
95. P.E. Lammert, X.L. Ke, J. Li, C. Nisoli, D.M. Garand, V.H. Crespi, P. Schiffer, Nat. Phys. **6**, 786 (2010)
96. Y. Li, T.X. Wang, Phys. Lett. A **374**, 4475 (2010)
97. J.P. Morgan, A. Stein, S. Langridge, C.H. Marrows, Nat. Phys. **7**, 75 (2011)

98. C. Castelnovo, R. Moessner, S.L. Sondhi, Nature **451**, 42 (2008)
99. P.A.M. Dirac, Proc. R. Soc. Lond. Ser. A-Containing Papers of a Mathematical and Physical Character **133**, 60 (1931)
100. A.S. Goldhaber, W.P. Trower, Am. J. Phys. **58**, 429 (1990)
101. D.J.P. Morris, D.A. Tennant, S.A. Grigera, B. Klemke, C. Castelnovo, R. Moessner, C. Czternasty, M. Meissner, K.C. Rule, J.U. Hoffmann, K. Kiefer, S. Gerischer, D. Slobinsky, R.S. Perry, Science **326**, 411 (2009)
102. T. Fennell, P.P. Deen, A.R. Wildes, K. Schmalzl, D. Prabhakaran, A.T. Boothroyd, R.J. Aldus, D.F. McMorrow, S.T. Bramwell, Science **326**, 415 (2009)
103. H. Kadowaki, N. Doi, Y. Aoki, Y. Tabata, T.J. Sato, J.W. Lynn, K. Matsuhira, Z. Hiroi, J. Phys. Soc. Jpn. **78**, 103706 (2009)
104. A. Imre, G. Csaba, L. Ji, A. Orlov, G.H. Bernstein, W. Porod, Science **311**, 205 (2006)
105. I.R. McFadyen, E.E. Fullerton, M.J. Carey, MRS Bull. **31**, 379 (2006)
106. S.N. Piramanayagam, J. Appl. Phys. **102**, 011301 (2007)
107. A. Moser, K. Takano, D.T. Margulies, M. Albrecht, Y. Sonobe, Y. Ikeda, S. Sun, E.E. Fullerton, J. Phys. D: Appl. Phys. **35**, R157 (2002)
108. Y. Shiroishi, K. Fukuda, I. Tagawa, H. Iwasaki, S. Takenoiri, H. Tanaka, H. Mutoh, N. Yoshikawa, IEEE Trans. Magn. **45**, 3816 (2009)
109. E.E. Fullerton, D. Margulies, M. Schabes, M. Doerner, M. Carey, B. Gurney, A. Moser, M. Best, G. Zeltzer, K. Rubin, H. Rosen, Appl. Phys. Lett. **77**, 3806 (2000)
110. K. Tang, X. Bian, G. Choe, K. Takano, M. Mirzamaani, G. Wang, J. Zhang, Q.-F. Xiao, Y. Ikeda, J. Risner-Jamtgaard, X. Xu, IEEE Trans. Magn. **45**, 786 (2009)
111. R.H. Victora, X. Shen, IEEE Trans. Magn. **41**, 2828 (2005)
112. D. Suess, J. Lee, J. Fidler, T. Schrefl, J. Magn. Magn. Mater. **321**, 545 (2009)
113. T. Hauet, S. Florez, D. Margulies, Y. Ikeda, B. Lengsfield, N. Supper, K. Takano, O. Hellwig, B.D. Terris, Appl. Phys. Lett. **95**, 222507 (2009)
114. Thomas P. Nolan, Bogdan F. Valcu, Hans J. Richter, IEEE Trans. Magn. **47**, 63 (2011)
115. G. Choe, J. Park, Y. Ikeda, B. Lengsfield, T. Olson, K. Zhang, S. Florez, Arien Ghaderi, IEEE Trans. Magn. **47**, 55 (2011)
116. G. Choe, Y. Ikeda, K. Zhang, K. Tang, M. Mirzamaani, IEEE Trans. Magn. **45**, 2694 (2010)
117. R. Wood, M. Williams, A. Kavcic, J. Miles, IEEE Trans. Magn. **45**, 917 (2009)
118. L. Zhang, Y.K. Takahashi, K. Hono, B.C. Stipe, J.-Y. Juang, M. Grobis, J. Appl. Phys. **109**, 07B703 (2011)
119. H. Yuan, A. Chernyshov, J. Mardinly, K. Srinivasan, R. Acharya, G. Bertero, T. Yamashita, J. Appl. Phys. **109**, 07B772 (2011)
120. H.J. Richter, A. Lyberatos, U. Nowak, R. Evans, R.W. Chantrell, J. Appl. Phys. **111**, 033909 (2012)
121. B.D. Terris, T. Thomson, J. Phys. D: Appl. Phys. **38**, R199 (2005)
122. T.R. Albrecht, O. Hellwig, R. Ruiz, M.E. Schabes, B.D. Terris, X.Z. Wu, in *Nanoscale Magnetic Materials and Applications*, ed. by J.P. Liu, E.E. Fullerton, O. Gutfleisch, D.J. Sellmyer (Springer Science + Business Media, New York, 2009), pp. 237–274
123. T. Bublat, D. Goll, J. Appl. Phys. **110**, 073908 (2011)
124. D. Goll, Int. J. Mat. Res. (formerly Z. Metallkd.) **100**, 5 (2009)
125. D. Makarov, J. Lee, C. Brombacher, C. Schubert, M. Fuger, D. Suess, J. Fidler, M. Albrecht, Appl. Phys. Lett. **96**, 062501 (2010)
126. A.T. McCallum, P. Krone, F. Springer, C. Brombacher, M. Albrecht, E. Dobisz, M. Grobis, D. Weller, O. Hellwig, Appl. Phys. Lett. **98**, 242503 (2011)
127. B.C. Stipe, T. Strand, C. Poon, H. Balamane, T. Boone, J. Katine, J-L Li, V. Rawat, H. Nemoto, A. Hirotsune, O. Hellwig, R. Ruiz, E. Dobisz, N. Robertson, T. Albrecht, B.D. Terris, Nat. Photonics **4**, 484 (2010)
128. M. Grobis, E. Dobisz, O. Hellwig, M. Schabes, T. Hauet, G. Zeltzer, T. Albrecht, Appl. Phys. Lett. **96**, 052509 (2010)
129. I. Tagawa, Y. Nakamura, IEEE Trans. Magn. **27**, 45 (1991)
130. A. Berger, Y. Xu, B. Lengsfield, Y. Ikeda, E.E. Fullerton, IEEE Trans. Magn. **41**, 3178 (2005)

131. A. Berger, B. Lengsfield, Y. Ikeda, J. Appl. Phys. **99**, 08E705 (2006)
132. O. Hovorka, R.F.L. Evans, R.W. Chantrell, A. Berger, Appl. Phys. Lett. **97**, 062504 (2010)
133. M. Grobis, Intermag talk Taipe, Taiwan (2011)
134. S. Hernandez, M. Kapoor, R.H Victora, Appl. Phys. Lett. **90**, 132505 (2007)
135. S.N. Piramanayagam, K.O. Aung, S. Deng, R. Sbiaa, J. Appl. Phys. **105**, 07C118 (2009)
136. S. Li, B. Livshitz, H.N. Bertram, A. Inomata, E.E. Fullerton, V. Lomakin, J. Appl. Phys. **105**, 07C121 (2009)
137. M.V. Lubarda, S. Li, B. Livshitz, E.E. Fullerton, V. Lomakin, Appl. Phys. Lett. **98**, 012513 (2011)
138. M.V. Lubarda, S. Li, B. Livshitz, E.E. Fullerton, V. Lomakin, IEEE Trans. Magn. **47**, 18 (2011)
139. J. Lee, C. Brombacher, J. Fidler, B. Dymerska, D. Suess, M. Albrecht, Appl. Phys. Lett. **99**, 062505 (2011)
140. M.E. Schabes, J. Magn. Magn. Mater. **320**, 2880 (2008)
141. J.M. Shaw, W.H. Rippard, S.E. Russek, T. Reith, C.M. Falco, J. Appl. Phys. **101**, 023909 (2007)
142. O. Hellwig, J.B. Kortright, A. Berger, E.E. Fullerton, J. Magn. Magn. Mater. **319**, 13 (2007)
143. J.M. Shaw, M. Olsen, J. Lau, M.L. Schneider, T.J. Silva, O. Hellwig, E. Dobisz, B.D. Terris, Phys. Rev. B. **82**, 144437 (2010)
144. J.W. Lau, R.D. McMichael, S.H. Chung, J.O. Rantschler, V. Parekh, D. Litvinov, Appl. Phys. Lett. **92**, 012506 (2008)
145. B. Pfau, C.M. Gnther, E. Guehrs, T. Hauet, E. Dobisz, D. Kercher, H. Yang, L. Vinh, X. Xu, D. Yaney, R.L. Rick, S. Eisebitt, O. Hellwig, Appl. Phys. Lett. **99**, 062502 (2011)
146. O. Hellwig, T. Hauet, T. Thomson, E. Dobisz, J.D. Risner-Jamtgaard, D. Yaney, B.D. Terris, E.E. Fullerton, Appl. Phys. Lett. **95**, 232505 (2009)
147. P. Krone, D. Makarov, T. Schrefl, M. Albrecht, J. Appl. Phys. **109**, 103901 (2011)
148. T. Hauet, E. Dobisz, S. Florez, J. Park, B. Lengsfield, B.D. Terris, O. Hellwig, Appl. Phys. Lett. **95**, 262504 (2009)
149. P. Krone, D. Makarov, T. Schrefl, M. Albrecht, Appl. Phys. Lett. **97**, 082501 (2010)
150. R. Ruiz, H. Kang, F.A. Detcheverry, E. Dobisz, D.S. Kercher, T.R. Albrecht, J.J. de Pablo, P.F. Nealey, Science **321**, 936 (2008)
151. O. Hellwig, J.K. Bosworth, E. Dobisz, D. Kercher, T. Hauet, G. Zeltzer, J.D. Risner-Jamtgaard, D. Yaney, R. Ruiz, Appl. Phys. Lett. **96**, 052511 (2010)
152. J. Moritz, B. Dieny, J.P. Nozieres, R.J.M. van de Veerdonk, T.M. Crawford, D. Weller, S. Landis, Appl. Phys. Lett. **86**, 063512 (2005)
153. T. Thomson, G. Hu, B.D. Terris, Phys. Rev. Lett. **96**, 257204 (2006)
154. O. Hellwig, A. Berger, T. Thomson, E. Dobisz, H. Yang, Z. Bandic, D. Kercher, E.E. Fullerton, Appl. Phys. Lett. **90**, 162516 (2007)
155. M. Grobis, O. Hellwig, T. Hauet, E. Dobisz, T.R. Albrecht, IEEE Trans. Mag. **47**, 6 (2011)
156. O. Hellwig, A. Moser, E. Dobisz, Z. Bandic, H. Yang, D.S. Kercher, J.D. Risner-Jamtgaard, D. Yaney, E.E. Fullerton, Appl. Phys. Lett. **93**, 192501 (2008)
157. J.M. Shaw, S.E. Russek, T. Thomson, M.J. Donahue, B.D. Terris, O. Hellwig, E. Dobisz, M.L. Schneider, Phys. Rev. B **78**, 024414 (2008)
158. R. Hyndman, P. Warin, J. Gierak, J. Ferre, J.N. Chapman, J.P. Jamet, V. Mathet, C. Chappert, J. Appl. Phys. **90**, 3843 (2001)
159. J. Fassbender, J. McCord, J. Magn. Magn. Mater. **320**, 579 (2008)
160. M.S. Martyn-Gonzalez, F. Briones, J.M. Garcya-Martyn, J. Montserrat, L. Vila, G. Faini, A.M. Testa, D. Fiorani, H. Rohrmann, J. Magn. Magn. Mater. **322**, 2762 (2010)
161. S. Sun, Adv. Mater. **18**, 393 (2006)
162. Q. Dai, D. Berman, K. Virwani, J. Frommer, P.-O. Jubert, M. Lam, T. Topuria, W. Imaino, A. Nelson, Nano Lett. **10**, 3216 (2010)
163. C.T. Black, C.B. Murray, R.L. Sandstrom, S. Sun, Science **290**, 1131 (2000)
164. I.S. Belobordodov, A.V. Lopatin, V.M. Vinokur, K.B. Efetov, Rev. Mod. Phys. **79**, 469 (2007)

165. S.A. Claridge, A.W. Castleman Jr, S.N. Khanna, C.B. Murray, A. Sen, P.S. Weiss, ACS Nano **3**, 244 (2009)
166. C.B. Murray, C.R. Kagan, M.G. Bawendi, Annu. Rev. Mater. Sci. **30**, 545 (2000)
167. K.J.M. Bishop, C.E. Wilmer, S. Soh, B.A. Grzybowski, Small **5**, 1600 (2009)
168. F. Marlow, Muldarisnur, P. Sharifi, R. Brinkmann, C. Mendive, Angew. Chem. Int. Ed. **48**, 6212 (2009)
169. G.M. Whitesides, B. Grzybowski, Science **295**, 2418 (2002)
170. A. Weddemann, I. Ennen, A. Regtmeier, C. Albon, A. Wolff, K. Eckstädt, N. Mill, M.K.-H. Peter, J. Mattay, C. Plattner, N. Sewald, A. Hütten, Beilstein J. Nanotechnol. **1**, 75 (2010)
171. X.-M. Lin, A.C. S Samia, J. Magn. Magn. Mater. **305**, 100 (2006)
172. J.R. Thomas, J. Appl. Phys. **37**, 2914 (1966)
173. Y. Lalatonne, J. Richardi, M.P. Pileni, Nat. Mater. **3**, 121 (2004)
174. E.L. Bizdoaca, M. Spasovaa, M. Farle, M. Hilgendorff, F. Caruso, J. Magnet, Magnet. Mater. **240**, 44 (2002)
175. F.X. Redl, C.T. Black, G.C. Papaefthymiou, R.L. Sandstrom, M. Yin, H. Zeng, C.B. Murray, S.P. O'Brien, J. Am. Chem. Soc. **126**, 14583 (2004)
176. M.J. Benitez, D. Mishra, P. Szary, G.A. Badini Confalonieri, M. Feyen, A.H. Lu, L. Agudo, G. Eggeler, O. Petracic, H. Zabel, J. Phys.: Condens. Matter **23**, 126003 (2011)
177. J.L. Dormann, D. Fiorani, E. Tronc, Adv. Chem. Phys. **98**, 283 (1997)
178. S.I. Woods, J.R. Kirtley, S. Sun, R.H. Koch, Phys. Rev. Lett. **87**, 137205 (2001)
179. V. Russier, J. Appl. Phys. **89**, 1287 (2001)
180. W. Kleemann, O. Petracic, Ch. Binek, G.N. Kakazei, YuG Pogorelov, J.B. Sousa, S. Cardoso, P.P. Freitas, Phys. Rev. B **63**, 134423 (2001)
181. X. Batlle, A. Labarta, J. Phys. D: Appl. Phys. **35**, R15 (2002)
182. P. Poddar, T. Telem-Shafir, T. Fried, G. Markovich, Phys. Rev. B **66**, 060403 (2002)
183. M. Porto, Eur. Phys. J. B **26**, 229 (2002)
184. F. Luis, F. Petroff, L.M. Garcia, J. Bartolome, J. Carrey, A. Vaures, Phys. Rev. Lett. **88**, 217205 (2002)
185. P. Joensson, Adv. Chem. Phys. **128**, 191 (2004)
186. C. Binns, K.N. Trohidou, J. Bansmann, S.H. Baker, J.A. Blackman, J.-P. Bucher, D. Kechrakos, A. Kleibert, S. Louch, K.-H. Meiwes-Broer, G.M. Pastor, A. Perez, Y. Xie, J. Phys. D: Appl. Phys. **38**, R357 (2005)
187. S.A. Majetich, M. Sachan, J. Phys. D: Appl. Phys. **39**, R407 (2006)
188. O. Petracic, X. Chen, S. Bedanta, W. Kleemann, S. Sahoo, S. Cardoso, P.P. Freitas, J. Magn. Magn. Mater. **300**, 192 (2006)
189. O. Iglesias, A. Labarta, X. Batlle, J. Nanosci. Nanotechnol. **8**, 2761 (2008)
190. O. Petracic, Superlatt. Microstruct. **47**, 569 (2010)
191. J.L. Dormann, D. Fiorani, R. Cherkaoui, E. Tronc, F. Lucari, F.D. Orazio, L. Spinu, M. Nogues, H. Kachkachi, J.P. Jolivet, J. Magnet, Magn. Mater. **203**, 23 (1999)
192. R. Lopez-Ruiz, F. Luis, J. Sese2, J. Bartolome, C. Deranlot, F. Petroff, Eur. Phys. Lett. **89**, 67011 (2010)
193. A. Mydosh, *Spin Glasses: An Experimental Introduction* (CRC Press, Boca Raton, 1993)
194. S. Bedanta, O. Petracic, E. Kentzinger, W. Kleemann, U. Rücker, A. Paul, Th Brückel, S. Cardoso, P.P. Freitas, Phys. Rev. B **72**, 024419 (2005)
195. E.Z. Meilikhov, R.M. Farzetdinova, J. Exp. Theo. Phys. **94**, 751 (2002)
196. P. Politi, M.G. Pini, R.L. Stamps, Phys. Rev. B **73**, 020405 (2006)
197. A. Ebbing, O. Hellwig, L. Agudo, G. Eggeler, O. Petracic, Phys. Rev. B **84**, 012405 (2011)
198. J. Briatico, J.-L. Maurice, J. Carrey, D. Imhoff, F. Petroff, A. Vaures, Eur. Phys. J. D **9**, 517 (1999)
199. S. Sankar, A.E. Berkowitz, D.J. Smith, Phys. Rev. B **62**, 14273 (2000)
200. D. Babonneau, F. Petroff, J.-L. Maurice, F. Fettar, A. Vaures, Appl. Phys. Lett. **76**, 2892 (2000)
201. S. Sahoo, O. Petracic, W. Kleemann, S. Stappert, G. Dumpich, S. Cardoso, P.P. Freitas, Appl. Phys. Lett. **82**, 4116 (2003)

202. Y.-C. Wu, L.-W. Wang, C.-H. Lai, Appl. Phys. Lett. **93**, 242501 (2008)
203. A. Sugawara, G.G. Hembree, M.R. Scheinfein, J. Appl. Phys. **82**, 5662 (1997)
204. N. Weiss, T. Cren, M. Epple, S. Rusponi, G. Baudot, S. Rohart, A. Tejada, V. Repain, S. Rousset, P. Ohresser, F. Scheurer, P. Bencok, H. Brune, Phys. Rev. Lett **95**, 157204 (2005)
205. F.X. Redl, K.-S. Cho, C.B. Murray, S. O'Brien, Nature **423**, 968 (2003)
206. E.V. Shevchenko, D.V. Talapin, N.A. Kotov, S. O'Brien, C.B. Murray, Nature **439**, 55 (2006)
207. E.V. Shevchenko, M. Ringler, A. Schwemer, D.V. Talapin, T.A. Klar, A.L. Rogach, J. Feldmann, A.P. Alivisatos, J. Am. Chem. Soc. **130**, 3274 (2008)
208. D.V. Talapin, E.V. Shevchenko, M.I. Bodnarchuk, X. Ye, J. Chen, C.B. Murray, Nature **461**, 964 (2009)
209. J. Chen, X. Ye, C.B. Murray, ACS Nano **4**, 2374 (2010)
210. A. Dong, J. Chen, P.M. Vora, J.M. Kikkawa, C.B. Murray, Nature **466**, 474 (2010)
211. A. Dong, X. Ye, J. Chen, C.B. Murray, Nano Lett. **11**, 1804 (2011)
212. P. Bartlett, R.H. Ottewill, P.N. Pusey, Phys. Rev. Lett. **68**, 3801 (1992)
213. J.V. Sanders, Phil. Mag. A **42**, 705 (1980)
214. M.D. Eldridge, P.A. Madden, D. Frenkel, Nature **365**, 35 (1993)
215. M.E. Leunissen, C.G. Christova, A.-P. Hynninen, C. Patrick Royall, A.I. Campbell, A. Imhof, M. Dijkstra, R. van Roij, A. van Blaaderen, Nature **437**, 235 (2005)
216. A.M. Kalsin, M. Fialkowski, M. Paszewski, S.K. Smoukov, K.J.M. Bishop, B.A. Grzybowski, Science **312**, 420 (2006)
217. N. Hunt, R. Jardine, P. Bartlett, Phys. Rev. E **62**, 900 (2000)
218. M. Grzelcak, J. Vermant, E.M. Furst, L.M. Liz-Marzan, ACS Nano **7**, 3591 (2010)
219. C.H. Lalander, Y. Zheng, S. Dhuey, S. Cabrini, U. Bach, ACS Nano **4**, 6153 (2010)
220. Q. Chen, S.C. Bae, S. Granick, Nature **469**, 381 (2011)
221. S.Y. Park, A.K.R. Lytton-Jean, B. Lee, S. Weigand, G.C. Schatz, C.A. Mirkin, Nature **451**, 553 (2008)
222. J.C. Crocker, Nature **451**, 528 (2008)
223. D. Nykypanchuk, M.M. Maye, D. van der Lelie, O. Gang, Nature **549**, 553 (2008)
224. M.M. Maye, M. Thilak Kumara, D. Nykypanchuk, W.B. Sherman, O. Gang, Nature Nanotechnol. **5**, 116 (2010)
225. Y. Yin, Y. Lu, B. Gates, Y. Xia, J. Am. Chem. Soc. **123**, 8718 (2001)
226. M.J. Benitez, P. Szary, D. Mishra, M. Feyen, A.H. Lu, O. Petracic, H. Zabel, (unpublished) arXiv:1010.4166
227. L. Jiang, W. Wang, H. Fuchs, L. Chi, Small **5**, 2819 (2009)
228. F. Juillerat, H.H. Solak, P. Bowen, H. Hofmann, Nanotechnology **16**, 1311 (2005)
229. J.Y. Cheng, A.M. Mayes, C.A. Ross, Nat. Mater. **3**, 823 (2004)
230. J.G. Son, W.K. Bae, H. Kang, P.F. Nealey, K. Char, ACS Nano **3**, 3927 (2009)
231. K. Naito, H. Hieda, M. Sakurai, Y. Kamata, K. Asakawa, IEEE Trans. Mag. **38**, 1949 (2002)
232. G.A. Badini Confalonieri, V. Vega, A. Ebbing, D. Mishra, P. Szary, V.M. Prida, O. Petracic, H. Zabel, Nanotechnology **22**, 285608 (2011)
233. U. Wiedwald, L. Han, J. Biskupek, U. Kaiser, P. Ziemann, Beilstein J. Nanotechnol. **1**, 24 (2010)
234. H. Masuda, K. Fukuda, Science **268**, 1466 (1995)
235. S.D. Bader, Rev. Mod. Phys. **78**, 1 (2006)

Quantum Dot Spintronics: Fundamentals and Applications

Arne Ludwig, Björn Sothmann, Henning Höpfner, Nils C. Gerhardt, Jörg Nannen, Tilmar Kümmell, Jürgen König, Martin R. Hofmann, Gerd Bacher and Andreas D. Wieck

1 Introduction

1.1 Introduction

Spintronics is a generalization of electronics: Electronics means charge carrier transport, spintronics adds to this transport the supplementary degree of freedom *spin* which has been neglected since the roots of electronics. In this sense, spintronics is opening a new dimension of functional devices which is even more mighty than it may look at a first glance: The electron spin and its orientation is a pure quantum mechanical phenomenon which leads in its complexity to much more information coding depth and combinatorial operations than the storage and transport of charges in classical electronics. That is why the *quantum bit* (qubit) concept has been introduced by Schumacher [1].

A. Ludwig (✉) · A. D. Wieck
Lehrstuhl für Angewandte Festkörperphysik, Ruhr-Universität Bochum,
44801 Bochum, Germany
e-mail: arne.ludwig@rub.de

B. Sothmann
Département de Physique Théorique, Université de Genève, CH-1211 Genève 4, , Switzerland

H. Höpfner · N. C. Gerhardt · M. R. Hofmann
Lehrstuhl für Photonik und Terahertztechnologie, Ruhr-Universität Bochum,
44801 Bochum, Germany

J. Nannen · T. Kümmell · G. Bacher
Werkstoffe der Elektrotechnik and CeNIDE, Universität Duisburg-Essen,
Bismarckstr. 81, D-47057 Duisburg, Germany

J. König
Theoretische Physik, Universität Duisburg-Essen and CeNIDE,
47048 Duisburg, Germany

H. Zabel and M. Farle (eds.), *Magnetic Nanostructures,*
Springer Tracts in Modern Physics 246, DOI: 10.1007/978-3-642-32042-2_7,

Quantum dots are of particular interest thereby as they provide three-dimensional confinement and thus exhibit a delta-distributed zero-dimensional density of states. This is why they are also called *artificial atoms* which can be intentionally tailored in terms of quantum confinement, emission wavelength, g-factors and other features. They may host even single electrons and their zero-dimensional character leads to a high degree of insulation from the surrounding solid state matrix. This results in spin states that are much more robust as compared to bulk materials, which is attractive not only for spintronic applications but also for the qubit concept.

There are three main issues for realizing *spintronics* [2] based on semiconductor quantum dots: First, defined and thus polarized spins must be injected from a spin reservoir, e.g. magnetized metals [3]. Second, these spins must be stored, transported or manipulated and third the spin orientation must be detected. In between, the spin information should not be lost. More precisely, since the spin precesses in the presence of magnetic fields, its phase should be maintained as long as possible. The stability of the spin e.g. depends on the dimensionality and the purity of the semiconductor, on interfaces in heterostructures and on the temperature. The goal is therefore to prepare a device with highest purity possible and which potentially still works at non-cryogenic temperatures, i.e. up to room temperature. This leads us to optoelectronic devices which are able to emit circularly polarized photons at room temperature even in the absence of an external magnetic field. The circular polarization stems from recombining spin polarized electrons and can be manipulated by changing the spin polarization.

In this article, we will present three exemplary approaches for spin injection into quantum dots from a spin reservoir that is separated by a barrier. First, the concept of a spin polarizing injector with out-of-plane magnetization is developed, fabricated and characterized [4]. The electrons get polarized by an effective exchange field when passing the magnetic multilayer. The spin-polarized electrons are injected into an underlying quantum dot light-emitting-diode (QD-LED) via a tunnel barrier. The growth of this LED is described in the following section. In the second section, we extend the spin injection concept to single quantum dots. Here, we compare spin injection from a magnetic semiconductor via drift/diffusion with a tunnel injection mechanism from a defined Zeeman-level in the n-contact. Schemes for getting spin injection on a sub-nanosecond time scale are developed and discussed. Finally, we provide a theoretical description of the minimal model for spin accumulation and relaxation in metal-semiconductor hybrids, a quantum dot coupled to spin-polarized electrodes. After deriving the kinetic equations that govern the coupled dynamics of the quantum dot's charge and spin degree of freedom, we extend the minimal model by taking into account a coupling of the quantum dot's spin to additional spin degrees of freedom.

2 Spin Injection in Metal-Semiconductor Hybrids and Quantum Dots: Spin LEDs

2.1 Introduction

Ferromagnetic systems, especially thin layers, always tend to close the internal magnetic field lines in polarized domains, stepwise changed in direction to closed loops. This is the easiest way for the system to minimize magnetic stray fields and thus its magnetic energy. However, if we are looking for spin aligning ferromagnetic contacts to inject spin-polarized electrons into a semiconductor, these loops are highly unintentional. Instead, we need a magnetization of the contact layer perpendicular to it, i.e. "out of plane". The development, fabrication and characterization of such special spin injection contacts is described in this section. Moreover, their integration on top of an underlying GaAs-light-emitting-diode (LED) and the carrier injection via a tunnel barrier is discussed here. We will describe in detail the epitaxial growth of the LED, leading us to optoelectronic devices which are able to emit and receive circular polarized photons which are unique fingerprints of spin polarized electrons in the solid.

2.2 Injector

The first essential element for the realization of a hybrid metal-semiconductor spin-optoelectronic device is the electrical spin injection from polarized ferromagnetic (FM) metal contacts into semiconductors at room temperature (RT) and under magnetic remanence, i.e., in zero applied magnetic field. Usually, electric spin injection into the semiconductor is detected via the circular polarization of the emitted electroluminescence (EL) from a spin light emitting diode (LED) [5–8]. The optical selection rules require to choose the so-called Faraday geometry, where the directions of photon emission and electron spin polarization are parallel, but both (and thus also the magnetic field) are parallel to the growth direction of the LED. However, conventional spin injection contacts are thin FM films which exhibit in-plane magnetization due to the shape anisotropy. This means that several ferromagnetic domains arrange themselves in closed loops within the film plane, minimizing their energy and the magnetic stray field. As a result, relatively strong external magnetic fields of about $B = 2\,\mathrm{T}$ are required to align the magnetization and the underlying electron spin polarization along the perpendicular direction. Such high fields, which have to be applied externally, are not very practical for future spintronic devices, of course.

Therefore, we develop here FM spin injection contacts with remanent out-of-plane magnetization, i.e. in Faraday geometry, which should still be magnetized at RT for spin-optoelectronic devices. To do this, knowledge about the magnetic state of the interface is essential for the tailoring of efficient spin injection devices [9].

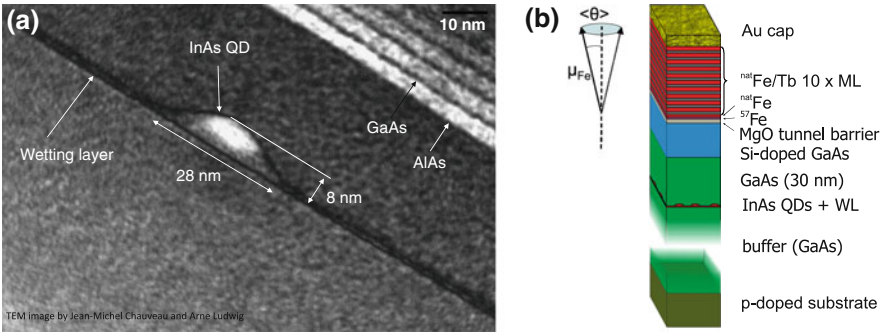

Fig. 1 **a** Transmission electron microscope (TEM) image of a single InAs quantum dot (QD). The Wetting layer (WL) and a current blocking layer made of epitaxial AlAs and GaAs (not present in the LED-structures) can be seen. **b** Definition of the Mössbauer tilting angle $\langle\Theta\rangle$ and layer sequence of our quantum dot spin-LEDs. The thickness of the undoped GaAs above the QD layer is varying from 30 nm to 150 nm for our sample series

Adelmann et al. [10] demonstrated remanent spin injection at $T = 2\,\mathrm{K}$ using FM δ-MnGa contacts. Gerhardt et al. [11] achieved remanent spin injection at 90 K employing Fe/Tb multilayer contacts. Later, Sinsarp et al. [12] used FePt/MgO tunnel contacts to demonstrate remanent spin injection at RT. Recently, we achieved efficient electrical spin injection [13] and electrical detection of photo-induced spins [14], both at RT and in remanence, using FM $[Fe/Tb]_{10}$/Fe and $[Fe/Tb]_{10}$/Fe/MgO multilayer contacts. Previously, we have reported the fabrication and characterization of [Fe/Tb]n/Fe contacts with perpendicular magnetic anisotropy (PMA) grown directly on a GaAs(100) based LED structure [15].

Here, we prepare a special structure to study the light emission and local magnetism of a $[Fe/Tb]_{10}$/Fe(001)/^{57}Fe[001]/MgO(001) spin aligner as a prototype layer system for remanent spin injection at room temperature (Fig. 1). An epitaxial Fe layer was grown on a clean GaAs(001)-based LED surface, with an epitaxial MgO interlayer serving as a tunnel barrier between both. Former studies revealed that MgO grows epitaxially on GaAs(001). The Fe film was followed by a $[Fe/Tb]_{10}$ multilayer to achieve the desired PMA. We monitor film growth and morphology at different stages in situ by reflection high-energy electron diffraction (RHEED). ^{57}Fe conversion-electron Mössbauer spectroscopy (CEMS) was applied to determine the Fe-spin structure at the buried ^{57}Fe(001)/MgO(001) interface. A conventional Mössbauer spectrometer and a ^{57}Co(Rh) source were used. The incidence of the γ-radiation was perpendicular to the film plane. A He/CH_4 proportional counter (channeltron detector) was employed for CEMS at room temperature and $T = 4.2\,\mathrm{K}$, respectively.

2.3 LED Growth

The GaAs-based LED-structures [16] were grown by molecular beam epitaxy on Zn-doped GaAs(001)-substrates, followed by a 3 μm undoped GaAs buffer layer to be far away from diffused or segregated impurities from the substrate. The InAs-QDs, 30 nm undoped GaAs and a 20 nm highly Si-doped injection layer are grown subsequently. Except for the QD growth in Stranski-Krastanov-mode, the growth temperature for the diode structure was kept at 600 °C. It is noteworthy that we do not apply p-doping in the MBE but that the use of a p-doped substrate is sufficient to obtain electroluminescence (EL) between the n-type epilayer and the p-type substrate. After growth, the sample is capped in-situ with an approx. 30 nm thick amorphous As_2 layer by increasing the As cracker zone temperature to 900 °C at a substrate temperature below 100 °C, and then transferred in air to a metal MBE system with a base residual gas pressure of 1×10^{-10} mbar for deposition of the spin aligner. After load-locking the sample in this second MBE-system, the As-cap layer was desorbed in UHV by heating the sample to 400 °C during a few minutes. The As-removal was monitored by RHEED and it was verified that this temperature did not yield an As-depletion of the GaAs. It resulted in a clean, As-terminated GaAs(001) surface, as evidenced by the 2×2 surface reconstruction in the RHEED pattern (Fig. 2a).

Subsequently, the cleaned GaAs-LED was held at 300 °C and a 3 nm-thin MgO(001) layer was deposited by evaporating MgO at a rate of 0.003 nm/s from an electron-beam heated effusion cell. As shown by Son et al. [17] UHV-deposited MgO is oxygen deficient. To achieve epitaxial growth of a stoichiometric MgO layer, the evaporation was carried out at an oxygen partial pressure of 10^{-7} mbar. Figure 2b shows the RHEED pattern of the 3 nm MgO(001)-layer. We conclude that the MgO growth was almost epitaxial, although the structure is less perfect than for the initial GaAs-LED surface. This is not surprising, since the lattice mismatch between GaAs and MgO is 25.5 % and strictly speaking MgO grows in a polycrystalline manner on GaAs with a texture along GaAs(001)[001] ∥ MgO(001)[001] [18]. Afterwards, a (001) film of 5 monolayers (ML) of ^{57}Fe(001) with 95 % isotopical enrichment was deposited at RT and 2×10^{-10} mbar onto the MgO(001) layer, followed by 1.88 nm of Fe of natural isotopical abundance (^{nat}Fe) under the same conditions. Both ^{57}Fe and ^{nat}Fe were deposited at a rate of 0.003 nm/s, as for the MgO layer. Figure 2c shows the RHEED pattern of the completed first iron layer (^{57}Fe plus ^{nat}Fe). We conclude from the somewhat broadened RHEED spots and their arrangement that Fe grows epitaxially in the Volmer–Weber (three-dimensional) mode, which leads to an atomically rough surface. In addition, there is evidence of weak Debye–Scherrer rings, indicating some polycrystalline growth in addition to the dominant epitaxial (001) growth. After this starting epitaxial iron layer, 1.4 nm Tb- and 2.6 nm ^{nat}Fe-layers were alternately deposited at a rate of 0.003 nm/s. The completed multilayer consisted of 10 Fe/Tb pairs. This was covered by a protective cap layer of 5 nm of Cr to enable ex situ studies. All of these layers, except the first iron layer and the MgO layer, were found to be polycrystalline.

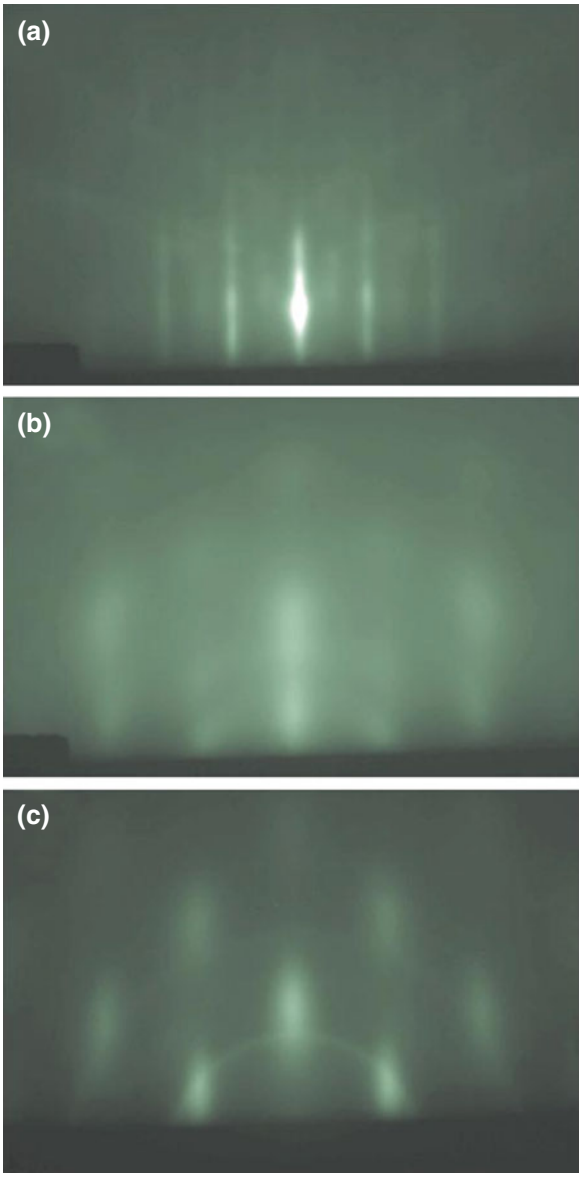

Fig. 2 RHEED diffraction patterns taken with 15 keV electrons along the [1$\bar{1}$0] azimuthal direction of **a** clean GaAs (001)-LED surface, **b** 3 nm thick MgO(001) layer on a GaAs(001)-LED surface, and **c** first iron layer (5 ML ^{57}Fe + 1.88 nm ^{nat}Fe) on a MgO(001) layer. (Reprinted with permission from [4]. Copyright 2010, American Institute of Physics)

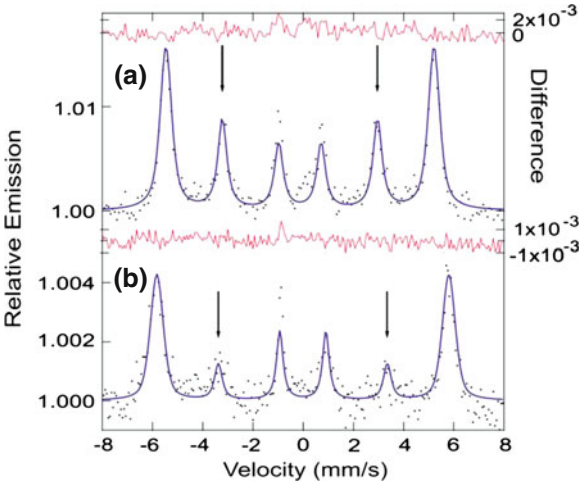

Fig. 3 ^{57}Fe tracer-layer CEMS spectra, taken in zero external magnetic field at $T = 295$ K **a** and 4.2 K **b**. Above each spectrum, the difference between the experimental data and the fit curve is shown, indicating the good fit matching. (Reprinted with permission from [4]. Copyright 2010, American Institute of Physics)

Table 1 Mössbauer spectral parameters of sample a obtained from least-squares fitting

Temperature [K]	$\langle B_{\mathrm{hf}} \rangle$ [T]	STD [T]	δ [mm/s]	R_{23}	$\langle \theta \rangle$ [deg]
295	33.1(1)	2.1(1)	0.00(1)	1.39(6)	46(5)
4.2	36.0(1)	2.6(1)	0.11(1)	0.58(6)	30(5)

Shown parameters are the average hyperfine magnetic field $\langle B_{\mathrm{hf}} \rangle$, isomer shift relative to bulk bcc Fe at RT δ, line intensity ratio R_{23}, and average Fe spin tilting angle relative to film normal direction $\langle \theta \rangle$. STD denotes the standard deviation of $\langle B_{\mathrm{hf}} \rangle$

It is well known that bcc Fe layers in nanoscale Fe/Tb multilayers may exhibit PMA (see e.g. [19–22]). The Fe/Tb interfaces play a dominant role in creating the PMA. The PMA is thought to originate from antiferromagnetically exchange-coupled Fe–Tb atomic pairs combined with the single-ion anisotropy and the large orbital moment of the Tb atom[20, 21]. An amorphous Fe–Tb alloy phase at the Fe/Tb interface which are a few atomic layers thick, as observed by Mössbauer spectroscopy [13–15, 17, 18], could be involved in creating PMA. In our sample, the 5 ML ^{57}Fe probe layer monitors the magnetic state at the Fe/MgO interface. However, since natural Fe contains approximately 2 % of ^{57}Fe, it is clear that about 40 % of our Mössbauer signal originates from the Fe/Tb multilayer and about 60 % from the ^{57}Fe probe layer. The CEMS spectra, measured at RT and 4.2 K, are shown in Fig. 3a, b, respectively. The spectra observed are Zeeman-split sextets typical for the bcc Fe phase, however with broadened lines. In least-square fits of these spectra, which are the solid lines in Fig. 3, we have used a continuous Gaussian distribution of hyperfine magnetic fields, $P(B_{\mathrm{hf}})$. The Mössbauer spectral parameters obtained from the fitting are given in Table 1.

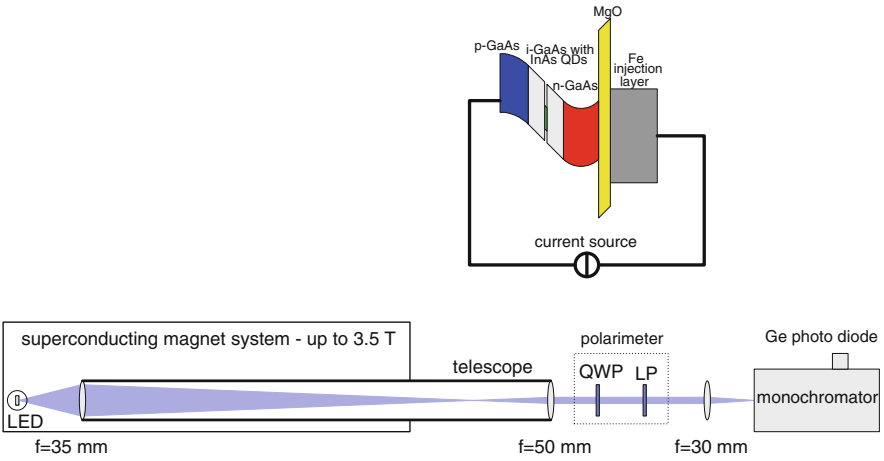

Fig. 4 Experimental setup for the optical characterization of the spin-LEDs. The inset shows the schematic band diagram of the LEDs connected to a constant current source

2.4 Optical Characterization of Spin-LEDs

The quantum dot spin-LEDs were characterized in the setup schematically shown in Fig. 4. The samples are placed inside a superconducting magnet system that can provide up to 3.5 T magnetic field strength. For temperature dependent measurements, the samples can be placed in a separate flow cryostat which itself can be placed within the superconducting magnet so that the samples can be analyzed for variable temperatures and magnetic fields. However, in this work, we restrict ourselves to the discussion of the behaviour at room temperature and (mainly) at zero magnetic field. The LED is operated with a constant current source. Its band diagram is shown schematically in the inset of Fig. 4.

The optical LED emission is collected using a telescope and directed towards a Stokes polarimeter for precise analysis of the polarization state of the emission. The polarimeter contains a rotating quarter wave plate (QWP) and a stationary linear polarizer (LP).

For spectrally resolved detection, the light is focused into a monochromator with a 1,200 lines per mm blazed grating providing a spectral resolution of 1 nm. Detection is performed in lock-in technique with a high sensitivity Germanium detector cooled with liquid nitrogen for low noise measurements in the 1,200 nm emission range of the LEDs.

In the Stokes polarimeter, the light intensity I_{det} is measured as a function of the rotation angle α of the QWP. The intensity measured with a polarization insensitive detector depends on the Stokes parameters S_0, S_1, S_2, and S_3 characterizing the polarization state:

$$I_{\mathrm{det}} = \begin{pmatrix} 1 & 0 & 0 & 0 \end{pmatrix} \cdot M_{\mathrm{LP}} \cdot M_{\mathrm{QWP}} \cdot \begin{pmatrix} S_0 \\ S_1 \\ S_2 \\ S_3 \end{pmatrix} \tag{1}$$

with M_{LP} and M_{QWP} being the Mueller matrices for the linear polarizer and the quarter wave plate, respectively [23, 24]. These matrices are given by:

$$M_{\mathrm{LP}} = \frac{1}{2} \begin{pmatrix} 1 & \cos 2\beta & \sin 2\beta & 0 \\ \cos 2\beta & \cos^2 2\beta & \cos 2\beta \sin 2\beta & 0 \\ \sin 2\beta & \cos 2\beta \sin 2\beta & \sin^2 2\beta & 0 \\ 0 & 0 & 0 & 0 \end{pmatrix} \tag{2}$$

and

$$M_{\mathrm{QWP}} = \begin{pmatrix} 1 & 0 & 0 & 0 \\ 0 & \frac{1}{2}(1+\cos 4\alpha) & \frac{1}{2}\sin 4\alpha & -\sin 2\alpha \\ 0 & \frac{1}{2}\sin 4\alpha & \frac{1}{2}(1-\cos 4\alpha) & \cos 2\alpha \\ 0 & \sin 2\alpha & -\cos 2\alpha & 0 \end{pmatrix} \tag{3}$$

with α being the angle between the fast axis of the QWP and the vertical and β being the angle of the transmission polarization direction with respect to the vertical.

The circular polarization is obtained from the ratio S_3/S_0, where S_0 corresponds to the total intensity. In most cases, the angle β is chosen to be 0. Then, I_{det} only depends on α, and Eq. (1) reduces to [23, 24]:

$$I_{\mathrm{det}} = \frac{1}{2}S_0 + \frac{1}{4}S_1(1+\cos 4\alpha) + \frac{1}{4}S_2 \sin 4\alpha - \frac{1}{2}S_3 \sin 2\alpha \tag{4}$$

It should be noted that Eq. (4) is only valid for ideal polarization optics. A non-ideality of the LP does not cause severe errors. A non-ideal LP provides an undesired signal with 90° phase difference but its signal strength is attenuated by the polarizer's contrast which is about 10^6 in our case so that the corresponding measurement error is negligible. In contrast, imperfections of the QWP are more severe and have to be considered. In detail, a wavelength dependent retardation error in the range of 5–10 % occurs even for achromatic QWPs. This has to be considered in the Mueller matrix for the QWP [23, 24]:

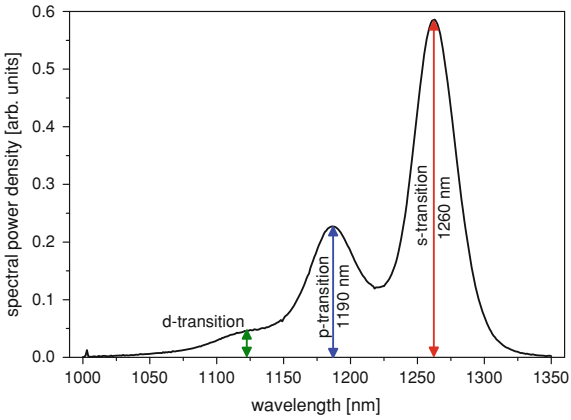

Fig. 5 Electroluminescence spectrum of our samples. Spectrum shown is for sample **e**, the other spectra are similar

$$M_{\mathrm{QWPr}} = \begin{pmatrix} 1 & 0 & 0 & 0 \\ 0 & \frac{1}{2}(1+\cos 4\alpha)(1-\sin\frac{\pi\varepsilon}{2}) & \frac{1}{2}\sin 4\alpha(1+\sin\frac{\pi\varepsilon}{2}) & -\sin 2\alpha\cos\frac{\pi\varepsilon}{2} \\ 0 & \frac{1}{2}\sin 4\alpha(1+\sin\frac{\pi\varepsilon}{2}) & \frac{1}{2}(1+\cos 4\alpha)(1-\sin\frac{\pi\varepsilon}{2}) & \cos 2\alpha\cos\frac{\pi\varepsilon}{2} \\ 0 & \sin 2\alpha\cos\frac{\pi\varepsilon}{2} & -\cos 2\alpha\cos\frac{\pi\varepsilon}{2} & -\sin\frac{\pi\varepsilon}{2} \end{pmatrix} \tag{5}$$

with the retardation error $\varepsilon = \frac{4\Delta s}{\lambda}$, Δs being the actual retardation and λ the wavelength. These values are usually provided by the manufacturer of the QWP. With Eq. (5) the intensity I_{det} measured with non-ideal polarization optics finally becomes [23]:

$$I_{\mathrm{det}} = \frac{1}{4}\left(2S_0 + S_1(1-\sin\frac{\pi\varepsilon}{2})(1+\cos 4\alpha) + S_2(1+\sin\frac{\pi\varepsilon}{2})\sin 4\alpha - 2S_3\cos\frac{\pi\varepsilon}{2}\sin 2\alpha\right). \tag{6}$$

Obviously, the contribution containing S_3, which is attributed to the circularly polarized signal component of interest in our measurements, scales with the cosine of the retardation error. Thus its variation is very small for small retardation errors as the first derivative of the cosine function is 0 around 0. However, the contributions associated with linear polarization suffer more significantly from retardation error as they scale with the sine of the retardation error. Thus, knowledge of the retardation error is obligatory in order to receive reliable quantitative data on the entire polarization state of the analyzed light.

Figure 5 shows a typical electroluminescence (EL) spectrum of one of our quantum dot LED samples, carrying the spin aligner. In the spectrum measured at room temperature in zero external magnetic field several transitions are visible, including the ground state emission (s-state) at about 0.98 eV. The emission wavelength corresponding to a transition between the ground states of the samples above is $\lambda_{\mathrm{max}} = 1260\,\mathrm{nm}$ with a FWHM $\approx 25\,\mathrm{meV}$ which means that there is a reasonable well ensemble homogeneity.

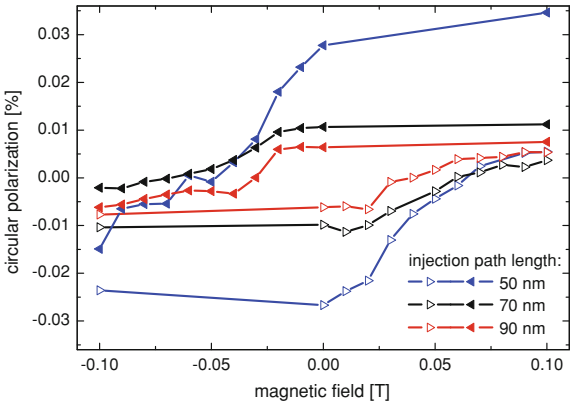

Fig. 6 Hysteresis curves of samples **a**, **b** and **c**. Filled (*open*) triangles represent decreasing (*increasing*) magnetic field strengths

In the following, only the ground state emission will be analyzed.

Figure 6 shows the measured circular polarization degree of the EL as a function of magnetic field for three different samples with different injector path lengths. All traces follow hysteresis loops. The maximum polarization degree of about 3 % is obtained for the sample with the shortest injection path. Note that even a polarization degree of 2.5 % is measured in remanence, i.e. without external magnetic field. This is an unambiguous confirmation of spin injection as magnetooptic effects due to the magnetic field are ruled out. The measured value for the circular polarization degree agrees well with values obtained earlier for quantum well spin-LEDs with similar injector design [11, 13, 25]. However, the circular polarization degree cannot be directly interpreted as spin injection efficiency because of spin relaxation effects. It is obvious from Fig. 6 that the LEDs with longer injection paths but with the same spin injector exhibit reduced circular polarization degrees. This is a consequence of spin relaxation. Thus, the influence of spin relaxation has to be quantitatively evaluated in order to determine the real spin injection efficiency.

2.5 Spin Relaxation and Real Spin Injection Efficiency

The relaxation mechanisms, which cause a polarization reduction in the spin injection process, are manifold. A systematic investigation of semiconductor structures with transport paths of different lengths should not only reveal the problems, but also be a guiding tool for the development and optimization of optoelectronic devices. In the following, the spin transport lengths in our LEDs are investigated under realistic conditions, i.e. at room temperature and without external magnetic fields and at reasonable current densities (up to 30 mA for a $300 \times 400\,\mu\text{m}^2$ device).

First, we analyze the spin-polarization and its dependence on the contact magnetization as revealed from SQUID measurements. Then, we compare the polarizations of samples with different injector lengths, evaluate the interface polarization and

Table 2 Injection path length and polarization values of our sample series

Sample	Injection path length (nm)	Measured polarization (%)	Mössbauer $\langle\cos^2\theta\rangle^{1/2}$	Calculated polarization (%)
a	50	2.69	0.60	4.47
b	70	1.71	0.69	2.46
c	90	1.19	0.78	1.52
d	120	0.77	0.73	1.05
e	170	0.49	0.67	0.73

extract the spin transport length from the exponential decrease of the polarization with increasing injector path length.

Our sample series consists of five samples which are nominally identical with exception of the layer thickness in between the spin injector layer and the quantum dot layer. At this place, the samples have layer thicknesses of 50, 70, 90, 120, and 170 nm. For further evaluation of our data on the circular polarization degree it has to be considered that the orientation of the magnetization of the ferromagnetic contact is not perfectly perpendicular to the surface but exhibits a certain angle with respect to the surface normal. This is accounted for by the quantities $\langle\cos^2(\theta)\rangle^{\frac{1}{2}}$ and the average Fe-spin canting angle $\langle\theta\rangle$. These values as obtained from conversion electron Mössbauer spectroscopy (CEMS) are listed for the different samples in Table 2 as well. Dividing the measured circular polarization values by the quantity $\langle\cos^2(\theta)\rangle^{\frac{1}{2}}$ provides the theoretical circular polarization degree that would be obtained for magnetization orthogonal to the film plane (see Table 2).

Further, it cannot be ruled out in our experimental geometry that a background polarization (P_{BG}) of the order of 1 % circular polarization degree appears due to magneto-optical effects during propagation of the light through the Fe/Tb contact. This is included into the data evaluation as a free fit parameter. According to calculations by Yu and Flatté [26] drift-based carrier transport should be assumed in non-degenerate semiconductors for reasonable electric field strengths. As this is valid for the injection paths in our devices, we fitted the data with an exponential decay according to [27]:

$$P(x) = P_0 \cdot e^{-\frac{x}{l_{\mathrm{r}}}} + P_{\mathrm{BG}} \tag{7}$$

From a least square fit of our data to Eq. (7) we obtain a background polarization of 0.7(1) %. The spin relaxation length l_r in remanence is calculated to 26(1) nm (see Fig. 7). This is on the lower end but still within the range interval predicted theoretically [28]. Extrapolating the polarization values towards shorter injection paths provides the interface polarization P_0 which accounts to 25(5) % in our case. Note that this is only a lower bound estimate because of spin relaxation in the active region prior to carrier recombination.

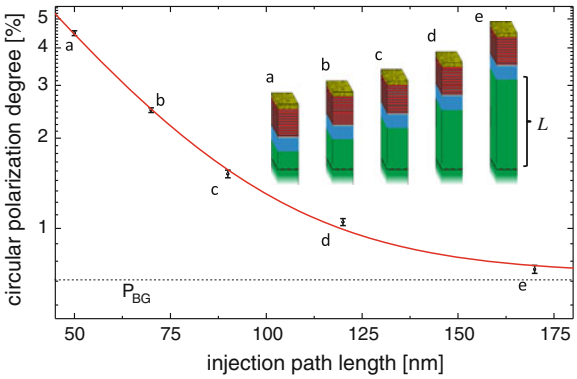

Fig. 7 Measured circular polarization as a function of injection path length L for samples **a**–**e**. The resulting relaxation length is 26(1) nm, the injection efficiency 25(5) % with a background polarization P_{BG} of 0.7(1) %

Additionally, we measured the polarization of the emission from our samples in an externally applied magnetic field of 0.5 T. In this case, the spin relaxation length inside magnetic fields increases to 36(1) nm, i.e. spin relaxation decreases. This effect is known [29] and emphasizes the necessity to measure spin relaxation without the use of external magnetic fields as those fields do have an impact on spin relaxation. A detailed study of this effect, particularly for magnetic fields below the coercive field strength of the magnetic layers, has yet to be carried out.

3 Spin Injection into Single Quantum Dots

3.1 Introduction

The key idea of our experiments is the coupling of a single quantum dot embedded in a p-i-n diode structure to a spin polarized source, which can be either a semiconductor in an external magnetic field or a ferromagnet. Spin polarized carriers from the source will affect the luminescence emitted from single quantum dots depending on the injection mechanisms and can be monitored by optical techniques both time integrated and time resolved.

Two approaches, which differ by the fundamental injection mechanism of spin-polarized electrons into the single quantum dots, have been developed and are sketched in Fig. 8. The first one is based on a light emitting device with quantum dots as the active area. As a model spin reservoir, a diluted magnetic semiconductor (DMS) is used, providing nearly 100 % spin polarization in external magnetic fields >2 T. When operating this device in forward direction, as indicated in Fig. 8a, spin-polarized electrons from the DMS layer will be transported via drift/diffusion into the quantum dots and will recombine with holes injected from the p-contact of the device. The high polarization in the spin source will ensure high spin polarization of the quantum dot electroluminescence albeit losses of the spin orientation during

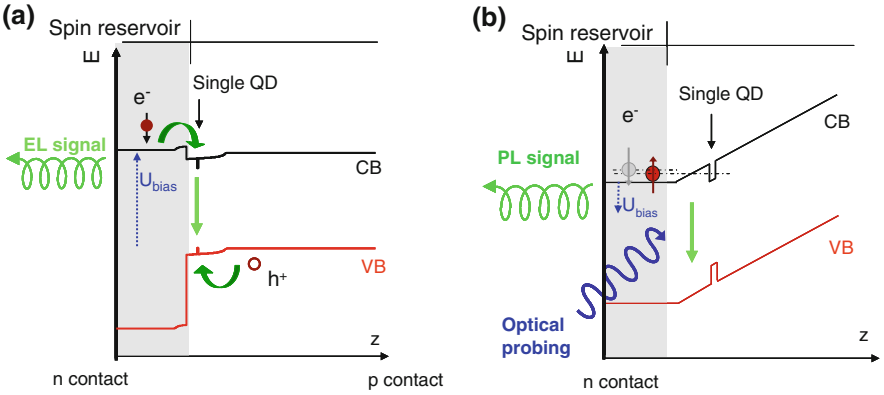

Fig. 8 Operation principle and schematic band structure of the two approaches coupling single quantum dots to a spin reservoir. **a** Spin injection via drift/diffusion into a spin LED **b** Tunnel injection of spin polarized electrons under reverse bias and optical probing

the transport. A different spin injection mechanism is used in the second approach. Here, the spin-polarized electrons are injected via tunneling, e.g. from a defined Zeeman level in the n-contact (Fig.8b). Although the spin alignment in the contact is lower than in the DMS, the high spin injection fidelity during the tunnel process still allows for significant spin polarization in the quantum dots that can be probed by photoluminescence spectroscopy.

3.2 Single Quantum Dot Based Spin LED

Let us consider at first the quantum dot LED device combined with a DMS spin aligner that is grown in a two chamber molecular beam epitaxy system. It is based on a p-doped GaAs substrate followed by a GaAs buffer and an i-GaAs layer with a thickness of 50 nm. Subsequently, self-assembled InAs quantum dots (QDs) with a nominal layer thickness of 1.7 monolayers, and 20 nm i-GaAs were grown. The transfer between the chamber equipped with the III–V materials and the chamber for the II–VI materials is performed under UHV conditions. In the second chamber, a 20 nm thick i-$Zn_{0.96}Mn_{0.04}Se$ layer was grown followed by a 150 nm thick layer of heavily doped (2×10^{18} cm^{-3}) n-$Zn_{0.96}Mn_{0.04}Se$. On the top of the sample, 10 nm of a heavily n-doped (1×10^{19} cm^{-3}) layer of ZnSe was deposited for the contact. Under a forward bias $U_{\text{bias}} = 1.5$ V, Fig. 8a gives a qualitative sketch of the band structure. The ZnMnSe layer will act as a very effective spin aligner in an external magnetic field (Faraday Geometry) and will accumulate spin-down electrons that are energetically lower than spin-up electrons due to the positive g factor. These spin polarized electrons from the DMS are transported under forward bias to the quantum dots, resulting in electroluminescent emission. As mentioned above, the strong spin

polarization in the DMS source is favorable in this experiment, because losses of the spin alignment are expected during transport into the single quantum dots.

For the electroluminescence measurements, lithographically defined nanoapertures in a 50 nm/25 nm thick chromium/gold (Cr/Au) mask with diameters ranging from 50 μm down to 300 nm were defined on top of the samples in order to get local access to individual QDs. The samples were contacted electrically and mounted inside a continuous flow cryostat, where the temperature can be controlled between 4 K and 300 K. We apply a magnetic field of up to 5 T in Faraday geometry and collect the electroluminescence using a 50 $\times$ objective. The signals were dispersed by a 0.55 m monochromator and detected using a LN_2-cooled CCD camera. In Fig. 9a, the EL emission of one individual QD is depicted at $T = 4.4$ K for different magnetic fields. The single quantum dot (SQD) emission is driven by a voltage of only 1.6 V in forward direction. Without external magnetic field, one single emission line is visible with a resolution limited FWHM of 0.15 meV. This is attributed to the recombination of an electron-hole pair in a single QD. With increasing magnetic field, the line splits with a Zeeman splitting of 0.82 meV at $B = 5$ T. The corresponding excitonic g-factor of $|g| = 2.8$ is typical for InAs quantum dots. Because g is generally negative in InGaAs quantum dots [30], actually $g = -2.8$. A striking feature is the significant circular polarization degree CPD $= (I^{\sigma+} - I^{\sigma-})/(I^{\sigma+} + I^{\sigma-})$, with $I^{\sigma+}$ ($I^{\sigma-}$) being the intensity of the right (left) circular polarized component of the quantum dot emission. The polarization degree reaches CPD = 65 % at 5 T, with an enhanced contribution of the high-energy line of the Zeeman doublet due to the negative excitonic g-factor. This non-thermal population of the Zeeman levels in the quantum dot is a clear indication of a successful spin injection from the DMS into the quantum dot. Remember that the electron g-factor is positive in ZnMnSe, but negative in the InAs QD. The spin alignment leads to a strong population of the lower Zeeman level in ZnMnSe by the electrons, thus the spin-polarized electrons injected into the InAs QD will occupy the higher Zeeman level of the SQD.

Analyzing the circular polarization degree CPD for individual single quantum dots, two interesting features can be observed. First, the CPD varies from dot to dot. Note that the DMS layer shows virtually 100 % spin polarization at $B = 5$ T and $T = 5$ K [31, 32]. While resonant tunnel processes are expected to be spin conserving, the drift/diffusion process can cause strong spin losses due to defects [33, 34] or to band bending at the interface [33]. The local environment and the individual energy level structure of each SQD, which may vary from dot to dot, can thus affect the spin injection efficiency significantly, in agreement with our experimental data (see Fig. 9b): While QD 1 reveals a maximum CPD of 65 % at 5 K, the corresponding value in QD 2 remains below 35 %. Most SQDs exhibit polarization degrees of more than 50 % and some reach nearly 100 % (see Fig. 9c).

Second, the current flow strongly affects the CPD (see Fig. 9b). It can be clearly seen that for higher injection current the polarization degree decreases. This is plausible, as for increasing currents the drift/diffusion based injection dominates over a possible tunnel injection. The effect has been observed already in ensemble structures [35, 36] and attributed to D'yakanov-Perel spin relaxation in the GaAs after

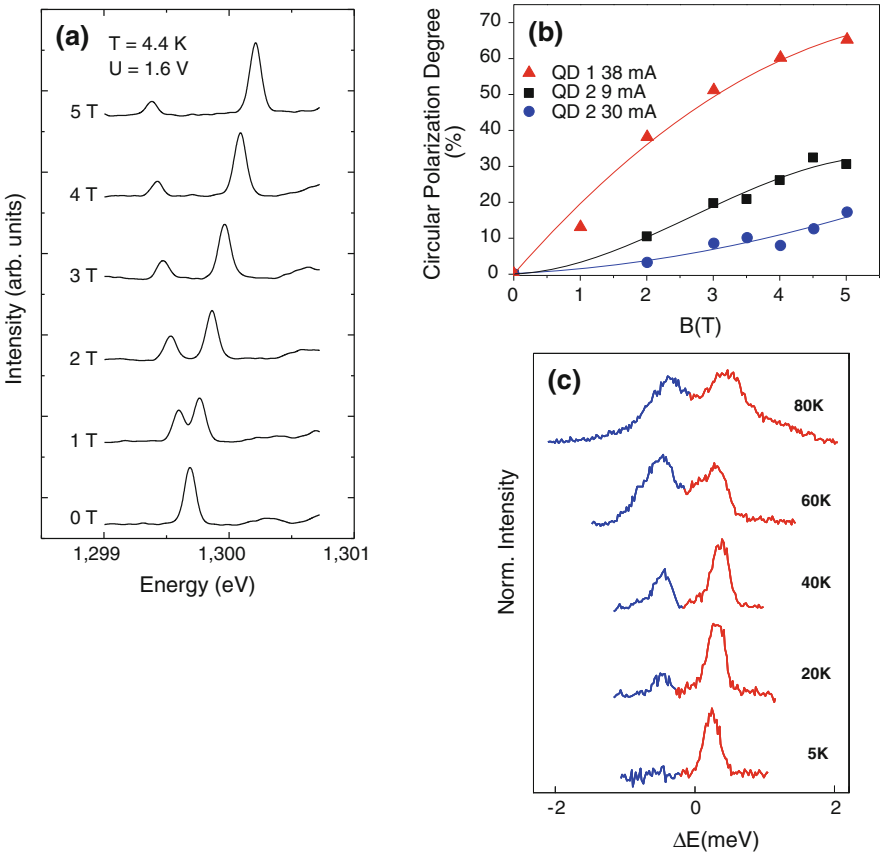

Fig. 9 **a** Electroluminescence of a SQD embedded in a p-i-n diode structure with a DMS spin aligner for different magnetic fields. **b** Circular polarization degree versus magnetic field for different SQDs and different current densities. **c** Temperature dependence of the SQD polarization

leaving the spin aligner. In addition, the local current flow might heat the sample thus reducing the spin alignment in the DMS.

The origin of the spin polarization in the DMS can be confirmed by performing a temperature dependent analysis of the CPD. The efficiency of the DMS as a spin reservoir is strongly dependent on temperature, because thermal disorder will destroy the spin alignment. In Fig. 9c, single quantum dot spectra at $B = 5\,\mathrm{T}$ are shown for temperatures between 4 K and 80 K. For clarity, the spectra are vertically shifted and the horizontal position is normalized to the center of the signal, therefore the typical Varshni shift of the bandgap with increasing T is not shown. This QD exhibits nearly 100 % spin polarization at 4 K. The polarization remains observable up to 40 K and quenches for higher temperatures, reflecting thus the typical DMS properties.

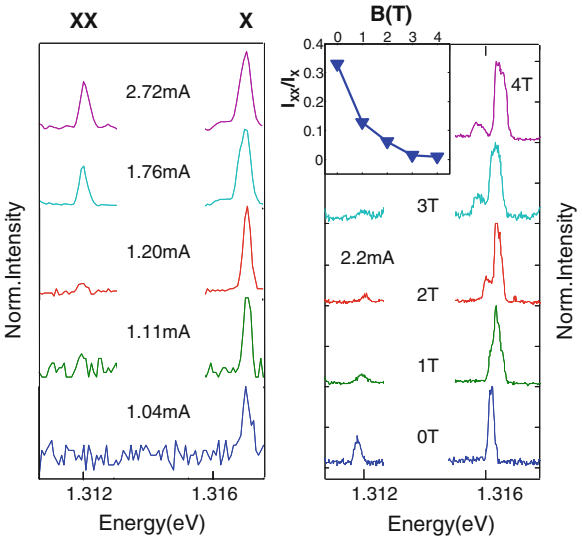

Fig. 10 Fingerprint of a biexciton. *Left*: Normalized EL-spectra of an exciton (X)—biexciton (XX) pair under different operation currents without external B-Field. *Right*: Normalized EL spectra of the same QD under different magnetic fields at constant current flow. The inset shows the ratio between the biexciton and the exciton emission as function of magnetic field

With increasing bias the number of charge carriers per quantum dot can be enhanced, leading to multi-exciton emission. In Fig. 10a, an exciton (X)–biexciton (XX) pair, separated by approximately 5 meV, is recorded for varying operation current in absence of an external magnetic field. Clearly, the biexciton emission increases non-linearly with increasing current. The biexciton emission XX reveals an atypical behavior in an external magnetic field: With increasing magnetic field, the XX line is strongly suppressed as compared to the single exciton emission X (Fig. 10b). The intensity ratio I_{XX}/I_X is plotted in the inset of Fig. 10b. For $B > 3\,\mathrm{T}$ the XX line is hardly detectable. This is a consequence of the injection of predominantly spin-down electrons with increasing magnetic field, whereas the formation of a biexciton requires two electrons with anti-parallel spins. Thus, the biexcitonic emission should be quenched with increasing magnetic field, in agreement with our measurements.

In order to gain insight into the dynamics of the spin injection, samples with a high frequency adaptation have been realized [37]: In close proximity to the nanoapertures selecting the individual QDs, bond pads consisting of a 200 nm thick Au layer with dimensions of approximately $100 \times 110\,\mu\mathrm{m}^2$ were deposited. By focused ion beam etching an area of approximately $115 \times 190\,\mu\mathrm{m}^2$ was separated from the remaining sample surface. A scanning electron microscopy image of the resulting sample surface is shown in Fig. 11a. A $50\,\Omega$ resistor was connected parallel to the sample for impedance matching, and the DC power source was replaced by a GHz pulse pattern generator. Measurements were performed at 4.7 K and an external magnetic field of 5 T. The pulse with an amplitude of 0.3 V switches between two states of the SQD

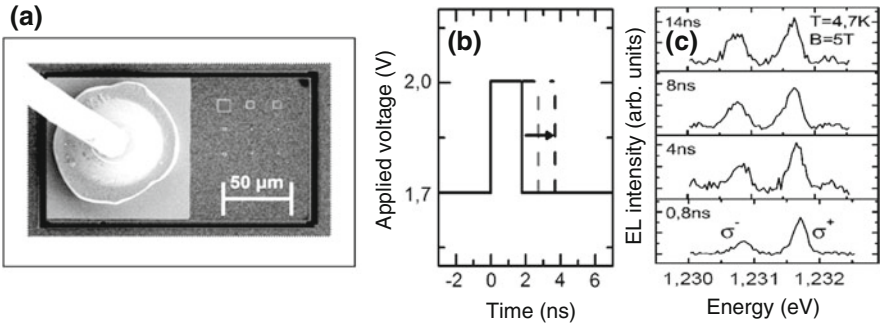

Fig. 11 High frequency adaptation of the device. **a** Scanning electron microscope image of the sample surface showing the bond wire (*left*), the apertures for optical access (*right*) and the focused ion beam etched trench. **b** Principle of device operation with variable pulse width. **c** EL emission spectra for different pulse widths

diode (see Fig. 11b): At 1.7 V, no EL emission is detected, while at the higher bias of 2 V, electroluminescence becomes visible. The pulse width was varied systematically between 800 ps and 14 ns. The resulting EL spectra are plotted in Fig. 11c. Even for sub-ns increasing pulse width, the CPD is reduced. As in addition a slight red shift of the EL signal is observed, we attribute the reduction of the CPD with increasing pulse width to current induced heating as the repetition rate of the pulse generator was hold constant and thus the duty cycle increased. It is interesting to note that time-dependent EL measurements with constant pulse width have shown a decrease of the CPD as well [38].

3.3 Tunnel Injection of Spin-Polarized Electrons into Single Quantum Dots

Because the drift/diffusion process seems to be generally less optimal for ultrafast spin injection, we will now concentrate on tunnel injection of spins. For that purpose, we study the coupling of a single quantum dot to a spin reservoir via tunneling in a charge-tunable device based on a p-i-n diode structure. These devices are intended for operation under reverse bias without current flow, as indicated in Fig. 8b. On a highly p-doped GaAs (100) substrate ($p = 1 \times 10^{19}\,\mathrm{cm}^{-3}$), an intrinsic GaAs layer with a thickness of 50 nm was deposited followed by 50 nm of intrinsic AlGaAs, which acts as a current blocking layer. This layer is followed by an intrinsic 160 nm thick GaAs layer, on top of which self-assembled quantum dots were formed by depositing 1.7 ML InAs. The quantum dots were capped by a thin tunnel barrier of 20 nm i-GaAs. On the latter layer 200 nm n-doped GaAs ($n = 3 \times 10^{18}\,\mathrm{cm}^{-3}$) were grown. Electrical contact to the sample was achieved by depositing 60 nm Cr and 10 nm Au on top of the heterostructure. Again, nanoapertures provide optical

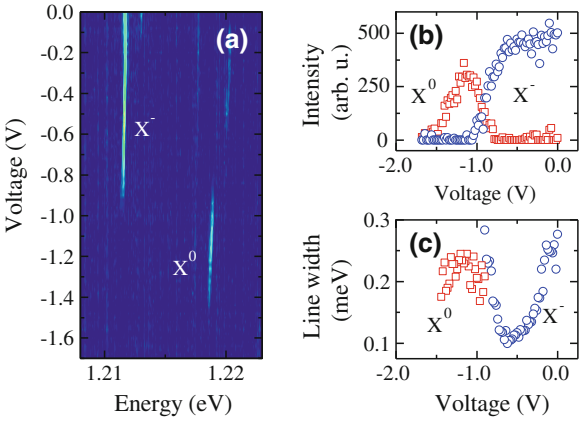

Fig. 12 **a** Contour plot of the PL spectra under dc biasing and pulsed laser excitation. **b** Spectrally integrated emission intensities of the neutral (X^0) and the charged exciton (X^-) versus dc voltage. **c** Bias-dependent line widths of the two emission lines

access to single quantum dots and the samples were prepared by FIB etching for high-frequency operation as described before.

The tunnel coupling of a single quantum dot to an electron reservoir can be used to charge the single quantum dot with a controlled number of electrons from the reservoir via an external bias voltage (Refs. [39–41]). This general operation principle is shown in Fig. 8b. By the application of an external voltage, the quantum dot's energy levels can be shifted with respect to the Fermi level, so that tunneling of electrons from the reservoir into the quantum dot can occur, as soon as an empty quantum dot state crosses the Fermi level. Applying an external magnetic field, the spin degeneracy is lifted and thus, the n-GaAs layer can act as a spin reservoir. We chose a thin tunnel barrier of only 20 nm to achieve a strong tunnel coupling of the reservoir with the quantum dot [40].

The sample was cooled down to a temperature of ∼4.3 K in a continuous flow cryostat and excited through the nanoapertures with a pulsed laser beam ($\lambda = 640$ nm, $f_{\mathrm{rep}} = 80$ MHz), focused with a 100 × microscope objective to a diameter of ∼1 μm. The resulting photoluminescence spectra vs. the applied bias voltage are shown as a contour plot in Fig. 12a. A very similar pattern as shown in Refs. [39, 40, 42] is obtained. Starting at ~ -1.45 V, the emission of a neutral exciton (X^0) is observed. At voltages above ~ -0.9 V, the emission energy switches to a ∼7 meV lower value, which indicates the emission of a single negatively charged exciton (X^-). The spectrally integrated emission intensities of both emission lines are shown in Fig. 12b versus voltage. The observed rather abrupt change between the two emission lines is an indication of a high tunneling probability of electrons from the n-contact into the quantum dot [40]. The line widths of the two emission lines are shown in Fig. 12c. As can be seen, the neutral exciton shows a line width of ∼0.2 meV over the respective voltage range, which is increased as compared to the X^- line width.

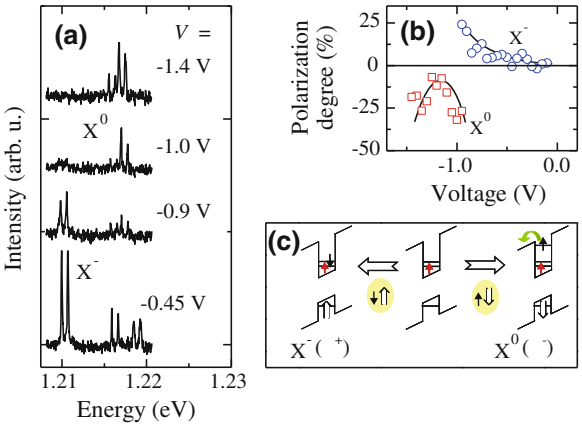

Fig. 13 **a** Photoluminescence spectra recorded in a magnetic field of 5 T for four different dc bias voltages. **b** Bias-dependent circular polarization degree CPD of the two emission lines. The solid lines are guides to the eye. **c** Scheme of the polarized emission of the charged/uncharged exciton in the regime of coexisting X^0 and X^- emission (Details see text)

We attribute this increase to the fine structure splitting of the neutral exciton [43], which is absent in the trion. The line width of the charged exciton shows a very characteristic behavior depending on the applied voltage. At a voltage of ~ -0.9 V, at the change of the emission from X^0 to X^-, it is increased to $\sim$0.25 meV. With rising voltage the line width drops down to $\sim$0.1 meV (limited by the spectral resolution of the optical system) at a voltage of approximately -0.6 V. After this minimum an increase to $\sim$0.25 meV can be observed again at ~ -0.2 V. The enhanced line width is a direct consequence of the fast resonant tunneling exchange of electrons between the quantum dot and the electron reservoir in the n-contact. At ~ -0.9 V, the quantum dot's X^- level is in resonance with the Fermi level, while at ~ -0.2 V the next charging resonance of the quantum dot occurs. Here, the p-level of conduction band of the SQD crosses the Fermi level, again leading to a tunnel exchange between the quantum dot and the reservoir.

In order to create a spin-polarized electron reservoir, we apply a magnetic field of 5 T in Faraday geometry. At low temperatures, the electrons in the reservoir become efficiently spin-polarized, so that charging of the quantum dot with electrons with a defined spin orientation via tunneling becomes possible.

Figure 13a shows photoluminescence spectra of the quantum dot at four representative voltages. The laser was linearly polarized in order to avoid any impact of the light polarization on the observed photoluminescence. The emission of the neutral exciton shows a clear polarization with the intensity of the σ^- line being larger than the intensity of the σ^+ one. The charged exciton reveals a polarized emission at -0.9 V with opposite sign, while at higher voltages both emission lines show the same intensity. The resulting voltage-dependent circular polarization degree (CPD) values are summarized in Fig. 13b. The solid lines are guides to the eye.

Both emission lines show a very characteristic dependence on the applied voltage. At low voltages, the neutral exciton emission shows a polarization of up to $|\mathrm{CPD}| > 30\,\%$, decreasing down to $|\mathrm{CPD}| < 10\,\%$ at $-1.2\,\mathrm{V}$. This behavior can be explained in terms of a co-tunneling process as described in Ref. [44]. At the low voltage edge of the emission plateau, the optically excited electron can leave the quantum dot via tunneling, leaving the quantum dot occupied by a single hole. An electron from the n-contact can now tunnel into the dot and recombine with the stored hole. As the electrons in the n-contact have a preferred spin-orientation, the resulting photoluminescence becomes polarized. With increasing voltage, this process is suppressed, leading to the observed decrease of the polarization degree. Further increasing the voltage leads to an increase of the polarization degree again. In this voltage regime again a co-tunneling process can lead to a polarization of the photoluminescence.

The polarization of the charged exciton emission has two different origins. It was shown in Ref. [45], that there exists a small voltage range, where an optically created X^0 can drag an additional electron into the dot in order to form the energetically lower X^- state. Assume that the electron reservoir is predominantly occupied with spin-up electrons. Due to the linear polarized excitation the probabilities to create an exciton with a total spin of $+1$ (e.g. spin-down electron and spin-up heavy hole) or -1 (e.g. spin-up electron and spin-down heavy hole) are equal. In case of optical excitation of a spin-down electron, an additional electron from the n-contact can tunnel into the quantum dot, forming the X^- state. The resulting photoluminescence will be σ^+ polarized. In the opposite case, when a spin-up electron is optically excited, tunneling from the n-contact into the s-state of the conduction band in the quantum dot is prohibited due to Pauli-blocking, so that recombination of the X^0 state with σ^- polarization will be recorded. This is exactly what is seen in the experiment.

Another process leading to a polarized emission of the charged exciton, based on the explanations given in Refs. [32, 40], is displayed in Fig. 13c. At higher voltages the quantum dot is occupied with an electron before optical excitation. Again, this electron is assumed to be in the spin-up state as it stems from the n-GaAs spin reservoir. As mentioned above, linear excitation can either lead to the creation of an electron hole pair with the electron spin-down and the hole spin-up (left part of Fig. 6c) or vice versa (right part). In the first case, the singlet X^- state is formed and recombination occurs under σ^+ polarization. In the second case, the optically excited electron can only occupy the quantum dot's p-level and will leave the quantum dot via tunneling. In this case, σ^- polarized photoluminescence of the X^0 state will be recorded. Further increasing the voltage will effectively decrease the tunneling time of electrons with suitable spin orientation from the reservoir into the quantum dot, so that the X^- state is formed, regardless of the spin orientation of the optically excited exciton, Hence, the polarization degree decreases and finally approaches zero.

In order to only probe the polarization of the injected electron we performed the following measurement, based on a technique introduced in Ref. [45]. As explained in the section before, the sample layout was designed for the application of high frequency voltage pulses. With this approach, charging and discharging of the SQD is possible within the sub-nanosecond range [37]. We used a 3.35 GHz pulse pattern

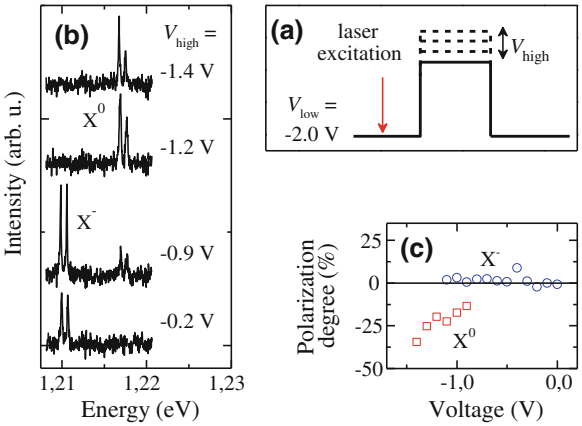

Fig. 14 **a** Technique for the preparation of a single hole and subsequent charging with electrons from the n-contact. **b** Luminescence spectra after optical preparation of a single hole and subsequent charging for four different charging voltages in a magnetic field of 5 T. **c** The resulting circular polarization degree for the two emission lines

generator to apply voltage pulses with a frequency of 80 MHz and rise times of ∼100 ps to the sample. The low level of the pulses was set to −2.0 V and the high level was varied. The laser excitation was triggered by the generator and set to take place in the center of the low level plateau, i.e. ∼3.1 ns before the change to the high level, as shown schematically in Fig. 14a. Optical excitation at such low voltages leads to the following scenario: due to the high electric field, the optically excited electron will leave the quantum dot via tunneling before radiative decay. Due to its higher effective mass, the tunneling time of the hole is significantly larger. This way, a single hole can be trapped within the quantum dot for several microseconds. Again, the laser was linearly polarized so that statistically every second hole captured within the quantum dot is in the spin-up or spin-down state, respectively. By the application of a time-delayed voltage pulse, an electron from the reservoir can be injected into the quantum dot and the polarization of the resulting luminescence is a direct measure of the spin-polarization in the reservoir.

Figure 14b shows the resulting luminescence for four different high voltage levels of the charging pulse. As can be seen, the neutral exciton emission shows a pronounced polarization, while the charged exciton emission is unpolarized. The circular polarization degree versus the high voltage level is displayed in Fig. 14c. The neutral exciton shows a polarized luminescence of up to $|\mathrm{CPD}| > 35\,\%$. As explained above, this reflects the spin-polarization of the adjacent electron reservoir. We attribute the observed decrease of the polarization degree at higher charging voltages to polarization losses during non-resonant spin injection. The charged exciton does not reveal any polarization throughout the complete voltage range. Here, two electrons from the n-contact tunnel into the quantum dot, one of which has to be in the spin-up and the other one in the spin-down state in order to form the singlet trion state. Due to

the two possible spin orientations of the optically prepared hole, both recombination paths become possible, so that the polarization degree is expected to be zero.

The two approaches presented here show well the pros and cons of different spin sources for spin injection into single quantum dots. While the drift/diffusion process seems to be a fairly robust concept for high spin polarization degrees in electroluminescence, there are limitations in a controlled ultrafast spin injection on the ns scale and a strong dependence on the current flow. In contrast, tunnel injection has the advantage of surprisingly high spin polarization degrees even on ns time scales although the spin polarization in the reservoir is only caused by the Zeeman splitting in the n-GaAs contact. On the other hand, an optical probing is necessary to extract the spin information from the single quantum dot. In principle, both concepts can be applied for hybrid devices consisting of single quantum dots coupled to any spin reservoir, in particular ferromagnetic leads.

4 Spin Excitations in Transport Through Quantum Dots

Spintronics extends the ideas of conventional electronics by making the electron's spin degree of freedom available for device functionalities. The extra handle introduced by the spin opens a huge variety of new routes towards controlled manipulation of nano-structured devices. A very important, and probably the most fundamental, novel aspect as compared to charge electronics is the possibility to generate a finite non-equilibrium spin polarization in semiconductors. For spatially confined regions such as quantum dots the number of participating electrons establishing the finite spin polarization can be small and may ultimately go down to one.

The problem of injecting spin into quantum dots in metal-semiconductor hybrids is a highly nontrivial issue but experimental success in that direction is growing, as described in this book chapter. In contrast to an optical generation of a finite spin polarization via the transfer of angular momentum from circularly polarized light to the electronic system, spin injection relies on the coupling to a reservoir of spin-polarized electrons. The latter may be provided by electrodes made of ferromagnetic metals or diluted magnetic semiconductors.

Intimately related to the issue of spin accumulation is the question of how long a finite spin polarization in the quantum dot survives before it relaxes. Spin accumulation and relaxation are the minimal ingredients that need to be taken into account in the description of the spintronics devices presented in this book chapter. This statement holds true irrespective of how the injected spin is detected. For spin injection into spin LEDs the most natural way is the optical detection of circularly polarized photons emitted from the spin-polarized electrons. This route is followed in the experiments presented in this chapter. Alternatively, spin accumulation in quantum dots contacted to source and drain electrodes may be probed by analyzing the electric current through the dot. In that case, considered in the present section of this book chapter, the coupling of the electronic degrees of freedom to the electro-magnetic field can be disregarded.

Another novel aspect, beyond spin accumulation and detection, introduced by the spin degree of freedom is spin dynamics. The latter may be invoked due to coupling of the quantum-dot spin to external magnetic and/or internal exchange fields. The minimal model exhibiting the physics of spin accumulation, relaxation and precession is a single-level quantum dot tunnel coupled to ferromagnetic electrodes with, in general, non-collinear magnetization directions. This so-called quantum-dot spin valve is described in the following section.

While the dynamics of the accumulated spin already introduces an interesting and non-trivial aspect that may be exploited in spintronics devices, the realm of possible extensions is seemingly infinite. What we will concentrate on in this section of the book chapter is the idea to couple the accumulated spins to additional spin degrees of freedom. We discuss two specific examples. First, we consider a model in which we allow for collective spin excitations, magnons, in the ferromagnetic electrodes. Electrons tunneling into or out of the dot can interact with excitations of the collective magnetic moment of the electrodes. As a consequence, additional transport channels that are mediated by the emission or absorption of magnons become possible. One can even drive, in the absence of a bias voltage, a finite charge current by different temperatures of the magnon reservoirs of source and drain electrode. Second, we will analyze a situation in which the additional spin degrees of freedom are provided by the internal magnetic structure of the quantum dot itself.

4.1 Quantum-Dot Spin Valve

A quantum-dot spin valve consists of a single-level quantum dot tunnel coupled to two ferromagnetic electrodes with magnetizations pointing in arbitrary directions $\mathbf{n}_{\mathrm{L}}$ and $\mathbf{n}_{\mathrm{R}}$. Its Hamiltonian consists of three parts, describing the electrodes, the quantum dot and their tunnel coupling,

$$H = \sum_r H_r + H_{\mathrm{dot}} + H_{\mathrm{tun}}. \tag{8}$$

The first term,

$$H_r = \sum_{\mathbf{k}\sigma} \varepsilon_{r\mathbf{k}\sigma} a^{\dagger}_{r\mathbf{k}\sigma} a_{r\mathbf{k}\sigma}, \tag{9}$$

describes the two ferromagnetic electrodes in terms of noninteracting electrons at chemical potential μ_r with spin quantized along the magnetization direction. Ferromagnetism is incorporated into the model by considering a spin-dependent density of states $\rho_{r\sigma}$ ($\sigma = +$ for majority and $\sigma = -$ for minority spins). In the following, we assume $\rho_{r\sigma}$ to be independent of energy. The density of states is related to the polarization via $p_r = (\rho_{r+} - \rho_{r-})/(\rho_{r+} + \rho_{r-})$ such that $p_r = 0$ corresponds to a normal metal and $p_r = 1$ to a half-metallic ferromagnet that contains only majority spins.

The quantum dot is described by

$$H_{\rm dot} = \sum_{\sigma} \varepsilon c_{\sigma}^{\dagger} c_{\sigma} + U c_{\uparrow}^{\dagger} c_{\uparrow} c_{\downarrow}^{\dagger} c_{\downarrow} \tag{10}$$

as a single level with spin-degenerate energy ε which experimentally can be tuned by a gate voltage. The Coulomb energy U is needed to doubly occupy the quantum dot. For simplicity, we choose the dot quantization axis along $\mathbf{n}_{\rm L} \times \mathbf{n}_{\rm R}$.

The tunnel Hamiltonian is given by

$$H_{\rm tun} = \sum_{r\mathbf{k}} \frac{t_r}{\sqrt{2}} \left[a_{r\mathbf{k}+}^{\dagger} \left(e^{{\rm i}\phi_r/2} c_{\uparrow} + e^{-{\rm i}\phi_r/2} c_{\downarrow} \right) + a_{r\mathbf{k}-}^{\dagger} \left(-e^{{\rm i}\phi_r/2} c_{\uparrow} + e^{-{\rm i}\phi_r/2} c_{\downarrow} \right) \right] + {\rm H.c.} \tag{11}$$

It couples majority (minority) spin electrons to both, spin up and spin down electrons on the dot due to the noncollinear geometry. The tunnel matrix elements t_r are related to the tunnel coupling strengths by $\Gamma_{r\sigma} = 2\pi |t_r|^2 \rho_{r\sigma}$. The dot-electrode coupling gives rise to a finite level width $\Gamma_r = \sum_{\sigma} \Gamma_{r\sigma}/2$.

To calculate the transport properties of a quantum-dot spin valve taking into account the Coulomb interaction on the dot exactly, we make use of a real-time diagrammatic approach [46, 47] adapted to systems with noncollinearly magnetized electrodes [48]. The main idea of this approach is to split the system into the non-interacting electrodes with many degrees of freedom and the quantum dot with a few, strongly interacting degrees of freedom. The former are then integrated out. The remaining system is described in terms of its reduced density matrix. The time evolution of the reduced density matrix is governed by a generalized master equation. The generalized transition rates that enter the master equation can be obtained diagrammatically as irreducible self-energy blocks of the dot propagator on the Keldysh contour in an perturbative expansion in the tunnel coupling strength.

For the quantum-dot spin valve, we can split the generalized master equation into one set that determines the probabilities $\mathbf{P} = (P_0, P_1, P_2)$ to find the dot empty, singly or doubly occupied. It takes the form

$$\frac{\rm d}{{\rm d}t} \mathbf{P} = \sum_{r} \mathbf{W}_r \mathbf{P} + \sum_{r} \mathbf{V}_r \left(\mathbf{S} \cdot \mathbf{n}_r \right). \tag{12}$$

The first term on the right-hand side describes transition between the different occupations due to electrons tunneling in and out of the dot. The second term describes a coupling of the occupations to the average spin on the dot projected onto the magnetizations of the electrodes and vanishes for vanishing polarizations $p_r = 0$. The second set of master equations describes the time evolution of the average dot spin. It takes the form of a Bloch equation,

$$\frac{\mathrm{d}\mathbf{S}}{\mathrm{d}t} = \left(\frac{\mathrm{d}\mathbf{S}}{\mathrm{d}t}\right)_{\mathrm{acc}} + \left(\frac{\mathrm{d}\mathbf{S}}{\mathrm{d}t}\right)_{\mathrm{rel}} + \left(\frac{\mathrm{d}\mathbf{S}}{\mathrm{d}t}\right)_{\mathrm{prec}} . \tag{13}$$

The first term on the right-hand side describes the accumulation of spin on the dot due to spin-dependent tunneling of electrons onto (off) the dot. The second term similarly describes a relaxation of the dot spin. Finally, the last term characterizes the precession of the dot spin in an energy-dependent exchange field that is generated by virtual tunneling processes between dot and leads. The interplay between spin accumulation and spin precession gives rise to a number of characteristic fingerprints in the transport properties that have been discussed in the literature [48–56].

4.2 Magnon-Assisted Transport

So far, we only discussed idealized quantum dot spin valves. In real devices, there will be additional spin degrees of freedom present as, e.g., spin waves in the electrodes [57], magnetic impurities embedded in the tunnel barriers or on the quantum dot [56] or quantum dots with more complex internal structure [58]. In the following, we discuss the influence of magnons that are excited in the leads by the tunneling electrons.

In order to model the spin wave degrees of freedom, we assume that each electrode contains one macroscopically large, localized spin that can be identified with the magnetization of the respective electrode. As the localized spin will point preferably into the magnetization direction, it is convenient to describe it in terms of Holstein-Primakoff bosons. Here, the spin operators are mapped onto bosonic operators. In the limit of large spins, this mapping takes a particular simple form: changing S_z by $\pm\hbar$ corresponds to the annihilation/creation of one boson. This leads to a particularly simple description of the localized spin in terms of noninteracting bosons, $H_{\mathrm{spin}} = \sum_r \omega_B b_r^\dagger b_r$. For simplicity, we assume an optical magnon mode with a momentum independent energy ω_B (Fig. 15).

The localized spin is coupled to the rest of system via an exchange interaction with the spins of the itinerant electrons in the leads. In terms of the bosonic degrees of freedom, this gives rise to an interaction between the magnons and electrons. As our real-time diagrammatic approach requires noninteracting lead electrons, we have to remove this interaction via a canonical transformation. The latter resembles a Lang-Firsov transformation that eliminates an electron-phonon coupling [59] but is slightly more complicated due to the spin degree of freedom involved in the problem. In particular, it can be performed only perturbatively in the electron-magnon coupling λ. After performing the canonical transformation, we obtain the Hamiltonian of the original quantum-dot spin valve as discussed above but with a modified tunneling part. In addition to ordinary tunneling events that conserve the spin of the tunneling electrons, we now have additional processes which flip the spin

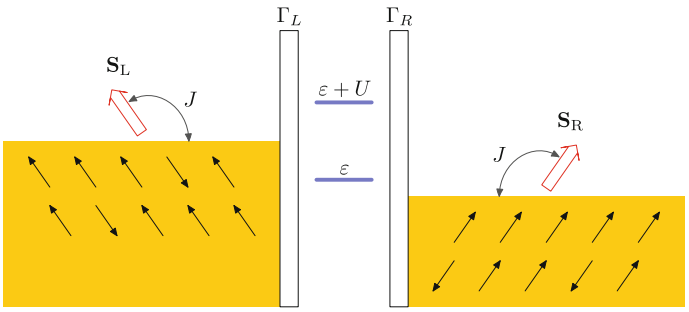

Fig. 15 Schematic model of a quantum-dot spin valve. Each electrode contains a large localized spin (*red arrow*) that couples via an exchange interaction J to the spins of the itinerant electrons (*black arrows*) (from Ref. [57])

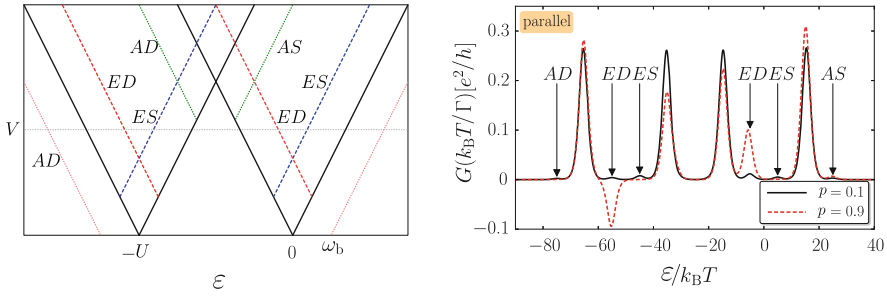

Fig. 16 *Left panel*: Schematic of the differential conductance as a function of bias voltage V and level position ε. The labels indicate whether a sideband is due to the emission (E) or absorption (A) of magnons in the source (S) or drain (D) lead. *Right panel*: Differential conductance for parallel magnetizations as a function of level position. Parameters are $V = 30\,k_\mathrm{B}T$, $U = 50\,k_\mathrm{B}T$, $\omega_B = 10\,k_\mathrm{B}T$, $\Gamma_\mathrm{L} = \Gamma_\mathrm{R}$, $\tau = 2/\Gamma$, $\lambda = 0.3$ and $T_B = 5T$ (from Ref. [57])

of the tunneling electron and at the same time emit or absorb a magnon in order to conserve the total angular momentum.

In order to make our model more realistic, we add a phenomenological relaxation term with relaxation time τ to the master equation that drives the magnon distribution in each lead towards its equilibrium distribution characterized by a temperature T_B (which we allow to differ from the electron temperature T). Apart from making the model more realistic, the relaxation also serves to prevent a runaway of the magnon number in the drain lead that would occur otherwise.

We now turn to the results, focusing first on the influence of magnons on the differential conductance. In Fig. 16, we show a schematic plot of the differential conductance as a function of level position and bias voltage. In addition to the standard conductance peaks (black lines) that indicate the onset of transport through the quantum dot, there are now sidebands associated with the emission and absorption of magnons in either the source or drain electrode. This is similar to the case of a quantum dot coupled to a phononic degree of freedom [59]. The main difference

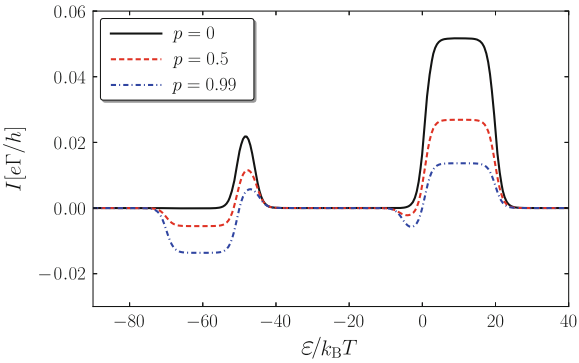

Fig. 17 Magnon-driven current at zero bias as a function of level position for $U = 50\,k_\mathrm{B}T$, $\omega_B = 20\,k_\mathrm{B}T$, $\Gamma_\mathrm{L} = \Gamma_\mathrm{R}$, $\tau = 1/\Gamma$, $\lambda = 1/3$ and $T_B = 10T$ (from Ref. [57])

is that due to the conservation of angular momentum at most one magnon can be emitted/absorbed in a tunneling process while the number of phonons is only limited by the applied bias voltage/the number of excited phonons.

The strength of the different sidebands depends on the polarization of the electrodes as well as on the magnetic configuration of the system. The most interesting effect occurs for large polarizations and parallel magnetizations when transport takes place through the singly and doubly occupied dot, cf. Fig. 16. If the dot is doubly occupied, a spin down electron can leave the dot by emitting a magnon. As the electron ends up in a spin up state, this process has a rather large probability to occur. It leaves the dot in a state with spin up. Hence, no second spin up electron can enter the dot, while tunneling of spin down electrons is suppressed by the large polarization. Thus, transport through the dot is blocked and a sideband of negative differential conductance appears.

So far, we discussed transport driven by an external bias voltage. However, if the magnon temperature is different from the electron temperature (this might be realized, e.g., by irradiating the ferromagnetic electrodes with microwaves), the system can also show a current without an applied bias. In order to obtain these magnon-driven currents, we need to break the left-right symmetry of the system. The easiest way to do this is by considering a setup where one electrode is ferromagnetic, while the other is an ordinary metal.

As shown in Fig. 17, we find a finite current at zero bias voltage driven by the temperature difference between electrons and magnons. The direction of the current depends on the level position. Its value depends on the polarization. Let us for the moment assume the dot level is above the Fermi level of the leads. A magnon is absorbed in the ferromagnet which gives the tunneling electron enough energy to reach the dot level which is out of reach energetically in the absence of magnons. The electron can then either tunnel back into the ferromagnet or leave the dot into the normal metal. Thus, we find a net current from the ferromagnet into the normal metal. Similar, if the dot level is deep below the Fermi level, a net current flows from the normal metal into the ferromagnet.

For the system at hands, the charge and magnon currents are proportional to each other as electrons can only enter the dot by absorbing a magnon. In the limit of a fully polarized ferromagnet, we find that one elementary charge is transferred for each magnon absorbed from the ferromagnet. This is known as the strong coupling limit in the thermoelectric literature and a necessary requirement for the device to reach Carnot efficiency in converting heat into useful work [60–62].

4.3 Spin-Inelastic Tunnel Spectroscopy

So far we discussed transport through a single-level quantum dot coupled to ferromagnetic electrodes. Our focus was on the influence of additional spin excitations in the electrodes. We now turn to transport through single magnetic atoms coupled to nonmagnetic electrodes. Here, the additional spin degrees of freedom that can be excited in transport are given by the complicated internal structure of the quantum dot formed by the atom.

The work discussed here has been motivated by a series of experiments where single magnetic atoms have been contacted with the tip of a scanning tunneling microscope [63–69]. The experimentally observed steps in the differential conductance could be explained by modeling the atom as a localized spin [66]. While the step position is determined by the excitation energies of the spin, the step heights are related to certain spin matrix elements. Later theoretical works [70–74] provided a more complete description of the experiments using perturbation theory in the tunnel coupling assuming equilibrium occupation of the spin states. Certain nonmonotonic features clearly visible in the experimental results of Ref. [66] remained, however, unexplained so far. In the following we demonstrate that they can be understood as a consequence of nonequilibrium spin occupations.

To this end, we model the experimental setup as a localized spin embedded in a tunnel barrier described by a Hamiltonian of the form $H = \sum_r H_r + H_{\text{spin}} + H_{\text{tun}}$. Here, H_r describes the nonmagnetic electrodes in terms of noninteracting electrons, i.e., it takes the same form as Eq. (9) above with $p_r = 0$. The magnetic atom is described by the spin Hamiltonian

$$H_{\text{spin}} = -DS_z^2 + E(S_x^2 - S_y^2) + g\mu_{\text{B}}\mathbf{B}\cdot\mathbf{S} \tag{14}$$

Here, the first term describes a uniaxial anisotropy. The second term characterizes the easy-plane anisotropy while the last term describes the coupling to an external magnetic field. In Ref. [66], the external field could point in arbitrary directions and take values up to 7 T. The parameters in the spin Hamiltonian extracted from the experiment for an Fe atom are $S = 2$, $D = 1.55\,\text{meV}$, $E = 0.31\,\text{meV}$ and $g = 2.11$.

The tunnel Hamiltonian describes an exchange interaction between the spin of the tunneling electron and the atom spin. It takes the form

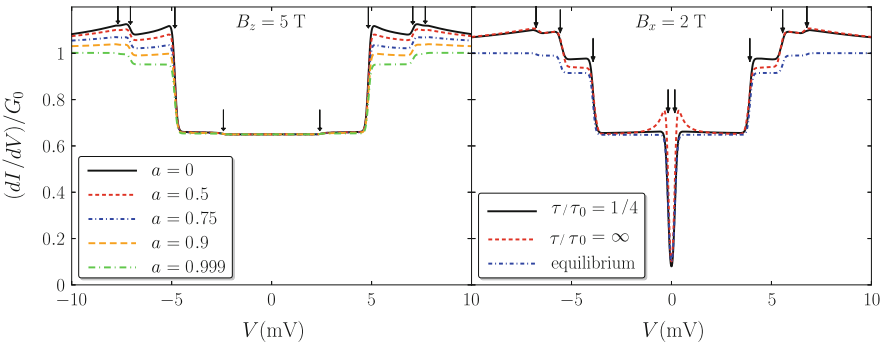

Fig. 18 Differential conductance in units of $G_0 = 4\pi e^2 S(S+1)|j_{\mathrm{LR}}|^2 \rho_{\mathrm{L}} \rho_{\mathrm{R}}$ as a function of bias voltage for $B_z = 5$ T (*left panel*) and $B_x = 2$ T (*right panel*)

$$H_{\mathrm{tun}} = \sum_{rr'\mathbf{k}\mathbf{k}'\sigma\sigma'} j_{rr'} a^{\dagger}_{r\mathbf{k}\sigma} \frac{\boldsymbol{\sigma}_{\sigma\sigma'} \cdot \mathbf{S}}{2} a_{r'\mathbf{k}'\sigma'}, \tag{15}$$

where $\boldsymbol{\sigma}$ denotes the Pauli matrix. We did not include direct tunneling into H_{tun} as it only gives rise to a constant background conductance (interference between direct and exchange tunneling can occur only for magnetic contacts or higher order tunneling processes). The processes described by j_{LR} and j_{RL} are responsible for the current flow though the atom and drive it out of equilibrium while the processes described by j_{LL} and j_{RR} do not contribute to the current but provide an intrinsic relaxation channel for the atom spin. We parametrize the couplings by the total coupling $J = j_{\mathrm{LL}} + j_{\mathrm{RR}}$ and the asymmetry $a = (j_{\mathrm{LL}} - j_{\mathrm{RR}})/J$ such that $j^2_{\mathrm{LL}} = (1+a)^2 J^2/4$, $j^2_{\mathrm{RR}} = (1-a)^2 J^2/4$ and $j^2_{\mathrm{LR}} = j^2_{\mathrm{RL}} = (1-a^2) J^2/4$.

Using a standard rate-equation approach we then obtain the current flowing through the atom taking into account nonequilibrium occupation of the spin states. The resulting differential conductance is shown in Fig. 18. For large asymmetries, $a \to 1$, we recover the equilibrium results with conductance steps followed by flat pleateaus. This results from the coupling to one electrode being very strong such that the atom is effectively brought to equilibrium after each current-carrying tunneling event. For smaller values of a, nonequilibrium effects become important. Now, the conductance overshoots at each step and subsequently decays in a powerlaw fashion towards the equilibrium conductance. Experimentally, the asymmetry a can be varied easily. While the adatom-substrate coupling is fixed in experiment, the adatom-tip coupling can easily be changed by changing the distance between the tip and the adatom. Recent experiments [69] with ferromagnetic STM tips confirmed that non-equilibrium effects become indeed more pronounced upon reducing the tip-sample distance.

In order to understand the physical origin of the overshooting, let us for the moment discuss a simple model system consisting of a spin 1/2 with Zeeman energy B embedded in the tunnel barrier at zero temperature. Transport can take place via

spin-conserving and spin-flip tunneling processes. The former contribute to the current according to

$$I_{\rm sc} = \pi e |j_{\rm LR}|^2 \rho_{\rm L} \rho_{\rm R} eV, \tag{16}$$

and, hence, to the differential conductance as $G = G_0/3$ where $G_0 = 4\pi e^2 S(S+1)|j_{\rm LR}|^2 \rho_{\rm L}\rho_{\rm R}$ is the conductance at infinite bias. As this contribution is independent of the spin occupations $P_\uparrow$ and $P_\downarrow$, nonequilibrium effects are only probed by spin-flip processes. Their contribution to the current is given by

$$I_{\rm sf} = 2\pi e |j_{\rm LR}|^2 \rho_{\rm L}\rho_{\rm R} \left[(eV - B)P_\uparrow + (eV + B)P_\downarrow\right]. \tag{17}$$

In equilibrium, we have $P_\uparrow = 1$ and $P_\downarrow = 0$. Therefore, only the first term contributes to the current and the associated differential conductance is given by $G = 2/3G_0$ which is constant. In a nonequilibrium situation, the solution of the master equation yields $P_\uparrow = 1 - P_\downarrow = 1 - (eV - B)/[2(eV + B)]$ for voltages above threshold. Hence, now both terms in the expression for the spin-flip current contribute. The total differential conductance above threshold is now given by

$$G = \frac{2}{3} G_0 \left(1 + \frac{2B^2}{(eV + B)^2}\right). \tag{18}$$

We, therefore, find an overshooting above the equilibrium value at threshold, followed by a subsequent powerlaw decay for large bias voltages as for $V \to \infty$ we have $P_\uparrow = P_\downarrow = 1/2$. The interplay between different current contributions from exciting and deexciting the spin and bias-dependent occupation probabilities thus gives rise to the overshooting at threshold. A similar effect is known from cotunneling through a quantum dot [75]. We emphasize that nonequilibrium features in the conductance are an overshooting, i.e., an increase of the conductance above the equilibrium value and not a signature of excited states carrying less current as speculated in Ref. [74]. Finally, we note that the nonequilibrium occupations also give rise to a super-Poissonian noise [58].

While our theory predicts an overshooting at each steps, experimentally it was observed that the first conductance step does not exhibit an overshooting when it is pronounced as for the case of a magnetic field along the x axis. This suggests the presence of a relaxation mechanism that only depopulates the first excited state $|1\rangle$ but does not affect the higher excited states. We find that the matrix element of S_z between the ground states $|0\rangle$ and $|1\rangle$ is large compared to the matrix elements of S_x and S_y as well as to matrix elements of $|0\rangle$ with other excited states. This suggests adding a phenomenological, spin-dependent relaxation term of the form

$$W^{\rm rel}_{mm'} = -|\langle m|S_z|m'\rangle|^2 \Theta(\Delta_{mm'})/\tau \tag{19}$$

to the master equation where $\Theta(x)$ is the step function and $\Delta_{mm'}$ the energy difference between states m and m'. For infinite relaxation time, $\tau \to \infty$, we obtain the nonequilibrium result with prominent overshootings at the first step. For $\tau \to 0$, we

similarly recover the equilibrium case without any overshooting. For suitably chosen finite relaxation times τ, we find, however, that the anisotropic relaxation can indeed remove the overshooting of the first step while leaving the nonequilibrium effects at the other steps basically unaffected, cf. Fig. 18.

Acknowledgments All authors gratefully acknowledge the fruitful cooperation under the direction of Hartmut Zabel within the SFB491 and the financial support via the DFG. We appreciated the collaboration with Ellen Schuster, Frank Stromberg, Heiko Wende and Werner Keune from the Universität Duisburg-Essen for fruitful discussions and regarding the growth of the ferromagnetic metal structures with perpendicular anisotropy, Dirk Reuter for his expert help in MBE, Astrid Ludwig, Nicole Stracke and Nadine Viteritti for expert sample preparation. We gratefully acknowledge the expert experimental assistance of Jie Huang and Sven Eliasson. We acknowledge financial support by the RUB Research School, the DFH/UFA DFDK-05-06, the SPP 1285, and the BMBF QuaHL-Rep 01BQ1035.

References

1. B. Schumacher, Phys. Rev. A **51**(4), 2738 (1995)
2. J. Fabian, S. Das Sarma, Rev. Mod. Phys. **76**(2), 323 (2004)
3. S. Hövel, N.C. Gerhardt, M.R. Hofmann, F.Y. Lo, D. Reuter, A.D. Wieck, E. Schuster, H. Wende, W. Keune, Physica Status Solidi (C) **6**(2), 436 (2009)
4. E. Schuster, R.A. Brand, F. Stromberg, F.Y. Lo, A. Ludwig, D. Reuter, A.D. Wieck, S. Hövel, N.C. Gerhardt, M.R. Hofmann, H. Wende, W. Keune, J. Appl. Phys. **108**(6), 063902 (2010)
5. H. Zhu, M. Ramsteiner, H. Kostial, M. Wassermeier, H.P. Schönherr, K. Ploog, Phys. Rev. Lett. **87**(1), 1 (2001)
6. A.T. Hanbicki, B.T. Jonker, G. Itskos, G. Kioseoglou, A. Petrou, Appl. Phys. Lett. **80**(7), 1240 (2002)
7. O.M.J. van 't Erve, G. Kioseoglou, A.T. Hanbicki, C.H. Li, B.T. Jonker, R. Mallory, M. Yasar, A. Petrou, Appl. Phys. Lett. **84**(21), 4334 (2004)
8. X. Jiang, R. Wang, R. Shelby, R. Macfarlane, S. Bank, J. Harris, S. Parkin, Phys. Rev. Lett. **94**(5), 1 (2005)
9. H. Zhao, D. Talbayev, G. Lüpke, A. Hanbicki, C. Li, M. van't Erve, G. Kioseoglou, B. Jonker, Phys. Rev. Lett. **95**(13), 1 (2005)
10. C. Adelmann, J.L. Hilton, B.D. Schultz, S. McKernan, C.J. Palmstrom, X. Lou, H.S. Chiang, Pa Crowell, Appl. Phys. Lett. **89**(11), 112511 (2006)
11. N.C. Gerhardt, S. Hövel, C. Brenner, M.R. Hofmann, F.Y. Lo, D. Reuter, A.D. Wieck, E. Schuster, W. Keune, K. Westerholt, Appl. Phys. Lett. **87**(3), 032502 (2005)
12. A. Sinsarp, T. Manago, F. Takano, H. Akinaga, Japanese J. Appl. Phys. **46**(1), L4 (2007)
13. S. Hövel, N.C. Gerhardt, M.R. Hofmann, F.Y. Lo, A. Ludwig, D. Reuter, A.D.Wieck, E. Schuster, H. Wende, W. Keune, O. Petracic, K. Westerholt, Appl. Phys. Lett. **93**(2), 021117(2008)
14. S. Hövel, N.C. Gerhardt, M.R. Hofmann, F.Y. Lo, D. Reuter, A.D. Wieck, E. Schuster, W. Keune, H. Wende, O. Petracic, K. Westerholt, Appl. Phys. Lett. **92**(24), 242102 (2008)
15. E. Schuster, W. Keune, F.Y. Lo, D. Reuter, A.D. Wieck, K. Westerholt, Superlattices Microstruct. **37**(5), 313 (2005)
16. A. Ludwig, R. Roescu, A.K. Rai, K. Trunov, F. Stromberg, M. Li, H. Soldat, A. Ebbing, N.C. Gerhardt, M.R. Hofmann, H. Wende, W. Keune, D. Reuter, A.D. Wieck, J. Cryst. Growth **323**, 376 (2011)
17. C. Son, J. Cho, J.W. Park, J. Vac. Sci. Technol. A **17**, 2619 (1999)
18. E.U. Schuster, Dissertation, Universität Duisburg-Essen (2007)

19. K. Cherifi, C. Dufour, M. Piecuch, A. Bruson, P. Bauer, G. Marchal, P. Mangin, J. Magn. Magn. Mater. **93**, 609 (1991)
20. K. Mibu, N. Hosoito, T. Shinjo, Hyperfine Interact. **68**, 341 (1991)
21. B. Scholz, R.A. Brand, W. Keune, Phys. Rev. B **50**, 2537 (1994)
22. J. Tappert, S. Neumann, R.A. Brand, W. Keune, F. Klose, H. Maletta, Europhys. Lett. **46**, 238 (1999)
23. H. Höpfner, M. Li, A. Ludwig, A. Ludwig, F. Stromberg, H. Wende, W. Keune, D. Reuter, A.D. Wieck, N.C. Gerhardt, M.R. Hofmann, in *Proceedings of SPIE* (2012) pp. 8260–09
24. K. Rochford, in *Encyclopedia of Physical Science and Technology*, ed. by R.A. Meyers (Elsevier Science Publishers B.V., 2004)
25. N.C. Gerhardt, S. Hövel, C. Brenner, M.R. Hofmann, F.Y. Lo, D. Reuter, A.D. Wieck, E. Schuster, W. Keune, S. Halm, G. Bacher, K. Westerholt, J. Appl. Phys. **99**(7), 073907 (2006)
26. Z. Yu, M. Flatté, Phys. Rev. B **66**(23), 1 (2002)
27. H. Soldat, M. Li, N.C. Gerhardt, M.R. Hofmann, A. Ludwig, A. Ebbing, D. Reuter, A.D. Wieck, F. Stromberg, W. Keune, H. Wende, Appl. Phys. Lett. **99**(5), 051102 (2011)
28. S. Saikin, M. Shen, M.C. Cheng, J. Phys. Condens. Matter **18**(5), 1535 (2006)
29. V.A. Marushchak, M.N. Stepanova, A.N. Titkov, J. Exp. Theore. Phys. Lett. **37**(7), 400 (1983)
30. T. Nakaoka, T. Saito, Y. Tatebayashi, Y. Arakawa, Phys. Rev. B **70**, 235337 (2004)
31. M. Ghali, T. Kümmel, J. Wenisch, K. Brunner, G. Bacher, Appl. Phys. Lett. **93**, 073107 (2008)
32. M. Ghali, R. Arians, T. Kümmel, G. Bacher, J. Wenisch, S. Mahapatra, K. Brunner, Appl. Phys. Lett. **90**, 093110 (2007)
33. G. Schmidt, C. Gould, P. Grabs, A. Lunde, G. Richter, A. Slobodskyy, L. Molenkamp, Phys. Rev. Lett. **92**, 226602 (2004)
34. R.M. Stroud, A.T. Hanbicki, Y.D. Park, G. Kioseoglou, A.G. Petukhov, B.T. Jonker, G. Itskos, A. Petrou, Phys. Rev. Lett. **89**, 166602 (2002)
35. R. Jiang, R. Wang, R. Shelby, R. MacFarlane, S. Bank, J. Harris, S. Parkin, Phys. Rev. Lett. **94**, 056601 (2005)
36. M. Hetterich, W. Löffler, J. Fallert, N. Höpcke, H. Burger, T. Passow, S. Li, B. Daniel, B. Ramadout, J. Lupaca-Schomber, J. Hetterich, D. Litvinov, D. Gerthsen, C. Klingshirn, K. H., Phys. Stat. Sol. (b) **243**, 3812 (2006)
37. J. Nannen, T. Kümmell, M. Bartsch, K. Brunner, G. Bacher, Appl. Phys. Lett. **97**, 173108 (2010)
38. P. Asshoff, W. Öffler, J. Zimmer, H. Füser, H. Flügge, H. Kalt, M. Hetterich. Appl. Phys. Lett. **95**, 202105 (2009)
39. R.J. Warburton, C. Schäflein, D. Haft, F. Bickel, A. Lorke, K. Karrai, J.M. Garcia, W. Schoenfeld, P.M. Petroff, Nature **405**, 926 (2000)
40. M. Baier, F. Findeis, A. Zrenner, M. Bichler, G. Abstreiter, Phys. Rev. B **64**, 195326 (2001)
41. F. Findeis, M. Baier, A. Zrenner, M. Bichler, G. Abstreiter, U. Hohenester, E. Molinari, Phys. Rev. B **64**, 121309(R) (2001)
42. S. Seidl, M. Kroner, P.A. Dalgarno, A. Högele, J.M. Smith, M. Ediger, B.D. Gerardot, J.M. Garcia, P.M. Petroff, K. Karrai, R.J. Warburton, Phys. Rev. B **72**, 195339 (2005)
43. M. Bayer, G. Ortner, O. Stern, A. Kuther, A.A. Gorbunov, A. Forchel, P. Hawrylak, S. Fafard, K. Hinzer, T.L. Reinecke, S.N. Walck, J.P. Reithmaier, F. Klopf, S. F. Phys. Rev. B **65**, 195315 (2002)
44. J.M. Smith, P.A. Dalgarno, R.J. Warburton, A.O. Govorov, K. Karrai, B.D. Gerardot, P.M. Petroff, Phys. Rev. Lett. **94**, 197402 (2005)
45. D. Heiss, V. Jovanov, M. Bichler, G. Abstreiter, J.J. Finley, Phys. Rev. B **77**, 235442 (2008)
46. J. König, H. Schoeller, G. Schön, Phys. Rev. Lett. **76**(10), 1715 (1996)
47. J. König, J. Schmid, H. Schoeller, G. Schön, Phys. Rev. B **54**(23), 16820 (1996)
48. M. Braun, J. König, J. Martinek, Phys. Rev. B **70**(19), 195345 (2004)
49. M. Braun, J. König, J. Martinek, Europhys. Lett. **72**(2), 294 (2005)
50. I. Weymann, J. Barnas, J. König, J. Martinek, G. Schön, Phys. Rev. B **72**(11), 113301 (2005)
51. I. Weymann, J. König, J. Martinek, J. Barnas, G. Schön, Phys. Rev. B **72**(11), 115334 (2005)
52. M. Braun, J. König, J. Martinek, Phys. Rev. B **74**(7), 075328 (2006)

53. R. Hornberger, S. Joller, G. Begemann, A. Donarini, M. Grifoni, Phys. Rev. B **77**(24), 245313 (2008)
54. S. Lindebaum, D. Urban, J. König, Phys. Rev. B **79**(24), 245303 (2009)
55. B. Sothmann, D. Futterer, M. Governale, J. König, Phys. Rev. B **82**(9), 094514 (2010)
56. B. Sothmann, J. König, Phys. Rev. B **82**(24), 245319 (2010)
57. B. Sothmann, J. König, A. Kadigrobov, Phys. Rev. B **82**(20), 205314 (2010)
58. B. Sothmann, J. König, New J. Phys. **12**(8), 083028 (2010)
59. J. Koch, F. von Oppen, A.V. Andreev, Phys. Rev. B **74**(20), 205438 (2006)
60. M. Esposito, K. Lindenberg, C. van den Broeck, Phys. Rev. Lett. **102**(13), 130602 (2009)
61. R. Sánchez, M. Büttiker, Phys. Rev. B **83**(8), 085428 (2011)
62. B. Sothmann, M. Büttiker, Europhys. Lett. **99**(2), 27001 (2012)
63. A.J. Heinrich, J.A. Gupta, C.P. Lutz, D.M. Eigler, Science **306**(5695), 466 (2004)
64. C.F. Hirjibehedin, C.P. Lutz, A.J. Heinrich, Science **312**(5776), 1021 (2006)
65. F. Meier, L. Zhou, J. Wiebe, R. Wiesendanger, Science **320**(5872), 82 (2008)
66. C.F. Hirjibehedin, C. Lin, A.F. Otte, M. Ternes, C.P. Lutz, B.A. Jones, A.J. Heinrich, Science **317**(5842), 1199 (2007)
67. A.F. Otte, M. Ternes, K. von Bergmann, S. Loth, H. Brune, C.P. Lutz, C.F. Hirjibehedin, A.J. Heinrich, Nat. Phys. **4**(11), 847 (2008)
68. A.F. Otte, M. Ternes, S. Loth, C.P. Lutz, C.F. Hirjibehedin, A.J. Heinrich, Phys. Rev. Lett. **103**(10), 107203 (2009)
69. S. Loth, K. von Bergmann, M. Ternes, A.F. Otte, C.P. Lutz, A.J. Heinrich, Nat. Phys. **6**(5), 340 (2010)
70. J. Fernández-Rossier, Phys. Rev. Lett. **102**(25), 256802 (2009)
71. J. Fransson, Nano Lett. **9**(6), 2414 (2009)
72. M. Persson, Phys. Rev. Lett. **103**(5), 050801 (2009)
73. N. Lorente, J. Gauyacq, Phys. Rev. Lett. **103**(17), 176601 (2009)
74. F. Delgado, J.J. Palacios, J. Fernández-Rossier, Phys. Rev. Lett. **104**(2), 026601 (2010)
75. J. Lehmann, D. Loss, Phys. Rev. B **73**(4), 045328 (2006)